Nuclear Science
NEA/NSC/R(2016)5
May 2017
www.oecd-nea.org

State-of-the-art Report on Structural Materials Modelling

OECD
BETTER POLICIES FOR BETTER LIVES

NEA
NUCLEAR ENERGY AGENCY

State-of-the-art Report on Structural Materials Modelling

ORGANISATION FOR ECONOMIC CO-OPERATION AND DEVELOPMENT

The OECD is a unique forum where the governments of 35 democracies work together to address the economic, social and environmental challenges of globalisation. The OECD is also at the forefront of efforts to understand and to help governments respond to new developments and concerns, such as corporate governance, the information economy and the challenges of an ageing population. The Organisation provides a setting where governments can compare policy experiences, seek answers to common problems, identify good practice and work to co-ordinate domestic and international policies.

The OECD member countries are: Australia, Austria, Belgium, Canada, Chile, the Czech Republic, Denmark, Estonia, Finland, France, Germany, Greece, Hungary, Iceland, Ireland, Israel, Italy, Japan, Korea, Latvia, Luxembourg, Mexico, the Netherlands, New Zealand, Norway, Poland, Portugal, the Slovak Republic, Slovenia, Spain, Sweden, Switzerland, Turkey, the United Kingdom and the United States. The European Commission takes part in the work of the OECD.

OECD Publishing disseminates widely the results of the Organisation's statistics gathering and research on economic, social and environmental issues, as well as the conventions, guidelines and standards agreed by its members.

NUCLEAR ENERGY AGENCY

The OECD Nuclear Energy Agency (NEA) was established on 1 February 1958. Current NEA membership consists of 31 countries: Australia, Austria, Belgium, Canada, the Czech Republic, Denmark, Finland, France, Germany, Greece, Hungary, Iceland, Ireland, Italy, Japan, Korea, Luxembourg, Mexico, the Netherlands, Norway, Poland, Portugal, Russia, the Slovak Republic, Slovenia, Spain, Sweden, Switzerland, Turkey, the United Kingdom and the United States. The European Commission also takes part in the work of the Agency.

The mission of the NEA is:

- to assist its member countries in maintaining and further developing, through international co-operation, the scientific, technological and legal bases required for a safe, environmentally friendly and economical use of nuclear energy for peaceful purposes;
- to provide authoritative assessments and to forge common understandings on key issues, as input to government decisions on nuclear energy policy and to broader OECD policy analyses in areas such as energy and sustainable development.

Specific areas of competence of the NEA include the safety and regulation of nuclear activities, radioactive waste management, radiological protection, nuclear science, economic and technical analyses of the nuclear fuel cycle, nuclear law and liability, and public information. The NEA Data Bank provides nuclear data and computer program services for participating countries.

Foreword

The Working Party on Multi-scale Modelling of Fuels and Structural Materials for Nuclear Systems (WPMM) has been established, under the auspices of the NEA Nuclear Science Committee (NSC), to review multi-scale models and simulations as validated predictive tools for fuels and structural materials needed in the design of nuclear systems, for fuel fabrication and for understanding performance. The WPMM's objective is to promote the exchange of information on theoretical and computational methods, experimental validation, and other topics related to modelling and simulation of nuclear materials.

The Expert Group on Structural Materials Modelling was established in 2009 to provide targeted critical reference reviews of the state-of-the-art concerning the use of multi-scale modelling to describe the changes induced by irradiation in structural nuclear materials. This expert group aims at reliably reproducing experimental data, while providing keys to understand and interpret existing experimental results, with a view to predicting the behaviour of structural nuclear materials under unexplored conditions and to support the choice and the development of new materials.

The topic of the present volume is the development of physical multi-scale models, with their root in computational physics, to describe the changes produced in steels by neutron irradiation. This is performed to underpin structural integrity and lifetime assessments of nuclear power plant components, namely current nuclear reactor vessel and core structural materials internals.

Acknowledgements

The NEA wishes to express its sincere gratitude to Professor Roger Smith (United Kingdom) and Dr Lorenzo Malerba (Belgium), who co-ordinated this report, to the members of the Expert Group on Structural Materials Modelling and to the authors for their contribution to this report.

Special thanks are also due to Dr Par Olsson (Sweden), Chair of the Expert Group on Structural Materials Modelling, and to Professor Dr Theodore M. Besmann (United States) and Dr Marius Stan (United States), current and former Chairs of the Working Party on Multi-scale Modelling of Fuels and Structural Materials for Nuclear Systems.

NEA editorial and publishing support was provided by Dr Simone Massara and Ms Reka Tarsi.

List of authors

R. Smith (Loughborough University, United Kingdom) Editor

L. Malerba (Centre d'Étude de l'Énergie Nucléaire - SCK•CEN, Belgium) Editor

D.J.Bacon (University of Liverpool, United Kingdom)

C. Becquart (École Nationale Supérieure de Chimie de Lille - ENSCL, France)

V.A. Borodin (Kurchatov Institute, Russia)

M.J. Caturla (Universidad de Alicante, Spain)

T. Couvant (Électricité de France - EDF, France)

A. Herbelin (Électricité de France - EDF, France)

Y. Kaji (Japan Atomic Energy Agency - JAEA, Japan)

M. Nastar (Commissariat à l'énergie atomique et aux énergies alternatives - CEA, France)

K. Nordlund (University of Helsinki, Finland)

S.R. Ortner (National Nuclear Laboratory - NNL, United Kingdom)

Y.N. Osetsky (Oak Ridge National Laboratory - ORNL, United States)

C. Pokor (Électricité de France - EDF, France)

N. Sakaguchi (Hokkaido University, Japan)

F. Soisson (Commissariat à l'énergie atomique et aux énergies alternatives - CEA, France)

R.E. Stoller (Oak Ridge National Laboratory - ORNL, United States)

M. Yamaguchi (Japan Atomic Energy Agency - JAEA, Japan)

List of abbreviations and acronyms

AISI/SAE	American Iron and Steel Institute/Society of Automotive Engineers
AKMC	Atomistic Kinetic Monte Carlo
ASTM	American Section of the International Association for Testing Materials
BBC	Body-centred cubic
BKL	Bortz, Kalos and Lebowitz
BWR	Boiling Water Reactor
CANDU	CANadian Deuterium Uranium
DBT	Ductile-to-brittle transition
DBTT	Ductile-to-brittle transition temperature
DD	Dislocation Dynamics
DFT	Density Functional Theory
EAM	Embedded-Atom-Method
ECP	Electrochemical (or corrosion) Potential
EKMC	Event Kinetic Monte Carlo
EGSMM	NEA Expert Group on Structural Materials Modelling
FCC	Face-centred cubic
FEM	Finite Element Method
FP	Frenkel pairs
GB	Grain boundaries
IASCC	Irradiation assisted stress corrosion cracking
IGSCC	Intergranular stress-corrosion cracking

KMC	Kinetic Monte Carlo
LWR	Light Water Reactor
MD	Molecular Dynamics
MD	Matrix damage
MTR	Materials Test Reactor
NDE	Non-destructive examination
NRT	Norgett, Robinson, and Torrens
ODS	Oxide dispersion strengthened
OKMC	Object Kinetic Monte Carlo
PAS	Positron Annihilation Spectroscopy
PKA	Primary knock-on atom
PWR	Pressurised Water Reactor
RCS	Replacement collision sequences
RIH	Radiation-induced hardening
RIS	Radiation-induced segregation
RPV	Reactor Pressure Vessel
SANS	Small Angle Neutron Scattering
SCC	Stress corrosion cracking
SFE	Stacking fault energy
SIA	Self-interstitial atom
SIPA	Stress-induced preferential absorption
SIPN	Stress-induced preferential nucleation
SRIM	Stopping and Range of Ions in Matter
SRO	Short range order
TEM	Transmission electron microscopy

TIP	Thermodynamics of irreversible processes
UTS	Ultimate Tensile Strength
WPMM	NEA Working Party on Multi-scale Modelling of Fuels and Structural Materials for Nuclear Systems
WS	Wigner-Seitz
WWER	Water-Water Energy Reactor

Table of contents

Executive summary

This report was produced by the Nuclear Energy Agency (NEA) Expert Group on Structural Materials Modelling. The mandate of this group, which was established in 2009, is to provide a critical review of the state-of-the-art concerning the use of the multi-scale modelling approach to describe the changes induced by irradiation in structural nuclear materials.

The volume will therefore concentrate mainly on steels and associated materials, i.e. polycrystalline metals. Other materials that are widely used for nuclear applications such as graphite or glasses to contain nuclear waste will not be considered in this review.

Since no single modelling technique can capture all the different aspects of what happens when structure materials are subjected to intense doses of radiation, the chapters in this state-of-the-art report form together a multi-scale approach to the understanding of this problem as shown in Figure 1.

Figure 1. A schematic illustration of the common models used in radiation damage studies and how they link time and length scales

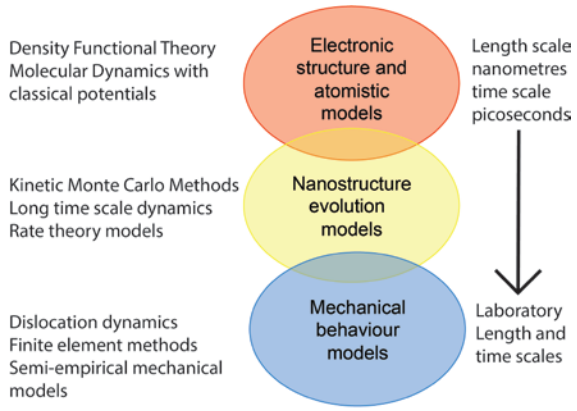

Thus the nanometre and sub-nanometre time scale Density Functional Theory (DFT) for electronic structure calculations, which is a quantum-mechanical method, can be used to determine such quantities as defect formation energies and defect migration barriers. Performing dynamics with these models is possible but limited to a few hundred atoms and picosecond time scales due to computational constraints. Nonetheless they have been used successfully to determine displacement energy thresholds (Ed) in some ceramic materials, albeit with a relatively small statistical sample. Thus as computing power continues to increase, one might expect that these methods will be used more often in the future for determination of Ed. The thresholds are important to help quantify radiation resistance and are essential inputs to Monte Carlo codes such as SRIM for predicting

depth profiles and radiation damage in materials over a larger length scale. This is one example of how fine scale models can be used to parameterise a coarser approach.

Data from DFT can be also used in the development of classical interatomic potentials that are used in Molecular Dynamics (MD) studies or in Kinetic Monte Carlo (KMC) models. A good example of the use of DFT to help refine interatomic potentials is the interstitial dumbbell defect in BCC Fe. Most early potentials showed that the ⟨111⟩ dumbbell was the preferred structure, in disagreement with the DFT results which showed ⟨110⟩ was favoured. This then led to more accurate interatomic potential development where the energetics of other defect structures determined from DFT, could be more accurately described. However the application of DFT to defect formation energies and diffusion barriers is not treated explicitly in this report. DFT codes such as SIESTA and VASP are under continual development and together with increased computing power are becoming standard tools for the investigation of structural material defect properties. It is expected that these models will be used much more in the future to study extended defects such as grain boundaries and dislocation loops as computing power continues to increase.

Currently classical MD as a technique is limited to systems of nanometre scale for time scales of the order on nanoseconds-microseconds. It is therefore very good for investigating collision cascades induced by a fast neutron or an alpha particle colliding with an atom in the structural material, particularly with the advent of the Finnis-Sinclair and embedded atom method potentials for metals that were introduced in the 1980's. These gave a much better description of the physical properties of structural materials.

The first MD simulations of a collision cascade were performed by Vineyard's group at Brookhaven in the 1960s where very small systems containing only 10's of atoms were studied. Even today MD cascade simulations are generally carried out over nanometre length scales and their ballistic phase is generally over in the space of several picoseconds. The main reason for this time limitation is the scaling involved in the integration of Newton's equations. Typically distances are given in Ångstroms, energies in eV, forces in eV/Å so that the integration time step for reasonable numerical accuracy is of the order of 1 femtosecond or less. Higher energy MD cascade simulations in metals were later (1970s) pioneered by Don Harrison's group in Monterey, mainly to investigate sputtering phenomena before being taken up by workers in the nuclear field.

To simulate 1 second of real time would require 10^{15} time steps where the forces on all the atoms in the system must be determined. This is clearly infeasible. Thus the models based on classical potentials can be used to parameterise dislocation dynamics or KMC models when it is too expensive to use DFT. They can also be used to determine diffusion coefficients for rate theory models. Luckily for structural materials, defect recombination and other such events happen relatively infrequently on the atomic time scale so that event driven KMC methods can be used. Such methods fall into two classes. The first class consists of those methods where all the transitions are pre-prescribed and given in an event table. The LAKIMOCA code is an example of this. The other method is where the transition barriers are calculated on-the-fly. This methodology is very computationally expensive and so far limited to small systems. It is not discussed in detail here but as a technique it is likely to grow in popularity as computing power continues to increase.

Other long time scale methods such as temperature accelerated dynamics have also been used to investigate the long time scale evolution of displacements cascades in nuclear materials.

Because of the time scale limitations, dose effects are very difficult to analyse using MD but a combination of MD together with one of the long time scale techniques offers the best prospect for future quantitative atomistic models of the microstructure development under radiation dose effects. So far this subject is only in its infancy and is therefore not discussed in detail in the report.

In concentrating on the latest methodologies it is sometimes easy to forget some of the early work in radiation damage modelling. The seminal work by Seitz and Brinkman contained sketches of the structure of what a typical collision cascade might look like, even postulating the displacement spike region and coining the phrase primary knock-on atom (PKA) for the first energetically displaced particle. Such cascade structures were subsequently verified by MD simulations, over a quarter of a century later. Even today a modified Kinchin-Pease formula first developed in the 1950s is used to determine the approximate number of defects produced in a collision cascade.

Similarly the widely-used SRIM programme which has been very successful in the investigation of range profiles and damage cause by ion bombardment of surfaces has its origins in the work of the Danish school in the 1940s and 1950s where the concept of the screened Coulomb interaction potential was implemented to investigate analytically the penetration of energetic atomic particles in matter. Programmes such as SRIM, in conjunction with simple analytic formulae such as that by Kinchin and Pease, then allow the determination of the number of permanently displaced particles in a collision cascade to be calculated leading to the concept of dpa (displacements per atom) as a quantitative measure of the cumulative effects of irradiation.

The SRIM programme works well for amorphous or polycrystalline materials but for crystalline materials channelling can take place. It could be argued that this was first discovered by computer when Mark Robinson at Oak Ridge left his binary collision code running overnight, only to discover the next day that the atom he had set in motion had hardly undergone any collisions and was merrily progressing down a channel in the crystal. The MARLOWE programme that developed from this became a leading binary collision code for the investigation of atomic collisions in crystalline structures.

There will inevitably be some gaps in this report. For example the formation of inert gas bubbles, especially in structural materials, is not treated in detail in the report although Chapter 11 touches on this. Such helium is a by-product of nuclear reactions, which can also adversely affect long-term structural stability. This is also a problem in fusion where under certain circumstances it can form a porous material (fuzz) in tungsten. There is a huge experimental literature on He bubble formation in metals which modelling could help explain. Beside accumulation at grain boundaries, bubbles can also form within grains and it seems they reach a preferred size depending on temperature and the composition of the secondary elements in the steel. At small concentrations the He is highly mobile and wants to form clusters. As the clusters grow in size the strain induced in the lattice combined with an increase in energy barriers for the He to diffuse into the clusters, prevents further clustering. However, further modelling is required to clarify this effect.

Dislocation dynamics is also not treated in detail in the report, although Chapters 4 and 5 touch on this. However the theory of dislocation dynamics provides a good link in the modelling between continuum elasticity theory and atomistic modelling. It might be expected that in the future atom probe and electron microscopy combined with dislocation dynamics modelling would throw more light on the role of dislocations in reactor structural materials.

The report is laid out as follows. In Chapter 1 an introduction to structural materials for the different reactor types is given; why the particular materials are used, together with an introduction to the various issues that they face over the lifetime of the plant operation, including hardening, embrittlement, creep and swelling.

In Chapter 2 the production of defects in an irradiation event is modelled in detail, through the use of classical MD with empirical potentials developed to describe the various material combinations, mainly applied to BCC and FCC structures. This allows the modelling of individual collision cascades and the defects that arise from them in the ballistic phase of a collision cascade where nuclear stopping dominates. Detailed models of electronic stopping are generally not considered in this chapter or in the overall report although there has been some recent progress in this direction, where MD models for the two-way transfer of energy between the electronic and ionic systems have been developed. So far such models require the use of some parameters, which are difficult to determine but linking them to *ab initio* models of electronic stopping should provide a useful avenue for future research.

Chapter 3 considers the long-time evolution of defects using KMC where the starting point is the initial distribution of defects in the system. In this case the atomic system evolves on an event driven basis rather than being integrated in time. The probability for an event to occur can be determined either from *ab initio* methods, empirical potentials or experiment. By combining the KMC with a source of defects, after sufficient time evolution, simulating a radiation event, dose and dose rate effects can be modelled at the atomistic level. In many cases good agreement between more coarse grained models such as those based on rate theory can be achieved. It is likely that such methods will become more popular in the future as more sophisticated models for determining the transition events on-the-fly become computationally feasible.

Chapters 4 and 5 describe techniques that can be used to model the segregation of defects. It is split into two parts. In the first part a discussion of the various models and mechanisms is given including rate theory, mean field and atomistic models. In the second part the use of rate theory to describe radiation-induced segregation to grain boundaries in reactor steels is described in detail. The parameters used in the model are explicitly given and it is shown that such segregation is critically dependent on the minor alloying elements.

Chapters 6 and 7 are a comprehensive review of irradiation creep and swelling including many ideas from the early literature on this topic. It contains many semi-empirical formulae that can be used to investigate creep and swelling. Unlike some of the other chapters it uses mainly theoretical ideas rather than computer simulation. In particular, data from experiments are used to determine parametric dependencies of irradiation swelling and creep, which are then correlated to the underlying microstructural evolution.

Chapter 8 investigates larger scale defects, such as cavities, dislocation loops, stacking fault tetrahedra and precipitates. It is shown how atomic scale modelling can be used in conjunction with dislocation dynamics models to understand how dislocations can interact with the larger scale defects. The chapter concentrates mostly on using empirical potentials for both static and dynamic simulation of interactions between moving dislocations and obstacles to their motion but a short review of the use of the coarser scale dislocation dynamics modelling is given and how the atomistic models could be used in their parameterisation.

Chapters 9 and 10 discuss irradiation-induced embrittlement from a continuum viewpoint rather than detailed computer simulation. A number of fracture models and simple formulae used to describe reactor pressure vessel embrittlement are given, together with their advantages and limitations. This is a topic that seems ripe for further development, especially through linking to atomistic models to examine on a finer scale the processes of crack propagation and fracture.

Finally, in Chapter 11 one of the least understood structural problems, that of irradiation assisted stress corrosion cracking (IASCC), is discussed. In this sense the topic is even more complicated than that discussed in Chapters 9 and 10 since it includes the extra effect of corrosion. Thus the subject has so many different aspects that are difficult to capture in simple models. In this chapter the different mechanisms leading to IASCC are described and some simple formulae for the growth of cracks are given and compared to experimental data on crack growth rates. However since no complete description of all the mechanisms involved have yet been found, this subject will provide a fertile research area for many years to come.

The chapters in this report provide an overview of the current state-of-the-art in structural materials modelling in the context of nuclear reactors. They demonstrate the link between many of the different methodologies such as how numerical quantum mechanics can be used to parameterise interatomic potentials which in themselves can be used together with dislocation dynamics to access greater length scales. What is so far missing in the structural materials modelling area is a direct link between atomistic modelling with potentials and continuum models where an atomistic region is embedded in a continuum. There have been many attempts in this direction over the years with some success, for example, in the subject of indentation testing but so far they have not been widely applied in the area of creep and swelling. Linking length scales through such models should also be a fertile area of future research.

The problem of linking time scales is rather more challenging. Linking nanometre sized length scales to reactor components of the size of centimetres requires a bridge of only seven orders of magnitude. However to link diffusion processes that can occur over years with molecular dynamics which is limited to microseconds at the most is rather more challenging. The last few years have seen many workshops focussed on such long time scale techniques where diffusive processes can be thought of as rare events compared to the frequency of phonon vibrations in a material. This subject itself has seen much progress driven by applications in other scientific areas such as the study of protein folding or chemical reactions. The nuclear community should be aware of such developments and the ever-increasing interdisciplinary nature of science and engineering provides both challenges and opportunities for future nuclear engineers.

Chapter 1.

Introduction on steels used as structural materials in current nuclear power plants and related modelling issues

L. Malerba
Institute of Nuclear Materials Science, SCK•CEN, Belgium

1. Introduction

Like all complex installations, nuclear power plants are built using a variety of materials. One can distinguish between two broad categories: structural and functional materials [1].

- **Structural materials** are those that bear load or stress, whichever the origin (mechanical, thermal, vibrations, etc.). The key properties of materials in relation to bearing load without undergoing unacceptable shape or dimension changes are the mechanical properties: elastic modulus, yield strength, ultimate tensile strength, hardness, ductility, fracture toughness, fatigue, and creep resistance (for a simple introduction to these properties [2].
- **Functional materials** display physical or chemical properties of use for a specific purpose, e.g. optical, electrical, thermal, and often simply of protection against external agents or separation between different environments that should not come into contact; alternatively, they are meant to facilitate the performance of a given operation (the list of properties of possible relevance is too wide to be summarised here).

Failure occurs when, due to unforeseen interference from external factors, or due to ageing, the material ceases to fulfil its structural or functional duty.

In many cases the above distinction becomes blurred: some functional materials end up having necessarily also a structural function, while structural materials have often also functions other than just bearing load or stress. Taking examples of relevance for a nuclear power plant (which should become clearer after reading the following sections of this chapter), a reactor pressure vessel steel is a structural material with safety functions: one small hole in it, though perhaps not affecting its ability to bear the stresses caused by high internal pressure, is not acceptable because it causes leakage, thereby compromising its important safety function of protection against the release of radioactive substances. Fuel cladding, which has mainly the function of keeping the fuel pellets together, allowing

refuelling and preventing contact with the outside coolant, has also some structural functions owing to the development of internal pressure with time, that imposes minimal, but not to be overlooked, requirements on ductility. Even fuel, which is neither structural nor functional (although one could argue that it fulfils the *function* of burning to produce energy) has some inherent functional properties and some structural requirements, related to the possibility of refuelling or to its integrity (e.g. bear thermal stresses).

This introductory chapter, and the whole volume, shall focus on structural materials, therefore restricting the scope to mechanical properties as well as dimensional and shape stability of materials.

The selection and optimisation of a structural material and the design of the component built with it are dictated by their "fitness for purpose" [3], which include suitability for the environment and the application, including the requirement of minimising the probability of failure, mainly by loss of integrity, as well as change of shape which might eventually also lead to loss of integrity. The criteria used for material choice and component design are mainly based on considerations of inherent capability of the material to fulfil its duty, when shaped as in the component, based on its properties, taking into account the possibility of interference from external factors. Some interferences are obvious, others less. Good criteria should be robust also against the least obvious external factors and for this purpose safety margins are duly applied to design the component. However, materials are not quintessentially incorruptible: they undergo with time internal changes due to use that almost invariably degrade their properties. Material ageing is, especially in nuclear power plants, the most significant threat to the integrity of components.

One of the main duties of materials engineers is to be able to foresee timely when, due to ageing, the material is no longer capable of fulfilling its duty, under any kind of external interference. This implies knowing what happens to the material and how its properties change while in operation. This knowledge is generally obtained by testing the material or the component under relevant conditions, and then by monitoring it during operation. Knowledge is then crystallised in models, that can be more or less detailed, specific or general, empirical or theoretical, or a mixture of both. Tests and monitoring are necessary to verify up to what extent models are followed in each specific case. In turn, models are needed to interpolate or extrapolate to conditions under which tests cannot be performed. Since materials in operation cannot be in general continuously tested, models are necessary to plan the maintenance and the inspection of the component and to foresee its lifetime.

Several significant ageing issues have affected nuclear power plants around the world along their history of operation (e.g. [4]). Most of them were not anticipated at the design stage and, by potentially threatening materials' integrity, have led for caution to costly interventions and replacements (though practically never to early shutdown). Many did not concern the nuclear components but the conventional ones. Fatigue, stress corrosion and delayed cracking due to either hydrogen or high temperature (high for the type of steel used) are the main issues. These are difficult issues to tackle in their own right but are not specific of the nuclear environment (although they may be affected by this environment, e.g. fatigue in pipes), so (with one partial exception, stress-corrosion cracking) they will not be addressed in the present volume.

By far the most threatening factor determining degradation in nuclear materials is that, in the reactor core, they are subjected to an intense field of irradiation, mainly energetic neutrons and gamma rays coming from the self-sustaining fission reactions of uranium nuclei that carry an exceptionally high energy density. The amount of neutrons received by a material is termed *fluence*, measured in neutrons per unit area, or *dose*, measured in displacements per atom, dpa. Dpa is a quantity that cannot be measured experimentally and is dependent on the particular model chosen to calculate it, given the neutron spectrum and the flux, i.e. how many neutrons of a given energy enter the material per unit time and area. It has the main advantage of allowing comparison between different types of irradiation. For neutron irradiation, the standards for calculation are given e.g. in [5]. For ion irradiation a standard is to use the SRIM (srim.org) or the PHITS (phits.jaea.go.jp) Monte Carlo simulation codes. For the scientific basis of these codes, see e.g. [6,7].

The present volume focusses on how radiation effects affect the mechanical properties of current nuclear reactor vessel and core structural materials, excluding cladding. As will be seen, these are essentially two types of steels: low alloy bainitic steels and austenitic stainless steels[1].

There are five key materials degradation effects due to irradiation [8]: (1) radiation-modified (induced or enhanced) solute segregation/precipitation, leading to local changes of composition with subsequent possible appearance of new, stable or metastable phases; (2) radiation hardening and embrittlement; (3) dimensional changes via void swelling and/or irradiation creep; (4) irradiation assisted stress corrosion cracking (IASCC); (5) helium embrittlement. The first effect reveals itself at the nano- or microscopic level and involves both nano/microstructural and microchemical changes, many of which are in fact at the origin of the other key issues. The second effect, radiation hardening and embrittlement, is mainly visible at "low" temperature, but in fact the concerned low temperature range corresponds in most cases, for steels, exactly to the operating temperature of current reactors: radiation embrittlement as a consequence of hardening, in the case of the reactor pressure vessel, is the most important factor that limits the lifetime of existing nuclear power plants [9,10]. The third effect, dimensional changes, is generally associated with a higher temperature than in current power reactors[2], but it is now suspected to be potentially threatening also for existing plants, in those components that accumulate significant dose [11,12]. The fourth effect, IASCC, which involves presence of stresses and interaction with the aqueous coolant environment, is the most critical one for core components of existing nuclear power plants made of austenitic steels [10,13]. Finally the fifth effect, He embrittlement, is associated mainly with fusion neutron spectra and high dose and temperature; in reactor core components of current plants He production by transmutation can be high (up to 15 appm/dpa – generally ~3-8 appm/dpa - in PWR, comparable with up to 14 appm/dpa – generally ~3-10 appm/dpa - in fusion [14]), but He embrittlement by promotion of intergranular fracture is generally

[1] In some reactor types Zr alloys are used not only as cladding, but also as structural materials (pressure tubes). However, Zr is not included in the present volume. In the 1960s, some reactors used austenitic steels as cladding.
[2] These are effects observed in fast reactors, of which at the moment only a few exist in the world, that operate at higher temperature and neutron flux and reach much higher fluence than ordinary power reactors (see Section 2).

not observed in the range of operation temperatures, although He production may have an effect to promote swelling.

In the present volume, all the above effects are addressed from a modelling standpoint: nanostructural and microchemical evolution are addressed in Chapters 2-5; swelling and irradiation creep are the subject of Chapters 6 and 7; hardening and embrittlement are treated in Chapters 8, 9 and 10; finally IASCC is the focus of Chapter 11. Helium effects, however, are addressed only as example of nanostructural modifications, mainly related with swelling, without considering its potential consequences on mechanical properties.

2. Brief description of main current nuclear reactor types

In a nuclear plant, very much as in a conventional power plant, the reactor core is a source of heat for the production of steam and subsequent production of electricity via a steam turbine and a generator, with subsequent condensation of the steam to continue the cycle. The difference is that the burning of fossil fuels, which is a *chemical* reaction, is replaced by the *nuclear* reactions that occur in the uranium contained in the reactor core, which are two orders of magnitude more efficient in terms of energy density than combustion reactions. The nuclear fuel is cooled by the circulation of a fluid through a (generally pressurised) circuit. In essentially all nuclear power reactors currently in operation this fluid is water.

The most diffuse reactor design worldwide is the pressurised water reactor (PWR), followed by the boiling water reactor (BWR). Together, these two designs, initially proposed by the USA, correspond to almost 90% of the installed nuclear electricity power in the world. They are jointly denoted as light water reactors (LWR). Heavy water[3] reactors (e.g. CANDU, CANadian Deuterium Uranium, of Canadian design) are the only other design that represents a non-negligible fraction of the share (6.4% of the installed power). Data are taken from [8]. All of these water-cooled reactors use mainly uranium dioxide (UO_2) ceramic fuel pellets (~1 cm in diameter), stacked inside 3-4 m long zirconium alloy tubes (fuel cladding) that transfer nuclear heat to flowing water, while acting as primary barrier to avoid leakage of volatile (gaseous) nuclear fission by-products.

In the PWR the water circulates through the core at high flow rate under a pressure of ~130 bar, without ever changing phase to vapour. The core is contained in a pressurised vessel which is connected, generally through piping, to one or more steam generators (up to four circulation loops, forming the so-called *primary* circuit). Here is where steam for the turbine is produced in a *secondary* circuit, by extracting heat from the primary circuit hot water (~300°C, more precisely the operating temperatures may vary between 270 and 330°C). To give an idea, the vessel is a massive structure of cylindrical shape, with a lower and an upper calotte. Its diameter, height and thickness can reach respectively 4 and 12 meters, and 25 cm (for a description of typical vessels, see [15]). The Russian variant of the PWR design is denoted as water-water energy reactors (WWERs): in it, the vessel is

[3] Heavy water is isotopically enriched water, in which most molecules contain deuterium (^2H = D) instead of hydrogen (^1H). This reduces the neutron absorption rate of water, allowing the use of natural uranium as fuel. The use of normal (light) water requires isotopic enrichment of uranium, up to a content of ^{235}U of ~3-3.5%.

somewhat more compact and the walls are thinner, to comply with the need that the vessel must be transportable by land. PWR type units are also used for submarine propulsion.

Figure 1. Frequently shown schematic diagram of (a) a PWR and (b) a BWR

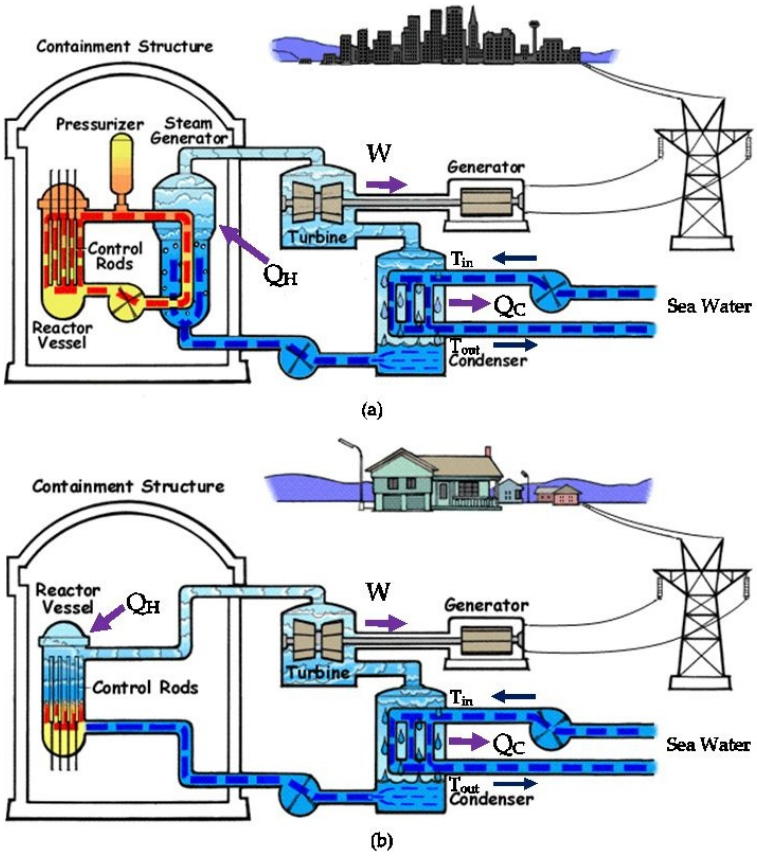

The heat transfer routes are also depicted: Q_H is the heat generated at high temperature, W is the energy extracted and Q_C the heat returned to the cold sink (that does not need to be see water, can be a river, a lake or a cooling tower)

Source: USNRC website: http://www.nrc.gov/reading-rm/basic-ref/students/reactors.html).

In the BWR, water does boil within the core, under the pressure of ~80 bar, at a temperature somewhat below 300°C: the steam is separated in the above region of the pressurised vessel and from there goes directly to the turbine. The vessel of a BWR is even larger than for a PWR. The process schemes of a PWR and a BWR are shown in Fig. 1 a & b, respectively.

The core of both the PWR and BWR, though different in the details, follows broadly similar design ideas. The zirconium alloy tubes with the fuel pellets inside (called fuel *pins* or fuel *rods*) are grouped into fuel assemblies that also contain control rods or blades. BWR assemblies are contained in channel boxes within which the water changes phase while flowing upward, whereas no channel separation exists in PWR and water can flow between assemblies. In both cases the core assemblies are contained inside a baffle-former assembly (PWR) or a core shroud (BWR) that guides the water through the core. The

different parts of all these components are kept together with bolts, springs, support pins and clips. Figure 2 shows how a PWR and BWR fuel assembly look like.

Figure 2. Aspect of a BWR (left) and PWR (right) fuel assembly, showing the fuel pin and a number of other components (spacer grids, guide tubes, etc.) made of austenitic steels

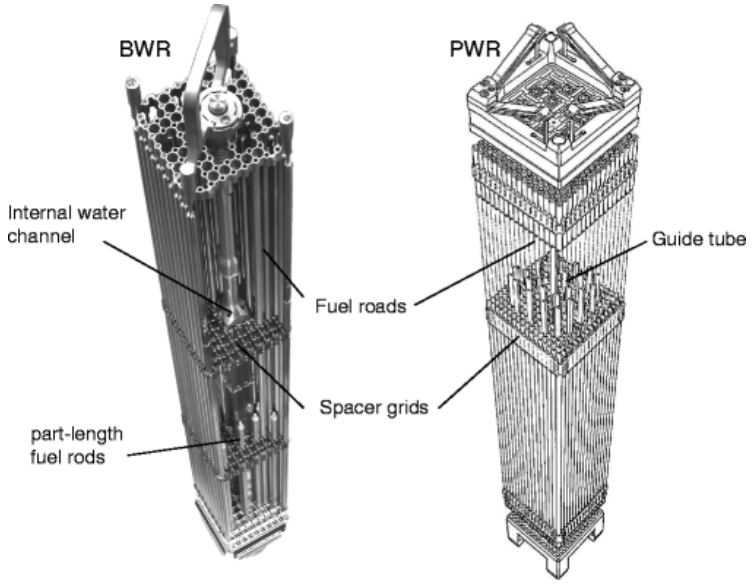

Source: P. Van Uffelen, R.J.M. Konings, C. Vitanza, J. Tulenko, "Analysis of Reactor Fuel Rod Behaviour", in: Handbook of Nuclear Engineering, D.G. Cacuci (Ed.), Springer Science & Business Media LLC 2010, pp. 1519-1627).

In heavy-water cooled reactors, each fuel assembly uses a separate power tube in which coolant flows. In the CANDU design, heavy-water acts as both coolant and moderator[4], while in the Russian version (RBMK) graphite is used as moderator.

A few gas-cooled reactors that use CO_2 as coolant still operate in the UK and consist of large graphite blocks used as moderator, into which fuel and coolant channels are opened; steam for the turbine flowing in a secondary system is produced in a generator from the primary circuit heat. Other reactor systems of which prototypes for power generation were built in the past, and which may be again used commercially in the future as so-called *Generation IV reactors*, are: (a) high-temperature gas-cooled reactors that use helium as coolant, with the possibility of direct power generation in a gas turbine; (b) fast breeder[5] reactors, that use fast neutron spectra by removing the moderator, i.e. using liquid metals as coolant instead of water. Sodium is essentially the only metal used for power generation so far, although lead is also considered for future reactors; He is also a possible coolant for a fast reactor. For more information on future reactor design, see e.g. [16].

[4] The moderator is a material that slows down neutrons efficiently by letting them bounce elastically against its atomic nuclei, without absorbing them. The best moderators are heavy-water and graphite. Light (i.e. normal) water moderates but absorbs neutrons as well, thereby requiring uranium enrichment to increase the number of neutrons produced at source: this is why PWR and BWR use 3-3.5% enriched uranium.

[5] Breeder reactors can potentially produce more fuel (i.e. fissile nuclei) than they use, by making much more efficient use of the uranium isotopes: typically, in addition to inducing the fission of ^{235}U, in these reactors neutrons also convert ^{238}U into ^{239}Pu, which is a fissile nucleus, as good to produce energy as ^{235}U.

3. Main materials for nuclear power plant components

The main pressure boundary components in LWRs, i.e. reactor pressure vessel (RPV), pressuriser, and steam generator shell, as well as turbine and condenser, are made of low-carbon, low alloy ferritic (bainitic) steels. Also secondary circuit piping in PWR is made from steels of this type. Austenitic stainless steels dominate as core structural materials, as liners on the inside surface of the RPV and the pressuriser and for the primary circuit piping. Steam generator tubes are made of nickel-base alloys. Austenitic stainless steels and nickel-base alloys are selected because of their good resistance to water corrosion up to high temperature.

General corrosion is a process of loss of metallic material via formation of superficial oxide layers from the oxidising species present in the water. Low corrosion rates are achieved in austenitic alloys by the formation of very stable chromium-containing oxide layers on the surface, which adhere very strongly to it and grow afterwards very slowly, thereby exerting an efficient protective function (passivation). Low alloy steels, on the other hand, are, like iron, easily corroded, i.e. surface layers of easily removable oxides (rust) are formed when in contact with water. Their formation and removal progressively thin the component walls: for this reason, for example, an austenitic steel liner is needed to protect the inner surface of the RPV and pressuriser from corrosion. Low-carbon, low alloy steels have, in turn, the advantage of relatively easy weldability through thick sections, which is important in large components, such as the pressurised vessel, that cannot be made of one single piece. Low alloy steels have also a significantly lower cost than austenitic steels (about a factor 4-5 [2]), which is of course an important point for large components such as vessel, pressuriser and steam generator.

Heavy-water reactors, mainly of CANDU design, make extensive use of zirconium alloys not only for fuel cladding, but also for the power tubes, or channels that contain each fuel assembly. The choice of zirconium alloys is dictated in these reactors by the need to "spare neutrons" when using natural uranium as fuel. Zirconium indeed absorbs much fewer neutrons than iron, thereby allowing the nuclear reactions to self-sustain, even based on the limited amount of neutrons emitted by the small number of fission events that are produced by the ~0.6% ^{235}U present in natural uranium. For more information on zirconium and its alloys for nuclear applications, see [17].

In future high temperature or fast breeder reactors, austenitic stainless steels and nickel-base alloys will still be used, but other materials are also envisaged, in view of the need to sustain higher temperature and/or higher neutron doses. For very high temperatures (ideally approaching 1000°C), ceramic materials such as silicon carbide composites (SiC_f/SiC, i.e. silicon carbide fibres in a silicon carbide matrix) are considered as the only possibility. For more moderate, but still higher temperatures than in current reactors, as well as for the higher dose expected in fast breeder reactors, high-chromium ferritic/martensitic steels are primary candidates, especially in the oxide-dispersion strengthened version for cladding applications.

In what follows, we focus on the two classes of steels used for structural purposes and mainly affected by irradiation in LWRs, namely low alloy ferritic (bainitic) steels used mainly for the RPV (almost ubiquitously denoted as RPV steels) and austenitic stainless steels used mainly for the internal core components.

3.1 Reactor pressure vessel steels

As mentioned, the vessels of LWR, as well as other primary circuit components, are made of low alloy ferritic (bainitic) steels. As a recent and extensive source of information on these steels and components, one can consult documents on the topic released by the International Atomic Energy Agency (IAEA), for example [18]. "Low alloy" refers to the fact that more than 95% of the composition of these steels is iron, in which other elements are found, either added on purpose or ended up there as a consequence of the manufacturing process. The carbon (C) content is low, <0.2-0.3wt%, i.e. these steels belong to the common low carbon steel category, typically used for large components: this low C content minimises cracking upon welding, while still giving some strength to the material, as compared to iron, by allowing carbide (globular cementite, Fe_3C, but also acicular Mo_2C carbides) formation upon thermal treatment. The microstructure obtained after *normalisation* (heating above the temperature where austenite is stable, followed by air-cooling) is bainite, an intermediate microstructure between the thermodynamically stable and ductile combination of pure ferrite and perlite obtained in annealed steels, and the hard but brittle martensite obtained by fast cooling (a good and easily readable source for metallurgical information is e.g. [19]). Bainite is essentially a complex form under which ferrite, that has a body-centred-cubic (BCC) crystal structure intermixed with cementite and other carbides, appears to optical microscope examination: this complexity provides a good compromise between the ductility of pure ferrite and the strength of martensite, in principle also without any need for further thermal treatments. However, RPV steels consist of *tempered* bainite, i.e. they do receive a subsequent tempering heat treatment to stabilise the microstructure; in this way bainite remains also stable upon welding.

Chemical elements that are added on purpose and characterise RPV steels are, in B/PWR, molybdenum (Mo), nickel (Ni), manganese (Mn) and silicon (Si); in WWER steels, also chromium (Cr) and in some steels vanadium (V) are added on purpose. The addition of Mo and Mn, as well as Ni and Si (the latter below a certain limit), aims mainly at strengthening further the steel, given that the carbon content is low. Both Mn and Mo contribute to stabilising bainite versus martensite formation upon cooling, leading to a fully bainitic microstructure; Ni and Cr (the latter within limits) also partly contribute to the latter purpose. Mn provides refined grain size, too, and decreases the ductile-brittle transition temperature, or nil-ductility transition temperature (RT_{NDT}[6]) [20], while Si provides better casting fluidity. The addition of Cr and V in WWER is meant to provide higher strength, especially in terms of resistance to thermal ageing, because of the type of carbides that Cr and especially V form (M_7C_3 and $M_{23}C_6$ in the case of Cr, where M stands for metallic atom; VC in the case of vanadium). Higher strength is required amongst other things because the WWER RPV walls must be thinner than B/PWR. However, the need to make welding easier led, in the larger version of WWER (WWER 1000), to increase significantly the Ni content, with basically complete removal of V. Other elements typically found in RPV steels, the presence of which is unwanted and that should be therefore kept under control, are copper (Cu), phosphorus (P) and sulphur (S), as well as

[6] Temperature below which the material does not show any ductility and behaves as brittle, i.e. when a crack is initiated it propagates completely and instantly through the specimen, which therefore breaks sharply without previous deformation.

traces of others, such as aluminium (Al), tin (Sn), nitrogen (N) and arsenic (As). Table 1 shows indicatively the ranges of concentration of these elements in B/PWR and WWER vessel steels and the somehow most typical values.

Table 1. Typical composition range of RPV steels (base metal) used in B/PWR (C < 0.3wt%) and WWER (C < 0.2wt%). In parenthesis the most typical value is indicated

wt%	Mo	Ni	Mn	Si	Cr	V	Cu	P	S
B/PWR	0.4-0.7 (~0.5)	0.4-1.2 (~0.7)	0.5-1.6 (~1.3)	0.1-0.4 (~0.2)	< 0.25	< 0.05	< 0.2-0.3 (~0.1)	< 0.035 (~0.01)	< 0.04
WWER	0.4-0.7 (~0.5)	0.3;1.9*	0.3-1.3 (~0.6)	0.15-0.45 (~0.2)	1.2-2.5 (~2.0)	0.1-0.35	<0.1	<0.01	<0.01

*Either they contain little Ni (<0.4wt%), or they have relatively high Ni content (1.5-1.9wt%).

The mechanical properties of these steels in the as-received form are obviously defined by their microstructure (bainitic or other), the corresponding distribution of carbides or other inclusions, and their chemical composition. To give an idea, the yield strength[7] at 20°C is around 350 MPa in PWR and around 450 MPa in the stronger WWER steels, and decreases at 350°C to ~300 and ~400 MPa, respectively. The ultimate tensile strength[8] is around 550 MPa in all steels, while the nil-ductility transition temperature, RT_{NDT}, is around 0°C, or somewhat below it.

The compositions given in Table 1 correspond to RPV base metals, i.e. parts of the component produced with a given steel in the form of rolled plates (i.e. obtained by machining) or - increasingly more often - of forged rings (i.e. given ring shape by exerting compressive forces). In the regions where the material is welded, on the other hand, the composition changes because of the impurities coming from the weld wire; in particular, if not controlled, the concentration of elements that are unwanted already in the base metal, such as Cu and P, increases, as well as the content of Ni. Because of the heat applied when welding and because of the change of composition, the microstructure of a weld will also generally differ from the microstructure of the base metal. Moreover, in the regions adjacent to the weld, affected by heat during welding (heat affected zones, HAZ), the microstructure is likely to be altered, as well. For this reason and because of the weak point that in any case a weld represents, with time the vessel fabrication techniques have improved to minimise the amount of welds needed, in particular to avoid longitudinal welds, i.e. parallel to the vertical axis of the vessel and normal to the highest load, using mainly forged rings instead. Moreover, strict control of the chemical elements added via the weld wire has been enforced. However, welding and subsequent local changes of composition cannot be completely avoided and the existence of welds and HAZ, together with the difficulty of guaranteeing at industrial level the compositional homogeneity of large plates or forgings, leads to the fact that the heterogeneity of the material over the different parts of such large components must be accounted for, when evaluating its ability to maintain structural integrity. Microstructural parameters may also be significantly

[7] The yield strength is the load that needs to be applied for the material to start to deform plastically, i.e. irreversibly; the yield point is the point on the load-displacement (stress-strain) curve above which deformation becomes irreversible.

[8] The ultimate tensile strength is the maximum uniaxial load that the material can withstand, once it has started to deform irreversibly.

different between the base metal and the weld; for example, the dislocation density[9] may vary from ~10^{12}-10^{13} m^{-2} in base metals, up to > 10^{14} m^{-2} in welds (as well as in WWER base steels); prior austenitic grains may vary in size between 10 and 40 μm, while the lath width is in the range 0.5-5 μm (larger sizes in welds).

Together with the heterogeneities, fabrication cannot completely avoid the presence of defects, or flaws, in the form of microcracks. The structural integrity assessment must include the possibility of verifying that these cracks are not such as to endanger the integrity of the component when it is delivered (pre-service inspection, PSI), as well as the verification that fatigue and pressurised thermal shocks do not cause these cracks to grow by reaching their critical size and subsequently propagate over the years during operation, thereby threatening the integrity of the component (in-service inspections, ISI). There are precise programmes, criteria and procedures for the ISI, obviously concentrated on the most critical locations (beltline, welds, etc.), the details of which can vary from country to country. Besides visual inspection, extensive use is made of non-destructive examination (NDE) techniques, such as ultrasonic testing, acoustic emission monitoring, eddy current testing, radiography, dye-penetrant tests, etc. These aspects are extensively discussed in [18].

3.2 Austenitic stainless steels

Most components located inside the vessel, in particular those constituting the core of the reactor that sustain the fuel pins and surround them, as well as primary circuit piping, are in constant contact with water and are for this reason made of austenitic stainless steels. Moreover, steels of this class are also used as liners for the inner wall of the vessel, the pressuriser and the steam generator, that are also constantly in contact with water. The reason for the choice of this material is quite obvious. On the one hand, these are steels that offer excellent mechanical properties, in particular high ductility, with low yield but high ultimate tensile strength and good fracture toughness over a wide range of temperatures; in particular, they are exempt from ductile-brittle transition, i.e. there is either no RT_{NDT}, or it is lower than -200°C, so the material always exhibits ductile behaviour. On the other, they are especially conceived to resist water corrosion. The essential difference in composition with respect to low alloy steels used in the RPV is that they contain high amounts of Ni (~10%) and Cr (15-20%): the former stabilises the austenitic phase down to room temperature, which otherwise in pure Fe would only appear above 910°C, while the latter slows down the transformation to non-austenitic forms, thereby guaranteeing that this structure remains stable during operation. Austenite has a face-centred cubic (FCC) crystallographic structure as opposed to the BCC structure of other Fe alloy allotropic forms. This is what provides the high ductility, thanks to the fact that the FCC system offers more dislocation glide planes than the bcc one. Ductility is also enhanced by low amounts of C with respect to the quantity that could be dissolved in FCC iron. Furthermore, the large amount of Cr leads, as mentioned already, to the

[9] Dislocations are planar defects that correspond to the insertion of additional atomic semi-planes or to the partial glide of atomic semi-planes with respect to one another. They are unavoidably produced during solidification and are the vehicles for irreversible (plastic) deformation in metals.

formation of a stable oxide layer[10] on the surface in contact with water, that provides corrosion resistance by preventing further advancement of the oxidation reaction and is generally rapidly reformed if it breaks. Stainless steels with 16-18% Cr have very good resistance to corrosive environments from room temperature up to ~300°C and the protective Cr oxide layer remains stable up to 550-600°C. The main shortcoming with respect to low alloy steels is the significantly higher cost of the material and the more delicate procedure for the welding (even though this does not mean that these steels cannot be welded). The latter is related among other things to the higher coefficient of expansion and lower thermal conductivity of austenitic versus ferritic alloys that lead potentially to high distortions and residual stresses during the increase of temperature experienced when welding. Care has to be taken also to avoid that the temperature increase leads to Cr depletion, by forming either locally too thick chromium oxide layers, which impair corrosion resistance and need to be removed, or stable chromium carbides at grain boundaries. The latter effect, called *sensitisation*, is especially detrimental, as it increases the susceptibility to stress corrosion cracking which, as discussed below, is the main problem that affects these steels. For general information on austenitic steels, see e.g. [19].

Typical commercial steel grades used for core structures and primary piping in nuclear reactors are (following the AISI/SAE standard for nomenclature) 304 and 316, as well as, to a lesser extent, 321 and 347. 308 and 309 grades are used for the liner of the vessel and other similar functions. The indicative compositions of these grades are given in Table 2. Most often these steels are used in the solution-annealed (SA) condition, i.e. with the alloying elements fully dissolved in the parent austenite phase and little or no precipitation. An alternative condition often use in nuclear components is cold-worked (CW), that is, plastically strained at low temperature, with a subsequent change in the microstructure, especially dislocation density.

The main difference between 304 and 316 is the presence in the latter of molybdenum, which increases amongst other things creep resistance (i.e. gives better high temperature strength), via formation of stable carbides, and provides better corrosion resistance (especially against pitting corrosion, in the presence of chlorides), while making the steel somewhat more expensive. Both these steels can be produced with low (L, <0.03%) or high (H, up to ~0.1%) carbon content: for nuclear applications, the low carbon versions (304L, 316L) are generally considered, in order to reduce the risk of sensitisation. High carbon, on the other hand, provides higher strength (the higher the C content, the higher the yield strength) and enhances the stability of austenite. The latter effects can however be also obtained, with less risk of sensitisation, by adding nitrogen (N), as in 304LN or 316LN. The addition of Ti (321) or Nb (347) induces the formation of specially stable carbides, that remain largely inert during operation and provide, therefore, higher strength, extended to high temperature (improved creep strength), as well as reduced risk of sensitisation. Finally, 308 and 309 are actually welding fillers for austenitic steels and are therefore especially suitable to be applied as liners to protect the walls of vessels from water corrosion, without having to fulfil any structural function.

[10] These are spinel-type oxides composed of a mixture of $NiFe_2O_4$, Fe_3O_4 and $FeCr_2O_4$. These are double-layer oxide films with the inner layer being a chromium-rich normal spinel (chromites), and the outer layer an inverse spinel magnetite/nickel ferrite (ferrites), the latter being formed by a metal cation dissolution/precipitation reaction.

Table 2. Typical composition range of austenitic steels used in nuclear reactors (300 AISI/SAE series)

wt%	Cr	Ni	Mo	Ti	Nb	Mn	Si	C	N
304	18-20 (18, 19)	8-12 (8,10)	-	-	-	1-2 (1.5)	0.75	0.04-0.08 <0.03 (L)	<0.03 <0.14 (LN)
316	16-18	10-14	2-4 (3)	-	-	2	0.75	0.04-0.08 <0.03 (L)	<0.03 <0.14 (LN)
321	17-19	9-13	-	0.2-0.4	-	1-2	0.75	0.04-0.08	<0.03
347	17-19	9-13	-		0.4-0.8	1-2	0.75	0.04-0.08	<0.03
308	19-21	10-12				2	1	0.08	
309	22-24	12-15				2	1	0.2	

L stands for low-carbon version; N for addition of nitrogen.

The mechanical properties of austenitic steels for structural use in nuclear reactors at room temperature and in the SA condition are fairly homogeneous, irrespective of the composition (besides addition of C and N). The yield strength (0.2% offset) is 250-300 MPa, while the ultimate tensile strength (UTS) can be as high as 600-700 MPa, and the total elongation exceeds largely 50%: large work-hardening (i.e. hardening during deformation, due to the creation of dislocations above yield point) is a distinct feature of this class of steels. Differences are seen in the variation of the mechanical properties with temperature. The yield strength of 316, which has better creep resistance than 304, declines to values around 150 MPa already at 500°C, remaining then almost unchanged up to ~650-750°C, while the UTS decreases in the same range of temperatures from 500 MPa to values comparable with the yield strength. On the contrary, certain versions of 347 may retain values of UTS as high as 200-300 MPa up to 800°C. Elongation is always >>50% at all temperatures for all these steels, which remain ductile down to -200°C.

Higher strength, with detriment of elongation, can be given by cold working, 20% cold-worked (CW) 316 may have yield strengths of 600-700 MPa at room temperature, although the elongation reduces then to a few per cents; in turn, the material will retain a more stable strength with increasing temperature, still having reasonable elongation, that increases with temperature.

Concerning the use of these steels both in BWR and PWR, 304 is the most common choice for relatively large components, such as shrouds (BWR) or baffle-former assemblies (PWR). PWR internals come in two basic types, welded and bolted. Bolts are generally made from harder steels, such as CW 316, although in some reactors SA 347 or even simply SA 304 bolts have been used. In WWER, on the other hand, typically 321 is used for baffle-former-barrels assemblies.

As mentioned, the main problem of these steels is that, although resistant to water corrosion up to relatively high temperature, they are susceptible to stress corrosion cracking (IASCC). This is a type of failure that occurs in corrosive environments under stresses lower than the yield strength, either deliberately applied or as a result of residual stresses in fabricated components, especially close to joints (welds, bolts, etc.). It is, therefore, the result of a critical combination of material, environment and stress, which might arise through the variation of just one of the three parameters. For example, difficulty in water chemistry control during operation, or the presence of residual stresses as a consequence of inadequate welding procedure during fabrication, or variations in the

materials' composition or microstructure, might produce the conditions for the appearance of IASCC. In turn, for a given material, provided that stresses and water chemistry are kept under appropriate control, the phenomenon can be avoided. Nevertheless, since the mechanisms triggering IASCC are still very imprecisely understood, this type of failure is very difficult to anticipate and to date in practice its appearance could only be minimised, but not completely avoided. The resulting crack is generally normal to the principal applied stress and propagates in a brittle-like way, i.e. with hardly any plastic deformation. It can be both transgranular (i.e. *through* grains) or intergranular (i.e. *between* grains), but the latter, a type of brittle fracture that is especially feared at engineering level, has been mainly observed in nuclear power plants. Thus, in connection with nuclear steels the main concern is intergranular stress-corrosion cracking, IGSCC. There is an important difference with respect to IGSCC between BWR and PWR. The closed primary circuit of the PWR results in very low levels of dissolved oxygen and in a more effective control of the water chemistry, with the possibility of dissolving hydrogen; in contrast, the open circuit of the BWR entails relatively high oxygen concentrations (200-300 parts per billion), while hydrogen cannot be retained because it partitions when the water boils. As a consequence, BWR materials are significantly more susceptible to IGSCC. On the other hand, also PWRs are affected by this problem, not only in the secondary circuit, but also in the primary, as a consequence of critical applied stresses and possibly also of materials choice. This is generally worse in BWR, where initially high carbon type of 304 or 316 steels were used (304H, 316H), which were especially prone to sensitisation on welding, i.e. formation of stable Cr carbides at grain boundaries. The reduction of carbon content proved beneficial in this respect, even though by no means was it sufficient to completely remove the problem of IGSCC. Similarly beneficial results are obtained using steels stabilised by Ti or Ni, such as 321 and 347, respectively, because the formation of TiC or NbC carbides also prevents Cr-carbide precipitation at grain boundaries.

It should be noted that IGSCC affects also other types of materials, namely nickel-base alloys used in steam generator tubes, which for this reason had to be replaced in several plants, at a very high price. However, the present chapter and volume deal with the effects of irradiation, to which steam generators are not exposed. Irradiation has been clearly observed to have the effect of enhancing the susceptibility of austenitic steels to IGSCC, both in BWR and PWR. This phenomenon, called irradiation-assisted SCC (IASCC), currently amongst the least understood of the radiation effects happening in nuclear reactor structural materials, will be described in Section 4.2.3.

Further information on austenitic steels in current and also future nuclear power plants, as well as on IGSCC, can be found in [8,13,14].

4. Radiation effects in nuclear steels

4.1 Hardening and embrittlement of RPV steels

The peculiarity of the RPV with respect to other LWR components made from low alloy steels is that, in the so-called beltline of the vessel that surrounds the reactor core, the material is subjected to a continuous neutron irradiation field during operation. Typically, the neutron flux received by the inner wall of the vessel at the beltline in PWR/WWER is on the order of 10^{10}-10^{11} n·cm^{-2}·s^{-1} (E > 1 MeV), leading to a lifetime (40 years) fluence of

10^{19}-10^{20} n·cm^{-2} (E > 1 MeV).[11] In displacements per atom (dpa), this corresponds to a dose-rate of 10^{-11}-10^{-10} dpa/s, so the foreseen lifetime dose hardly reaches 0.1-0.15 dpa. Because of the need of land transport, WWER vessels are somewhat smaller and, therefore, their vessel walls are closer to the core and receive, as a consequence, flux and fluence on the upper bound given here, as compared to PWR. In contrast, BWR vessels, due to a design characterised by a larger distance between core and vessel wall, are much less affected by neutron irradiation; the flux and fluence seen by the RPV material are one to two orders of magnitude smaller than in PWR/WWER.

The dose received by the beltline wall over the vessel lifetime is very small when compared to, for example, the one received by in-core components, which can reach tens of dpa (see Section 4.2), or the dose expected in future Generation IV or fusion systems, which in some components might abundantly exceed 100 dpa. Yet, it raises concerns because, as mentioned, at the temperature of operation of the RPV neutron irradiation leads to hardening (yield strength increase) and subsequent embrittlement, the RPV being a key component for the safety of the plant. Specifically, irradiation reduces the fracture toughness of the material, which is an index of its ability to delay fracture propagation. If the fracture toughness decreases, the steel becomes more prone to fast fracture, closer to the behaviour of a brittle material, so that its ability to maintain its integrity under both normal and especially off-normal load becomes progressively questionable. This problem is especially delicate for the vessel, because its replacement is not foreseen and its failure to fulfil the safety criteria in a structural integrity assessment might lead to the shutdown of the whole reactor unit. AIrradiation embrittlement of RPV steels is therefore one of the main concerns for nuclear power plants operators, who are required to guarantee that the material remains within safety margins in terms of fracture toughness during the whole lifetime of the plant [9,10].

In virtually all commercial nuclear power plants the in-service verification that the fracture toughness (or more generally the impact properties) of the RPV steel are within margins is needed to obtain the authorisation of the safety authorities to run further the plant, after demonstrating that there is no danger of vessel loss of integrity. This is performed via a systematic and specifically regulated *surveillance programme*. Such a programme has to be designed before starting operation, by locating on the inner wall of the vessel, at the height of the beltline, capsules that contain specimens ready to be tested, as shown in Figure 3. These capsules are periodically extracted and, since they receive higher flux and therefore fluence than the wall itself, they allow the properties of the steel to be sampled *ahead of time*. The implicit assumption is that the higher flux does not represent a determining factor that would influence significantly the level of irradiation embrittlement. The ratio between the fluence at the capsule and at the wall is called *lead factor* and provides a measure of the fraction of component lifetime that the capsule specimens are representative of. For example, if the capsule is extracted after 10 years of operation and the lead factor is 2.0, the samples are representative of the expected properties of the vessel material after 20 years of operation, i.e. 10 years later (about half

[11] The beltline is defined as the "region adjacent to the reactor core that must be evaluated to account for the effects of radiation on fracture toughness". The US NRC has used a neutron fluence value of 1x10^{17} n/cm2 E > 1 MeV) at the end-of-license (EOL) to define the extent of the RPV beltline [21].

the typical design life-time). The samples in the capsule should include both base and weld metal and possibly also HAZ material; un-irradiated archive material should also be kept outside the capsules for comparison. The samples should fulfil the standards to perform certifiable tests, providing all data needed for the structural integrity assessment. The actual rules and standards applied may vary from country to country, as well as between B/PWR and WWER. However, in essence the parameter that is sought for is the *increase*, due to irradiation, of the temperature conventionally representative of the nil-ductility transition (ΔRT_{NDT}). In this way the fracture toughness change can be assessed and, based on the assumed flaw size (via NDE, see Section 3.1), one can determine the response of the vessel to a given pressure at a given temperature (pressure-temperature curve, PTC). But what is here said in a few lines is, in practical terms, far from simple: it requires establishing all standards for the tests to be performed, the way to extract from there the parameters needed, the knowledge of the correlation between properties obtained with one test and properties obtained with another test, or between tested properties and real properties, or at least with the properties needed for the assessment, and so on. An idea on the problems that need to be solved to face these issues is given in [18].

By testing specimens in surveillance capsules and applying all the standard procedures that follow, one can obtain a "vessel-specific" structural integrity assessment for a given fraction of its life-time. However, one also needs to be able to know, possibly in advance, whether a given material used in a given reactor behaves as *should be expected* or else presents signs of deviation from *normal behaviour*. In order to do so, one should know what "normal behaviour" is, i.e. one should be able to correlate the embrittlement measured in terms of ΔRT_{NDT} with the variables that define the environment, including irradiation (mainly temperature, fluence and flux, but also neutron spectrum), and the steel (chemical composition, but also initial microstructure or type of material, plate, forging, weld, …). These correlations would provide the "trend" to be expected, so that one can check whether or not a material is behaving *as expected*. Based on data from surveillance, decommissioned plants, accelerated irradiation in materials test reactors and, up to a certain extent, also on some physical and/or mechanistic considerations, several empirical trend curves (ETC) have been developed in the last decades. (They are also called DDR: dose-damage relationships). These are supposed to be able to predict, within scatter, the embrittlement of RPV steels as a function of fluence. [9]. The elaboration of these curves is also required in order to correlate surveillance data with a high lead factor (i.e. from capsules that received a given dose at significantly higher flux than the one received by the vessel wall), or high-flux materials test reactor (MTR) data, with the actual behaviour of the vessel material in operation.

Figure 3. Drawing of surveillance capsules showing specimens for Charpy and fracture toughness tests (above), position of surveillance capsules on the cross-section of a PWR vessel (denoted by CH numbers) (below)

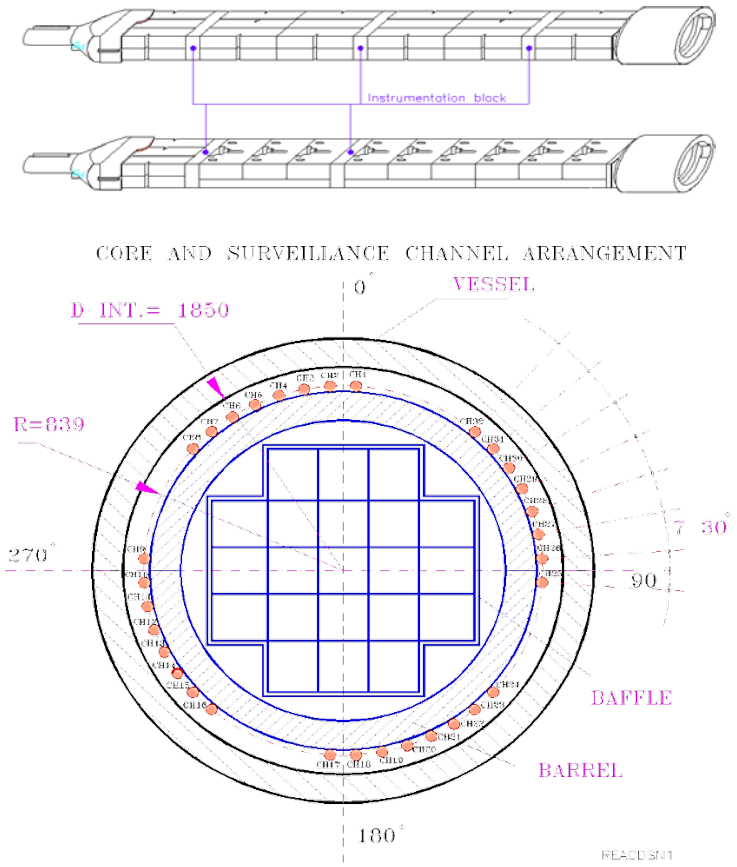

Source: SCK•CEN

The development of ETCs highlighted that some variables are clearly more important than others; for example the initial microstructure does not seem to be an issue, but the chemical composition, especially the amount of Cu, P, and Ni, and possibly also Mn, seem to play a crucial role, as well as irradiation temperature. Steels that contain relatively high amounts of Cu (~0.3wt%) exhibit higher levels of embrittlement than steels that contain negligible Cu (<<0.1wt%); the presence of high levels of Ni (> 1wt%), especially together with Cu, further enhances embrittlement. However, high Cu content leads to saturation of embrittlement at very low dose. In contrast, no clear saturation is observed, according to the latest data, when Cu is virtually absent and high contents or Ni and Mn are present instead. (Figure 4).

Concerning temperature, the trend is that hardening would decrease linearly in the range 100-350°C [9]. Above this temperature range, hardening and embrittlement cease to be an issue and radiation hardening fast disappears for increasing irradiation temperature between 350 and 450°C. Furthermore, radiation damage is annealed by keeping the material for sufficient time at temperatures > 400°C, the higher the temperature the faster the recovery; so much so that annealing treatments are in some instances considered as a

(costly) measure for mitigation of embrittlement, without need to replace the component, in particular for WWER [22].

The effect of other extremely important variables, like flux, is still debated. It is unclear whether the embrittlement of a given material irradiated to a given fluence at a given temperature is the same or not if that fluence is reached with a different flux, i.e. over different times (Fig. 4 gives a pictorial idea of possible differences for high Cu RPV steels). This problem is key in view of deciding about the possibility of extending the lifetime of nuclear power plants, i.e. the lifetime of the vessel. As a matter of fact, in order to do so within safety requirements, one needs to be able to predict in a proven way the behaviour of the steel at higher fluence than initially foreseen, for which there is no operational experience (e.g. after 60 or 80 years of operation). Some indications of this type come from surveillance specimens with a high lead factor or extracted at an advanced fraction of the vessel lifetime, but data remain too scarce to be able to make safe high fluence predictions. These should take into account correctly all variables and, in addition, need to be correlated with the behaviour of the material at operational flux. Moreover, recent data of this type clearly suggest that existing ETCs worryingly underestimate the embrittlement to be expected at high fluence (see Figure 4). High fluences (for RPV standards) can be reached in high-flux MTRs in a short time (a few months) but the data obtained from there are only usable for prediction provided that it can be demonstrated that the effect of flux is clearly understood, so that one can correct the data accordingly. The scarcity of data, and the long time and high amount of resources required to overcome this scarcity, make the goal of mastering the flux effect elusive. It is in this framework of high fluence and flux effect, *not yet fully mastered by the existing ETCs*, where the development of models supported by physical understanding of the mechanisms responsible for the changes produced in the material by irradiation becomes important, to underpin structural integrity assessments beyond vessel design lifetime.

Figure 4. Qualitative illustration of the shape of ETC for high Cu (~0.3%), low/high flux, and low Cu (<0.1%) as compared with recent data for low flux/low Cu at high fluence and corresponding emerging trend

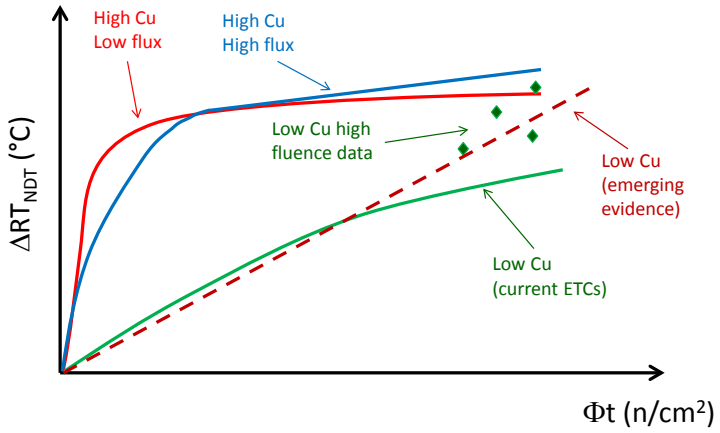

Low Cu RPV steels always contain Ni and Mn.

4.2 Irradiation and environment effects in austenitic steels

Austenitic steels are used as structural materials for LWR and WWER core components, i.e. they are immersed in water and located very close to the fuel pins, therefore they receive substantially higher fluxes of neutrons and, as a consequence, higher fluences than RPV steels. A typical dose-rate received by core components is ~$5 \cdot 10^{-8}$ dpa/s in PWR and WWER[12] and one order of magnitude less in BWR, where not only the vessel, but also the shrouds that enclose the core are located further away from the fuel pins than the baffle-former assembly in PWR. This means that in PWR, in certain near-core locations, the material can accumulate several tens of dpa and over 40 years of lifetime even approach 80-100 dpa. Moreover, the temperature maybe as high as 340°C and hot spots reaching 400°C may be produced locally, due to heating by gamma irradiation, as a consequence of very close fuel elements. These conditions produce three main types of consequences, all of them potentially dangerous for the integrity of the components [12,14]:

- Similarly to RPV steels, core reactor materials will become harder; moreover, even though in austenitic steels there is no problem of increase of RT_{NDT}, because they do not undergo ductile-brittle transition, i.e. fractures are always ductile[13], "embrittlement" appears in terms of loss of uniform elongation, i.e. the material breaks after progressively less deformation than before irradiation, without work-hardening, approaching quasi-brittle behaviour. An important feature that accompanies this loss of ductility is the localisation of plastic deformation: when observed in the electron microscope, deformed specimens reveal the presence of clear bands in which the plastic strain can be up to an order of magnitude higher than in the rest of the material.

- With increasing fluence volume and shape change, leading to progressive distortion. This is worrying because design separations and tolerances might not be sufficient to accommodate these changes, resulting in separation of parts or cracking at constrained joints, and therefore failure. The main causes of change of dimension are swelling and irradiation creep.

- Sudden appearance of intergranular (brittle) cracks, due to the phenomenon known as irradiation assisted stress corrosion cracking. , which stems from a combination of irradiation (with the above consequences), mechanical load and contact with water and is no doubt the main concern related to irradiation in austenitic steels in LWRs. It is a complex phenomenon, the susceptibility to which is most likely affected and determined by both previously listed radiation effects, (1) and (2), and possibly others, too. It has been observed first in BWR shrouds but it also affects for example the bolts that keep together the baffle-former assembly in PWR or WWER.

An underlying process that might influence all three above-listed consequences of irradiation is radiation-induced segregation (RIS), i.e. the redistribution of chemical elements inside the material according to patterns that differ significantly from the initial one, potentially leading to the destabilisation of certain phases and the appearance of new

[12] However, in some regions located especially close to the core, the dose rate may reach ~10^{-7} dpa/s.
[13] So long as the swelling level remains modest, see [12].

ones, in all cases with subsequent, sometimes dramatic, changes in the macroscopic features of the steel.

The complexity of radiation effects in austenitic steels is higher than in RPV steels, also due to the higher doses and temperature range they are subjected to, as well as to the fact that they are concentrated alloys, with more complex composition. There is, however, an important practical difference in impact between the problems that affect austenitic stainless steels in a nuclear reactor and RPV steels. The latter fulfils a fundamental safety function, so its integrity is of paramount importance and decides the lifetime of the plant, given that its replacement is not possible. In contrast, core components failure will impact mainly the efficiency of the plant, although of course any failure has also potential safety implications, in particular for professionally exposed workers. Furthermore, these components can be generally replaced, even though the operation is costly. Parts of them can in any case be extracted from the reactor during recharge, to be examined. This explains why no measure equivalent to the surveillance programme and safety integrity assessment of RPV steels is enforced in the case of core components. Yet, preventing failure in core components remains a primary issue for reactor operators, because of the huge economic impact that component replacements have.

4.2.1 Mechanical property changes

Neutron irradiation at the temperatures of operation of LWRs, i.e. < 350°C, causes in austenitic steels dramatic hardening, i.e. increase of yield strength, as well as reduction of elongation, as qualitatively shown in Figure 5. Hardening and loss of elongation are evident since the early stage of irradiation, at very low dpa, but clearly saturate at < 10 dpa. If irradiated at temperatures > 350°C, the saturation level to which yield strength increases (and elongation decreases) becomes significantly lower (higher), until no radiation hardening or loss of elongation occur anymore above 450-500°C. Saturation at ~10 dpa occurs also for fracture toughness reduction (it decreases by about one order of magnitude, 400-500 $kJ/m^2 \rightarrow$ 40-50 kJ/m^2, after irradiation at ~400°C).

Differently from the case of RPV steels, the significance of these effects depends much more on the initial microstructure than on the detailed composition, at least within the series 300 of austenitic steels typically used in nuclear power plants. Both the increase of yield strength and the loss of elongation at saturation are only modest in initially CW steels, but are dramatic in stainless austenitic (SA) steels. Table 3 gives a quantitative idea of the difference. However, it is interesting to note that, even though the change of property is more dramatic in the SA than in the CW steels, in absolute values if the SA and CW version of the same steel are irradiated at the same temperature and dose rate, they eventually saturate at the same level of yield strength and reduced elongation [12]. This remains true also at temperatures > 350°C, at which the increase of yield strength becomes more modest. In that case, CW steels might even *soften* during irradiation, until they reach the same absolute yield strength saturation level as irradiated SA steels [12]. This is illustrated in Fig. 6. Also the absolute value at saturation of the fracture toughness is largely independent of the initial value, i.e. there is convergence to the same level after irradiation. Departure from this convergence between SA and CW steels may, however, occur occasionally, because modes of deformation active in the CW steel are not active in

the SA steel (e.g. twinning): this depends mainly on composition, more precisely on stacking fault energy, which is a property influenced by composition[14].

Figure 5. Illustration of the change of shape of the stress-strain curve obtained in a tensile test on austenitic steels irradiated to increasing neutron dose at "low" temperature

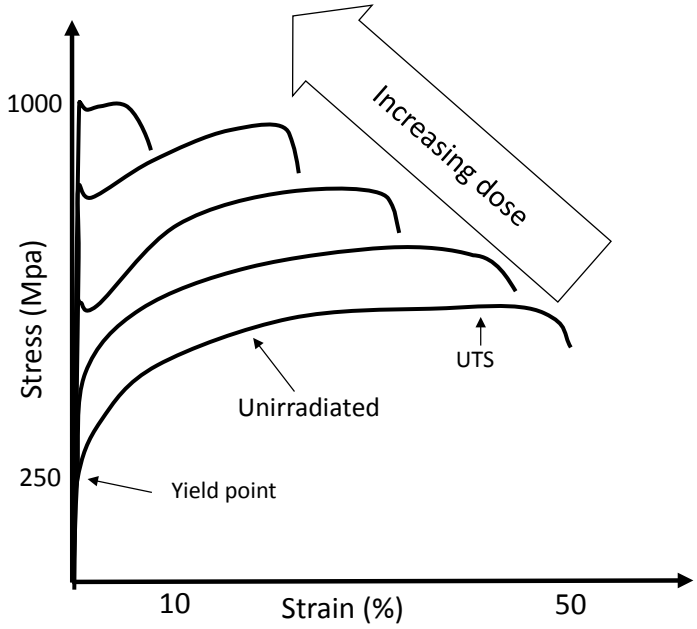

The material hardens spectacularly (yield point increase) and its elongation reduces increasingly.

In the case of RPV steels, the effect of flux (dose-rate) on mechanical properties is still harshly debated. Part of the problem comes from the fact that, in the RPV case, data corresponding to relatively high dose at the very low flux received in operation are scarce, so any comparison with data for the same material irradiated at the same temperature, but different dose rate, will be statistically questionable. Moreover, the "high doses" of interest are in fact very low, so saturation, except when Cu content is "high", is often not observed. In the case of austenitic steels the operational dose rate and dose in current reactors are much higher than in RPV steels, so much so that saturation is always reached; moreover, the use of this class of steels for fast breeder reactors produced a wealth of data for higher flux. This allows the effect of flux to be better known in the case of austenitic steels, namely data for exposure until saturation at different fluxes reveal a weak dependence of hardening on dose rate. This can be expressed as a power law with exponent ¼ [12].

[14] The stacking fault energy, measured in energy per unit area, is the increase in the energy of the crystal due to the fact that the regular sequence of atomic planes corresponding to a given crystallographic structure is (locally) broken. This energy is generally low in FCC metals (with differences depending on the metal), but very high in bcc metals. This has important consequences on the mechanical behaviour of the two classes of metals.

Table 3. Hardening and loss of elongation in austenitic steels before and after irradiation depending on initial microstructure (from [14])

Type of steel	Un-irradiated		Irradiated		
	Yield Strength (MPa)	Uniform elongation (%)	Yield Strength (MPa)	YS increase (MPa)	Uniform elongation (%)
SA	250-300	50	800-1000	550-750	<10
CW	600-700	<10%	800-1000	200-300	<10%

Figure 6. Illustration of the evolution of the yield strength of austenitic steels with dose, depending on irradiation temperature and initial microstructure (SA vs CW)

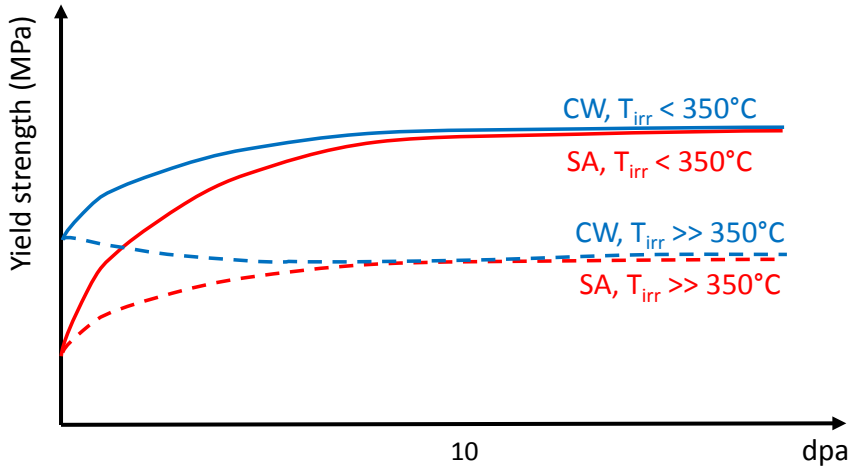

To conclude on the effect of irradiation on the mechanical behaviour of austenitic steels, the progressive loss of work-hardening with increasing dose leads the ultimate tensile strength to coincide with the yield strength, i.e. uniform elongation is suppressed and, as soon as the specimen starts deforming plastically (irreversibly), it starts necking (its cross section starts decreasing) and becomes less resistant to further deformation. From that moment on, lower and lower (engineering, i.e. calculated as constant cross-sectional specimen area) stress is sufficient to allow the deformation to proceed, with progressive thinning of the sample, until fracture occurs. When the radiation dose at which this happens is exceeded, the material starts to deform in a localised way. Examination under the electron microscope reveals that plastic deformation occurs constrained within narrow clear bands, so-called because they appear clearer with respect to the rest of the steel. These bands are generally parallel to each other (although families of them may cross each other), have a thickness of a few tens of nm at most and are separated by distances on the order of 1 μm. Their length spans the whole grain. The strain in the bands can be as high as 100%, much higher than in the rest of the material. This phenomenon, although not observed in RPV steels, is actually common to most steels and essentially to all pure metals [23]. It is considered that this phenomenon may promote intergranular fracture.

This would happen because of the high stresses that accumulate at the end of the band on the grain boundary (one should remember that inside the band the material is highly strained while almost no strain occurs outside), that may locally induce separation between grains. .

Even though all these effects severely degrade the properties of the material, the fact that there is saturation after a certain level of dpa and that there are experimental data indicating the level of degradation that can be reached make these changes not especially worrying in themselves, as they can be foreseen and allowed for. Hardening and loss of elongation, especially plastic flow localisation, are mainly a concern as precursors of or contributors to IASCC, which is a cause of brittle inter-granular cracking that, to date, remains largely unpredictable (see Section 4.2.3).

4.2.2 Dimensional changes

The possibility that components shrink or grow in volume or get distorted in shape while in service is especially worrying from an engineering standpoint. If it happens, operations that imply that different parts must move with respect to one another (insertion/extraction of bars …) will be complicated or prevented. Moreover in the case of constrained immobile parts, either welded or bolted, stresses due to distortion will appear that may lead to cracking and therefore failure. These types of processes do take place under irradiation and can be classified in terms of being volume conservative or non-conservative, isotropic or anisotropic, stress-driven or not. Austenitic stainless steels are especially prone to:

- swelling, which does not need stress to be triggered, is isotropic and is volume non-conservative, and
- irradiation creep, which is driven by stress but is anisotropic and is volume conservative.

These two processes are actually not independent. Irradiation creep may appear under stress before swelling, or swelling may develop without creep in the absence of stress, but as soon as swelling appears the internal stresses caused by this process trigger creep, while the development of creep has an enhancing effect on swelling development. The combination of the two and the order in which they appear will change the type of distortion that is induced in the material [12].

An important point about irradiation creep and swelling is that these and especially the latter, differently from hardening and loss of elongation, *do not saturate with increasing dose in austenitic steels*; in contrast, their rate does saturate, i.e. at steady-state the deformation due to these processes proceeds indefinitely, but at constant speed.

- Swelling

Swelling in steels depends on irradiation dose in a characteristic way, illustrated in Figure 7. Up to a critical dose, d_C, it increases at a relatively slow rate, remaining in practice almost negligible. This is the *transient*, or *incubation*, *regime*. Above d_C, the swelling rate increases very quickly and reaches a steady-state value, $\dot{S}_{ss}$, that remains thereafter constant, leading to *unlimited volume increase*. Based on available data, mainly from fast reactor irradiation but not only, $\dot{S}_{ss}$ in austenitic steels seems to be a constant, irrespective of the detailed

composition and microstructure of the steel or the irradiation conditions (dose-rate, temperature, etc.), equal to ~1%/dpa [12]. Interestingly, in ferritic/bainitic/martensitic steels, this constant steady-state swelling rate would be 5 times smaller, i.e. ~0.2%/dpa [24]. In contrast, d_C depends crucially on not only steel crystallography (in ferritic/bainitic/martensitic steels d_C is much higher, easily in excess of 100 dpa, while in austenitic steels it can reduce to 10 dpa), detailed composition (amount of Cr vs Ni, presence of impurities such as Si and P, …) and microstructure (presence of phases and carbides), but also on the material's history (SA vs CW), neutron spectrum (leading or not to He and H production via transmutation), temperature and, very importantly, dose-rate. Here is a summary of the effect of the different parameters on d_C, according to [12]:

- Composition: generally, an increase in Cr content shortens the transient, while an increase in Ni content, up to 40-60%, delays the onset of steady-state swelling (but higher Ni amounts reverse the tendency). The presence of minor alloying elements (concentration << 1%), especially Si and P, shortens the transient in low amounts but delays steady-state swelling in higher amounts.

- Microstructure and material history: CW is a primary way to delay swelling, optimal results being obtained with 20-25% CW, although too high CW levels may be counter-productive. Ageing with the creation of phases, especially fully-formed carbides, increases significantly the susceptibility to swelling, which implies that C in solution plays a role to hinder swelling.

- Neutron spectrum: Production of gaseous elements via transmutation, mainly He and H, is well-known to favour swelling; so, neutron spectra that produce higher transmutation rates will enhance it.

- Irradiation temperature: Susceptibility to swelling increases at higher irradiation temperature, as well as in presence of any temperature gradient or if changes of temperature occurred during irradiation.

- Dose rate: This effect was historically underrated, but is now believed to be crucial. In the last decade plenty of experimental studies revealed that lower dose rate shortens tremendously the transient to steady-state swelling. The lower the temperature, the stronger the swelling enhancement by decreasing the dose-rate.

Besides affecting the dimension of components, swelling has quite dramatic effects on the mechanical properties. For values of swelling in excess of a few % not only the elongation, total and uniform, but also the yield strength and the ultimate tensile strength decrease sharply; i.e. the material suddenly becomes *softer and more brittle at the same time* [11], which is an unusual combination. The brittleness can be so extreme that, in fact, it is the main reason for avoiding swelling above 2-3%, even more than the change of shape. Citing [25]: "a new form of embrittlement associated with void swelling arises with increasing swelling above ~5 to 10%. Based on fast reactor data available to date, when ~10% volume change is exceeded, the tearing modulus at PWR operating temperatures of Type 300-series stainless steels is dramatically reduced, producing severe embrittlement with little energy required to propagate any crack. Another origin of concern is *differential* swelling; i.e. the fact that parts that are in contact but are constructed from different steels may swell differently, thereby creating stress concentrations even after modest change of volume.

Figure 7. Schematic illustration of the evolution of the swelling of steels with dose: the final steady-state swelling rate, $\dot{S}_{SS}$, is roughly a material's constant, but the critical dose for the onset of steady-state swelling, d_c, depends on several factors, the increase of which may shift d_c to lower or higher values, as indicated

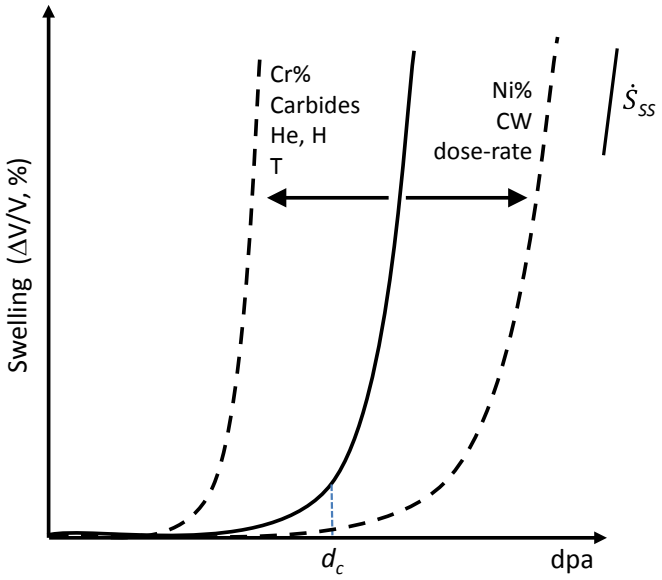

Until recently, swelling was not considered an issue in LWRs. One reason for this was that swelling was perceived to exhibit a strong dependence on irradiation temperature. The so-called peak swelling temperature, i.e. the temperature at which swelling would reach a maximum, was experimentally found well above 400°C, while any change of volume under irradiation was found to vanish below ~350°C. This perception is now believed to be the result of the fact that most data came from experiments conducted in fast reactors [11]. These reactors are compact, so different specimens not only experience different irradiation doses, but are also simultaneously subjected to different dose-rates while being kept at different temperatures, higher than LWR operating temperature. The deconvolution of the separate role of each parameter is not obvious and the observed disappearance of swelling in specimens irradiated at the lowest temperatures conveyed the idea that LWRs would be immune to it. It is now known that, while a low irradiation temperature certainly hinders the onset of swelling, it is by no means true that swelling may not occur at the temperature of operation of LWRs. In addition, hot spots may be created in specific locations of the core barrel, where the temperature may approach 400°C. Moreover, while in BWR the distance between core and shroud is such that the lifetime dose received by structural components remains low (5 dpa over 40 years), in PWR baffle-former assemblies the dose may be significant (80 dpa or more in 40 years) and even higher from the perspective of prolongation of the life of nuclear power plants. At the same time, the dose rate would be much lower than in fast reactors. Thus, low dose rates would shorten the transient to steady state swelling[15], and high doses might lead

[15] Under especially low dose rates (~$2 \cdot 10^{-9}$ dpa/s) at ~350°C swelling has been detected already after accumulating only 0.64 dpa [26].

it to unacceptable levels. Finally, the production rate of He and H in LWRs is several tens of times higher than the rate typical of fast reactors, this being another factor that enhances swelling.

For all these reasons, the correct assessment of the critical dose for steady-state swelling onset under LWR conditions of operation, for which only very limited experimental data are available, is an increasing concern. In this framework, deeper physical insight into the causes of swelling and its consequences and the subsequent development of models capable of predicting swelling onset is become increasingly important for safe and competitive management of nuclear power plants, especially in view of life extension.

- Irradiation creep

Thermal creep is a very well-known problem that affects components operating at high temperature for a long time (e.g. in steels above 500°C for several tens of thousands of hours). It corresponds to plastic (i.e. irreversible) deformation even if the load the component is subject to remains constant and below the nominal yield strength of the material (i.e. in principle only elastic, reversible, deformation should occur). Creep is anisotropic (it occurs in the direction of the principal load) and is volume conservative (i.e. if the material elongates in one direction it will shrink in the normal one). Thermal creep leads not only to change of shape, but also potentially to cracking. Irradiation creep is a similar phenomenon of sub-yield straining but it occurs under irradiation at any temperature, also well below 500°C, being in fact virtually temperature independent (paradoxically, it even exacerbates at very low temperature, e.g. close to room temperature [27]).

Irradiation creep strain is observable since the early irradiation stages, although it needs relatively high doses to become evident: at ~10 dpa it may produce at any temperature (300°C and higher) strains comparable to those observed after the same amount of time is spent at 700°C, i.e. only at relatively high temperature does the irradiation creep contribution become negligible as compared to thermal creep [12]. After a short transient, in which the strain increases relatively fast versus time/dose, it reaches a constant (for the applied stress) strain rate. This strain rate scales linearly with the applied stress (on the contrary, thermal creep strain rate grows with stress according to a power law that may have a fairly large exponent). During this stage, the constant ratio between strain-rate and stress, sometimes called *creep compliance* seems to be a sort of material constant, like the steady-state swelling rate: it is independent of initial material state, temperature and dose rate [12]. Even though the issue is debated, it seems [12] that irradiation creep would not lead to cracking in the same way as thermal creep. As a matter of fact, irradiation creep can be seen as a process that results mainly in the removal of stresses via straining, with potentially harmful consequences but also, in some cases, beneficial effects, depending on the specific material, component and operating conditions.

Generally irradiation creep straining starts to be measurable before swelling. However, as soon as swelling onset occurs, the internal stresses it causes enhance creep strain rate and rapidly (in terms of time/dose) the swelling-controlled component of irradiation creep becomes dominant. At that point, creep strain increases following the same pattern as swelling, also in terms of dependences. Yet, when swelling exceeds a certain amount (a

few per cent), its effect on creep vanishes and, from that moment on, irradiation creep straining virtually stops. The evolution of creep strain with dose including the effect of swelling is illustrated in Figure 8.

Figure 8. Schematic illustration of the evolution of swelling and irradiation creep with dose, including their interconnection

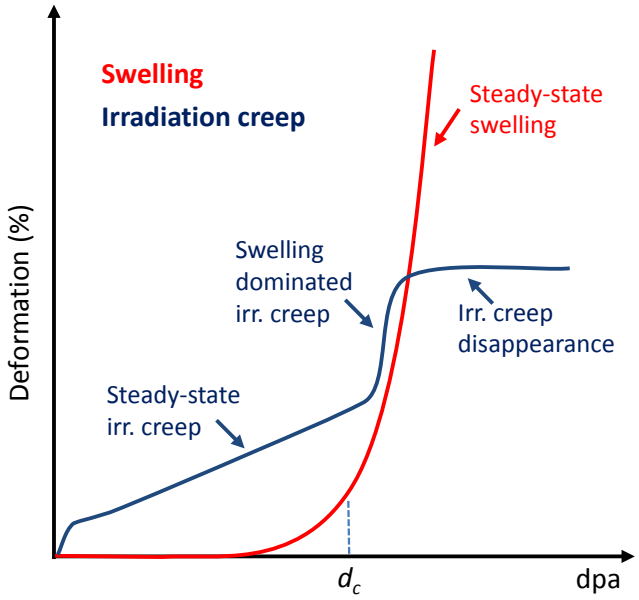

Qualitative interpretation of data from [12].

The most evident consequence of irradiation creep is the relaxation and removal of any preload and, combined with swelling, the creation of complex stress/strain histories to which components are subject in operation. The best example are 316L bolts which are tightened to keep baffle plates joined to former plates in a PWR core. If the bolt becomes looser due to irradiation creep, it will reduce the grip with risk of separation between baffle and former; at the same time, however, under irradiation the 304 plates will swell more than the 316 bolts, leading eventually to their reloading. As will be seen, these changing local stresses have an influence on the appearance of IASCC (see Section 4.2.3).

Because of the still many aspects obscure for what concerns irradiation creep and its synergy with swelling and possible connection with IASCC onset, a better physical understanding of the fundamental processes and the concomitant development of physical models would be of high relevance for LWRs.

4.2.3 Irradiation assisted stress corrosion cracking

IASCC is a particular case of inter-granular stress-corrosion cracking that affects austenitic steels in the core of light water reactors at temperatures between 270 and 340°C, leading to failure [13]. It is a form of corrosion, i.e. a process of loss of metallic material via formation of superficial oxide layers, because of the oxidising species present in the water. The initiation of the crack and its propagation are therefore connected with the rupture of the oxide layer and its capability (or not) of reforming and grow, and how. The fact that the contact with aqueous environment is necessary for cracking is revealed by the

observation of crack initiation always on the water side. Moreover, the crack is invariably found to be inter-granular, while only ductile, trans-granular cracks are observed in austenitic steels, both in as-received and in post-irradiation mechanical tests in inert environment; thus it is a different process from just cracking because of the application of stress. However, stress is clearly always a fundamental component of cracking, which explains why IASCC is observed almost exclusively near the welds of the BRW's core shroud, where residual stresses remain, or in PWR's baffle bolts, where the stress is due to the tightening of the bolt. These stresses are, however, lower than the yield strength and thus definitely much lower than the fracture strength, again pointing to the special nature of the cracking and to the need for other factors than just stress to explain it. Experiments in water on un-irradiated materials provide a framework useful to understand some of the factors that influence inter-granular stress corrosion cracking in the absence of irradiation. These show that there is a steep increase in cracking kinetics when the electrochemical (or corrosion) potential (ECP) of the water rises. The ECP increases with oxygen dissolution in the water and even more if impurities –chlorides, sulfates– that increase its conductivity are added, while it decreases with hydrogen dissolution in the water. Thus, what makes the BWR environment more favourable to give early IASCC is the higher ECP than in PWRs. Geometrical factors, such as crevices, may also influence local water chemistry and therefore ECP, making these locations more prone to IASCC. Nevertheless, IASCC is nowadays essentially as frequently observed in BWR and PWR core components. This happens because another, equally important factor, reaches a higher level in PWR that compensates for the low level of ECP; namely, neutron fluence is higher in PWRs. Thus the key feature of IASCC is that three factors must act simultaneously to produce it: stress, aqueous environment, and irradiation [13].

Strictly speaking, IASCC should be evaluated in terms of factors that influence crack initiation (at which stress the crack is produced and after how long exposure to water and irradiation) and growth (how fast it propagates depending on the conditions). Crack initiation has been studied in constant load experiments [10], revealing that the triggering stress decreases with increasing irradiation dose and saturates to an *average* value of ~40% of the yield strength above 10 (BWR) and 30-40 (PWR) dpa; the time to initiation decreases with increasing dose and applied stress, depending also on water chemistry. The crack growth rate increases with dose and roughly saturates above 5 dpa (with large scatter) and the saturation level grows with the ECP. However, the difficulty of these studies makes that most data are given in terms of "susceptibility to IASCC", i.e. probability of observing IASCC in slow strain rate tensile (SSRT) tests under given conditions. Susceptibility varies by definition between 0 and 100% and, generally, does so in a narrow range of values of the studied variable. For example, the susceptibility is observed to rise steeply when the ECP exceeds 100 mV (vs standard hydrogen electrode). A steep rise is also seen above fractions of dpa in BWR and a few dpa in PWR environment. These steep increases of susceptibility above a certain value, or the fact that the initiation stress saturates at about 40% of the yield strength, provide the impression that one can identify *thresholds* below which IASCC cannot be observed. This is a very convenient concept for engineering purposes, that suggests the opportunity of mapping operational conditions within which IASCC should not be expected, which is indeed what is attempted at industrial level. Physically, however, the threshold concept is not applicable, because one parameter can compensate for another, so in reality there is no threshold ECP, applied stress or fluence below which IASCC is absolutely impossible to be observed: the

existence of thresholds is valid only in statistical sense. Moreover, IASCC is also influenced by factors such as material composition, in particular in connection with the stacking fault energy (SFE) that the composition leads to, and materials history (CW or SA steel, sensitization – i.e. presence of Cr carbides at grain boundaries, …).

This inherent difficulty to predict the conditions for the appearance of IASCC is further complicated by the fact that it is also hard to identify which, of the several effects of irradiation, is determinant to trigger IASCC. The expression itself, irradiation "assisted" SCC, is an implicit admission of ignorance: irradiation "assists", "helps" intergranular stress-corrosion cracking; probably causes it, but not alone, i.e. IASCC is always due to a combination of several factors, of which none is dominant and all are necessary.[16]

Irradiation causes at least three phenomena in the material that have been found to lead to an increase of IASCC susceptibility, namely:

- Radiation-induced segregation, leading to Cr depletion at grain boundaries and surfaces;
- Radiation-induced hardening;
- Localisation of plastic deformation.

To these, one should add first of all the influence of irradiation conditions, such as temperature and flux or even spectrum; secondly, the less conspicuous role of effects such as irradiation creep and swelling (see Section 4.2.2); and, finally but importantly, the fact that irradiation induces changes also in the water (radiolysis).

The difficulty of identifying the dominant radiation effect to trigger IASCC (if any) is that again the IASCC susceptibility exhibits, in experimental studies, almost always a *threshold-like* behaviour, rising steeply above a certain value of fluence, until reaching 100%, while quantities such as radiation-induced hardening or radiation-induced segregation, for which also an apparent threshold for IASCC to appear may be found, grow fast at low fluences but then tend to saturate, and often do so before IASCC susceptibility rises. This is illustrated in a simplified way in Figure 9. So, no clear correlation between IASCC and specific factors can be empirically deduced; in particular, it becomes impossible to separate factors as in any single variable plot it appears that the susceptibility may vary between 0 and 100% also above the threshold. This is also illustrated in Figure 9. Deeper physical understanding is hence needed, with a view to developing models that go beyond the simple mapping of conditions where IASCC likeliness remains supposedly low, without really knowing why, to avoid unexpected failures.

[16]"Irradiation has a complex effect on SCC susceptibility. While radiation segregation and radiation hardening increase susceptibility, radiation creep relaxation of constant displacement loads (e.g., bolts and welds) tends to reduce susceptibility. For these reasons, SCC in BWR shrouds and PWR baffle bolts does not always correlate strongly with fluence. SCC can be interpreted and predicted only by accounting for the conjoint effects of multiple factors." [28].

Figure 9. Schematic illustration of the evolution with dose of IASCC susceptibility and of other effects of irradiation, such as radiation-induced hardening (RIH) or segregation (RIS), including representative distribution of experimental points: while RIH and RIS follow a clear law with dose, IASCC susceptibility may exhibit low values also above the supposed threshold (simplification and combination of figures from [13])

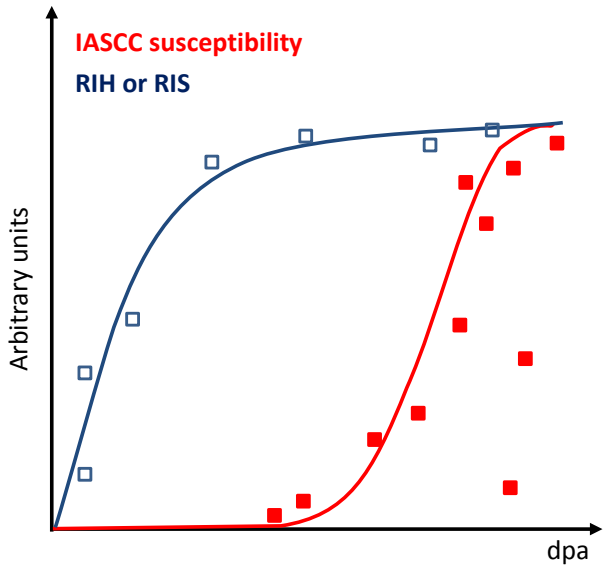

5. Modelling the behaviour of nuclear steels under irradiation

The topic of the present volume is the development of physical multi-scale models, with their root in computational physics, to describe the changes produced in steels by neutron irradiation. This is done to underpin structural integrity and lifetime assessments of nuclear power plant components, namely RPV and internals. The principle of multi-scale modelling is that the physical description of the behaviour of a material requires the use of models that address the correct scale for the phenomenon at hand. It also requires that the information about the behaviour of the material at a certain scale is somehow transferred to the higher scale, so that the model at this higher level can be more accurate [29]. As a matter of fact, radiation effects are inherently a multi-scale problem and all macroscopic changes described in the previous section are the result of processes that occur at much lower scales.

At their origin is the collision of neutrons with the nuclei of the atoms that compose the material. Besides changing the nuclear properties, if the impinging neutron carries enough energy it may kick the corresponding atom out of its lattice position and produce a sequence of atomic collisions and subsequent displacements inside the material, a process generally known as collision cascade, or displacement cascade. This process is repeated over and over in different points of the material while the irradiation goes. It lasts only a few picoseconds and affects a region of linear size not larger than a few tens of nanometres, but produces in that region a large amount of lattice point-defects, namely vacancies (missing atoms) and self-interstitials (atoms occupying an interstitial position in the lattice), both isolated and in clusters. Moreover, cascades produce ballistic mixing of atoms, with several possible effects, depending on the material, amongst which local loss

of crystallinity, destruction of pre-existing chemical order (if any), destruction of phases and, possibly, also destruction of previously produced defects. However, the relevance of the latter effects in metals, and in steels in particular, is limited.

The defects produced in cascades are mobile according to specific atomic-level mechanisms; for example in metals interstitials are more mobile than vacancies. By diffusion within the material over time scales ranging from nanoseconds to years, they bring about several processes, until they are absorbed by extended pre-existing material defects that act as sinks (these are mainly dislocations and grain boundaries). These processes essentially consist of (i) formation of clusters of defects and (ii) transport of chemical elements.

Clusters of defects can grow until they become visible in the electron microscope. A difference between vacancy and interstitial clusters is that the former can agglomerate both in two-dimensional and three-dimensional form, while the latter are constrained to be two-dimensional. Vacancies form cavities, which may be classified as voids or bubbles. The former are often crystallographically facetted and correspond to removed parts of the crystal that contain no atoms, whereas the latter tend to be smaller and are filled with atoms of gaseous elements, generally He and possibly H, thereby assuming a more spherical shape because of internal pressure; He clusters forming bubbles are considered to be the nuclei for voids. In contrast, interstitials form only dislocation loops, planar defects corresponding to platelets of point defects, delimited by a close dislocation line, because in the platelet there are extra atomic layers. Vacancies may also form dislocation loops (in this case atomic layers are removed), but vacancy loops are less frequently formed than interstitial loops in metals. In face-centred cubic crystals with low stacking fault energies, vacancies produce so-called stacking-fault tetrahedra, which are the result of the partial glide of a pyramidal portion of crystal along crystallographic planes, made possible by the agglomeration of vacancies into a planar structure that leaves space for the atomic rearrangement. Once grown, all these defects become in turn sinks for other lattice point-defects.

The transport of chemical elements is due to the fact that under irradiation there is a large supersaturation of point defects. The subsequent redistribution of the corresponding atoms occurs according to a pattern that is dictated by a combination of thermodynamic driving forces that push the system towards equilibrium, with kinetic effects, that may delay or even counteract the evolution towards equilibrium. The latter, sustained by the continuous production of migrating defects, may indeed keep the material in a thermodynamically metastable state or produce locally the conditions for a different thermodynamic equilibrium to be reached, moving locally the system to a state that the nominal composition would not allow. This redistribution of chemical species is observed in terms of accumulation or depletion of certain elements in specific regions of the material. One mechanism causing this is that point-defects may bind with specific types of atoms. The gradient of defect concentration between bulk (where defects are produced) and sinks (where defects disappear) is a path down which the bound chemical elements will follow the transporting point defects (solute drag), so that their concentration at sinks increases. Even in the absence of drag, differences in the diffusional speed (diffusion

coefficient) between chemical species via exchange with vacancies [17] lead to the accumulation of the slowest species close to sinks (inverse Kirkendall effect). Since not only extended defects, but also radiation induced defects act as sinks, accumulation of chemical species may occur close to bubbles, voids or dislocation loops. Chemical species transport mechanisms are illustrated in Figure 10.

Figure 10. Schematic illustration of the different possible mechanisms leading to chemical species redistribution

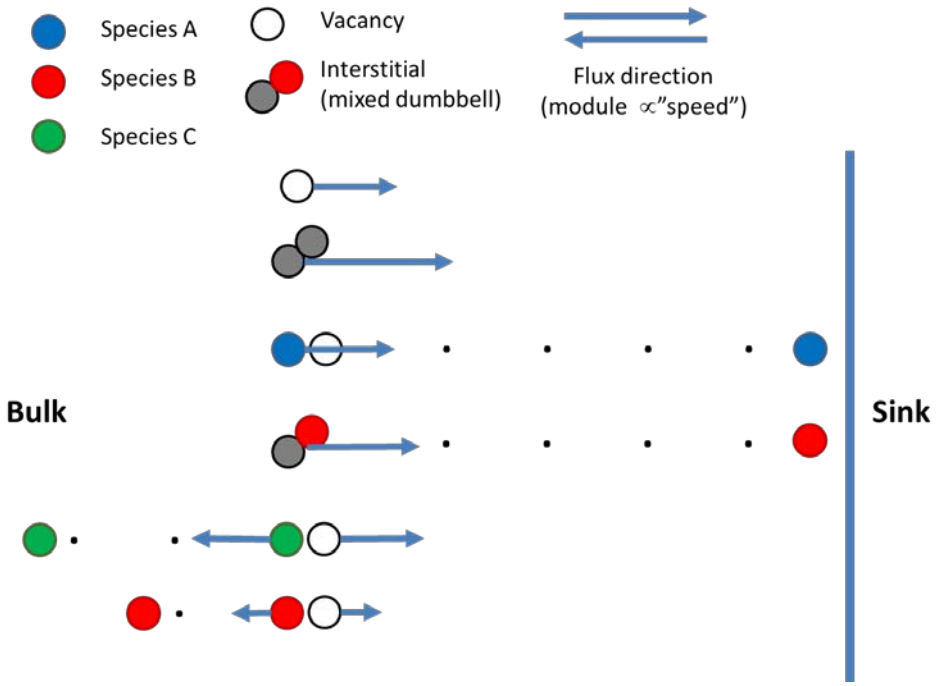

Top-down: (i) both vacancies and self-interstitials produced in bulk migrate towards sinks; (ii) species A can be dragged by vacancies, so it will tend to accumulate at sinks; (iii) species B forms mixed dumbbells (two atoms sharing a lattice position, self-interstitial configuration in metals), so it will be dragged by self-interstitials to sinks; (iv) species C cannot be dragged by vacancies and is a fast diffuser in the opposite direction, so it will tend to move away from sinks (depletion at sinks); (v) species B is also not dragged by vacancies but is a slower diffuser than C, so it will remain closer to sinks (plus it is brought there by self-interstitials).

Typically, clusters of redistributed solute atoms form and grow creating a separate phase, i.e. becoming precipitates, which might be stable from a classic thermodynamic point of view (radiation-enhanced) or might not (radiation-induced). Alternatively, if given chemical species simply accumulate or become depleted in the proximity of sinks, without forming separate phases, as described above, the process is known as radiation-induced segregation, which may but does not need to be also thermodynamically favoured. Segregation may in turn lead to produce, locally, the conditions for different stable thermodynamic phases to form (e.g. local ferritisation where Ni depletes, or formation of Ni and Si rich phases where the opposite occurs, in austenitic steels). The combination of diffusional atomic redistribution with ballistic mixing in cascades might also lead to destabilisation of phases. These processes are illustrated pictorially in Figure 11.

[17] Note that in this case the chemical species will move away from the sinks towards which vacancies are heading.

Figure 11. Schematic illustration of examples of chemical species redistribution processes brought about by irradiation (symbols are as in Figure 10)

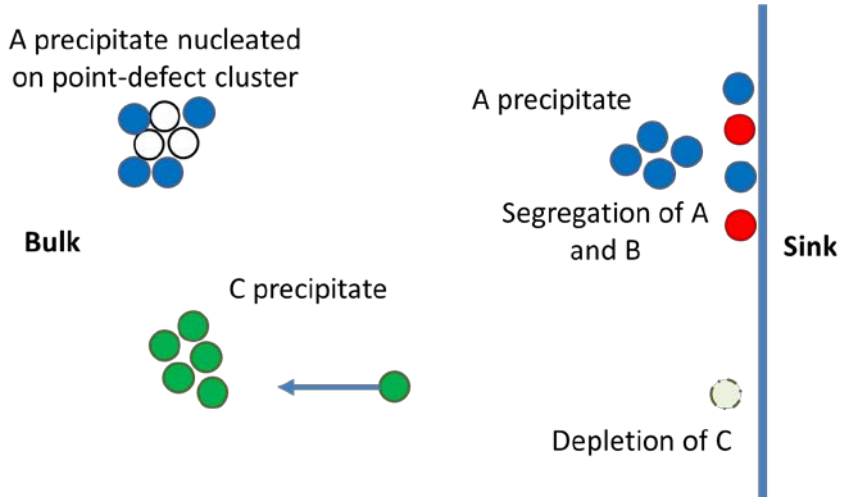

The accumulation of C in the bulk may lead to exceeding the solubility limit with subsequent thermodynamics-driven precipitation (precipitationof C may also occur if initially C is in solid solution but should precipitate); the depletion of C at the sink (e.g. grain boundary) may lead to destabilisation of the matrix, if C is instrumental to keep its stability. Accumulation of A and B at the sink is called segregation; accumulation of A close to sink may lead to local A precipitation, if the solubility limit is locally exceeded.

As a consequence of these changes, driven by atomic-level mechanisms, the properties of the irradiated material will not be the same as before irradiation. The presence of cavities, dislocation loops and precipitates, as well as segregation at dislocations, will obstruct dislocation motion when load is applied: the lower the temperature, the more effectively. Since dislocations are vehicles for irreversible deformation in metals, the material will become harder (more difficult to set dislocations into motion) and also more brittle (emission of dislocations from crack tips as means to arrest or delay crack propagation will be more difficult). This happens especially when the material is irradiated at low temperature, because these conditions lead to a higher density of surviving radiation defects. Embrittlement may also be caused by changes in the cohesion between grains as a consequence of (radiation-induced) segregation that alters the grain boundary chemistry, leading to a shift to inter-granular fracture instead of the normal transgranular fracture, when subjected to a load high enough to allow crack growth. Since this process leads to embrittlement without involving dislocations and radiation defects, it is referred to as non-hardening embrittlement and may occur also at high temperature.

Some classes of radiation defects, especially dislocation loops, can be absorbed by impinging dislocations. When dislocation loops are the dominant radiation-induced nanostructural features, absorption of defects by dislocations during plastic deformation may result in the formation of bands devoided of defects parallel to the dislocation glide plane. These are the clear bands observed under the electronic microscope in deformed metals, especially in austenitic steels (see Section 4.2), for this reason called also dislocation channels. Plastic deformation becomes then localised in these series of narrow parallel bands. Usually, a band crosses an entire grain. The key point is that plastic deformation in a dislocation channel can be several times greater than in the matrix, leading to a series of generally deleterious consequences. The yield strength increase is

followed by a dramatic loss of work-hardening and reduction of elongation. As soon as the material starts to deform irreversibly, it meets little resistance to deformation inside the bands and rapidly fails, after very little uniform engineering strain (Figure 5), although it is suspected that in fact locally the material does retain some capability of strain hardening. Furthermore, the accumulation of dislocations at the grain boundary at the end of the band, if no transmission to the adjacent grain occurs, may lead to a local accumulation of stress and to the possible creation of microcracks there [30]. The latter is considered as an important process to promote intergranular mode of fracture when loaded, also in connection with IASCC.

Microchemical modifications in regions close to grain boundaries or free surfaces due to RIS might also impede the formation of stable oxide layers in contact with water, thereby decreasing corrosion resistance; typically, Cr depletion is considered deleterious in this sense, because Cr-containing oxides are especially stable and effectively protect from further corrosion. The accumulation of voids implies that the removed atoms will be accumulated elsewhere, leading to swelling, i.e. increase of the volume of the piece of material. Finally, the anisotropic absorption of point-defects by dislocations and grain boundaries in a material under stress in the elastic regime will lead to irreversible deformation even though the applied stress is lower than the nominal yield strength, via mechanisms that my differ from generalized dislocation glide, producing deformation in the direction of the load, i.e. irradiation creep and so on.

As can be seen, therefore, all the effects of irradiation described in section 4 from a macroscopic point of view are in fact manifestations of complex physical processes that involve atoms or agglomeration of atoms at the nanometric scale. Physical models and advanced physical modelling tools are thus expected to be able to help in the quantitative understanding of the mechanisms that lead to these effects, including evaluation of their kinetics and of the factors that may accelerate or hinder their occurrence, thanks to the fact that some modelling tools give access also to scales or mechanisms that cannot be studied experimentally. This understanding, that in any case can only be achieved if models are developed on adequate experimental studies, is expected to guide the elaboration of better correlations used in the procedures applied for structural integrity assessments or – if applicable - in the elaboration of design rules, or else of better maps that define the conditions for the occurrence or not of specific pernicious effects, by not only increasing our predictive capability, but possibly also allowing the anticipation of unexpected problems.

5.1 Modelling of hardening and embrittlement in RPV steels

As explained above, the understanding of the processes that lead to changes due to irradiation in the properties of low alloy bainitic steels, specifically the decrease of their fracture toughness, and the subsequent development of reliable quantitative models, is very important in view of underpinning the structural integrity assessment of RPV. Large research efforts are devoted worldwide to this issue, encompassing all aspects: experimental evaluation of the effect of environmental (fluence, flux, temperature, etc.) and metallurgical (mainly composition, but also manufacturing process) variables; extensive use of advanced microstructural examination techniques; evaluation of the mechanical behaviour and its rationalisation; and the development of ETCs. The

development of physical multi-scale models, which include experimental programmes on model alloys and is the focus of the present volume, is also part of this effort.

Based on microstructural analysis of RPV steels and indications from early radiation damage, thermodynamic and dislocation models, the origin of hardening and embrittlement of RPV steels is currently understood in terms of three main contributions: (i) formation of matrix damage, interpreted in terms of small voids and dislocation loops (so small that they cannot be seen in the electron microscope, i.e. their size is below ~2 nm); (ii) precipitation of Cu (insoluble in Fe), but also of Mn and Ni, together with Si and P, forming nanometric (2-4 nm) aggregates or solute clusters; (iii) segregation of P at grain boundaries leading to non-hardening embrittlement. By superposing semi-empirically terms corresponding to each of these processes, different "mechanistic" ETCs have been produced and re-elaborated over the years, based on both new data on which to fit the correlations and new insight on the role of one or another variable (see Fig. 4 as illustrative example). However, the attempt at improving these correlations led also to an ever more complex fauna of nanostructural features that are invoked to contribute to hardening and embrittlement, depending on temperature, flux, fluence and composition. There is not just matrix damage (MD), but stable and unstable MD, the latter having an effect mainly if flux is high and temperature low; there are not just precipitates, but Cu-rich precipitates (CRP) as well as Mn-Ni-rich precipitates (MNP), the latter being favoured in low-Cu steels, when the Ni (and Mn) content is high, at low temperature and high fluence; and so on [31]. MNPs have been postulated to be the precursors of stable hardening phases that, above a certain fluence, would start to *bloom*, i.e. to form in large volume fractions (late blooming phases) [32]. Complexity is growing and even by exploiting in a combined fashion the most advanced microstructural examination techniques, such as atom probe tomography [3,34], high resolution transmission electron microscopy [35], small-angle neutron scattering [36], positron annihilation spectroscopy [37], and others, applied to both irradiated and irradiated-annealed specimens, it remains difficult to come up with a full rationalisation of the RPV embrittlement data and a proper understanding of the relevance of the different mechanisms and variables. For example, the nature of matrix damage in all of its postulated forms remains elusive, while the observation of late blooming phases is controversial. The most recent experimental observations and models suggest that matrix damage is likely not to be separate from precipitates, because the latter would be the consequence of the segregation of solute atoms on point-defect clusters (heterogeneous nucleation). The difficulty of rationalising data is due not only to the limitations and uncertainties of the experimental techniques, but also to the large scatter deriving from inhomogeneities in real steels, to the practical inaccessibility of certain irradiation conditions (e.g. low flux / high fluence) and to the difficulty (and the cost) of having the same material irradiated under conditions where only one variable is changed at a time, to be characterised with several techniques.

Physical models are therefore called to give indications capable of casting some light on all the shaded areas of understanding that still linger. The multi-scale approach is expected to provide tools to explore, for example:

- how and up to what extent different fluxes lead to different nanostructural evolution and with what impact on mechanical properties, so as to have an appraisal of the validity of materials test reactors and surveillance data for high fluence effect prediction with respect to operation;
- how large these differences would become when projected to high fluences, in order to assess the possibility of extending the life of vessels and therefore nuclear power plants beyond the initially envisaged time;
- which, of all possible nanofeatures formed under irradiation that have been theorised or observed (matrix damage and precipitates in all their forms), are the main ones responsible for hardening and subsequent embrittlement and what is their thermal stability and actual mechanical effect. By knowing which compositions and conditions favour the formation of those features, one can identify potentially risky situations, including the consequences of inhomogeneities, as well as being able to devise more effective mitigation strategies.

The above examples highlight the direction that multi-scale modelling developments should follow for RPV steels and emphasises the importance of pursuing this approach.

5.2 Modelling irradiation and environmental effects in austenitic steels

As explained above, the understanding of the processes that lead to changes due to irradiation in the properties of austenitic steels is important in order to avoid unexpected failures in core components that, even if with limited impact on safety, reduce the availability of the plant. The failed component will generally be replaceable, but its replacement is costly and will oblige to prolonged plant outage. A correct understanding should allow failure to be avoided and the elaboration of suitable replacement interventions.

Radiation effects in austenitic steels are more complex and more diversified, although interconnected, than in RPV steels, mainly because of the higher neutron dose received and because of the simultaneous exposure to aqueous environment, as well as because of the somewhat higher temperature in some locations. Their underlying physics and the open questions that physical models are meant to address are separately described in the following subsections.

5.2.1 Microstructural and microchemical evolution

The microstructural examination of irradiated austenitic steels reveals high levels of complexity, with a strong influence of initial conditions, temperature, and variations of local chemical composition [14]. Electron microscope studies reveal that the main players in determining radiation hardening and loss of elongation are different families of defects, namely: "black dots" (so called because this is how they appear in the microscope), dislocation loops of interstitial nature, dislocation networks and also cavities that include both voids and bubbles. Interstitial dislocation loops may exist in two forms: faulted and unfaulted (i.e. perfect). Faulted loops are called Frank loops and are easily obtained as platelets of interstitials, by adding only one atomic layer, although this results in a stacking fault inside the loop. Since the stacking fault energy is low in austenitic steels, this situation is stable (while it would not be in a body-centred cubic structure, such as ferritic/martensitic or bainitic alloys). However, when the loops grow this configuration

becomes progressively more energetically untenable, so larger loops become more stable by unfaulting, i.e. by removing the stacking fault, thereby becoming perfect loops. A key difference between Frank loops and perfect loops is that the former are immobile, while the latter may glide along the direction normal to their habit plane.

In all types of steels irradiated at <250°C, a high density of uniformly distributed black dots (2-4 nm) is detected already at low dose. In SA steels, large (10-50 nm) Frank loops appear as well at growing dose, but no dislocation network exists, although it may develop if dose grows further. In CW steels the initial dislocation network starts recovering under irradiation and, while this process continues, no Frank loops are observed. These start to form only when the dislocation network falls below a critical dislocation density, most likely because, so long as many dislocations exist, these effectively absorb interstitials, preventing the formation of loops. Note that, although it is most likely that black dots are nothing else than small Frank loops, there is no full consensus on this issue, in particular there is evidence that these defects could be a mixture of interstitial and vacancy type defects, the latter in the form of dislocation loops instead of cavities [38]. So here too, like in RPV steels, there remains an elusive part in the damage component that models are expected to help to remove.

By irradiating at ~300-330°C the picture changes; no black dots are seen, but only large Frank loops and a dislocation network is present, also in SA steels, superposed on the initial one in the case of the CW steels. Note that the recovery of the dislocation network explains the initial softening observed at relatively high irradiation temperature versus dose, as exemplified in Figure 6. Furthermore, small cavities (He and maybe also H bubbles) start to appear, depending on the dose. Electron microscope examination has revealed the presence of small cavities, especially along grain boundaries, in specimens that received ~70 dpa at 330°C [39], with production of ~600 appm of He and 2500 appm of H.

Irradiation at higher temperature, > 330°C, results in the appearance of visible populations of cavities and dislocation networks, in addition to loops, since the earliest stages. Cavities become somehow the dominant feature. Below this temperature, the dominance of loops as nanostructural features results in frequent creation of dislocation channels and localised plastic deformation. Above it, swelling is considered to be the dominant radiation effect.

In concomitance with the formation of loops and cavities, chemical species redistribution occurs. RIS leads in austenitic steels to Cr depletion and Ni enrichment close to all sinks, because the diffusion of Cr via vacancy mechanisms by exchange (no drag) is much faster than the diffusion of Ni. Mo is also depleted via a similar mechanism. Small atoms such as Si and P seem to be efficiently dragged by interstitials, so they also accumulate close to sinks. Ni atoms can be probably dragged to sinks by interstitials as well. A very clear proof of sink enrichment by Si, Ni and P under irradiation has been recently obtained by examining with atom probe austenitic alloys ion irradiated at 360°C [40] and 450°C [41], revealing clouds of Ni and Si close to dislocation lines and loops. Overall, this redistribution of atomic species leads to the local formation of Ni and Si (and to a lesser extent P) rich phases, for example the Ni_3Si γ' phase that is abundantly formed in reactor-irradiated SA 316, or enrichment of existing phases in these elements (e.g. carbides), while removing these species from solution [12,14]. It should be noted that the

formation of Ni_3Si is purely a radiation effect, as this phase would not form under thermal ageing, although it is puzzling that this phase appears in the bulk and not at grain boundaries, where the Si and Ni content is even higher [13]. Cr enrichment and Ni depletion in the bulk, if extreme, may cause ferritisation of the austenite away from voids, while Ni-Si-rich phases are typically observed to form close to voids. Cr depletion close to grain boundaries and surfaces will reduce the capability of the material to create protective oxide layers, because Cr oxides are the stable ones. RIS processes are especially efficient at higher temperature (>400-450°C) than LWRs operation, but they are also significantly active at lower temperature.

Physical models are expected, in this framework, to contribute to: unravelling the nature of black dots; anticipating the kinetics of void formation and loop unfaulting, as well as the likeliness of new phase formation; foreseeing RIS and any non-homogeneous redistribution of chemical species, including formation of new phases or destabilization of existing ones, with a view to establishing a quantitative link with macroscopic radiation effects. The mechanisms behind these are illustrated in the sections below.

5.2.2. Hardening, embrittlement and plastic strain localisation

Even though the microstructural changes in austenitic steels are overall better known than in the case of RPV steels, because more easily detected via electron microscope examination, it remains not obvious how to identify which component of the damage plays the dominant role as cause of hardening. In particular, the dramatic hardening observed in SA steels (up to 5 times the un-irradiated value) is not straightforwardly correlated with the densities of defects detected by electron microscopy. In general, a simple dispersed barrier model [42] allows a good correlation with the loop population to be found [10,13]. However, this result is obtained by ascribing empirically to the loops a strength, as obstacles, that they should not have; more sophisticated approaches show the importance of specific dislocation/loop interaction mechanisms, involving mainly small defects [43]. Moreover, it is likely that the formation of secondary phases such as Ni_3Si will also contribute to hardening, and that the different chemical composition around loops may have an effect on their strength as obstacles to dislocation motion. When also voids are considered, the relative importance of these contributions to hardening is not easily deconvoluted.

In addition to this, the full mechanical behaviour under load after irradiation to sufficiently high dose will involve localisation of plastic deformation, especially if loop hardening is dominant, and so, because of the impingement of channels on grain boundaries, inter-granular crack initiation becomes likely to occur. This is a critical condition that is not easily predicted, either from the point of view of dislocation channel appearance, or from the point of view of its propagation and consequences. Physical modelling is expected here to provide substantial support to identify hardening and dislocation channelling mechanisms and to inform polycrystal models capable of anticipating potentially dangerous conditions, under realistic, multiaxial loads.

5.2.3 Swelling and irradiation creep

- Swelling

Swelling is associated with the observation, via electron microscope examination, of massive formation of cavities, especially large voids, inside the material. This is why the

phenomenon that occurs in austenitic steels is more precisely denoted as *void* swelling. The increase in volume is due to the transfer of the material initially located inside the cavities to other locations. Any circumstance leading to efficient removal of interstitials from the bulk towards sinks, leaving behind an excess of vacancies, and to the nucleation and growth of voids, will favour swelling; in contrast, conditions that favour recombination of vacancies with interstitials or more efficient absorption of vacancies at sinks will counteract swelling.

Three mechanisms can be proposed to explain why interstitials are more efficiently removed from the bulk than vacancies (biases):

- diffusion bias: interstitials in metals are more mobile than vacancies, so they are more readily absorbed by sinks;
- dislocation bias: the strain field created by an interstitial is more extended than the one created by a vacancy, so interstitials will be attractively interacting with dislocations from further away than vacancies and thus more efficiently absorbed;
- production bias: interstitial clusters are produced in cascades in different quantities than vacancy clusters and are, if not faulted, more mobile, because they can glide normal to their habit plane. This one-dimensional motion is a very efficient way to remove interstitials from the bulk.

The third bias, which operates only under cascade irradiation conditions, seems to be especially important in connection with the incubation dose of swelling. Microstructural examinations suggest that the two listed below are the microstructural conditions required to give rise to steady-state swelling [11,12]:

- attainment of a quasi-equilibrium dislocation network, that does not vary anymore with time/dose (dislocation density $\sim 3 \cdot 10^{14}$ m^{-2}).
- creation of a glissile type of dislocation network, i.e. Frank loops should unfault and become perfect loops that can freely glide to sinks.

Several of the factors affecting swelling susceptibility of austenitic steels mentioned in Section 4.2.2 can be rationalised with the above concepts in mind:

- The effect of composition can generally be associated with the influence of specific chemical species on vacancy diffusion. Species that *decrease* the effective mobility of vacancies (assuming unchanged mobility of interstitials), like Cr in austenitic steels, will increase the diffusion bias and therefore favour swelling (less vacancies will be disappearing at sinks and their excess in the bulk will increase). The effect of Ni (fast diffuser) and other species on vacancy diffusion is non-monotonic, hence the effect will differ depending on the actual concentration. The occurrence of RIS and subsequent local change of chemical species concentrations will thus make the situation change in time and space during irradiation.
- CW, by providing a high concentration of sinks, increases vacancy removal, so *a priori* decreases swelling susceptibility, although the result obtained will depend on the balance between interstitial and vacancy removal, i.e. on the actual biases. The

effect will be a delay of swelling, by removing more defects of both kind, rather than a suppression.

- Gaseous elements favour cavity nucleation by stabilising small vacancy clusters. At the same time, they will decrease vacancy and vacancy cluster mobility, increasing the diffusion bias. Both effects favour swelling, even though the growth of voids will be slower.

- High enough irradiation temperatures are needed for small vacancy clusters to become thermally unstable, thereby providing a source of single vacancies that make the growth of nucleated cavities effective at the expenses of smaller clusters, that otherwise would not coalesce. However, high temperature will also increase mobility and the removal of vacancies at sinks and very high temperatures will even make voids thermally unstable; the overall net effect will be a balance between these opposing tendencies.

- Lower dose-rate will provide more time for nucleated cavities to grow at the expenses of small ones, before new cavities are nucleated, leading to lower densities but larger volume fractions, while allowing more efficient absorption of interstitials by sinks. The lower the temperature, the longer the time required for larger cavities to grow at the expenses of small ones because of lower diffusivity and lower emission, which explains why the lower the temperature the lower the dose-rate needs to be to have effective swelling. This is exactly the situation with LWRs which operate at low temperature, but also low dose-rate. However, what plays a major role here is not the growth of voids, but the growth of loops. Lower dose-rates lead to the formation of less but larger Frank loops and larger loops will favourably unfault, leading earlier (in terms of dose) to a microstructure of gliding dislocations, that will determine the onset of swelling [44].

Clearly, the key parameter that must be known to be able to accommodate swelling when designing or operating components is the critical dose above which the onset of steady-state swelling occurs, d_c. From a fundamental point of view, it is also important and challenging to understand and explain in terms of physical mechanisms the non-saturating nature of swelling, i.e. the fact that, when steady-state is reached, it continues to develop indefinitely at constant rate, at least in steels.

Even though conceptually the fundamental mechanisms responsible for swelling have been most likely all identified and their identification allows one to understand qualitatively the effect of different factors on delaying or anticipating d_c, to date this parameter can only be predicted based on extensive experimental data that, because of the wide range of conditions that should be explored in terms of temperature, flux and fluence, are not easy to obtain. Moreover, the strong dependence of this parameter on initial material microstructure and composition means that empirical swelling rules are only valid for a specific type of material, with defined composition and microstructure. The expectation from physical models is that they should be able to include correctly all the important physical variables that play a role in swelling, so that the same model can be reliably transferred to conditions and compositions that cannot be explored experimentally, or to materials with different compositions and microstructure, including the possibility of allowing an assessment of the effects of local inhomogeneity and solute

redistribution on swelling onset. For example, this would allow fast reactor data, which are fairly abundant, to be extrapolated to LWR conditions.

So, the expectation from physical models is that they should, ideally:

- Describe the nanostructural evolution in the given material up to doses on the order of d_C, as a function of steel composition, sink density (dislocations, grain boundaries), temperature, dose-rate;
- Include the correct mechanism of onset of steady-state swelling, which should only become activated at d_C; i.e. the model should correctly and spontaneously predict the value of d_C; Spontaneously provide the correct $\dot{S}_{ss}$, for the given material. The complexity of the problem, the large number of variables involved (especially evolving local composition and dislocation microstructure) and the high doses generally required to reach swelling steady-state (with subsequent high activation of the concerned materials) make the problem especially difficult and expensive to address. A very useful and deep discussion of the difficulty of developing swelling models, especially focused on the problem of the non-saturability of swelling, can be found in [45].

▪ Irradiation creep

Of all irradiation effects, creep is probably one of the least understood. Several possible mechanisms exist whereby stress removal might be occurring, but there is no consensus on the dominant ones in each case.

Qualitatively, the appearance of irradiation creep can be explained as follows. In the presence of tensile stress, dislocation loops will be preferentially oriented in the direction that minimises their energy, i.e. with the compressive region of the strain field oriented as the tensile strain, which means that their habit plane will be as close to being normal to the principal stress as the crystallographic orientation permits. By growing in this way until meeting the grain boundary, each loop will add atomic layers, all of them normal to the principal stress, thereby creating expansion in that direction (Figure 12). What, however, is not clear is whether loops are preferentially *created* (*nucleated*) in the favourable orientation (stress-induced preferential nucleation, SIPN), or only those that are in favourable orientation manage to *grow*, while those that are not preferentially oriented shrink (stress-induced preferential absorption, SIPA).

Stress is also assumed to polarise migrating point-defects, making their diffusion and absorption by sinks, especially dislocations, anisotropic. Specifically, vacancies will tend to be absorbed by dislocations that are *squeezed* by the applied stress, while interstitials will tend to be absorbed by dislocations that are *pushed* by the applied stress, leading to jog formation and dislocation climb and subsequent plastic deformation in accordance with the load, even if this is not sufficient to make dislocations glide (Figure 13a). The preferential climb of dislocation lines may also lead to the overcoming of obstacles and subsequent glide. At low temperature, when vacancies are immobile, climb will occur exclusively via interstitials, so always in the same direction, thereby exacerbating irradiation creep (Figure 13b).

Figure 12. Atomic configuration of a ½⟨111⟩ loop in BCC, showing the compressed region, where the additional atomic layer is (actually three extra layers) and the tensed region around the edge of the loop (left), schematic representation of the ideal orientation of loops to decrease the free energy of the system (centre), schematic illustration of the mechanism whereby an expanding loop that reaches a grain boundary produces an elongation in the direction of the load (right)

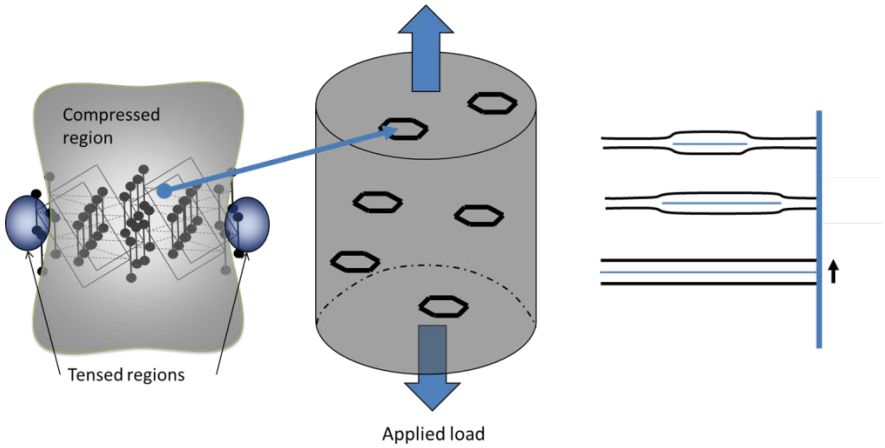

Figure 13. Preferential and anisotropic absorption of vacancies (V) and interstitials (I) depending on the orientation of the dislocation with respect to load

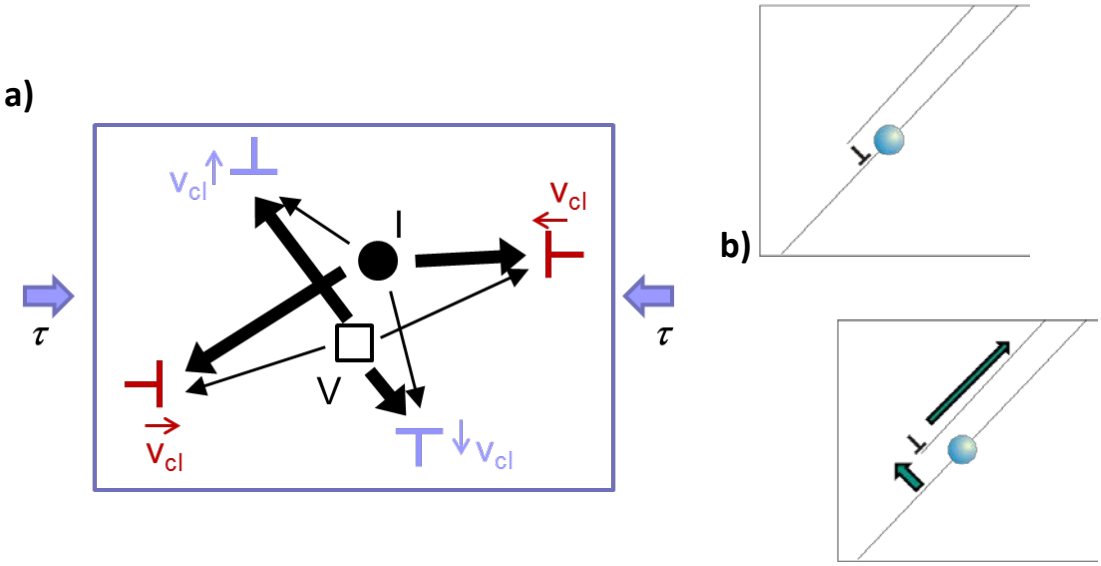

Under normal conditions the climb direction will be isotropic. Under stress and under irradiation, interstitials will tend to be absorbed by dislocations that by doing so will climb along the direction of the load, while vacancies by dislocations that will climb normal to it. The result is shrinking and expansion according to the load (a) Preferential climb will also lead to dislocations get around obstacles that prevented glide, giving them the possibility to do so and leading to further deformation (b) .

Source: E. Clouet.

In summary, irradiation creep is in essence the result of how stress influences the way point-defect clusters, especially interstitial clusters, are created and grow, as well as the way point-defects diffuse and are absorbed by sinks, mainly dislocation loops and lines. Preferential absorption of some defects versus others is also, as seen, the origin of swelling, hence the strong connection between the two phenomena. Early overviews on possible irradiation creep mechanisms can be found in [46].

Irrespective of the general qualitative understanding of the mechanisms responsible for irradiation creep, quantitatively it is far from simple to provide a correct estimate of the relative importance of each of them, even more in synergy with swelling. Moreover, these are inherently atomic-level processes that call for a physical modelling approach to be properly evaluated and then inserted in higher level models that are expected to allow the plastic creep strain to be properly predicted and included in the evaluation of macroscopic shape changes. A physical model predicting plastic deformation due to irradiation creep should thus be able to:

- Describe the influence of a stress field on the nanostructure evolution under irradiation, including preferential nucleation and/or growth of loops and anisotropic diffusion and absorption, as well as the influence of stress below yield on the dislocation network, translating these changes into a plastic deformation contribution;
- Allow the derivation of climb-driven dislocation mobility laws, as well as other plastic flow laws, to be used in continuum models of viscoplasticity, coupled to models describing nanostructural and dislocation network evolution under irradiation;
- Take into account the synergistic interaction of irradiation creep with void swelling;
- Enable the performance of finite element type simulation of the mechanical behaviour of components in operation, taking correctly into account irradiation creep effects.

As progressive steps towards these objectives, physical models should enable:

- The development and use of atomic-level simulation tools to assess the influence of a sub-yield applied stress field on stability and mobility of defects. This will allow the evaluation of the relative importance of irradiation creep mechanisms, such as SIPN, SIPA, and anisotropic diffusion and absorption, as well as a study of climb;
- Development and use of dislocation-level simulation tools based on either discrete dislocations or dislocations densities, possibly coupled with nanostructure evolution tools, to investigate climb & glide mechanisms. This should allow the derivation of relevant dislocation mobility laws.

5.2.4 Irradiation assisted stress corrosion cracking (IASCC)

If irradiation creep is the least understood of the effects of irradiation, it is easy to guess that the understanding of IASCC - a process of creation of inter-granular cracks that depends not only on irradiation, but also on the applied stress (in this similarly to creep), as well as on the environment (contact with water) -remains to a large extent elusive.

The eluding nature of IASCC is due to the fact that, even though some factors are often dominant to increase the susceptibility to it, and the simultaneous presence of environment, stress and radiation effects is mandatory, there are almost invariably cases in which intergranular cracking is observed even when generally dominant variables take a very low value (see Section 4.2.3). In those cases some other variables reach a sufficiently high value to compensate for the lack of the normally dominant ones. In other words, IASCC is a continuous function of several variables that cannot be separated and all have more or less the same importance. Thus, predicting the combination of levels of factors that will lead to the appearance of intergranular cracking under conditions of stress-corrosion and irradiation is extremely challenging and, in practice, statistical approaches are often adopted.

The radiation effects that are thought to influence IASCC susceptibility are: radiation induced segregation, radiation defect production and subsequent macroscopic effects, such as radiation hardening and localised deformation, as well as increased stress from differential swelling. The effect of irradiation creep can be tricky: residual stress relaxation at welds or bolts will decrease IASCC susceptibility, but eventually the strain produced might assist the production of intergranular cracks. The latter might be the reason why the dependence of IASCC on fluence is complex: increasing fluence leads to hardening and localisation of deformation, as well as stress accumulation when swelling occurs, but the concomitant stress relaxation due to irradiation creep will counteract these effects, until the moment it might add to them. Another effect of irradiation that assists intergranular cracking in contact with water is radiolysis, i.e. the creation of oxidising ionic species in water by neutron bombardment: the effect of this is to increase the ECP, thereby increasing the susceptibility to IASCC.

RIS is considered as one major factor in increasing the susceptibility to intergranular cracking. In austenitic Fe-Cr-Ni model alloys RIS leads Ni to segregate to GB, while both Cr and Fe deplete. In commercial austenitic stainless steels about the same happens, although Fe might both enrich or deplete, because of the influence of other solutes. Amongst these, Si, generally present in fair amount in austentic stainless steels, enriches at the GB up to 10 times the bulk concentration. As mentioned, Cr depletion and Ni enrichment is the consequence of the fact that in these materials Ni is the slow diffuser, Cr is the fast diffuser, and Fe is intermediate, thus the exchange of atomic position of these species with vacancies that move towards sinks, here grain boundaries, creates a flux of atomic species in the opposite direction, i.e. away from grain boundaries. This separation will be most efficient for Cr (and Fe), thereby leaving Ni behind, while Si enrichment is most likely the consequence of transport via interstitial mechanism (see Fig. 10).

Several studies show that IASCC susceptibility increases when the grain boundary Cr level decreases: this happens because of the progressively lower capability of recreating a stable oxide layer to protect against further corrosion while the crack propagates through the GB, possibly with abnormal growth of the oxide, leading to further cracking. However, while Cr depletion saturates at ~5 dpa (300°C), IASCC susceptibility generally appears above a certain dose and then grows fast to 100%, in a non-saturating fashion, at fluences where the RIS evolution has already saturated [13], as illustrated in Figure 9. Likewise, annealing experiments in which radiation damage recovers with time show that RIS takes a long time to be removed, while IASCC susceptibility in this case drops almost

immediately to zero, again suggesting no direct correlation between the two. In addition, there is a significant amount of scatter in the data. More to the point, while Cr levels above 16-18% effectively protect against intergranular cracking, lower Cr levels admit a susceptibility that may vary from 0 to 100%. All this leads to the conclusion that GB Cr depletion is an important, but insufficient condition for IASCC to occur. Probably one should not even say that Cr depletion induces IASCC, but more correctly that a sufficiently high Cr concentration at GB is a good guarantee that IASCC susceptibility will remain low, probably overruling other important factors, without implying that Cr depletion necessarily causes it. Also the increase in Si content at grain boundaries seems to promote intergranular cracking due to stress-corrosion, but the connection to IASCC is not fully proven.

Hardening is often cited as an additional necessary condition to increase intergranular stress-corrosion cracking susceptibility [47], given the good correlation found experimentally between the two, again in a threshold-like fashion (IASCC susceptibility appears above 500-600 MPa of yield strength and increases with it [10]), even irrespective of whether the yield strength increase is due to cold-working or irradiation [13]. However, once again, while the density and size of hardening radiation defects, and therefore radiation hardening as well, grow versus fluence with a power exponent less than 1 and tends to saturate from ~5 dpa (see illustration in Figure 9), this does not apply to IASCC susceptibility. Likewise, in annealing experiments the drop of IASCC susceptibility over time is much faster than the recovery from hardening. Finally, samples showing the same level of hardening, but obtained from different combinations of irradiation and cold-working, showed different levels of intergranular stress-corrosion cracking susceptibility, suggesting that it is not hardening as such, but rather a specific microstructure that favours or hinders crack initiation in water under stress. This observation shifts the attention to microstructural consequences of hardening, such as localisation of plastic deformation in clear bands, rather than hardening itself: these will be more or less likely, depending on the type of microstructure that causes hardening.

A correlation is found between decreasing stacking fault energy (SFE) and increasing susceptibility to stress corrosion cracking: this correlation has been attributed to the fact that low SFE leads to split dislocations and makes cross-slip (change of dislocation glide plane to a plane inclined with respect to the initial one) more difficult, thereby enhancing the tendency to planar plastic deformation and hence to plastic flow localisation [13]. Similarly, the microstructure produced by irradiation leads to plastic deformation localised in clear bands, as already mentioned. The large plastic strain inside bands translates into a pile-up of dislocations at the end of the channels, i.e. impinging on grain boundaries. In general terms, this situation is expected to initiate cracks at grain boundaries, promoting intergranular fracture, regardless of the environment, when a critical local stress is exceeded. Recent work shows indeed that early models to calculate the stress induced by clear bands impinging on grain boundaries led to values that are half the real ones [30]. It is therefore sensible to believe that a localised and planar mode of deformation, whether due to low SFE or to irradiation, will enhance the appearance of IASCC. In environment, the large amount of strain inside the bands that must be accommodated by the grain boundary results in a high local stress leading there to the rupture of the oxide layer, causing the initiation of an intergranular crack with exposure of the metal to water and subsequent corrosion. Also the propagation of existing grain boundary cracks will be

promoted if the clear band impinges on the crack tip, supplying dislocations that result in continual rupture of the crack tip oxide and therefore crack extension and faster crack growth. The fact that irradiation was more effective than CW in initiating intergranular stress-corrosion cracking is possibly a sign of the importance of planar localised deformation for IASCC [12]. Recent investigations seem to lead to the conclusion that indeed localised deformation could be the most important factor in IASCC [48].

Other radiation-induced factors that may further contribute to promoting IASCC are on the one hand internal stresses induced by swelling, especially differential swelling, as well as strain due to irradiation creep, but also the possibility of accumulating He bubbles at grain boundaries, especially in LWRs where He production is higher than in fast reactors, and, possibly, grain cohesion decreased by specific segregating solute atoms, such as P.

It is clear that IASCC is a real challenge for modelling. From experiments many uncertainties remain as to the important factors and the mechanisms: it is difficult even to build a conceptual model to be used as a guide for a quantitative one. Moreover, modelling IASCC to estimate its likeliness implies combining a series of models for several simultaneous processes:

- Correct microstructural (radiation defects) and microchemical (RIS) evolution under irradiation;
- Effects of this microstructure on mechanical properties and deformation modes: prediction of hardening and clear band formation;
- Details of interaction between clear bands and grain boundaries to evaluate crack initiation;
- Stability of oxide layer and kinetics of formation when the local composition has been altered by RIS, in interaction with water;
- Correct evaluation of the electrochemical corrosion potential including effect of irradiation and local geometry;
- Correct evaluation of the local stresses, including the effect of differential swelling and irradiation creep, the latter being beneficial or exacerbating depending on the competition between stress relaxation and level of strain;

Models should ideally provide both the probability of crack initiation and an evaluation of the crack growth rate. For the latter tentative models have been proposed based on the evaluation of the oxide rupture rate due to crack tip strain: they include the increase of yield strength due to irradiation and the effect of RIS on oxidation and re-passivation rates [10]. But models that predict initiation beyond statistical approaches at the moment do not exist.

5.3 The importance of modelling-oriented experiments

In the previous sections the results of experiments in which materials of different composition and history have been exposed to irradiation using different means, under different conditions and, if relevant, in a specific environment, have been summarily reviewed, based on authoritative publications and on some theoretical studies. This

allowed "conceptual models" to be deduced and described. Conceptual models are frameworks based on the observed correlations between variables (a good example are ETCs for RPV steels), in which a combination of plausible physical mechanisms is used to rationalise the experimental observations. Without the support of a conceptual model it is essentially impossible to develop any quantitative model endowed with some predictive capability. When the processes of interest are especially complex, as is generally the case for radiation effects on materials, model development is therefore crucially based on the performance of "modelling-oriented" experiments. These are designed explicitly to explore the effect of different values of variables and parameters that are considered of importance, under as properly controlled conditions as possible, so as to identify the underlying physical mechanisms. Modelling-oriented experiments strive to separate effects and, in this endeavour, model materials are often used, instead of materials of technological relevance. Model materials either have a simpler chemical composition or have been treated in such a way that the consequences of specific microstructures are analysed separately: even though eventually models have to be validated against the materials of technological interest, experimenting on model materials is an essential part of any modelling effort.

Physical materials modelling is based on the assumption that macroscopic effects such as embrittlement or swelling are the consequences of microstructural modifications undergone when the material is exposed to specific conditions, such as irradiation at a certain temperature. Physical multiscale models are built following this fundamental assumption, i.e. assuming that each physical process needs to be modelled at the relevant length and time scales and that somehow the output of this model needs to be the input for higher scale and coarser models. There are scales that *are not* observable experimentally; but for those that *are* accessible to experiments it is of paramount importance to extract as much information as possible. This is why advanced and refined microstructural examination techniques, like electron microscopy in all of its forms and varieties [35], and analytical techniques such as atom probe tomography [33,34], small-angle neutron scattering [36], positron annihilation spectroscopy [37], x-ray absorption spectroscopy [49], internal friction [50], magnetic after-effect [51], and so on, are by now, all combined, irreplaceable tools in the development of physical models that describe radiation effects: their use makes integral part of modelling. These are the techniques that allow plausible physical mechanisms to be identified and conceptual models to be built. Models must include these physical mechanisms and, if properly parameterised, they provide tools to verify quantitatively if those physical mechanisms are actually capable of producing the effects observed at macroscopic level, i.e. to give a prediction. The comparison of this prediction with the experimental measurements allows the model to be validated, but in fact the model has been developed with its roots in the experimental observations as well. Often, the reason why a model does not provide correct predictions is because the parameters are not correct, because there are quantities whose values are not known and cannot be measured experimentally, or else because there are missing mechanisms, that no experimental techniques can observe and explore and/or no-one thought of. In the latter case the problem is essentially the lack of a correct or complete conceptual model, which calls for further experimental investigations, but also for the development of different interpretative paradigms that may be based on the use of physical modelling tools, in particular computer simulation. In the other cases, unknown values are typically fitted or calibrated to known conditions, hoping that their validity can be extended beyond the

range of fitting or calibration. It is quite obvious that, the more adherent to physics a model, the higher the probability that it will be valid beyond calibration range. Furthermore, it is also obvious that, if the parameters to be calibrated have a precise physical meaning, it is possible to evaluate in which range they should vary and even to anticipate that their values will have to change, if the conditions to which the material is subjected change in a certain way. This is the essential strength of physical modelling as compared to the development of empirical correlations between effects and variables.

But the strength of modern modelling techniques goes beyond this. Nowadays (and actually for long in some cases) there are modelling tools that "see where experiments cannot see". Obviously, the validation of these models is difficult or impossible, uncertainties remain that are sometimes hard to evaluate; in some cases an "act of faith" in the model has to be taken. Yet, in the absence of experimental ways to measure certain materials properties or to quantify and explore specific mechanisms, these modelling tools offer a way to improve greatly the accuracy of higher scale models, especially the parameters and variables used there. The result of these higher scale models can be then compared with experimental results and a favourable comparison will be an indirect proof that the parameters and mechanisms obtained with the underlying models are probably sufficiently correct. Furthermore, the approach based on the idea that modelling tools for the correct length and time scales need to be applied allows often the identification of physical mechanisms that could not be guessed from experiments, or at least provides a number of possibilities that can be then used to guide experiments, that will be performed to search traces of those mechanisms. This discussion should clarify once and for all that - as has always been in science- experiments and models are two intimately connected tools in our hands to try to understand physical reality better and possibly predict the course of the events based on this understanding, in a quantitative way. The fact that modern modelling tools with their roots in computer science have become very sophisticated and precise calls for equally sophisticated and precise experimental techniques to match them. Together, these tools and techniques provide very powerful means to advance in our comprehension of, in this case, materials behaviour, including the possibility of progressing in technological applications beyond empirical qualification of systems and components.

6. Conclusions

In this chapter an attempt has been made to introduce the reader step by step to the main features of steels used in current nuclear power plants, the reasons why they have been chosen and are still used, the problems they face when subjected to irradiation (in a certain chemical environment) and the origin of these problems. The last point has been especially expanded, in order to provide an idea of existing conceptual models, thereby highlighting what is understood and what is not. This led to discuss why models are necessary and what they are in principle expected to provide. Obviously, the ultimate goal is that, by understanding the origin of the problems, it should be possible to mitigate their effects.

Table 4 summarises what the models are expected to address and provide, in connection with the different issues that affect nuclear steels used in current nuclear power plants.

The chapters of this volume will overview different important effects of irradiation on steels used in the core of current nuclear power plants, through different length and time scales, providing examples of physical models that have been developed to address them. Conclusions can be drawn from them to further improve the conceptual models that, unavoidably, constitute the necessary framework for correct (or incorrect, if the framework is wrong) decisions of technological relevance to be made.

Table 4. Summary of problems that physical modelling should address for different issues affecting nuclear steels used in current power plants

Materials → Issues ↓	RPV steels	Austenitic steels
Microstructural and microchemical evolution	Mechanism and kinetics of formation of solute clusters and precipitates, in connection or not with matrix damage; spatial distribution of matrix damage and precipitates; segregation at dislocations and grain boundaries; dependence on temperature and dose-rate	Nature of black dots; kinetics of void formation and loop unfaulting (identification of d_C for swelling) as a function of composition and sink microstructure, versus temperature and dose-rate; likeliness of new phase formation or destabilisation; kinetics and extent of radiation-induced segregation
Hardening and embrittlement Plastic flow localisation (if relevant)	Dominant nanostructural feature as to hardening and embrittlement Effect of flux on nanostructural/microchemical evolution and impact on mechanical properties, both tensile behaviour and fracture toughness (MTR vs surveillance) Reliable extrapolation of data (microstructure and mechanical properties) to high fluence, beyond what has been reached in current vessels	Hardening and dislocation channelling mechanisms; polycrystal models capable of anticipating potentially dangerous conditions, under realistic, multiaxial loads
Swelling		Include all important physical variables to guarantee transferability to inexplored conditions and compositions / microstructures, allowing for effects of local inhomogeneity: Nanostructural evolution up d_C, vs composition, sink density, temperature, dose-rate, … (predict d_C); Mechanism of onset of steady-state swelling, at d_C Provide $S_{ss}^{\cdot}$
Irradiation creep		Stress field influence on nanostructure evolution under irradiation: preferential nucleation and/or growth of loops; anisotropic diffusion and absorption; influence of stress below yield on dislocation network; corresponding plastic deformation contribution. Climb-driven dislocation mobility laws for continuum viscoplasticity models, coupled to nanostructural and dislocation network evolution models under irradiation; Synergistic interaction irradiation creep / void swelling; Mechanical behaviour of components in operation, taking into account irradiation creep strain
Irradiation assisted stress corrosion cracking		*See hardening, embrittlement and plastic flow localisation*, moreover: Interaction between dislocation channels and grain boundaries (crack initiation); Stability of oxide layer and kinetics of formation when the local composition is altered by RIS, in interaction with water; Electrochemical corrosion potential including effect of irradiation and local geometry; Local stresses, including effect of differential swelling and irradiation creep.

References

[1] H.V. Atkinson "Structural and Functional Materials", Material Science and Engineering, Vol. II, UNESCO Encyclopedia of Life Support Systems, www.eolss.net .

[2] M.F. Ashby, D.R. Jones, "Engineering Materials 1 – An Introduction to their Properties and Applications", 3rd Edition, Elsevier Butterworth-Heinemann (2005).

[3] B. R. T. Frost, in "Nuclear materials.", Volumes 10A and 10B of Materials Science and Technology – A Comprehensive Treatment, R. W. Cahn, P. Huusen, and E. J. Kramer, Eds., Weinheim, VCH 1994, p. 557.

[4] B. Tomkins, "Structural integrity issues in the nuclear industry", in: "Comprehensive Structural Integrity" – Vol. I (2003) 173-192.

[5] ASTM Standard E293-01 (2007), "Standard Practice for Characterizing Neutron Exposure in Iron and Low Alloy Steels in Terms of Displacements Per Atom (DPA)", E706 (ID), vol. 12.02, American Society for Testing and Materials, West Conshohocken, PA.

[6] J.F. Ziegler, J.P. Biersack and U. Littmark, "The Stopping and Range of Ions in Solids", Pergamon, New York (1985).

[7] T. Sato, K. Niita, N. Matsuda, S. Hashimoto, Y. Iwamoto, S. Noda, T. Ogawa, H. Iwase, H. Nakashima, T. Fukahori, K. Okumura, T. Kai, S. Chiba, T. Furuta and L. Sihver, "Particle and Heavy Ion Transport Code System PHITS, Version 2.52", Journal of Nuclear Science & Technology 50(9) (2013) 913-923..

[8] S.J. Zinkle and G.S. Was, "Materials challenges in nuclear energy", Acta Materialia 61 (2013) 735-758.

[9] C. English, J. Hyde, "Radiation damage of Reactor Pressure Vessel Steels", in "Comprehensive Nuclear Materials", *R.J.M. Konings Ed.-in-chief, Elsevier Ltd. (2012), 4.05.*

[10] K. Fukuya*, "Current understanding of radiation-induced degradation in light water reactor structural materials", Journal of Nuclear Science and Technology 50(3) (2013) 213-254.*

[11] *F.A.* Garner, "Void swelling and irradiation creep in light water reactor (LWR) environments", in: "Understanding and mitigating ageing in nuclear power plants", P.G. Tipping Ed., Woodhead Publishing Ltd (2010).

[12] F.A. Garner, "Radiation Damage in Austenitic Steels", in "Comprehensive Nuclear Materials", *R.J.M. Konings Ed.-in-chief, Elsevier Ltd. (2012), 4.02.*

[13] G.S. Was and P.L. Andresen, "Stress Corrosion Cracking Behaviour of Alloys in Aggressive Nuclear Reactor Core Environments", Corrosion 63 (2007) 19-45.

[14] P.J. Maziasz and J.T. Busby, "Properties of Austenitic Steels for Nuclear Reactor Applications", in "Comprehensive Nuclear Materials", *R.J.M. Konings Ed.-in-chief, Elsevier Ltd. (2012), 2.09.*

[15] L.E. Steele and R.H. Sterne, Nuclear Engineering & Design 10 (1969) 259-307.

[16] TECHNOLOGY ROADMAP UPDATE FOR GENERATION IV NUCLEAR ENERGY SYSTEMS – JANUARY 2014, published by the nuclear energy association (NEA) of the OECD, (https://www.gen-4.org/gif/jcms/c_60729/technology-roadmap-update-2013).

[17] C. Lemaignan, A.T. Motta "Zirconium Alloys in Nuclear Applications", Wiley (2006).

[18] "Integrity of reactor pressure vessels in nuclear power plants: assessment of irradiation embrittlement effects in reactor pressure vessel steels", IAEA nuclear energy series, ISSN 1995-7807 ; no. NP-T-3.11, STI/PUB/1382 ISBN 978-92-0-101709-3, Vienna (April 2009) – available at http://www-pub.iaea.org/MTCD/publications/PDF/Pub1382_web.pdf .

[19] R.W.K. Honeycombe, "Steels – Microstructure and Properties", Edward Arnold Ltd. (1981).

[20] R.B. Jones, International Materials Reviews 56 (2011) 167.

[21] NUREG-1511, "Reactor Pressure Vessel Status Report," U.S. Nuclear Regulatory Commission, December 1994.

[22] M. Brumowski "Reactor pressure vessel (RPV) annealing and mitigation in nuclear power plants", in: "Understanding and mitigating ageing in nuclear power plants", P.G. Tipping Ed., Woodhead Publishing Ltd. 2010, pp. 374-386 (chapter 12).

[23] T. Byun, K. Farrell, "Plastic instability in polycrystalline metals after low temperature irradiation", Acta Materialia 52 (2004) 1597.

[24] F.A. Garner, M.B. Toloczko, B.H. Sencer, Journal of Nuclear Materials 276 (2000) 123.

[25] EPRI Materials Degradation Matrix, Revision 3. EPRI, Palo Alto, CA: 2013. 3002000628.

[26] S.I. Porollo, A.M Dvoriashin, Yu.V. Konobeev, A.A. Ivanov, S.V. Shulepin, F.A. Garner, J. Nucl. Mater. 359 (2006) 41-49.

[27] A.R. Causey, C.K.C. Carpenter, S.R. McEwen, J. Nucl. Mater. 90 (1980) 216-223.

[28] NUREG/CR-7153, Vol. 2, ORNL/TM-2013/532, Expanded Materials Degradation Assessment (EMDA) Volume 2, October 2014.

[29] L. Malerba, "Multi-scale modelling of irradiation effects in nuclear power plant materials", in: *Understanding and mitigating ageing in nuclear power plants: Materials and operational aspects of plant life management (PLiM)*, Tipping, P.G. (Ed.), Woodhead Publishing Ltd., 2010, p. 456 (Chapter 15).

[30] M. Sauzay and K. Vor, "Influence of plastic slip localization on grain boundary stress fields and microcrack nucleation", Engineering Fracture Mechanics 110 (2013) 330-349.

[31] G.R. Odette, G.E. Lucas, " Embrittlement of nuclear reactor pressure vessels",JOM-Journal of the Minerals Metals & Materials Society 53 (2001) 18.

[32] G.R. Odette, R.K. Nanstad, " Predictive reactor pressure vessel steel irradiation embrittlement models: Issues and opportunities",JOM- Journal of the Minerals Metals & Materials Society 61 (2009) 17.

[33] B. Gault, M.P. Moody, J.M. Cairney, S.P. Ringer, "Atom Probe Microscopy", Springer Series in Materials Science, vol. 160 (2011).

[34] M.K. Miller and R.G. Forbes "Atom Probe Tomography", Materials Characterization 60 (2009) 461-469.

[35] M. Jenkins, M. Kirk, *Characterization of Radiation-Damage by Transmission Electron Microscopy*, Taylor Francis Ltd, London, 2000.

[36] I. Grillo, "Small-Angle Neutron Scattering and Applications in Soft Condensed Matter", in Soft matter characterization, Eds. R. Borsali, R. Pecora, Springer Verlag (2008), chapter 13.

[37] P. Hautojärvi, C. Corbel, Positron spectroscopy of defects in metals and semiconductors", in: "Positron Spectroscopy of Solids, Eds. A. Dupasquier, A.P. Mills, IOS Press (1995).

[38] J.T. Busby, M.M. Sowa, G.S. Was, E.P. Simonen, Phil. Mag. 85 4-7 (2005) 609-617.

[39] D.J. Edwards, F.A. Garner, S.M. Bruemmer, P. Efsing, " Nano-cavities observed in a 316SS PWR flux thimble tube irradiated to 33 and 70 dpa", J. Nucl. Mater. 384 (2009) 249-255.

[40] Z. Jiao, G.S. Was, "Novel features of radiation-induced segregation and radiation-induced precipitation in austenitic stainless steels", Acta Mater. 59 (2011) 1220.

[41] A. Volgin, "Characterization and understanding of ion irradiation effect on the microstructure of austenitic stainless steels", PhD disseration, U. Rouen, (2012).

[42] A.K. Seeger, "On the theory of radiation damage and radiation hardening", in:Proceedings of the Second United Nations International Conference on The Peaceful Uses of Atomic Energy, vol. 6, pp. 250–273, Geneva, September 1958, United Nations, New York.

[43] G. Monnet, "New insights into radiation hardening in face-centered cubic alloys", Scripta Materialia, in press, http://dx.doi.org/10.1016/j.scriptamat.2014.12.003.

[44] T. Okita, T. Sato, N. Sekimura, T. Iwai, F.A. Garner, " The synergistic influence of temperature and displacement rate on microstructural evolution of ion-irradiated Fe–15Cr–16Ni model austenitic alloy", JNM 367-370 (2007) 930-934.

[45] A.V. Barashev, S.I. Golubov, "Unlimited Damage Accumulation in Metallic Materials Under Cascade-Damage Conditions", Report nr. ORNL/TM-2008/141 (September 2008).

[46] J.R. Matthews, M.W. Finnis, "Irradiation creep models – An oveview", Journal of Nuclear Materials 159 (1988) 257.

[47] K. Chatani, Y. Kitsunai, M. Kodama, S. Suzuki, Y. Tanaka, S. Ooki, S. Tanaka, T. Nakamura, "Irradiation assisted stress corrosion cracking susceptbility of core component materials", Proc. 12th Intl. Conf. On "Environmental Degradation of

Materials in Nuclear Power System – Water Reactors", Edited by T.R. Allen, P.J. King, L. Nelson, TMS (The Minerals, Metals and Materials Society), 2005.

[48] Z. Jiao, G.S. Was, " Impact of localized deformation on IASCC in austenitic stainless steels", JNM 408 (2011) 246.

[49] G. Bunker, Introduction to XAFS, Cambridge (2010).

[50] "Mechanical Spectroscopy Q^{-1} 2001 with Applications to Materials Science", Ed. by R. Schaller, G. Fantozzi, R. Gremaud, Trans Tech Publ. (2001).

[51] B. Minov, M. Konstantinovic, L. Dupré, Electr. Rev. 87 (2011) 120

Chapter 2.

Displacement cascade damage production in metals

R.E. Stoller[1], K. Nordlund[2], L. Malerba[3]
[1]Materials Science and Technology Division, Oak Ridge National Laboratory, US,
[2]Department of Physics, University of Helsinki, Finland
[3]Structural Materials Modelling and Microstructure, Institute of Nuclear Materials Science, SCK•CEN, Belgium

Abstract

Radiation-induced changes in microstructure and mechanical properties in structural materials are the result of a complex set of physical processes initiated by the collision between an energetic particle (neutron or ion) and an atom in the lattice. This primary damage event is called an atomic displacement cascade. The simplest description of a displacement cascade is to view it as a series of many billiard-ball-like elastic collisions among the atoms in the material. This chapter describes the formation and evolution of this primary radiation damage mechanism to provide an overview of how stable defects are formed by displacement cascades, as well as the nature and morphology of the defects themselves. The impact of the relevant variables such as cascade energy and irradiation temperature is discussed, and defect formation in different materials is compared.

1. Introduction

Radiation damage in structural materials employed in nuclear energy systems is a result of exposure to high-energy neutrons which are a by-product of the energy-producing nuclear reactions. In the fission reactors, the neutrons are the result of uranium fission, whereas in future fusion reactors employing deuterium (D) and tritium (T) as fuel, the neutrons will be the result of DT fusion. In addition, spallation neutron sources generate neutrons as a result of spallation reactions between a high-energy proton beam and a heavy metal target. Neutron exposure leads to substantial changes in the microstructure of the materials, which are ultimately manifested as observable changes in the material's physical and mechanical properties. For example, radiation-induced void swelling has produced density changes greater than 50% in some grades of austenitic stainless steels [1] and changes in

the ductile-to-brittle transition temperature greater than 200°C have been observed in the low-alloy steels used in the fabrication of reactor pressure vessels [2,3]. Phenomena known as irradiation creep and radiation-induced solute segregation are also discussed extensively in the literature [4]. The objective of this chapter is to describe the process of primary radiation damage production that gives rise to the macroscopic changes. This primary radiation damage event, which is referred to as an atomic displacement cascade (or alternatively a collision cascade or a displacement spike), was first proposed by Brinkman in 1954 [5,6]. Many aspects of the cascade damage production discussed below were anticipated in Brinkman's conceptual description.

The time scale of a displacement cascade is from femtoseconds to a few tens of pico-seconds. The size scale of displacement cascades, is on the order of a few $nm^{3.}$ The disparity between the size and time scales of displacement cascades and the resultant property changes has been a primary driving-force for the development of so-called multi-scale modelling [7]. Although interest in displacement cascades was initially limited to the nuclear industry, cascade damage production has also become important in the solid state processing practices of the electronics industry [8], and for the modification of surface layers by ion beam implantation to improve wear or corrosion resistance of materials [9]. The energy and mass of the particle that initiates the cascade provide the principal differences between the nuclear and ion beam applications. Neutrons from nuclear fission and DT fusion have energies up to about 20 MeV and 14.1 MeV, respectively, while ion beam applications typically involve relatively low energy ions, a few tens of keV.

This chapter focuses on the cascade energies of relevance to metals and alloys employed in nuclear energy systems. However, the description of the basic physical mechanisms of displacement cascade formation and evolution given below is generally valid for any crystalline material. Although additional physical processes may come into play to alter the final defect state in ionic or covalent materials due to atomic charge states [10], the ballistic processes observed in metals due to displacement cascades are quite similar in these materials. This has been demonstrated in molecular dynamics (MD) simulations in a range of ceramic materials [11-15].

2. Description of atomic displacement cascades

An atomic displacement cascade can be visualised as a series of elastic collisions which is initiated when a given atom is struck by a high-energy particle (typically a neutron in nuclear environments, although it could also be a fission fragment or alpha particle created in a nuclear decay process). The initial atom, which is called the primary knock-on atom (PKA), will recoil with a given amount of kinetic energy which it dissipates in a sequence of collisions with other atoms. The first of these are termed secondary knock-on atoms and they will in turn lose energy to third and subsequently higher ordered knock-ons until all of the energy initially imparted to the PKA has been dissipated. The physical mechanisms are similar to billiard ball collisions, with one primary difference. Unlike a billiard ball, an atom in a crystalline solid experiences the binding forces that arise from the presence of the other atoms. This binding stabilises the crystalline lattice, leading to the requirement that a certain minimum kinetic energy must be transferred to an atom before it can be displaced from its lattice site. This minimum energy is called the displacement threshold energy (E_d) and is typically 20 to 40 eV for most metals and alloys

used in structural applications [16]. Another consequence of the interaction between atoms is that, differently from billiard balls, collective (or many-body) mechanisms and effects, that cannot be described in terms of simple binary collisions, play an important role in determining the redistribution of atoms during the displacement cascade process.

If an atom receives kinetic energy in excess of E_d, it can be displaced from its original lattice site and come to rest within the interstices of the lattice. Such an atom constitutes a point defect in the lattice and is called an interstitial or interstitial atom. In the case of an alloy, the interstitial atom may be referred to as a self-interstitial atom (SIA) if the atom is the primary alloy component (e.g. iron in steel) to distinguish it from impurity or solute interstitials. The SIA nomenclature is also used for pure metals although it is somewhat redundant in that case. The complementary point defect is formed if the original lattice site remains vacant; such a site is called a vacancy. Although vacancies are thermal equilibrium defects and exist in any crystal at finite temperature, the interstitial formation energy is so high that the concentration is always negligible. However, vacancies and interstitials are created in equal numbers by irradiation and the name Frenkel pair is used to describe a single, stable interstitial and its related vacancy. In addition, small clusters of both point defect types can be formed within a displacement cascade.

For the case of nonrelativistic particle energies with one particle initially in motion with kinetic energy E_o and the other at rest, the kinematics of the displacement cascade can be described as follows. In an elastic collision between two such particles, the maximum energy transfer (E_m) from particle (1) to particle (2) is given by:

$$E_m = 4E_o A_1A_2 / (A_1+A_2)^2, \quad (1)$$

where A_1 and A_2 are the atomic masses of the two particles. Two limiting cases are of interest. If particle 1 is a neutron and particle 2 is a relatively heavy element such as iron, $E_m \sim 4E_o/A$. Alternately, if $A_1=A_2$, any energy up to E_o can be transferred. The former case corresponds to the initial collision between a neutron and the PKA, while the latter approximately corresponds to the collisions between lattice atoms of the same mass.

Various models have been proposed to compute the total number of atoms displaced by a given PKA as a function of energy. The most widely cited model is that of Kinchin and Pease [17]. Their model assumed that between a specified threshold energy and an upper energy cut-off, there was a linear relationship between the number of Frenkel pair produced and the PKA energy. Below the threshold energy, no new displacements would be produced. It was assumed that the energy above the high-energy cut-off was dissipated in electronic excitation and ionisation. Later, Lindhard and co-workers developed a detailed theory for energy partitioning that could be used to compute the fraction of the PKA energy that was dissipated in elastic collisions and in electronic losses [18]. This work was used by Norgett, Robinson, and Torrens (NRT) to develop a secondary displacement model that is still used as a standard in the nuclear industry and elsewhere to compute atomic displacement rates [19].

The NRT model gives the total number of displaced atoms produced by a PKA with kinetic energy E_{PKA} as:

$$\nu_{NRT} = 0.8\, T_d\, (E_{PKA})/2\, E_d \quad (2)$$

where E_d is an average displacement threshold energy [16]. The determination of an appropriate average displacement threshold energy is somewhat complex because the displacement threshold is strongly dependent on crystallographic direction. An example of the angular dependence is shown for iron in Figure 1 [20], based on molecular dynamics (MD) simulations using the Finnis-Sinclair potential [21]. In order to apply a single value in Eq. (2), an appropriate angular averaged value must be used. Defining this average is further complicated by the fact that MD simulations also show that the threshold is not a single value for any one direction due to thermal effects. Reference [22] provides a comparison of threshold behaviour obtained with eleven different iron potentials and discusses several different possible definitions of the displacement threshold energy. The factor T_d in Equation (2) is called the damage energy and is a function of E_{PKA}. The damage energy is the amount of the initial PKA energy dissipated in atomic displacements, with electronic excitation responsible for the difference between E_{PKA} and T_d. The ratio of T_d to E_{PKA} for iron is shown in Figure 2 as a function of PKA energy, where the analytical fit to Lindhard's theory described in [19] has been used to obtain T_d.

Note that a significant fraction of the PKA energy is dissipated in electronic processes even for energies as low as few keV [23]. The factor of 0.8 in Equation (2) accounts for the effects of realistic (i.e. other than hard sphere) atomic scattering; the value was obtained from an extensive cascade study using the binary collision approximation (BCA) [24-25].

Figure 1. Angular dependence of displacement threshold energy for iron at 0K [20]

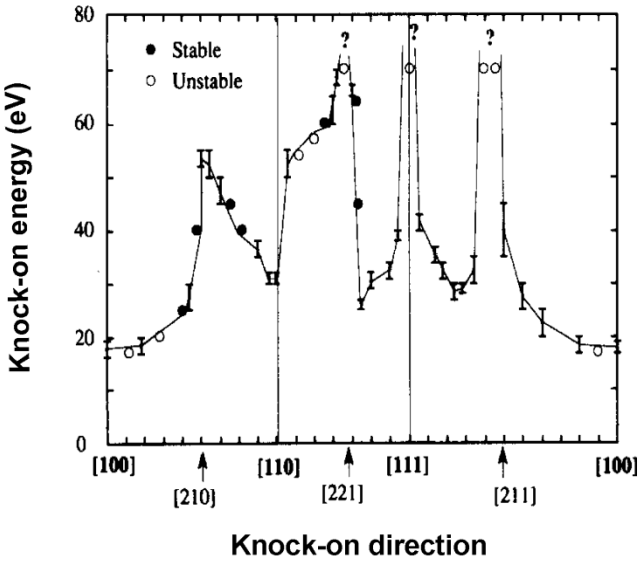

Figure 2. Ratio of damage energy (T_d) to PKA energy (E_{PKA}) as a function of PKA energy

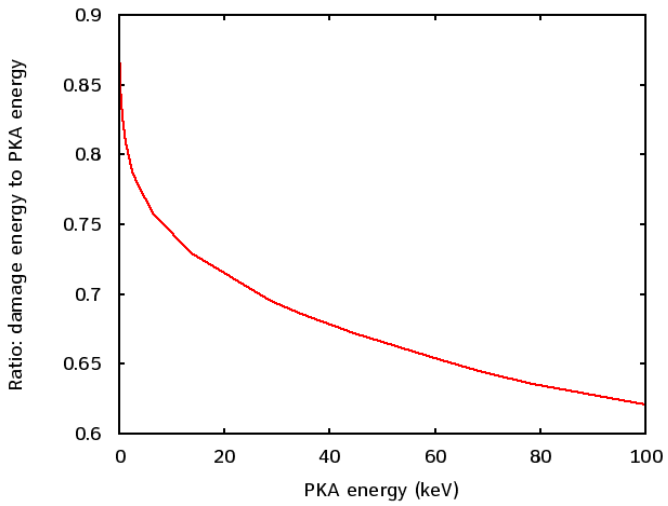

The number of stable displacements (Frenkel pair) predicted by both the original Kinchin-Pease model and the NRT model is shown in Figure 3 as a function of the PKA energy. The third curve in the figure will be discussed below. MD simulations (see Section 2) indicate that ν_{NRT} over-estimates the total number of Frenkel pair that remains after the excess kinetic energy in a displacement cascade has been dissipated at about 10 ps. Many more defects than this are formed during the collisional phase of the cascade; however, most of these disappear as vacancies and interstitials annihilate one another in spontaneous recombination reactions.

Figure 3. Predicted Frenkel pair production as a function of PKA energy for alternate displacement models (see text for explanation of models)

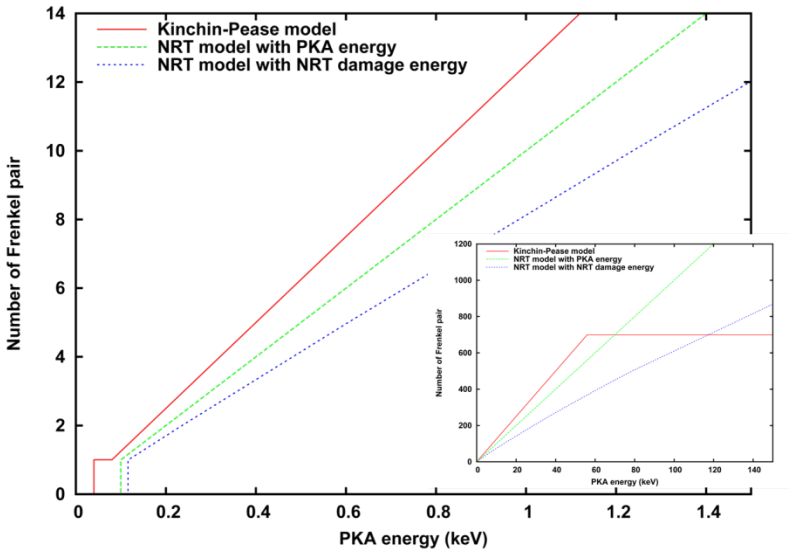

One valuable aspect of the NRT model is that it enabled the use of atomic displacements per atom (dpa) as an exposure parameter which provides a common basis of comparison for data obtained in different types of irradiation sources, e.g. different neutron energy spectra, ion irradiation, or electron irradiation. The neutron energy spectrum can vary significantly from one reactor to another depending on the reactor coolant and/or moderator (water, heavy water, sodium, graphite), which leads to differences in the PKA energy spectrum as discussed below. This can confound attempts to correlate irradiation effects data on the basis of parameters such as total neutron fluence or the fluence above some threshold energy, commonly 0.1 or 1.0 MeV. More importantly, it is impossible to relate any given neutron fluence with a charged particle fluence. However, in any of these cases, the PKA energy spectrum and corresponding damage energies can be calculated, and the total number of displacements obtained using Equation (2) in an integral calculation. Thus, dpa provides an environment-independent radiation exposure parameter that in many cases can be successfully used as a radiation damage correlation parameter [26].

3. Computational approach to simulating displacement cascades

Given the short time scale and small volume associated with atomic displacement cascades, it is not currently possible to directly observe their behaviour by any available experimental method. Some of their characteristics have been inferred by experimental techniques that can examine the fine microstructural features that form after low doses of irradiation. The experimental work that provides the best estimate of stable Frenkel pair production involves cryogenic irradiation and subsequent annealing while measuring a parameter such as electrical resistivity [27,28]. These data are consistent with the results of MD simulations which indicate that the number of stable Frenkel pair produced by a cascade is about 20-35% of ν_{NRT}. Less direct experimental measurements include small angle neutron scattering [29], x-ray scattering [30], positron annihilation spectroscopy [31], and field ion microscopy [32]. More broadly, transmission electron microscopy has been used to characterize the small point defect clusters such as microvoids, dislocation loops, and stacking fault tetrahedra that are formed as the cascade collapses [33-37].

Experiments only provide indirect information on displacement cascades; a single cascade cannot be experimentally seen and studied while it happens. As a result, most of our knowledge on displacement cascades is obtained from computer simulations. The primary computational tool for investigating radiation damage formation in displacement cascades has been molecular dynamics, which is a computationally intensive method for modeling atomic systems on the time and length scales appropriate to displacement cascades. The method was pioneered for radiation effects by Vineyard and co-workers at Brookhaven National Laboratory [38], and much of the early work on atomistic simulations is collected in a review by Beeler [39]. The approach was applied to study the near-surface effects of ion implantation such as sputtering by Harrison and co-workers [40,41]. Other methods, such as those based on the binary collision approximation [24, 25], have also been used to study displacement cascades. Binary collision models are well suited for very high energy events which require that the interatomic potential accurately simulates only close encounters between pairs of atoms. This method requires substantially less computer time than MD, but provides less detailed information about lower energy collisions where many-body effects become important. In addition, in-

cascade recombination and clustering can only be treated parametrically in the BCA. When the necessary parameters have been calibrated using the results of an appropriate database of MD cascade results, the BCA codes have been shown to reproduce the results of MD simulations reasonably well [42, 43].

A detailed description of the MD method can be found elsewhere [44]. Briefly, the method relies on obtaining a sufficiently accurate analytical interatomic potential function that describes the energy of the atomic system and the forces on each atom as a function of its position relative to the other atoms in the system. It is also possible to obtain the forces from quantum mechanical simulations, but this approach is too slow for almost all radiation cascade simulations. This function must account for both attractive and repulsive forces to obtain the appropriate stable lattice configuration. Specific values for the adjustable coefficients in the function are obtained by ensuring that the interatomic potential leads to reasonable agreement with measured material parameters such as the lattice parameter, lattice cohesive energy, single crystal elastic constants, melting temperature, and point defect formation energies. The process of developing and fitting interatomic potentials is described in a recent review [45]. Critical aspects of cascade behaviour can be sensitive to the details of the interatomic potential [22,46-48].

The total energy of the system of atoms being simulated can be calculated by summing over all the atoms, with the forces on the atoms obtained from the gradient of the interatomic potential. These forces can be used to calculate the atom's accelerations according to Newton's second law, the familiar F=ma (force=mass times acceleration), and the equations of motion for the atoms can be solved by numerical integration using a suitably small time step. At the end of the time step, the forces are recalculated for the new atomic positions and this process is repeated as long as necessary to reach the time or state of interest. For energetic PKAs, the initial time step may range from ~1 to $10x10^{-18}$ s, with the maximum time step limited to ~1 to $10x10^{-15}$ s to maintain acceptable numerical accuracy in the integration and avoid violation of fundamental principles such as energy conservation. As a result, MD cascade simulations are typically not run for times longer than 10 to 100 ps. With periodic boundary conditions, the size of the simulation cell needs to be large enough to prevent the cascade from interacting with periodic images of itself. Higher energy events therefore require a larger number of atoms in the cell.

The process of conducting a cascade simulation requires two steps. First, a block of atoms of the desired size is thermally equilibrated. This permits the lattice thermal vibrations (phonon waves) to be established for the simulated temperature and typically requires a simulation time of approximately 10 ps. This equilibrated atom block can be saved and used as the starting point for several subsequent cascade simulations. Subsequently, the cascade simulations are initiated by giving one of the atoms a defined amount of kinetic energy, E_{MD}, in a specified direction. Statistical variability can be introduced by either further equilibration of the starting block, choosing a different PKA or PKA direction, or some combination of these. The number of simulations required at any one condition to obtain a good statistical description of defect production is not large. Typically, only about 8 to 10 simulations are required to obtain a small standard error about the mean number of defects produced; the scatter in defect clustering parameters is larger. This topic will be discussed further below when the results are presented. It is common to use a high index crystallographic direction for the PKA (e.g. [135]) to minimise directional effects such as channelling and directions with particularly low or

high displacement thresholds. Investigations of the effect of PKA direction generally indicate that mean values obtained from [135] cascades are representative of the average defect production expected in cascades greater than about 1 keV [49]. A stronger influence of PKA direction can be observed at lower energies as discussed in Refs. [50,51].

Various procedures have been applied to characterize cascade-produced defects. One approach is to search the volume of a Wigner-Seitz (WS) cell which is centered on one of the original, perfect lattice sites. An empty cell indicates the presence of a vacancy and a cell containing more than one atom indicates an interstitial-type defect. The advantage of the WS cell method is that WS cells cover the entire volume without overlap and permit an unambiguous definition of vacancy and interstitial type defects, leading immediately to their exact count. A simpler geometric criterion can also be used which provides a more intuitive visualization of clusters. A small sphere can be centered on the perfect lattice sites, and a search similar to that just described for the Wigner-Seitz cell is carried out. Any atom that is not within such a sphere is identified as part of an interstitial defect and each empty sphere identifies the location of a vacancy. The diameter of the effective sphere should be slightly less than the spacing of the two atoms in a dumbbell interstitial (see below); in the case of iron this is ~30% of a lattice parameter. Comparison of the effective sphere and Wigner-Seitz cell approaches indicate essentially no difference in the number of stable point defects identified at the end of cascade simulation in bcc metals, although the WS method may offer some advantages for some extended defects in fcc metals. The advantage of the effective sphere approach is that the visualization gives a better indication of the local defect geometry, while the drawback to this approach is that the number of apparent defects identified cans be greater than the number of Frenkel pairs. For example, the dumbbell interstitial appears to be two atoms and one vacancy. In order to minimize the lattice strain energy, most interstitials are found in the dumbbell configuration; the energy is reduced by distributing the distortion over multiple lattice sites. For the crowdion interstitial, which involves displacements in a close-packed direction, the defect is typically visualized as n-interstitials and (n-1)-vacancies. The value of n depends on the radius of the analysis sphere, which is a measure of the local lattice strain, as shown in Figure 4. A simple post-processing code can be used to determine the true number of point defects which are reported below.

Most of the MD displacement cascade simulations reported for metals have accounted for only the elastic collisions between atoms; i.e. they did not account for energy loss mechanisms such as electronic excitation and ionization. Thus, the initial kinetic energy, E_{MD}, given to the simulated PKA in MD simulations is more analogous to T_d in Equation (2) than it is to the PKA energy which is the initial kinetic energy of the recoil atom. Using the values of E_{MD} in Table 1 as a basis, the corresponding E_{PKA} and ν_{NRT} for iron, and the ratio of the damage energy to the PKA energy, have been calculated using the procedure described in [19] and the recommended 40 eV displacement threshold [16]. These values are also listed in Table 1, along with the neutron energy that would yield E_{PKA} as the average recoil energy in iron. This is one-half the maximum energy given by Equation (1).

Figure 4. Influence of analysis sphere on visualisation of a <111> crowdion interstitial; red spheres are lattice sites determined to be vacancies and green spheres are atoms identified as being in interstitial positions

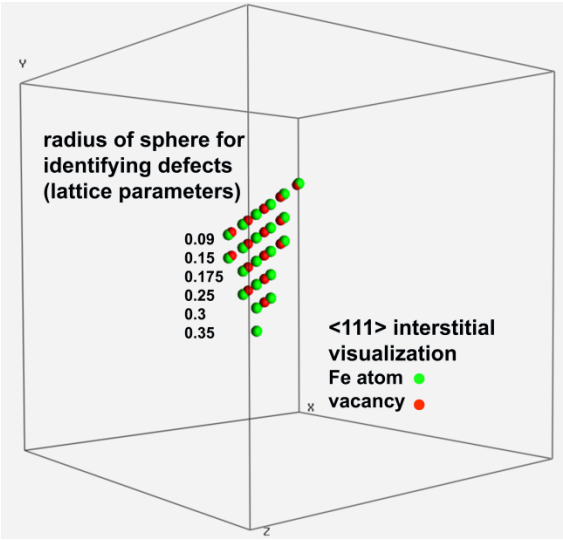

As mentioned above, the difference between the MD cascade energy, or damage energy, and the PKA energy increases as the PKA energy increases. Discussions of cascade energy in the literature on MD cascade simulations are not consistent with respect to the use of the term PKA energy. The third curve in Figure 2 shows the calculated number of Frenkel pair predicted by the NRT model if the PKA energy is used in Eqn. (2) rather than the damage energy. The difference between the two sets of NRT values is substantial and is a measure of the ambiguity associated with the vague use of terminology. It is recommended that the MD cascade energy should not be referred to as the PKA energy, and that authors always report whether and how they account for electronic stopping. For the purpose of comparing MD results to the NRT model, the MD cascade energy should be considered as approximately equal to the damage energy (T_d in Eqn. 2).

Recoil atoms lose energy continuously by a combination of electronic and nuclear reactions, and the approximation in MD simulations involves essentially deleting the electronic component at time zero. The effects of continuous energy loss on defect production have been investigated in the past using a damping term to slowly remove kinetic energy [52], an approach which is consistent with the inclusion of electronic stopping power in both BCA and MD ion range calculations [53-56]. Very recent simulations have compared cascade simulations with and without electronic stopping. These results indicate that the final damage production is sensitive to the approach used, and it remains unclear which approach is most appropriate [57,58]. The related issues of how this extracted energy heats the electron system and the effects of electron-phonon coupling on local temperature have also been examined [59-62]. More recently, computational and algorithmic advances have enabled these phenomena to be investigated with higher fidelity [58,59]. Some of the work just referenced has shown that accounting for the electronic system has a modest quantitative effect on defect formation in displacement cascades. For example, Gao, et al. found a systematic increase in defect formation as they increased the effective electron-phonon coupling in 2, 5, and 10 keV

cascade simulations in iron [62], and a similar effect was reported in Ref. [59]. However, the primary physical mechanisms of defect formation that are the focus of this chapter can be understood in the absence of these effects.

Table 1. Typical iron atomic displacement cascade parameters

Neutron Energy (MeV)	Average PKA Energy (keV) [1]	Corresponding T_d (keV) [2] ~E_{MD}	NRT Displacements	Ratio: T_d/E_{PKA}	Typical simulation cell size (atoms)
0.00335	0.116	0.1	1	0.8634	3,456
0.00682	0.236	0.2	2	0.8487	6,750
0.0175	0.605	0.5	5	0.8269	
0.0358	1.24	1.0	10	0.8085	54,000
0.0734	2.54	2.0	20	0.7881	
0.191	6.6	5.0	50	0.7570	128,000
0.397	13.7	10.0	100	0.7292	250,000
0.832	28.8	20.0	200	0.6954	~500k
2.28	78.7	50.0	500	0.6354	~2.5M
5.09	175.8	100.0	1000	0.5690	~5 to 10 M
12.3	425.5	200.0	2000	0.4700	~10 to 20 M
14.1[3]	487.3	220.4	2204	0.4523	

1. This is the average iron recoil energy from an elastic collision with a neutron of the specified energy
2. Damage energy calculated using Robinson's approximation to LSS theory [19]
3. Relevant to D-T fusion energy production

4. Results of MD cascade simulations in iron

MD simulations have been employed to investigate displacement cascade evolution in a wide range of materials. The literature is sufficiently broad that any list of references will be necessarily incomplete; Refs. [46, 47, 49, 64-82] provide only a representative sample. Additional references will be given below as specific topics are discussed. The recent reviews by Malerba [46] and Stoller [47] provide good summaries of the research that has been done on iron. MD investigations of displacement cascades have established several consistent trends in primary damage formation in a number of metals. These trends include: (1) the total number of stable point defects produced follows a power-law dependence on the cascade energy over a broad energy range, (2) the ratio of MD stable displacements divided by the number obtained from the NRT model decreases with energy until subcascade formation becomes prominent, (3) the in-cascade clustering

fraction of the surviving defects increases with cascade energy, and (4) the effect of lattice temperature on the MD results is rather weak. Two additional observations have been made regarding in-cascade clustering in iron, although the fidelity of these statements depends on the interatomic potential employed. First, the interstitial clusters have a complex, three-dimensional morphology, with both sessile and glissile configurations. Mobile interstitial clusters appear to glide with a low activation energy similar to that of the mono-interstitial (~0.1-0.2 eV) [83]. Second, the fraction of the vacancies contained in clusters is much lower than that of interstitials. Each of these points will be discussed further below.

The influence of the interatomic potential on cascade damage production has been investigated by several researchers [48,84-86]. Such comparisons generally show only minor quantitative differences between results obtained with interatomic potentials of the same general type, although the differences in clustering behaviour are more significant with some potentials. Variants of embedded atom or Finnis-Sinclair type potential functions [45] have most often been used. However, more substantial differences are sometimes observed that are difficult to correlate with any known aspect of the potentials. The analysis recently reported by Malerba [46] is one example. In this case, it appears that the formation of replacement collision sequences was very sensitive to the range over which the equilibrium part of the potential was joined to the more repulsive pair potential which controls short-range interactions. This changed the effective cascade energy density and thereby the number of stable defects produced.

In order to provide a self-consistent database for illustrating cascade damage production over a range of temperatures and energies, and to provide examples of secondary variables that can influence this production, the results presented in this chapter will focus on MD simulations in iron using a single interatomic potential [49, 75-79]. This potential was originally developed by Finnis and Sinclair [21] and later modified for cascade simulations by Calder and Bacon [70]. The calculations were carried out using a modified version of the MOLDY code written by Finnis [87]. The computing time with this code is almost linearly proportional to the number of atoms in the simulation. Simulations were carried out using periodic, Parrinello-Rahman boundary conditions at constant pressure [88]. Electronic stopping was not included in the simulations (see discussion above). Since no thermostat was applied to the boundaries, the average temperature of the simulation cell was increased as the kinetic energy of the PKA was dissipated. The impact of this heating appears to be modest based on the observed effects of irradiation temperature discussed below, and on the results observed in the work of Gao et al. [89]. A comparison of the iron cascade results with those obtained in other metals will be presented in the next section.

The primary variables studied in these cascade simulations is the cascade energy, E_{MD}, and the irradiation temperature. The database of iron cascades includes cascade energies from near the displacement threshold (~100 eV) to 200 keV and temperatures in the range of 100 to 900 K. In all cases, the evolution of the cascade has been followed to completion and the final defect state determined. Typically this is reached after a few ps for the low energy cascades and up to ~15 ps for the highest energy cascades. Because of the variability in final defect production for similar initial conditions, several simulations were conducted at each energy to produce statistically meaningful average values. The parameters of most interest from these studies are the number of surviving point defects,

the fraction of these defects that are found in clusters, and the size distribution of the point defect clusters. The total number of point defects is a direct measure of the residual radiation damage and the potential for long-range mass transport and microstructural evolution. In-cascade defect clustering is important because it can promote microstructural evolution by eliminating the cluster nucleation phase.

The parameters used in the following discussion to describe results of MD cascade simulations are the total number of surviving point defects and the fraction of the surviving defects contained in clusters. The number of surviving defects will be expressed as a fraction of the NRT displacements listed in Table 1, whereas the number of defects in clusters will be expressed as either a fraction of the NRT displacements or a fraction of the total surviving MD defects. Alternate criteria were used to define a point defect cluster in this study. In the case of interstitial clusters, it was usually determined by direct visualization of the defect structures. The coordinated movement of interstitials in a given cluster can be clearly observed. Interstitials bound in a given cluster were typically within a second nearest-neighbour distance, although some were bound at third nearest-neighbours. The situation for vacancy clusters will be discussed further below, but vacancy clustering was assessed using first, second, third and fourth nearest-neighbour distances as the criteria. The vacancy clusters observed in iron tend to not exhibit a compact structure according these definitions. In order to analyse the statistical variation in the primary damage parameters, the mean value (M), the standard deviation about the mean (σ), and the standard error of the mean (ε) have been calculated for each set of cascades conducted at a given energy and temperature. The standard error of the mean is calculated as $\varepsilon = \sigma/n^{0.5}$, where n is the number of cascade simulations completed [90]. The standard error of the mean provides a measure of how well the sample mean represents the actual mean. For example, a 90% confidence limit on the mean is obtained from $1.86 \times \varepsilon$ for a sample size of nine [91]. These statistical quantities are summarized in Table 2 for a representative subset of the iron cascade database.

Table 2. Statistical analysis of primary damage parameters derived from MD cascade simulations

Cascade Energy (keV)	Temperature (K)	Number of cascades	Surviving displacements (mean / standard deviation / standard error)		Clustered interstitials (mean / standard deviation / standard error)		
			Number	per NRT	Number	per NRT	per MD surviving defects
0.5	100	16	3.94 0.380 0.170	0.790 0.136 0.0340	1.25 1.39 0.348	0.250 0.278 0.0695	0.310 0.329 0.0822
1	100	12	6.08 1.38 0.398	0.608 0.138 0.0398	2.25 1.66 0.479	0.225 0.166 0.0479	0.341 0.248 0.0715
2	100	10	10.1 2.64 0.836	0.505 0.132 0.0418	4.60 2.80 0.884	0.230 0.140 0.442	0.432 0.0214 0.0678
5	100	9	22.0 2.12 0.707	0.440 0.0424 0.0141	11.4 2.40 0.801	0.229 0.0481 0.0160	0.523 0.113 0.0375
10	100	15	33.6 5.29 1.37	0.336 0.0529 0.0137	17.0 4.02 1.04	0.170 0.0402 0.0104	0.506 0.101 0.0261
	600	8	30.5 10.35 3.66	0.305 0.104 0.0366	18.1 8.46 2.99	0.181 0.0846 0.0299	0.579 0.115 0.0406
	900	7	27.3 5.65 2.14	0.273 0.0565 0.0214	18.6 6.05 2.29	0.186 0.0605 0.0229	0.679 0.0160 0.0606
20	100	10	60.2 8.73 2.76	0.301 0.0437 0.0138	36.7 6.50 2.06	0.184 0.0325 0.0103	0.610 0.0630 0.0199
	600	8	55.8 5.90 2.09	0.281 0.0290 0.0103	41.6 5.85 2.07	0.211 0.0285 0.0101	0.746 0.0796 0.0281
	900	10	51.7 9.76 3.09	0.259 0.0488 0.0154	35.4 8.94 2.83	0.177 0.0447 0.0141	0.682 0.0944 0.0299
30	100	16	94.9 13.2 3.29	0.316 0.0440 0.0110	57.2 11.5 2.88	0.191 0.0385 0.00963	0.602 0.0837 0.0209
40	100	8	131.0 12.6 4.45	0.328 0.0315 0.0111	74.5 15.0 5.30	0.186 0.0375 0.0133	0.570 0.102 0.0361
50	100	9	168.3 12.1 4.04	0.337 0.0242 0.00807	93.6 6.95 2.32	0.187 0.0139 0.00463	0.557 0.0432 0.0144
100	100	10	329.7 28.2 8.93	0.330 0.0283 0.0089	184.8 20.5 6.47	0.185 0.0205 0.00650	0.561 0.0386 0.0122
	600	20	282.4 26.6 5.95	0.282 0.0266 0.00595	185.5 26.9 6.01	0.186 0.0269 0.00601	0.656 0.0556 0.0124
	900	18	261.0 17.5 4.13	0.261 0.0175 0.00413	168.7 17.3 4.08	0.169 0.0173 0.00408	0.646 0.0498 0.0117
200	100	9	676.7 37.9 12.6	0.338 0.0190 0.00632	370.3 29.5 9.83	0.185 0.0147 0.00491	0.548 0.0464 0.0155

- Cascade evolution and structure

The evolution of displacement cascades is similar at all energies, with the development of a highly energetic, disordered core region during the initial, collisional phase of the cascade. Vacancies and interstitials are created in equal numbers and the number of point defects increases sharply until a peak value is reached. Depending on the cascade energy, this occurs at a time in the range of 0.1 to 1 ps. This evolution is illustrated in Figure 5 for a range of cascade energies, where the number of vacancies is shown as a function of the cascade time. Many vacancy-interstitial pairs are in quite close proximity at the time of peak disorder. An essentially athermal process of in-cascade recombination of these close pairs takes places as they lose their kinetic energy. This leads to a reduction in the number of defects until a quasi-steady-state value is reached after about 5 to 10 ps. Since interstitials in iron are mobile even at 100 K, further short-term recombination occurs between some vacancy-interstitial pairs which were initially separated by only a few atomic jump distances. Finally, a stage is reached where the remaining point defects are sufficiently well separated that further recombination is unlikely on the time scale (a few hundred ps) accessible by MD. Note that the number of stable Frenkel pairs is actually somewhat lower than the value shown in Figure 5 because the values obtained using the effective sphere identification procedure were not corrected to account for the interstitial structure discussed above.

Figure 5. Time evolution of defects formed during displacement cascades

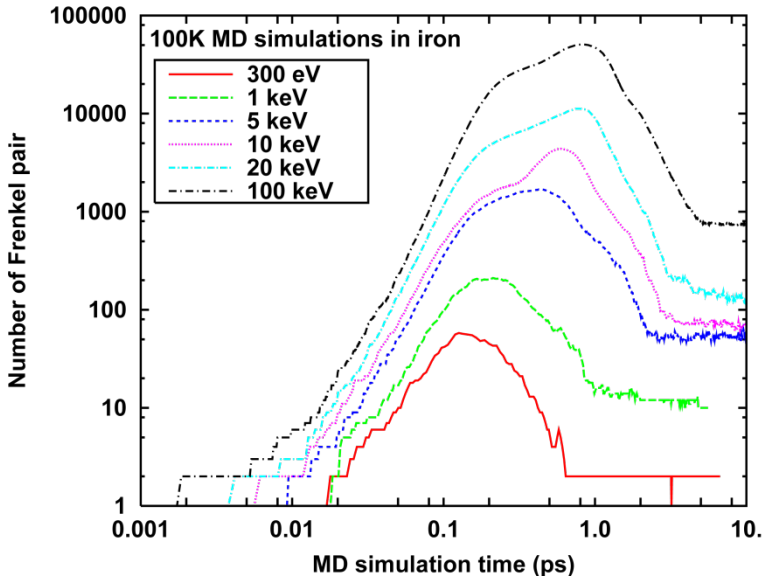

A mechanism known as replacement collision sequences (RCS) may help explain some aspects of cascade structure [25,46]. An RCS can be visualized as an extended defect along a close-packed row of atoms. When the first atom is pushed off its site, it dissipates some energy and pushes a second atom into a third, etc. along the same crystallographic direction (an RCS is sometimes also called a "focus-on"). When the last atom in this chain is unable to displace another, it is left in an interstitial site with the original vacancy several atomic jumps away. Thus, RCSs provide a mechanism of mass transport that can efficiently separate vacancies from interstitials. The explanation is consistent with the

observed tendency for the final cascade state to be characterised by a vacancy-rich central region that is surrounded by a region rich in interstitial type defects. However, although RCSs are observed, particularly in low energy cascades, they do not appear to be prominent enough to explain the defect separation observed in higher energy cascades [70]. In these cases, visualisation of cascade dynamics indicates that the separation occurs by a more collective motion of multiple atoms, and recent work by Calder and co-workers has identified a shock-wave-induced mechanism that leads to the formation of large interstitial clusters at the cascade periphery [92]. This mechanism will be discussed further below. Coherent displacement events involving many atoms have also been reported by Nordlund et al. [93] and Osetsky, et al. [94] for near-surface cascades.

Defect production tends to be dominated by a series of simple binary collisions at low PKA energies, while the more collective, cascade-like behaviour dominates at higher energies. The structure of typical 1 keV and 20 keV cascades is shown in Figure 6, where parts (a) and (b) show the peak damage state, and (c) and (d) show the final defect configurations. The MD cells contained 54,000 and 432,000 atoms for the 1 and 20 keV simulations, respectively. Only the vacant lattice sites and interstitial atoms identified by the effective sphere approach described above are shown. The separation of vacancies from interstitials can be seen in the final defect configurations; it is more obvious in the 1 keV cascade because there are fewer defects present. In addition to isolated point defects, small interstitial clusters are also clearly observed in the 20 keV cascade debris in Figure 6d. In-cascade clustering is discussed further in Section 37.4.3.

Figure 6. Structure of typical 1 keV (a,c) and 20 keV (b,d) cascades. Peak damage state is shown in (a and b) and the final stable defect configuration is shown in (b and d)

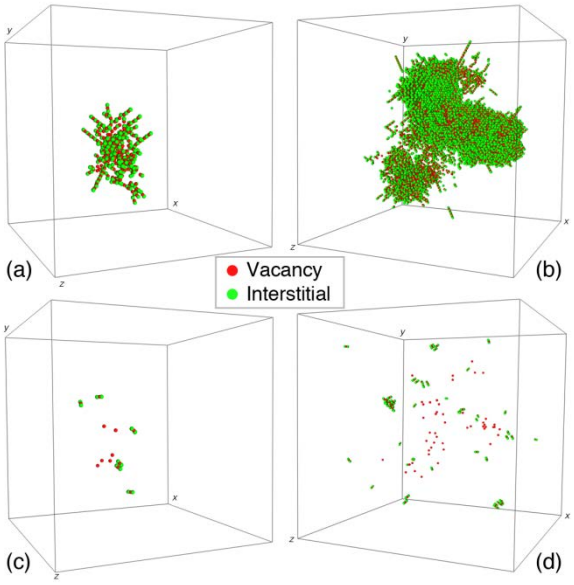

The morphology of the 20 keV cascade in Figure 6b exhibits several lobes which are evidence of a phenomenon known as subcascade formation [95]. At low energies, the PKA energy tends to be dissipated in a small volume and the cascades appear as compact, sphere-like entities as illustrated by the 1 keV cascade in Figure 6a. However, at higher

energies, some channelling [95,96] of recoil atoms may occur. This is a result of the atom being scattered into a relatively open lattice direction, which may permit it to travel some distance while losing relatively little energy in low-angle scattering events. The channelling is typically terminated in a high-angle collision in which a significant fraction of the recoil atom's energy is transmitted to the next generation knock-on atom. When significant subcascade formation occurs, the region between high-angle collisions can be relatively defect free as the cascade develops. This evolution is clearly shown in Figure 7 for a 40 keV cascade, where the branching due to high angle collisions is observed on a time scale of a few hundreds of femtoseconds. One practical implication of subcascade formation is that very high energy cascades break up into what looks like a group of lower energy cascades. An example of subcascade formation in a 100 keV cascade is shown in Figure 8 where the results of 5 and 10 keV cascades have been superimposed into the same block of atoms for comparison. The impact of subcascade formation on stable defect production will be discussed in the next section.

Figure 7. Evolution of a 40 keV cascade in iron at 100 K, illustrating subcascade formation

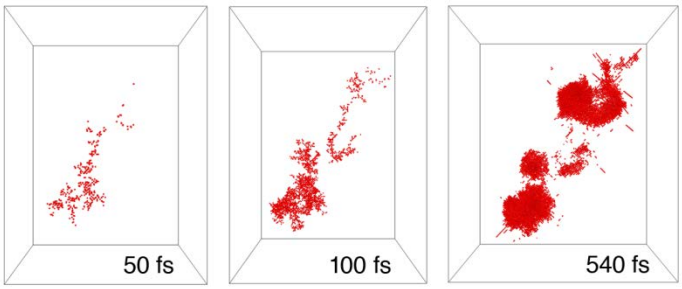

Figure 8. Energy dependence of subcascade formation

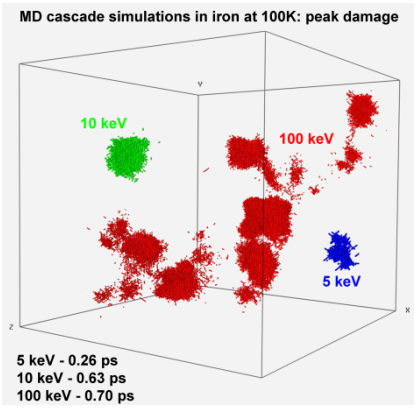

- Stable defect formation

Initial work of Bacon and co-workers indicated that the number of stable displacements remaining at the end of a cascade simulation, N_D, exhibited a power-law dependence on cascade energy [97]. For example, their analysis of iron cascade simulations between 0.5 and 10 keV at 100K, showed that the total number of surviving point defects could be expressed as:

$$N_D = 5.67E_{MD}^{0.779}, \quad (3)$$

where E_{MD} is given in keV. This relationship is not followed below about 0.5 keV because true cascade-like behaviour does not occur at these low energies. Subsequent work by Stoller [47,75-78] indicated that N_D also begins to deviate from this energy dependence above 20 keV when extensive subcascade formation occurs. This is illustrated in Figure 9a where the values of N_D obtained in cascade simulations at 100K is plotted as a function of cascade energy. At each energy, the data point is an average of between 7 and 26 cascades, and the error bars indicate the standard error of the mean. It appears that three well-defined regions with different energy dependencies exist. A power-law fit to the points in each energy region is also shown in Figure 9a. The best-fit exponent in the absence of true cascade conditions below 0.5 keV is 0.485. From 0.5 to 20 keV, the exponent is 0.75. This is marginally lower than the value in Equation (2), possibly because the 20 keV data were used in the current fitting. An exponent of 1.03 was found in the range above 20 keV which is dominated by subcascade formation. Only in the highest energy range do the MD results approach the linear energy dependence predicted by the NRT model. The range of plus or minus one standard error is barely detectable around the data points, indicating that the change in slope is statistically significant.

The data from Figure 9a are replotted in Figure 9b where the number of surviving displacements is divided by the NRT displacements at each energy. The rapid decrease in this MD defect survival ratio at low energies was first measured in 1978 and is well known [69,98]. The error bars again reflect the standard error and the dashed line through the points is only a guide to the eye. The MD/NRT ratio is greater than 1.0 at the lowest values of E_{MD}, indicating that the NRT formulation underestimates defect production in this energy range. This is consistent with the low energy (near threshold) simulations preferentially producing displacements in the "easy" directions [27]. The actual displacement threshold varies with crystallographic direction and is as low as ~19 eV in the [100] direction [20,99]. Thus, use of the recommended average value of 40 eV for E_d in Equation (2) will predict fewer defects at low energies. The average value is more appropriate for the higher energy events where true cascade-like behaviour occurs. In the cascade-dominated regime, the defect density within the cascade increases with energy. Although many more defects are produced, their close proximity leads to a higher probability of in-cascade recombination and a lower defect survival fraction.

Figure 9. Cascade energy dependence of stable point defect formation in iron MD cascade simulations at 100K: (a) total number of interstitials or vacancies and (b) ratio of MD defects to NRT displacements. Data points indicate mean values at each energy and error bars are standard error of the mean

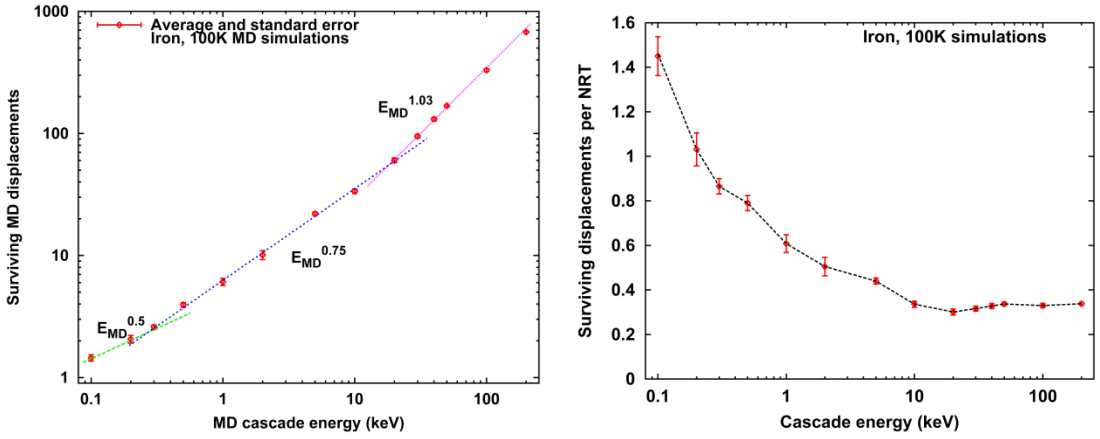

a) b)

The surviving defect fraction shows a slight increase as the cascade energy increases above 20, and the indicated standard errors make it arguable that the increase is statistically significant. If significant, the increase appears to be associated with subcascade formation, which becomes prominent above 10 to 20 keV. In the channelling regions between the high angle collisions that produce the subcascades shown in Figures 7 and 8, the moving atom loses energy in many low angle scattering events that produce low energy recoils. These are essentially like low energy cascades which have higher-than-average defect survival fractions (Figure 9). These events could contribute to the incremental increase in defect survival at the highest energies. The average defect survival fraction of ~0.3·NRT shown for cascade energies greater than about 10 keV is consistent with values of Frenkel pair formation obtained from resistivity change measurements following low-temperature neutron irradiation and ion irradiation [27,28,69,98].

The effect of irradiation temperature is shown in Figure 10, which compares the defect survival fractions obtained from simulations at 100, 600, and 900 K. Although it is difficult to discern a consistent effect of temperature between the 600 and 900 K data points, the defect survival fraction at 100 K is always somewhat greater than at either of the two higher temperatures. A similar result for iron was reported in [97]. In addition to an interest in radiation temperature itself, the effect of temperature is relevant to the simulations presented here because no thermostat was applied to the simulation cell to control temperature. As mentioned above, the energy introduced by the PKA will lead to some heating if the simulation cell temperature is not controlled by a thermostat. For example, in a 1 keV cascade simulation with 54 000 atoms, the average temperature rise will be about 140 K when all the kinetic energy of the PKA is distributed in the system. This change in temperature should be more significant at 100K than at higher temperatures. The fact that defect survival at 600 K and 900 K is lower than at 100 K suggests that the 100 K results may be somewhat biased toward lower survival values by

the PKA-induced heating. This is in agreement with the effect of temperature reported by Gao et al. [98] in their study of 2 and 5 keV cascades with a hybrid MD model that extracted heat from the simulation cell. On the other hand, the difference between the 100 K and 600 K results is not large, so the effect of ~200 K of cascade-induced heating may be modest.

Figure 10. Temperature dependence of stable defect formation in MD simulations: ratio of MD defects to NRT displacements

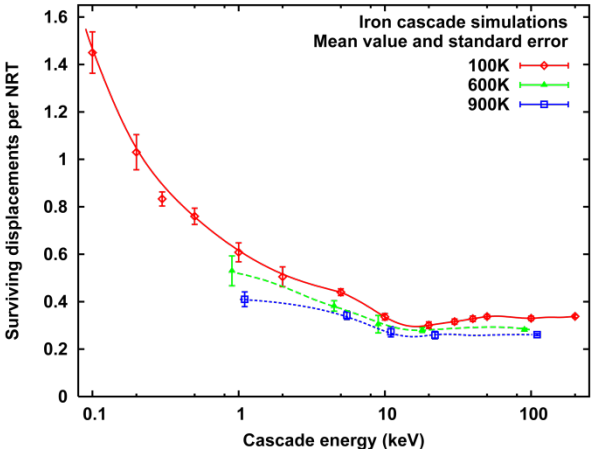

A simple assessment of this cascade-induced heating was carried out using 10 keV cascades at 100 K. Two independent sets of simulations were carried out, seven simulations in a cell of 128k atoms and eight simulations in a cell of 250 k atoms. A 10 keV cascade will raise the average temperature by 604 and 309 K, respectively, for these two cell sizes. The results of these simulations are summarised in Figure 11, where the parameters plotted are the surviving defect fraction (per NRT), the fraction of interstitials in clusters (per NRT), and the fraction of interstitials in clusters (per surviving MD defect). In each case, the range of values for the two populations are shown, along with their respective mean values with the standard error indicated. The mean and standard error for the combined data sets is also shown. Although the heating differed by a factor of two, it is clear that the defect survival fraction is essentially identical for both populations. There is a slight trend in the interstitial clustering results which indicates that a higher temperature (due to a smaller number of atoms) promotes interstitial clustering. This is consistent with the results that will be discussed below.

Figure 11. Effect of cascade heating on defect formation in 10 keV cascades at 100 K

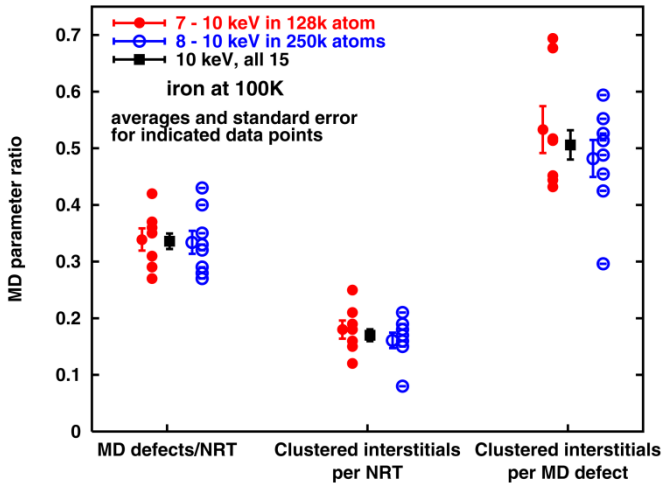

- In-cascade clustering of point defects

Among the features visible in the two cascades shown in Figure 6 are a number of small interstitial clusters. For example, the cascade debris from the 1 keV cascade in Figure 6c contains only seven stable interstitials, but five of them (71%) are in clusters: one di-interstitial and one tri-interstitial. This tendency for point defects to cluster is characteristic of energetic displacement cascades, and it differentiates neutron and ion irradiation from typical 0.5 to 1 MeV electron irradiation which primarily produces only isolated Frenkel pair defects. The differences between in-cascade vacancy and interstitial clustering discussed below, and the fact that their migration behaviour is also quite different, have a profound influence on radiation-induced microstructural evolution at longer times. This impact of point defect clusters on microstructural evolution is discussed in detail in a recent review of mean field reaction theory [99].

- Interstitial clustering

The dependence of in-cascade interstitial clustering on cascade energy is shown in Figure 12 for a simulation temperature of 100K, where the average number of interstitials in clusters of size two or larger at each energy has been divided by the total number of surviving interstitials in part (a), and by the number of displaced atoms predicted by the NRT model for that energy in part (b). The data points and error bars in Figure 12 indicate the mean and standard error at each energy. The error bars can be used to make two significant comments. First, the relative scatter is much higher at lower energies, which is similar to the case of defect survival shown in Figure 10. Second, comparing again with Figure 10, the standard errors about the mean for interstitial clustering are greater at each energy than they are for defect survival.

Figure 12. Fraction of surviving interstitials contained in clusters at 100K; the fraction in (a) is relative to the total number of MD defects created and in (b) is relative to the NRT displacements

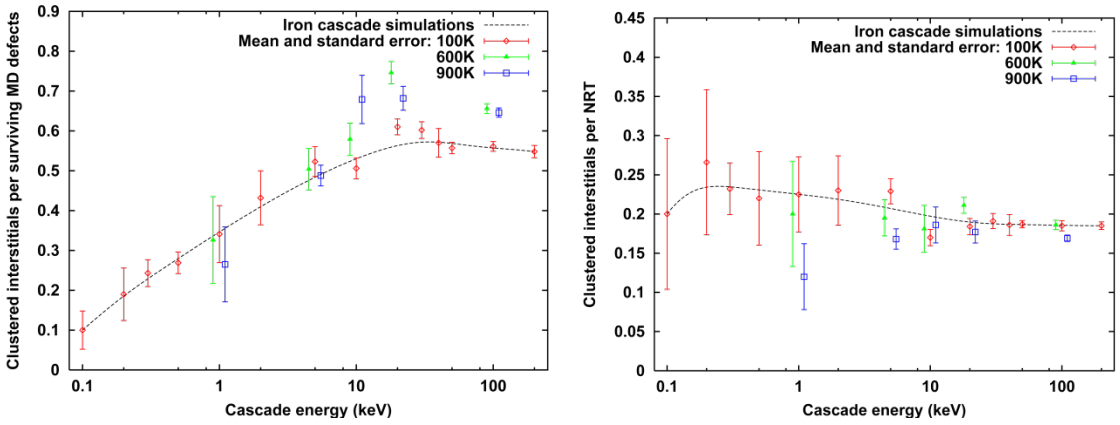

a) b)

The fact that the interstitial clustering fraction exhibits greater variability between cascades at a given energy than does defect survival is essentially related to the variety of defect configurations that are possible. A given amount of kinetic energy tends to produce a given number of stable point defects; this simple observation is embedded in the NRT model, i.e. the number of predicted defects is linear in the ratio of the energy available to the energy per defect. However, any specific number of point defects can be arranged in many different ways. At the lowest energies, where relatively few defects are created, some cascades produce no interstitial clusters and this is primarily responsible for the larger error bars at these energies. The average fraction of interstitials in clusters is about 20% of the NRT displacements above 5 keV, which corresponds to about 60% of the total surviving interstitials. Although it is not possible to discern a systematic effect of temperature below 10 keV, there is a trend toward greater clustering with increasing temperature at higher energies. This can be more clearly seen in Figure 12a where the ratio of clustered interstitials to surviving interstitials is shown, and in the high-energy values in Table 2. This effect of temperature on interstitial clustering in these adiabatic simulations is consistent with the observations of Gao et al. [100] mentioned above, i.e. they found that the interstitial clustering fraction increases with temperature. At the same time, the rate of increase with temperature that is found will be quantitatively influenced by the interatomic potential used [46,48].

The interstitial cluster size distributions exhibit a consistent dependence on cascade energy and temperature as shown in Figure 13 (where a size of 1 denotes the single interstitial). The cascade energy dependence at 100 K is shown in Figure 13a, where the size distributions from 10 and 50 keV are included. The influence of cascade temperature is shown for 10 keV cascades in Figure 13b, and for 20 keV cascades in Figure 13c. All interstitial clusters larger than size 10 are combined into a single class in the histograms in Figure 13. The interstitial cluster size distribution shifts to larger sizes as either the cascade energy or temperature increases. An increase in the clustering fraction at the higher temperatures is most clearly seen as a decrease in the number of mono-interstitials. Comparing Figures 13b and 13c demonstrates that the temperature dependence increases

as the cascade energy increases. The largest interstitial cluster observed in these simulations was contained in a 20 keV cascade at 600K as shown in Figure 14. This large cluster was composed of 33 interstitials (<111> crowdions), and exhibited considerable mobility via what appeared to be one-dimensional glide in a <111> direction [76,78].

Figure 13. Fractional size distributions of interstitial clusters formed directly within the cascade, comparison of: (a) 10 and 50 keV cascades at 100 K, (b) 10 keV cascades at 100 and 900 K, and (c) 20 keV cascades at 100 and 600 K

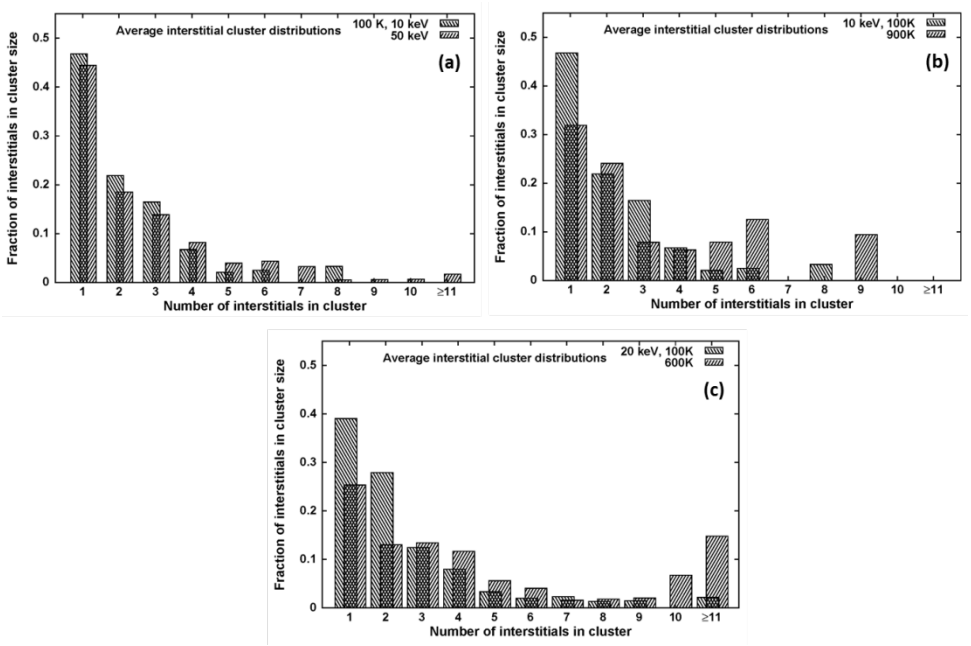

Figure 14. Residual defects at ~30 ps from a 20 keV cascade at 100 K containing a 33-interstitial cluster

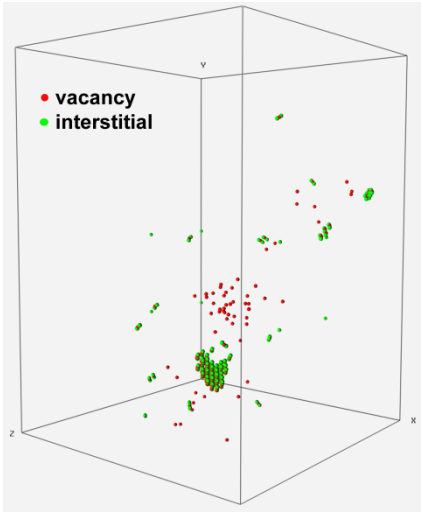

Although the number of point defects produced and the fraction of interstitials in clusters was shown to be relatively independent of neutron energy spectrum [95], the increase in the number of large clusters at higher energies suggested that the in-cascade cluster size distributions may exhibit more sensitivity to neutron energy spectrum than did these other parameters. At 100K, there are no interstitial clusters larger than 8 for cascade energies of 10 keV or less. Therefore, the fraction of interstitials in clusters of 10 or more was chosen as an initial parameter for evaluation of the size distributions. This partial interstitial clustering fraction is shown in Figure 15. Since the large clusters are relatively uncommon, the fraction of interstitials contained in them is correspondingly small. This leads to the relatively large standard errors shown in the figure. However, it is clear that the energy dependence of the formation of these large clusters is much stronger than simply the total fraction of interstitials in clusters. Infrequent large clusters such as the 33-interstitial cluster shown in Figure 14 play a significant role in the sharp increase in this clustering fraction observed between 100 and 600K for the 20 keV cascades.

Figure 15. Cascade energy dependence of interstitials contained in clusters of 10 or more: clustered interstitials divided by NRT displacements

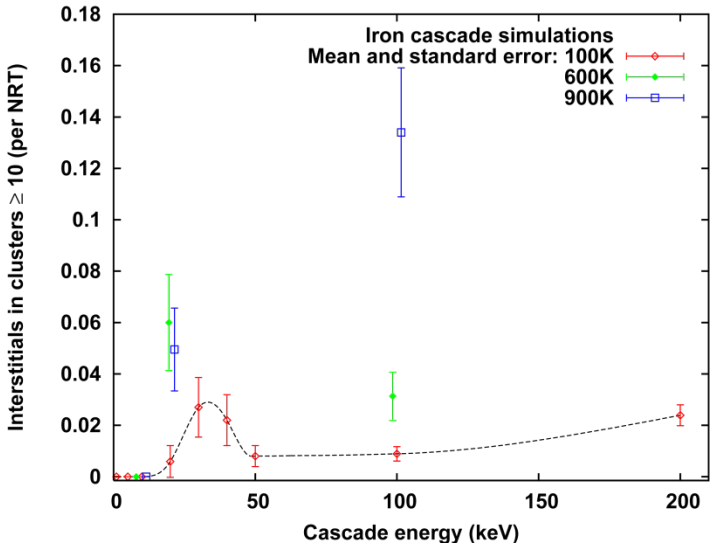

One unusual observation reported in [72,100] was that some of the interstitial clusters exhibited a complex three-dimensional morphology rather than collapsing into planar dislocation loops which are expected to have lower energy. Similar clusters have been seen in materials such as copper, although they appear to be less frequent in copper [66]. The existence of such clusters has been confirmed with interatomic potentials that were developed more recently and with *ab initio* calculations [99]. Representative examples of these clusters from the current iron database are shown in Figure 16, where a ring-like four-interstitial cluster is shown in (a) and a five-interstitial cluster is shown in (b). Unlike the mobile clusters that are composed of [111] crowdions such as the one shown in Figure 14, the SIA clusters in Figure 16 are not mobile. As such, they have the potential for long lifetimes and may act as nucleation sites for larger interstitial-type defects. Figure 17 shows a somewhat larger sessile cluster containing eight SIA. This particular cluster

was examined in detail by searching a large number of low-order crystallographic projections in an attempt to find a projection in which it would appear as a loop. Such a projection could not be found. Rather, the cluster was clearly three-dimensional with a single di-interstitial, tri- interstitial, and di-interstitial on adjacent, close-packed (110) planes as shown in the figure. The eighth interstitial is a [110] dumbbell that lies perpendicular to the others and on the left side in Figure 17a. Figures 16(b-d) are [101] projections through the three centre (101) planes in Figure 17a.

Figure 16. Two examples of sessile interstitial configurations formed in 20 keV, 600K displacement cascades: clusters in (a) and (b) consist of 4 and 5 SIA, respectively (see the glissile cluster configuration in Figure 14)

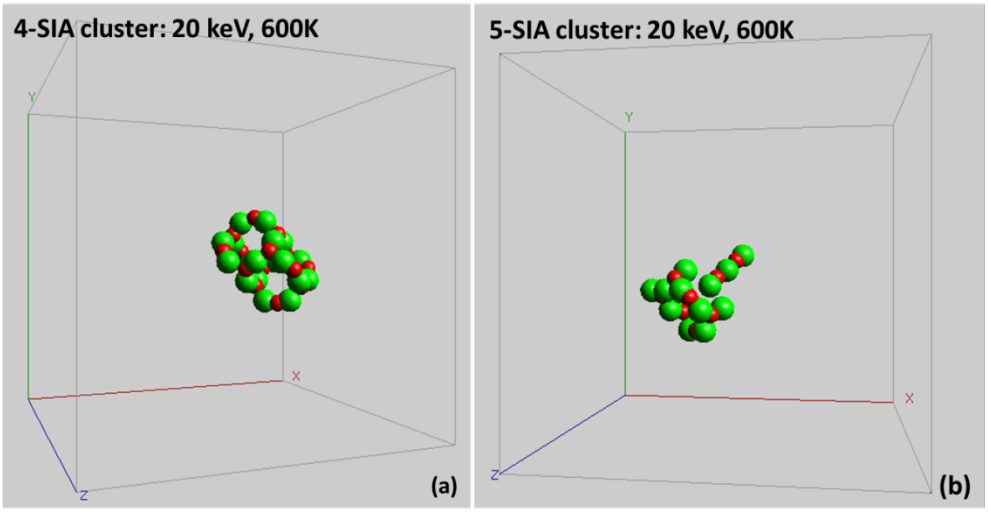

Figure 17. Three dimensional sessile interstitial cluster in 10 keV, 100K cascade: (a) [010] projection normal to five adjacent {110} planes, (b-d) projections through three of the {110} planes

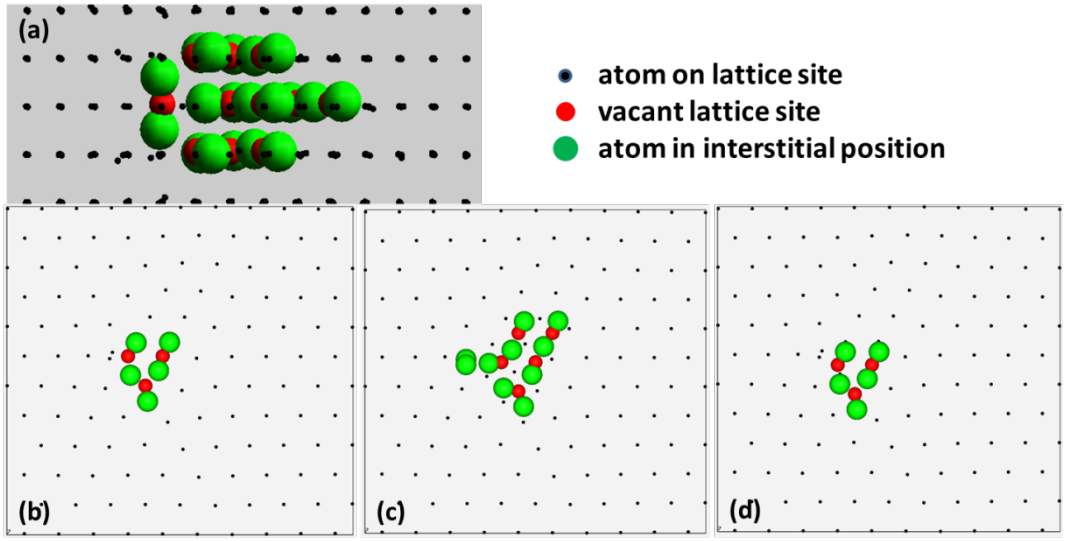

It is possible that the typical 10 to 15 ps MD simulation was not sufficient for the cluster to reorient and collapse. To examine this possibility, the simulation time of a 10 keV cascade at 100K that contained a similar eight SIA cluster was continued up to 100 ps. Very little cluster restructuring was seen over the time from 10 to 100 ps. In fact, the cluster had coalesced into nearly its final configuration by 10 ps. Gao, et al. [100] carried out a more systematic investigation of sessile cluster configurations with extended simulations at 300 and 500K. They found that many sessile clusters had converted to glissile within a few hundred ps, but at least one eight SIA cluster remained sessile for ~500 ps even after aging at temperatures up to 1 500 K. Given the impact that stable sessile clusters would have on the longer timescale microstructural evolution [101], further research is needed to characterize the long-term evolution of cascade-created point defect clusters. It is significant to point out that the conversion of glissile SIA clusters into sessile clusters has also been observed. For example, in a 20 keV cascade at 100K, a glissile eight SIA cluster was trapped and converted into a sessile nine SIA cluster when it reacted with a single [110] dumbell. The simulation was continued for more than 200 ps and the cluster remained sessile.

The mechanism responsible for interstitial clustering has not been fully understood. For example, it has not been possible to determine whether the motion and agglomeration of individual interstitials and small interstitial clusters during the cascade event contributes to the formation of the larger clusters that are observed at the end of the event. Alternate clustering mechanisms in the literature include the suggestion by Diaz de la Rubia and Guinan [102] that large clusters could be produced by a loop punching mechanism. Nordlund, et al. [74] proposed a "liquid isolation" model in which solidification of a melt zone isolates regions with excess atoms.

However, a new mechanism has recently been elucidated by Calder, et al. [103] which seems to explain how both vacancy and interstitial clusters are formed, particularly the less frequent large clusters. Their analysis of cluster formation followed an investigation of the effects of PKA mass and energy which demonstrated that the probability of producing large vacancy and SIA clusters increases as these parameters increase [103]. The conditions of this study produced a unique dataset that motivated the effort to unravel how the clusters were produced. They developed a detailed visualisation technique that enabled them to connect the individual displacements of atoms that resulted in defect formation by comparing the start and end positions of atoms in the simulation cell. This defined a continuous series of links between each vacancy and interstitial that were ultimately produced by a chain of displacements. These chains could be displayed in what are called lines of "spaghetti" [92]. Regions of tangled spaghetti define a volume in which atoms are highly agitated and a certain fraction of which are displaced. Stable interstitials and interstitial clusters are observed on the surface on this volume.

From their analysis of cascade development and the final damage state, Calder and co-workers were able to demonstrate a correlation between the production of large SIA clusters and a process taking place very early in the development of a cascade. Specifically, they established a direct connection between such clusters and the formation of a hypersonic recoil atom that passed through the supersonic pressure wave created by the initiation of the cascade. This highly energetic recoil may create a subcascade and a secondary supersonic shockwave at an appropriate distance from the primary shockwave. In this case, SIA clusters tend to be formed at the point where the primary and secondary

shockwaves interfere with one another. This process is illustrated in Figure 18 [92]. Atoms may be transferred from the primary shockwave volume into the secondary shockwave volume, creating an interstitial supersaturation in the latter and a vacancy supersaturation in the former. In this case, the mechanism of creating large SIA clusters early in the cascade process correspondingly leads to the formation of large vacancy clusters by the end of the thermal spike phase, i.e. after several picoseconds. It is notable that the location of the SIA cluster is determined well before the onset of the thermal spike phase, by about 0.1 ps. Calder's spaghetti analysis provides the opportunity for improved definition of parameters such as cascade volume and energy density; the interested reader is directed to [92] for more details.

Figure 18. Schematic representation of cascade development leading to the formation of interstitial and vacancy clusters formation [92]

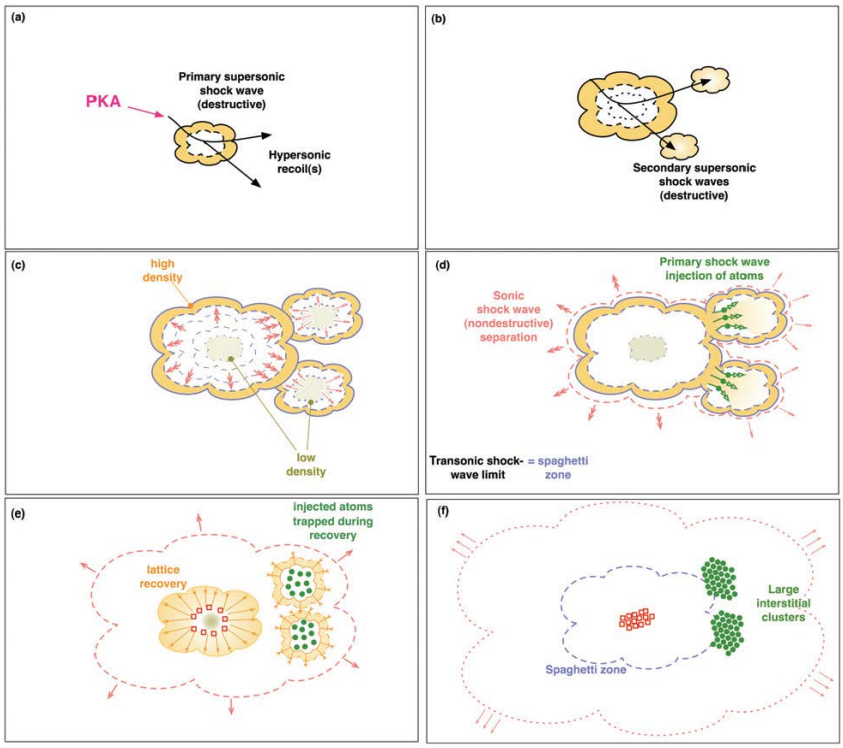

- Vacancy clustering

As discussed elsewhere [71,75,77], in-cascade vacancy clustering in iron is quite low (~10% of NRT) when a nearest-neighbor (nn) criterion for clustering is applied. This was identified as one of the differences between iron and copper in the comparison of these two materials reported in [62]. However, when the coordinates of the surviving vacancies in 10, 20, and 40 keV cascades were analyzed, clear spatial correlations were observed. Peaks in the distributions of vacancy-vacancy separation distances were obtained for the second (2-nn) and fourth (4-nn) nearest neighbor locations [76]. These radial distributions are shown in Figure 19. Similar results were obtained from the analysis of the vacancy distributions in higher energy cascades at 100 K and 600 K. The peak observed for vacancies in 2-nn locations is consistent with the di-vacancy binding energy being greater

for 2-nn (0.22 eV) than for 1-nn (0.09 eV) [104]. In addition, work discussed in Ref. [105] indicates that there is a small binding energy between two vacancies at the 4-nn distance.

Figure 19. Spatial correlation of all vacancies observed in 10, 20, 40 and 50 keV cascades at 100 K

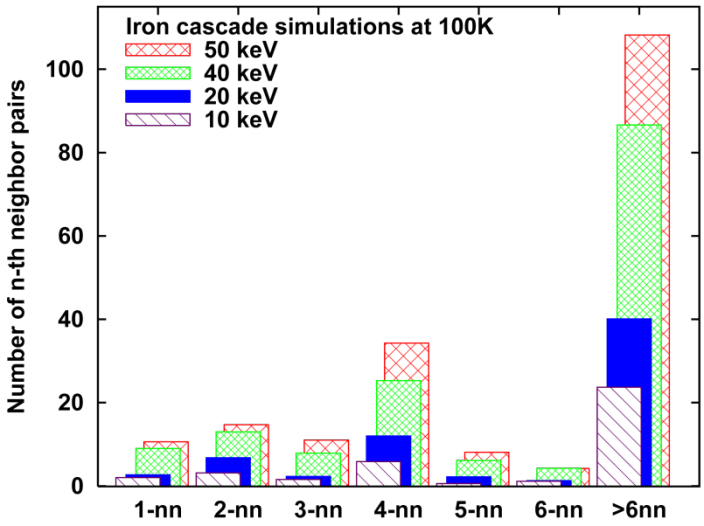

An example of a locally vacancy-rich region in a 50 keV, 100K cascade is shown in Figure 20, where the region around a collection of 14 vacancies has been extracted from the larger simulation cell. This appears to be a nascent or uncollapsed vacancy cluster. Each of the vacancies has at least one other vacancy within the fourth-nearest-neighbour spacing of $1.66a_o$, where a_o is the iron lattice parameter. Such an arrangement of vacancies is similar to some of the vacancy clusters observed by Sato et al. in field ion microscope images of irradiated tungsten [106]. Since the time period of the MD simulations is too short to allow vacancies to jump (<100 ps), the possibility that these closely correlated vacancies might collapse into clusters over somewhat longer times has been investigated using Monte Carlo (MC) simulations. The vacancy coordinates at the end of the MD simulations were extracted and used as the starting configuration in MC cascade annealing simulations. The expectation of vacancy clustering was confirmed in the MC simulations, where many of the isolated vacancies had clustered within 70 ms [104,107].

The energy and temperature dependence of in-cascade vacancy clustering as a fraction of the NRT displacements is shown in Figure 21 for cascade energies of 10 to 50 keV. Results are shown for clustering criteria of 1-nn, 2-nn, 3-nn, and 4-nn. A comparison of Figure 21 and Figure 12 demonstrates that in-cascade vacancy clustering in iron remains lower than that of interstitials even when the 4-nn criterion is used. This is consistent with the experimentally observed difficulty of forming visible vacancy clusters in iron as discussed in [71], and the fact that only relatively small vacancy clusters are found in positron annihilation studies of irradiated ferritic alloys [108]. However, it should be pointed out that work with more recently developed iron potentials finds less difference between vacancy and interstitial clustering [86]. The cascade energy dependence of vacancy clustering is similar to that of interstitials; there is essentially zero clustering at the lowest energies but it rapidly increases with cascade energy and is relatively independent

of energy above ~10 keV. However, vacancy clustering decreases as the temperature increases, which is consistent with vacancy clusters being thermally unstable. Moreover, the rate of increase of vacancy clustering with cascade energy is generally less pronounced than for interstitial clusters and will depend on the interatomic potential used [46,48].

Figure 20. Typical uncollapsed or nascent vacancy cluster from 50 keV cascade at 100K; 14 vacancies are contained, each of which is within the fourth nearest-neighbor distance ($1.66a_o$)

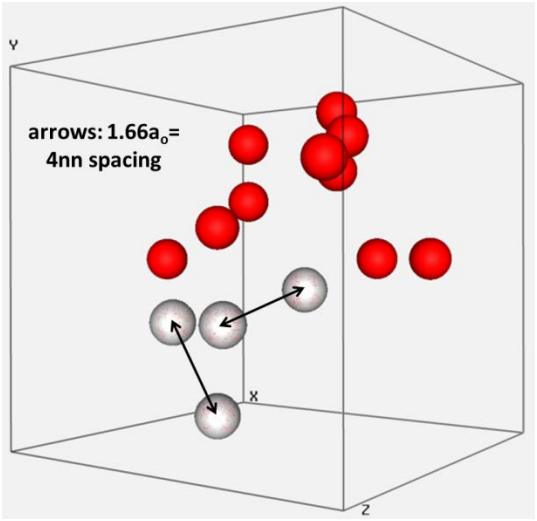

Figure 21. Cascade energy dependence of vacancy clustering: Clustered vacancies divided by NRT displacements

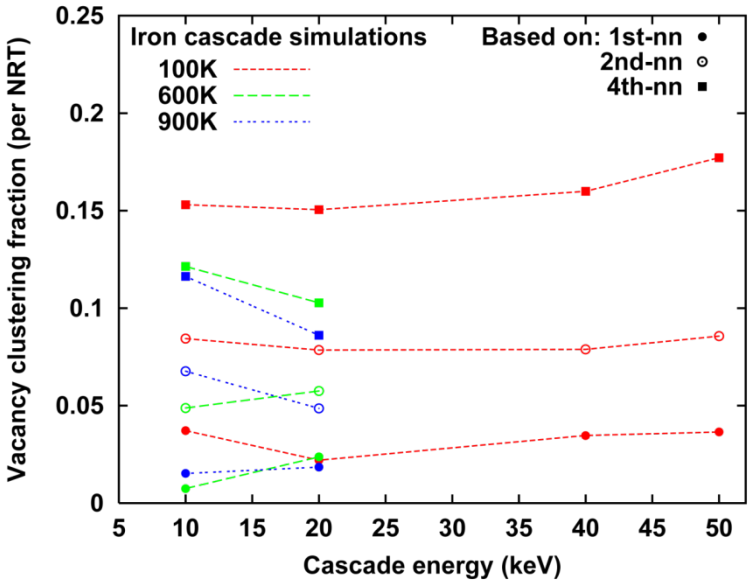

Data points indicate mean values and error bars are standard error of the mean.

Fractional vacancy cluster size distributions are shown in Figure 22, for which the 4-nn clustering criterion has been used. Figure 22a illustrates that the vacancy cluster size distribution shifts to larger sizes as the cascade energy increases from 10 to 50 keV. This is similar to the change shown for interstitial clusters in Figure 13a. There is a corresponding reduction in the fraction of single vacancies. However, as mentioned above, the effect of cascade temperature shown in Figure 22b and 22c is the opposite of that observed for interstitials. The magnitude of the temperature effect on the vacancy cluster size distributions also appears to be weaker than in the case of interstitial clusters. The fraction of single vacancies increases and the size distribution shifts to smaller sizes as the temperature increases from 100 to 900 K for the 10 keV cascades, and from 100 to 600K for 20 keV cascades. Similar to the case of interstitial clusters, the effect of temperature seems to be greater at 20 keV than at 10 keV.

Figure 22. Fractional size distributions of loosely-coupled vacancy clusters (all within 4th nn) formed directly within the cascade, comparison of: (a) 10 and 50 keV cascades at 100 K, (b) 10 keV cascades at 100 and 900 K, and (c) 20 keV cascades at 100 and 600 K

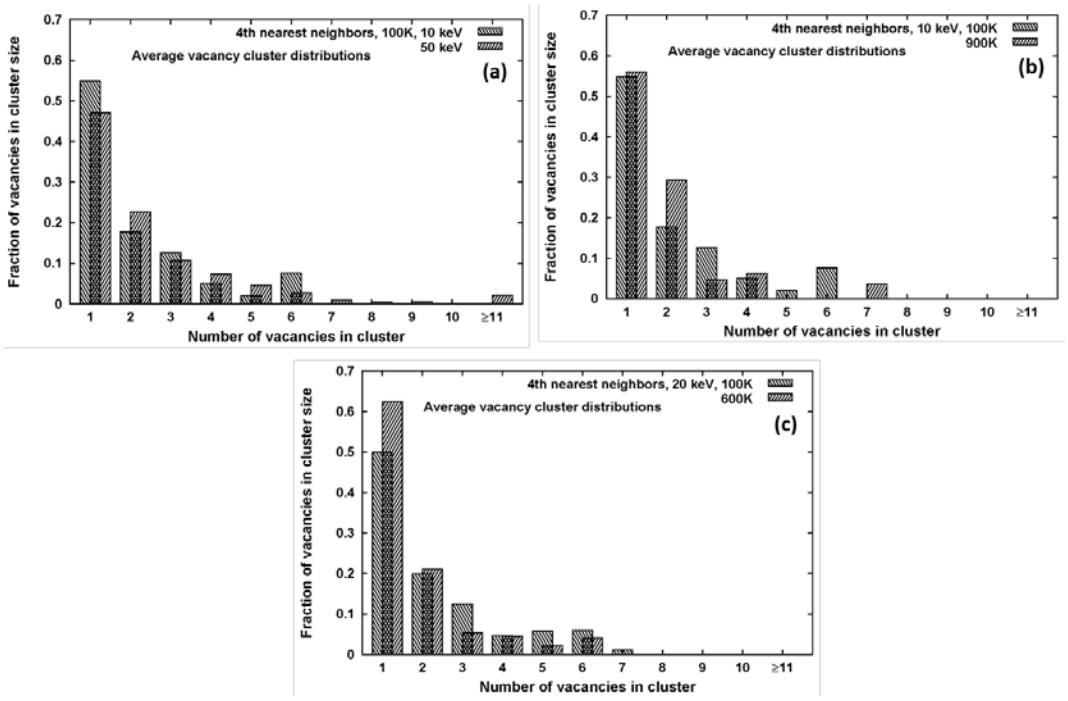

- Secondary Factors Influencing Cascade Damage Formation

The results of simulations such as those presented above should not be viewed as proving a quantitatively accurate accounting of radiation-induced defect formation. As already mentioned, subtle changes in the fitting of the interatomic potential can alter the cascade simulations both qualitatively and quantitatively. Even if a sufficiently accurate potential can be identified, the results represent a certain limiting case of what may be observed experimentally. This is because all the simulations mentioned so far were carried out in perfect material – computer-pure material. Nowhere in nature can such perfect metal be found, particularly for iron which is easily contaminated with minor interstitial impurities such as carbon. Moreover, even if a well-annealed, nearly defect-free, single crystal

material is selected for irradiation, radiation-induced defects will rapidly change the state of the material. A simple calculation employing typical elastic scattering cross sections for fast neutrons and the cascade volumes observed in MD simulations will demonstrate that by the time a dose of ~0.01 dpa is reached, essentially the complete volume will have experienced at least one cascade. A number of studies have been carried out to investigate how a more realistic description of material microstructure could influence the formation of defects from displacement cascades. These include assessments of the influence of pre-existing defects, free surfaces, and grain boundaries as discussed in [47]. Some of the primary findings are summarised below.

There are relatively few studies of how cascade damage production may be different in material with defects [109-112]. The pre-existing defect structures in these studies included small voids, dislocation loops, and random distributions of point defects and small clusters typical of cascade debris. The cascade energy investigated ranged from 1 to 20 keV. Cascade energies of 10 and 20 keV are high enough to initiate in-cascade clustering, are near the plateau region of the defect survival curve, and involve a limited degree of subcascade formation. Substantial variation was observed among different simulations for any given pre-existing defect configuration; in some cases the cascade produced more defects than in perfect crystal, while in others fewer were produced. On average, a significant reduction in defect formation was observed for the configurations most typical of cascade debris. The number of surviving defects, decreases in the presence of loops, with the size of the surviving loops decreasing as well, as a consequence of recombination with vacancies. Small voids and loops can be dissolved by a cascade, but they often re-form, although their configuration may be altered and the loops may have a different Burgers vector.

Some of the statistical variation among different cascades was shown by Gao et al. [100] to be related to the distance between the center of mass of the new cascade and that of the pre-existing damage. A good correlation was found between this spacing and the number of new defects produced. Many more simulations need to be carried out at different energies to develop a more complete picture of cascade damage formation in material with typical defect densities, particularly to assess the clustering behavior. Overall, the reduced defect survival observed in material containing defects suggests that it may be appropriate to employ somewhat lower defect formation values than that obtained for perfect crystal material in kinetic models used to simulate microstructural evolution over long times.

The rationale for investigating the impact of free surfaces on cascade evolution is the existence of an influential body of experimental data provided by experiments in which thin foils are irradiated by high-energy electrons and/or heavy ions [113-121]. In most cases, the experimental observations are carried out *in situ* by transmission electron microscopy and the results of MD simulations are in general agreement with the data from these experiments. For example, some material-to-material differences observed in the MD simulations, such as differences in in-cascade clustering between bcc iron and FCC copper, also appear in the experimental data [71,122,123]. However, the yield of large point defect clusters in the simulations is lower than would be expected from the thin foil irradiations, particularly for vacancy clusters. It is desirable to investigate the source of this difference because of the influence this data has on our understanding of cascade damage formation.

Both simulations [50, 93,94, 124-126] and experimental work [120,121] indicate that the presence of a nearby free surface can influence primary damage formation. For example, interesting effects of foil thickness have been observed in some experiments [120]. Unlike cascades in bulk material, which produce vacancies and interstitials in equal numbers, the number of surviving vacancies and interstitials in surface-influenced cascades can be quite different because of defect transport to the surface. This leads to the formation of larger vacancy clusters and may account for the differences in visible defect yield observed between the results of MD cascade simulations conducted in bulk material and the thin-film, *in situ* experiments. Initial modeling by Nordlund and co-workers [93] and Ghaly and Averback [124] demonstrated the nature of effects that could occur. Subsequently Stoller and co-workers [50,125] and Osetsky and co-workers [94] conducted more systematic studies involving a larger number of simulations at 10 to 25 keV to examine the statistical behavior. Typically, such studies involve creating a free surface on one face of a cubic simulation cell and injecting an atom with the specified kinetic energy through the surface. Periodic boundary conditions are otherwise imposed.

Work by Calder et al. [92] demonstrated the significant role of the cascade-induced pressure wave in defect formation in bulk cascades, particularly its role in cluster formation discussed above. This pressure wave or shock front plays a dominant role in surface cascades when the constraining force of the surface atoms is removed. Examination of the population of surface cascades revealed three broad categories which were distinguished by the distance from the surface at which the shock front changes from supersonic to sonic speeds:

(1) Cascades in which the initial high-angle collisions with the PKA occurred deeply enough that the transformation from a supersonic to sonic shock front speed (transonic transformation) was far from the free surface that little or no direct surface damage was produced. These are generally similar to cascades that occur in bulk material.

(2) Cascades in which the transonic transformation occurs close to the surface produce a significant surface damage, many adatoms, sputtered atoms and large <100> vacancy loops – some of which may glide to the surface. Because of the atom and vacancy movement to the surface, there is a significant imbalance between the number of vacancies and interstitials left in the material.

(3) Cascades in which the supersonic front-shock interacts directly with the free surface produce the greatest degree of surface damage, including deep craters with rims of adatoms and large <100> vacancy loops.

The largest vacancy loops observed the category (2) and (3) cascades were more than 2.5 nm in diameter, which would be visible in the transmission electron microscope. This suggests that the free surface-shock front interaction could be responsible for the visible defect yield observed thin-film, *in situ* experiments mentioned above. Further work such as that described in [94,103] would help assess this issue and improve the ability to make quantitative comparisons between simulations and experiments.

Depending on the complexity of the microstructure, internal interfaces such as grain boundaries, twins, and lath and packet boundaries (in ferritic/martensitic steels) can provide a significant sink in the material for point defects. As such, they may play a significant role in radiation-induced microstructural evolution. For example, the effect of

grain size on austenitic stainless steels was observed as early as 1972 [127-129]. The swelling effect was more closely associated with damage accumulation than damage production, but current understanding of the role of mobile interstitial clusters has provided a link to damage production as well [101,130]. More recently, there has been considerable interest in the properties of nanograined materials because the high sink strength could lead to very efficient point defect recombination and improved radiation resistance. It is reasonable to expect that primary damage production could be influenced in nanograined material because the grain sizes can be of comparable size to high energy displacement cascades. Moreover, investigation of grain size effects by MD would be computationally limited to nanograin sizes in any case.

There have been a limited number of studies carried out to investigate whether and how primary damage formation would be altered in nanograined metals [131-137], and quite strong effects have been observed [131]. The results from [137] can be used to illustrate the phenomenon because the results of that study can be directly compared with the existing single crystal database that has been discussed above. In that work, the nanocrystalline structure was created by choosing random grain nucleation sites and orientations, and completing the grains using a Voronoi technique [138]. MD cascade simulations were carried out in the same manner discussed above, although the analysis was somewhat more difficult due to the need to differentiate cascade-produced defects from the defect structure associated with the grain boundaries.

The results demonstrate that the creation of primary radiation damage can be substantially different in nanograined material due to the influence of nearby grain boundaries. The number of surviving point defects, particularly interstitials, was strongly reduced in the nanograined material. The relative reduction in the point defect clustering fraction is somewhat less than the change in the total number of defects in clusters, is still substantial for interstitial defects. Notably, the temperature dependence of clustering between 100 and 600 K observed in the single crystal 20 keV cascades is reversed in nanograined material. Between 100 and 600 K, the fraction of interstitials in clusters increases for single crystal iron but decreases for nanograined iron. Conversely, the vacancy cluster fraction decreases for single crystal iron and increases for nanograined iron. Both the effects and the mechanisms observed in the iron simulations appear to be consistent with previous work in nickel [131,135], in which very efficient transport of interstitial defects to the grain boundaries was observed. In both iron and nickel, this leads to an asymmetry in point defect survival. Many more vacancies than interstitials survive at the end of the cascade event in nanograined material while equal numbers of these two types of point defects survive in single grain material. There appears to be both a reduction in the number of large interstitial clusters formed directly in the cascade and less coalescence of small mobile interstitial clusters since the latter are being transported to the grain boundaries.

The changes in defect survival observed in these simulations are qualitatively consistent with the limited available experimental observations [132-135]. For example, Rose, et al. [132] carried out room-temperature ion irradiation experiments of Pd and ZrO_2 with grain sizes in the range of 10 to 300 nm, and observed a systematic reduction in the number of visible defects produced. Chimi, et al. [133] measured the resistivity of ion irradiated gold specimens following ion irradiation and found that resistivity changes were lower in nanograined material after room temperature irradiation. However, they

observed an increased change in nanograined material following irradiation at 15K. The low temperature results could be related to the accumulation of excess vacancy defects since they would be immobile at 15 K.

5. Cascade simulations in other metals and alloys

As mentioned above, Bacon and co-workers [97,122] have shown that the number of stable point defects produced in many materials follows a simple power-law dependence over a broad range of cascade energies, see Equation (3). This behaviour is shown in Figure 23 for several pure metals and Ni_3Al [122]. This figure also includes a line labelled NRT which is obtained from Equation (2) if the displacement threshold is taken as 40 eV which is the recommended average value for iron [16]. The difference between the NRT and Fe lines reflect the ratio plotted in Figure 9. Since the displacement threshold is different for different metals (e.g. 30 eV is recommended for Cu [16]), the other lines should not be compared directly with the NRT values. When normalised using the appropriate NRT displacements, the difference in the survival ratio between Fe and Cu can be seen in Figure 24 [122]. Although the stable defect production in the other metals may be either somewhat lower or higher than in iron, the behaviour is clearly similar across this group of BCC, FCC, and hcp materials. Since the energies involved in displacement cascades are so much greater than the energy per atom in a perfect lattice or the vacancy and interstitial formation energies, it is not surprising that ballistic defect production would be similar.

Figure 23. Stable defect formation as a function of cascade energy for several pure metals and Ni_3Al 100 K, and for Al and Ni at 10 K

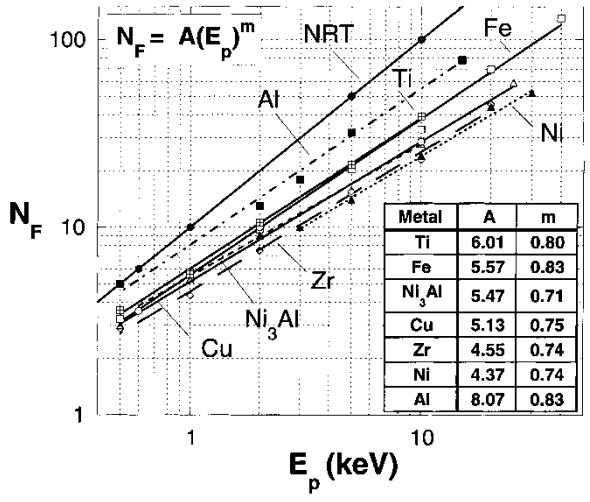

The inset table shows the values of m and A (with E_p in keV) yielding the best power-law fit to the data [122].

Figure 24. Total surviving Frenkel pair divided by the corresponding number of NRT displacements for Fe and Cu [73]

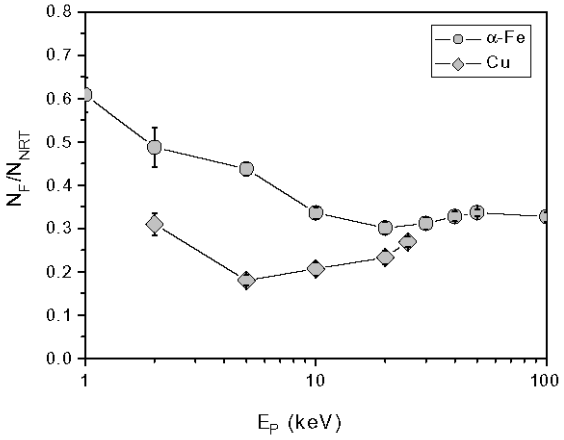

Displacement thresholds of 40 eV and 30 eV were used for Fe and Cu, respectively [16].

5.1 Face-centered cubic (FCC) metals

Cascades in FCC metals have been studied extensively by MD simulations [139-150]. Among the first simulations of relatively energetic cascades in these metals were those in Cu by Diaz de la Rubia and coworkers [139]. Although these simulations were carried out with a purely repulsive interatomic potential, they demonstrated the main features of cascade development that have subsequently been observed in all dense metals, (see Figure 25). In fact, since the FCC crystal structure is close-packed, these features are in many respects most pronounced in this crystal structure. These features include the formation of an under-dense cascade core, formation of a highly-disordered, molten-like region, and recrystallisation of the material during the cooling stage. All these features are qualitatively similar to the behavior of iron discussed above; here we review some particular aspects of cascade evolution in FCC metals.

As in Fe, defect clusters can be produced directly in collision cascades in FCC metals. However, although in Fe the vacancy clusters are disordered, in Cu the formation of geometrically highly symmetric stacking fault tetrahedra (SFT) have been observed experimentally, even at 30 K where no defect migration should occur [140,151,152]. This observation was reproduced by MD simulations of Nordlund and Gao [153], who showed that formation of geometrically perfect SFT's is indeed possible directly in a heat spike carried out even at an ambient temperature of 0 K, i.e. the formation is possible completely without thermally activated equilibrium defect migration, (see Figure 26).

Figure 25. Results from the first molecular dynamics cascade simulations carried out in the heat spike regime [139]

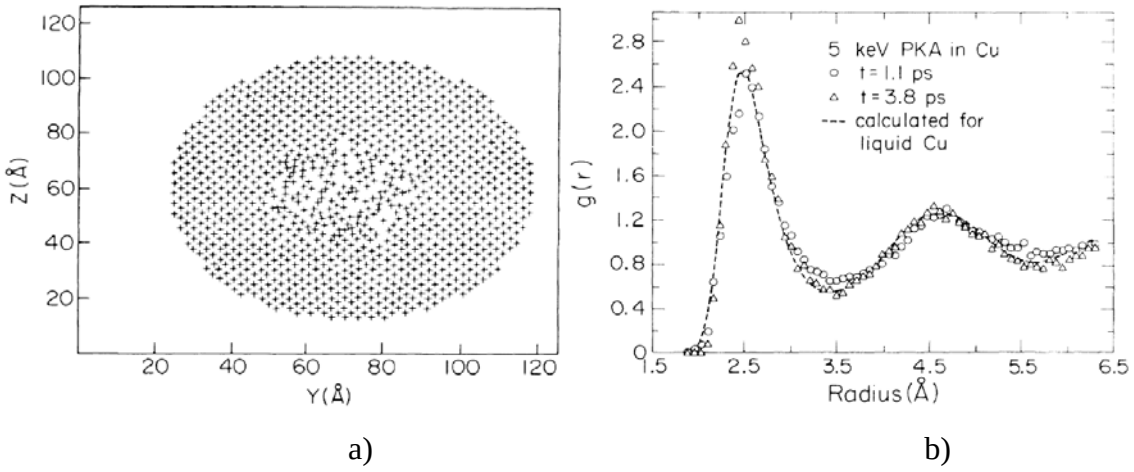

Left: snapshot of the collision cascade. Right: Analysis of the pair correlation function g(r) for the atoms in the heat spike, showing that the disordered atom state corresponds to that of regular liquid Cu, From Ref. **[**139**]** with permission from the authors. Copyright the American Physical Society (1987).

Figure 26. Geometrically perfect stacking fault tetrahedron formed in a 50 keV cascade in Cu

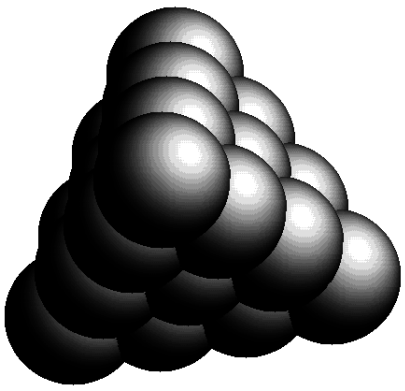

The figure is made based on the same data used for [153].

Cascades have been simulated in several different FCC metals, including the noble metals Cu and Au, the coinage metals Ni, Pd and Pt, as well as Al [143,147]. These metals are interesting to study in that they share not only the same crystal structure, but also (with the exception of Al) a relatively simple electronic structure and hence nature of bonding. Moreover, there are interatomic potentials available for these developed in the same framework by the same groups [154-157], removing some of the general uncertainty of interatomic potential reliability in MD simulations.

On the other hand, these metals have fairly large differences in properties such as mass, melting point and elastic constants. Thus comparison of cascades in them can be instructive to get insight into how these properties affect the cascade evolution. In a systematic comparative study of these metals, Nordlund et al. [143] found that the melting point affects the recrystallization rate of the material and hence also the damage production mechanisms. Later studies on bilayer interfaces of Ni/Cu and Co/Cu interfaces showed conclusively that vacancies are pushed towards the center of the cascade by the recrystallisation front and that at an interface they end up on the side of the lower-melting point metal since the heat spike survives longer in this material [158]. Also studies of cratering at surfaces for model metals where the melting point was changed without modifying the equilibrium properties pointed to the major importance of the value of the melting point on cascade development [159].

Ion beam mixing, i.e. the relocation and replacement of atoms by ion irradiation [160], has also been examined extensively by MD simulations especially in FCC metals [161-163] (although also Fe was considered recently [164]). Since ion beam mixing is a direct outcome of a collision cascade, and usually not affected by diffusive processes [165,166], simulating the ion beam mixing provides a way of testing how well MD simulations describe collision cascades without the major uncertainties in the long-term evolution that in most cases complicates comparison of defect production with experiments.

Comparison of ion beam mixing between Cu, Au, Ni, Pd and Pt showed that also the ion beam mixing clearly depends on the melting point of the material [161]. Since the coinage metals Ni, Pd, Pt have higher melting points than the noble metals Cu and Au, the heat spike cools down faster and thus the time for atom position exchange (mixing) is shorter. Thus mixing in Ni is smaller than in Cu, and that in Pt smaller than in Au, respectively, even though the densities and thus ballistic properties of the element pairs are almost identical [161,162]. This trend agrees well with experiments [166].

The overlap of cascades with pre-existing damage has also been examined in fcc metals. This was motivated by ion beam experiments, where defect production was measured with resistivity, which showed that during prolonged irradiation, the damage level in Cu and Ag saturated at a level of about 1% Frenkel pairs [167]. To explain this, Nordlund and Averback carried out simulations of 5 keV cascades in Al, Cu, Au, Pd and Pt with various levels of pre-existing interstitials. The results showed that when the damage level exceeds about 1%, the new heat spikes promote recombination of damage, such that the final damage level is lower than the initial one. Moreover, Gao et al. considered cascade overlap in Fe, and showed that also extended defects can recombine [100]. Taken together, these results show that the observed damage saturation can be understood as being related to existing defects recombining in subsequent cascade events.

5.2 Influence of alloying elements in Fe

Although the development of alloy potentials is relatively recent, there have been a sufficient number of investigations to provide a comparison of displacement cascade evolution in pure iron with that in four binary alloys, Fe-C, Fe-Cu, Fe-Cr and FeNi [168-184]. The motivation for each of these binary systems is clear. Carbon must be added to iron to make steel, and as a small interstitial solute it could interact with and influence interstitial-type defects. Copper is of interest largely because it is a primary contributor to reactor pressure vessel embrittlement when it is present as an impurity in concentrations

greater than about 0.05 atom-%. Steels containing 7 to 12 atom-% chromium are the basis of a number of modern ferritic and ferritic-martensitic steels that are of interest to nuclear energy systems [184]. Finally, addition of sufficient nickel stabilises the FCC structure and provides a model system for FCC austenitic stainless steels.

5.2.1 Defect Production in Fe-C

Calder et al. examined the effect of carbon on defect production in the Fe-C system with the carbon concentration between 0 and 1.0 atom-% [168]. The Fe potential was developed by Ackland and co-workers [176]. The form of this potential is similar to the Finnis-Sinclair potential discussed throughout this chapter, but the absolute level of defect production is somewhat lower. Simulations were carried out at temperatures of 100 and 600K for cascade energies of 5, 10, and 20 keV. Thirty simulations were carried out at each condition to ensure a good statistical sampling. No systematic effect of carbon was observed on either stable defect formation or the clustering of vacancies and interstitials. Analysis of the octahedral sites around vacancies and interstitials revealed a statistically significant association of carbon atoms with both vacancies and SIAs. This indicates an effective trapping which is consistent with the solute-defect binding energies. Although primary damage formation was not affected by carbon, the trapping mechanism could have an effect on damage accumulation.

5.2.2 Defect Production in Fe-Cu

Copper concentrations as high as ~0.4 atom-% were found in early reactor pressure steels, largely due to both steel recycling and the use of copper as a corrosion-resistant coating on steel welding rods. Research that began in the 1970s demonstrated that this minor impurity was responsible for a significant fraction of the observed vessel embrittlement due to its segregation into a high density of very small (a few nm diameter) copper-rich solute clusters [169]. Becquart, et al. employed MD cascade simulations to determine whether displacement cascades could play a role in the Cu-segregation process, e.g. by coalescing with vacancies in the cascade core during the cooling phase. The set of interatomic potentials used is described in [169]. Cascade energies of 5, 10, and 20 keV were employed in simulations at 600 K, with copper concentrations of 0, 0.2, and 2.0 atom-%. Similar to the case for Fe-C, no effect of copper was found on either stable defect formation or point defect clustering. The tendency for copper to be found bound with either a vacancy or an interstitial in solute-defect complex was observed. The copper-vacancy complexes may play role in the formation of copper-rich clusters over longer times, but no evidence for copper clustering was observed in the cascade debris. Similar results were found in an earlier study by Calder and Bacon [170]. Overall, the results of the Fe-Cu studies completed to date are consistent with the fact that Fe and Cu have similar masses and do not strongly interact.

5.2.3 Defect Production in Fe-Cr

Interest in ferritic and ferritic-martensitic steels has stimulated the development of Fe-Cr potentials such as those discussed in [172]. These potentials have been applied to investigate the influence of Cr on displacement cascades [173,174] and on point defect diffusion [175]. The MD cascade study by Malerba, et al. in [173] involved cascade energies from 0.5 to 15 keV at 300K. In contrast to the Fe-C and Fe-Cu results discussed above, a slight increase in stable defect formation was observed in Fe-10%Cr relative to

pure Fe. The asymptotic value of the defect survival ratio (relative to the NRT) at the highest energies was 0.28 for Fe and 0.31 for Fe-10%Cr. In a later study by the same authors which involved a larger number of simulations and energies up to 40 keV, they also concluded that the presence of 10% Cr did not lead to a change in the collisional phase of the cascade but rather reduced the amount of recombination during the cooling phase [135]. Additional detailed studies performed with more recent Fe-Cr potentials essentially confirmed the absence of any significant effect of Cr on primary damage in Fe-Cr alloys as compared to pure Fe [178-180].

The lack of a Cr effect on the collisional or ballistic phase of the cascade may be expected because, like Cu, the mass of Cr is similar to Fe. The reduced recombination appears to be related to the formation of highly stable mixed Fe-Cr dumbbell interstitials. About 60% of interstitial dumbbells contain a Cr atom, which is substantially higher than the overall Cr concentration of 10%. In spite of the strong mixed dumbbell formation, the fraction of point defects in clusters did not seem to be significantly different than in pure Fe. However, if the stability and mobility of the mixed dumbbells and clusters containing them proves to be appreciably different than pure iron dumbbells [175], there could be an influence on damage accumulation at longer times. Experimental results that are consistent with this hypothesis [174] are mentioned in [185].

5.2.4 Defect Production in Fe-Ni

The damage production in Fe-Ni alloys at variable compositions (with 10, 40, 50, and 75% Ni content), both in the bcc and FCC structure, were examined by molecular dynamics simulations by Vörtler et al. [184]. For comparison, also BCC Fe-Cr cells with Cr compositions in the range of 0 to 15% were examined. Some of the cells had an atomic arrangement in a completely random distribution of Ni and Fe (solid solution), while $Fe_{50}Ni_{50}$ was also simulated in an ordered intermetallic configuration. The effect of prolonged irradiation was studied by carrying out simulations of the overlapping of single 5 keV displacement cascades events. Analysis of the short range order showed that the initially ordered cells were driven towards an disordered configuration, while the random alloys remained disordered.

In the particular case of the $Fe_{60}Ni_{40}$ configuration simulated starting from an FCC structure, it was found that although the system is initially stable, after generating a sufficient number of overlapping cascades, the structure collapsed into a strongly disordered state. This is consistent with the phase diagram in which the $Fe_{60}Ni_{40}$ should be unstable. This study demonstrates that irradiation-induced defects can destabilise a metastable phase even in a structure with no surface or other initial seeds for a phase change.

One main difference in the Frenkel pair production due to an increasing number of cascades in the bcc and FCC simulation cells was identified [184]. In bcc cells, the number of Frenkel pair was observed to saturate, i.e. the overlapping of multiple cascades tends to produce fewer new defects with each subsequent cascade In the FCC alloys, stacking-faults, including stacking fault tetrahedral were observed with an increasing number of cascades in the cell as shown in Figure 27. Due to these stacking faults, the cell did not re-crystallise in its original orientation and the number of Frenkel pair did not saturate and was higher than in bcc cells. With an increasing number of overlapping of cascades, the initially perfect FCC crystals became polycrystalline. The fraction of SIAs in clusters

saturated at about 80% in the bcc and 90% in the FCC cells. The most striking effect of the Cr content in Fe-Cr was preferential enrichment of Cr in SIA positions, with a concentration about twice that of the matrix for Fe-5%Cr. The concentration of Cr was not enriched in large 1D-migrating SIA clusters in any of the Fe-Cr alloys. Analysis of the SIA cluster size after ~200 cascades had been simulated in the cell showed that more small clusters containing 2 to 5 SIAs were present in bcc material, while the number of large clusters is higher in FCC than in BCC metals [186].

Figure 27. Stacking fault tetrahedral (top) and other extended defects observed after 64 overlapping 5 keV cascades in initially ordered Fe50Ni50

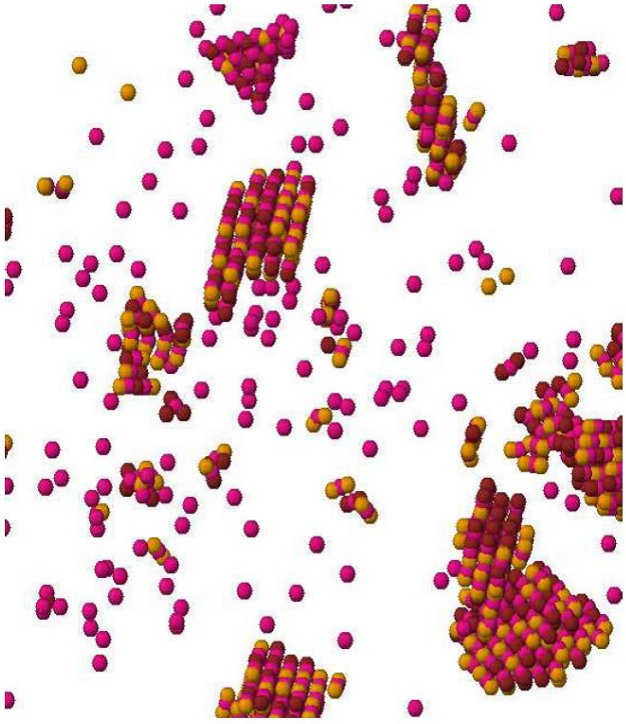

The magenta spheres are vacant atom positions, the dark red spheres are Ni and the beige ones Fe [192].

6. Summary and needs for further work

The use of molecular dynamics to simulate primary damage formation has become widespread and relatively mature. In addition to the research involving metals discussed above, the approach has also been applied to common structural ceramics [11-14, 187] and ceramics of interest to the nuclear fuel [15,188,189]. However, there are a number of areas that require further research. Some of these have to do with the most basic aspect of MD simulations, i.e. the interatomic potentials that are used. In addition to the Finnis-Sinclair potential for iron that was used as a reference case in this chapter, results from several other iron potentials were mentioned. The choice of potential is never an obvious one, and there have been few studies to systematically compare them. In one such study, the details of how the equilibrium part of the potential was joined to a screened Coulomb potential to account for short range interactions were shown to significantly influence cascade evolution and defect formation [47]. Although a clear difference has been

demonstrated, there is no clear path to determining what constitutes the "correct" way to join these potentials.

In the case of iron and other magnetic elements such as chromium, research to address the issue of how magnetism may influence defect formation and behaviour has only recently begun [190-192]. The effect may be modest in the ballistic phase of the cascade when energies are high, but magnetism must certainly influence the configuration and properties of stable defects. Magnetic effects may also determine critical properties of interstitial clusters such as their migration energy and primary diffusion mechanism, which will strongly influence the nature of radiation damage accumulation. Since the standard density functional theory fails to fully account for magnetic effects, further developments in electronic structure theory are required in order to provide data for fitting new and more accurate potentials. Moreover, in order to allow explicitly for these effects new interatomic potential formalisms will be likely to be required, the challenge being that they should be computationally affordable in order to allow the study of large systems. Alternatively, as is done at the moment [193,194], magnetic effects can be "effectively" included by taking them into account when fitting potentials of Finnis-Sinclair or Embedded Atom Method type.

The interaction between the atomic and electronic system has largely been neglected in most of the work discussed above. This may impact the results of MD simulations in at least two ways. First, energetic atoms lose energy in a continuous slowing down process that involves both the elastic collisions MD currently models and electronic excitation and ionization between these elastic collisions with lattice atoms. Because of the energy dependence of elastic scattering cross-sections, neglecting the energy loss between atomic collisions could lead to more diffuse cascades and higher predicted defect survival. The second effect is related to inaccuracies in temperature when energy transfer between the electronic and atomic systems (electron-phonon coupling) is neglected. To first order, the atoms remain hotter when energy loss to the electron system is not accounted for. Given the temperature dependence of defect survival and defect clustering discussed above, this clearly has the potential to be significant in any one material. In addition, since electron-phonon coupling varies from one material to another, its neglect may obscure real differences in defect formation between materials.

Finally, the issue of rare events requires more investigation. The need to carry out sufficient simulations at a given condition to obtain an accurate estimate for mean behaviour was emphasised in the chapter. However, it may be that rare events are also important for the prediction of radiation damage accumulation at longer times or higher doses. If nucleation of extended defects is difficult, which is typically the case at higher temperatures and lower point defect supersaturations, rare events that seed the microstructure with large clusters may largely control the process. One example of a potentially significant rare event is provided by the work of Soneda, et al. [195]. They carried out 100 50 keV simulations at 600 K to obtain a good statistical description of defect formation at this condition. In one of these simulations, 223 stable point defects were created, which was much greater than the average of 130 defects. In addition, a <100> vacancy loop containing 153 vacancies was created. The diameter of the loop was about 2.9 nm, which is large enough to be visible by transmission electron microscopy. The impact of the one-in-a-hundred type events should not be underestimated without further study.

Acknowledgments

Various aspects of RES's research discussed in this chapter were supported by the Division of Materials Sciences and Engineering, and the Office of Fusion Energy Sciences, U.S. Department of Energy and the Office of Nuclear Regulatory Research, U.S. Nuclear Regulatory Commission at the Oak Ridge National Laboratory under contract DE-AC05-00OR22725 with UT-Battelle, LLC. This work has also been carried out within the framework of the EURO fusion Consortium and has received funding from the Euratom research and training programme 2014-2018 under grant agreement No 633053. The views and opinions expressed herein do not necessarily reflect those of the European Commission.

References

[1] F. A. Garner, "Overview of the Swelling Behavior of 316 Stainless Steel," Optimizing Materials for Nuclear Applications, F. A. Garner, D. S. Gelles, and F. W. Wiffen. Eds., The Metallurgical Society, Warrandale, PA, 1984, pp. 111-141.

[2] J. A. Wang, F. B. K. Kam, and F. W. Stallman, "The Embrittlement Data Base (EDB) and Its Applications," Effects of Radiation on Materials, ASTM STP 1270, D. S. Gelles, R. K. Nanstad, A. S. Kumar, and E. A. Little, Eds., American Society of Testing and Materials, Philadelphia, 1996, pp. 500-521.

[3] R. E. Stoller, "Pressure Vessel Embrittlement Predictions Based on a Composite Model of Copper Precipitation and Point Defect Clustering," Effects of Radiation on Materials, ASTM STP 1270, D. S. Gelles, R. K. Nanstad, A. S. Kumar, and E. A. Little, Eds., American Society for Testing and Materials, Philadelphia, 1996, pp. 25-58.

[4] For example, see the proceedings from a series of two international conferences: (a) The Effects of Radiation on Materials, published in a series of Special Technical Publications by the ASTM International, West Conshohocken, PA, and (b) the International Conference on Fusion Reactor Materials published in the Journal of Nuclear Materials.

[5] J.A. Brinkman, J. Appl. Phys. 25 (1954) 961-969.

[6] J.A. Brinkman, Amer. J. Phys. 24 (1956) 246-267.

[7] E. Weinan *Principles of Multiscale Modelling*, Cambridge University Press, (2011).

[8] A. F. Tasch, Nucl. Inst. and Meth. in Physics Research B74 (1993) 3-6.

[9] Ion Mixing and Surface Layer Alloying, M-A. Nicolet and S. T. Picraux, Eds., Noyes Publications, Park Ridge, NJ, 1984.

[10] L. W. Hobbs and M.R. Pascucci, J. Phys. Colloques 41 (1980) C6-237-C6-242

[11] B. P. Uberuaga, A. F. Voter, K. E. Sickafus, A. Cleave, R. W. Grimes, and R. Smith, J Computer-Aided Mater Des (2007) 14:183–189.

[12] R. Cleave, R. W. Grimes, R. Smith, B. P. Uberuaga and K. E. Sickafus, Nucl. Instr. and Meth. B 250 (2006) 28-35.

[13] J. M. Perlado, L. Malerba, A. Sanchez-Rubio, and T. Diaz de la Rubia, J. Nucl. Mater. 276 (2000) 235-242.

[14] F. Gao, W. J. Weber and R. Devanathan, Nucl. Instr. and Meth. B 180 (2001) 176-186.

[15] R. Devanathan and W. J. Weber, Nucl. Instr. and Meth. B 268 (2010) 2857-2862

[16] ASTM E521, Standard Practice for Neutron Radiation Damage Simulation by Charged Particle Irradiation, Annual Book of ASTM Standards, Vol. 12.02, ASTM International, West Conshohocken, PA.

[17] G. H. Kinchin and R. S. Pease, Prog. Phys. 18 (1955) 1.

[18] J. Lindhard, M. Scharff and H.E. Schiott, Mat. Fys. Medd. Dan. Vid. Selsk. 33 (1963) 1.

[19] M. J. Norgett, M. T. Robinson, and I. M. Torrens, Nucl. Eng. and Des. 33 (1975) 50-54, and see ASTM E693, Standard Practice for Characterizing Neutron Exposures in Ferritic Steels in Terms of Displacements per Atom (dpa), Annual Book of ASTM Standards, Vol. 12.02, ASTM International, West Conshohocken, PA.

[20] D.J. Bacon, A.F. Calder, J. M. Harder, and S.J. Wooding, J. Nucl. Mater. 205 (1993) 52-58

[21] M.W. Finnis and J.E. Sinclair, Phil. Mag. A50 (1984) 45-55 and Erratum, Phil. Mag A53 (1986) 161.

[22] K. Nordlund, J. Wallenius, and L. Malerba, Nucl. Instr. and Meth. B, 246 (2006) 322-332

[23] D. E. Harrison and M. M. Jakas, Nucl. Inst. and Meth. B15 (1986) 25-28.

[24] I. M. Torrens and M. T. Robinson, "Computer Simulation of Atomic Displacement Cascades in Metals," Radiation-Induced Voids in Metals, U.S. AEC CONF-710601, 1972, pp. 739-756

[25] M. T. Robinson, J. Nucl. Mater. 216 (1994) 1-28.

[26] R. E. Stoller and G. R. Odette, J. Nucl. Mater 186 (1992) 203-205).

[27] P. Jung, Phys. Rev. B 23 (1981) 664-670.

[28] G. Wallner, M. S. Anand, L. R. Greenwood, M. A. Kirk, W. Mansel, and W. Waschkowski, J. Nucl. Mater. 152 (1988) 146-153.

[29] F. Bergner, A. Ulbrichta, M. Hernandez-Mayoral and P. K. Pranzas, J. Nucl. Mater. 374 (2008) 334-337.

[30] H. Franz, G. Wallner, J. Peisl, Radiat. Eff. Def. Solids 128 (1994) 189.

[31] P. Asoka-Kumar and K.G. Lynns, Journal de Physique IV Colloque C1, supplement to Journal de Physique 111 (5) 1995 C1-C15.

[32] L. A. Beaven, R. M. Scanlan, and D. N. Seidman, "The Defect Structure of Depleted Zones in Irradiated Tungsten," U.S. AEC Report NYO-3504-50, Cornell University, Ithaca, NY, 1971.

[33] C.A. English and M.L. Jenkins, Mater. Sci. Forum 15-18 (1987) 1003-1022.

[34] M.L. Jenkins, M.A. Kirk and W.J. Phythian, J. Nucl. Mater. 205 (1993) 16-30.

[35] M. A. Kirk, "Production of Defects in Metals by Collision Cascades: TEM Experiments," Microstructure of Irradiated Materials, I. M. Robertson, L. E. Rehn, S. J. Zinkle, and W. J. Phythian, Eds. Materials Research Society, Pittsburgh, PA, 1995, pp. 47-56.

[36] S. J. Zinkle and B. N. Singh, C

[37] M. Kiritani, J. Nucl. Mater. 276 (2000) 41-49.

[38] J. B. Gibson, A. N. Goland, M. Milgram, and G. H. Vineyard, Phys. Rev. 120 (1960) 1229.

[39] J. R. Beeler, Jr., "Computer Simulation of Radiation-Induced Void Nucleation and Growth in Metals," Radiation-Induced Voids in Metals, U.S. AEC CONF-710601, 1972, pp. 684-738.

[40] D. E. Harrison, P. W. Kelly, B. J. Garrison, and N. Winograd, Surc. Sci 76 (1978) 311-322.

[41] D. E. Harrison and M. M. Jakas, Rad. Eff. 99 (1986) 153-169.

[42] H. L. Heinisch and B. N. Singh, J. Nucl. Mater. 191-194 (1992) 1083-1087.

[43] M. Hou, A. Souidi, C. S. Becquart, C. Domain, L. Malerba, J. Nucl. Mater. 382 (2008) 103-111.

[44] W. Cai, J. Li, and S. Yip, "Molecular Dynamics," in *Comprehensive Nuclear Materials*, R. J. M. Konings, T. R. Allen, R. E. Stoller, and S. Yamanaka, Editors, Elsevier Ltd., Amsterdam, 2012, pp. 249-265.

[45] G. J. Ackland, "Interatomic Potential Development," in *Comprehensive Nuclear Materials*, R. J. M. Konings, T. R. Allen, R. E. Stoller, and S. Yamanaka, Editors, Elsevier Ltd., Amsterdam, 2012, pp. 267-291.

[46] L. Malerba, J. Nucl. Mater. 351 (2006) 28-38.

[47] R. E. Stoller, "Primary Radiation Damage," in *Comprehensive Nuclear Materials*, R. J. M. Konings, T. R. Allen, R. E. Stoller, and S. Yamanaka, Editors, Elsevier Ltd., Amsterdam, 2012, pp. 293-332.

[48] D. Terentyev, C. Lagerstedt, P. Olsson, K. Nordlund, J. Wallenius, C.S. Becquart, and L. Malerba, J. Nucl. Mater. 351 (2006) 65-77.

[49] R. E. Stoller, J. Nucl. Mater. 233-237 (1996) 999-1003.

[50] R. E. Stoller and S. G. Guiriec, J. Nucl. Mater. 329-333 (2004) 1228-1232.

[51]R. E. Stoller, "The influence of PKA Direction on Displacement Cascade Evolution," Microstructural Processes in Irradiated Materials, MRS Vol. 650, G. E. Lucas, L. L. Snead, M. A. Kirk, and R. G. Elliman, Eds, Materials Research Society, Warrandale, PA, 2001, pp. R3.5.1-6

[52] D. R. Mason, J. le Page, C. P. Race, W. M. C. Foulkes, M. W. Finnis and A. P. Sutton, J. Phys.: Condens. Matter 19 (2007) 436209 (13 pp).

[53] K. Gärtner et. al., Nucl. Instr. Meth. Phys. Res. B, 102(1-4):183, 1995

[54] L. Leblanc and G. G. Ross. Nucl. Instr. Meth. Phys. Res. B, 83:15, 1993.

[55] K. Nordlund, Comput. Mater. Sci., 3:448, 1995.

[56] K. M. Beardmore and N. Gronbech-Jensen, Phys. Rev. E, 57:7278, 1998.

[57] C. Bjorkas and K. Nordlund, Nucl. Instr. Meth. Phys. Res. B, 267:1830--1836, 2009

[58] A. E. Sand, S. L. Dudarev, and K. Nordlund. High energy collision cascades in tungsten: dislocation loops structure and clustering scaling laws EPL, 103:46003, 2013

[59] M. W. Finnis, P. Agnew and A. J. E. Foreman, Phys. Rev. B 44 (1991) 567–574.

[60] C. P. Flynn and R. S. Averback, Phys. Rev. B 38 (1988) 7118–7120.

[61] A. Caro A and M. Victoria, Phys. Rev. A 40 (1989) 2287–2291

[62] F. Gao, D. J. Bacon, P. E. J. Flewitt, and T. A. Lewis, Mod. Simul Mater. Sci. Eng 6 (1998) 543-556

[63] C. P. Race, D. R. Mason, M. W. Finnis, W. M. C. Foulkes, A. P. Horsfield and A. P. Sutton, Rep. Prog. Phys. 73 (2010) 116501 (40pp).

[64] R. S. Averback, T. Diaz de la Rubia and R. Benedek, Nucl. Instr. and Meth. in Physics Research B 33 (1988) 693-700.

[65] T. Diaz de la Rubia and M. W. Guinan, J. Nucl. Mat. 274 (1990) 151-157.

[66] A.J.E. Foreman, C.A. English and W.J. Phythian, Phil. Mag. A66 (1992) 655-669.

[67] T. Diaz de la Rubia and M. W. Guinan, Mater. Sci. Forum 97-99 (1992) 23-42.

[68] R. S. Averback, J. Nucl. Mater. 216 (1994) 49-62.

[69] J. B. Adams, A. Rockett, J. Kieffer, W. Xu, M. Nomura, K. A. Kilian, D. F. Richards, and R. Ramprasand, J. Nucl. Mater. 216 (1994) 265-274.

[70] A.F. Calder and D.J. Bacon, J. Nucl. Mat. 207 (1993) 25-45.

[71] W. J. Phythian, R. E. Stoller, A. J. E. Foreman, A. F. Calder, and D. J. Bacon, J. Nucl. Mater. 223 (1995) 245-261.

[72] S.J. Wooding, D.J. Bacon, and W.J. Phythian, Phil. Mag. A 72 (1995) 1261-1279.

[73] D.J. Bacon, Yu.N. Osetsky, R.E. Stoller, R.E. Voskoboinikov, J. Nucl. Mater. 323 (2003) 152-162.

[74] Nordlund, M. Ghaly, R. S. Averback, M. Caturla, T. Diaz de la Rubia, and J. Tarus, Physical Review B 57 (1998) 7556-7570

[75] R. E. Stoller, "Molecular Dynamics Simulations of High Energy Cascades in Iron," Microstructure of Irradiated Materials, Vol. 373, I. M. Robertson, L. E. Rehn, S. J. Zinkle, and W. J. Phythian, Eds., Materials Research Society, Pittsburgh, PA, 1995, pp. 21-26.

[76] R. E. Stoller, G. R. Odette, and B. D. Wirth, J. Nucl. Mater. 251 (1997) 49-60.

[77] R. E. Stoller, "Point Defect Cluster Formation in Iron Displacement Cascades up to 50 keV," Microstructural Processes in Irradiated Materials, Vol. 540, S. J. Zinkle, G. E. Lucas, R. C. Ewing, and J. S. Williams, Eds., Materials Research Society, Pittsburgh, PA, 1999, pp. 679-684.

[78] R. E. Stoller, J. Nucl. Mater. 276 (2000) 22-32.

[79] R. E. Stoller and A. F. Calder, J. Nucl. Mater. 283-287 (2000) 746-752.

[80] M. J. Caturla, T. D. De la Rubia, M. Victoria, R. K. Corzine, M. R. James, and G. A. Greene, J. Nucl. Mater. 296 (2001) 90.

[81] J. Fikar and R. Schäublin, J. Nucl. Mater. 386–388 (2009) 97–101.

[82] S. J. Wooding and D. J. Bacon, Phil. Mag. A 76 (1997) 1033-1051.

[83] B.D. Wirth, G.R. Odette, D. Maroudas, and G.E. Lucas, J. Nucl. Mater. 244 (1997) 185-194.

[84] C.S. Becquart, C. Domain, A. Legris, and J.C. Van Duysen, J. Nucl. Mater. 280 (2000) 73-85.

[85] C. Björkas and K. Nordlund, NIMB 259 (2007) 853-860.

[86] L. Malerba, M.C. Marinica, N. Anento, C. Björkas, H. Nguyen, C. Domain, F. Djurabekova, P. Olsson, K. Nordlund, A. Serra, D. Terentyev, F. Willaime, C.S. Becquart, J. Nucl. Mater. 406 (2010) 19-38.

[87] M.W. Finnis, "MOLDY6 A Molecular Dynamics Program for Simulation of Pure Metals," AERE R 13182, U.K.A.E.A. Harwell Laboratory, 1988.

[88] M. Parrinello and A. Rahman, Phys. Rev. Lett. 45 (1980) 1196–1199 and M. Parrinello and A. Rahman, J. Appl. Phys. 52 (1981) 7182.

[89] F. Gao, D. J. Bacon, P. E. J. Flewitt, and T. A. Lewis, J. Nucl. Mater. 249 (1997) 77-86.

[90] Kendall's Advanced Theory of Statistics, Volume 1, A. Stuart and J. K. Ord, Charles Griffin and Company, Ltd., London, 1987

[91] Manual on Presentation of Data and Chart Control Analysis, Sixth Edition, American Society for Testing and Materials, West Conshohocken, PA, 1992.

[92] A. F. Calder, D. J. Bacon, A. V. Barashev, Yu.N. Osetsky, Phil. Mag. 90 (2010) 863-884.

[93] K. Nordlund, J. Keinonen, M. Ghaly, and R. S. Averback, Nature 398 (1999) 49-51

[94] Y. N. Osetsky, A. F. Calder, and R. E. Stoller, " How do energetic ions damage metallic surfaces?," accepted for publication in Current Opinion in Solid State & Materials Science (2015).

[95] R. E. Stoller and L. E. Greenwood, J. Nucl. Mater. 271&272 (1999) 57-62.

[96] O. S. Oen and Mark T. Robinson, Appl. Phys. Lett. 2 (1963) 83-85.

[97] D.J. Bacon, A.F. Calder, F. Gao, V.G. Kapinos, and S.J. Wooding, Nucl. Instr. and Meth. in Physics Research B102 (1995) 37-46.

[98] R.S. Averback, R. Benedek, and K.L. Merkle, Phys. Rev. B 18 (1978) 4156-4171.

[99] S. I. Golubov, A. V. Barashev, and R. E. Stoller, "Radiation Damage Theory," in *Comprehensive Nuclear Materials*, R. J. M. Konings, T. R. Allen, R. E. Stoller, and S. Yamanaka, Editors, Elsevier Ltd., Amsterdam, 2012, pp. 357-391.

[100] D. A. Terentyev, T. P. C. Klaver, P. Olsson, M.-C. Marinica, F. Willaime, C. Domain, and L. Malerba, Physical Review Letters 100 (2008) 145003.

[101] F. Gao, D. J. Bacon, Yu. N. Osetskiy, P. E. J. Flewitt, and T. A. Lewis, *J. Nucl. Mater.* 276 (2000) 213-220.

[102] T. Diaz de la Rubia and M.W. Guinan, Physical Review Letters 66 (1991) 2766.

[103] A.F. Calder, D.J. Bacon, A.V. Barashev and Yu.N. Osetsky, Phil. Mag. Lett. 88 (2008) 43.

[104] B. D. Wirth, "On the Character of Nano-scale Features in Reactor Pressure Vessel Steels Under Neutron Irradiation," Ph. D. Dissertation, University of California, Santa Barbara (1998).

[105] F. Djurabekova, L. Malerba, R. C. Pasianotcd, P. Olssone, and K. Nordlund, Phil Mag, 90 (2010) 2585–2595.

[106] S. Sato, A. Kohyama, and N. Igata, *Appl. Surf. Sci.* 76&77 (1994) 285-290.

[107] B. D. Wirth and G. R. Odette, "Kinetic Lattice Monte Carlo Simulations of Cascade Aging in Iron and Dilute Iron-Copper Alloys," Multiscale Modeling of Materials, Symp. Proc. Vol. 527, V. V. Butalov, T. Diaz de la Rubia, P. Phillips, E. Kaxiras, and N. Ghoniem, Eds. Materials Research Society, Pittsburgh, PA, 1999, pp. 211-216.

[108] M. Valo, R. Krause, K. Saarinen, P. Hautojarvi, and J. R. Hawthorne, "Irradiation Response and Annealing Behavior of Pressure Vessel Model Steels and Iron Ternary Alloys Measured with Positron Techniques," Effects of Radiation on Materials, ASTM STP 1125, R. E. Stoller, A. S. Kumar, and D. S. Gelles, Eds., American Society for Testing and Materials, West Conshohocken, PA, 1992, pp. 172-185.

[109] A. J. E. Foreman, W. J. Phythian, and C. A. English, private communication, unpublished.

[110] F. Gao, D. J. Bacon, A. F. Calder, P. E. J. Flewitt, and T. A. Lewis, J. Nucl. Mater. 276 (1996) 47-56

[111] R. E. Stoller and S. G. Guiriec, J. Nucl. Mater. 329-333 (2004) 1228-1232.

[112] D. Terentyev, K. Vortler, C. Bjorkas, K. Nordlund, and L. Malerba, J. Nucl. Mater. 417 (2011) 1063.

[113] M. L. Jenkins, C. A. English, and B. L. Eyre, Phil. Mag. 38 (1978) 97.

[114] I. M. Robertson, M. A. Kirk, and W. E. King, Scripta Met. 18 (1984) 317-320.

[115] C. A. English and M. L. Jenkins, Mat. Sci. Forum 15-18 (1987) 1003-1022.

[116] M. A. Kirk, I. M. Robertson, M. L. Jenkins, C. A. English, T. J. Black, and J. S. Vetrano, J. Nucl. Mater. 149 (1987) 21-28.

[117] J. S. Vetrano, M. W. Bench, I. M. Robertson, and M. A. Kirk, Met. Trans. 20A (1989) 2673-2680.

[118] M. L. Jenkins, M. A. Kirk, and W. J. Phythian, J. Nucl. Mater. 205 (1993) 160.

[119] T. L. Daulton, M. A. Kirk, and L. E. Rehn, J. Nucl. Mater. 276 (2000) 258-268.

[120] M. Kiritani, Mat. Sci. Forum 15-18 (1987) 1023-1046.

[121] T. Muroga, N. Yoshida, N. Tsukuda, K. Kitajima, and M. Eguchi, Mat. Sci. Forum 15-18 (1987) 1097-1092.

[122] D. J. Bacon, F. Gao, and Yu. N. Osetsky, J. Nucl. Mater. 276 (2000) 1-12.

[123] M. J. Caturla, N. Soneda, E. Alonso, B. D. Wirth, T. Diaz de la Rubia, and J. M. Perlado, J. Nucl. Mater. 276 (2000) 13-21.

[124] M. Ghaly and R.S. Averback, Phys. Rev. Let. 72 (1994) 364.

[125] R. E. Stoller, J. Nucl. Mater. 307-311 (2002) 935-940.

[126] A. F. Calder, D. J. Bacon, A. V. Barashev, Yu.N. Osetsky, Phil. Mag. 88 (2008) 43-53.

[127] J. M. Leitnaker, E. E. Bloom, and J. O. Stiegler, Fuels and Materials Development: Quarterly Progress Report, ORNL-TM-4105, Oak Ridge National Laboratory, December, 1972, pp. 3.19-3.29.

[128] A. Horsewell and B. N. Singh, "Role of Dislocations, Dislocation Walls, and Grain Boundaries in Void Formation During Early Stages of Fast Neutron Irradiation," Effects of Radiation on Materials, ASTM STP 870, F. A. Garner and J. S. Perrin, Eds., ASTM, Philadelphia, 1985, pp. 248-261.

[129] W. van Witzenburg and A. Mastenbroek, J. Nucl. Mater. 133&134 (1985) 553-557.

[130] B. N. Singh, M. Eldrup, J. J. Zinkle, and S. I. Golubov, Phil. Mag. A 82 (2002) 1137-1158.

[131] M. Samaras, P. M. Derlet, H. Van Swygenhoven, and M. Victoria, Phys. Rev. Lett. 88, 125505 (2002).

[132] M. Rose, A. G. Balogh, and H. Hahn, Nucl. Instr. Meth. Phys. Res., Sect. B 127-128, 119 (1997).

[133] Y. Chimi, A. Iwase, N. Ishikawa, M. Kobiyama, T. Inami, and S. Okuda., J. Nucl. Mater. 297, 355 (2001).

[134] T. D. Shen, S. Feng, M. Tang, J. A. Valdez, Y. Wang and K. E. Sickafus, Appl. Phys. Lett. 90, 263115 (2007).

[135] M. Samaras, P. M. Derlet, and H. Van Swygenhoven, Phys. Rev. B 68, 224111 (2003).

[136] M. Samaras, P. M. Derlet, H. Van Swygenhoven, M. Victoria, Phil. Mag. 83 (2003) 3599-3607.

[137] R. E. Stoller, P. J. Kamenski, and Yu. N. Osetskiy, "Length-scale Effects in Cascade Damage Production in Iron," Materials for Future Fusion and Fission Technologies,

Vol. 1125, C. C. Fu, A. Kimura, M. Samaras, M. Serrano de Caro, and R. E. Stoller, Eds., Materials Research Society, Warrendale, PA, 2009, pp. 109-120.

[138] G. Z. Voronoi and J. Reine, Journal für die reine und angewandte Mathematik 134 (2008) 198-287.

[139] T. Diaz de la Rubia, R. S. Averback, R. Benedek, and W. E. King,, Phys. Rev. Lett., 59:1930--1933, 1987. See also erratum: Phys. Rev. Lett. 60 (1988) 76.

[140] A. F. Calder, D. J. Bacon, W. J. Phythian, and C. A. English,, Mater. Sci. Forum, 97--99:183, 1992.

[141] Mai Ghaly and R. S. Averback, Phys. Rev. Lett., 72(3):364--367, 1994.

[142] A. J. E. Foreman, W. J. Phythian, and C. A. English,. Rad. Eff. & Def. in Sol., 129(1-2):25, 1994.

[143] K. Nordlund, M. Ghaly, R. S. Averback, M. Caturla, T. Diaz de la Rubia, and J. Tarus, Phys. Rev. B, 57(13):7556--7570, 1998.

[144] A. Wucher and B. J. Garrison, J. Chem. Phys., 105(14):5999, 1996.

[145] F. Karetta and H. M. Urbassek, Appl. Phys. A, 55:364--371, 1992.

[146] H. Gades and H. M. Urbassek, Phys. Rev. B, 51:14559, 1995.

[147] A. Almazouzi, M. J. Caturla, M. Alurralde, d. Diaz, T. Rubia, and M. Victoria, Nucl. Instr. Meth. Phys. Res. B, 153(1-4):105--15, 1999.

[148] X. W. Zhou, H. N. G. Wadley, R. A. Johnson, D. J. Larson, N. Tabat, A. Cerezo, A. K. Petford-Long, Acta Materialia, 49(19):4005--4015, 2001.

[149] J. Samela, J. Kotakoski, K. Nordlund, and J. Keinonen, Nucl. Instr. Meth. Phys. Res. B, 239(4):331--346, 2005.

[150] J. Samela and K. Nordlund, Phys. Rev. Lett., 101:027601, 2008. and cover of issue 2. Also selected to Virtual Journal of Nanoscale Science and Technology Vol. 18 Issue 3 (2008).

[151] M. A. Kirk, I. M. Robertson, M. L. Jenkins, C. A. English, T. J. Black, and J. S. Vetrano, J. Nucl. Mater., 149:21, 1987.

[152] T. L. Dalton and M. Ozima, Science, 271:1260, 1996.

[153] K. Nordlund and F. Gao, Appl. Phys. Lett., 74(18):2720--2722, 1999.

[154] S. M. Foiles, M. I. Baskes, and M. S. Daw, Phys. Rev. B, 33(12):7983, 1986. Erratum: ibid, Phys. Rev. B 37, 10378 (1988).

[155] M. S. Daw, S. M. Foiles, and M. I. Baskes, Mat. Sci. Rep., 9:251, 1993.

[156] M. A. Karolewski, Rad. Eff. and Def. in Solids, 153(3):239--255, 2001.

[157] D. G. Pettifor, M. W. Finnis, D. Nguyen-Manh, D. A. Murdick, X. W. Zhou, and H. N. G. Wadley, Mater. Sci. and Eng. A, 365:2--13, 2004.

[158] K. Nordlund and R. S. Averback, Phys. Rev. B, 59:20--23, 1999.

[159] K. Nordlund, K. O. E. Henriksson, and J. Keinonen, Appl. Phys. Lett., 79(22):3624, 2001.

[160] B. M. Paine and R. S. Averback, Nucl. Instr. Meth. Phys. Res. B 7/8, 666 (1985).

[161] K. Nordlund and R. S. Averback, Appl. Phys. Lett., 70(23):3103--3105, 1997.

[162] K. Nordlund, M. Ghaly, and R. S. Averback, J. Appl. Phys., 83(3):1238--1246, 1998.

[163] K. Nordlund, L. Wei, Y. Zhong, and R. S. Averback, Phys. Rev. B (Rapid Comm.), 57:13965--13968, 1998.

[164] C. Bjorkas and K. Nordlund, Nucl. Instr. Meth. Phys. Res. B, 267:1830--1836, 2009.

[165] B. M. Paine, M.-A. Nicolet, R. G. Newcombe, and D. A. Thompson, Nucl. Instr. Meth. Phys. Res. B, 182/183:115, 1981

[166] S.-J. Kim, M-A. Nicolet, R. S. Averback, and D. Peak, Phys. Rev. B, 37(1):38, 1988.

[167] R. S. Averback and K. L. Merkle, Phys. Rev. B, 16:3860, 1977.

[168] A. F. Calder, D. J. Bacon, A. V. Barashev, and Yu. N. Osetsky, J. Nucl. Mater. 382 (2008) 91–95.

[169] C. S. Becquart, C. Domain, J. C. van Duysen, and J. M. Raulot, J. Nucl. Mater. 394 (2001) 274-287.

[170] A. F. Calder and D. J. Bacon, "Computer Simulation Study of the Effects of Copper Solutes on Cascade Damage in Fe-Cu Alloys," Microstructure Evolution During Irradiation, Ian M. Robertson, Gary S. Was, Linn W. Hobbs, Tomas Diaz de la Rubia, Eds., Materials Research Society Symposium Proceedings Vol. 439, Pittsburgh, PA 1997, pp 521.

[171] J. Wallenius, I. A. Abrikosov, R. Chajarova, C. Lagerstedt, L. Malerba, P. Olsson, V. Pontikis, N. Sandberg, and D. Terentyev, J. Nucl. Mater. 329-333 (2004) 1175-1179.

[172] L. Malerba, A. Caro, and J. Wallenius, J. Nucl. Mater. 382 (2008) 112.

[173] L. Malerba, D. Terentyev, P. Olsson, R. Chajarova, and J. Wallenius, J. Nucl. Mater. 329-333 (2004) 1156-1160.

[174] D. Terentyev, L. Malerba, and M. Hou, Nucl. Instr. and Meth. B 228 (2005) 164-162.

[175] D. Terentyev and L. Malerba, J. Nucl. Mater. 329-333 (2004) 1161-1165.

[176] G. J. Ackland, M. I. Mendelev, D. J. Srolovitz, S. Han, and A. V. Barashev, J. Phys.: Cond. Mat. 16 (2004) S2629.

[177] A. Okada, H. Maeda, K. Hamada, and I. Ishida, J. Nucl. Mater. 256 (1999) 247.

[178] K. Vörtler, C. Björkas, D. Terentyev, L. Malerba, K. Nordlund, J. Nucl. Mater. 382 (2008) 24.

[179] C. Björkas, K. Nordlund, L. Malerba, D. Terentyev, P. Olsson, J. Nucl. Mater. 372 (2008) 312.

[180] D. Terentyev, L. Malerba, R. Chakarova, K. Nordlund, P. Olsson, M. Rieth, J. Wallenius, J. Nucl. Mater. 349 (2006) 119.

[181] R. E. Voskoboinikov, Yu. N. Osetsky, and D. J. Bacon, J. Nucl. Mater. 377 (2008) 385-395.

[182] R. E. Voskoboinikov, Yu. N. Osetsky, and D. J. Bacon, Nuclear Instruments & Methods In Physics Research Section B 242 (2006) 68-70.

[183] R. E. Voskoboinikov, Yu. N. Osetsky, and D. J. Bacon, "Atomic-scale Simulation of Defect Cluster Formation in High-Energy Displacement Cascades in Zirconium," Effects of Radiation on Materials, STP 1475, T. R. Allen, R. G. Lott, J. T. Busby, and A. S. Kumar, Eds., ASTM International, West Conshohocken, PA, 2006, pp. 299-313.

[184] K. Vortler, N. Juslin, G. Bonny, L Malerba, and K Nordlund, J. Phys.: Condens. Matter., 23:355007, 2011.

[185] R. L. Klueh and D. R. Harries, "High-Chromium Ferritic and Martensitic Steels for Nuclear Applications," Monograph 3, ASTM International, West Conshohocken, PA, 2001.

[186] B. N. Singh and J. H. Evans, J. Nucl. Mater. 226 (1995) 277.

[187] D. Bacorisen, R. Smith, B. P. Uberuaga, K. E. Sickafus, J. A. Ball, and R. W. Grimes, Nucl. Instr. and Meth. B 250 (2006) 28-35.

[188] C. L. Bishop, R. W. Grimes, and D. C. Parfitt, Nucl. Instr. and Meth. B 268 (2010) 2915-2917.

[189] D. S. Aidhy, P. C. Millett, T. Desai, D. Wolf, S. R. Phillpot, Phys. Rev. B 80 (2009) 104107.

[190] S. L. Dudarev, P. M. Derlet, J. Phys.: Cond. Mat. 17 (2005) 7097-7118

[191] G. J. Ackland, J. Nucl. Mater. 351 (2006) 20-27.

[192] L. Malerba, G. J. Ackland, C. S. Becquart, G. Bonny, C. Domain, S. L. Dudarev, C-C. Fu, D. Hepburn, M. C. Marinica, P. Olsson, R. C. Pasianot, J. M. Raulot. F. Soisson, D. Terentyev, E. Vincent, F. Willaime, J. Nucl. Mater. 406 (2010) 7-18.

[193] P. Olsson, J. Wallenius, C. Domain, K. Nordlund, L. Malerba, Physical review B 72 (2005) 214119, and Erratum, Phys. Rev. B 74, 229906 (2006);

[194] G. Bonny, R.C. Pasianot, D. Terentyev, L. Malerba, Philosophical Magazine 91 (2011) 1724

[195] N. Soneda, I. Ishino, and T. Diaz de la Rubia, Phil. Mag. Let. 81 (2001) 649-659.

Chapter 3.

Damage evolution in structural materials

M.J. Caturla[1], C. Becquart[2]
[1]Dept. Física Aplicada, Universidad de Alicante, Spain
[2]Unité Matériaux et Transformations (UMET), Ecole Nationale Supérieure de Chimie de Lille, France,
Laboratoire commun EDF-CNRS Etude et Modélisation des Microstructures pour le Vieillissement des Matériaux (EM2VM), France

Abstract

In this chapter we present an overview of long-term damage evolution in structural materials. We mostly focus on the simulation methods available to study damage evolution, and provide a short introduction on the experimental techniques used to explore the microstructure evolution in irradiated materials. We describe the kinetic Monte Carlo method, a powerful tool to study damage evolution over long time scales, and give examples of applications of these models for the case of Fe under different irradiation conditions. The effect of impurities such as helium is also addressed. Although the overview is mostly devoted to iron-based materials, we also describe briefly other structural materials such as tungsten. Finally, the limitations in the simulation models to study damage evolution are discussed.

Introduction

Structural materials for nuclear applications must be selected to comply severe restrictions to guarantee safe, reliable and economically viable reactors. New generation reactors, in particular, must withstand high neutron radiation levels, high temperatures and very corrosive environments [49]. Some of the materials considered for next generation nuclear reactors are ferritic/martensitic steels (9-12% Cr steels), austenitic stainless steels (such as 316LN), oxide dispersion strengthened (ODS) steels, Ni-base alloys, W-Re alloys or SiC/SiC composites [40,49].

These materials must be resistant to radiation damage effects such as dimensional changes due to void swelling, embrittlement or radiation induced segregation, among

others. For example, ferritic/martensitic (F-M) steels are selected due to their resistance to void swelling as well as creep. Moreover, these materials have reduced activation which makes them good candidates also for fusion applications. However, they present problems of embrittlement as well as concerns about phase stability under irradiation. Austenitic steels, on the other hand, avoid the embrittlement problem but present significant void swelling under irradiation. Like with F-M steels, phase stability is also an issue in these materials.

The selection of the most appropriate materials can be improved if we have an understanding of the underlying processes of defect production and evolution in these complex systems as well as how they interact with elements of the microstructure such as dislocations, grain boundaries, solute atoms and so on. In order to achieve such an understanding it is necessary to use a combination of experimental methods, to characterise the damage produced by the irradiation, and modelling tools, that are able to predict the behaviour of these materials under irradiation.

In this chapter we first review briefly the characterisation tools used to study defects in irradiated materials. Then we describe the models used to study long term damage evolution with emphasis on kinetic Monte Carlo models. Examples are then given for damage production and evolution in Fe, including the effect of He and C. We conclude with a discussion about the limitations in the simulation methods.

Experimental methods to study damage evolution in irradiated materials

There is a wide range of characterisation tools that are used to study irradiated materials at different levels. We describe here, very briefly, the type of information that can be obtained from different experimental methods, and how that data can be used to validate long term-damage evolution models, such as those described in the next section.

Figure 1. TEM image of ultra-high-pure Fe irradiated with Fe^{2+} ions of 150 keV at 300^{0}C for irradiation doses (a) 1×10^{15} ions/cm^{2} and (b) 2×10^{15} ions/cm^{2} [30]

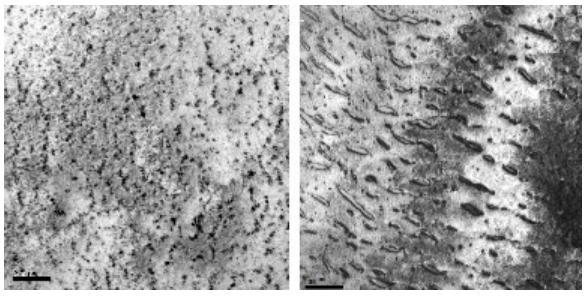

a) b)

Transmission electron microscopy (TEM) is a powerful tool that provides information about defect densities, sizes and types. The resolution of this method has increased significantly in the last few years [69]. However, even with these improvements, it should be remembered that not all defect sizes can be resolved with this method. Typically the resolution for damage of irradiated materials is around 1nm. Figure 1 shows a TEM image of ultra-high-pure Fe irradiated with Fe2+ ions of 150 keV at 300ºC from

[30]. Figure 1a shows the damage produced after 1×10^{15} ions/cm^2 and 2×10^{15} ions/cm^2. The image shows how the damage is distributed homogeneously in the matrix and how loops grow with irradiation dose. Moreover, *in-situ* TEM experiments allow to observe the formation and evolution of defects as the sample is being irradiated [46]. The dynamical information obtained from these experiments show, for example, how defects are able to migrate in Fe [2] and even change their Burgers vector [1], as well as information about defect-defect interactions.

Other methods that can also provide information about defect densities, sizes and types are Small Angle Neutron Scattering (SANS) and positron annihilation spectroscopy (PAS). Small Angle Neutron Scattering is a technique that involves sending a beam of neutrons parallel to the sample and measuring the intensity and the scattering angle after their interactions with matter. The ratio of the scattered intensities in the direction perpendicular to those scattered in the parallel direction (A ratio) provides information on the chemical composition of the particles, if the magnetic contrast is known [9]. The positron is the antiparticle of the electron [54]. In a material, the positron is attracted by the electrons and repelled by the atoms nuclei. Therefore, this antiparticle is attracted by the cavities in which the repulsions are weaker. PAS experiments can thus detect open defects such as vacancies or voids of all sizes [37]. However, the interpretation of these experiments can be complicated when there is a large variety of defect types.

Atom probe tomography [47] has been particularly important to understand the composition of radiation induced precipitation of clusters in Fe-Cu alloys [33,48]. Atom probe is based on the principle of evaporation. The tip is evaporated by field effect, atomic layer by atomic layer in the form of ions. This occurs due to the superposition of high voltage pulses to a dc electrical potential applied. The ions extracted pass through the amplifier where they transform into an electron cloud that bombards a detector measuring their positions and flight.

Besides the characterisation techniques described above, measurements of macroscopic properties can also provide very valuable information about defects in metals. For example, electrical resistivity measurements of irradiated samples have been used for several decades to obtain information about basic processes such as single and small defect cluster migration. The experiments consist of irradiating a sample at low temperatures to create defects, usually by electron irradiation [59] although there are also experiments performed by neutron implantation [45]. After the irradiation the sample is then annealed, increasing the temperature in time intervals, while measuring the electrical resistivity. As the temperature is increased, different mechanisms get activated such as single self-interstitial migration. As defects become mobile they recombine with other defects of the same type or opposite type (vacancies and self-interstitials). The recombination between defects results in damage recovery and, therefore, in the decrease of electrical resistivity of the sample. The derivative of the electrical resistivity measurements with temperature shows peaks at different temperatures that correspond to different mechanisms being activated. These temperatures indicate activation energies that can then be related to migration or dissociation energies of defects obtained from density functional calculations (DFT) or molecular dynamics or statics with empirical potentials.

All these experimental techniques can be used to validate simulation models being developed to understand damage evolution in irradiated materials. However, the

comparison between the experimental data and the models is never straightforward as for instance, the experimental signal has to be interpreted using models which rely on the knowledge one has of the physics involved. Furthermore, "simulated materials" are perfect in contrast with real materials. Many of the experiments available nowadays were made 30 or 40 years ago. Since then, the influence of impurities, even in very residual amount, has been pointed out, and one research direction that needs to be pursued to characterise more properly the interactions between point defects and solute atoms is the setting up of new sets of simple experiments, such as the recovery experiments, on materials with the highest purity possible in order to eliminate unwanted effects, as well as experiments on model alloys with increasing chemical complexity to validate the models developed.

To progress in this field, one needs to design dedicated experiments in a close collaboration between experimentalists and modellers. The goal is to perform experiments on model alloys with the same number of elements that simulation can currently safely take into account (and some inevitable impurities) and also with simplified irradiation conditions (electrons irradiations, simple or joint ion irradiation, before treating neutron irradiation).

Both experimentalists and modellers benefit from this type of collaboration, because it gives access to experimental conditions where the numerous possible interactions defects, elements, and microstructure features have been de-correlated from one another (compared to the complex industrial multicomponent case), which makes it possible to test one by one the experimental and numerical models describing these interactions.

In the next section we describe the main simulation methods used to study damage evolution in structural materials.

Long-term damage evolution models

Object Kinetic Monte Carlo

The Object kinetic Monte Carlo (OKMC) method is based on the residence time algorithm (RTA), also known as the BKL method (for Bortz, Kalos and Lebowitz) [36]. This algorithm is used to evolve a set of objects that can undergo different events. Given a set of possible events involving these objects, $\{e_i; i=1,\ldots,N_e\}$, each with a known rate of occurrence, Γ_i, a total rate, R, is computed as the sum over all N_e events of the product $\Gamma_i n_i$, where n_i is the number of events of the same type with the same rate:

$$R = \sum_{i=1}^{N_e} n_i \Gamma_i \qquad (1)$$

A Monte Carlo step is initiated by selecting an event from all N_e based on a random number between 0 and R. The value of this number determines which event is selected since the increment due to each event in the interval [0:R] in Equation (1) is known. If more than one object can undergo the selected event, one is chosen at random. Once the event and the corresponding object are selected, the appropriate actions are performed to make that event occur and the time is updated, by adding a time increment proportional to the inverse of R:

$$\delta\tau = \frac{-\log\xi}{R} \qquad (2)$$

where ξ is a random number in the interval [0,1], which is included to ensure a Poisson distribution of the time increments. In the limit of long times, it is easy to demonstrate that the average, $\delta\tau \rightarrow 1/R$, which is the average time increment. Thus, this average value can also be used in the KMC algorithm as initially proposed by [67]. This general algorithm can be applied to study a wide variety of processes. In the case of the long-term evolution of radiation damage the objects are the intrinsic defects (vacancies and self-interstitials) or impurities, and their clusters which are located at known (and traced) positions in a simulation volume. The events are all the possible actions that these objects can perform and the reactions that they may undergo, such as: (a) migration, (b) dissociation (emission of a smaller defect from a bigger one), (c) aggregation of like defects or of defects and impurities, and (d) annihilation between opposite defects (self-interstitials and vacancies).

The probability for a migration event is given by the corresponding jump frequency, expressed as a thermally activated process, following the Arrhenius dependence:

$$\Gamma_m = \Gamma_0 \exp\left(\frac{-E_m}{k_B T}\right) \qquad (3)$$

where Γ_0 is the attempt frequency, which can be taken as a constant prefactor, on the order of the Debye frequency; E_m is the migration energy of that particular object; T is the temperature; and k_B the Boltzmann constant.

For the dissociation events, the probability is given in terms of a jump frequency, with an activation energy equal to the sum of the migration energy plus the binding energy between the emitted defect and a cluster of the size that remains after emission, E_b:

$$\Gamma_d = \Gamma_0 \exp\left(-\frac{E_m + E_b}{k_B T}\right) \qquad (4)$$

E_b will in general depend on the type of emitted and emitting object, as well as on the emitting object's size. For the case of events of type (c) and (d), which are reactions between defects, it is generally assumed that they are *diffusion-limited*. That is, the reaction occurs as soon as the two objects are within a pre-defined capture radius, but no energy barrier is associated with the reaction. These events occur therefore only on the basis of geometrical considerations (overlap of reaction volumes) and do not participate in defining the progressing of time. Events of this type also include the absorption of objects by sinks (dislocations, grain boundaries, …).

Other events due to external processes, which influence the rate at which time progresses, need to be included in a radiation damage simulation. These are events producing damage, such as the appearance of isolated Frenkel pairs (FP), as in electron irradiation, or of the debris of a displacement cascade (i.e. the point defects and clusters remaining at the end of the cascade), as in ion or neutron irradiation. The rates of these events must be included in the computation of the total rate, R.

Difficulties in applying the OKMC algorithm are not due to the method itself, which is fairly straightforward. These stem, instead, from the fact that all the possible events that each object can undergo according to a specific physical mechanism, their appropriate probability, and their defining properties must be pre-defined. The problem of pre-defining possible actions, reactions, mechanisms and parameters for all possible objects is addressed in a latter section.

Event Kinetic Monte Carlo

The OKMC method is not the only Monte Carlo method to study the evolution in time of a set of events of known probability. A second type of Monte Carlo method is known as Event kinetic Monte Carlo (EKMC). This method has been implemented in the code JERK [14,38]. In contrast to the residence time algorithm, where all rates are lumped into one total rate to obtain the time increment (Equations 1 and 2), in an EKMC scheme the time delays of all possible events are calculated separately and sorted by increasing order in a list. The event corresponding to the shortest delay, τ_s, is processed first, and the remaining list of delay times for other events is modified accordingly by eliminating the delay time associated with the particle that just disappeared, adding delay times for a new mobile object, etc. The actual time is increased by τ_s and the next event on the list is processed until all possible events that can happen before time Δt have occurred. The delay times that include a migration step are calculated according to continuous laws of diffusion, after converting jump frequencies Γ_i into diffusion coefficients D_i. For a walker starting at a distance d from a partner of radius r, the probability that they will meet is given by:

$$P(d,t) = \frac{r}{d} erfc\left\{\frac{d-r}{2\sqrt{Dt}}\right\} \qquad (6)$$

which is easily inverted to yield the time delay under the form:

$$\tau = \frac{1}{4\mathrm{D}} \frac{(d-r)^2}{\left\{erfc^{-1}(\xi / r)\right\}^2} \qquad (7)$$

where $erfc^{-1}$ is the inverse of the complementary error function and ξ is a random number uniformly distributed over the interval 0-1. This delay is calculated in the framework of a binary collision approximation, i.e. as if the two partners were alone in an infinite volume. This assumption is not exact, but it was extensively checked using JERK that this approximation remains quantitatively correct as long as the time interval Δt is not too large. Otherwise, the probability of encounter with a third partner would be no longer negligible. The advantage of EKMC is that it is more rapid when they are only few possible events.

The choice of Δt is a matter of compromise: too small a value would approach the limits of atomic Monte-Carlo or OKMC and too large a value would probe the delay probability law given above in a time window where it is less and less correct. In addition the number of events to be processed would grow too large. An important difference between OKMC and EKMC is that the latter does not easily treat one-dimensional (1D) motion, although in principle the corresponding probabilities can be calculated and introduced in parallel with the three-dimensional (3D) ones.

The above procedure includes delay times of different types. Some delay times are associated with events defined by a frequency of occurrence consistent with a Poisson distribution (for example, the jump monitoring the emission of a monomer from a cluster), whereas the others account for encounters between objects which are the result of diffusion and not a Poisson process. It has been shown in the past that for problems where Poisson processes act in parallel, the RTA is equivalent to the brute force Metropolis scheme [3]. No formal proof has been established up to now for the case of event based Monte-Carlo. However, a recent reformulation of Jerk called First Passage Kinetic Monte-Carlo (FPKMC) has been numerically checked extensively against the RTA treatment of the same diffusion problem and no detectable difference could be found between the two approaches [50].

Rate theory models

Rate theory models have been used for several decades to study defect production and defect evolution in irradiated materials [39]. It is a powerful technique with almost no restriction on sample size or time to be simulated. Rate theory or cluster dynamics methods typically compute the changes in concentration as a function of time for different defect types. This requires the resolution of coupled differential equations, and the number of equations that must be solved can be extremely large, depending on the problem. There are, therefore, different approximations used in the literature to solve systems up to very large cluster sizes [27,58,51].

The information needed for these simulations in terms of defect mobilities, stabilities or interaction radius are exactly the same as those needed in kinetic Monte Carlo methods and will be described in the next section.

Parametrisation of the models: the example of Fe

The problem of determining an initial parameter set is common to any model used to simulate microstructure evolution. By parameter set we mean the whole set of physical mechanisms included in the model, along with the physical or materials parameters that quantitatively define them, such as characteristic energies, attempt frequencies and capture radii. Clearly, the appropriateness of a parameter set should be decided on the basis of its ability to reproduce available experimental results in a large enough range of conditions. However, the work of identifying a suitable parameter set and of its corresponding validation is far from straightforward. Here we describe the main parameters used in the literature for pure Fe as an example of the information needed in these models. The parameters needed for these simulations are: migration energies, attempt frequencies, binding energies, interaction radii and defect-defect interaction mechanisms. Moreover, the initial defect distribution must also be provided, and it will depend on the type of

experiment being simulated. Migration energies for mono-defects or small defect clusters can be obtained from DFT methods. In particular, for the case of Fe we have information about vacancy clusters up to size 4 and self-interstitials up to size 3 from DFT calculations [18,24,25], shown in table I. However, DFT simulations of clusters with more than 4 or 5 defects, particularly to obtain their migration barriers, are difficult to perform. Therefore, above those values information must be obtained from other simulation methods, such as molecular dynamics (MD) with empirical potentials [53,55]. In general, the behaviour of large defect clusters is one of the difficult parameters to incorporate in these kinetic models since it implies knowing about the mobility and interactions of defects of any type and size. This is particularly complicated in the case of self-interstitial clusters in Fe. For vacancies in Fe in some cases [11] the DFT values are used for vacancies up to 4 and larger vacancy clusters are considered immobile. Other kinetic Monte Carlo simulations [19] use a migration energy of 0.65 eV and a prefactor decreasing with size according to the law $\nu_0 p^{-(n-2)}$ for $n \geq 2$, with p=100 and $\nu_0 = 6\times10^{12}\ \mathrm{s}^{-1}$ [7]. For self-interstitial atoms (SIA), MD has shown that SIA clusters of <111> type are able to diffuse one-dimensionally and almost athermally [53,55]. For example, MD simulations by Osetsky show that SIA clusters migrate with a migration energy E_m=0.04 eV and a prefactor decreasing with size according to the law: $\nu_0 \cdot n^{-s}$ ($\nu_0 = 6\times10^{12}\ \mathrm{s}^{-1}$, s=0.51). The difference in migration energies between small and large SIA clusters comes from the different configurations: the lowest energy configuration of small clusters, below 5 defects, are of <110> type migrating in 3D while the largest clusters have a <111> configuration [42], with low migration energies in 1D. However, recent ab initio results show that small clusters of size with non-planar configurations are more stable than <110> clusters and immobile [60]. As mentioned above, one main difficulty in modelling damage evolution in Fe is that the behaviour of large SIA clusters is not fully understood. According to simulations all large SIA clusters are <111> type and highly mobile while experiments show two types of loops <100> and <111> [66], with mobilities for <111> clusters on the order of 1.3 eV [2], well above the MD values. This discrepancy is often explained by the presence of impurities such as carbon, that can act as traps for defects, and it is included in the simulations in an effective manner, either by adding traps with a binding energy to SIA clusters of about 1 eV [12,19] or by assuming that all SIA clusters above a certain size are immobile [11]. The general conclusion of these studies [11,19], is that it is only possible to reproduce the observed experimental data when some mechanism for immobilisation or slowing down of large self-interstitial clusters is included in the model.

Binding energies of single-defects to clusters are also important parameters for the OKMC simulations since they determine the rate of dissociation of a cluster. Binding energies for small clusters can be obtained by ab initio techniques [18,20,24,25,26]. For larger clusters, the data can be obtained from empirical interatomic potentials and then extrapolated [11,19,25]. Often, the capillary approximation is used for larger vacancy and self-interstitial clusters [25].

Examples of binding energies used in the OKMC model of Figure 2 below are presented in Table 2.

Defect-defect interactions are often assumed to be diffusion limited: when a defect is within the capture radius of a second defect they recombine. The recombination can result in annihilation of the defects, in the case of recombination of a vacancy with a self-

interstitial, in the growth of a defect cluster (a vacancy recombining with a vacancy cluster, for example) or the formation of mixed clusters, with two or more types of defects, such as He-vacancy clusters. Moreover, very complex reactions could also take place particularly when we have large mobile clusters, as in the case of Fe. Mechanisms such as the formation of <100> loops from the reaction between two <111> loops proposed by Marian et al. based on MD simulations [41] have been included in some OKMC simulations [30]. This is, again, an area where many open questions remain in terms of loop growth and loop interaction in Fe. For all these recombination reactions a recombination or capture radius (or capture volume) must be defined. The interaction bias between self-interstitials is often included into this parameter.

Finally, the initial defect distribution used in the kinetic model will depend on the type of experiment to be studied. For the case of electron irradiation experiments a random distribution of Frenkel-pairs (vacancies and self-interstitials) separated a given distance is assumed as initial distribution [25]. For the case of ion implantation or neutron irradiation, cascade damage must be introduced taking into account the irradiation energy. MD simulations of collision cascade damage is generally used as input [8,11,19,20]. Binary collision approximation calculations, such as those performed by Marlowe [43], can also be used in some cases [4-6,31]. In fact, for energies higher than several 10s of eV a combination of Marlowe and MD simulations must be used. The information obtained from these calculations can serve as input both to kinetic Monte Carlo models and rate theory models. In KMC models the actual 3D location of vacancies and self-interstitials obtained from MD or BCA calculation is directly used in the simulations. In rate theory, the concentration of clusters of different sizes obtained from the MD or BCA simulations are used as input to the calculations [28,64].

In the following section we present some examples of calculations of defect accumulation and evolution in Fe using kinetic models.

Table 1. Migration energies of vacancies and self-interstitials used in the OKMC simulations of Fe of Figure 2 (given as an example of input parameters)

SIA cluster size	E_m (eV)	Vacancy cluster size	E_m (eV)
1	0.34	1	0.67
2	0.42	2	0.62
3	0.43	3	0.35
> 3	Immobile	4	0.48
		> 4	Immobile

Table 2. Binding energies (eV) of defect clusters used in the OKMC simulations of Fe of Figure 2 (given as an example of input parameters)

SIA cluster size	E_b (eV)	Vacancy cluster size	E_b (eV)
1	0.8	1	0.3
2	0.92	2	0.37
3	1.64	3	0.62

E_f is the formation energy used for the capillary law.

Damage accumulation and evolution in Fe

Electron irradiation and thermal annealing

As mentioned above, irradiation and annealing of a sample while measuring electrical resistivity can provide important information about basic processes related to defect migration and defect stability. In the case of Fe the resistivity recovery curve after electron irradiation was modelled by C. C. Fu et al. [25] using Event kinetic Monte Carlo with parameters for defect stability and defect migration from DFT calculations. The calculations provide an explanation for the different peaks observed in experiments performed by Takaki et al. [59] and the position of those peaks correlate well with the values obtained from the DFT calculations. Figure 2 shows the derivative of the number of defects (N) with temperature as a function of temperature obtained in this case from an Object kinetic Monte Carlo model with the parameters included in tables I and II (same as those in reference [25] for a dose of 2x10 dpa. The location of the peaks found experimentally in [59] is marked in the same figure with arrows. These simulations show that the first peak, corresponding to stage ID2, appears because of the recombination of correlated Frenkel-pairs, that is, a vacancy and a self-interstitial of the same Frenkel-pair. With one single self-interstitial jump these defects recombine and the total number of defects decreases giving rise to this peak. The second stage, named IE, also corresponds to the recombination between vacancies and self-interstitials but for pairs of defects that are far away from each other, so more than one jump of the self-interstitial must occur for the defects to recombine. Therefore, this peak appears at a temperature that corresponds to that of self-interstitial migration. The next stage, stage II, is due to the migration of self-interstitial clusters while stage III is due to vacancy migration.

Figure 2. Derivative of the number of defects with temperature as a function of temperature for electron irradiation at a dose of 2x10^{-6} dpa from OKMC calculations and parameters from [25]

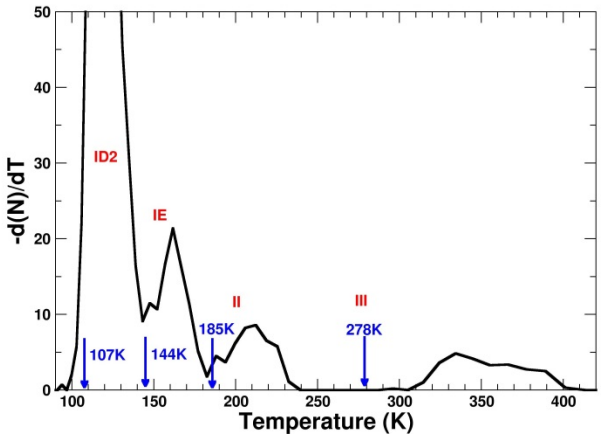

Neutron irradiation and comparison to TEM and PAS

One particularly clean and complete experiment, very suitable for modeling, is the positron annihilation study performed by Eldrup and coworkers [21,22] on high-purity Fe specimens, neutron-irradiated in the range of about 0.0001-0.8 dpa in the HFIR at Oak Ridge National Laboratory. This work provides a precise and detailed experimental assessment of the density and size distribution of vacancy clusters (nanovoids) versus dose in Fe, which is extremely valuable for the validation of microstructure evolution models. For similarly irradiated pure Fe, the total density of visible clusters (mostly self-interstitial clusters) versus dose is also available [63].

A dose-rate corresponding to HFIR (~10^{-6} dpa/s) was used for OKMC simulations with LAKIMOCA, where 0.23 dpa were accumulated at 70°C in a ~1.22x10^{-22} m^3 pure Fe box, with periodic boundary conditions. This equals the maximum dose for which results of void size distribution are provided in [21]. The HFIR spectrum was decomposed into 3x10^{16} FP cm^{-3} s^{-1}, 4x10^{14} 10 keV cascade-debris cm^{-3} s^{-1} and 2x10^{14} 20 keV cascade-debris cm^{-3} s^{-1}, in accordance with INCAS package results [35] (for the exact values of the parameters used in this simulation [7]). As mentioned above, in order to reproduce the experimental data it was necessary to introduce traps for SIA and their clusters. In this case a concentration of 100 ppm of traps was used with a binding energy between trap and object of 0.9 eV, and a capture radius for traps of 5 Å. A good agreement obtained with the experimental data, i.e. the saturation of the damage versus dose as shown in Figure 3 for a number of slightly different choices of parameters that hardly affect the overall result.

Figure 3. Density of vacancy clusters in pure Fe at different doses after a neutron irradiation in HFIR at 70°C including experimental uncertainty [21,22]

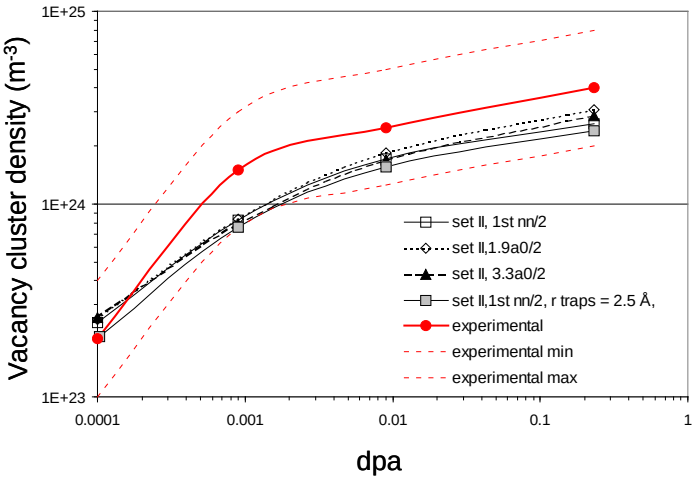

OKMC with set II with traps for interstitials (binding energy of 0.9 eV and capture radius of 2.5 Å) for three different capture radii. Set II with traps for interstitials with a binding energy of 0.9 eV and a recombination distance of 2.5 Å is also represented in the figure. ($200a_0$x$200a_0$x$200a_0$ simulation box, periodic boundary conditions).

Figure 4. Vacancy cluster size distribution versus dose according to the OKMC simulation using set II with traps and a 1nn capture radius

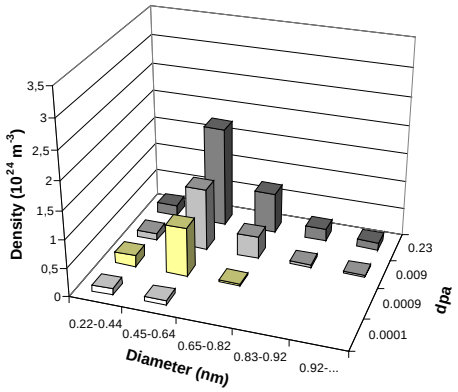

The size for a cluster of N vacancies is given by an equivalent diameter, i.e. the diameter of a sphere with a volume equal to N vacancies. To be compared with experimental results in [21,22].

The main outcome of these simulations is that it is necessary to allow for SIA cluster 1D (fast) migration, while introducing traps for them, in order to reproduce the reference experimental results. The capture radius is found to have a very limited effect on the results, although at low dose the smallest radius provides the best agreement, fully contained in the experimental error bar (Figure 3). The vacancy cluster size distribution versus dose obtained from the simulation and 100 ppm of SIA traps and the smallest capture radius is shown in Figure 4. This figure can be directly compared with Figure 4 in [21] and Figure 6 in [22]. The agreement between simulation and experiment is excellent. The only noticeable difference between simulation results and experimental

measurements is that the former tends to shift the size distribution towards somewhat larger clusters, thereby predicting a slightly lower density.

Nucleation of He-V clusters in Fe

Our next example shows the evolution of damage in Fe in the presence of He. In this case one needs to define all the parameters describing the migration of the Helium atom in Fe as well as the interaction of He with other defects. To model the desorption experiments performed by Vassen et. al. [62], an OKMC model [12], as well as a rate theory model [52], were used, where the migration mechanisms for He described by C. C. Fu and F. Willaime [26] were implemented.

According to their calculations He at an interstitial position (Hei) can migrate with a barrier of 0.06 eV. When He is at a substitutional position (Hes) it can migrate through a vacancy mechanism with a barrier of 1.1 eV, or through the dissociative mechanism: Hes. - >Hei + V, with a barrier of 2.36 eV. A substitutional He can also move to an interstitial position through the replacement mechanism, also known as the kick-out mechanism [61,39]. This mechanism occurs in the presence of defects since it involves a self-interstitial atom replacing the position of the He substitutional: $He_s + I -> He_i$.

Binding energies of small He-V clusters were also calculated by C. C. Fu and F. Willaime [26] and were included in the model. Using these input data the desorption experiments in [62] were simulated. In these experiments Fe samples of different thickness were homogeneously implanted with He at different concentrations and annealed at constant temperature, monitoring in time the amount of He released.

In the simulations a homogeneous distribution of He at interstitial sites, vacancies and self-interstitials is used as the initial damage distribution after implantation. TRIM [68] calculations show that for the energies used in these experiments a total of approximately 200 Frenkel-pairs per implanted He is expected for a threshold displacement energy of 40eV. Assuming this initial condition the evolution of these defects was simulated at room temperature until steady state is reached. After the room temperature simulation, He desorption during isothermal annealing was simulated using the BIGMAC code for the temperature conditions of the experiments in [62]. Due to the issues described above regarding SIA clusters in Fe, different assumptions were used in the simulations.

Figure 5 shows the released fraction of He obtained from the OKMC calculation with all self-interstitial clusters mobile (solid line) together with the experimental data obtained by Vassen et al. for annealing temperature of 667 K. Clearly the simulations with these conditions fail to reproduce the experimental observations. The time scale for He release is too long as compared to the experiment, and the total fraction is also much lower. The results from the simulation when all self-interstitial clusters are immobile (also shown in Figure 5) are in better agreement with the experiments, although it still underestimates the fraction of He released. From the results shown in Figure 5 it seems that a better agreement with the experiment is obtained when self-interstitial clusters are considered immobile. This assumption has been used successfully by A. Hardouin Duparc [29] to simulate electron irradiation of Fe within a rate theory model. The work of Domain et al [19] described in the previous section has shown that it is necessary to include the mobility of self-interstitial clusters and the presence of traps for these clusters to be able to reproduce neutron irradiation experiments on Fe. Using the same approach traps for

self-interstitial clusters were included with a binding energy of 1.0 eV. Calculations for two different conditions, annealing at 667 K of an irradiated sample of 2.6 micron depth and a He concentration of 0.109 appm, and for a case of annealing at lower temperature, 559 K were performed. For this last case the sample depth was 2.5 microns and the initial He concentration 1.39 appm. A trap concentration of 12 appm was used. Figure 6 shows the results of the simulations under these conditions (lines) compared with the experimental measurements (circles). Clearly a much better agreement with the experimental observations is now obtained. These results indicate that the role of traps for self-interstitial clusters in crucial not only for the evolution of SIA and vacancy clusters, but also for the migration and nucleation of He and He-V clusters.

Figure 5. He desorbed fraction for annealing at 667 K and at 559 K. Comparison between experiments

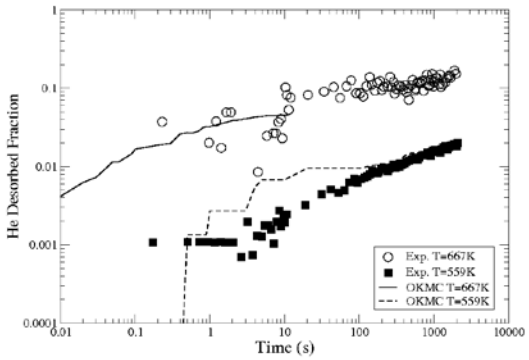

Rate theory vs. kinetic Monte Carlo calculations

Mean-field rate theory has been used for decades to study the evolution of defects produced during irradiation. From simple to very complex models have been used to study, for example, void growth in different materials [27]. Rate theory has the advantage of being a very efficient tool, allowing for calculations of large systems as well as long time scales, therefore suitable to study damage in materials during the lifetime of a reactor. However, it lacks spatial correlations between defects due to its mean-filed character. Several recent studies have addressed this issue by comparing calculations performed with rate theory and with kinetic Monte Carlo using the same input parameters [15,34,51, 52,57].

The work of Stoller et al. [57] has shown that there is a good agreement between the two methods for conditions of high defect density, for example, low temperature and high displacement rates, as well as for cases where there is a high density of fixed sinks such as dislocations.

On the other hand, the work of Dalla Torre [15] and Ortiz et al. [51,52] has shown that a perfect agreement can be achieved between rate theory and kinetic Monte Carlo when using a combination of both models. For example, for the case of the resistivity recovery curves described above and shown in Figure 2, the initial defect distribution after implantation is first modelled with EKMC or OKMC. Therefore, correlated recombination between Frenkel-pairs that can not be accounted for in rate theory, is done in the Monte Carlo models. The concentration of defects obtained in the Monte Carlo

models is then used as input for cluster dynamics achieving a very good agreement with the Monte Carlo results. Recent work by Jourdan and Crocombette [34] shows a method to combine kinetic Monte Carlo and cluster dynamics to account for spatial correlations in displacement cascades, which is necessary to perform continuous irradiation studies such as those required for damage evolution in reactor materials.

Damage evolution in other structural materials (W)

Implantation of He in tungsten has been modelled in a similar manner to what has been described for Fe. The OKMC technique, parameterised on DFT data has been used to model the implantation and subsequent annealing sequence of 800 keV ^{3}He atoms implanted at room temperature in tungsten. Different fluences were investigated ranging from 10^{17} to 5×10^{20} ions m^{-2} and comparisons were made with Positron Annihilation Spectroscopy (PAS) results [16]. These simulations showed that He atoms play the role of nuclei (of which the most probable is the He.*v* complex) for the formation of vacancy clusters and that a high vacancy to nuclei ratio at the end of the implantation causes the formation of large vacancy clusters during the clustering. One interesting consequence of this, is that the higher the fluence, the smaller the nanovoids in the track region, i.e. the region where very few He atoms are implanted [16].The track region of the W slab was modelled using a box of 195 × 203 × 2208 lattice unit cells (64 × 64 × 700 nm) with periodic boundary conditions in the two small directions and recombining surfaces in the third one (which corresponds to the thickness of the track region). Similar to the experimental procedure, the simulation proceeds in two steps: the implantation followed by the isochronal annealing sequence. The implantation stage was done at 300 K using the experimental implantation flux and fluence by introducing randomly in the box «cascade debris» obtained with Marlowe [32].

Figure 6a shows the mean number of vacancies in the clusters versus distance from the surface for the high and low fluences, it reflects thus the depth distribution of the mean size. Figure 6b shows the cluster concentrations versus distance from the surface for the low and high fluences implantation. From Figures 5(a) and (b) it is evidenced that the width and the position of the maximum size of the depth distribution strongly depend on the implantation fluence. For the high fluence (HF), the vacancy clusters are larger in the first 100 nm close to the surface and then slightly decrease in size as depth increases. For the low fluence (LF) case, the maximum of the vacancy cluster distribution is observed around 200 nm from the surface. In this last case, for depths larger than 300 nm from the surface, the mean size of clusters significantly decreases. However, the simulations reveal that in both cases, the concentration of clusters increases with depth and follows the same trend.

Figure 6. (a) mean number of vacancies in the clusters (containing more than one vacancy) versus distance (averaged on slices 35 nm thick) from the surface for the low and high fluences. (b) nHe.mv (m>1) cluster concentration versus distance from the surface for the low and high fluences (the low fluence concentration has been multiplied by 50 in 800 keV ^{3}He implanted W after annealing at 900 K)

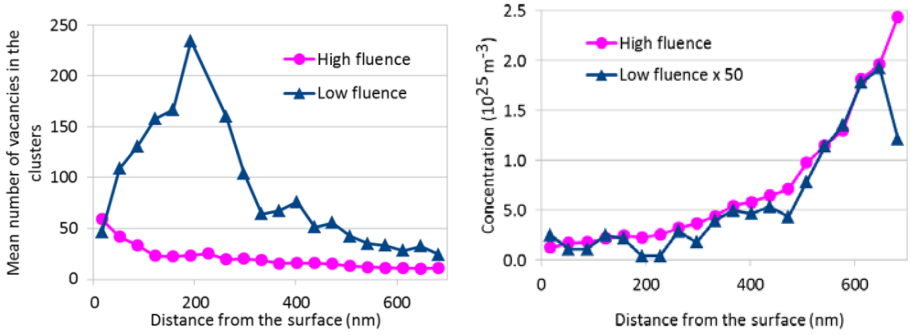

Due to the damage and implantation profiles which are not homogeneous and the recombination events which do not occur in a homogeneous manner in the sample, the He, SIA and vacancy profiles are not uniform at the end of the implantation. The simulations showed that whatever the fluence, the vacancy clusters are smaller very close to the surface. The width and the position of the maximum size of the distribution, however, depend on fluence. For the high implantation fluence, the vacancy clusters are the largest close to the surface, whereas, for the low implantation fluence, the vacancy cluster distribution is more uniform in size and larger between 100 and 300 nm from the surface. The trends observed are in good agreement with the experimental PAS results. The OKMC model was thus able to reproduce the experimental tendencies and as it provides spatial information as the depth profiles of the concentrations, sizes and He to vacancy ratio of the pure and mixed vacancy clusters, can help to interpret the PAS data which result from a complicated combination of cluster size, concentration, He/vacancy ratio and position in the sample.

Limitations of the models and outlook

The main difficulty in all the models described above is to ensure that all relevant parameters and mechanisms have actually been accounted for in the model. Nowadays DFT calculations can provide accurate values of basic defect properties, such as defect formation energies or defect migrations, for systems with a few (4 to 5) defects, , but alloys containing a large number of elements, such as steels for instance, are still difficult to model using DFT because of the size of the supercells which can be used. Information for larger cluster sizes can be obtained from other methods with empirical potentials such as molecular dynamics or molecular statics, but in this approach also the number of alloying elements is limited. However, even with the more accurate values possible for all defect sizes and types nothing ensures that all possible, and relevant, types of interactions have been included into the kinetic model. The only way available to understand the limitations of these models is to contrast the results of the calculations with experiments performed under different conditions (temperatures, type of irradiation, doses, etc.). A robust kinetic model should be able to reproduce, with the same set of defect parameters (migration energies, binding energies, recombination radius, etc.), experiments performed

under very different conditions. Concentrated alloys are also more difficult to model, as one has to find a clever way of introducing a concentration dependent parameterisation.

One of the effects that is often included only in an effective manner in these models (both Monte Carlo and rate theory) is the interaction between defects due to their strain field. In most cases this is modelled through a bias factor included in the capture radius. Recent work by Chen et al shows how this effect can actually be included in a kinetic model [13]. On the other hand, the Langevin approach developed by Derlet et al. [17] can describe the long-range elastic interactions existing between, for example, clusters of defects in an irradiated material.

Modelling damage evolution becomes particularly difficult when dealing with complex systems such as alloys, especially for concentrated alloys. In that case, the properties of defects can depend on the local environment and tabulating all possible defect configurations and reactions can become an infinite task. There are several methods that try to overcome this difficulty. Neural networks could be used to create this list of parameters in an efficient manner [10]. On the other hand, on-the-fly Monte Carlo methods [23,65] allow for the calculation of the defect energetics for the particular structure at any given point in the simulation.

All these very complex systems require efficient kinetic algorithms, specially for the case of object and kinetic Monte Carlo methods. Parallel algorithms, that can make use of large supercomputer facilities, is an obvious improvement. However, for the case of object kinetic Monte Carlo, parallelisation is not straightforward, although there are methods being developed [44].

Conclusions

In this chapter we have described how models such as object kinetic Monte Carlo, event kinetic Monte Carlo and rate theory can follow the evolution of defects in time for time and length scales that can be compared to those measured experimentally. We have presented different examples of calculations compared to experiments for the case of electron and neutron irradiation of Fe, thermal desorption of He implanted Fe and irradiation of W. The main limitations and breakthroughs in these models have been discussed in the final part of this chapter.

Acknowledgements

This work is part of the research programme of the EDF-CNRS joint laboratory EM2VM (Study and Modelling of the Microstructure for Ageing of Materials).

It has been supported by theCEA under the collaborative contract number V 3542.001 on Fusion engineering issues. By the CNRS under the programme interdisciplinaire énergie CHETEX, the European Commission FP7 project PERFORM-60, under grant agreement number 232612, the European Commission FP7 project GETMAT under grant agreement number 212175 and the ACOMP/2012/126 from the Generalitat Valenciana, Spain.

References

[1] K. Arakawa, M. Hatanaka, E. Kuramoto, K. Ono, H. Mori, Phys. Rev. Lett. 96 (2006) 125506

[2] K. Arakawa, K. Ono, M. Isshiki, K. Mimura, M. Uchikoshi, H. Mori, *Science* 318 (2007) 956.

[3] M. Athenes, P. Bellon, G. Martin, Phil. Mag. A76 (1997) 565.

[4] C.S. Becquart, A. Souidi, M. Hou, Phys. Rev. B66 (2002) 134104.

[5] C.S. Becquart, C. Domain, L. Malerba, M. Hou, Nucl. Instr. Methods B228 (2005) 181.

[6] C.S. Becquart, A. Souidi, C. Domain, M. Hou, L. Malerba, R.E. Stoller, J. Nucl. Mater. 351 (2006) 39.

[7] C. S. Becquart, A. Barbu, J. L. Bocquet, M. J. Caturla, C. Domain, C-C. Fu, S. I. Golubov, M. Hou, L. Malerba, C. J. Ortiz, A. Souidi, R. E. Stoller, J. Nucl. Mater. 406 (2010) 39.

[8] C. Björkas, K. Nordlund, M.J. Caturla, Phys. Rev. B 85 (2012) 024105.

[9] R. G. Carter, N. Soneda, K. Dohi, J. M. Hyde, C. A. English, W. L. Server, J. Nucl. Met. 295 (2001) 211

[10] N. Castin, L. Malerba, G. Bonny, M.I. Pascuet, M. Hou, Nucl. Inst. Meth. Phys. Res. B: 267 (2009) 3002.

[11] M.J. Caturla, N. Soneda, E. Alonso, B.D. Wirth, T. Díaz de la Rubia, J.M. Perlado, J. Nucl. Mater. 276 (2000) 1

[12] M. J. Caturla, C. J. Ortiz, J. of Nucl. Mat. 362 (2007) 141.

[13] Z. Chen, N. Kioussis, N. Ghoniem, D. Seif, Phys. Rev. B 81 (2010) 094102

[14] J. Dalla Torre, J-L. Bocquet, N.V. Doan E. Adam, A. Barbu, Phil. Mag. 85 (2005) 549.

[15] J. Dalla Torre, C. C. Fu, F.Willaime, A. Barbu, and J.-L. Bocquet, J. Nucl. Mater. 352, 42 (2006).

[16] A. De Backer, P.E. Lhuillier, C.S. Becquart, M.F. Barthe, J. Nucl. Mater.429 (2012) 78.

[17] P. M. Derlet, M. R. Gilber, S. L. Dudarev, Phys. Rev. B 84 (2011) 134109

[18] C. Domain, C.S. Becquart, Phys. Rev. B 65 (2002) 024103.

[19] C. Domain, C.S. Becquart, L. Malerba, J. Nucl. Mater. 335 (2004) 121.

[20] C. Domain, C.S. Becquart, J. Foct, Phys. Rev. B 69 (2004) 144112. see Ma 2011

[21] M. Eldrup, B.N. Singh, S.J. Zinkle, T.S. Byun, K. Farrell, J. Nucl. Mater. 307-311 (2002) 912.

[22] M. Eldrup, B.N. Singh, J. Nucl. Mater. 323 (2003) 346.

[23] F. El-Mellouhi, N. Mousseau, and L.J. Lewis, Phys. Rev. B. 78 (2008) 153202.

[24] C-C. Fu, F. Willaime, P. Ordejón, Phys. Rev. Lett. 92 (2004) 175503.

[25] C.C. Fu, J. DallaTorre, F. Willaime, J.L. Bocquet, A. Barbu, Nature Mat. **4** (2005) 68.

[26] C.C. Fu, F. Willaime, Phys. Rev. B72 (2005) 064117.

[27] N. Ghoniem, J.N. Alhajji, J. Nucl. Mater. 136 (1985) 192.

[28] A. Gokhman, A. Ulbricht, U. Birkenheuer, F. Bergner, Diff. Def. Data Pt.B: Sol. St. Ph., 172-174 (2011) 449.

[29] A. Hardouin-Duparc, C. Moingeon, N. Smetniansky-De-Grande, A, Barbu, J. Nucl. Mater. 302 (2002) 143.

[30] M. Hernández-Mayoral, M. J. Caturla, D. Gómez-Briceño, J. M. Perlado, E. Martínez, J. Marian, Proceedings of the Structural Materials for Innovative Nuclear Systems (SMINS) conference, NEA No. 6260 (2008)

[31] M. Hou, A. Souidi, C.S. Becquart, C. Domain, L. Malerba, J. Nucl. Mater. 382 (2008) 103.

[32] M. Hou, C. Ortiz, C.S. Becquart, C. Domain, U. Sarkar, A. De Backer, J. Nucl. Mater. 403 (2010) 89.

[33] E. Hornbogen, R.C. Glenn, Trans. Metall. Soc. Aime 218 (1960) 1064

[34] T. Jourdan, J.-P. Crocombette, Phys. Rev. B 86 (2012) 54113

[35] S. Jumel, J.-C. van Duysen, J. Nucl. Mater. 238 (2004) 251.

[36] *Monte Carlo Methods. Volume I: Basics*, by M. H. Kalos & P. A. Whitlock, John Wiley & sons (1986).

[37] J. Kuriplach, App. Surf. Sci. 194 (2002) 61.

[38] J.M. Lanore, Rad. Effects 22 (1974) 153.

[39] L.K. Mansur, Kinetics of Nonhomogeneous Processes, Wiley-Interscience, New York, 1987. p. 377.

[40] L. K. Mansur, A. F. Rowcliffe, R. K. Nanstad, S. J. Zinkle, W. R. Corwin, R. E. Stoller, J. Nucl. Mat. 329-333 (2004) 166-172

[41] J. Marian, B. D. Wirth, J. M. Perlado, Phys. Rev. Lett. 88 (2002) 255507.

[42] M.C. Marinica, F. Willaime, Diff. Def. Data B: Sol. Stat. Phen. 129 (2007) 67.

[43] M. T. Robinson, Phys. Rev. B 40 (1989) 10717

[44] E. Martínez, P.R. Monasterio, J. Marian, J. Comp. Phys. 230 (2011) 1359.

[45] H. Matsui, S. Takehana, M. W. Guinan, J. Nucl. Mater. 155-157 (1988) 1284.

[46] Y. Matsukawa, S. J. Zinkle, Science 318 (2007) 959

[47] M. K. Miller, Atom Probe Tomography, Kluwer Academic/Plenum, New York, 2000

[48] M.K. Miller, B.D. Wirth and G.R. Odette, Mater. Sci. Eng. A353 (2003) 133.

[49] K. L. Murty, I. Charit, J. Nucl. Mat. 383 (2008) 189-195 (Structural materials for Gen-IV nuclear reactors: challenges and opportunities)

[50] T. Opplestrup, V. Bulatov, G.H. Gilmer, M.H. Kalos, B. Sadigh, Phys. Rev. Lett. 97 (2006) 230602.

[51] C. J. Ortiz, M. -J. Caturla, Phys. Rev. B 75 (2007), 184101.

[52] C. J. Ortiz, M. J. Caturla, C. C. Fu, F. Willaime, Phys. Rev. B 75 (2007) 100102.

[53] Yu. N. Osetsky, D. J. Bacon, A. Serra, B. N. Singh, S. I. Golubov, J. Nucl. Mater. 276 (2000) 65.

[54] M.J. Puska, R.M. Nieminen, Rev. Mod. Phys. 66 (1994) 841.

[55] N. Soneda, T. Diaz de la Rubia, Phil. Mag. A 78 (1998) 995.

[56] N. Soneda, T. Díaz de la Rubia, Phil. Mag. A 81 (2001) 331.

[57] R.E. Stoller, S.I. Golubov, C. Domain, C.S. Becquart, J. Nucl. Mat. 382 (2008) 77.

[58] M.P. Surh, J.B. Sturgeon, W.G. Wolfer, J. Nucl. Mater. 325 (2004)

[59] S. Takaki, J. Fuss, H. Kugler, U. Dedek, H. Schultz, Rad. Effects 79 (1983) 87.

[60] D. A. Terentyev, T. P. Klaver, P. Olsson, M.-C. Marinica, F. Willaime, C. Domain, L. Malerba, Phys. Rev. Lett. 100 (2008) 145503.

[61] Ullmaier, Landolt-Börnstein, New Series III/25 (1991)

[62] R. Vassen, H. Trinkaus and P. Jung, Phys. Rev. B 44 (1991) 4206

[63] M. Victoria, N. Baluc, C. Bailat, Y. Dai, M. I. Luppo, R. Schäublin, B. N. Singh, J. Nucl. Mater. 276 (2000) 114.

[64] C.H. Woo, B Singh, H.L. Heinisch, J. Nucl. Mater. 179-181 (1991) 951.

[65] H. Xu, Yu. N. Osetsky, R. E. Stoller, Phys. Rev. B 84 (2011) 132103.

[66] Z. Yao, M. Hernandez-Mayoral, M.L. Jenkins, M.A. Kirk, Phil. Mag. 88 (2008) 2851.

[67] W.M. Young, E.W. Elcock, Proc. Phys. Soc., 89 **(**1966) 735.

[68] J.F. Ziegler, J. P. Biersack, U. Littmark, in: *The Stopping, Range of Ions in Solids*, J. F. Ziegler (Ed.), vol. 1, Perfamon, New York, 1985, p.22.

[69] S.J. Zinkle, G. E. Ice, M. K. Miller, S. J. Pennycook, Z.-L. Wang, J. Nucl. Mat. 386-388 (2009) 8-14

Chapter 4

Radiation-induced segregation

F. Soisson, M. Nastar
CEA, DEN, Service de Recherches de Métallurgie Physique, Gif-sur-Yvette, France

Abstract

We present here the basic mechanisms of radiation-induced segregation, typical experimental results, phenomenological and atomistic models. RIS has been first modelled with continuous methods. They are based on the thermodynamics of irreversible processes in which partial diffusion coefficients are estimated from diffusion experiments. To compensate the lack of diffusion data, a multi-scale approach has been developed. Atomic jump frequencies are parameterised from first principles calculations, leading to the partial diffusion coefficients when diffusion theory is available. The same atomic jump frequency models can be introduced in direct atomic-scale simulation methods.

Introduction

Permanent irradiation of materials sustains fluxes of vacancies and self-interstitials towards point defect sinks, such as dislocations, grain boundaries, free surfaces where they can annihilate. In an alloy, these fluxes of defects induce fluxes of chemical elements, leading to a local modification of the composition, the so-called Radiation-Induced Segregation phenomenon. The objective of this article is to provide a first introduction to RIS, emphasizing its basic mechanisms and their connection with point defect diffusion properties. More extensive reviews can be found in [1,2], and a detailed modeling of RIS in austenitic steels can be found in a companion paper by Sakaguchi [3].

We will show that simple rate theory models, based on extended Fickian diffusion equations can successfully explain the experimental observations, especially when consistently built within the framework of the Thermodynamics of Irreversible Processes (TIP). However, a quantitative prediction of RIS in real systems is often limited by a lack of experimental diffusion data: this is especially true for the diffusion by interstitials but also, to a lesser degree, for the diffusion by vacancies. Multi-scale approaches, coupling *ab initio* calculations and atomic diffusion models offer an alternative way to get reliable information on the missing RIS parameters, or to directly simulate – at the atomic scale –

the microstructure evolution: we present the recent progress achieved in that direction and the difficulties that remain to be overcome.

Equilibrium vs. non-equilibrium segregation

Segregation is commonly observed in alloys at thermal equilibrium: the composition of solid solutions that are homogeneous in the bulk usually differs near the dislocations, the grain-boundaries, the free surfaces, etc. This equilibrium segregation results from the difference of interactions between the chemical elements and these extended defects, and is controlled by the minimization of the free energy of the system [4]. Diffusion properties of the materials affect the kinetics of such segregation processes, but not the final equilibrium states. By comparison, non-equilibrium segregation phenomena result from the coupling between fluxes of excess point defects and fluxes of alloying elements, and can occur e.g. during quenching from high temperatures, during sintering or under irradiation. They are non-equilibrium phenomena: they tend to disappear when external forces are switched off and the system reaches its equilibrium. They are controlled by the external forcing, but also by point defect properties.

A classical and simple case of non-equilibrium segregation has been observed by Anthony in Al-Zn dilute alloys after quenching from high temperatures [5]. During the quench, the equilibrium vacancy concentration strongly decreases and excess vacancies may in some special conditions eliminate by forming small pyramidal cavities, just below the oxidised surface. An enrichment of Zn is measured near the cavities. Anthony explained this phenomenon by the fact that the flux of vacancies toward a cavity must be balanced by a flux of Al and Zn atoms in the opposite direction. The fluxes of Al and the flux of Zn depend on their respective diffusion coefficients and are usually not simply proportional to their concentration. Therefore, the local composition of the alloy is modified. Anthony predicted that similar phenomena may be much stronger in alloys under irradiation, where fluxes of excess point defects are sustained for long times [6]. Soon afterwards, radiation induced segregation was observed in austenitic steels by Okamoto et al. [7] and since then have been observed in many other alloys [1,2].

RIS mechanisms

While it is clear from the start that RIS is due to the coupling between fluxes of point defects and fluxes of chemical elements, several mechanisms involving either vacancies or interstitials may lead to a preferential transport of some alloying elements at the sinks. The very details of these mechanisms affect the direction and the amount of RIS. As we will see below, their full physical description requires the knowledge of the L_{ij} phenomenological coefficients of the Onsager matrix. In many systems of practical interest, one only knows some diffusion coefficients (typically some tracer diffusion coefficients) that do not provide the equivalent information. Nevertheless, they often give some insights on the underlying mechanisms and a first estimation for the tendency to segregate one element or the other.

In a binary alloy for example, one may define some partial diffusion coefficients for A and B atoms: D_A^V and D_B^V for the diffusion by vacancies and D_A^I and D_B^I for the diffusion by interstitials. If the A and B fluxes occur both in the opposite direction of the vacancy

flux, the vacancy contribution drives an enrichment of the slow diffusing element at sinks: this mechanism (Figure 1a) is usually referred to as the inverse-Kirkendall effect. In dilute alloys, a strong attraction between vacancies and B solute atoms may also lead to an enrichment of B through a vacancy-drag mechanism (Figure 1b): in such a case the flux of B and vacancies are in the same direction, and an enrichment of B is observed even if they diffuse more rapidly than A atoms. Finally, fluxes of interstitials and fluxes of atoms usually occur in the same direction and one may expect that the interstitial contribution favours the segregation of the fast diffusing element (Figure 1c). RIS therefore results from several mechanisms that can oppose or reinforce each other, depending on the material diffusion properties: one difficulty for the understanding and ultimately, the prediction of RIS phenomena, comes from the lack of reliable diffusion data, especially for the interstitial defects. In such a case, a multi-scale modelling approach can be useful to provide additional information.

Figure 1. Some possible RIS mechanisms, depending on the partial diffusion coefficients. Coupling with the vacancy flux (resulting from the plotted vacancy concentration profile): (a) if the A and B fluxes are in the same direction, an enrichment of B occurs if $D_B^V < D_A^V$ and a depletion if $D_B^V > D_A^V$, (b) when the vacancies drag the solute, an enrichment of B occurs, even if $D_B^V > D_A^V$. Coupling with the interstitial flux (resulting from the plotted interstitial concentration profile): (c) an enrichment of B occurs when $D_B^I > D_A^I$.

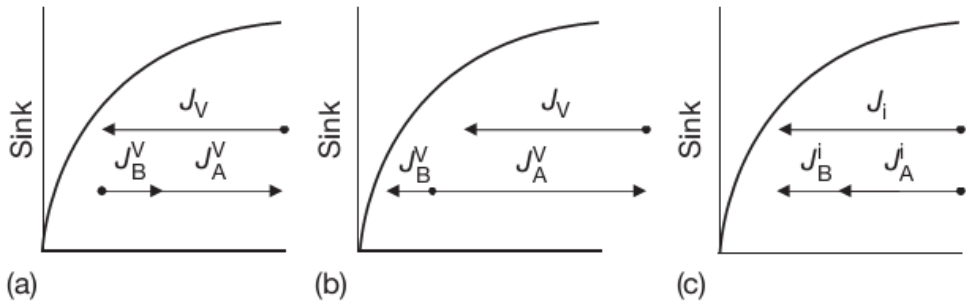

Experimental observations and general trends

Segregating elements. As must be clear from the previous discussion, the prediction of the segregating elements is usually difficult. General trends may be identified only when one mechanism is dominant: in binary alloys with strong size effects for example, undersized atoms usually segregate at point defects sinks [8]. This can be explained by a preferential occupation of interstitial positions by small atoms, leading to the situation illustrated onFigure 1c.

Temperature and dose-rate effects. RIS may occur when significant fluxes of defects are sustained towards sinks, which typically happens only in a range of temperatures between 0.3 and 0.6 times the melting point T_m. At lower temperatures, point defects are immobile and will annihilate mainly by mutual recombination. At higher temperatures, the point defects annihilate rapidly at sinks and their supersaturation is too low for sustaining sufficient fluxes. RIS can be observed for irradiation doses much smaller than for void swelling or ballistic disordering effects. An increase in the dose rate K_0 results in higher

point defect concentrations and fluxes. The transition between the different regimes is then shifted towards higher temperatures (Figure 2). However, because point defect concentrations slowly evolves with the radiation fluxes (usually as its square root in the range where RIS occurs), while point defect mobility increases exponentially with the temperature, a high increase of the dose rate is necessary to get a significant shift.

Figure 2. Temperature and dose rate effect on the radiation-induced segregation

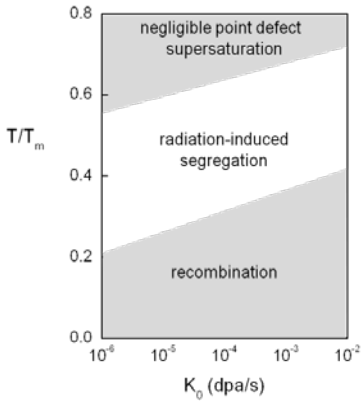

Concentration profiles. RIS often leads to concentration profiles with specific features: they can spread over relatively "large" distances: a few tens of nanometers (see e.g. Figures 3 and 4) while equilibrium segregation is often limited to the range of atomic interactions, i.e. to a few angstroms. Equilibrium segregation profiles are monotonous, except in alloys with ordering tendencies where some oscillations can appear with atomic wavelengths. By contrast, non-equilibrium segregation profiles may be non-monotonous, with sometimes at grain boundaries typical "W-shape" profiles. A typical case is RIS of Cr in austenitic or ferritic steels (Figure 3).

Figure 3. Examples of radiation induced segregation of Cr at grain boundaries, with "W-shape" concentration profiles: (a) in a 316 austenitic steel, after irradiation of ~1 dpa by protons (at 360°C, closed circles) or neutrons (at 280°C, open circles) [9]; (b) in a PE16 Ninomic alloy, after neutron irradiation at 425°C [10]; (c) in a ferritic steel, after an ion irradiation of ~0.5 dpa at 350°C [11]

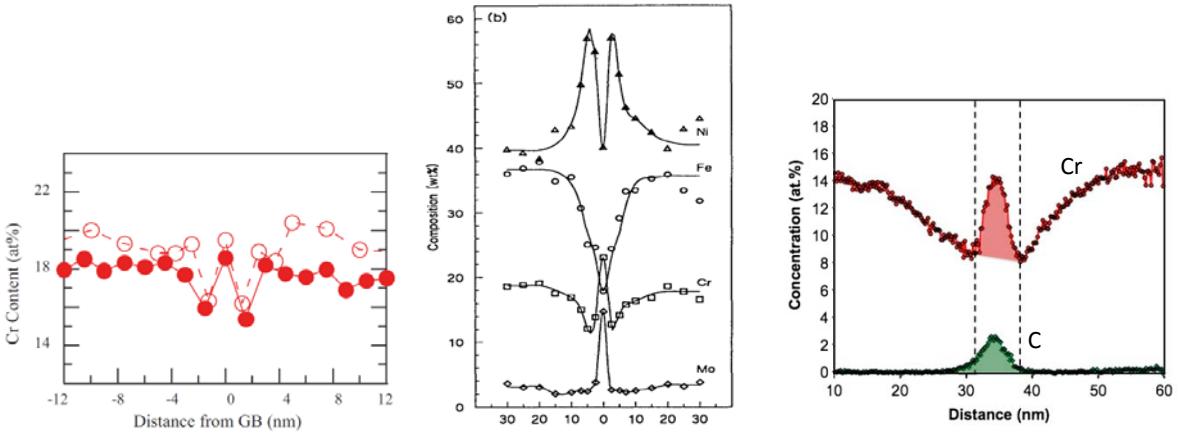

- RIS in steels

In austenitic steels, an enrichment of Ni and Si and a depletion of Cr is usually observed on the cavities or at grain boundaries. The depletion of Cr is suspected to play a role in irradiation-assisted stress corrosion cracking (IASCC). The enrichment of Ni and the depletion of Cr can also stabilise the austenite near the sinks and favor a transition to ferrite in the matrix [12]. The segregation of minor elements can lead to the formation of various phases, such as γ'-precipitates (e.g. Ni_3Si) or $M_{23}C_6$ carbides. The mechanisms controlling the segregation of major elements (Fe, Ni and Cr) are still debated. The order of tracer diffusion coefficients at thermal equilibrium ($D_{Ni} < D_{Fe} < D_{Cr}$) suggests that Inverse-Kirkendall by vacancy diffusion could explain the observed behaviors of major elements, but some models also suggest a significant contribution of interstitials [2]. The segregation of minor elements seems to be dominated by size effects and interstitial diffusion, with an enrichment of undersized (e.g. Si [13]) and a depletion of oversized atoms (e.g. Mo [14]). RIS in ferritic and ferritic-martensitic steels has recently drawn some attention because they are considered as candidates for future fission and fusion reactors. In highly concentrated alloys, a depletion of Cr [11,15] and enrichment of Ni [15] at grain boundaries have been observed, reminding the general trends in austenitic steels. Carbon segregation has been sometimes found to go with the Cr one (Figure 3c.). RIS of phosphorus at grain boundaries has been observed and the addition of Hf atoms has been found to reduce the Cr segregation, in austenitic [16] and more recently in ferritic [17] steels.

Radiation Induced Precipitation and Dissolution. A direct consequence of RIS is the modification of the precipitate stability and microstructure. In case of solute enrichment near a sink, if the concentration reaches the solubility limit, precipitation may occur even in an overall under-saturated alloy. Radiation Induced Precipitation of the ordered Ni_3Si phase has been observed in under saturated Ni-Si alloys, at free surfaces or on small interstitials loops [18]. Inversely, in case of solute depletion, a dissolution of precipitates may occur in super-saturated alloys: this has been observed for example near dislocation loops in Ni-Al alloys [19].

Diffusion equations in the framework of the thermodynamics of irreversible processes

- Diffusion equations

The evolution of concentration profiles in the vicinity of a sink, during the segregation, is given by generalized diffusion equations. For a binary A-B alloy, for example:

$$\begin{aligned} \frac{\partial c_v}{\partial t} &= K_0 - R c_i c_v - \operatorname{div} J_v \\ \frac{\partial c_i}{\partial t} &= K_0 - R c_i c_v - \operatorname{div} J_i \\ \frac{\partial c_B}{\partial t} &= -\operatorname{div} J_B \end{aligned} \qquad (1)$$

where K_0 is the point defect production rate in dpa.s^{-1} (i.e. the number of displacements per atom per second) and R the recombination rate. The equilibrium point defect concentrations are imposed at the sink, as a boundary condition. The solution of

these equations requires the knowledge of the relation between the fluxes *J* and the concentrations *c*. The Thermodynamics of Irreversible Processes (TIP) [20] provides such a relation: the flux of specie α is a linear combination of the thermodynamics driving forces, i.e. the gradients of chemical potentials $\nabla\mu_\beta$:

$$J_\alpha = -\sum_\beta L_{\alpha\beta}\nabla\mu_\beta , \qquad (2)$$

with $\alpha,\beta = i,v,B$. The L-coefficients are the phenomenological or Onsager coefficients. The Onsager matrix is symmetric and positive and the sign of the non-diagonal terms (such as L_{Bv} or L_{Bi}) determines if the flux of B and point defects are in the same ($L>0$) or in the opposite ($L<0$) direction. An equivalent description in terms of diffusion coefficients and gradients of concentrations can be established. For example in a binary alloy (AB), fluxes are separated into two contributions, the first one induced by the point defect concentration gradients and the second one appearing after the formation of chemical concentration gradients near the point defect sink [2,21].

$$\begin{aligned} J_A &= C_A(d_{AV}\nabla C_V - d_{AI}\nabla C_I) - (d^c_{AV}C_V + d^c_{AI}C_I)\Phi\nabla C_A \\ J_V &= -(C_A d_{AV} + C_B d_{BV})\nabla C_V + C_V\Phi(d^c_{AV} - d^c_{BV})\nabla C_A \\ J_I &= (C_A d_{AI} + C_B d_{BI})\nabla C_I + C_I\Phi(d^c_{AI} - d^c_{BI})\nabla C_A \end{aligned} , \qquad (3)$$

where the thermodynamic factor Φ relating the alloy chemical potential to the solute concentration, is proportional to the second derivative of the Gibbs free energy, *G*, of the alloy with respect to the concentration of one of the components. The partial diffusion coefficients are defined in terms of the *L*-coefficients and the equilibrium vacancy concentration C_V^{eq}:

$$\begin{aligned} d_{AV} &= \frac{L^V_{AA} + L^V_{AB}}{C_A C_V} \\ d^c_{AV} &= \frac{L^V_{AA}}{C_A C_V} - \frac{L^V_{AB}}{C_B C_V} + C_A d_{AV}\frac{1}{\Phi}\frac{\partial \ln C_V^{eq}}{\partial \ln C_A} \end{aligned} . \qquad (4)$$

The flux of B is deduced from the flux of A by inverting A and B letters. Interstitial partial diffusion coefficients are obtained from the vacancy ones by replacing letter V by letter I.

- Steady-state concentration profile

An analytical solution of the coupled equations is obtained within steady state conditions. At the boundary plane, variation of composition is controlled by a unique flux coming from the bulk. A steady state condition implies the latter flux to be zero and step by step every flux to be zero. In a binary alloy, equations (3) lead to a relationship between concentration gradients:

$$\nabla C_A = \frac{C_A C_B d_{BI} d_{BV}}{(C_B d_{BI} D_A + C_A d_{AI} D_B)} \left(\frac{d_{AV}}{d_{BV}} - \frac{d_{AI}}{d_{BI}} \right) \nabla C_V \,, \qquad (5)$$

where the intrinsic diffusion coefficient is equal to $D_\alpha = (d^c_{\alpha V} C_V + d^c_{\alpha I} C_I)\Phi$. The spatial extent of segregation coincides with the region of non-vanishing defect gradients. Therefore, if the chemical potentials and the Onsager coefficients are known, the stationary state of RIS can be predicted by Equation (5). However, to take into account the variation of the L coefficients with local composition, numerical integration of the diffusion equations is required.

Figure 4. Surface Radiation Induced Segregation in Ni-10%Cu alloys: Evolution of the Cu concentration profiles with the dose rate at different temperatures

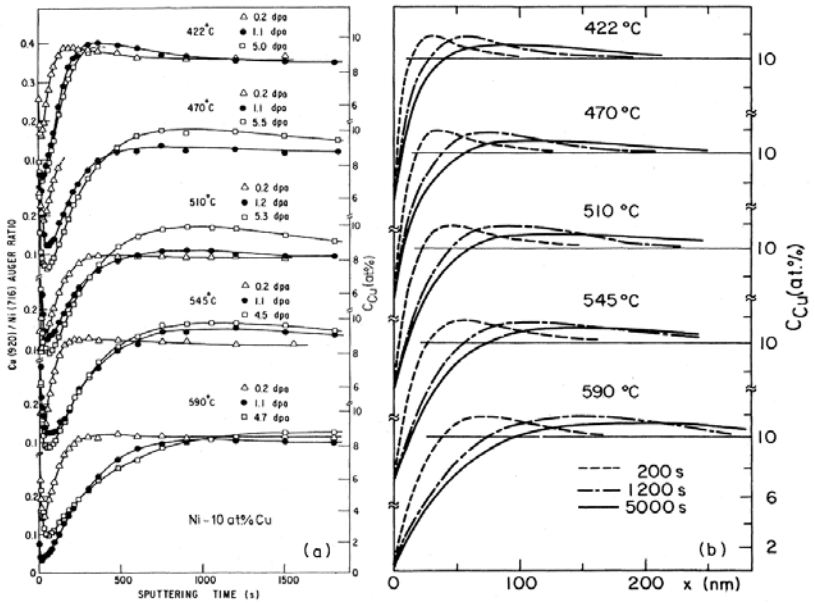

On the left: Auger spectroscopy measurements (the distance to the surface is proportional to the sputtering time), on the right: solution of the diffusion equations [22].

- Experimental determination of the phenomenological parameters

Experimental data for the determination of the chemical potentials are available for the most usual systems. Unfortunately, a complete experimental determination of the L coefficients is much more difficult. Even for the vacancy terms, it requires the measurements of the intrinsic diffusion coefficients D_A and D_B (i.e. in principle an interdiffusion experiment *and* the determination of the Kirkendall velocity for each composition), but also the measurement of additional diffusion coefficients [2]. Anthony's experiments in Al alloys were precisely devised to get this extra information. Unfortunately, they were only possible thanks to the very specific configuration of vacancy clusters in Al alloys (pyramidal cavities growing under an Al_20_3 film), and appear to be difficult to measure in other – especially iron based – alloys. Moreover, the contribution of interstitials are difficult to separate from the one of vacancies, and the experimental determination of the corresponding Onsager coefficients is even more challenging. As a consequence, equations (1)-(3) have been used mainly as a

phenomenological tool, with parameters partly coming from available data and partly fitted to the experimental segregation profiles. Such approaches have been quite successful to reproduce RIS phenomena in Ni-Cu [22], Ni-Si alloys, austenitic steels, etc. A typical example is shown on Figure 4: a depletion of Cu atoms at the surface on a Ni-10%Cu alloy, observed under ion irradiation by Auger spectroscopy, is well reproduced by diffusion equations. In that special case, vacancy and interstitial diffusion where fitted to the segregation profile: the conclusion was that RIS is due to a preferential diffusion of Ni by interstitials and to a more rapid diffusion of Cu by vacancies [22]. An application of a similar approach to multi-component austenitic steels can be found in this volume [3].

Atomistic modelling

Alternatively, the *L* coefficients for the diffusion equations can be directly derived from the point defect jump frequencies. If the vacancy and self-interstitial jump frequencies are known, it is possible to compute the *L* from analytical models or to measure them in Molecular Dynamics or Kinetic Monte Carlo simulations. Jump frequencies may also be used directly in atomic models, to simulate the microstructure evolution.

Jump frequencies

According to the transition state theory, the exchange frequency between e.g. a vacancy and a neighboring atom A is given by:

$$\Gamma_{AV} = \nu_A \exp\left(-\frac{\Delta G_{AV}^{mig}}{k_B T}\right) = \nu_A \exp\left(\frac{\Delta S_{AV}^{mig}}{k_B}\right)\exp\left(-\frac{\Delta H_{AV}^{mig}}{k_B T}\right) \quad (6)$$

where ν_A is an "attempt frequency", of the order of the Debye frequency and ΔG_{AV}^{mig}, ΔH_{AV}^{mig} and ΔS_{AV}^{mig} are respectively the Gibbs free energy, the enthalpy and the entropy of migration (they correspond to the change when the atom A goes from its original position on the crystal lattice to the saddle point between the initial and final positions). One of the key points of kinetics studies is the description of the jumps frequencies (6) and the way they depend on the local atomic environment. This description encompasses all the information on the thermodynamic and kinetic properties of the system. The variations of ΔH_{AV}^{mig} are the most crucial ones, because they control the thermally activated part of the jump frequencies: even small variations of ΔH_{AV}^{mig} usually result in strong variations of Γ_{AV}.

First-principle methods, especially those developed in the framework of the density functional theory (DFT) now provide a reliable way to compute the jump frequencies. Migration enthalpies may be computed by the drag or the nudged elastic band methods. The entropies of migration are usually dominated by the vibrational contribution, which may be computed in the harmonic approximation – even if it requires heavier calculations. DFT studies on self-interstitial properties are of particular interest, due to the lack of experimental data. However, the computational cost of DFT calculations is still very high: typical applications are the calculations of self-diffusion or impurity diffusion coefficients in dilute alloys, which require the estimation of only a few jump frequencies [23,24]. Onsager coefficients and the resulting coupling between point defects and solute atoms have also been calculated directly from DFT calculations in a few binary dilute alloys [25-27]. Systematic studies in concentrated alloys remain very challenging. In iron based alloys, the effect of the ferro-to-paramagnetic transition that strongly accelerates diffusion at

high temperature is still only taken into account by empirical corrections [24]. Above all, DFT methods are limited to small systems (typically a few hundreds of atoms) and they are still too time consuming to allow either "on-the-fly" calculations of the jump frequencies, or their tabulation for all possible local configurations (especially in concentrated alloys). More approximated models are therefore required, that can be fitted to *ab initio* calculations and/or experimental data.

Empirical or semi-empirical potentials can be used: the problem is to develop potentials giving a reliable description of point defect properties in alloys, by no means an easy task. D and L coefficients can then be directly measured in Molecular Dynamics for the interstitials, due to their small migration barriers [28,29] and for the vacancies at high temperatures [30]. At lower temperatures, Atomistic Kinetic Monte Carlo (AKMC) simulations must be used, but full on-the-fly calculations of the jump frequencies, including the entropic contributions, remain time consuming and have been again limited to the calculations of diffusion coefficients [31]. To go beyond and follow the segregation or precipitation kinetics, Monte Carlo simulations using approximate estimations of the migration barriers (i.e. without calculations of the entropic migration entropy or without considering the actual saddle-point configuration) have been proposed [32-35]: one advantage of such methods is that they take into account long range elastic interactions that may affect diffusion properties.

For the time being however [2,36-39], most AKMC simulations of segregation and precipitation under irradiation still rely on broken-bond models based on rigid lattice approximations, which are even faster. The enthalpy of the system is considered to be a sum of pair interactions, fitted on DFT calculations or experimental data, such as the phase diagram, point-defect properties or diffusion coefficients [40,41]. Specific interactions can be introduced for the description of the saddle-point configurations [42]. Other possible improvement are the introduction of many-body-interactions [43,44] or concentration-dependent pair interactions [45] to reproduce no-symmetrical thermodynamic behaviours, and temperature-dependent pair interactions, to take into account vibrational entropies and other finite temperature effects [45].

Determination of the Onsager coefficients from the jump frequencies

Once the point defect jump frequencies are known, the theory of diffusion in alloys establishes the connection with the Onsager coefficients, at least in some simple cases. The main difficulty is to take into account the correlation effects [46]. In dilute alloys, reliable expressions are available for the vacancy mechanism in the faced centered cubic (FCC) and the body centered cubic (BCC) structures if the interactions are limited to first nearest neighbors. Some models have been proposed for specific interstitial diffusion mechanisms [47].

In concentrated alloys, diffusion models require additional assumptions [48]. The alloy is assimilated to a random lattice gas model where atoms do not interact and where vacancies jump at a frequency which only depends on the species they exchange with (two frequencies in a binary alloy). Such diffusion models which consider a limited number of jump frequencies give reliable results for the simulation of the inverse-Kirkendall flux coupling. However, they do not account for the effect of the binding energies between neighboring species and the resulting short range order (SRO) parameters, on the L-coefficients. Indeed, one knows that RIS behaviour is often explained by means of a

competition between binding energies of point defects with atomic species especially in dilute alloys. A unified description of flux coupling in dilute and concentrated alloys including the effect of short range order parameters would allow a simultaneous prediction of two different mechanisms leading to RIS, the solute drag by vacancies and an inverse-Kirkendall effect involving the major elements. Diffusion models including SRO were developed in BCC alloys [49]. The extension to FCC solid solutions provided a model of the composition effect on solute drag by vacancies [50,51]. Recently, an interstitial diffusion model including SRO was proposed in BCC concentrated alloys [47].

Finally, when reliable diffusion models are lacking, it is possible to measure the displacements $\Delta\mathbf{r}$ of point defects and atoms during the time interval t in a Molecular Dynamic or Monte Carlo simulation [52,39], the Onsager coefficients are then given by the generalised Einstein relations [46]:

$$L_{ij} = \frac{1}{6Vk_BT}\frac{\left\langle \Delta\mathbf{r}_i.\Delta\mathbf{r}_j \right\rangle}{t}, \qquad (7)$$

where V is the atomic volume.

Mean-Field and Monte Carlo simulations

Atomistic simulations may also be used to follow directly the whole RIS process and the evolution of the microstructure. One advantage is that in addition to the segregation itself, kinetics of precipitation (or of precipitate dissolution) can be modeled (Figure 6).

Figure 5. Mean Field simulation of the evolution of the Cr concentration profile near a grain boundary in Fe-12at.%Ni-19at.%Cr at 635 K, as a function of the irradiation dose [53]

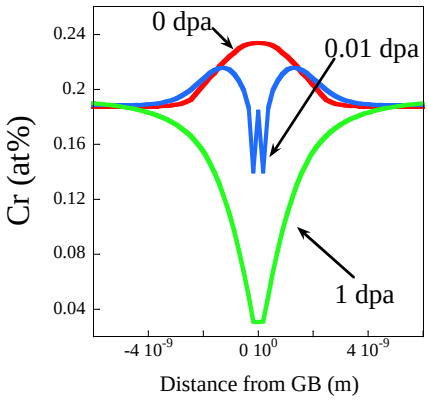

In Atomistic Kinetic Mean-Field simulations, evolution of average point defect and atom concentration on lattice sites, or planes, are computed by solving rate equations that directly include the point defect jump frequencies, computed with broken-bond models. The mean-field approximation is used to compute the activation enthalpies of the jump frequencies. The method has applied to Ni-Cu [54] and Fe-Ni-Cr [53] alloys. In the later case, "W-shape" profiles have been obtained, in agreement with experimental observations (Figure 5).

AKMC simulations have been quite successful to model the kinetics of phase transformations during thermal ageing. Applications to alloys under irradiation have been introduced only recently, because of the complex parameterisation required, especially for interstitial properties. An example of simulation in a model system A-B is shown onFigure 6: here A atoms diffuse more rapidly than B atoms by vacancy jumps ($D_A^V > D_B^V$) and more slowly by interstitial jumps ($D_A^I < D_B^I$). The flux of vacancy and interstitials towards a grain boundary located in the middle of the simulation box both results in an enrichment of B. When the local concentration exceeds the solubility, a precipitation occurs [36]. Copper segregation and precipitation in Fe-Cu alloys under irradiation has been especially studied. Experimental data and DFT calculations show that Cu diffuses more rapidly than Fe by the vacancy mechanism. However, direct measurements of the L_{CuV} coupling coefficients in AKMC simulations [39,52] show that at low temperature, vacancy and copper fluxes operate in the same direction: in a bcc alloy, this drag effect is due to the strong attraction between Cu atoms and vacancies, up to the second nearest-neighbour positions. At high temperature, Cu-V pairs dissociate and Cu and V fluxes are in opposite directions. AKMC simulations show that irradiation at low temperature favours the segregation of Cu and its heterogeneous precipitation at point defect sinks [2,39]. The same simulations suggest that the contribution of interstitial diffusion (with ⟨110⟩ dumbbell configuration) to the segregation is very limited. AKMC simulations with displacement cascades have shown the formation of vacancy clusters surrounded by copper atoms [37,38] and that other solutes elements (Mn, Ni, Si) can precipitate with copper [37,38,55]. The segregation and precipitation of Mn, seems to be controlled by a positive coupling with the interstitial flux, because of a significant attraction between Mn atoms and ⟨110⟩ dumbbells.

Figure 6. Monte Carlo simulation of Radiation Induced Segregation at a grain boundary in an under supersaturated binary A-B alloy, with $c_B = 0.05$ at 800 K with a dose rate of 10^{-6} dpa.s^{-1} (only B atoms are shown)

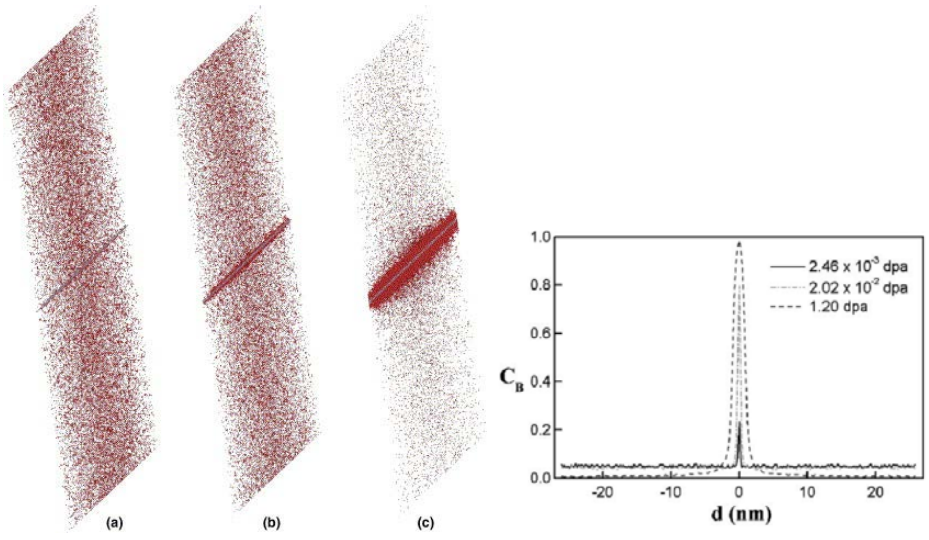

When the solute concentration (right) goes beyond the solubility limit ($c_B = 0.08$ here) precipitation takes place.

Conclusion

Intensive experimental work has been devoted to the observations of RIS profiles mainly in austenitic steels and its model alloys and more recently to ferritic steels. A strong variation of RIS with irradiation flux and dose, temperature, composition and GB type was observed. Non-monotonous concentration profiles such as the "W-shaped' transitory profile of Cr in steels were discovered at irradiation doses of a few dpa, although the mechanisms involved are still not fully understood. However, the main RIS mechanisms were known before RIS was observed. Since the first models, diffusion enhancement and point defect driving forces were accounted for. The kinetic equations of these models are based on general Fick's laws. While in dilute alloys one knows how to deduce such equations from atomic jump frequencies, in concentrated alloys more empirical methods are used. This can be explained by the lack of diffusion data and diffusion theory to determine the L-coefficients from atomic jump frequencies. However recent improvements of the mean-field diffusion theories including short range order effects for both vacancy and interstitial diffusion mechanism are such that we can expect the development of more rigorous RIS models for concentrated alloys. Meanwhile, first principle methods relying on the DFT have significantly improved and they are able to provide activation energies of both vacancy and interstitial jump frequencies as a function of local environment, as least at 0 K. It remains difficult to deal with finite temperature effects in the DFT framework: the ferro-to-paramagnetic transition in iron based alloys, vibration entropic contributions in concentrated alloys, etc. The problem is critical in austenitic steels which are stable at high temperature only. But in spite of these difficulties, it seems now easier to calculate the partial diffusion coefficients from first principle calculations rather than to estimate them from diffusion experiments. An alternative approach to continuous diffusion equations is to develop atomistic scaled simulations such as mean field equations or Monte Carlo simulations which are quite appropriate to study the nanoscale RIS phenomena. Monte Carlo simulations are now able to embrace the full complexity of RIS phenomena including vacancy and split interstitial diffusion mechanisms, the whole flux coupling, the resulting segregation and eventual nucleation at grain-boundaries. But it is still a computationally intensive method when correlation effects are important.

References

[1] G. Was, *Fundamentals of Radiation Materials Science* (Springer-Verlag, Berlin, 2007).

[2] M. Nastar and F. Soisson, in *Comprehensive Nuclear Materials* (Elsevier, Oxford, 2012), pp. 471–496.

[3] N. Sakaguchi, (this volume).

[4] W. C. Johnson and J. M. Blakely, *Interfacial Segregation* (ASM, Metals Park, 1979).

[5] T. R. Anthony, Acta Metall. 18, 307–314 (1970).

[6] T. R. Anthony, J. Appl. Phys. 41, 3969–3976 (1970).

[7] P. R. Okamoto, S. D. Harkness, and J. J. Laidler, Trans. Am. Nucl. Soc. 16, 70–70 (1973).

[8] L. E. Rehn and P. R. Okamoto, in *Phase transformations during irradiation*, edited by F. V. Nolfi (Applied Science Publishers, 1983).

[9] E. A. Kenik and J. T. Busby, Mater. Sci. Eng. R 73, 67–83 (2012).

[10] S. Dumbill, R. M. Boothby, and T. M. Williams, Mater. Sci. Tech. 7, 385–390 (1991).

[11] E. A. Marquis, R. Hu, and T. Rousseau, J. Nucl. Mater. 413, 1–4 (2011).

[12] P. R. Okamoto and L. E. Rehn, J. Nucl. Mater. 83, 2–23 (1979).

[13] P. R. Okamoto and H. Wiedersich, J. Nucl. Mater. 53, 336–345 (1974).

[14] V. K. Sethi and P. R. Okamoto, Journal of Metals 32, 5–6 (1980).

[15] E. A. Little, Mater. Sci. Technol. 22, 491–518 (2006).

[16] T. Kato, H. Takahashi, and M. Izumiya, J. Nucl. Mater. 189, 167–174 (1992).

[17] Z. Lu, R. G. Faulkner, G. Was, and B. D. Wirth, Scr. Mater. 58, 878–881 (2008).

[18] A. Barbu and A. J. Ardell, Scr. Metall. 9, 1233–1237 (1975).

[19] D. I. Potter and D. G. Ryding, J. Nucl. Mater. 71, 14–24 (1977).

[20] P. Glansdorff and I. Prigogine, *Thermodynamic Theory of Structure, Stability and Fluctuations* (John Wiley & Sons Ltd, 1971).

[21] W. G. Wolfer, J. Nucl. Mater. 114, 292–304 (1983).

[22] W. Wagner, L. E. Rehn, H. Wiedersich, and V. Naundorf, Phys. Rev. B 28, 6780–6794 (1983).

[23] M. Mantina, Y. Wang, L. Q. Chen, Z. K. Liu, and C. Wolverton, Acta Mater. 57, 4102–4108 (2009).

[24] S. Huang, D. L. Worthington, M. Asta, V. Ozolins, G. Ghosh, and P. K. Liaw, Acta Mater. 58, 1982–1993 (2010).

[25] J. D. Tucker, R. Najafabadi, T. R. Allen, and D. Morgan, J. Nucl. Mater. 405, 216–234 (2010).

[26] S. Choudhury, L. Barnard, J. D. Tucker, T. R. Allen, B. D. Wirth, M. Asta, and D. Morgan, J. Nucl. Mater. 411, 1–14 (2011).

[27] L. Barnard, J. D. Tucker, S. Choudhury, T. R. Allen, and D. Morgan, J. Nucl. Mater. 425, 8–15 (2012).

[28] J. Marian, B. D. Wirth, J. M. Perlado, G. R. Odette, and T. Diaz de la Rubia, Phys. Rev. B 64, 094303 (2001).

[29] M. I. Mendelev and Y. Mishin, Phys. Rev. B 80, 144111 (2009).

[30] A. C. Arokiam, A. V. Barashev, D. J. Bacon, and Y. N. Osetsky, Phys. Rev. B 71, 174205 (2005).

[31] J.-L. Bocquet, Defects and Diffusion in Metals: An Annual Retrospective IV 203-2, 81–112 (2002).

[32] A. Finel, in *Phase transformations and evolution in materials* (TMS, Warrendale, 2000), p. 371.

[33] C. Pareige, C. Domain, and P. Olsson, J. Appl. Phys. 106, 104906 (2009).

[34] C. Pareige, M. Roussel, S. Novy, V. Kuksenko, P. Olsson, C. Domain, and P. Pareige, Acta Mater. 59, 2404–2411 (2011).

[35] G. Bonny, D. Terentyev, L. Malerba, and D. Van Neck, Phys. Rev. B 79, 104207 (2009).

[36] F. Soisson, J. Nucl. Mater. 349, 235–250 (2006).

[37] E. Vincent, C. S. Becquart, and C. Domain, Nucl. Instrum. Methods Phys. Res., Sect. B 255, 78–84 (2007).

[38] E. Vincent, C. S. Becquart, and C. Domain, J. Nucl. Mater. 382, 154–159 (2008).

[39] F. Soisson and C.-C. Fu, Solid State Phenomena 139, 107 (2008).

[40] G. Martin and F. Soisson, in *Handbook of Materials Modeling*, edited by S. Yip (Springer Netherlands, 2005), pp. 2223–2248.

[41] C. S. Becquart and C. Domain, Phys. status Solidi B 247, 9–22 (2010).

[42] L. A. Girifalco, J. Phys. Chem. Solids 25, 323–333 (1964).

[43] E. Clouet and M. Nastar, in *Complex Inorganic Solids: Structural, Stability, and Magnetic*, edited by P. E. A. Turchi, A. Gonis, K. Rajan, and A. Meike (Springer Verlag, New York, 2005), pp. 215–239.

[44] F. De Geuser, B. M. Gable, and B. C. Muddle, Philos. Mag. 91, 327–348 (2011).

[45] E. Martínez, O. Senninger, C.-C. Fu, and F. Soisson, Phys. Rev. B 86, 224109 (2012).

[46] A. R. Allnatt and A. B. Lidiard, *Atomic Transport in Solids* (Cambridge University Press, 2003).

[47] V. Barbe and M. Nastar, Phys. Rev. B 76, 054206 (2007).

[48] J. R. Manning, Phys. Rev. B 4, 1111 (1971).

[49] R. Kikuchi and H. Sato, J. Chem. Phys. 53, 2702–2713 (1970).

[50] N. A. Stolwijk, Phys. Status Solidi A 105, 223–232 (1981).

[51] M. Nastar and V. Barbe, Faraday discuss. 134, 331–342 (2007).

[52] A. V. Barashev and A. C. Arokiam, Philos. Mag. Lett. 86, 321 (2006).

[53] M. Nastar, Philos. Mag. 85, 641–647 (2005).

[54] Y. Grandjean, P. Bellon, and G. Martin, Phys. Rev. B 50, 4228–4231 (1994).

[55] B. Wirth and G. Odette, Mater. Res. Soc. Symp. P. 540, 637–642 (1999).

Chapter 5

Modelling of radiation-induced segregation at grain boundaries in austenitic stainless steels

N. Sakaguchi
Hokkaido University, Japan

Abstract

A model for radiation-induced segregation (RIS) at grain boundaries was developed based on the rate equations including the inverse-Kirkendall fluxes and the interactions between point defects and minor alloying elements. The dependencies of irradiation temperature and damage rate on the RIS were theoretically predicted by the present model. The effect of the additional minor alloying elements on the RIS was also examined. The multi-component RIS model, which includes the contribution of the minor alloying elements, successfully reproduced the RIS behaviour in neutron irradiated type 304L and 316L austenitic stainless steels.

Introduction

Solute redistribution in a concentrated alloy under irradiation occurs due to the preferential interaction between the solute atoms and excess point defects migrating toward sinks, such as surfaces or grain boundaries. In the austenitic stainless steels type 304 and 316, which are used as a light-water reactor core materials, radiation-induced segregation (RIS) near the grain boundaries significantly degrades their mechanical chemical properties. The seriousness of this problem has been considered as irradiation-assisted stress corrosion cracking (IASCC) induced by the RIS because of the depletion of chromium atoms near grain boundaries. It is thus important to investigate the mechanism for retardation of radiation-induced solute redistribution near the grain boundaries.

In the present paper, defect kinetic rate equations were used to evaluate the RIS behaviour around the grain boundaries in austenitic stainless steels. To clarify the validity of the present model and a set of physical parameters, the calculated results were compared to some experimental results obtained by electron and neutron irradiation experiments.

Simulation method

Simultaneous solutions to rate equations describe solute redistribution induced by vacancies and interstitials fluxes to grain boundaries and by solute interactions with those defect fluxes. The present RIS model is based on a simple model for ternary Fe-Cr-Ni system described by Marwick et al. [5]. The composition-dependent diffusion coefficients introduced by Allen et al. [1] is not considered in the present model. Finite difference methods and the LSODE subroutine [4] have been used to solve the rate equations.

Continuity equations for point defects and major alloying elements

The approach is to solve the coupled diffusion equations for vacancies, interstitials and alloying elements to obtain the terms coupling the defect and solute fluxes. The continuity equations are

$$\frac{\partial C_v}{\partial t} = -\frac{\partial J_v}{\partial x} + \eta G_{dpa} - R_{vi} D_i C_v C_i - S_v D_v (C_v - C_v^{th}) \quad (1)$$

$$\frac{\partial C_i}{\partial t} = -\frac{\partial J_i}{\partial x} + \eta G_{dpa} - R_{vi} D_i C_v C_i - S_i D_i C_i \quad (2)$$

$$\frac{\partial C_k}{\partial t} = -\frac{\partial J_k}{\partial x} \quad (k = Fe, Cr, Ni) \quad (3)$$

where C_v and C_i are the concentrations of vacancy and interstitial, C_k is the concentration of alloying element k, η is the damage efficiency, G_{dpa} is the displacement production rate of point defects, R_{vi} is the mutual recombination coefficient, D_v and D_i are the diffusivities of vacancy and interstitial, S_v and S_i are the internal sink strength for vacancy and interstitial, and C_v^{th} is the thermal equilibrium concentration of vacancy. The fluxes, J_v, J_i and J_k, are defined by:

$$J_v = -D_v \frac{\partial C_v}{\partial x} + C_v \sum_k d_k^v \frac{\partial C_k}{\partial x} \quad (4)$$

$$J_i = -D_i \frac{\partial C_i}{\partial x} - C_i \sum_k d_k^i \frac{\partial C_k}{\partial x} \quad (5)$$

$$J_k = -D_k \frac{\partial C_k}{\partial x} + C_k \left(d_k^v \frac{\partial C_v}{\partial x} - d_k^i \frac{\partial C_i}{\partial x} \right) \quad (6)$$

where D_k is the diffusivity of alloying element k, d_k^v and d_k^i are the partial diffusion coefficients of solutes by vacancies and by interstitials. In the flux equations (4) and (5) for point defects, the last term shows the contribution of the Kirkendall flux due to the concentration gradient of the solute atoms. In the flux equation (6) for alloying elements, the last two terms indicate the inverse-Kirkendall fluxes due to the concentration gradients of vacancies and interstitials respectively. Of main interest are the coupling parameters, d_k^v and d_k^i, determined by

$$d_k^v = a_0^2 \nu_k^v \exp(-E_m^v / k_B T) \quad (7)$$

$$d_k^i = a_0^2 \nu_k^i \exp(-E_m^i / k_B T) \quad (8)$$

where ν_k^v and ν_k^i are the jump frequencies of vacancy and interstitial via the k-atom, a_0 is the lattice constant, E_m^v and E_m^i are the migration energies of the vacancy and interstitials, respectively. The diffusivities of point defects and the solute atoms are the given by

$$D_v = \sum_k d_k^v C_k \quad (9)$$

$$D_i = \sum_k d_k^i C_k \quad (10)$$

$$D_k = d_k^v C_v + d_k^i C_i \ . \quad (11)$$

Continuity equations for minor alloying elements

Considering the flux of minor alloying elements and the interaction with the point defects, a few additional parameters should be introduced to the continuity equations. Since the additives, silicon and phosphorous, are the undersized solute elements in austenitic stainless steels, they are thought to preferentially interact with interstitial atoms and form mixed-dumbbells [8]. On the other hand, the minor alloying elements such as manganese and molybdenum are the oversized solutes in the austenitic stainless steels. These oversized elements only interact with vacancies and form additive-vacancy complexes [2,6].

For the undersized solute elements, we introduced a new coupling parameter in the flux equations (5) and (6). The flux equation is rewritten as:

$$J_i = -D_i \frac{\partial C_i}{\partial x} - C_i \sum_k d_k^i \beta_k \frac{\partial C_k}{\partial x} \quad (12)$$

$$J_k = -D_k \frac{\partial C_k}{\partial x} + C_k \left(d_k^v \frac{\partial C_v}{\partial x} - d_k^i \beta_k \frac{\partial C_i}{\partial x} \right) . \quad (13)$$

The important parameter here is the coupling parameter between interstitial and solute atoms described by:

$$\beta_k = \frac{C_k \exp\left(E_{k-i}^b / k_B T\right)}{\sum_m C_m \exp\left(E_{m-i}^b / k_B T\right)} \quad (14)$$

where $E_{k\text{-}i}^{\ b}$ is the binding energy between an interstitial atom and solute atom. This parameter provides the fraction of each solute element forming the mixed-dumbbell in all of the mixed-dumbbells, and the magnitude of β_k becomes large with increase in binding energy. Undersized-solute elements such as silicon and phosphorus, which are expected to easily form a mixed-dumbbell, are thought to have larger β that those of the other solute elements. In the present calculation, the binding energies were selected to be positive values for silicon and phosphorus, and zero for the other alloying elements. The diffusivities of interstitials and solute atoms are also rewritten as:

$$D_i = \sum_k d_k^i \beta_k C_k \quad (15)$$

$$D_k = d_k^v C_v + d_k^i \beta_k C_i \ . \quad (16)$$

For the oversized solutes, the continuity equations for the point defects and oversized solutes *M* are rewritten as:

$$\frac{\partial C_v}{\partial t} = -\frac{\partial J_v}{\partial x} + G_{dpa} - R_{vi} D_i C_v C_i - S_v D_v (C_v - C_v^{th}) - K_{Mv} D_v C_M C_v + K_{Mv}^r D_v C_{Mv} \quad (17)$$

$$\frac{\partial C_i}{\partial t} = -\frac{\partial J_i}{\partial x} + G_{dpa} - R_{vi} D_i C_v C_i - S_i D_i C_i - R_{vi} D_i C_i C_{Mv} \quad (18)$$

$$\frac{\partial C_M}{\partial t} = -\frac{\partial J_M}{\partial x} - K_{Mv} D_v C_M C_v + K_{Mv}^r D_v C_{Mv} + R_{vi} D_i C_i C_{Mv} \quad (19)$$

where K_{Mv} is the reaction coefficient between a vacancy and solute atom, K_{Mv}^{r} is the thermal dissociation rate of the vacancy-solute complex, and C_{Mv} is the concentration of the vacancy-solute complexes. The dissociation rate of the complex is determined by

$$K_{Mv}^{r} = Z_{Mv} \exp\left(-E_{M-v}^{b}/k_B T\right) \quad (20)$$

where E_{M-v}^{b} is the binding energy between a vacancy and solute atom and Z_{Mv} is the geometrical co-ordination number of the complexes. The binding energies were selected to be positive values for manganese, molybdenum and other oversized additives, and zero for the other alloying elements. The migration of the vacancy-solute complexes was neglected in the present calculation and the reaction rate equation for the complexes is described by

$$\frac{\partial C_{Mv}}{\partial t} = K_{Mv} D_v C_M C_v - K_{Mv}^{r} D_v C_{Mv} - R_{vi} D_i C_i C_{Mv} \, . \quad (21)$$

Boundary condition at grain boundaries

The continuity equations were evaluated as functions of the one-dimensional coordinate perpendicular to the grain boundary and of the irradiation time. The boundary conditions for the alloying elements are zero flux at the grain boundary and at the centre of a grain. Similarly, the defect fluxes are assumed to be zero at the centre of a grain, but the grain boundary concentrations are fixed at the equilibrium concentration for vacancies and zero for interstitial atoms , so-called "perfect sink condition", described by

$$C_v|_{GB} = C_v^{th} \quad (22)$$

$$C_i|_{GB} = 0 \, . \quad (23)$$

However, the "perfect sink condition" sometimes overestimates the segregation behaviour at the small angle boundaries and coincidence site lattice (CSL) boundaries. These boundaries do not act as a perfect sink, thus we additionally defined the sink strength of the grain boundary and equations (1) and (2) are rewritten as

$$\left.\frac{\partial C_v}{\partial t}\right|_{GB} = -\frac{\partial J_v}{\partial x} + G_{dpa} - R_{vi} D_i C_v C_i - S_v D_v (C_v - C_v^{th}) - S_{GB} D_v (C_v - C_v^{th}) \quad (24)$$

$$\left.\frac{\partial C_i}{\partial t}\right|_{GB} = -\frac{\partial J_i}{\partial x} + G_{dpa} - R_{vi} D_i C_v C_i - S_i D_i C_i - S_{GB} D_i C_i \quad (25)$$

where S_{GB} is the sink strength of the grain boundary, which is a function of the misorientation angle and Σ value [7,10].

Effect of probe size on TEM/EDX measurement

Comparing the calculated concentration profiles to the experimental profiles obtained by the TEM/EDX, it is important to consider the averaging effect due to the finite size probe (about 1 nm in FEG-TEM) in the EDX analysis [9]. The one-dimensional calculated concentration profile is convoluted by the normalised two-dimensional Gaussian function (see Figure 1), which is expressed by:

$$C^{EDX}(x) = \frac{\sqrt{a/\pi}}{1-\exp(-aR^2)} \int_{-R}^{R} \exp(-ar^2) \times \mathrm{Erf}\left[\sqrt{a(R^2 - r^2)}\right] \times C(x - r) dr \quad (26)$$

where C^{EDX} is the averaged concentration profile, i.e., series of concentrations obtained by the TEM/EDX analysis, R is the probe radius, and *a* is the deviation constant described as

$$a = \frac{1}{2R^2} . \quad (27)$$

This procedure is of importance for simulating the actual profile data taken by the TEM/EDX.

Figure 1. Schematic illustration of one-dimensional concentration profile and electron probe intensity

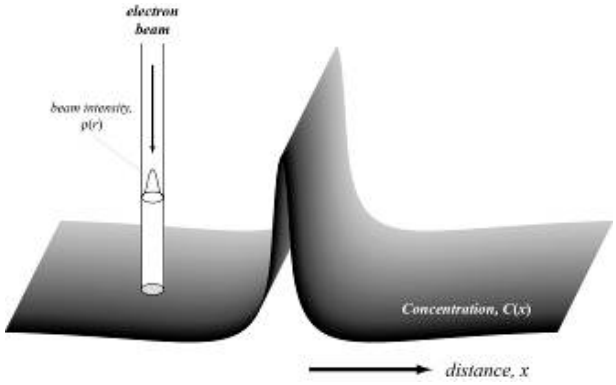

Determination of physical parameters

The material constants used in the present calculations are listed in Table 1. The solute-defect interactions are ignored for the major alloying elements (Fe, Cr and Ni). It is assumed that the interstitial only interacts with the undersized minor alloying elements (Si, P), whereas the vacancy forms the vacancy-solute complex with the oversized minor alloying elements (Mn, Mo).

Table 1. Summary of main parameters used in the present calculations

Vacancy migration energy	E_m^v	1.05eV
Fe-vacancy jump frequency	ν_{Fe}^v	5.0e13s^{-1}
Cr-vacancy jump frequency	ν_{Cr}^v	8.0e13s^{-1}
Ni-vacancy jump frequency	ν_{Ni}^v	2.5e13s^{-1}
Mn-vacancy jump frequency	ν_{Mn}^v	1.0e14s^{-1}
Mo-vacancy jump frequency	ν_{Mo}^v	1.2e14s^{-1}
Si-vacancy jump frequency	ν_{Si}^v	5.0e14s^{-1}
P-vacancy jump frequency	ν_{P}^v	5.0e14s^{-1}
Interstitial migration energy	E_m^i	0.85eV
Interstitial jump frequency	ν^i	5.0e12s^{-1}

Si-interstitial dumbbell migration energy	ν_{Si}^{i}	1.2eV
P-interstitial dumbbell migration energy	ν_{P}^{i}	1.4eV
Mn-vacancy binding energy	$E_{Mn\text{-}v}^{b}$	0.2eV
Mo-vacancy binding energy	$E_{Mo\text{-}v}^{b}$	0.4eV
Si-interstitial dumbbell binding energy	$E_{Si\text{-}i}^{b}$	0.5eV
P-interstitial dumbbell binding energy	$E_{P\text{-}i}^{b}$	0.7eV
Mutual recombination coefficient	R_{vi}	$500/a_0^2$
Vacancy-solute reaction coefficient	K_{Mv}	$30/a_0^2$
Vacancy-solute dissociation coefficient	Z_{Mv}	$14/a_0^2$
Point defect production rate	η	
electron irradiation		1.0
neutron irradiation		0.03
Internal sink strength for vacancy	S_v	
electron irradiation		$1.0e14m^{-2}$
neutron irradiation		$1.0e15m^{-2}$
Internal sink strength for interstitial	S_i	1.1 S_v

Calculations

RIS behaviour in Fe-Cr-Ni ternary alloy

A typical theoretical prediction of solute segregation near a random grain boundary in Fe-15Cr-20Ni alloy after electron irradiation to 1 dpa at 673 K is shown in Figure 2. Experimental data also are also plotted in the figure. Irradiation-induced nickel enrichment and chromium depletion at the grain boundary were quantitatively reproduced by the present RIS model. Figure 3 shows the temperature dependencies of nickel and chromium concentrations at the random grain boundaries after electron irradiation to 1 dpa. Both the theoretical and experimental data suggest that the peak temperature of the RIS is about 800 K in the present irradiation conditions. This peak temperature depends on the displacement production rate of point defects. To clarify this, calculated three-dimensional plots of the RIS at a grain boundary after irradiation to 0.1 dpa are shown in Figure 4. The maxima in nickel and minima in chromium by the RIS with temperature change are clearly seen, and their shift with the damage rate is manifest. We can see that the peak temperature of the RIS falls with decrease of the damage rate but the magnitude of the RIS increases. Figure 5 shows a schematic drawing of the relationship the RIS between the temperature and the damage rate. The RIS at a grain boundary is suppressed at higher temperature because of the back diffusion of solute elements that counters segregation driven by the irradiation; on the other hand, suppression of the RIS also

occurs at lower temperature because the short-range mutual recombination of the vacancies and interstitials becomes dominant. Hence, a maximum of the RIS is expected at intermediate temperature and the higher damage rate elevates the peak temperature of the RIS.

Figure 2. Solute concentration profiles near a random grain boundary after electron irradiation to 1 dpa at 673 K in Fe-15Cr-20Ni ternary alloy

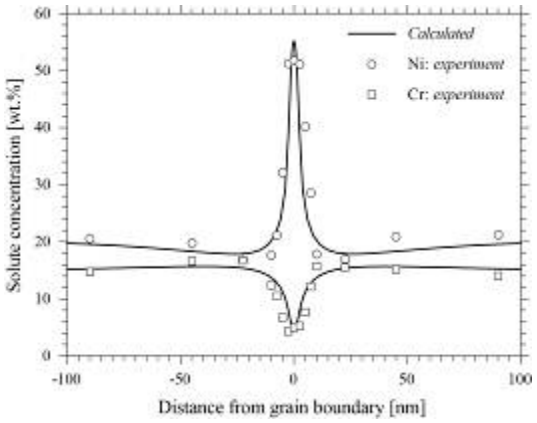

Figure 3. Temperature dependence of RIS at random grain boundaries after electron irradiation to 1 dpa at 2×10^{-3} dpa/s

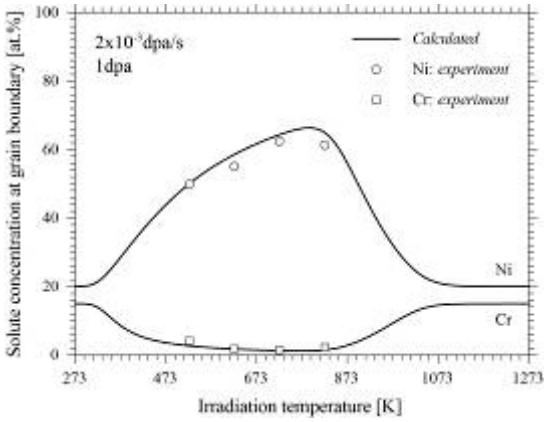

Figure 4. Three-dimensional plots of temperature and damage rate dependence of RIS at a grain boundary in Fe-15Cr-20Ni alloy after irradiation to 0.1 dpa

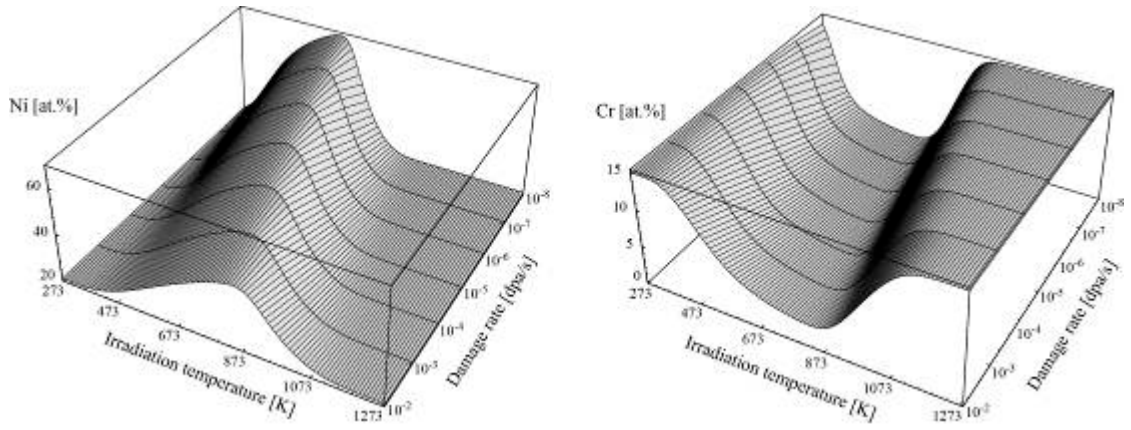

Figure 5. Schematic diagram of the relationship between the temperature and the damage rate, showing the RIS region

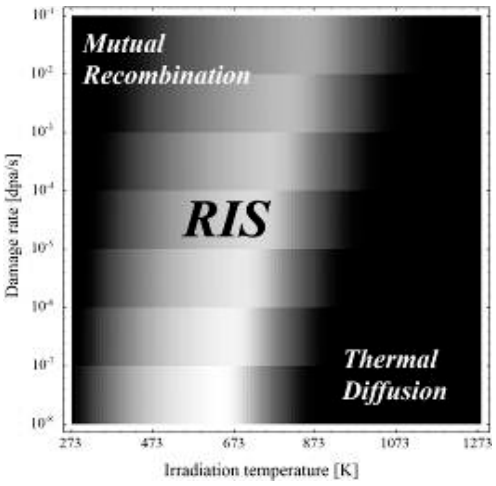

Effect of additional minor alloying element on RIS

In order to overview the effect of addition of a minor alloying element, a typical theoretical prediction of the temperature dependence on the RIS at a grain boundary in Fe-15Cr-20Ni with or without the additional element after irradiation to 3 dpa is shown in Figure 6. In this calculation, we assumed that the additional element only interacted with vacancies, and the diffusion of the additional element was neglected. The concentration of the additional element and the additive-vacancy binding energy were 0.5 at.% and 0.5 eV, respectively. It was predicted that the amount of segregation at the grain boundary decreased in the presence of the additional element at elevated temperature. Here we divide the temperature dependence of the RIS into three stages.

Figure 6. Temperature dependence of RIS in Fe-15Cr-20Ni alloy with and without an oversized additional element at a grain boundary after electron irradiation to 3 dpa

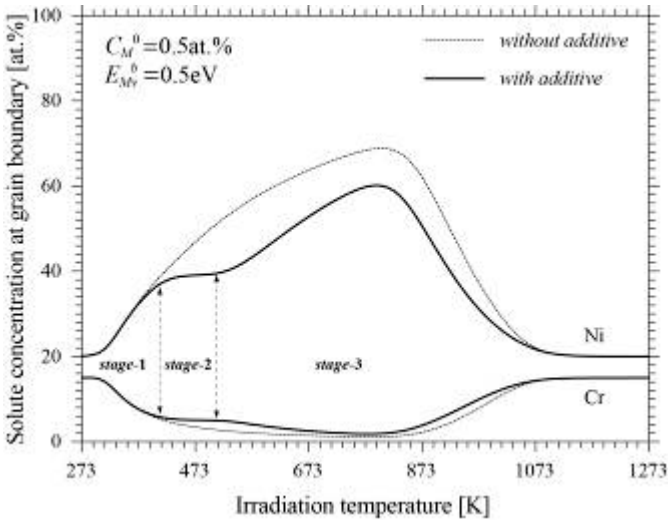

- At the temperatures below 400 K, the RIS is not affected by the additional minor element which interacts with the vacancies (stage-1). At this stage, the mobility of the vacancies is too small to form the additive-vacancy complexes. Almost all of the vacancies annihilate due to the mutual recombination of the neighbouring interstitial atoms.

- Above that temperature, the temperature region in which the amount of the RIS is kept constant appears (stage-2). Almost all of the vacancies are trapped by the additional elements in this temperature regime, and the dominant defect reaction is the recombination between the additive-vacancy complexes and the interstitial atoms. In the present situation, radiation-enhanced diffusivities of the alloying elements do not depend on the temperature.

- After a further increase of temperature, the amount RIS increases (stage-3), but then decreases in the Fe-Cr-Ni ternary alloy. At this stage, the dissociation of the additive-vacancy complexes occurs and some of the free-vacancies diffuse again to the grain boundary and annihilate there. The appearance activation energy of the vacancy diffusion equals to the sum of the vacancy migration energy and the additive-vacancy binding energy.

The additive concentration dependencies on solute segregation at a grain boundary after irradiation to 3 dpa are shown in Figure 7. The binding energy between the additive and vacancies used was 0.5 eV. The amount of the RIS decreased with increases of the additive concentration in the temperature ranges of stage-2 and stage-3. The magnitude of the decrement gradually became saturated at higher additive concentrations and the transient temperatures of each stage ($T_{\text{stage1-2}}$ and $T_{\text{stage2-3}}$) did not depend on the additive concentration. Figure 8 shows the additive-vacancy binding energy dependencies on solute segregation at a grain boundary. The concentration of the additional element used was 0.5 at.%. It was also predicted that the amount of the RIS decreased with increase of the additive-vacancy binding energy in the temperature ranges of the stage-2 and stage-3.

The transient temperature from stage-1 to stage-2 ($T_{stage1\text{-}2}$) did not depend on the additive-vacancy binding energy; however, the transient temperature from stage-2 to stage-3 ($T_{stage2\text{-}3}$) shifted to higher temperature with increasing of the binding energy and the RIS was strongly suppressed at the temperatures corresponding to the stage-3. It was expected that the additive-vacancy binding energy was correlated with the size factor of oversized additional elements [2,6]. For examples, addition of hafnium and zirconium, which were the oversized additional elements with large additive-vacancy binding energy (~ 1 eV), to type 316L stainless steels nearly suppressed the RIS on the grain boundaries at the stage-3 temperature regime [3].

Figure 7. Three-dimensional plots of temperature and additive concentration dependence of RIS at a grain boundary in Fe-15Cr-20Ni alloy with oversized additional alloying elements

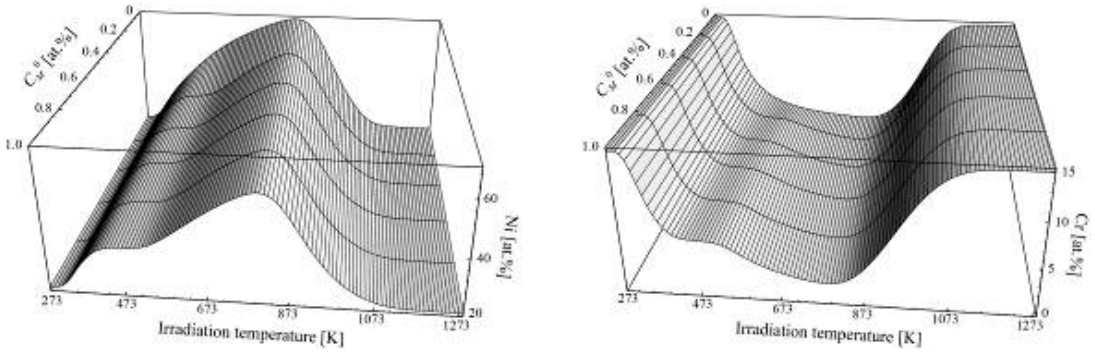

Figure 8. Three-dimensional plots of temperature and additive-vacancy binding energy dependence of RIS at a grain boundary in Fe-15Cr-20Ni alloy with oversized additional alloying elements

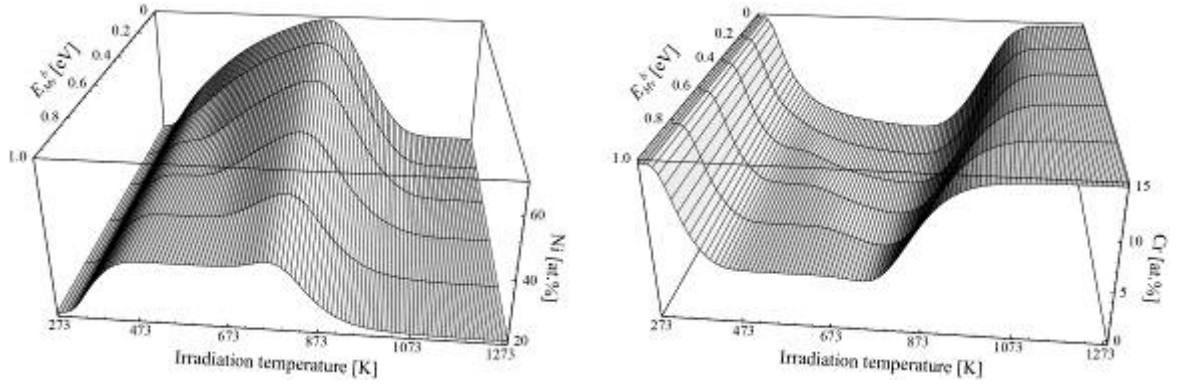

As with the oversized additional elements, the undersized elements preferentially interact with the interstitial atoms and form mixed-dumbbells. In general, the migration energy of the mixed-dumbbell is higher than that the migration energy of the self-interstitials, so that the appearance activation energy of the interstitial diffusion increases. Figure 9 shows the temperature dependence on the RIS at a grain boundary with or without the undersized additional element after irradiation to 3dpa. The migration of the mixed-dumbbells was neglected in the present calculation. The amount of the RIS decreased in the presence of the undersized additional element at elevated temperature and the same stages appear as a function of temperature. It has been reported that the addition of the undersized additional elements such as silicon and phosphorous drastically suppress the RIS at the grain boundaries [8]. It was suggested that the phosphorous suppresses the RIS more effectively because of a strong interaction with the interstitial atoms.

Figure 9. Temperature dependence of RIS in Fe-15Cr-20Ni alloy with and without undersized additional element at the grain boundary after electron irradiation to 3 dpa

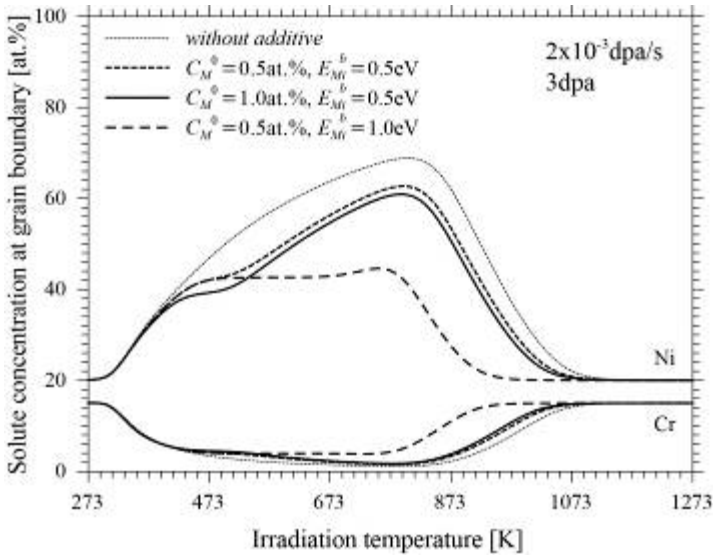

Prediction by multi-component RIS model

It was reconfirmed that the addition of the minor alloying elements strongly influenced the RIS behaviour of the major alloying elements like chromium. The theoretical prediction using the multi-component RIS model is needed to estimate quantitatively the RIS behaviour in neutron irradiated materials. Figure 10 shows the calculated concentration profiles of nickel, chromium and silicon in Fe-21Cr-8Ni-1Si-0.05P-1.5Mn alloy after irradiation to 1 dpa at 561 K. The experimental data was obtained by the neutron irradiated type 304L stainless steel. In the present parameter set (see Table 1), silicon and phosphorous interact with the interstitial atoms, whereas the manganese acts as the vacancy trapping element. Fairly good agreement between the calculated and experimental concentration profiles was achieved. It can be seen that the Fe-Cr-Ni ternary RIS model fails to reproduce the solute profiles and the RIS at the grain boundary is overestimated. In Figure 11, the concentration profiles of nickel, chromium and silicon in neutron irradiated type 316L stainless steel are plotted with the theoretical values. The

irradiation dose and the temperature were 3 dpa and 561 K, respectively. In the theoretical prediction, we considered the Fe-18Cr-12Ni-0.5Si-0.05P-1.5Mn-2.5Mo alloy system as a model for the 316L stainless steel. Molybdenum is assumed to be the vacancy trapping element, the same as manganese. The binding energy between the molybdenum and vacancy used (0.4 eV) was higher than that of the manganese (0.2 eV). Even though the irradiation dose was higher than the former case, the amount of the RIS at the grain boundary was less than that in the type 304 stainless steel. This reflects the fact that the molybdenum acts as a stronger vacancy trapping element than the manganese, as assumed in the calculations.

Figure 10. Concentration profiles of nickel, chromium and silicon near grain boundary in 304L stainless steel after neutron irradiation to 1 dpa

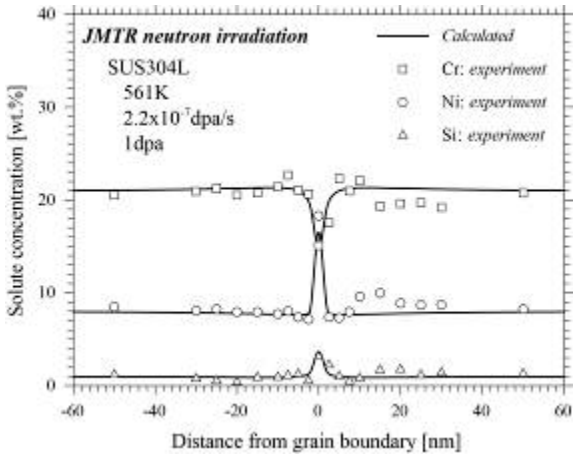

Figure 11. Concentration profiles of nickel, chromium and silicon near grain boundary in 316L stainless steel after neutron irradiation to 3 dpa

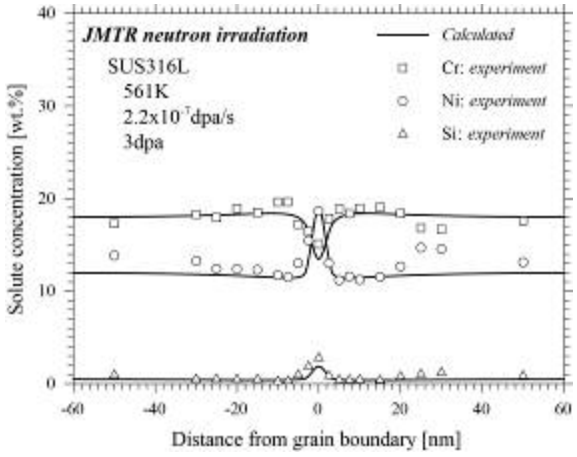

Conclusion

We proposed a model for radiation-induced segregation (RIS) at grain boundaries based on the rate equations including the inverse-Kirakendall fluxes and the interactions between point defects and minor alloying elements. The relationship between irradiation temperature, damage rate and the RIS on the grain boundaries were theoretically predicted by the present model. It was confirmed that the peak temperature of the RIS falls in decreases of the damage rate but the magnitude of the RIS increases. It was revealed that the RIS was significantly affected by the additional minor alloying elements which interacted with the vacancies or interstitials. The multi-component RIS model can successfully reproduce the RIS behaviour in neutron irradiated type 304L and 316L austenitic stainless steels.

References

[1] T.R. Allen, G.S. Was, E.A. Kenik, J. Nucl. Mater. 244 (1997) 278.

[2] M.J. Hackett, R. Najafabadi, G.S. Was, J. Nucl. Mater. 389 (2009) 279.

[3] T. Kato, H. Takahashi, M. Izumiya, J. Nucl. Mater. 189 (1992) 167.

[4] A.C. Hindmarsh, LSODE: Livermore Solver for Ordinary Differential Equations, Lowrence Livermore National Laboratory, (1980).

[5] A.D. Marwick, R.C. Piller and M.E. Horton, AERE-R 10895, (1983).

[6] N. Sakaguchi, S. Watanabe, H. Takahashi ", Nucl. Inst. Meth. Phys. Res. B, 153 (1999), 142.

[7] N. Sakaguchi, S. Watanabe, H. Takahashi, R.G. Faulkner, J. Nucl. Mater., 329-333 (2004), 1166.

[8] N. Sakaguchi, H. Takahashi, H. Ichinose, Materials Transaction, 46 (2005), 440.

[9] S. Watanabe, N. Sakaguchi, N. Hashimoto, H. Takahashi, J. Nucl. Mater., 224 (1995), 158.

[10] S. Watanabe, Y. Takamatsu, N. Sakaguchi, H. Takahashi, J. Nucl. Mater., 283-287 (2000), 152.

Chapter 6.

Radiation induced swelling

V.A. Borodin
National Research Centre "Kurchatov Institute", Kurchatov pl. 1, 123182, Russia
National Research Nuclear University "MEPhI", Kashirskoe sh. 31, 115409, Russia

Abstract

Swelling and radiation creep are specific modes of material deformation under irradiation. The main fundamental reason for both effects is the ability of high-energy radiation to produce damage in the form of interstitial atoms and vacancies that move in the irradiated material and interact with other components of material microstructure. Potentially, all solids under irradiation are able to change shape and volume as a result of the matter transport promoted by irradiation, but the degree to which these changes are manifested in particular operation conditions depends on many factors, including the basic properties of the material itself, the microstructural state of material created by its thermo-mechanical treatment, and the particular operation conditions. The chapter describes the macroscopic manifestations of radiation-induced dimensional instability of metals, discusses the origins of these effects at the level of microstructure development and presents the commonly used theoretical approaches used to understand and predict the parametric dependencies of swelling.

1. Introduction

Swelling and creep as two different deformation modes of solids are commonly met in everyday life. For example, wood placed into water increases its volume, while a straight metal bar kept strongly bent for a long time adopts this bent shape on its own. However, when solid materials are subject to fast particle irradiation, the irradiation can so strongly enhance both swelling and creep that the resulting dimensional instability becomes a serious risk for the safe operation of industrial facilities, first of all - nuclear power plants, where material irradiation is an indispensable part of the reactor operation. In order to emphasise the radiation origin of the effects, the terms "irradiation swelling" and 'irradiation creep' are used in radiation materials science in order to describe these two modes of deformation of irradiated solids, though in the case of swelling the word 'irradiation' is often skipped for brevity.

Due to the practical importance of irradiation swelling and creep, enormous efforts have been devoted to the investigation of both these effects in various materials since the middle of the 20th century, when both of these effects were discovered. Especially thoroughly were studied metallic materials most widely used as structural and functional components of fission and fusion facilities, and first of all - steels of various types. However, quite a number of non-metallic materials were investigated as well (graphite, silicon carbide, various ceramics), indicating that volume and shape modification under irradiation is a common physical phenomenon in solids, including metals, semiconductors and insulators.

The basic difference between the swelling and creep modes of deformation is that radiation swelling commonly refers to the change of the material volume as a result of irradiation, but not to its shape change. In order to describe the shape change, one commonly uses the terms irradiation growth (in unstrained material) or irradiation creep (as a reaction of material to the external loads). In mathematical terms, the total accumulated deformation in the irradiated solid can be written down as

$$\varepsilon_{ij} = \tilde{\varepsilon}_{ij}^{g} + \tilde{\varepsilon}_{ij}^{c} + \frac{1}{3}\delta_{ij} S\,, \tag{1.1}$$

where ε_{ij} stands for the total (generally - tensor) strain of material, $\tilde{\varepsilon}_{ij}^{c}$ and $\tilde{\varepsilon}_{ij}^{c}$ stand for the volume conserving (deviatoric) strain tensors due to irradiation growth and irradiation creep, δ_{ij} is the Kronecker tensor and S - the volume change (swelling).

It should be kept in mind, however, that the separation of the total strain tensor into three parts is no more than a convention. In real life all three effects can be manifested at the same time and it is not an easy task to unequivocally discern between them because at the microstructural level all of them originate from closely interrelated processes. For example, under the action of non-hydrostatic external loads and/or in intrinsically anisotropic material the volume can change anisotropically due to the evolution of essentially the same microstructural features that are responsible for the isotropic (free of shape change) swelling in a hydrostatically loaded material, so that it can equally well be treated as anisotropic swelling. However, strain separation according to eq. (1.1) is often convenient from the practical point of view, especially when only one of three contributions to overall strain dominate.

When talking about irradiation creep, it is usually assumed that the applied loads remain below the current yield stress of material (which in irradiated material can be different from that in non-irradiated one due to hardening or softening). At higher loads one usually speaks about plastic flow and not creep. Though at the microscopic level the origins of creep and flow are often similar, the plastic flow occurs fast on the life-size time scale and quickly leads to the loss of material integrity, while creep is a long-term deformation that can last for years without detrimental consequences. In fact, creep is often even beneficial as a mechanism of relieving strains that accumulate in reactor materials during their operation in radiation environment (e.g. due to non-uniform swelling of rector core components).

This chapter deals mostly with the discussion of the physical reasons and microstructural mechanisms that lead to swelling and irradiation creep, without going into too much detail of experimental observations and without trying to discuss all the aspects of these phenomena. Both effects are very complicated and lots of investigations are devoted to various aspects of swelling and creep. Many reviews of experimental data on swelling and creep manifestation in different materials and in specific irradiation conditions are available in the literature (e.g. [1-6], also various chapters in a recent handbook [7]) and those interested in a deeper understanding of these topics of radiation materials science are referred to them. One more thing to mention is that this chapter is in no way a literature review; while relevant citations are given to support various statements, no attempts were made to provide an exhaustive reference list.

2. Basic experimental features of irradiation swelling and creep

Many factors affect the macroscopic manifestation of swelling and creep in irradiated materials, including in particular:

- properties of the material itself (crystal structure, chemical composition, the strength of interatomic interactions, possible types of point and extended defects, the strength of interaction between different microstructural features, etc.)
- the particular state of defect microstructure (the grain size, shape and structure, dislocation density, impurity contents, the availability and size of phase inclusions, etc.). These properties are largely determined by the methods of material preparation and thermal-mechanical treatment prior to irradiation, but can be completely changed as a result of sufficiently long irradiation itself.
- the external operation conditions (the shape and fixation modes of particular structural parts in nuclear facilities, the type and energy of irradiating fast particles, the intensity and duration of irradiation in particular locations of a particular facility, the temperature distribution in the irradiated materials, the availability and type of external loads in each particular material location, etc.). Additional complications arise from the fact that these conditions can change during material operation (sometimes very quickly, e.g. at reactor shutdowns) causing various transient effects.

With so many variables, it is virtually impossible to predict *a priori* the irradiation-induced deformation of a particular material in a particular irradiation facility. However, experimental investigations suggest some common trends in the material behaviour under

irradiation that provide qualitative feeling for the expected material response to the action of that or other factor.

In terms of three groups of factors affecting swelling and creep, trends related to the basic material parameters are the easiest to identify because these parameters themselves can be either measured or estimated with reasonable accuracy using simulation methods that have become now as important an investigation tool, as the experimental measurements. This holds true even for complicated multicomponent materials, such as steels, where the necessary microstructural parameters can be determined for the pure base alloys (e.g. Fe-Cr for ferritic and Fe-Cr-Ni for austenitic steels), while the effects of minor alloying elements can be determined as the local perturbations as compared to the base alloy.

At this level, the best known trend is that bcc and hcp metals are noticeably more resistant to swelling than FCC metals. Possibly the most illustrative demonstration of the effect of crystalline structure on swelling was obtained in an experiment [8], where dual-phase steel with both FCC and bcc grains of essentially the same chemical composition was irradiated by 1 MeV electrons and exhibited swelling only in FCC grains. This does not mean, however, that a particular crystal structure slows down the swelling. For example, the steady-state swelling rate of bcc vanadium with unfavorable alloying elements (Cr,Fe) can be higher than that of FCC austenitic stainless steels. However, it is much harder to create appropriate conditions (in particular - the optimum dislocation density [9-11]) for the onset of swelling in bcc and hcp metals, which means much longer swelling lag time as compared to FCC metals [6]. On the other hand, the steady-state irradiation creep rate is fairly insensitive to the metal crystal structure.

The influence on the swelling behaviour from two other groups of factors is much harder to predict because both the material microstructure and the operation conditions can vary with time. Therefore, when discussing the trends of material response to the variation of any particular parameter it is implicitly assumed that other parameters remain invariable. This should be kept in mind in considering the experimental examples below because in the real experiments this condition seldom holds. This is especially true for long-term reactor experiments and to less extent for simulation experiments on fast particle accelerators, where irradiation conditions can be controlled much better. Unfortunately, simulation experiments with fast charged particles also have features (first of all, spatial non-uniformness of damage production) that make the observed trends at best qualitative.

With this in mind let us summarise some trends in the irradiation swelling and creep response to variations of operation conditions and microstructural parameters. It should be emphasised that only the basic trends are described and even these should not be considered as unbreakable rules. Irradiation creep and especially swelling are very complicated phenomena, highly sensitive to the synergetic action of multiple metallurgical parameters and environmental conditions. Whatever the trend, especially where swelling is concerned, it is always possible to find in the literature some data that disobey it.

2.1. Dose dependence

One of the most important trends is the dependence of swelling and creep on irradiation duration, which is usually expressed in terms of irradiation dose Φ, that is the product of

flux of fast particles on the irradiation time. A typical swelling dependence of irradiated material on the accumulated dose is shown in Figure 1.

Figure 1. Schematic representation of the dose dependence of irradiation swelling: I - incubation stage; II - void nucleation stage; III - steady-state stage; IV - deceleration stage

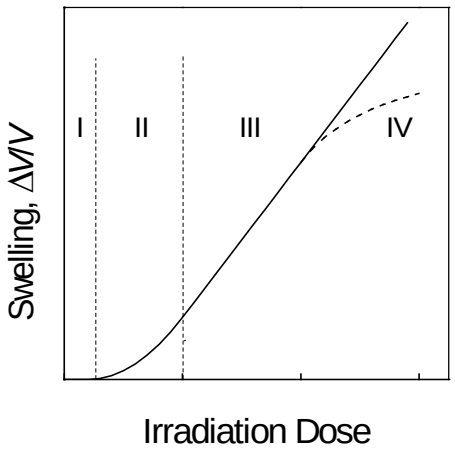

As can be seen, several stages are present on the swelling-dose curve, though not all of them are necessarily observed in particular experiments. First of all, the offset of swelling takes place only after some incubation dose Φ_0. To get a feeling of the incubation dose value, Φ_0~1-3 dpa is typical for austenitic steels in fission reactors [6], but in other materials it can vary from 10^{-4} dpa to tens of dpas, depending on the material properties and the irradiation conditions. It is very sensitive to the particular state of material, such as the dislocation density level, stress state, material chemical composition (in alloys), the impurity types and contents, the irradiation flux and temperature [12]. Two examples are shown in Figure 2. The duration of the transient stage is essentially the main factor that differentiates materials in terms of their resistance to swelling.

Figure 2. (a) The effects of the level of cold-work on the swelling, void number densities N_v and average sizes in steel 09Kh16N15M3B irradiated with Cr ions to 100 dpa: 1 - austenitized, 2- 10% cw, 3 - 20 % cw. (from [13]) (b) The effect of impurity type on the swelling of V-Cr alloys (from [14])

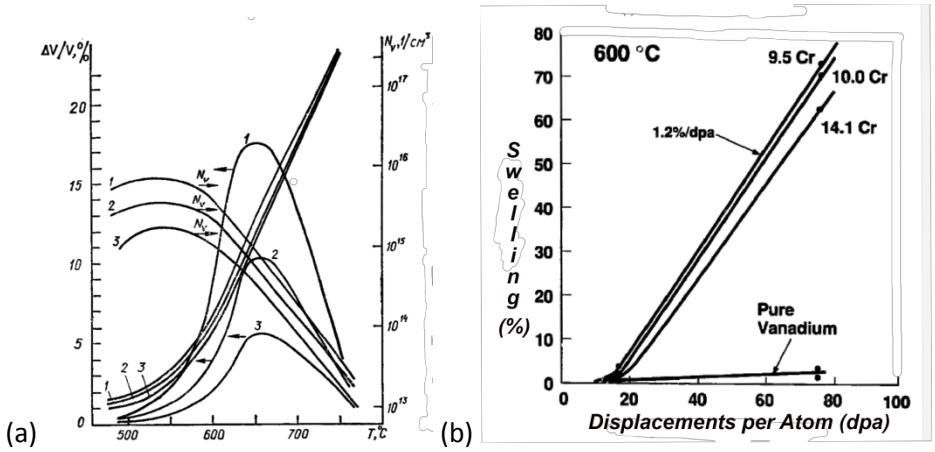

Following the incubation stage, there is a transient stage, where the swelling grows nonlinearly as a function of the irradiation dose, i.e. $S \propto (\Phi-\Phi_0)^n$ with $n > 1$, which is eventually replaced by the so called steady-state swelling stage, where the swelling rate, $\dot{S}$, does not vary with the irradiation dose. In contrast to incubation time, the swelling rate at the steady stage is remarkably insensitive to material parameters, being close to ~ 0.1-1%/dpa [6,15]. Finally, at high fluences the swelling rate can fall down and sometimes swelling can saturate completely [16-19]. In practice, swelling saturation is only seldom observed at application-relevant fluences, whereas the steady-state swelling can persist to very high doses (hundreds of dpa) without any signs of saturation [20].

In contrast to swelling, irradiation creep has practically no incubation time and starts immediately after the onset of irradiation or application of loads, whatever happens later. Typically, the irradiation creep starts with a transient stage, which after some dose transforms into the steady-state one, Figure 3. The creep strain ε^c at the transient stage is typically a gradually decreasing function of the dose, $\varepsilon^c \propto \Phi^n$ with $n < 1$, and the duration of the transient stage is also sensitive to the material state, but to much less degree as compared to swelling; typically the transient doses are of the order of 0.01-1 dpa. In other words, the transient creep stage in loaded irradiated materials usually terminates well before the onset of swelling.

Figure 3. Schematic representation of the dose dependence of irradiation creep. I – primary creep, II – steady-state creep, III – accelerated creep, IV – creep cessation

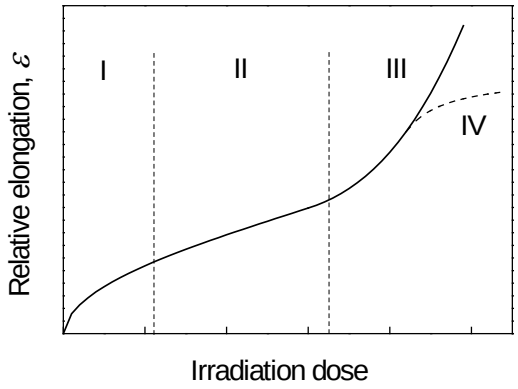

At the steady-state the irradiation creep rate, similar to swelling rate, is weakly sensitive to particular material, having typically the value of $\dot{\varepsilon}^c \sim 10^{-6}$-$10^{-5}$ (MPa dpa)$^{-1}$ for in-reactor irradiation and roughly an order magnitude higher (for the same material) in simulation experiments with charged fast particles. The differences between in-reactor and simulation experiments are usually ascribed to different test setups and to the problems of consistent dpa determination for neutrons and charged particles.

In cases where irradiation creep tests take sufficient time for the swelling to start, an additional acceleration of creep rate (stage III) is often observed after the swelling onset (i.e. after 3-30 dpa), though the new creep strain is usually also a steady-state one. It is a common practice to interpret the third stage of creep in terms of the creep acceleration by swelling. There are multiple evidences in favour of the fact that the development of the void system in irradiated material modifies irradiation creep rate. In addition to the

concurrence of the third creep stage with an appreciable swelling [21-24], one notices also similarities in the temperature dependencies of irradiation creep and swelling [15,25-29] and their similar reaction to thermo-mechanical treatment and to changes in material microchemistry (in particular, the solutes that reduce swelling in AISI 316 steel also reduce the irradiation creep strain [30,31]). Also, the creation of voids by irradiation prior to loading forces the irradiation creep rate to quickly reach the third stage, going through the first two stages much faster than usual [32-35].

Correspondingly, the dose dependence of irradiation creep rate $\dot{\varepsilon}$ at the third stage is often described not in terms of the dose itself, but in terms of the swelling rate, $\dot{S}$ (which is expected from theoretical considerations and allows nice fit to experimental data),

$$\dot{\varepsilon} = BG\sigma + D\sigma\dot{S}, \qquad (2.1)$$

where B is a constant (called the steady-state creep modulus) and D is a numerical factor, which falls into a rather narrow range of $D \sim 10^{-5} - 10^{-2}$ MPa^{-1} for various steels [12].

In spite of the abundance of experimental data in support of equation (2.1), the correlation between the irradiation creep and swelling should be addressed with certain caution [36]. Indeed, a typical irradiation creep experiment involves measurements of the overall relative change $\Delta L/L$ of some linear parameter L of a sample (length of a tensile sample, tube diameter, etc.), which contains contributions from both the volume conserving deformation (i.e. the true irradiation creep strain ε) and deformation caused by the swelling S, according to eq. (1.1). In order to extract from the overall length change only the creep-related deformation, one should measure at the same time the accumulated swelling. This means, however, the destructive analysis of samples for each data point, which is very expensive and technically inconvenient. Therefore, the value of swelling taken from independent experiments on stress-free samples, S_0, is usually employed to extract creep strains with the help of eq. (2.1). It is known, however, that the external stress accelerates swelling as a result of its effect on void nucleation, e.g. reducing the void nucleation time lag [15,37,38] and/or increasing the void number density [39]. Hence, the neglect of stress enhancement of swelling can lead to artificial conclusions concerning creep behaviour at the third stage. The estimates of irradiation creep rate taking into account the stress dependence of swelling, show (first for stainless steel 316 irradiated by fast neutrons [36,40] and later on for other steels [41-43]) that at some swelling levels the irradiation creep rate falls much below the values typical for the steady-state stage, maybe even to zero (Figure 4). Hence at the doses corresponding to high swelling levels the true creep strain probably vanishes completely.

Figure 4. Calculated creep strain for two pressurised pins of type AISI 316 SS, showing how the use of stress-free swelling camouflages the onset of the saturation stage of creep [44]

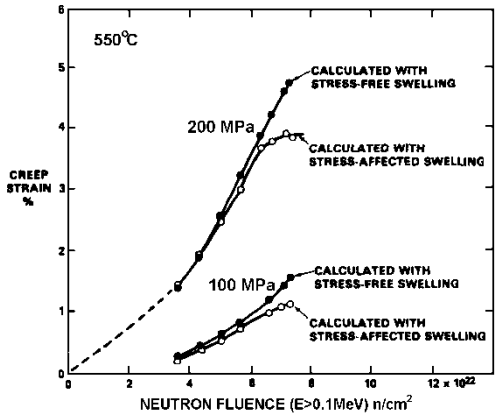

Having in mind the observed correlation between the creep and swelling rates, it is a common practice to state that irradiation creep is always accelerated by swelling, which is however not true. There exist results, indicating the lack of proportionality between irradiation creep and swelling [45-47], or even directly contradicting such a correlation. For example, no irradiation creep rate modification was observed in samples irradiated to very high doses (~40-60 dpa) [48], when the swelling is quite pronounced, and, on the contrary, the third stage of creep was observed in martensitic steel 1.4914 [49] and in PCA (Primary Candidate Alloy) [47] with practically no swelling. It seems more reasonable to conclude that both the irradiation creep acceleration and the development of swelling are independent consequences of microstructural and micro-chemical changes in the irradiated material.

Finally, it is worth mentioning that although it is a general trend to discuss the behaviour of swelling as a function of irradiation dose, it does not mean that swelling is not sensitive to the irradiation flux. The most pronounced effect of the flux variation is the shift of the temperature dependence of swelling, (see Figure 5). Typically, with the increase of irradiation flux the peak swelling temperature shifts towards higher temperatures. For example, simulation experiments on fast particle accelerators (with the typical damage production rate $G \sim 10^{-3}$ dpa/s) predict the swelling peak at 100-200 K higher temperatures than in reactor experiments (with $G \sim 10^{-7}$ - 10^{-6} dpa/s). On the other hand, irradiation creep in typical reactor operation conditions, at least at the steady-state, is insensitive to irradiation flux other than through the dose [50-52].

Figure 5. The temperature dependence of swelling in Ni irradiated with 2.8 MeV Ni ions up to 13 dpa. $G = 7\times10^{-4}$ dpa/s (LDR) and (2) $G = 7\times10^{-2}$ dpa/s (HDR) [53]

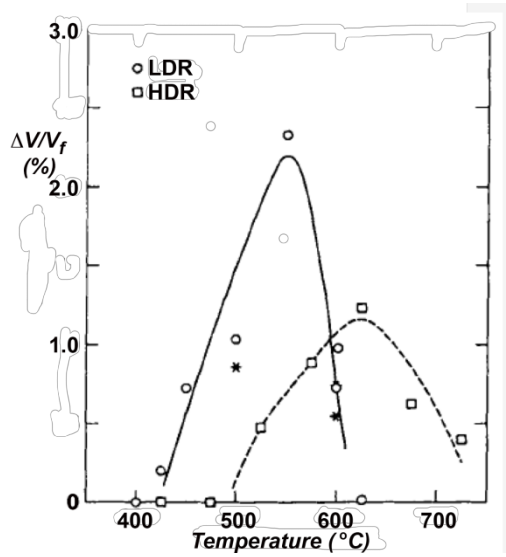

2.2. Temperature dependence

The temperature dependence of swelling is one of the most important parametric dependencies. The most typical is the bell-shaped temperature dependence as shown in Figure 2(a). The position of the swelling peak falls as a rule within 0.3-0.55 T_m, where T_m is the melting temperature of the material. While the height of the peak is determined by the accumulated dose, the width of the temperature 'bell' is quite sensitive to material properties (first of all - the energy characteristics of point defects and of small complexes thereof) and the material microstructure and chemistry, which affect the transport and capture of point defects. The swelling curves look very similar when drawn as a function of the homologous temperature T/T_m, which is largely due to the known fact that the energies of point defect formation and migration in metals roughly scale with the material melting temperature.

Such sensitivity of swelling to the point defect parameters is explained by the fact that noticeable swelling in reactor structural materials is correlated with the development of an ensemble of cavities arising as a result of vacancy clustering and subsequent growth of vacancy clusters from vacancies generated by irradiation. At too low temperatures the vacancy mobility is low and they are mostly annihilated by more mobile interstitial atoms, rather than collect in cavities. On the contrary, at high temperatures vacancy clusters are very unstable and it is hard to form a noticeable amount of void nuclei, which prevents the development of voids at high temperatures. This is demonstrated in Figure 2(a), where the curves showing number densities and average sizes of voids are superimposed over the swelling curves at the same irradiation dose. At low temperatures many small vacancy clusters form but cannot grow efficiently due to the low vacancy mobility, while at high temperatures a relatively small number of cavities can overcome the nucleation barrier, though the nucleated voids can become quite large. As a result of a competition between these two trends, noticeable swelling is possible only in a restricted temperature window, where they do not completely cancel out each other. Typically, this range is quite narrow,

no more than 200-300°C, but unfortunately the reactor operation temperatures (close to 300ºC) fall within this window for many structural materials (first of all - austenitic stainless steels), which makes the problem of swelling so important for radiation materials science.

The bell-shaped temperature dependence is the dominant, but not the only type of swelling temperature dependence observed in reactor materials. Sometimes a double-bell shaped temperature dependence of swelling is also reported. As a rule, the second peak of swelling is due to the action of some impurities stabilising cavities and lies at higher temperatures than the peak related to purely vacancy cavities (voids). One of the most known is the effect of cavity stabilisation by insoluble gases [54-58], first of all He, that accumulate in irradiated metals as a result of transmutation nuclear reactions. The helium-induced swelling is often much more dangerous than that due to vacancy voids, because He tends to accumulate at grain boundaries and promotes there the nucleation of helium-containing voids (bubbles) [59-61] that weaken the grain boundaries and cause the so-called 'high-temperature helium embrittlement'. However, He is not the only impurity that is able to promote double-peak swelling temperature dependence, the same effect can be caused by other impurities such as e.g. carbon in austenitic stainless steels [12].

Finally, it is worth mentioning the swelling at relatively low temperatures, where voids do not form. In some materials (refractory metals and ceramics) one observes noticeable swelling, not related to voids. An example is shown in Figure 6.

Figure 6. The temperature dependence of swelling in neutron irradiated molybdenum

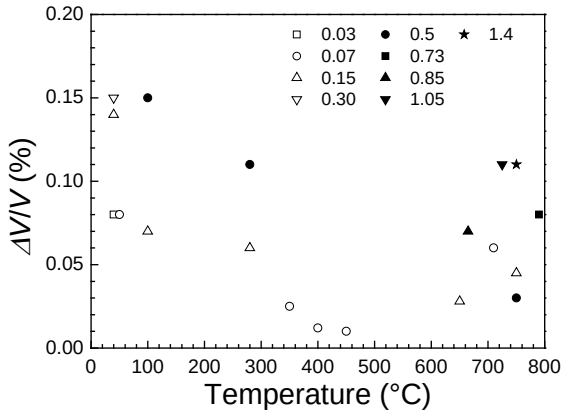

Fluences of fast neutrons (to be multipled by 10^{21} n/cm^2) corresponding to different points are indicated in the legend. Drawn based on the data reported in [62].

In-reactor creep occurs at all reactor relevant temperatures but, in contrast to swelling, creep has not only an irradiation-induced counterpart, but also a thermal one. Thermal creep dominates at temperatures exceeding ~ $0.5T_m$, where its rate grows exponentially with temperature increase. At high temperatures, the creep activation energies under irradiation and without it are practically identical and are close to the self-diffusion energy via vacancy mechanism [63,64], indicating that it is controlled by thermal vacancy production and transport. In other words, irradiation creep *per se* is observed only below $0.5T_m$, which is relevant to operation conditions of structural materials in fission and currently designed fusion reactors.

The major body of the available data concerning irradiation creep falls within the temperature range of 0.25-0.5 T_m. In this temperature range the irradiation creep dependence on temperature is rather weak. Usually, in experiments with a limited number of temperature points no pronounced temperature dependence at the typical working temperatures of nuclear reactors is noticed, though weak increase or decrease of irradiation creep with the increase of temperature are reported as well. Several detailed studies of the temperature dependence of creep in irradiated materials show that at lower temperatures a monotonous increase of the creep rate with temperature increase is observed, whereas at temperatures closer to the transition from irradiation to thermal creep a depression in the creep rate takes place, leading to a characteristic "hump" in the creep temperature dependence [46,65-69], see an example in Figure 7. Such temperature dependence is more typical for pre-irradiation cold-worked materials [65,66,68], as well as for ferritic-type steels with inherently high dislocation density [67].

Figure 7. Temperature dependence of irradiation creep in type AISI 316 CW [65]

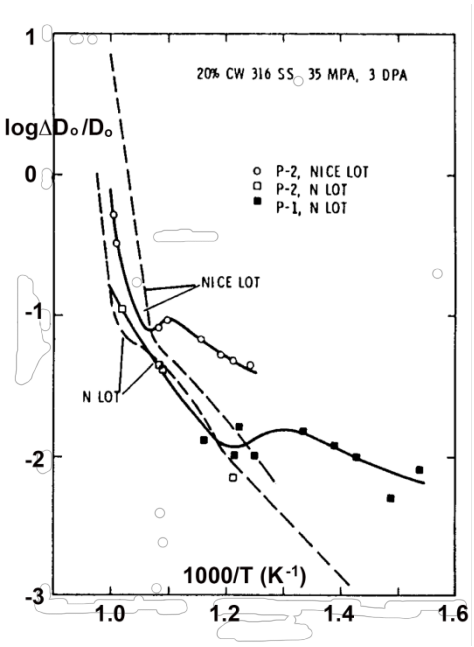

The "hump" on the temperature dependence of irradiation creep is usually located in the same temperature range where the "bell-shaped" temperature dependence of swelling is observed, which is often considered as a proof of the direct correlation between swelling and irradiation creep [70]. This interpretation should, however, be taken with

caution because the "hump" in the irradiation creep is observed also when no swelling is experimentally detected [66] or the doses are too low for noticeable swelling (< 3 dpa) [65]. Moreover, the responses of creep and swelling to a progressive temperature decrease are not correlated [71]. Finally, in a comparative study of SS 316 tubes in annealed and cold-worked states [66], the normal "bell-shaped" dependence of swelling was noticed in both types of tubes, whereas the "hump" on the temperature dependence of irradiation creep was observed only in cold-worked samples.

The results of irradiation creep measurements in copper [72] indicate, however, that the temperature variation of the creep rate inversely reflects the changes in the material yield stress, Figure 2.8, indicating correlation between irradiation creep and hardening. Moreover, the increase of the copper purity completely removes the "pit" in the irradiation creep curve (curve 3 in Figure 8).

Figure 8. Temperature dependence of the reactor (1,2) and the thermal (3, 4) copper (99.95%) creep rate and of the yield stress (5): the grain size are 35 μm (1, 3) and 50 μm (2, 4). [72]

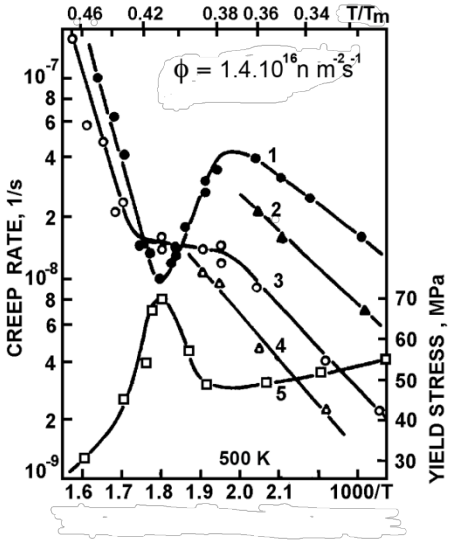

At temperatures below 0,25T_m the irradiation creep is investigated poorly. However, several measurements indicate that the irradiation creep rate at 60ºC is of the same order of magnitude or even larger than at higher temperatures [73-75]. Moreover, even at temperatures of some tens Kelvin irradiation was shown to accelerate the creep in pure W and Mo, while the creep rate values were comparable to those observed at higher temperatures [76-78].

2.3. Stress dependence

Irradiation-induced swelling does not require the assistance of external loading to occur, but there is ample evidence that material straining affects swelling. The effect of external stress on swelling is usually described by the relation

$$S = S_0(1 + D^S(T)\sigma_H), \qquad (2.2)$$

where σ_H is the hydrostatic component of stress and the factor D^S is typically of the order of 2-5x10^{-3} MPa^{-1} for steels [79-83], while in nickel irradiated to doses of appr. 10 dpa the value of D^S = 6x10^{-2} MPa^{-1} was found [84]. Microstructural reasons for swelling acceleration are usually associated with the influence of stress on void nucleation, which leads either to the reduction of void nucleation time lag [6,37,38,85] or to the increase of void number density [39]. On the other hand, the rate of steady-state swelling is insensitive to the action of external stresses [86,87]. According to relation (2.2), it is commonly expected that only the hydrostatic part of applied stress affects swelling. However, recently it was claimed that all stress states, including pure shear, can affect both void swelling and the correlation between irradiation creep and swelling [88].

While the effect of stresses is not crucial for swelling, the irradiation creep by definition vanishes in the absence of external loads. However, the discussion of the stress-dependence of creep is complicated by the fact that stress is a tensor variable and quite different combinations of stress tensor components can be involved in particular experiments. The most common loading schemes for creep tests are (i) uniaxial tension of rods, wires or thin film samples, (ii) nearly bi-axial loading of tubular samples, and (iii) nearly pure shear loading (stretching of thin wire springs or torsion of wires, tubes or rods). In the uniaxial tests, the stress σ_1 and strain ε_1 in the loading direction are measured, in the case of internally loaded tubes one considers usually the hoop stress and strain, σ_θ and ε_θ, while shear experiments involve the measurement of shear stress τ and shear strain γ. Luckily, the results of such tests can be compared rather easily through the reduction of the actual stress and strain to the so-called equivalent stress σ and equivalent strain ε using Soderberg relations [89]

$$\frac{\varepsilon}{\sigma} = \frac{\varepsilon_1}{\sigma_1} = \frac{4\varepsilon_\theta}{3\sigma_\theta} = \frac{\gamma}{3\tau}. \quad (2.3)$$

Hence, in the discussion below, by stress and strain we imply the equivalent values, if not explicitly stated otherwise.

The experimental dependence of irradiation creep rate on the applied stress is usually described in terms of a power law, $\dot{\varepsilon} \propto \sigma^n$, where n can vary depending on the stress range considered. Generally, it is possible to allocate up to three ranges of stresses characterized by different values of stress exponent [90] and separated by critical values σ^* and σ^{**}, (see Figure 9). At low stress levels ($\sigma < \sigma^*$) n = 1 and this linear creep rate dependence on stress is a universal law for quite different materials under different irradiation conditions and loading schemes.

Figure 9. Schematic stress dependence of irradiation creep

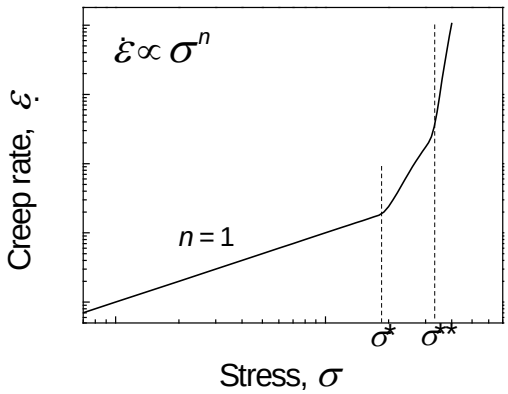

In some materials the linear stress range is followed by the one where the stress exponent exceeds unity, even though more common is the case where the non-linearity is not observed at all (see e.g. [91,92]). In particular, there are observed values of $n \sim 1.5$ (e.g. [93-97]) or $n = 2$ (e.g. [98-102]), (see Figure 10). These stress exponents are too low for plastic flow or thermal creep and the creep at this stage is believed to be caused by irradiation, while the change of the stress exponent is ascribed to the change of the governing microstructural mechanism of creep. In any case, the quadratic stress dependence is valid only within a limited stress range ($\sigma^* < \sigma < \sigma^{**}$). The values of σ^* in those reactor structural materials, where the stress nonlinearity is observed, have typically the order of 100-200 MPa [90], but are sensitive to the studied material and the experimental conditions.

Figure 10. Stress dependence of the irradiation creep rate for 20% cold-worked 316L stainless steel [103]

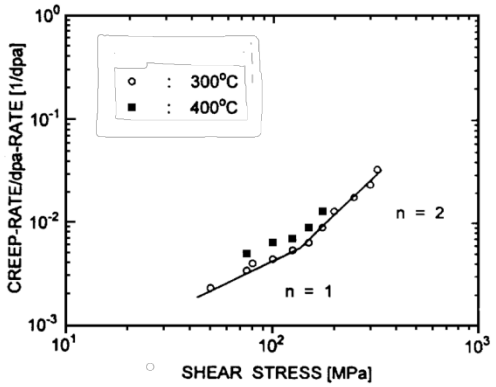

Finally, at high stresses ($\sigma > \sigma^{**}$) the stress exponents are in the range of 3 to 10 [49,92,104-106]. In this situation one deals already with the plastic flow of material and the value of σ^{**} correlates well with the yield stress (e.g. with $\sigma_{0.2}$). For example, a correlation $\sigma^{**} = 1.3\ \sigma_{0.2}$ was proposed in [107] based on the analysis of creep behaviour in a number of pure metals. The pre-factor exceeding unity is reasonable in this relation, since the yield stress of un-irradiated materials was used for the comparison, while more

appropriate correlation would be to that of irradiated materials, which is usually somewhat higher due to radiation hardening.

3. Theoretical models of swelling

3.1. The swelling equation

The main cause for many radiation effects in solids is the production of primary damage, which includes first of all atom-size defects (interstitials and vacancies), but also small clusters of interstitials and vacancies, if irradiating fast particles are energetic enough to produce localized atomic collision cascades. The generated point defects accumulate in the lattice, recombine, cluster to form larger point defect agglomerations (dislocation loops, cavities) or become captured by sinks, which include both those existed prior to the irradiation onset (network dislocations, precipitates, grain boundaries, etc.) and those evolved during the irradiation. Due to the small sizes of interstitial and vacancies, as well as clusters thereof, the defects can be considered as 'point-size' stress concentrators because an individual defect introduced into the crystal lattice creates elastic strains in the surrounding matrix. The contribution of each such stress concentrator to the volume change can be estimated using the Eshelby theorem [108], which states that the overall (i.e. macroscopic) volume increase is equal to the elastic misfit between the introduced defect and the surrounding matrix. Having in mind that interstitials and vacancies have the volume of the order of atomic volume ω, it is convenient to define the misfit of a point defect i as $e_i\omega$, where the factor e_i is named the point defect dilatation. It should be emphasized that as far as the solid can be considered as elastic continuum, it absolutely does not matter, in which particular place the defect is located inside the solid, or whether the misfit is spherically symmetric or not. The only requirement is that the material is not subject to the action of external constraints and is able to expand or contract freely. Hence, the relative increase of material volume (i.e. swelling) due to all point defects contained in the matrix can be written down simply as

$$S = \frac{\omega}{\Omega}\sum_i e_i \qquad (3.1)$$

where Ω is the volume of material and summation is over all point defects introduced into the matrix during irradiation, no matter whether they exist as a single defects or are consumed by the sinks available in the matrix. In writing Equation (3.1) we consider the onset of irradiation as a reference state, assuming that at that moment the swelling is vanishing.

While being exact, equation (3.1) itself is not very practical for the determination of the total swelling, because each point defect in this equation has, strictly speaking, its own dilatation determined by its nature and its local surroundings, which may change with time. Moreover, the number of defects is also varying all the time during irradiation. Hence, one needs some approximations to proceed further.

The first approximation that we introduce is that only intrinsic point defects (self-interstitials and vacancies) are taken into account in the subsequent discussion. With this approximation we rule out quite a number of contributions to swelling, e.g. those coming from impurity atoms, which are present in most of the relevant structural materials at

quite high levels (up to percent), often much higher than the levels of intrinsic point defects that can be reached during irradiation. In macroscopic terms, this means that we completely forget about contributions from aging, as well as from other forms of second phase precipitation and re-solution. However, in practice this approximation is reasonable, because intrinsic point defects are permanently generated in irradiated materials and are the most important defects responsible for large volume changes, which are of practical interest where the behaviour of structural components in irradiation facilities is concerned.

The next step is to look in more detail, which particular local environments are met for single point defects. It makes sense to differentiate, first of all, between single point defects in the bulk and point defects incorporated into sinks. The dilatations of single point defects are determined by forces of interatomic interaction in the lattice and are essentially the same for all defects belonging to the same type. The characteristic dilatation values for single interstitials and vacancies in metals are e_{I0} = 1.1 - 2.0 and e_{V0} = -0.1 - -0.2 [109]. When an atom is added or extracted at the edge of a dislocation extra-plane, the sample volume changes by ω or -ω, respectively [110], so that e_{Id} = 1 and e_{Vd} = -1. The same is true for interstitials and vacancies consumed at grain boundaries and external (free) surfaces of material. In the case, when a point defect is consumed by a point defect cluster, such as a dislocation loop, the point defect dilatations differ from unity only if the cluster is very small (no more than several atoms) and the cluster strength as a local stress concentrator is sensitive to the addition or removal of one atom. Finally, when an interstitial or a vacancy are consumed on internal surfaces (such as surfaces of internal cavities), their dilatations vanish, because the shift of an internal surface does not contribute to the change of the macroscopic volume. Strictly speaking, the last statement is not fully correct for those internal surfaces that are strongly curved (as is the case of small cavities), because in this case the addition or removal of a point defect changes the local stress distribution due to the action of capillarity forces. For example, a spherical cavity sufficiently large to be described in terms of surface tension causes the elastic relaxation at its surface, which is equivalent to the average dilatation of $\sim\gamma/\mu R$ per one vacancy in the cavity, where γ is the free surface energy, μ - the shear modulus and R - the cavity radius. However, for typical values of $\gamma \sim 1$ J/m^2 and $\mu \sim 100$ GPa, this dilatation is negligible even for cavity radius as small as 1 nm.

Having in mind the introduced approximations, equation (3.1) can be rewritten as

$$S = \frac{\omega}{\Omega}[N_I e_{I0} + N_V e_{V0} + \sum_s (e_{Is} N_{Is} - e_{Vs} N_{Vs})] \qquad (3.2)$$

where N_α is the total number of single point defects of type α ($\alpha = I$ for interstitials or $\alpha = V$ for vacancies) generated in the material by irradiation, N_{α_s} - the total number of interstitials and vacancies consumed by sink s starting from the irradiation onset and summation is over all point defects sinks available in the material. This can be written down in a more compact form by introducing the average concentrations of point defects as $C_\alpha = N_\alpha\omega/\Omega$ and substituting the values of point defect dilatations for different sinks, as discussed above,

$$S_t = C_I e_{I0} + C_V e_{V0} + \omega \sum_s^{\text{ext}} (n_{Is} - n_{Vs}) \qquad (3.3)$$

where $n_{\alpha_s} = N/\Omega$ and superscript 'ext' at the summation sign indicates that only the sinks contributing to the external increase of the material volume are taken into account. Though essentially the same as Equation (3.2), this relation does not contain direct reference to the total volume of material and can be considered as a local one.

At this junction it makes sense to make several comments as related to irradiation swelling:

- (i) First of all, it can be seen that, contrary to common belief, the availability of point defect sinks is not a prerequisite for swelling to occur. As shown above, each Frenkel pair (i.e. a pair of single interstitial and single vacancy created by irradiation) introduces the volume increase of the order of ω, and only the pair recombination or the simultaneous capture of interstitial and vacancy on the same sink nullifies their contribution to swelling. Even in the absence of whatever sinks the swelling due to accumulation of free point defects is non-zero (though in normal in-reactor conditions it is negligible as compared to that from sinks).
- (ii) The sum over sinks in the right hand side (r.h.s.) of Equation (3.3) does not contain contributions from cavities. It is the capture of excess interstitials at dislocations and grain boundaries that is responsible for the material volume growth under irradiation. The statement that cavities themselves do not contribute to swelling might sounds quite unexpected because it is a common practice to set the equality sign between swelling and the development of cavities (voids or gas-filled bubbles). The latter statement is, however, often true, being the consequence of the matter conservation, which requires the equality

$$C_I^G + \omega \sum_s^{ext} n_{Is}^G + \omega \sum_s^{\text{int}} n_{Is}^G = C_V^G + \omega \sum_s^{ext} n_{Vs}^G + \omega \sum_s^{\text{int}} n_{Vs}^G \qquad (3.4)$$

where the superscript G indicates the defects generated by atomic displacements caused by the irradiation and the superscript 'int' indicates summation over the sinks that do not contribute to the external growth of the material volume. Combining Equations (3.3) and (3.4), one gets:

$$S = C_I^G (e_{I0} - 1) + C_V^G (e_{V0} + 1) + C_I^N e_I + C_V^N e_V + \omega \sum_s^{\text{ext}} (n_{Is}^N - n_{Vs}^N) - \omega \sum_s^{\text{int}} (n_{Is}^G - n_{Ns}^G) \qquad (3.5)$$

where superscript N indicates defects introduced into the material during irradiation in the ways other than the direct displacement by irradiating particles. The common examples are vacancies introduced via thermal emission from surfaces and dislocations (with the equal number of extra atoms added to corresponding sinks) or extra atoms introduced during ion implantations. For materials operating in the conditions where the production of point defects is dominated by radiation, one gets

$$S \approx C_I^G (e_{I0} - 1) + C_V^G (1 + e_{V0}) + \omega \sum_s^{\text{int}} (n_{Vs}^G - n_{Is}^G) \qquad (3.6)$$

so that the swelling is indeed determined by the internal defect-absorbing surfaces. Strictly speaking, all such surfaces should be considered here, not only the cavity surfaces. But in practice only cavities are able to accumulate non-equal numbers of vacancies and interstitials, whereas the other similar sinks (such as e.g. surfaces of incoherent second phase precipitates) consume interstitials and vacancies in exactly the same numbers. Taking finally into account that the concentrations of single interstitials and vacancies in relevant structural and functional materials during reactor operation are usually quite low ($C_I^G << C_V^G < 10^{-7}$), the swelling is given by the uncompensated vacancies accumulated in cavities, i.e.

$$S_t \approx \omega \sum_s^{\text{cav}} (n_{Vs}^G - n_{Is}^G) = \sum_s^{\text{cav}} V_s \qquad (3.7)$$

where summation is over all the cavities in the material and $V_s = \omega(n_{Vs}^G - n_{Is}^G)$ is essentially the volume of cavity *s*. So, the matching between swelling and the total volume of cavities in the material can indeed be true, but it is no more that an approximation for special conditions, albeit quite common in dealing with reactor materials.

Forgetting that the real cause for swelling is the loss of interstitials can lead to unsupported conclusions as far as the relevant approximations do not hold true. For example, the fact that cavities in most metals have nearly spherical shape in no way implies that the associated deformation of irradiated material is isotropic as well. Since interstitials are preferentially captured on dislocations and/or grain boundaries, any noticeable anisotropy in the distribution of these sinks can induce material shape modification concurrent with the volume increase "non-hydrostatic swelling". Another example is met in simulation experiments that involve material implantation with self-ions. It is sometimes stated that the supply of additional interstitials by ion implantation suppresses swelling, which is not necessarily true. In fact, it is the void growth which is suppressed by injected ions, whereas swelling can equally well increase (after all, the matter is added to the investigated sample by implantation). Finally, in deriving eq. (3.7) it was nowhere required that the cavities themselves were produced by irradiation. For instance, when the material prior to irradiation has some amount of internal porosity and these pores preferentially absorb interstitials, one can easily observe 'negative' swelling (densification) until the pores are completely dissolved (a common situation with irradiated graphite).

- (iii) The contributions to swelling from different sinks are additive. It is absolutely unnecessary that the irradiation-generated interstitials were captured at the outer material surface or grain boundaries in order for swelling to occur. Interstitial capture by dislocations has exactly the same effect and in realistic metals (with grains sizes of the order of tens of micrometers) it is the interstitial capture on dislocations that gives the dominant contribution to the overall swelling.

In order to further simplify eq. (3.3) (or Equation (3.7), when applicable), it is convenient to group together the equivalent sinks (i.e. sinks with the same behaviour in terms of their contribution to swelling) into sink classes, such as e.g. various kinds of network dislocations (edge or screw) and dislocations loops (vacancy or interstitial, faulted or glissile), planar defects (grain and subgrain boundaries, coherent or incoherent), precipitates (with coherent and incoherent interfaces), cavities (empty or gas-filled), as well as mixed sinks (e.g. cavities on grain boundaries or precipitates), etc. Then the expression (3.3) for swelling can be written down as

$$S_t = C_I e_{I0} + C_V e_{V0} + \sum_c {}^{\text{ext}} \sum_{sc} \Delta\Omega_{sc} \qquad (3.8)$$

where Σ_c means the sum over sink classes, Σ_{sc} -summation over the sinks within each class and $\Delta\Omega_{sc} = \omega(n_{Isc} - n_{Vsc})$ - the contribution to the total volume change from sink *sc*. Though essentially equivalent to Equation (3.3), this relation allows $\Delta\Omega_{sc}$ to be expressed in terms of parameters appropriate to sinks of each particular type, while the whole system of similar sinks can be described in purely statistical terms instead of counting individual sinks. For example, in the case of circular interstitial dislocation loops the only parameters that characterise individual dislocation loop are loop diameter D and loop Burgers vector $\boldsymbol{b}_l$, while the contribution of the whole class of such dislocation loops ($c = l$) into swelling can be written down as:

$$\sum_{sl} \Delta\Omega_{sl} = \frac{\pi}{4} \sum_m b_l^m \int D^2 f_l^m(D,t)\, dD \qquad (3.9)$$

where $b_l^m = |\boldsymbol{b}_l^m|$, $f_l^m(D,t)$ is the probability (per unit volume of material) to meet a dislocation loop with diameter D at the moment of time t and summation is over all (usually of a quite limited number) types of Burgers vectors in the considered material. Similarly, when spherical cavities are considered, the sum in the r.h.s. of eq. (3.7) can be written down as

$$\sum_s {}^{\text{cav}} V_s = \frac{4\pi}{3} \sum_\xi \int R^3 f_c(R,t \mid \xi)\, dR \qquad (3.10)$$

where $f_c(R,t|\,\xi)$ is the probability (per unit volume of material) to find a cavity with radius R at the moment of time t and ξ stands for a set of additional parameters (e.g. the amount of impurity atoms contained inside or at the surface of a cavity) that can be used to characterise an individual cavity. In the case when the cavity contains only vacancies (in this case it is referred to as 'void'), summation in Equation (3.10) should be omitted.

The basic disadvantage of Equation (3.8) for theoretical treatment is the fact that the instantaneous value of swelling is determined by total numbers of point defects absorbed by all the sinks that were present in the material during the whole irradiation history, including even those that have already disappeared by the observation time t. Such "lost" sinks include e.g. the dissolved pores present prior to irradiation, boundaries of grains that have disappeared via recrystallisation, dislocations annealed out at grain boundaries, etc. For this reason, it is a common practice in the theory of swelling to deal not with the

swelling itself, but with the swelling rate, $\dot{S} = dS/dt$, which depends only on the instantaneous material microstructure,

$$\dot{S} = e_{I0}\frac{dC_I}{dt} + e_{V0}\frac{dC_V}{dt} + \sum_c {}^{\text{ext}} \sum_{sc} \frac{d(\Delta\Omega_{sc})}{dt} \qquad (3.11)$$

or, when Equation (3.6) is applicable,

$$\dot{S} = (e_{I0} - 1)\frac{dC_I^G}{dt} + (1 + e_{V0})\frac{dC_V^G}{dt} + \frac{4\pi}{3}\sum_{\xi}\int R^3 \frac{df_c(R,t\,|\,\xi)}{dt}dR \qquad (3.12)$$

In addition to making the description sensitive to only the current microstructure, the transition to swelling rate allows us to simplify the description for those sink classes, where the accumulated volume $\Delta\Omega_{sc}$ is hard to estimate, whereas the rate of volume change is determined easily. For example, if we consider the class of straight edge dislocation (a quite common approximation for dislocation network in irradiated materials), its contribution to the overall swelling rate can be described as:

$$\sum_{sd}\frac{d(\Delta\Omega_{sd})}{dt} = \sum_k b_d^k \rho_d^k V_{dc}^k \qquad (3.13)$$

where b_d^k is the length of the dislocation Burgers vector, ρ_d^k - the dislocation density (i.e. the total length of dislocations of type k per unit volume of material), V_{dc}^k - the velocity of dislocation climb (assumed to be positive when the dislocation builds up its extraplane) and summation is over dislocations with the different types and orientations of dislocation Burgers vector $\boldsymbol{b}_d^k$.

An additional advantage in using the swelling rate rather than swelling is that the concentrations of point defects vary little during irradiation (except during sharp transients) and thus their derivatives can be nearly always safely neglected, so that e.g. eq. (3.12) can be written down as:

$$\dot{S} = \frac{4\pi}{3}\sum_{\xi}\int R^3 \frac{df_c(R,t\,|\,\xi)}{dt}dR \qquad (3.14)$$

In what follows, we deal with Equation (3.14), which in theoretical treatments of swelling is usually postulated without any justification. It should be pointed out, however, that there exist situations where the assumptions used in the derivation of Equation (3.14) do not hold and in these cases one should use Equation (3.11), which is always applicable. An example of such situation is given in Section 3.7 below dealing with the low-temperature swelling of refractory metals and ceramics. An additional price to pay where the material deformation is anisotropic is that Equation (3.11) can be straightforwardly generalized in order to describe the full strain tensor ε_{ij} comprising both volume and shape modification, while Equation (3.14) cannot.

3.2. Analytical equations for the description of swelling

Let us assume that the cavities considered are voids, so that no additional parameters ξ affect cavity growth and no summation in eq. (3.14) is involved. Then the swelling rate is exclusively determined by the law of temporal evolution of the void distribution function in the space of void sizes. This law is sensitive to the particular events that result in the variation of void sizes. In irradiated materials this is only possible when the transport of vacancy-type defects is allowed, which means that void swelling cannot be observed at temperatures where vacancy diffusion is suppressed. A common assumption is that the only mobile defects in irradiated materials are single vacancies and interstitials. In the discussion below we accept it, even though it is not strictly true. First of all, small clusters of vacancies and especially interstitials are often also very mobile, sometimes even more mobile than single defects. One, but not the only example is the mobility of small defect clusters in pure iron, where e.g. tri-vacancies have a lower migration barrier than single vacancies [111], while small interstitial clusters form glissile dislocation loops that glide in <111> lattice directions much faster than single interstitials are able to diffuse [112-114]. Second, the voids themselves are able to move, and though the void diffusion coefficient sharply falls down with the growth of void size [115], the effect can be non-negligible in situations where dense arrays of small voids are created in the material. Typical examples where the direct coalescence of cavities is non negligible is the development of planar arrays of helium bubbles (on grain boundaries, or at the end of range of ions implanted into subsurface sample layers in simulation experiments on fast particle accelerators).

In the approximation where only single vacancies and interstitials (monomers) are able to move, the change of a cavity size takes place in discrete steps, so it is more convenient (especially for small clusters) to introduce the cavity distribution function $f_n(t)$, which defines the probability to find a void that contains n vacancies at time t. The sum over void sizes,

$$N_c(t) = \sum_{n=2}^{\infty} f_n(t), \qquad (3.15)$$

defines the number density of voids N_c (normalised per one lattice site). Summation starts here from di-vacancies, which are considered as the smallest immobile clusters. Equation (3.14) in this case can be rewritten as

$$\dot{S} = \sum_{n=2}^{\infty} n \frac{df_n(t)}{dt} = \frac{d}{dt}(N_c \bar{n}), \qquad (3.16)$$

where $\bar{n}$ is the average number of vacancies in a void.

While seemingly straightforward, the transition from (3.14) to (3.16) involves two more approximations that are seldom overtly declared. First of all, it is implicitly assumed that all voids with n vacancies have essentially the same shape. This statement is more or less reasonable for large voids ($n >> 1$), which are roughly spherical, but may be not a good approximation for clusters containing only several vacancies ($n < 10$), where clusters of different shapes can exist with competing probabilities and, in the most unfavourable cases, some vacancy clusters can belong to the types that are not void-like at all (e.g. stacking fault tetrahedra in fcc metals). Second, while in Equation (3.14) the distribution

function f_c is the average over the whole volume of material and as such does not depend on the particular position in space, the function $f_n(t)$ is usually introduced as a local function and should be generally considered as spatially dependent, $f_n(\mathbf{r},t)$. The neglect of this spatial dependence implies that the ensemble of cavities is uniform over the whole material volume or, at least, changes relatively weakly at the length scales of interest for particular application. If this is not the case (e.g. in simulation experiments on particle accelerators), the spatial dependence of the distribution function should be taken into account explicitly.

The equation for the time evolution of the density function via the capture and emission of monomers can be written down in the form of a balance equation that directly counts the processes that change the number of clusters of each size per unit time. Originally this kind of equation ('master equation') was introduced in [116] and has the most simple form when the sink size changes as a result of a capture of individual monomers [117]:

$$\frac{\partial f_n}{\partial t} = G_n + P_{n-1} f_{n-1} + Q_{n+1} f_{n+1} - (P_n + Q_n) f_n, \qquad (n \geq 2), \tag{3.17}$$

where G_n is the rate of direct production of vacancy clusters of size n and the kinetic coefficients $P_n(t)$ and $Q_n(t)$ are the rates of monomer attachment to and detachment from clusters of size n. This equation is broadly applied to the nucleation of voids, even though two kinds of monomers (vacancies and interstitials) are produced during irradiation. This does not change the basic assumption that the sink kinetics is determined by the capture of monomers; simply the kinetic coefficients are presented as additive contributions from vacancies and interstitials [118,119],

$$P_n = p_{nV} + q_{nI} \qquad \text{and} \qquad Q_n = p_{nI} + q_{nV} \tag{3.18}$$

where $p_n\alpha$ and $q_n\alpha$ are the rates of absorption at and desorption from a void of size n for point defects of type α. The values of q_{nI} are usually set to zero, which is nearly always reasonable because the energies of interstitial formation in reactor structural material are typically several electron-Volts [109] and the probability of interstitial expulsion from a vacancy cluster into the bulk is absolutely negligible for any relevant application temperature unless one deals with the cavities strongly over-pressurised with gas atoms (such as helium or other noble gases).

Though the master equation was broadly used for the analytical description of void formation in irradiated metals from the early 1970s, it misses many important features of defect kinetics that were brought to light by later research. For example, in many metals small clusters of interstitials and vacancies (consisting of 2-3 point defects of the same kind) are mobile and so the basic assumption of the cluster size modification by ±1 is not strictly valid. The inclusion of a non-vanishing term G_n into master equation (3.17) is also a generalization of the original formulation that accounts for the fact that clusters of several vacancies can be directly produced in cascades of atomic collisions. Equally well, collision cascades can be expected to completely destroy small vacancy clusters [120], which is not taken into account in Equation (3.17). It is commonly expected that these

complications do not change the overall qualitative picture of void nucleation but, to the best of the author's knowledge, no qualitative proof of this statement has been given.

One more simplification in (3.17) that should be mentioned for completeness is the neglect of direct interaction of clusters (in terms of coalescence or coagulation). This simplification is generally not a very severe one because such interaction becomes of any importance only when the relative volume occupied by voids becomes large, i.e. at $S \sim 1$. At this swelling stage the application of the "master equation" is excessive because the kinetics of a system of large voids usually can be nicely described in deterministic way (see Section 3.6).

Equation set (3.17) is essentially a diffusion equation in the space of void sizes, which is used for the description of void evolution also in the alternative form (e.g. in [121])

$$\frac{\partial f_n}{\partial t} = \frac{\partial}{\partial n}(A_n f_n) + \frac{\partial}{\partial n} B_n \frac{\partial f_n}{\partial n} \qquad (3.19)$$

where the void size is treated as a continuous variable, while A_n and B_n are presented either as:

$$A_n = P_n - Q_n, \; B_n = (P_n + Q_n)/2,$$

or

$$A_n = P_n \ln(Q_n/P_n), \; B_n = P_n.$$

In the first case eq. (3.19) is called Fokker-Planck equation, in the second - Zeldovich-Frenkel equation. The advantage of using a partial differential equation instead of a discrete equation set is in much easier analytical treatment and analysis of the overall qualitative behaviour of the void size distribution function. The difference between the treatments of cluster size as a continuous or a discrete variable should not be really important for $n >> 1$, indeed. However, the transition to the differential equation is accurate only provided the kinetic coefficients P_n and Q_n vary smoothly as a function of n and that $P_n \approx Q_n$ (more precisely, $|P_n - Q_n| << (P_n + Q_n)/2$). While the first approximation is invalid only for relatively small clusters (less than ~10 vacancies) in the worst case, the second one is rather an exception, applicable at best for a limited range of cluster sizes. Hence, eq. (3.19) is useful mostly for the understanding of the void kinetics in qualitative terms; quantitative predictions based on it are usually poor.

Substituting Equation (3.17) into Equation (3.16), it is easy to get two useful alternative expressions for the swelling rate, namely:

$$\dot{S} = \sum_{n=2}^{\infty} n G_n + \sum_{n=1}^{\infty} (1 + \delta_{n1}) J_n \qquad (3.20)$$

where $J_n = P_n f_n - Q_{n+1} f_{n+1}$ is the cluster current in the space of sizes, and

$$\dot{S} = \sum_{n=2}^{\infty} n G_n + (2P_1 f_1 - Q_2 f_2) + \sum_{n=2}^{\infty} (P_n - Q_n) f_n \qquad (3.21)$$

Quite generally, various kinds of relations between the kinetic coefficients can be met. First of all, consider the case, where $Q_n > P_n$ for all cluster sizes. Such a situation is met in the case of high-temperature irradiation, where void decomposition due to thermal vacancy emission dominates. Evidently, in this case no void development is possible because any void cluster, even if formed athermally or fluctuatively, eventually dissolves. In the opposite case, where $Q_n < P_n$, all clusters tend to grow. This situation is not very common for voids but is relevant for clustering of interstitials into interstitial loops.

More complicated are situations, when the void size space is separated in regions, where the difference $j_n = P_n - Q_n$ changes sign. In this case, there exist some void sizes n^*, called critical sizes, separating adjacent regions with different signs of j_n. If $j_n > 0$ at $n < n^*$, then the voids with the sizes both below and above the critical size tend to reach size n^*. On the contrary, when $j_n < 0$ at $n < n^*$, the clusters with $n < n^*$ tend to dissolve, whereas those with $n > n^*$ tend to grow. The latter situation is very typical for vacancy voids in reactor structural metals, as discussed later in Section 3.6.

In order to study the particular kinetics of void ensemble evolution, it is necessary to specify the kinetic coefficients as functions of the void size and to specify the initial and boundary conditions. For the initial conditions one can select essentially any reasonable distribution function. For example, the condition $f_n(0) = 0$ for $n \geq 2$ is a realistic choice, implying no voids exist prior to the onset of irradiation. Equally easy is the assignment of a boundary condition at the large void sizes,

$$f_n(n \to \infty) = 0 . \qquad (3.22)$$

The trickiest part is the introduction of a condition for the vacancy and interstitial concentrations. Remaining in the framework of the assumptions used to formulate Equation (3.17), one has to assume that monomers (both interstitials and vacancies) are described by some spatially uniform concentrations $C_{\alpha 0}$, which are determined by the balance of point defect generation, recombination and absorption on voids, as well as on other possible sinks. Then, by definition

$$f_1 = C_{V0} \qquad (3.23)$$

The balance equation for C_{V0} can be written down as:

$$\frac{dC_{V0}}{dt} = G_V - \sum_{n=2}^{\infty} (p_{nV} - q_{nV}) f_n + ((q_{2V} + p_{2I}) f_2 - p_{1V} C_{V0}) - \kappa_V^2 - \gamma_{IV} C_{I0} C_{V0} \qquad (3.24)$$

where GV is the rate of vacancy production, the second term in the r.h.s. (the sum over vacancy cluster sizes) describes the balance of vacancy capture and emission at voids in a way consistent with equations (3.17) and (3.18), the third term describes the balance between the vacancy production and removal as a result of divacancy dissociation and creation, κV in the fourth term describes the integral loss and creation of vacancies on sinks other than voids, and the last term describes interstitial-vacancy recombination. A similar equation for CI0 looks like:

$$\frac{dC_{I0}}{dt} = G_I - \sum_{n=2}^{\infty} p_{nI} f_n - \kappa_I^2 - \gamma_{IV} C_{I0} C_{V0} \tag{3.25}$$

where G_I and κ_I are the rates of interstitial generation and loss on sinks other than vacancy clusters, respectively. The rate of interstitial emission from vacancy clusters, q_{nI}, is set here to zero for the reasons discussed in the paragraph following Equation (3.18). Since both interstitial and vacancy defects are generated by irradiation at exactly the same rate, G, the following additional relation must hold:

$$G_I + \sum_{n=2}^{n_V^{\max}} nG_{nI} = G_V + \sum_{n=2}^{n_I^{\max}} nG_{nV} = G \tag{3.26}$$

where $G_{n\alpha}$ are the generation rates for clusters of size n and type α, which are directly created by irradiation, and $n_\alpha^{\max}$ - the maximum sizes of clusters that a particular type of irradiation is able to produce. When no clustered defects are produced by irradiation, the rates of single interstitial and single vacancy generation are naturally equal.

The rates of point defect absorption and desorption on sinks should evidently depend on the concentrations of point defects available in the material. It is also intuitively clear that they are proportional to point defect diffusion coefficients, D_α, as a measure of the point defect transfer rate by diffusion, which is the principal mechanism of point defect movement in crystals. Hence, it is a common practice to present the rates of point defect capture by a cavity in the form:

$$p_{n\alpha} = k_{n\alpha}^2 D_\alpha C_{\alpha 0} \tag{3.27}$$

where $k_{n\alpha}^2$ is a proportionality factor, usually referred to as cavity 'sink strength'. Similarly, the rate of point defect emission from the cavity is written down as:

$$q_{n\alpha} = k_{n\alpha}^2 D_\alpha C_{n\alpha}^{th} \tag{3.28}$$

where $C_{n\alpha}^{th}$ is some measure of point defect emission from the cavity, which may depend on both the point defect type and the properties of the cavity itself. The superscript *th* refers here to the fact that the emission of defects from cavities is usually thermofluctuative and so it is reasonable to expect that $C_{n\alpha}^{th}$ is proportional to the thermally equilibrium concentration of point defects, $C_{\alpha 0}^{th}$.

Since the reasoning leading to relations (3.27) and (3.28) does not rely on the particular nature of sinks, similar relations should hold for sinks of any type, so that the efficiencies of point defect capture by sinks other than voids in equations (3.24) and (3.25) can be written down as:

$$\kappa_\alpha^2 = k_\alpha^2 D_\alpha (C_{\alpha 0} - \bar{C}_\alpha^{th}) \tag{3.29}$$

where $k_\alpha^2 = \sum_s k_{s\alpha}^2$ is the sum of sink strengths $k_{s\alpha}^2$ and $\bar{C}_\alpha^{th} = k_\alpha^{-2} \sum_s k_{s\alpha}^2 C_{s\alpha}^{th}$ is the weighted average of point defect emission efficiencies from all sinks types s other than cavities.

A common implicit assumption in writing relations (3.27) - (3.29) is that both sink strengths and the emission efficiencies C_α^{th} of individual sinks are the properties of sinks themselves and do not depend on the point defect concentrations. At this point, these assumptions are no more than intuitive, but they can indeed be justified in the framework of the so called chemical rate theory, as described in Section 3.3 below. The same theory suggests also the ways to calculate sink strengths and sink emission efficiencies for different sink types. In particular, it can be shown that $C_{s\alpha}^{th}$ coincides with the thermal equilibrium concentration of α-type point defects at the surfaces of relevant sinks, which will be used in the discussion below. In particular, for network dislocations and planar sinks (first of all, grain boundaries) the thermal equilibrium concentrations are simply equal to $C_{\alpha 0}^{th}$ and so for these sinks $\bar{C}_\alpha^{th}$ in eq. (3.29) can be replaced with $C_{\alpha 0}^{th}$.

Using relations (3.27) - (3.29), equations (3.24) and (3.25) can be written down as:

$$\frac{dC_{V0}}{dt} = G - k_{cV}^2 D_V (C_{V0} - \bar{C}_{cV}^{th}) - k_V^2 D_V (C_{V0} - C_{V0}^{th}) - \gamma_{IV} C_{I0} C_{V0} \tag{3.30}$$

$$\frac{dC_{I0}}{dt} = G - k_{cI}^2 D_I C_{I0} - k_I^2 D_I C_{I0} - \gamma_{IV} C_{I0} C_{V0} \tag{3.31}$$

where

$$k_{cV}^2 = \sum_{n=2}^{\infty} f_n k_{nV}^2 \quad \text{and} \quad \bar{C}_{cV}^{th} = k_{cV}^{-2} \sum_{n=2}^{\infty} f_n k_{nV}^2 C_{nV}^{th} \tag{3.32}$$

and several minor simplification were introduced, including the neglect of direct generation of defect clusters and of inessential term accounting for divacancy creation correction in eq. (3.24).

Equations (3.17) - (3.23) and (3.30) - (3.32) constitute the boundary-value problem for consistent description of void swelling in irradiated materials. This statistical problem is too complicated to be solved either analytically or numerically without certain simplifications. However, before describing the methods of its solution, let us describe how to determine the sink strengths introduced *ad hoc* in relations (3.27) - (3.29).

3.3 The effective medium theory

When dealing with the statistical description of void ensemble development in irradiated materials, one uses the intuitive concept of spatially uniform efficient concentrations of point defects. Evidently, these concentrations are not the real concentrations of point defects that are created and diffuse in the material matrix. The real concentrations c_α are defined only in the space between the sinks and their spatial

dependence is determined by the solution of diffusion equations that can be written down as:

$$\frac{\partial c_\alpha}{\partial t} + \mathrm{div}\, \boldsymbol{j}_\alpha = G - \gamma_{IV} c_I c_V \ , \qquad (3.33)$$

where G is the rate of point defect creation (which can depend on both the time and the spatial position $\boldsymbol{r}$) and the point defect current $\boldsymbol{j}_\alpha$ is defined as:

$$j_{\alpha n} = -D_{\alpha nm} \frac{\partial c_\alpha}{\partial x_m} \ , \qquad (3.34)$$

where $D_{\alpha_{mn}}$ is the tensor of diffusion coefficients; indices n and m (from 1 to 3) enumerate Cartesian coordinates, and the rule of summation over the repeated subscript indices is implied. In completely isotropic materials, the diffusion tensor has the diagonal form, $D_{\alpha_{mn}} = D_\alpha \delta_{mn}$, where δ_{mn} is the Kronecker tensor. Correspondingly, equation (3.34) is reduced to the isotropic form:

$$\boldsymbol{j}_\alpha = -D_\alpha \nabla C_\alpha \, . \qquad (3.35)$$

The diffusion equations are to be supplied with boundary conditions on sinks, which are the regions in the material that can capture diffusing defects at their surfaces. Realistic materials have multiple sinks that can be roughly grouped as belonging to one of three groups:

- local sinks, with their largest size much less than some characteristic length scale in the matrix; voids, bubbles and small dislocation loops are representative of this group;
- linear sinks, whose length in one dimension is comparable to or noticeably exceeds the characteristic length scale in the matrix (e.g. network dislocations);
- planar sinks (e.g. grain boundaries), whose sizes in two dimensions exceed the characteristic length scale in the matrix.

As long as one is interested in point defect absorption by sinks, the relevant length scale referred to in this classification is the average distance L_s travelled by a point defect before it is captured by a sink. When the generated point defects are eliminated from the material mostly via capture at sinks and not via mutual recombination, L_s is of the order of inter-sink distance. The requirement that the average inter-sink distance exceeds considerably the typical sink sizes implies that the total volume of sinks constitutes only a small fraction of the whole volume of material. When applied to swelling, this means that the considerations below are valid only when $S \ll 1$.

At the sink surfaces the concentration of point defects is normally maintained equal to the thermal equilibrium concentration of defects in contact with a particular sink. Defining this concentration at the surface of sink i ($1 \le i \le N$, where N is the total

number of sinks in the material) as $C_{i\alpha}^{th}$, we can write down a set of the boundary conditions as:

$$c_\alpha(\boldsymbol{r}_i^s, t) = C_{i\alpha}^{th}(\gamma_i), \tag{3.36}$$

where $\boldsymbol{r}_i^s$ is the radius-vector of a point on the surface S_i of the sink and γ_i denotes the set of parameters, characterising the sink. The choice and the number of these parameters depend on particular sink type. For example, for a spherical void γ_i includes only void radius R_i, while e.g. for second phase particles this set of parameters can include information about the particle shape, composition, grain boundary coherence to the matrix, etc.

Thus it is necessary to specify the relation between the true point defect concentrations and the effective concentrations $C_{\alpha 0}$. A possible way to do it is suggested by the chemical rate theory, introduced originally for the description of chemical reactions in solutions. This concept was applied to the investigation of sink kinetics in irradiated materials in [122,123] on a largely intuitive basis. The general philosophy of such an approach is very similar to the approaches used in analogous situations for the theoretical description of many-body problems [124]. The chemical rate theory describes point defect absorption by sinks in an "average" manner, by assuming that on the length scales noticeably exceeding the inter-sink separation the material behaves as a spatially uniform "lossy medium" where sinks are 'smeared' over the material volume, while the efficiency of point defect capture by individual sinks is determined in some self-consistent way. As a result, the exact concentration c_α is replaced with the average concentration $C_{\alpha 0}$, which coincides with c_α only in those regions of the matrix, where the sinks are absent.

Several attempts to rigorously justify the rate theory can be found in the literature [125-131]. Below we illustrate in a simplified manner the basic steps of the transition from the boundary value problem (3.33) - (3.36) to the effective medium, considering only the local sinks and neglecting the point defect loss term by recombination in equation (3.33). A more detailed treatment, including in particular linear sinks and the effects of external stresses on point defect diffusion, can be found in [130,131]. Having in mind that the neglect of recombination term uncouples diffusion equations for vacancies and interstitials, subscripts indicating particular type of point defects will be omitted in section 3.3, if not explicitly stated otherwise. In the presentation below, we also neglect the temporal evolution of the sink system when dealing with the problem of point defect diffusion to sinks. This approximation is valid when the time scale of point defect concentration redistribution around the sinks, τ_s, is much shorter than that for evolution of the sink system itself, which is valid practically always except at very sharp transients (e.g. sudden switch on or switch off of irradiation).

As already said, an arbitrary local sink i can be characterised by a set of parameters $\xi_i = (\boldsymbol{r}_i, \gamma_i)$, which includes sink position in the matrix, $\boldsymbol{r}_i$, and a set of other parameters, which we have denoted as γ_i. The complete set of parameters for all sinks will be briefly denoted as $\Xi = (\xi_1, ..., \xi_N)$ and the space of all possible parameter sets Ξ - as $\{\Xi\}$. For any particular realization of the sink system the concentration c of point defects in the space between the sinks satisfies the equation

$$\frac{dc}{dt} = G + D\nabla^2 c \qquad (3.37)$$

with boundary conditions (3.36). Generally, an appropriate boundary condition should be defined on the outer surface of material as well. However, to simplify matters one may assume that the volume of material Ω tends to infinity (and also $N \to \infty$, so that the ratio N/Ω would remain finite) and only demand the boundedness of c everywhere in the matrix. Evidently, the point defect concentration defined by this boundary-value problem depends not only on the spatial position $\boldsymbol{r}$ and time, but also on the spatial distribution and parameter of sinks, i.e. $c = c(\boldsymbol{r},t|\Xi)$.

Because Equation (3.37) is defined only in the domain between the sinks and for different realisations of the sink system the domains of definition of equation (3.37) are different, it is convenient to rewrite it in an alternative way, so that it were defined in the whole volume of material and would automatically give correct values of concentration in the domain between the sinks, regardless of particular sink realisation. This can be achieved by incorporating the boundary conditions at sink surfaces into the diffusion equation itself,

$$\frac{dc}{dt} = G + D\nabla^2 c - \sum_{n=1}^{N} (\boldsymbol{j}\mathbf{e}^{(n)})\delta(S_n) \qquad (3.38)$$

where $\mathbf{e}^{(n)}$ is the unit normal vector to the sink surface in a surface point $\boldsymbol{r}_n^s$, $\delta(S_n)$ is the surface delta-function, defined as (see e.g. [132])

$$\delta(S_n) = \int_{S_n} \delta(\boldsymbol{r} - \boldsymbol{r}_n^s)\, dS, \qquad (3.39)$$

where $\delta(\boldsymbol{r} - \boldsymbol{r}_n^s)$ is the three-dimensional Dirac delta function and the integration is over the points $\boldsymbol{r}_n^s$ belonging to the surface S_n of the n-th sink. This function has the property that for any function of spatial co-ordinates $f(\boldsymbol{r})$ the following relation holds [132]:

$$\int_{\Omega} f(\boldsymbol{r})\delta(S_n)\, d\boldsymbol{r} = \int_{S_n} f(\boldsymbol{r}_n^s)\, dS$$

Equation (3.38) coincides with (3.37) in the domain of definition of the latter, while integration of (3.38) over the volume of material provides the correct point defect currents to sinks, if the integral over the internal volume of sinks can be neglected. This latter is reasonable for dilute sink systems and corresponds to the neglect of point defect generation and diffusional transport inside the sinks (which is self-evident where voids are concerned).

Now, let us assume that the probability dP to find a system of sinks in a small volume $d\Xi = d\xi_1 d\xi_2 ... d\xi_N$ of the parameter space $\{\Xi\}$ around a point Ξ is given by some N-sink probability distribution function $f_N(\Xi)$ such that

$$dP = \Omega^{-N} f_N(\Xi) d\Xi \ . \qquad (3.40)$$

The normalisation condition is, evidently,

$$\Omega^{-N}\int_{\Omega} f_N(\Xi)d\Xi = 1$$

Because we would like to describe the system of sinks in an average way, it is reasonable to define the average concentration of point defects as an average over various sink ensemble realisations, that is:

$$C_0(\boldsymbol{r}) = \Omega^{-N}\int c(\boldsymbol{r},t\,|\,\Xi)\, f_N(\Xi)d\Xi, \tag{3.41}$$

where the integral is over the whole configurational space $\{\Xi\}$.

An equation for C_0 can be obtained by averaging Equation (3.38) over parameters of all sinks,

$$\frac{dC_0}{dt} = K + D\nabla^2 C_0 - \sum_{n=1}^{N} I_1^{(n)} \tag{3.42}$$

where the point defect loss intensities at sinks, $I_1^{(n)}$, are given by:

$$I_1^{(n)}(\boldsymbol{r}) = \Omega^{-1}\int d\gamma_n f_1^{(n)}(\boldsymbol{r},\gamma_n) J_1^{(n)}(\boldsymbol{r},\gamma_n) \tag{3.43}$$

where $f_1^{(n)}$ is the probability to find sink n with the parameter set γ_n in point $\boldsymbol{r}$;

$$J_1^{(n)}(\boldsymbol{r},\gamma_n) = D\int_{S_n} (\mathbf{e}^{(n)}\nabla C_1^{(n)})\Big|_{\boldsymbol{r}_n=\boldsymbol{r}-\boldsymbol{b}_n^S} dS \tag{3.44}$$

$\boldsymbol{b}_n^S$ is the radius vector of the surface point, defined in the local coordinate system originating at the sink centre and

$$C_1^{(n)} = \frac{V^{1-N}}{f_1^{(n)}}\int c(r,t\,|\,\Xi)\, f_N(\Xi)d\Xi_{(n)} \tag{3.45}$$

where $d\Xi_{(n)}$ indicates that integration in configurational space $\{\Xi\}$ is over all sinks except the n-th one.

As can be seen, in order to determine the average concentration C0 at an arbitrary point r in the matrix, one must know the concentration moment C1 for any sink placed near this point r in such a way that it "touches" r with some point of its surface. The latter requirement makes calculation of $J_1^{(n)}(\boldsymbol{r},\gamma_n)$ quite a non-trivial task but, luckily, in dilute systems of local sinks $J_1^{(n)}$ can be nicely approximated simply with the point-defect current to the n-th sink located in point r [130], so that

$$J_1^{(n)}(\boldsymbol{r},\gamma_n) = D\int_{S_n} (\mathbf{e}^{(n)}\nabla C_1^{(n)})\Big|_{\boldsymbol{r}_n=\boldsymbol{r}} dS. \tag{3.46}$$

In order to find the equation for concentration $C_1^{(n)}$ around any fixed sink n, one can average out Equation (3.38) over the parameters of all sinks, except the n-th one. This gives us a set of N equations,

$$\frac{dC_1^{(n)}}{dt} = K + D\nabla^2 C_1^{(n)} - \sum_{\substack{m=1 \\ m\neq n}}^{N} I_2^{(m|n)} \tag{3.47}$$

where

$$I_2^{(m|n)} = \Omega^{-1} D \int (\mathbf{e}^{(m)} \nabla C_2^{(mn)}) f_2^{(m|n)} \delta(S_m)\, d\xi_m \tag{3.48}$$

$f_2^{(m|n)}$ is a conditional probability to find sink *m* with the parameter set ξ_m provided sink *n* has a predefined parameter set ξ_n and the second concentration moment is defined as:

$$C_2^{(mn)} = \frac{\Omega^{2-N}}{f_2^{(mn)}} \int c(r,t\,|\,\Xi)\, f_N(\Xi) d\Xi_{(mn)} \tag{3.49}$$

The boundary conditions for C_1 can be found by averaging Equation (3.36) over the positions of all sinks except the *n*-th one,

$$C_1^{(n)}(\boldsymbol{r}_n^s) = C_n^{th}(\gamma_n)\,. \tag{3.50}$$

A second boundary condition should be defined far from the sink (for a local sink it can be considered as a boundary condition at infinity). In general, the only limitation on this boundary condition is the requirement of C_1 boundedness. To be more specific, it is possible to impose a heuristic "concentration locality principle", postulating that any sink *n* contributes to the concentration field *c* only at distances not exceeding some "extinction length" λ_n from the sink, while its contribution to *c* quickly vanishes as $|\boldsymbol{r}\text{-}\boldsymbol{r}_n|/\lambda_n \to \infty$. This principle is physically reasonable and usually can be justified *a posteriori* [125,126,130]. An immediate consequence of the locality principle is that the *n*-th sink contributes to the concentration in a matrix point $\boldsymbol{r}$ only provided it is located at distances within λ_n from this point. It is easy to show [130] that the "concentration locality principle" is equivalent to the requirement

$$C_1^{(n)}(\boldsymbol{r} \to \infty) \to C_0\,, \tag{3.51}$$

with the restriction on C_0 that it should remain finite everywhere in the studied volume.

According to Equation (3.47), in order to find the first concentration moments $C_1^{(n)}$, one must know the second concentration moments $C_2^{(mn)}$ for all sink pairs including sink *n*. Averaging Equation (3.38) over the parameters of all sinks except two fixed ones gives a set of equation that depends on the third concentration moments and so on. Eventually

one gets a hierarchy of equations, where in order to determine the concentration moment C_k in a point $\boldsymbol{r}$ in the matrix encompassing k fixed sinks one needs to know the concentration moments C_{k+1} for all systems, consisting of these sinks plus one more "probe" sink. Since the application of statistical treatment is reasonable only in the case when $N \gg 1$, the total number of equations in the hierarchy, though finite, is extremely large. However, the hierarchy can be truncated at any fixed value of k invoking physical arguments and using standard methods of equation hierarchy uncoupling in statistical physics [124].

For example, having in mind the concentration locality principle, it may be shown that far from any pair of sinks the concentration moment C_2 tends to the average concentration C_0. This can be reformulated in a way that the concentration deviation near the sink pair, $\delta_2 = C_0 - C_2$ is non-zero only at finite distances form sinks. Moreover, when sinks are separated by a distance largely exceeding the extinction length, the deviation δ_2 in the vicinity of each sink should not be very different from δ_1. Both these requirements can be satisfied approximating $\delta_2^{(mn)}(\boldsymbol{r}|\,\xi_n,\xi_m)$ for an arbitrary pair (n,m) of sinks with a sum of local concentration deviations $\delta_1^{(n)}(\boldsymbol{r}|\,\xi_n)$ and $\delta_1^{(m)}(\boldsymbol{r}|\,\xi_m)$, or, equivalently,

$$C_2^{(nm)}(\boldsymbol{r}\,|\,\xi_n,\xi_m) = C_1^{(n)}(\boldsymbol{r}\,|\,\xi_n) + C_1^{(m)}(\boldsymbol{r}\,|\,\xi_m) - C_0(\boldsymbol{r}). \tag{3.52}$$

This relation constitutes the "mean-field" approximation for the concentration moments. Its substitution into $I_2^{(m|n)}$ gives:

$$I_2^{(m|n)} \approx \Omega^{-1}\int d\gamma_m\, f_2^{(m|n)}(\boldsymbol{r},\gamma_m\,|\,\xi_n) J_1^{(m)}(\boldsymbol{r},\gamma_m) \tag{3.53}$$

where $J_1^{(n)}$ is given by (3.46) and depends on the first-order concentration moment. Hence, substitution of $I_2^{(m|n)}$ into (3.47) results in a closed-form equation set for $C_1^{(n)}$ (n = 1,...,N). These equations look out very similar to the equation for C_0. Indeed, the point defect loss efficiencies (3.43) and (3.48), entering equations for C_0 and C_1, respectively, differ only because of the difference between distribution functions $f_1^{(n)}$ and $f_2^{(m|n)}$. If all sinks were statistically independent (that is - their positions were completely uncorrelated), one would have

$$f_2^{(m|n)} = f_1^{(m)} \tag{3.54}$$

In reality, this assumption can never be strictly correct; sink positions cannot be completely uncorrelated because e.g. the overlapping of sinks is in any case prohibited. But close sink configurations should be very rare for a dilute system of randomly distributed sinks and the correlation can be neglected in the zero order approximation. When Equation (3.54) is valid, I2(m|n) = I1(n) and the following equations can be written down for the local concentration perturbations δ1(i) by combining Equations (3.42) and (3.47):

$$\frac{d\delta_1^{(n)}}{dt} = D\nabla^2\delta_1^{(n)}, \tag{3.55}$$

with the boundary conditions

$$\delta_1^{(n)}(\boldsymbol{r}_n^s) = C_n^{th} - C_0(\boldsymbol{r}_n^s) \qquad (3.56)$$

and

$$\delta_1^{(n)} \to 0 \qquad \text{far from the sink.}$$

The average point defect concentration C_0 does not vary much at the length scale of the order of sink size and in the boundary conditions we may replace the average concentration $C_0(\boldsymbol{r}_n^s)$, defined in the sink surface point $\boldsymbol{r}_n^s$, with its value $C_0(\boldsymbol{r}_n)$ in the sink position point $\boldsymbol{r}_n$. After this substitution it is possible to introduce a non-dimensional function $v_1^{(n)}$ via

$$\delta_1^{(n)} = \left[C_n^{th} - C_0(\boldsymbol{r}_n) \right] v_1^{(n)} \qquad (3.57)$$

and the equation for the average concentration C_0 is finally reduced to:

$$\frac{dC_0}{dt} = G + G^{th} + D\nabla^2 C_0 - k_0^2 D C_0 \qquad (3.58)$$

where G^{th} describes point defect emission from sinks,

$$G^{th} = \frac{D}{\Omega} \sum_{n=1}^{N} \int C_n^{th}(\gamma_n) f_1^{(n)}(\boldsymbol{r}, \gamma_n) j_1^{(n)}(\boldsymbol{r}, \gamma_n) d\gamma_n \qquad (3.59)$$

and k02 is the sink strength, defined as:

$$k_0^2 = \frac{1}{\Omega} \sum_{n=1}^{N} \int f_1^{(n)}(\boldsymbol{r}, \gamma_n) j_1^{(n)}(\boldsymbol{r}, \gamma_n) d\gamma_n , \qquad (3.60)$$

where

$$j_1^{(n)}(\boldsymbol{r}, \gamma_n) = -\int_{S_n} (\mathbf{e}^{(n)} \nabla v_1^{(n)}) \Big|_{\boldsymbol{r}_n = \boldsymbol{r}} dS \qquad (3.61)$$

and $v_1^{(n)}$ satisfies the boundary value problem

$$\frac{dv_1^{(n)}}{dt} = D\nabla^2 v_1^{(n)} , \qquad (3.62)$$

$$v_1^{(n)}(\boldsymbol{r}_n^s) = 1 \qquad (3.63)$$

and $v_1^{(n)} \to 0$ far from the sink. Equation (3.58) is the balance equation for the average point defect concentration in the matrix (see Equations (3.30) - (3.32)), while the set of equations (3.60) - (3.62) justifies the conventional procedure of sink strength calculation, as proposed in [122,123], where each sink is inserted into a "lossy" continuum with some average point defect concentration C_0 and the local deviations of concentration are found in the sink vicinity, to be used afterwards to find k_0^2.

As can be seen, the sink strength is a function of sink distribution and geometry only, but it does not depend on any parameters of material and irradiation, as is usually postulated. However, in contrast to the intuitive introduction of the sink strength as a spatially invariable value, k_0^2 in Equation (3.60) can depend on spatial positions of sinks (through the distribution function $f_1^{(n)}$) and thus the Laplace operator in Equation (3.58) cannot, generally, be omitted. Only when the distribution of sinks is uniform in space (that is $f_1^{(n)} = f_1^{(n)}(\xi_n)$), the sink strength k_0^2 and concentration C_0 are constant throughout the matrix.

While the sink strength in Equation (3.60) is defined as a sum over individual sinks, its calculation is considerably simplified by the fact that sinks in real physical systems belong to a limited number of different types, while all sinks of the same type are equivalent in terms of point defect absorption. Let us suppose that the material contains K different sink types, each comprising $N_p \gg 1$ individual sinks ($p = 1,...,K$), so that $\sum_p N_p = N$. Since all sinks of the same type are equivalent, the probability distribution function $f_N(\Xi)$ is symmetric with respect to the permutation of parameter sets ξ_n corresponding to sinks of the same type. Therefore both $f_1^{(n)}$ and Equation (3.61) for the point defect current are the same for all sinks of the same type. Hence, equation (3.60) for the sink strength can be re-written as a sum over different sink types:

$$k_0^2 = \sum_{p=1}^{K} n_p k_p^2, \tag{3.64}$$

where

$$k_p^2 = \int f_1^{(p)}(\mathbf{r}, \gamma_p)\, j_1^{(p)}(\mathbf{r}, \gamma_p) d\gamma_p \tag{3.65}$$

and $n_p = N_p/\Omega$ is the average concentration of p-type sinks in a unit volume of material. That is, in agreement with the standard rate theory formulations, the total sink strength is a sum of sink strengths for all sink classes in a material, and thus only K boundary-value problems of the type (3.60) - (3.62) should be solved in order to find the total sink strength.

Similarly, equation (3.59) can be rewritten as:

$$G^{th} = D \sum_{p=1}^{K} n_p G_p^{th} \tag{3.66}$$

where

$$G_p^{th} = \int C_p^{th}(\gamma_p)\, f_1^{(p)}(\mathbf{r}, \gamma_p)\, j_1^{(p)}(\mathbf{r}, \gamma_p) d\gamma_p \tag{3.67}$$

In case, where the thermal point defect concentration is not sensitive to parameters of a particular sink type, $G_p^{th} = k_p^2 C_p^{th}$.

Finally, let us discuss how to correlate the kinetic coefficients in the master equation (3.17) for void growth and the mean-field description of diffusion problem. As can be easily realised, the effective concentrations $C_{\alpha 0}$ in Equations (3.30) and (3.31) are essentially those corresponding to the mean field approximation and are obtained by the averaging over possible realisations of sink ensembles. Evidently, the kinetic coefficients should be obtained using the same approach from the growth equation for individual sinks. Let us demonstrate how this can be done using the simplest case of a spherical sink n growing due to the diffusional inflow of individual point defects. Let the sink radius be denoted as R_n. and the sink volume as V_n.

When an individual sink is a part of an ensemble of other sinks, the rate of its volume change can be described as:

$$\frac{dV_n}{dt} = 4\pi R_n^2 \beta \left(c(R_n + \lambda) - C_n^{th}(R_n) \right) \tag{3.68}$$

where c is the true concentration of point defects specified at a shortest distance λ from the sink surface (the 'last jump' separation) such that point defect can still be considered as an entity, β is the frequency of point defect jumps leading to their attachment to the sink surface and C_n^{th} is the concentration of point defects emitted from the sink. Usually one can take $\lambda \approx a$ (where a is the interatomic distance). In order to specify the rate of the fixed sink growth in the mean-field theory sense, one must average eq. (3.68) over all possible realisations of other sinks, thus obtaining

$$\frac{dV_n}{dt} = 4\pi R_n^2 \beta (C_1^{(n)}(R_n + \lambda) - C_n^{th}(R_n)) \tag{3.69}$$

which gives the kinetic coefficients p_n and q_n in the form:

$$p_n = 4\pi R_n^2 \beta C_1^{(n)}(R_n + \lambda) \quad \text{and} \quad q_n = 4\pi R_n^2 \beta C_n^{th}(R_n) \tag{3.70}$$

In order to specify the value of $C_1^{(n)}(R_n + \lambda)$, the continuity of the point defect current through the sphere with the radius $R_n+\lambda$ can be required,

$$-D \nabla c\big|_{r=R_n+\lambda} = \beta (c(R_n + \lambda) - C_n^{th}(R_n)) \tag{3.71}$$

After the averaging over the statistical realisations of sinks other than the considered one, one gets:

$$-D \nabla C_1^{(n)}\Big|_{r=R_n+\lambda} = \beta (C_1^{(n)}(R_n + \lambda) - C_n^{th}(R_n)) \tag{3.72}$$

In the mean-field approximation, $C_1^{(n)}$ can be expresses through a dimensionless function $v_1^{(n)}$ as

$$C_1^{(n)} = C_0 + (C_n^{th} - C_0) v_1^{(n)}$$

where $v_1^{(n)}$ satisfies eq. (3.62), but the boundary condition at the sink now looks like

$$D\nabla v_1^{(n)}\Big|_{r=R_n+\lambda} = \beta(v_1^{(n)}(R_n+\lambda)-1) \qquad (3.73)$$

Having in mind that the accommodation of point defect concentration profile near a sink occurs much faster than the change of the sink size [133], the time derivative in Equation (3.62) can be safely neglected. The steady-state version of Equation (3.62) satisfying boundary condition (3.73) and vanishing far from the sink can be easily solved [3,134], and after simple calculations p_n can be presented as:

$$p_n = 4\pi R_n^2[\beta C_n^{th} + \frac{D}{R_n + (D/\beta)}(C_0 - C_n^{th})] \qquad (3.74)$$

Writing down the 'last jump' rate β as:

$$\beta = \frac{D}{a}\exp(-E_n^S / k_B T)$$

where E_n^S is the energy barrier for the point defect absorption at the sink surface, k_B - the Boltzmann constant and T - the absolute temperature, eq. (3.74) can be reduced to

$$p_n = 4\pi R_n^2[\beta C_n^{th} + \frac{D}{R_n + a\exp(E_n^S / k_B T)}(C_0 - C_n^{th})] \qquad (3.75)$$

When the surface barrier for point defect absorption is high, i.e. $\exp(E_n^S / k_B T) >> R_n / a$, eq. (3.75) is reduced to:

$$p_n = 4\pi R_n^2 \beta C_0 \qquad (3.76)$$

This case is often referred to as "reaction limited" kinetics of point defect absorption by sinks. The rate of point defect capture at the sink surface is so slow that the point defect depletion in the vicinity of a sink does not form and a uniform average point defect concentration is kept in the volume enclosing the sink practically up to the sink surface. As a result, relation (3.76) resembles very much that used in the classical nucleation theory of a new phase [135-137]. The opposite case of $\exp(E_n^S / k_B T) << R_n / a$ corresponds to 'diffusion limited' kinetics because the sink volume change is limited by the diffusional transport of matter to the sink surface. In materials applied in nuclear power facilities the diffusion-limited case is commonly realised. In this case Equation (3.75) is reduced to:

$$p_n = 4\pi R_n^2[\beta C_n^{th} + \frac{D}{R_n}(C_0 - C_n^{th})] \qquad (3.77)$$

As can be easily checked, in the diffusion limited case the boundary condition (3.73) weakly differs from (3.63).

To conclude this section, it is worth mentioning that in the studies devoted to the modeling of cavity nucleation it is a common practice to write the kinetic coefficients p_n and q_n in the form

$$p_n = 4\pi R_n D C_0 \quad \text{and} \quad q_n = 4\pi R_n D C_n^{th} \tag{3.78}$$

This approximation for p_n is only valid when the cluster kinetics is dominated by the 'drag' term in the diffusion equation in the size space (e.g. by the first derivative term in the r.h.s. of Fokker-Planck equation (3.19)).

3.4. The early stage of void development (nucleation stage)

Investigations of the void nucleation based on either the master equation (3.17) or partial differential Equation (3.19) were started in [118,119], where the first of two principal improvements of the classical nucleation theory were introduced. That is, it was taken into account that although voids are purely vacancy clusters, both vacancies and interstitials contribute to their kinetics (see Equation (3.18)). It took more time and efforts to realise that the kinetic coefficients for both interstitials and vacancies should be determined in the framework of the mean-field theory because the spatially uniform concentration of monomers used in the master equation approach is not the real concentration of point defects, which is depleted in the vicinity of immobile sinks (e.g. [138-140]).

Even with rather strong simplifications involved in the formulation of the master equation (3.17), its direct solution with analytical methods is impossible, while numerical integration of cluster equations requires powerful computers because of the large number of equations needed to describe clusters of reasonable sizes. For instance, a void of only 2 nm in diameter, the smallest size reliably identified in transmission electron microscopes, contains ~ 500 vacancies, while for realistic void sizes of tens of nanometers, the number of vacancies reaches hundreds of thousands). The only case, where the solution can be obtained in analytic form is the "steady state" one, where the time derivative vanishes in the master equation [117]. Non-steady-state systems are comprehensively described only for very special forms of cluster size dependence of absorption and desorption kinetic coefficients [117], while for the time-dependent master equation only approximate models at different levels of sophistication are available in the literature (a good review can be found e.g. in [141]).

The true steady-state distribution function implies the fulfillment of the detailed balance condition [142],

$$P_{n-1} f_{n-1} = Q_n f_n \,, \tag{3.79}$$

which uniquely defines the "equilibrium" distribution function as:

$$f_n^e = f_1 \prod_{m=2}^{n} \left(\frac{P_{m-1}}{Q_m} \right) = f_1 \exp\left[\sum_{m=2}^{n} \ln\left(\frac{P_{m-1}}{Q_m} \right) \right] \tag{3.80}$$

provided all generation terms G_n in Equation (3.17) vanish. One should have in mind, however, that this function provides only a formal solution of the "steady-state" master equation and can be reached in a physical system if f_1 is maintained at a constant level and the equilibrium function vanishes as n tends to infinity. The latter implies that P_n/Q_n <1 is satisfied at all n above some finite value n*. For example, when neither the attachment, nor detachment rate depend on the cluster size (that is $P_n = P$ and $Q_n = Q$),

$$f_n^e == A \exp\left[n \ln\left(\frac{P}{Q} \right) \right], \tag{3.81}$$

and the “equilibrium” distribution function does not diverge at $n \to \infty$ only provided $P < Q$.

Let us thus discuss how the ratio P_n/Q_n depends on the void size for the irradiation conditions. Having in mind relations (3.70) and (3.74), this ratio is written down as:

$$\frac{P_n}{Q_n} = 1 + \frac{1}{\beta_V (R_n + D_V/\beta_V)} \frac{D_V (C_{V0} - C_{nV}^{th})}{D_V C_{nV}^{th}} - \frac{1}{\beta_V (R_n + D_I/\beta_I)} \frac{D_I C_{I0}}{D_V C_{nV}^{th}} \tag{3.82}$$

where all parameters referring to particular defect types are now marked with relevant subscripts. In the case of diffusion limited point defect absorption ($D_\alpha/\beta_\alpha \approx a << R_n$) this equation is reduced to

$$\frac{P_n}{Q_n} = 1 + \frac{a}{R_n} \frac{D_V (C_{V0} - C_{nV}^{th}) - D_I C_{I0}}{D_V C_{nV}^{th}} \tag{3.83}$$

It can be seen that the sign of the difference P_n/Q_n -1 is determined by the net currents of vacancies and interstitials into the void. In order to have $P_n > Q_n$, the following relation must hold,

$$D_V C_{V0} - D_I C_{I0} > D_V C_{nV}^{th} \tag{3.84}$$

The equilibrium concentration at the void surface is defined as:

$$C_{nV}^{th} = C_{V0}^{th} \exp(-E_{nV}^b / k_B T) \tag{3.85}$$

where E_{nV}^{b} is the energy of vacancy binding to a void with n vacancies. For large voids (where the concept of the surface tension can be introduced) E_{nV}^{b} can be approximated as:

$$E_{nV}^{b} \approx \frac{2\gamma^{s}\omega}{R_n} \tag{3.86}$$

where γ^s is the surface energy density. The typical value of γ^s in metals is ~1 J/m^2 so that for a typical temperature T ~ 300ºC in the nuclear reactor core during reactor operation, one gets:

$$R^{s} = \frac{2\gamma^{s}\omega}{k_B T} \approx 7 \text{ nm}$$

For voids of only several nanometers in size, the approximation (3.86) is a bad one; for clusters of several vacancies the typical values of E_{nV}^{b} are of the order of some tenths of electron-Volt, while extrapolation of (3.86) to $R_n \sim a$ would give $E_{nV}^{b} \approx 1.5$ eV and the ratio $C_{nV}^{th} / C_{V0}^{th}$ would exceed unity too much. Hence it is a common practice to replace relation (3.85) with a linearised form (Gibbs-Thomson relation)

$$C_{nV}^{th} \approx C_{V0}^{th}\left(1+\frac{R^{s}}{R_n}\right) \tag{3.87}$$

in spite of the fact that is strictly applicable only for voids with $R_n >> R^s$. Substituting (3.87) into (3.84), it is easy to show that a void absorbs more vacancies than interstitials (in other words, grows), only provided $D_V C_{V0} > D_I C_{I0}$ and the void radius exceeds the critical value R^*, equal to:

$$R^{*} = R^{s}\frac{D_V C_{nV}^{th}}{D_V C_{V0} - D_I C_{I0}} \tag{3.88}$$

In other words, in the case of void nucleation one meets the situation when $P_n < Q_n$ for $n < n^* = 4\pi(R^*)^3/\omega$ and $P_n > Q_n$ otherwise. This mode of cluster nucleation is commonly referred to as the 'barrier-type' nucleation. The origin of this name becomes clear, if one rewrites eq. (3.80) as:

$$f_n^{e} = f_1 \exp\left(-\frac{\delta G_n}{k_B T}\right) \tag{3.89}$$

which is a known relation for a probability of a fluctuation that requires the change of Gibbs free energy δG_n, even though in our case the function

$$\delta G_n = -k_B T \sum_{m=2}^{n} \ln\left(\frac{P_{m-1}}{Q_m}\right) \tag{3.90}$$

can be treated as the free energy change only when one kind of monomers is active and the absorption of monomers on clusters is reaction-limited (i.e. when the conditions for thermal equilibrium are satisfied). In our case the dependence of δG_n on n looks qualitatively as shown in Figure 11(a), so the transition of a fluctuation into the supercritical region $n>n^*$ can be interpreted as the overcoming of a 'pseudo-thermodynamic' barrier.

Figure 11. (a) Qualitative dependence of δG_n on the cluster size n for barrier-type nucleation (b) schematic evolution of the distribution function $f_n(t)$ for different moments of time: curve 0 - equilibrium function, curves 1 and 2 - intermediate times ($t_2 > t_1$), 3 - distribution function corresponding to the steady-state current in the size space

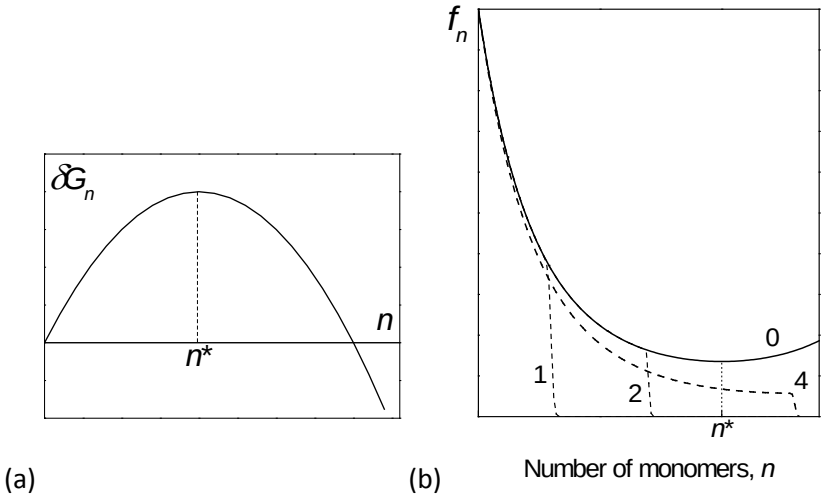

The 'equilibrium' cluster distribution function looks schematically as shown with curve 0 in Figure 11(b) and can never be achieved. However, when no clusters are initially present in the matrix, the qualitative behaviour of the cluster distribution function can be described as a gradual approximation to the equilibrium profile in the subcritical region (see curves 1 and 2 in Figure 11(b)) until the front of the distribution function reaches the critical size. Evidently, this takes a certain time (referred to as 'incubation time'), during which the clusters remain exclusively in the subcritical region and the cluster current into the region of stable growth is absent. As the front of the distribution function reaches the critical size, the clusters falling into the supercritical region do not require fluctuations to grow and thus do not return back into the subcritical region. Eventually there evolves a regime (called 'steady-state nucleation'), where the profile of the distribution function in the subcritical region corresponds to a constant cluster current in the size space, that is

$$P_{n-1} f_{n-1} - Q_n f_n = I_0 = \text{ const} \qquad (3.91)$$

for all cluster sizes from $n = 2$ up to the distribution function front position $n_m > n^*$. At the front the following relation holds

$$P_{n_m} f_{n_m} = I_0 \qquad (3.92)$$

Equations (3.91) and (3.92) are easily solved, giving:

$$I_0 = \frac{P_1 f_1}{1 + \sum_{n=2}^{n_m} \exp\left(\frac{\delta G_m}{k_B T}\right)} \tag{3.93}$$

where δG_n is specified by Equation (3.90). The sum in the denominator is usually approximated with an integral, which is evaluated by the saddle point method, giving

$$I_0 \approx \sqrt{\frac{|\delta G_{n^*}^{''}|}{2\pi k_B T}} P_1 f_1 \exp\left(-\frac{\delta G_{n^*}}{k_B T}\right) \tag{3.94}$$

where $\delta G_{n^*}^{''}$ denotes the second derivative of δG_n in the point $n = n^*$. As can be noticed, I_0 is insensitive to the exact position of the distribution function front and is completely determined by the behaviour of δG_n at the critical size.

As more and more voids overcome the critical size, the average concentrations of point defects gradually fall down, thus increasing the critical radius for void nucleation. As a result, the void nucleation eventually terminates because of the sharp increase of δG_{n^*} and the void system development reaches the stage where all already formed voids grow.

In order to estimate the critical void size according to Equation (3.88), one must know concentrations $C_{\alpha 0}$. Neglecting for simplicity the time derivative of point defect concentrations and the point defect recombination (which is only important at low temperatures, where voids do not nucleate), one gets from Equations (3.30) and (3.31)

$$D_V C_{V0} = \frac{G + k_{cV}^2 D_V \bar{C}_{cV}^{th} + k_V^2 D_V C_{V0}^{th}}{(k_{cV}^2 + k_V^2)} \tag{3.95}$$

and

$$D_I C_{I0} = \frac{G}{(k_{cI}^2 + k_I^2)} \tag{3.96}$$

So that

$$\frac{P_n}{Q_n} - 1 = \frac{a}{R_n}\left[\frac{G}{D_V C_{nV}^{th}}\left(\frac{1}{(k_{cV}^2 + k_V^2)} - \frac{1}{(k_{cI}^2 + k_I^2)}\right) + \left(\frac{k_{cV}^2 \bar{C}_{cV}^{th} + k_V^2 C_{V0}^{th}}{(k_{cV}^2 + k_V^2) C_{nV}^{th}} - 1\right)\right] \tag{3.97}$$

For the practically relevant case of diffusion controlled point defect absorption, the factor $k_{n\alpha}^2$ in eq. (3.28) is given by $k_{n\alpha}^2 = 4\pi R_n$, while for the total sink strength of the cavity ensemble one gets $k_{c\alpha}^2 = 4\pi N_c \bar{R}$, where $\bar{R}$ is the average void radius (the line over a value means its averaging over the void ensemble).

If the void sink strength is the same for both interstitials and vacancies, eq. (3.97) can be reduced to

$$\frac{P_n}{Q_n} - 1 = \frac{a}{R_n D_V C_{nV}^{th}} \left[\frac{(k_I^2 - k_V^2)G}{(4\pi N_c \bar{R} + k_V^2)(4\pi N_c \bar{R} + k_I^2)} - D_V C_{nV}^{th} \frac{R^s}{R_n} \left(1 - \frac{4\pi N_c R_n}{4\pi N_c \bar{R} + k_V^2} \right) \right] \qquad (3.98)$$

where approximation (3.87) for C_{nV}^{th} is adopted. As can be easily checked, the second term in the brackets can be positive only for very large voids (much larger than the average size). So, small voids can grow only when the first term in (3.98) is positive, which physically means that more radiation produced vacancies that interstitials are captured by voids in a unit time.

The rate equation derivation described in sect. 3.3 did not differentiate between interstitials and vacancies, implying that $k_I^2 - k_V^2 = 0.$ To make the sink strengths depend on particular types of point defects, one should take into account that the diffusion of point defects to individual sinks takes place in the stress fields existing in their vicinity. The account of the local stress fields modifies the equations for the first concentration moment $C_1^{(n)}$ [130,131] so that they become sensitive to the particular defect type. Without going into detail, the sink strength of an individual spherical void that takes into account the effects of stresses on the point defect diffusion can be written down as

$$k_{n\alpha}^2 = 4\pi R_n (1 + Y_\alpha(R_n)) \qquad (3.99)$$

where the correction Y_α depends on the particular mechanism of point defect interaction with the stress field of a cavity. In the literature one can meet the expressions for Y_α describing the effect of elastic modulus (MD) interaction of point defects with the stress field [143], the image (IM) interaction of point defects with the cavity surface [144], and the influence of the anisotropy of elastic fields near a cavity on the point defect energies in either equilibrium positions (EA) [145,146] or in the saddle points of diffusion jumps (DA) [147]. The largest values of Y_α and the slowest decrease law, $Y_\alpha = R_\alpha/R_n$, are predicted for the image interaction and the effect of stress on the diffusion barriers ('elastodiffusion'), (Figure 12). In particular, one gets for the image interaction mechanism:

$$R_\alpha^{IM} \approx \frac{a}{3} \left(\frac{\mu\omega}{k_B T} \right)^{1/3} e_{\alpha 0}^{2/3}$$

and for the elastodiffusion mechanism:

$$R_\alpha^{da} \approx q_\alpha R^s$$

where the typical values of q_α are q_V = -0.05 for vacancies and q_I = 0.05 for interstitial atoms [147].

Figure 12. Estimated void bias factors in α-iron and copper as functions of void radius for various models, as specified by the keys at the curves (the keys are explained in the text)

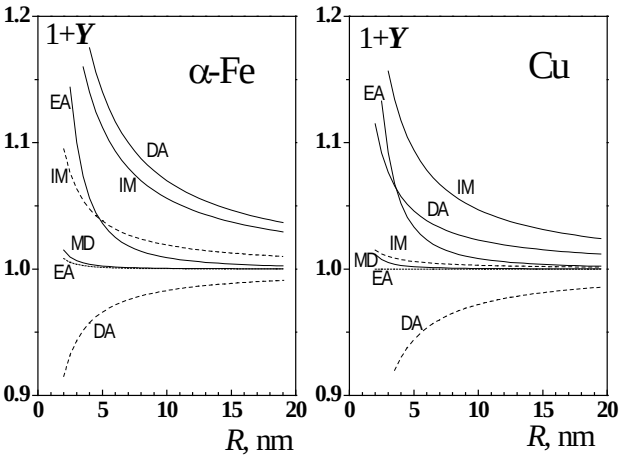

Solid lines correspond to interstitials and dashed lines - to vacancies. [147].

In the case of dislocations, the sink strength $k_{d\alpha}^2$ can be written down as

$$k_{d\alpha}^2 = Z_\alpha \rho_d \qquad (3.100)$$

where ρ_d is the dislocation density and the factors Z_α (usually referred to as dislocation bias factors) differ for vacancies and interstitials because of the effect of dislocation elastic fields on the point defect diffusion in the vicinity of dislocations. The most commonly used relation for dislocation bias factor is [148]

$$Z_\alpha = 2\pi \ln^{-1}(R_d / R_{d\alpha}) \qquad (3.101)$$

where $R_d = (\pi\rho_d)^{-1/2}$ and $R_{d\alpha}$ are some parameters with the dimension of length (elastic interaction radii), which are determined by a particular mechanism of interaction between point defects and the elastic field of dislocations. The typical values of dislocation bias factors are $Z_\alpha \approx 3$. Similar to voids, the point defect modulus effect [149,150] and the elastodiffusion [151,152] are often considered as the reason for the difference between the values of R_{dI} and R_{dV}, though for both mechanisms $R_{dI} > R_{dV}$ and thus $Z_I > Z_V$. There exist also models [153-157] that take into account possible restrictions on the point defect capture at dislocation lines (similar to reaction-limited kinetics of point defect absorption by voids).

Having in mind eq. (3.100) and taking into account that at the void nucleation stage the sink strength of voids can be neglected as compared to that of other sinks, $4\pi N_c \overline{R} << k_\alpha^2$, relation (3.98) can be further reduced to:

$$\frac{P_n}{Q_n} - 1 \approx \frac{a}{R_n D_V C_{nV}^{th}} \left[\frac{B_d \rho_d G}{(\rho_d + k_0^2 / Z_I)(\rho_d + k_0^2 / Z_V)} - D_V C_{V0}^{th} \frac{R^s}{R_n} \right] \quad (3.102)$$

where it is assumed that dislocations are the only 'biased' sinks in the material (i.e. the corrections Y_α in the void bias factors are temporarily neglected), k_0^2 stands for the sink strength of all unbiased sinks other than voids (e.g. grain boundaries), and B_d is the dislocation bias, defined as:

$$B_d = \frac{Z_I - Z_V}{Z_I Z_V}$$

The value of B_d is usually relatively small (typically several percent). Nevertheless, dislocation bias is the crucial parameter in the theory of swelling because the preferential absorption of interstitials at dislocations is one of the most important factors that enable the nucleation of voids. For a long time it was considered as the only driving force for swelling, though in the early 1990-s an alternative mechanism leading to the unbalanced absorption of vacancies and interstitials on sinks (the so-called 'production bias') was suggested [158,159]. The latter mechanism is less universal than that described above, acting only in some metals (typically with bcc lattice) and only under cascade-producing irradiation, which generates not only single interstitials, but also highly mobile small interstitial clusters (glissile dislocation loops) [112,160,161]. The one-dimensional mode of loop diffusion not only modifies the interstitial bias factors for dislocations and voids [162,163], but also makes grain boundaries biased sinks with the preference for interstitial capture [164]. This mechanism is not considered here, however, in order not to make presentation too complicated.

Though the sign variation of the difference $(P_n - Q_n)/Q_n$ predicted by Equation (3.102) gives a key to the understanding of the qualitative features of void nucleation in irradiated metals (such as the existence of the nucleation time lag and the steady state rate of void nucleation for a limited time), it is currently believed that the treatment applied above to explain the sign change requires serious improvements in order to explain the experimental observations in quantitative terms. To make this clear, let us estimate the value of the critical radius for void growth, which at the early stages of void growth can be approximated with

$$R^* \approx R^s \frac{D_{V0} \exp(-Q_V / k_B T) \rho_d}{B_d G} \quad (3.103)$$

where D_{V0} is the prefactor of vacancy diffusion coefficient (~1 cm^2/s) and Q_V - the self-diffusion energy via vacancy mechanism. Using the typical values of $Q_V \approx 3$ eV, $B_d \approx 0.3$ and the standard parameters of in-reactor neutron irradiation, namely $G \approx 10^{-7}$ dpa/s,

$\rho_d \approx 10^{10}$ cm^{-2}, and $T \approx 300$ºC, one obtains $R^* \approx 10^{-8}$ R^c, which means that the vacancy emission even from the smallest vacancy clusters is absolutely negligible. In fact, the thermal emission of vacancies from voids can strongly counteract vacancy clustering for typical in-reactor irradiation fluxes only at temperatures exceeding ~ 500 – 600 ºC. Since, however, the void nucleation regime under irradiation resembles very much the "barrier-type" regime, there should be some other reasons for it.

One of such reasons may be the experimentally observed trend that the void nucleation starts only after the dislocation density in the material achieves a favorable value [12]. Indeed, the first term in the brackets in Equation (3.102) reaches maximum at a certain dislocation density ($\rho_d^* = k_0^2 / \sqrt{Z_I Z_V} \approx k_0^2 / 3$). At lower values of ρ_d the decrease of dislocation density decreases the misbalance of interstitial and vacancy absorption on dislocations, thus leading to the decrease of the single vacancy supersaturation in the matrix. On the contrary, at too large dislocation densities the vacancy supersaturation falls down because nearly all the vacancies are consumed by dislocations, leaving no free vacancies to be captured by void nuclei. One can thus expect that the nucleation of voids is especially efficient for dislocation densities comparable to ρ_d^*.

The latter statement is supported by an experiment dedicated to the evaluation of the dislocation density effect on the void nucleation in thin copper films irradiated with fast electrons in transmission electron microscope [10]. In TEM samples the main unbiased sinks are the film free surfaces, with the sink strength $k_0^2 \sim 5\times10^9$ cm^{-2} [165], which gives $\rho_d^* \sim 2\times10^9$ cm^{-2}. Indeed, the most efficient void nucleation was observed for dislocation densities of ~(2-3)$\times10^9$ cm^{-2}.

On the other hand, the barrier-type nucleation can be due the fact that, according to Equation (3.99), small voids are not neutral sinks for point defects but have preference for interstitial absorption. Taking into account the corrections to the void bias in the form $Y_\alpha = R_\alpha / R_n$ and neglecting the Gibbs-Thomson correction to the vacancy thermal emission from voids, one obtains instead of Equation (3.102) the relation

$$\frac{P_n}{Q_n} - 1 \approx \frac{aB_d \rho_d G}{R_n D_V C_{nV}^{th} (\rho_d + k_0^2 / Z_I)(\rho_d + k_0^2 / Z_V)} \left(1 - \frac{R_{IV}^*}{R_n}\right) \qquad (3.104)$$

with

$$R_{IV}^* = \frac{R_I Z_V - R_V Z_I}{(Z_I - Z_V)} \qquad (3.105)$$

Equation (3.104) has the same type of dependence on the void radius as Equation (3.102), but the critical radius R_{IV}^* is relatively weakly dependent on the temperature. Using the values for R_α for α-Fe and Cu from [147], one gets the estimates $R_{IV}^* \approx 0.9$ nm in α-Fe and $R_{IV}^* \approx 0.5$ nm in Cu. These values look very similar but one should not forget that they correspond to the numbers of vacancies in a critical nucleus of $n^* \sim 100$ and $n^* \sim 20$ in bcc α-Fe and FCC Cu, respectively. This is in agreement with the known trend

that it is much harder to create voids in BCC metals as compared to FCC ones. However, it is highly improbable that even twenty vacancies would collect in the same place purely fluctuatively. Hence it is believed that the nucleation of voids is usually promoted by impurities (first of all - gas atoms) that stabilise small vacancy clusters. Indeed, it is well known that voids do not form in copper unless it is contaminated with oxygen, helium or hydrogen [166,167].

3.5. Gas driven void nucleation

Helium atoms are known to be badly solvable in metals (the He solution energy constitutes typically several electron-Volts [168]) and are captured at the first empty space they are able to find. When accumulated in cavities, helium behaves as gas or even liquid; its pressure counteracts the surface tension and thus strongly suppresses the efficiency of thermal vacancy emission form cavities. The kinetics of cavity growth in the presence of helium atoms can be qualitatively understood, if we note that the relation (3.87) for the equilibrium vacancy concentration in the presence of helium atoms inside the cavity changes to

$$C_{nV}^{th} = C_{V0}^{th}\left(1 - \frac{(p - 2\gamma^s / R_n)\omega}{k_B T}\right) \tag{3.106}$$

where p is the pressure of gas atoms within the cavity. Hence the equation for the critical radius of a He-filled cavity (or He bubble) becomes

$$\frac{R^s}{R*} - \frac{p\omega}{k_b T} = \frac{D_V C_{V0} - D_I C_{I0}}{D_V C_{nV}^{th}} \tag{3.107}$$

Assuming the ideal gas law for He atoms, this relation can be reformulated as

$$\frac{R^s}{R^*} - \frac{3n_g}{4\pi(R^*)^3} = \ln\frac{D_V C_{V0} - D_I C_{I0}}{D_V C_{nV}^{th}} \tag{3.108}$$

where n_g is the number of He atoms in the cavity. This is a cubic equation with respect to R*, which at sufficiently small values of n_g has two positive roots, R_1^* and R_2^*. The larger root R_2^* is similar to the critical radius of a void in a sense that $P_n > Q_n$ for $R > R_2^*$ and $P_n < Q_n$ for $R_1^* < R < R_2^*$. However, at $R < R_1^*$ one has again $P_n > Q_n$, so that a He bubble with the radius less than R_1^* tends to grow. In other words R_1^* corresponds to the stable equilibrium cluster size and a cavity with the size $R_1^* < R < R_2^*$ can not dissolve completely, but rather stops shrinking on reaching the size R_1^*. Physically it is evident, the cavity shrinkage is strongly counteracted by the helium atoms contained in the cavity. Strictly speaking, the ideal gas approximation is not really a good one when dealing with He in very small bubbles, but the qualitative picture described above does not change when the He equation of state is replaced with a more realistic one (e.g. van der Waals or more sophisticated).

Possibly the most ostensive way to explain the kinetics of He-driven cavity nucleation is in terms of the pseudo-free energy function δG_n introduced with Equation (3.90). A schematic representation of this function at different numbers of gas atoms in the bubble is shown in Figure 13.

Figure 13. Schematic representation of the function δG_n versus cavity size n for different amounts of gas atoms n_g in the cavity. Curve 0 corresponds to $n_g = 0$, curve 1 - $0 < n_g < n_g^*$, curve 2 - $n_g = n_g^*$ and curve 3 - $n_g > n_g^*$

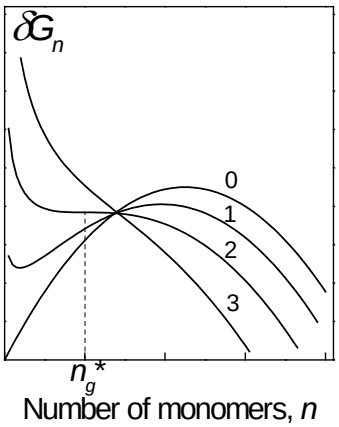

Let us assume that there are no vacancy clusters in the matrix prior to irradiation. While in the absence of He atoms the most probable fate of any fluctuatively created subcritical vacancy cluster is dissociation into separate vacancies, the capture of gas atoms stabilizes small clusters at the size R_1^* corresponding to the minimum of δG_n. As far as a cluster captures more He atoms, the equilibrium size R_1^* increases, and the size of the bubble follows R_1^*, being entirely determined by the number of gas atoms n_g contained in the cavity. At the same time, the second equilibrium size R_2^* falls down with the increase of n_g and at a certain number of gas atoms, n_g^*, the minimum and maximum on the δG_n function curve converge into a flex point. From this moment on, the growth of cavity does not require more gas atoms, the cavity grows at the expense of the vacancy excess in the irradiated material. As a result, the gas pressure in supercritical bubbles gradually decreases, while the bubble itself more and more resembles a void.

As more and more bubbles overcome the critical size, the excess vacancy supersaturation drops down, while the critical gas atom number n_g^* increases. The bubbles that had not managed to overcome the initial nucleation barrier remain forever at the size dictated by the available number of gas atoms in them. In other words, the gas-driven kinetics of void ensemble often results in a bi-modal distribution of cavities with sharply different sizes, that is - small gas bubbles and large voids with relatively low gas content inside [55-58,169].

In this chapter we restrict ourselves with this simple qualitative description of gas-driven cavity nucleation. More detailed qualitative discussion with appropriate referencing

of relevant papers can be found in [170], while for a detailed quantitative treatment the reader is referred to [171].

3.6. Swelling after the nucleation stage

After the termination of the void nucleation stage the number density of voids does not change and all nucleated voids continue to grow as long as the irradiation persists. The established concentration of voids is usually strongly temperature dependent; the higher is the temperature, the lower is the void number density (see Figure 2(a)).

Due to the fact that the number density N_c of voids does not change and all the voids are larger than the critical size ($n \geq n_{\min} > n^*$), the description of swelling is considerably simplified. First of all, the diffusion equation for the distribution function over void radii is reduced to that for deterministic growth,

$$\frac{\partial f_n}{\partial t} = J_{n-1} f_{n-1} - J_n f_n \tag{3.109}$$

or, in the differential form,

$$\frac{\partial f_n}{\partial t} = -\frac{\partial}{\partial n}(J_n f_n) \tag{3.110}$$

where Jn is the rate of the cluster growth,

$$J_n = P_n - Q_{n+1} > 0 \tag{3.111}$$

Substituting eq. (3.109) into (3.14), one immediately obtains

$$\dot{S} = \sum_{n=n_{\min}}^{\infty} J_n f_n = N_c \overline{J} \tag{3.112}$$

where $\overline{J}$ is the average rate of void growth.

For large voids one can forget about the size dependence of the void bias factors and neglect the dependence of the thermal vacancy concentration at the void surface on the void size, setting $C_{nV}^{th} = C_{V0}^{th}$. The rate of growth of an individual void is then given by

$$J_n = 4\pi R_n (D_V (C_{V0} - C_{V0}^{th}) - D_I C_I) \tag{3.113}$$

where we have used relations (3.70) and (3.77) for kinetic coefficients P_n and Q_n. Substitution of (3.113) into (3.112) gives

$$\dot{S} = 4\pi N_c \overline{R} (D_V (C_{V0} - C_{V0}^{th}) - D_I C_I) \tag{3.114}$$

As can be seen, the rate of swelling is determined by the growth kinetics of voids with the average size. So there is no need to know the exact form of the void size distribution function in order to find swelling rate after the termination of nucleation stage.

The growth of voids with the average radius $\overline{R}$ is evidently defined by equation

$$4\pi\bar{R}^2\frac{d\bar{R}}{dt} = J(\bar{R}) \qquad (3.115)$$

or, using expressions (3.95) and (3.96) for $C_{\alpha 0}$,

$$\frac{d\bar{R}}{d\Phi} = \frac{1}{\bar{R}}\frac{(Z_I - Z_V)\rho_d}{(4\pi N_c\bar{R} + k_V^2)(4\pi N_c\bar{R} + k_I^2)} \qquad (3.116)$$

where $\Phi = Gt$ is the irradiation dose. Equation (3.116) is easily integrated, especially if we neglect a small difference between the sink strengths of sinks other than voids and set $k_I^2 = k_V^2 = k^2$. The result is an implicit relation:

$$B(\frac{\bar{R}}{\bar{R}_k}) = B(\frac{\bar{R}_{nuc}}{\bar{R}_k}) + \frac{\Phi - \Phi_{nuc}}{\Phi_k} \qquad (3.117)$$

where B is a function of the form

$$B(x) = x^2(1 + \frac{4}{3}x + \frac{1}{2}x^2)$$

Φ_{nuc} is the dose at which the void nucleation stage terminates, $\bar{R}_{nuc}$ is the average radius of voids at this dose, $\bar{R}_k = k^2/4\pi N_c$ is the average radius of voids at which the sink strength of voids become the same as that of other sinks, and

$$\Phi_k = \frac{k^8}{2(Z_I - Z_V)\rho_d(4\pi N_c)^2}$$

Taking $k^2 = Z_I\rho_d$ and the typical parameter values $\rho_d \approx 10^{10}$ cm^{-2}, $N_c \approx 10^{15}$ cm^{-3}, $Z_I \approx 3$, and $(Z_I - Z_V)/Z_I = 0.3$, one gets $\bar{R}_k \approx 20$ nm and $\Phi_k \approx 0.3$ dpa. The dependence of the normalized swelling value $s = 3S/4\pi N_c\bar{R}_k^3$ on the normalised dose $\phi - \phi_{nuc} = (\Phi - \Phi_{nuc})/\Phi_k$ is shown in Figure 14.

Figure 14. The normalised swelling *s* as a function of the normalised dose $\phi - \phi_{nuc}$. Here $\phi_{nuc} = \Phi_{nuc}/\Phi_k$.

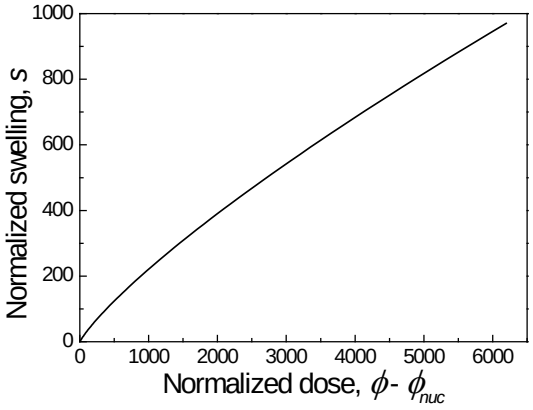

As can be seen, when the average void size falls in the range of $\overline{R} \le (1 \div 3)\overline{R}_k$, the average void size grows approximately as $\overline{R} \propto \Phi^{1/3}$, implying the constant swelling rate and thus corresponding to steady-state swelling. At the larger average void sizes the expected law of void growth is $\overline{R} \propto \Phi^{1/4}$, which means slow swelling deceleration, with $S \propto \Phi^{3/4}$. One should keep in mind, however, that already at $\overline{R} = 5\overline{R}_k \sim 50$ nm and the void number density of $N_c \approx 10^{15}$ cm^{-3} the swelling reaches ~ 100 %, which means that the voids occupy half of the whole material volume. In other words, the deceleration of swelling can take place only at quite noticeable swelling levels. With swelling at the levels of 100 % and higher the whole theory described above becomes poorly justified.

To conclude this section, it should be emphasised that only the basic picture of swelling at the steady state is outlined here. In practical situations the swelling behaviour can be more complicated and the parametric dependencies of the steady state swelling rate can be different from those presented.

3.7 Swelling without voids

Finally, an example of swelling which is not related to void formation is given. This kind of swelling is observed at low temperatures, when vacancies generated by irradiation are immobile and the only mobile defects are interstitials. The migration energy barriers for interstitials, E_{mI}, in metals are known to be generally very low (typically < 0.1 eV [5,109]) and interstitials are mobile down to temperatures well below room temperature. At such low temperatures radiation-produced vacancies are unable to agglomerate into voids and can only disappear via recombination with interstitials. However, interstitials can annihilate not only with vacancies, but also on network dislocations and on dislocation loops created as a result of interstitial clustering. Vacancies can compete with the dislocation structure as sinks for interstitials only provided their concentration is high enough. Comparing the interstitial loss terms on sinks and via recombination in eq. (3.31), it can be easily verified that to be competitive with other interstitial sinks, vacancies should have concentration at the level of

$$C_{V0} \approx \frac{k_I^2 D_I}{q_{IV}} \approx \frac{a^2 k_I^2}{z_{IV}} \sim (0.1 \div 1) \times 10^{-3}$$

where we have used the usual expression for recombination coefficient $q_{IV} = z_{IV} D_I / a^2$, where the prefactor is $z_{IV} \approx 2$ - 3 [172]. For the typical dislocation densities in the range of 10^{10}-10^{11} cm^{-2} this gives $C_{V0} \sim$ (0.1-1)$\times 10^{-2}$. On the other hand, for highly mobile interstitials only a very short time (parts of a second) is needed to establish extremely low quasi-steady state concentration C_{I0} as a balance between interstitial production by irradiation and annihilation at extended microstructural defects. Having this in mind and recalling eq. (3.6), one gets

$$S = (1 + e_V) C_{V0} \approx (0.8 \div 0.9) C_{V0} \qquad (3.118)$$

implying quite measurable swelling in materials with high dislocation densities (e.g. bcc metals).

Let us discuss the swelling kinetics in the case of low-temperature irradiation, assuming that the main microstructural components responsible for interstitial loss are network dislocations and irradiation produced dislocation loops. The loop number density N_l can be considered constant because it is known to saturate extremely quickly after the onset of irradiation [173-176]. The distribution of loops over sizes will be neglected and all loops will be supposed to have the same radius R_l that depends on irradiation time.

The rate theory equations (3.30) and (3.31) together with the dislocation loop growth equation can be written down as

$$\frac{dC_{\alpha 0}}{dt} = G - Z_\alpha (\rho_d + \rho_l) D_\alpha C_{\alpha 0} - z_{IV} D_I C_{I0} C_{V0} \qquad (3.119)$$

$$\frac{dR_l}{dt} = \frac{1}{b} [Z_I D_I C_{I0} - Z_V D_V C_{V0}] \qquad (3.120)$$

where $\rho_l = 2\pi N_l R_l$ is the dislocation density contained in loops, b - the value of Burgers vector of dislocation loops, and the bias factors for α-type point defects Z_α are assumed here to be the same for network dislocations and dislocation loops. The thermal vacancy concentration C_{V0}^{th} is omitted in these equations because at the temperatures of interest it is negligible. The initial conditions are taken in the form

$$C_{\alpha 0}(t = 0) = 0 \qquad (3.121)$$

$$R_l(t = 0) = 0 \qquad (3.122)$$

The set of equations (3.119)-(3.120) has an integral that represents, in fact, the law of matter conservation:

$$C_{I0} + b\rho_d R_l + \pi N_l b R_l^2 = C_{V0} \qquad (3.123)$$

With this relation in mind, equation (3.120) can be reduced to [177]:

$$\frac{dr}{dt} = \frac{1}{\tau_1}\frac{1}{(2r+r^2)} - \frac{1}{\tau_2}(2r+r^2) \qquad (3.124)$$

while the time dependence of swelling is given implicitly as

$$S = (1+e_V)S_c(r^2+2r) \qquad (3.125)$$

where $r = R_l/R_c$, $R_c = \rho_d/2\pi N_l$ is the loop radius, at which the sink strength of loops becomes equal to that of network dislocations, $S_c = \pi N_l b R_c^2$ is the total volume of loops with $R_l = R_c$, and the time constants are

$$\tau_1 = \frac{z_{IV}\rho_d^3}{8\pi^2 Z_I N_l^2 G} \quad \text{and} \quad \tau_2 = \frac{2}{Z_V D_{V0}\rho_d}$$

For typical values of dislocation densities ($\rho_d \sim 10^{10}$ cm^{-2}), loop volume densities ($N_l \sim 10^{15}$-10^{18} cm^{-3}), in-reactor point defect generation rate ($G = 10^{-7}$ dpa/s), $Z_\alpha \approx 3$, and $z_{IV} \approx 5/a^2$ one gets $R_c \approx 1.5$ nm, $S_c \approx 2.5\times10^{-5}$ and $\tau_1 \approx 4\times10^4$ s. The value of τ_2 is strongly temperature dependent; assuming e.g. the vacancy migration energy $E_{mV} = 1.2$ eV one obtains at room temperature $\tau_2 \approx 10^{10}$ s. In other words, the loop kinetics is mainly determined by the first term in the r.h.s. of eq. (3.124). So let us consider the loop growth kinetics and the related swelling at two time scales, namely $t << \tau_2$ and $t \sim \tau_2$.

At the early stage of loop growth ($t << \tau_2$) the second term in eq. (3.124) can be omitted and the equation is easily integrated to give

$$3r^2 + r^3 = \varphi \qquad (3.126)$$

where $\varphi = t/\tau_1$. When loops are small ($R \le R_c$) and point defects are absorbed mainly by dislocations, one gets $R \propto (Gt)^{1/2}$ (this type of dose dependence was observed e.g. in neutron irradiated annealed 316 SS [176]), whereas at $R \ge R_c$, when loops become principal sinks for interstitials, $R \propto (Gt)^{1/3}$, which is the loop growth low commonly observed at low temperatures [174,175]. Correspondingly, the dose dependence of swelling varies from $S \propto \varphi^{0.5}$ at $t << \tau_1$ to $S \propto \varphi^{2/3}$ at $\tau_1 << t << \tau_2$.

As t $\rightarrow \infty$, the average loop radius tends to a constant value r∞, defined by the equation (r∞2+2 r∞)2 = τ2/τ1. Taking into account that τ2/τ1 >> 1, one gets

$$R_\infty = r_\infty R_c = \left(\frac{Z_I}{\pi^2 z_{IV} Z_V}\right)^{1/4}\left(\frac{G}{D_V N_l^2}\right)^{1/4} \qquad (3.127)$$

or $R_\infty \approx 30$ nm for the selected set of parameters. Therefore, on the large time scale ($t \sim \tau_2$) it is more convenient to introduce another dimensionless loop radius, $r_1 = R/R_\infty$. Taking into account that $R_c/R_\infty << 1$, the solution of Equation (3.124) is given by the implicit equation [177]

$$\ln\left(\frac{1+r_1}{1-r_1}\right) - 2\arctan r_1 = \varphi_1 \qquad (3.128)$$

where $\varphi_1 = Gt/\Phi_\infty$ and $\Phi_\infty = G\tau_1^{1/4}\tau_2^{3/4}/4$ is the characteristic dose of swelling saturation. With the parameter values used above, $\Phi_\infty \approx 10$ dpa. The swelling value can be approximated by the dependence $S = S_\infty r_1^2$, which is plotted in Figure 15. The saturation swelling, S_∞, is given by:

$$S_\infty = (1+e_V)\pi N_l b R_\infty^2 = (1+e_V)\left(\frac{Z_I}{z_{IV}Z_V}\right)^{1/2}\left(\frac{Gb^2}{D_V}\right)^{1/2} \qquad (3.129)$$

With the parameters used above, $S_\infty \approx 5\%$.

Figure 15. Long-time swelling behaviour at low temperatures as a function of φ_1

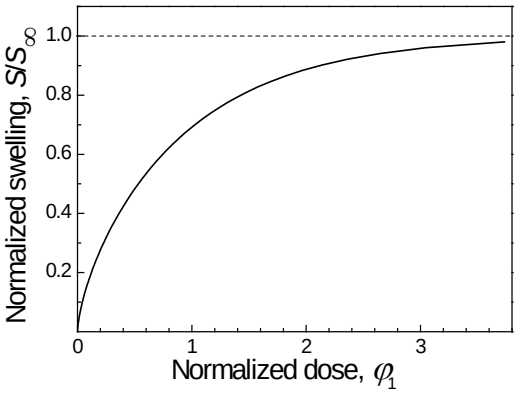

It can be seen that irradiation at sufficiently low homologous temperatures can cause quite noticeable, even though saturable swelling due to the accumulation of interstitials in dislocations and dislocation loops, while the immobile vacancies remain in the matrix. There is little doubt that the described kinetics of microstructural evolution is valid when applied to metals. Indeed, fast formation and subsequent growth of interstitial dislocation loops in metals even at low temperatures is well documented (see e.g. [176]). Also, the kinetics of loop growth predicted by the model correlates with experimental observations. Therefore, observation of low-temperature swelling in metals under proper conditions seems to be relatively easy. However, to our knowledge the only observation of low-temperature swelling was reported for molybdenum [62,178] (see Figure 2.6). The lack of observations may result from the fact that void-free swelling takes place at temperatures well below those relevant for material operation in nuclear reactors. Indeed, with the increase of irradiation temperature the non-void swelling becomes less pronounced and, at some threshold temperature, disappears completely. A simple estimate of the upper threshold temperature $T_{\max}$ for the observation of low temperature swelling can be done based on eq. (3.124), if one demands that at $T_{\max}$ even the smallest loops (with the relative radius of $r_0 \sim a/R_d$) do not grow,

$$k_B T_{\max} = \frac{E_{mV}}{2} \ln^{-1}(2r_0 + r_0^2) \approx \frac{E_{mV}}{30}$$

for the parameter values used above. For the majority of metals (EmV ~ 0.8-1.3 eV [5,109]) the threshold temperatures are quite low, Tmax ≈ 300-500 K. In fact, the temperatures where the swelling can become measurable should be well below Tmax. Interestingly, for molybdenum with EmV ~ 1.3-1.7 eV [6] the observed threshold temperature for the low-temperature swelling (~ 100°C [178]) is in reasonable agreement with this estimate. For comparison, the interstitial migration energy in Mo is very low, EmI ≈ 0.05-0.06 eV [179,180], so that the requirement of high interstitial mobility at such temperatures is satisfied.

At temperatures relevant for nuclear reactors, the effect of low-temperature swelling can be observed only in refractory metals with EmV ~ 2 eV (such as tungsten or tantalum [6]), which are of little interest for fission reactors. On the other hand, tungsten is currently considered as a potential material for fusion reactor applications. If vacancy-

mediated swelling will be indeed discovered for tungsten, it will add one more problem to using it as a structural material in reactor technologies.

While observations of low-temperature swelling are rare in metals, they are quite common for ceramic materials [181,182], for which temperatures as large as 1000 K still remain 'low' on homologous temperature scale. Even having in mind that the simple model outlined above should be applied to ceramics with a certain caution, it reproduces the kinetics of microstructural development and swelling remarkably well. The general character of microstructure development in ceramics resembles closely that of metals. Dislocation loops are observed in ceramics during low-temperature irradiation (see e.g. [181-184]). For example, loops constitute an important part of microstructure in SiC at low-temperature irradiation, whereas voids in this compound are found only at much higher temperatures [185]. Accumulation of vacancies in 6H SiC samples during fast electron, neutron and Xe+ irradiation at low temperatures was evidenced by positron annihilation [186], the dose dependence of this process being nearly independent of the type of fast particles. Because vacancies in ceramics, in contrast to metals, can be charged, they can be detected by luminescence measurements, which demonstrate e.g. the accumulation of carbon vacancies during neutron irradiation of SiC samples [187,188].

Observations in ceramics give additional credits to the model described above. For example, low-temperature swelling is shown to be completely eliminated by subsequent annealing at high temperatures (the effect was observed e.g. for neutron irradiated samples of SiC [188] and AlN [189]). Indeed, at high temperatures the bulk vacancies become mobile and are captured by dislocations and other sinks. Interestingly, the temperature dependencies of macroscopic volume and lattice parameter annealing are very similar [188], indicating that the volume shrinkage indeed occurs in parallel with the vacancy elimination.

References

[1] E.R. Gilbert, Reactor Technology 14, 258 (1971).

[2] D.I.R. Norris, Rad. Effects, 14, 1 (1972); ibid. 15, 1 (1972).

[3] L.K. Mansur, Nucl.Techn. 40, 5 (1978).

[4] J.R. Matthews, M.W. Finnis, J. Nucl. Mater. 159, 257 (1988).

[5] V.F. Zelenksyi, I.M. Neklyudov, T.P. Chernyaeva, Radiation Defects and Swelling of Metals (Naukova Dumka, Kiev, 1988) – in Russian.

[6] F.A. Garner, in: Materials Science and Technology: A Comprehensive Treatment, vol. 10A (VCH, Weinheim, 1994) p. 419.

[7] Comprehensive Nuclear Materials, Konings R.J.M. (ed.) (Elsevier, 2012)

[8] D. Blasl, H. Tsunakawa, K. Miyahara, N. Igata, J.Nucl.Mater. 133-134, 517 (1985).

[9] J.E. Harbottle, Philos. Mag. 27, 147 (1973).

[10] E. Kenik, T.E. Mitchell, Rad. Effects 24, 155 (1975).

[11] K. Kitajima, K. Futagami, E. Kuramoto, J. Nucl. Mater. 85-86, 725 (1979).

[12] F.A. Garner, [7], vol.4, p.33.

[13] M.Yu. Bredikhin, V.V. Bryk, V.N. Voevodin, I.M. Neklyudov, P.V. Platonov, in: Problems of Atomic Science and Technology. Series: Physics of Irradiation Damage and Radiation Study of Materials, No. 3 (17) (Kharkov, 1981) p. 56. (in Russian)

[14] F.A. Garner, D.S. Gelles, H. Takahashi, S. Ohnuki, H. Kinoshita, B.A. Loomis, J.Nucl. Mater. 191–194, 948 (1992).

[15] F.A. Garner, J. Nucl. Mater. 122-123, 459 (1984).

[16] J.A. Hudson, D.J. Mazey, R.S. Nelson, J. Nucl. Mater. 41, 241 (1971).

[17] D.J. Mazey, J.A. Hudson, R.S. Nelson, J. Nucl. Mater. 41, 257 (1971).

[18] G.L. Kulcinski, J.L. Brimhall, H.E. Kissinger, J. Nucl. Mater. 40, 166 (1971).

[19] J.L. Brimhall, G.L. Kulcinski, Rad. Effects 20, 25 (1973).

[20] E.A. Kenik, Scr. Met. 10, 733 (1976).

[21] J.P. Foster, R.V. Strain, W.G. Wolfer, Nucl. Eng. Des. 31, 117 (1973).

[22] H.J. Bergmann, W. Dietz, D. Haas, J. Nucl. Mater. 65, 224 (1977).

[23] H.J. Bergmann, D. Haas, K. Herschbach, in: Radiation Effects in Breeder Reactor Structural Materials. Proc.Int.Conf., Scottsdale, AZ, 1977 (Met. Soc. of AIME, 1977), p.241.

[24] W. Schneider, K. Herschbach, K. Ehrlich, in: Effects of Radiation on Materials, 11th Conf. ASTM STP 782, H.R. Brager and J.S. Perrin, Eds. (ASTM, Phil., 1982) p.30.

[25] E.R. Gilbert, B.A. Chin, Trans. ANS 28, 141 (1978).

[26] M.M. Paxton, B.A. Chin, E.R.Gilbert, J.Nucl.Mater. 95, 185 (1980).

[27] R.J. Puigh, E.R. Gilbert, B.A. Chin, in: Effects of Radiation on Materials, 11th Conf., ASTM STP 782, H.R. Brager and J.S. Perrin, Eds., (ASTM, Phil., 1982) p.108.

[28] B.A. Chin, R.J. Puigh, in: Effects of Radiation on Materials, 11th Conf., ASTM STP 782, H.R. Brager and J.S.Perrin, Eds., (ASTM, Phil., 1982) p.122.

[29] J.L. Boutard, Y. Carteret, R. Cauvin, Y. Guerin, A. Maillard, in: Dimensional Stability and Mechanical Behaviour of Irradiated Metals and Alloys. Proc. BNES Conf., vol.1 (BNES, London, 1984) p.109.

[30] J.F. Bates, R.W. Powell, E.R. Gilbert, in: Effects of Radiation on Materials, 10th Conf., ASTM STP 725 (ASTM, Phil., 1981) p.713.

[31] V.S. Neustroev, V.K. Shamardin, J. Nucl. Mater. 307-311, 343 (2002).

[32] S.R. MacEwen, V. Fidleris, J. Nucl. Mater. 65, 250 (1977).

[33] G.L. Wire, J.L. Straalsund, J. Nucl. Mater. 64, 254 (1977).

[34] B.A. Chin, J.L. Straalsund, G.L.Wire, J. Nucl. Mater. 75, 274 (1978).

[35] F.A. Garner, B.J. Makenas, S.A. Chastain, J. Nucl. Mater. 413, 53 (2011).

[36] D.L. Porter, F.A. Garner, HEDL-SA-3615 (1986).

[37] F.A.Garner, E.R.Gilbert, D.L.Porter, in: Effects of Radiation on Materials, 10th Conf., ASTM STP 725 (ASTM, Phil., 1981) p.680.

[38] G.L. McVay, R.E. Einziger, G.L. Hofman, L.C. Walters, J. Nucl. Mater. 78, 201 (1978).

[39] H.R. Brager, F.A. Garner, G.L. Gutrie, J. Nucl. Mater. 66, 301 (1977).

[40] F.A. Garner, D.L. Porter, B.J. Makenas, J. Nucl. Mater. 148, 279 (1987).

[41] K. Herschbach, H.J. Bergmann, J. Nucl. Mater. 175, 143 (1990).

[42] A. Uehira, S. Ukai, S. Mizuta, R.J. Puigh, in: Effects of Radiation on Materials: 20th Int.Symp., ASTM STP 1405 (ASTM, Phil., 2001), p. 487.

[43] E.R. Gilbert, F.A. Garner, J. Nucl. Mater. 367-370, 954 (2007).

[44] D.L. Porter, F.A. Garner, in: Influence of Radiation on Material Properties : 13th Int. Symp., part II. ASTM STP 956 (ASTM, Phil., 1988) p. 11.

[45] J.M. Dupouy, J. Erler, G. Allegrand, A. Bisson, P. Blanchard, M. Vouillon, J. Sagot, M. Weisz, in: Fuel and Fuel Elements for Fast Reactors, Proc.Symp.IAEA, vol.2. (IAEA, Vienna, 1974) p.253.

[46] D. Mosedale, D.R. Harries, J.A. Hudson, G.W. Lewthwaite, R.J. McElroy, in: Radiation Effects in Breeder Reactor Structural Materials. Proc.Int.Conf., Scottsdale, AZ, 1977 (Met. Soc. of AIME, 1977), p.209.

[47] R.J. Puigh, J. Nucl. Mater. 141-143, 954 (1986).

[48] J.M. Dupouy, J. Lehmann, J.L. Boutard, in: Reactor Materials Science (Moscow, 1978) p.280. (in Russian).

[49] K. Herschbach, J. Nucl. Mater. 127, 239 (1985).

[50] A.S. Kruglov, M.G. Bulkanov, V.N. Bykov, Yu.M. Pevchikh, Soviet Atomic Energy, 48, 266 (1980).

[51] F.A. Garner, M.B. Toloczko, J. Nucl. Mater. 251, 252 (1997).

[52] F.A. Garner, M.B. Toloczko, M.L. Grossbeck, J. Nucl. Mater. 258-263, 1718 (1998).

[53] J.E. Westmoreland, J.A. Sprague, F.A. Smidt Jr.,P.R. Malmberg, Rad. Effects 26, 1 (1975).

[54] D.J. Mazey, R. Bullough, A.D. Brailsford, J.Nucl.Mater. 62, 273 (1976).

[55] D.J. Mazey, R.S. Nelson, J. Nucl. Mater. 85-86, 671 (1979).

[56] N. Igata, A. Kohiyama, Y. Kohno, K. Suzuki, G. Ayrault, J. Nucl. Mater. 122-123, 214 (1984).

[57] A. Kohiyama, G. Ayrault, N. Igata, J. Nucl. Mater. 122-123, 224 (1984).

[58] M. Victoria, W.V. Green, B.N. Singh, T. Leffers, J. Nucl. Mater. 122-123, 737 (1984).

[59] W. Kesternich, J. Nucl. Mater. 78, 261 (1983).

[60] P.L. Lane, P.J. Goodhew, J. Nucl. Mater. 122-123, 509 (1984).

[61] H. Ullmaier, H. Trinkaus, Mater. Sci. Forum 97-99, 451 (1992).

[62] J.L. Brimhall, E.P. Simonen, H.E. Kissinger, J. Nucl. Mater. 48, 339 (1973).

[63] K.D. Closs, K. Hershbach, L. Schmidt, H. Van den Boorn, J. Nucl. Mater. 65, 244 (1977).

[64] T.C. Reiley, R.L. Auble, R.H. Shannon, J. Nucl. Mater. 90, 271 (1980).

[65] E.R. Gilbert, A.J. Lovell, in: Radiation Effects in Breeder Reactor Structural Materials. Proc.Int.Conf., Scottsdale, AZ, 1977 (Met. Soc. of AIME, 1977), p.269.

[66] J. Lehmann, J.M. Dupouy, H. Broudeur, J.L. Boutard, A. Maillard, in: Irradiation Behaviour of Metallic Materials for Fast Reactor Core Components, Proc.Int.Conf., Ajaccio, France, 1979, p.409.

[67] D.S. Gelles, R.J. Puigh, in: Effects of Radiation on Materials. 12th Int. Symp., ASTM STP 870, vol.1 (ASTM, Phil., 1985) p.19.

[68] R.J. Puigh, J. Nucl. Mater. 141-143, 954 (1986).

[69] P. Jung, H. Klein, J. Nucl. Mater. 159, 360 (1988).

[70] F.A. Garner, J. Nucl. Mater. 122, 459 (1984).

[71] F.A. Garner, E.R. Gilbert, D.S. Gelles, J.P. Foster, in: Effects of Radiation on Materials, 10th Conf., ASTM STP 725 (ASTM, Phil., 1981) p.665.

[72] E.S. Aitkhozhin, E.V. Chumakov, J. Nucl. Mater. 233-237, 537 (1996).

[73] A.R. Causey, C.K.C. Carpenter, S.R. MacEwen, J. Nucl. Mater. 90, 216 (1980).

[74] M.L.Grossbeck, L.L.Horton, L.K.Mansur, Trans. ANS 60, 295 (1989).

[75] M.L. Grossbeck, L.K. Mansur, J. Nucl. Mater. 179-181, 130 (1991).

[76] J. Ponsoye, Rad. Effects 8, 13 (1971).

[77] J.L. Pouchou, L. Zuppiroli, J. Ardonceau, J. Leteurtre, Rad. Effects 29, 225 (1976).

[78] L. Zuppiroli, J.L. Pouchou, A. Francois, J. Leteurtre, Y. Quere, Phil.Mag. 35, 853 (1977).

[79] J.F. Bates,E.R. Gilbert, J. Nucl. Mater. 59, 95 (1975).

[80] J.L. Boutard, G. Brun, J. Lehmann, J.L. Seran, J.M. Dupouy, in: Irradiation Behaviour of Metallic Materials for Fast Reactor Core Components. Proc.Int.Conf., Ajaccio, France, 1979, p. 137.

[81] K. Herschbach, W. Schneider, K. Ehrlich, J. Nucl. Mater. 101, 326 (1981).

[82] K. Herschbach, W. Schneider, H.J. Bergmann, in: Effects of Radiation on Materials: 14th Int. Symp., ASTM STP 1046, vol. 2 (ASTM, Phil., 1990) p.570.

[83] A.N. Vorobyev, N.I. Budylkin, E.G. Mironova, S.I. Porollo, Yu.V. Konobeev, F.A. Garner, J. Nucl. Mater. 258-263, 1618 (1998).

[84] S.Ya. Lebedev, V.G. Bagdinov, S.Ya.Surkov, Fiz. Met. Metallov. 54, 595 (1982).

[85] S.K. Khera, C. Schwaiger, H. Ullmaier, J. Nucl. Mater. 85-86, 299 (1979).

[86] K. Ehrlich, J.Nucl.Mater. 100, 149 (1981).

[87] D.L. Porter, M.L. Takata, E.L. Wood, J. Nucl. Mater. 116, 272 (1983).

[88] M.M. Hall Jr., J.E. Flinn, J. Nucl. Mater. 396, 119 (2010).

[89] I. Finnie, W.R. Heller, Creep of Engineering Materials (Mc Graw Hill, NY, 1959).

[90] V. Fidleris, J. Nucl. Mater. 159, 22 (1988).

[91] J. Nagakawa, Trans. Nat. Res. Inst. Met. 26, 183 (1984).

[92] J. Nagakawa, V.K. Sethi, A.P.L. Turner, J. Nucl. Mater. 104, 1275 (1981).

[93] D. Mosedale, G.W. Lewthwaite, in: Creep Strength in Steel and High-temperature Alloys, Proc. of a meeting, Univ. of Sheffild, 20-22 Sept. 1972. The Metals Soc., 1974, p.169.

[94] S.D. Harkness, F.L. Yaggee, F.V. Nolfi, in: Irradiation Embrittlement and Creep in Fuel Cladding and Core Components (BNES, London, 1972) p.259.

[95] M.L. Grossbeck, J.A. Horak, J. Nucl. Mater. 155-157, 1001 (1988).

[96] M. Ando, M. Li, H. Tanigawa, M.L. Grossbeck, S. Kim, T. Sawai, K. Shiba, Y. Kohno, A. Kohyama, J. Nucl. Mater. 367–370 (2007) 122.

[97] J. Nagakawa, S. Uchio, Y. Murase, N. Yamamoto, K. Shiba, J.Nucl.Mater. 386-388, 264 (2009)

[98] P.L. Hendrick, A.G. Pieper, D.J.M. Michel, R.E. Surrat, A.L. Bement, in: Radiation Effects and Tritium Technology for Fusion Reactors, vol.2. CONF-750989, 1976, p.84.

[99] T.C. Reiley, R.L. Auble, R.H. Shannon, J. Nucl. Mater. 90, 271 (1980).

[100] P. Jung, J. Nucl. Mater. 113, 133 (1983).

[101] N. Kishimoto, H. Shiraishi, N. Yamamoto, J. Nucl. Mater. 155-157, 1014 (1988).

[102] J. Chen, P. Jung, J. Henry, Y. de Carlan, T. Sauvage, F. Duval, M.F. Barthe, W. Hoffelner, J. Nucl. Mater. 437, 432 (2013).

[103] R. Scholz, R. Mueller, J. Nucl. Mater. 233-237, 169 (1996).

[104] F.A. Nichols, Trans. ANS 12, 572 (1969).

[105] J.P. Foster, W.G. Wolfer, A. Biancheria, A. Boltax, in: Irradiation Embrittlement and Creep in Fuel Cladding and Core Components (BNES, London, 1972) p.273.

[106] A.R. Causey, J. Nucl. Mater. 54, 64 (1974).

[107] P. Jung, M.I. Ansari, J. Nucl. Mater. 138, 40 (1986).

[108] J.D. Eshelby, Solid State Physics, vol.3 (NY, 1956) p.79.

[109] H. Wollenberger, in: Physical Metallurgy, 3rd Edn. (Elsevier, Amsterdam, 1983) p.1140.

[110] D.T. Keating, A.N. Goland, J. Appl .Phys. 39, 6018 (1968).

[111] C.-C. Fu, J.D. Torre, F. Willaime, J.L. Bocquet, A. Barbu, Nature Mater. 4, 68 (2005).

[112] A.J.E. Foreman, W.J. Phytian, C.A. English, Philos. Mag. A 66, 671 (1992).

[113] B.D. Wirth, G.R. Odette, D. Maroudas, G.E. Lucas, J. Nucl. Mater. 244, 185 (1997).

[114] Yu.N. Osetsky, D.J. Bacon, A. Serra, Philos. Mag. Lett. 79, 273 (1999).

[115] Ya.E. Geruzin, M.A. Krivoglaz, Motion of macroscopic inclusions in solids (Metallurgia, Moscow 1971). (in Russian)

[116] L. Farkas, Z. Phys. Chem. 125, 239 (1927).

[117] C.W. Gardiner, Handbook of stochastic methods. Springer Series in Synergetics, vol. 13 (Springer, Berlin, 1983).

[118] J.L. Katz, H. Wiedersich, J. Chem. Phys. 55, 1414 (1971).

[119] K.C. Russel, Acta Met. 19, 753 (1971).

[120] H. Trinkaus, J. Nucl. Mater. 318, 234 (2003)

[121] M.F. Wehner, W.G. Wolfer, Philos. Mag. A 52, 189 (1985).

[122] A.D. Brailsford, R. Bullough, J. Nucl. Mater. 44, 121 (1972).

[123] A.D. Brailsford, R. Bullough, M.R. Hayns, J.Nucl.Mater. 60, 246 (1976).

[124] R. Balescu, Equilibrium and Non-Equilibrium Statistical Mechanics (Wiley-Interscience, New York, 1975).

[125] A.D. Brailsford, J. Nucl. Mater. 60, 257 (1976).

[126] B.U. Felderhof, J.M. Deutch, J. Chem. Phys. 64, 4551 (1976).

[127] H. Gurol, Trans. ANS 28, 196 (1978).

[128] A.D. Brailsford, R. Bullough, Phil. Trans. Roy. Soc. London 302, 78 (1981).

[129] J.A. Marqusee, J. Ross, J. Chem. Phys. 80, 536 (1984).

[130] V.A. Borodin, Physica A 211, 279 (1994).

[131] V.A. Borodin, M.G. Ganchenkova, in: Handbook of Theoretical and Computational Nanotechnology, Ch. 65, vol.5, M. Rieth and W. Schommers, Eds. (American Scientific, Stevenson Ranch, 2006) p.437.

[132] R. de Wit, J. Res. Nat. Bur. Stand. 77A, 49 (1973).

[133] A.M. Kosevich, Z.K. Saralidze, V.V. Slezov, Fizika Tvedogo Tela 9, 895 (1967). (in Russian)

[134] A.E. Volkov, Physica A 323, 336 (2003).

[135] M. Volmer, Kinetik der Phasenbildung (Dresden, 1939).

[136] J. Frenkel, Kinetic Theory of Liquids (Oxford Univ., Oxford, 1946).

[137] J.B. Zeldovich, Acta Physicochim. URSS 18, 1 (1943).

[138] U. Gösele, J. Nucl. Mater. 78, 83 (1978).

[139] D. Peak, J. W. Corbett, Rad. Effects 36, 197 (1978).

[140] S.T. Weidman, R.A. Johnson, J. Phys. Chem. Solids 49, 243 (1988).

[141] K.F. Kelton, A.L. Greer, C.V. Thompson, J. Chem. Phys. 79, 6261 (1983).

[142] R. Becker, W. Döring, Ann. Phys. 24, 719 (1935).

[143] W.G. Wolfer, M. Ashkin, J. Appl. Phys. 46, 547 (1974).

[144] W.G.Wolfer, in Fundamntal Aspects of Radiation Damage in Metals, vol.2 (US ERDA CONF-751/006, 1975) p. 812

[145] V.A. Borodin, V.M. Manichev, A.I.Ryazanov, Fiz. Met. Metalloved. 63, 435 (1987).

[146] A.I. Ryazanov, D.G. Sherstennikov, J. Nucl. Mater. 186, 33 (1991).

[147] V.A. Borodin, A.I. Ryazanov, C. Abromeit, J. Nucl. Mater. 210, 242 (1993).

[148] F.S. Ham, J. Appl. Phys. 30, 915 (1959).

[149] P.T. Heald, M.V. Speight, Acta Met. 23, 1389 (1975).

[150] W.G. Wolfer, M. Ashkin, J.Appl.Phys. 47, 791 (1976).

[151] B.C. Skinner, C.H. Woo, Phys. Rev. B 30, 3084 (1984).

[152] V.A. Borodin and A.I. Ryazanov, J. Nucl. Mater. 210, 258 (1994).

[153] R.W. Balluffi, Phys. Stat. Sol. 31, 443 (1969).

[154] A.D. Brailsford, R. Bullough, in: Vacancies'76 (Metals Society, London, 1977), p. 108.

[155] A.I. Ryazanov, V.A. Borodin, Rad. Effects 55, 157 (1981).

[156] V.V. Ivanov, V.M. Chernov, Soviet Atomic Energy 61, 1011 (1986); ibid 61, 1018 (1986).

[157] H. Kamiyama, H. Rafii-Tabar, Y. Kawazoe, H. Matsui, J. Nucl. Mater. 212-215, 231 (1994).

[158] C.H. Woo, B.N. Singh, Philos. Mag. A 65, 889 (1992).

[159] H. Trinkaus, B.N. Singh, A.J.E. Foreman, J. Nucl. Mater. 206, 200 (1993).

[160] A.J.E. Foreman, C.A. English, W.J. Phytian, Philos. Mag. A 66, 655 (1992)

[161] Yu.N. Osetsky, D.J. Bacon, Nucl. Instr.Meth. Phys.R es. B 202 31 (2003).

[162] V.A. Borodin, Phisica A 260, 467 (1998).

[163] A.V. Barashev, S.I. Golubov, H. Trinkaus, Phil. Mag. A 81, 2515 (2001).

[164] S.I. Golubov, B.N. Singh, H. Trinkaus, J. Nucl. Mater. 276, 78 (2000).

[165] F. Fortuna, V. A. Borodin, M.-O. Ruault, E. Oliviero, M. A. Kirk, Phys. Rev. B 84, 144118 (2011).

[166] J.S. Lally, P.G. Partridge, Phil. Mag. 13, 9 (1966).

[167] S.Z. Zinkle, W.G. Wolfer, G.L. Kulcinski, L.E. Seitzman, Phil. Mag. A 55, 127 (1987).

[168] H. Ullmaier , Nucl. Fusion 24, 1039 (1984).

[169] H.R. Brager, J.L. Straalsund, J. Nucl. Mater. 46, 134 (1973).

[170] L.K. Mansur, W.A. Coghlan, J.Nucl. Mater. 119, 1 (1983).

[171] V.I. Dubinko, J.Nucl. Mater. 225, 26 (1995).

[172] T. Leffers, B.N. Singh, J. Nucl. Mater. 91, 336 (1980).

[173] J.M. Makin, in: Electron Microscopy 1978, vol.3 (Toronto 1978) p.330.

[174] R. Nakai, C. Kinoshita, Y. Muroo, S. Kitajama, Philos. Mag. A 48, 215 (1984).

[175] Y. Satoh, C. Kinoshita, K. Nakai, J. Nucl. Mater. 179-181, 399 (1991).

[176] A. Kohyama, K. Asano, Y. Katoh, Y. Kohno, in: Effects of Radiation on Materials: 15th Int. Symp., ASTM STP 1125 (ASTM, Phil.,1992) p.1051.

[177] V.A. Borodin, A.I. Ryazanov, D.G. Sherstennikov, J. Nucl. Mater. 202, 169 (1993).

[178] J.L. Brimhall, H.E. Kissinger, G.L Kulcinski, in Radiation-induced Voids in Metals (USAEC Technical Information Center, Oak Ridge, 1972) p. 338.

[179] S. Okuda, J. Atom. Energy Soc. Jap. 17, 223 (1975).

[180] M. Kiritani, H. Takata, J. Nucl. Mater. 69-70, 277 (1978).

[181] M.S. Kovalchenko, V.V. Ogorodnikov, Yu.I. Rogovoy, A.G.Krainiy, Irradiation damage in refractory compounds (Atomizdat, Moscow, 1979). (in Russian)

[182] G.P. Pells, J.Nucl.Mater. 122-123, 1338 (1984).

[183] C.J. McHargue, P.S.Sklad, C.W.White, Nucl. Instr. Meth. B 46, 79 (1990).

[184] S.J. Zinkle, in: Effects of Radiation on Materials: 15th Int. Symp., ASTM STP 1125 (ASTM, Phil.,1992) p.749.

[185] R.P. Thorne, V.C. Howard, B. Hope, Proc. Brit. Ceram. Soc. 7, 449 (1967).

[186] A.I. Girka, A.D. Mokrushin, E.N. Mokhov, V.M. Osadchiev, S.V. Svirida, A.V. Shishkin, Sov. Phys. – JETP, 70, 322 (1990).

[187] Yu.A. Vodakov, G.A. Lomakin, E.N. Mokhov et al., Fiz. Tech. Poluprovodnikov 20, 2153 (1986).

[188] R.N. Kyutt, A.A. Lepneva, B.A. Lomakina, E.N. Mokhov, A.S. Tregubova, V.V. Tscheglov, G.F. Yuldashev, Fiz. Tv. Tela 30, 2606 (1988)..

[189] T. Yano, M. Tezuka, H. Myazaki, T. Iseki, J. Nucl. Mater. 191-194, 635 (1992).

Chapter 7.

Radiation induced creep

V.A. Borodin
National Research Centre "Kurchatov Institute", Kurchatov pl. 1, 123182, Russia
National Research Nuclear University "MEPhI", Kashirskoe sh. 31, 115409, Russia

Abstract

Whereas radiation induced swelling produces an isotropic expansion of a material, it is also possible for the material to expand (or contract) anisotropically as a result of the non-uniform arrangement of vacancies and interstitials in the material. This is what is termed radiation-induced creep. In addition reactor vessel structural materials subjected to stress may show enhanced creep as a result of weakening due to irradiation.

Radiation enhanced creep is usually associated with point defect interaction with loops and dislocations. In this chapter various continuum models are proposed based on the movement of dislocations. Dislocation climb is discussed in terms of point defect flux per unit dislocation length as well as stress-induced anisotropy of point defect diffusion. The stress-modified efficiency of point defect absorption by dislocations leads to mechanisms based on climb-controlled dislocation glide and a formula for the average glide distance in the presence of obstacles is given. Finally the relationship between creep and swelling is discussed in terms of the relative attraction of point defects into voids as opposed to dislocations.

1. Theoretical models of irradiation creep

1.1 Governing equations of irradiation creep

In contrast to swelling, the description of irradiation creep requires in a general case the use of the second-order strain tensor, ε_{ij}. Having in mind that the main reason for the material deformation is usually the movement of dislocations, the strain rate can be expressed in terms of dislocation velocities $\boldsymbol{V}$ as [1]

$$\dot{\varepsilon}_{ij} = \Omega^{-1} e_{imn} \int V_m t_n b_j dl, \qquad (1.1)$$

where $\boldsymbol{t}$ is a unit vector along the dislocation line, $\boldsymbol{b}$ is the Burgers vector of the dislocation, e_{imn} is the anti-symmetric Kronecker tensor and integration is along all dislocation lines in the material. Here and below a dot over a symbol means time derivative and the Einstein summation rule over repeated subscripts is implied as before.

In order to simplify this equation, let us introduce some simplifications regarding the nature of the dislocation structure. Let us assume, first of all, that network dislocations are of purely edge type and are straight, while dislocation loops are perfectly circular. Since contributions to the strain from network dislocations and from loops are additive, let us discuss them separately.

It is usually safe to assume that a straight dislocation moves as a whole with the same average velocity which, however, can depend on the dislocation orientation in the material. Usually the number K of possible dislocation orientations in a crystal is limited. Then the dislocation network contribution to the total creep rate can be reduced to

$$\dot{\varepsilon}_{ij}^{D} = e_{imn} \rho \left\langle V_m t_n b_j \right\rangle. \qquad (1.2)$$

The angular brackets for an arbitrary function F^k of dislocation orientation k ($1 < k < K$) mean here and below the averaging over dislocation orientations,

$$\left\langle F \right\rangle = \sum_{k=1}^{K} f^k F^k, \qquad (1.3)$$

with the weights $f^k = \rho_d^k / \rho_d$, where ρ_d^k is the density of dislocations with orientation k and ρ_d - the total network dislocation density in the sample.

Due to the symmetry reasons, the dislocation velocity is normal to the dislocation line direction $\boldsymbol{t}$. Having in mind that the Burgers vector of an edge dislocation is also normal to $\boldsymbol{t}$, we can write down $\boldsymbol{V}$ as a sum of two contributions:

$$\mathbf{V}^k = -V_c^k \mathbf{n}^k + V_g^k \hat{\mathbf{b}}^k, \qquad (1.4)$$

where $\hat{\mathbf{b}}^k = \mathbf{b}^k / b$, $\mathbf{n}^k = [\hat{\mathbf{b}}^k \times \mathbf{t}^k]$, b is the absolute value of the dislocation Burgers vector (assumed for simplicity to be independent of dislocation orientation), V_g^k is the velocity of dislocation parallel to the dislocation Burgers vector and V_c^k is the velocity of dislocation in the direction of its extra plane. The movement in the direction of the Burgers vector (called slide or glide) involves only the shift of dislocation extra-plane and occurs under the action of local shear stresses. On the contrary, the movement in the direction normal to the Burgers vector (climb) involves the dissolution or build-up of the

extra plane. The signs before the terms in the r.h.s. of eq. (4.4) are chosen so that $V_c > 0$, when the dislocation climbs by extra plane build-up, while $V_g > 0$ when the dislocation glides in the direction of the Burgers vector.

Substituting (4.4) into (4.2), one obtains (cf. [150,2]):

$$\dot{\varepsilon}_{ij}^{D} = \rho_d b \left\langle \hat{b}_i \hat{b}_j V_c \right\rangle + \frac{1}{2} \rho_d b \left\langle (\hat{b}_i n_j + n_i \hat{b}_j) V_g \right\rangle . \qquad (1.5)$$

According to Equation (4.5), one can consider contributions to creep rate from dislocation climb and glide as additive.

In contrast to network dislocations, interstitial loops can glide only under the action of shear stress gradients [3], which are seldom created in the irradiation creep experiments and, even if present, are not large enough to force the glide of the loops with the sizes of several tens to hundreds nanometers, which are of interest for the transient creep stage. Hence, the glide mode of dislocation loop movement is little relevant for irradiation creep. Strictly speaking, another movement mechanism is possible for very small (< 1 nm) perfect interstitial loops formed directly in collision cascades, as observed in Molecular Dynamics (MD) computer simulations [112-114,160,4,5]. This mechanism is very similar to glide, since it is one-dimensional and involves no absorption or desorption of point defects. However, small dislocation loops move in a stochastic manner even in the absence of external stresses and can contribute to irradiation creep in the case of cascade producing irradiation, which serves as a source of dislocation loops that operates over the whole experiment duration. However, here we do not consider this mechanism because up to now no discussion of the contribution of one-dimensionally moving small dislocation loops to irradiation creep are reported in the literature.

Similar to network dislocations, the number of possible loop orientations, M, is usually finite. In agreement with experimental data, one can assume that practically immediately after the onset of irradiation the volume number densities of loops attain the steady-state values, N_L^m ($1 < m < M$), and do not change until the loops grow very large, intersect with other dislocations and loops and incorporate into the dislocation network. Let us introduce for the loops with orientation m the distribution function over radii R at time t, $f_l^m(R,t)$, such that

$$\int f_l^m(R,t)dR = N_L^m / N_L ,$$

where N_L is the total volume density of loops. The loop contribution to the creep rate will then be given by

$$\dot{\varepsilon}_{ij}^{L} = 2\pi b \sum_{m=1}^{M} \hat{b}_i \hat{b}_j \int_0^{R_{\max}} f_l^m(R,t) V_l^m(R) R dR , \qquad (1.6)$$

where V_l^m is the loop growth rate. To simplify matters, one can assume that all loops of the same orientation have the same radius R^m. Then the contribution to the irradiation creep rate from the growing dislocation loops, $\dot{\varepsilon}_{ij}^{L}$, can be written down as

$$\dot{\varepsilon}_{ij}^{L} = 2\pi N_L b \left\langle \hat{b}_i \hat{b}_j R V_l \right\rangle , \qquad (1.7)$$

where the orientational average is performed similar to relation (4.3), but with the weight of $f^m = N_L^m / N_L$. As can be seen, two different reasons give rise to creep, namely the dislocation movement and the evolution of the dislocation structure, which includes both the variation of total dislocation density and the redistribution of dislocations over orientations.

It is convenient to discuss first the creep mechanisms associated with the dislocation movement, assuming that the dislocation structure is stabilized and consists predominantly of network dislocations, as appropriate to the steady-state creep stage. The effects of microstructure development on irradiation creep will be discussed later in sections dealing with the primary creep and the swelling-accelerated creep.

At the steady-state stage, the rate of irradiation creep is given by equation (1.5) and contains two terms, one of which is due to dislocation climb and another to dislocation glide. Let us consider these terms separately, starting from the climb mode of dislocation motion.

1.2 Steady-state irradiation creep: mechanisms based on dislocation climb

As follows from equation (4.5), the dislocation climb contribution to the creep rate is determined by the climb velocity V_c^k, which can be expressed in terms of point defect currents per unit dislocation length, $J_\alpha^k (\alpha = I,V)$ as

$$V_c^k = b^{-1}(J_I^k - J_V^k), \tag{1.8}$$

where the currents are given by:

$$J_\alpha^k = Z_\alpha^k D_\alpha (C_{\alpha 0} - C_{k\alpha}^{th}), \tag{1.9}$$

Z_α^k are the bias factors for dislocations with orientation k and $C_{\square\square}$ - the mean-field average concentrations of point defects (see Equation (3.41)). The mean-field balance equations for $C_{\square 0}$ is taken in this section in the form

$$G - \rho_d \langle J_\alpha \rangle - q_{IV} C_{I0} C_{V0} = 0. \tag{1.10}$$

Solving the set of equations (1.10) with the point defect currents given by eq. (1.9), one can re-write the dislocation velocity as:

$$V_c^k = V_{cT}^k + V_{cI}^k, \tag{1.11}$$

where V_{cT} is the thermal climb velocity arising due to the sensitivity of the equilibrium vacancy concentration to dislocation orientation:

$$V_{cT}^k = \frac{Z_V^k D_V}{b}\left(C_{kV}^{th} - \frac{< Z_V C_V^{th} >}{< Z_V >} \right), \tag{1.12}$$

and V_{cI} is the climb rate due to the effect of irradiation,

$$V_{cI}^k = \left(\frac{Z_I^k - < Z_I >}{< Z_I >} - \frac{Z_V^k - < Z_V >}{< Z_V >} \right) \frac{G}{b\rho_d} \Phi\left(\frac{G}{G_R} \right), \tag{1.13}$$

Where:

$$G_R = < Z_I >< Z_V > \frac{D_I D_V \rho_d^2}{4 q_{IV}}$$

and $\Phi(x) = 2/(1+\sqrt{1+x})$. The thermal contribution to the dislocation climb velocity can be omitted in the range of irradiation parameters where the creep rate is determined by irradiation and is not considered below.

The most important feature of equation (1.13) is the dependence of the climb rate on dislocation bias factors Z_α for vacancies and interstitials. The irradiation leads to dislocation climb only provided the external load leads in some way to the "double" asymmetry of point defect absorption by dislocations. First of all, dislocation bias factors should depend on dislocation orientation with respect to external loads and, second, this dependence should be different for vacancies and interstitials. In other words, in the absence of alternative point defect sinks, such as cavities, the climb of dislocations occurs exclusively through the unbalanced partitioning of interstitials and vacancies between dislocations differently oriented with respect to the external loads. Having in mind relation (2.3), we restrict ourselves below to the simplest loading scheme of uniaxial tension with the applied stress σ.

The climb-controlled contribution to the irradiation creep rate, $\dot{\varepsilon}_{ij}^I$, is obtained by straightforward substitution of equation (1.13) into the first term in the r.h.s. of equation (1.5):

$$\dot{\varepsilon}_{ij}^I = \left(\frac{< \hat{b}_i \hat{b}_j Z_I >}{< Z_I >} - \frac{< \hat{b}_i \hat{b}_j Z_V >}{< Z_V >} \right) G \Phi \left(\frac{G}{G_R} \right). \qquad (1.14)$$

Using this relation, it is possible to analyse the dependence of the steady-state irradiation creep on irradiation parameters even not knowing which particular microstructural mechanism is responsible for the stress-induced anisotropy of dislocation bias factors.

The dependence of in-reactor creep rate on the point defects generation rate G is markedly different for three temperature intervals. In the low-temperature region, where the point defect loss is mostly due to the direct recombination, $\dot{\varepsilon}_{ij}^I \propto \sqrt{G}$ (cf. [46,6,7]). At intermediate temperatures the creep rate is described by the usual linear law $\dot{\varepsilon}_{ij}^I \propto G$. Finally, in the high-temperature region the irradiation creep is negligible as compared to the thermal component of creep. It should be emphasised that such qualitative behaviour is quite general and is due exclusively to the variation of point defect annihilation regimes, but the transition temperatures T^* and T^{**} between the three temperature regions can be sensitive to details of point defect capture by sinks.

The irradiation creep dependence on the load intensity can also be obtained from quite general considerations. As long as the applied stress σ is sufficiently low, the bias factors $Z_\square$ can be expanded to the first order in σ (or, more conveniently, in dimensionless parameter σ/μ):

$$Z_\alpha^k = Z_\alpha^0\left(1+\delta_\alpha^k\frac{\sigma}{\mu}\right), \qquad (1.15)$$

where Z_α^0 is the stress-free value of the corresponding bias factor and δ_α^k is the first derivative of Z_α with respect to the normalised stress (σ/μ). Substitution of (4.15) into (4.14) gives

$$\dot{\varepsilon}_{ij}^I = B_{ij}\frac{\sigma}{\mu}G\Phi\left(\frac{G}{G_R}\right), \qquad (1.16)$$

where $B_{kl}$is the creep compliance (a tensor analog of the creep modulus) defined as

$$B_{ij} = \left\langle \hat{b}_i\hat{b}_j(\delta_I-\delta_V-<\delta_I-\delta_V>)\right\rangle. \qquad (1.17)$$

Relation (4.16) demonstrates that the in-reactor creep rate dependence on the applied stress at comparatively small stresses is universally described by a linear law and only the applicability range of this law (that is, the upper threshold stress σ*) depends on the particular mechanism ensuring the anisotropy of point defect absorption by dislocations.

When the bias factor anisotropy is due to the stress influence on the elastic interaction of point defects with dislocations, σ* is of the order of the elastic moduli of the material. Because so large stresses are well above the yield stress of reactor materials and are never used in creep experiments, the linear dependence of the creep rate on stress can be expected at any relevant stress. On the other hand, when bias factor modification is due to the stress effect on point defect energetics (e.g. diffusion barriers, energies of jog nucleation on dislocations, etc.), the critical stress is $\sigma^* \sim k_BT/\omega$, which gives for σ* the values of about several hundreds MPa at typical reactor temperatures of 300-600°C. It is interesting to note, that for many reactor structural materials these values are of the same order of magnitude as the yield stress.

The temperature dependence of irradiation creep rate is also little sensitive to the particular mechanism of dislocation bias modification by external stresses, being mostly determined by the temperature dependence of the function Φ entering equation (4.16). One generally meets two temperature ranges, separated by a certain temperature T*. At lower temperatures ($T < T$*) the basic mode of point defect annealing is their mutual recombination and the temperature dependence is dominated by the exponential term,

$$\dot{\varepsilon}_{ij}^I \propto \exp\left(-\frac{E_{mV}}{2k_BT}\right), \qquad (1.18)$$

where E_{mV} is the vacancy migration energy. On the contrary, at temperatures $T > T$*, where point defects are mostly absorbed by dislocations, Φ ≈ 1 and the temperature dependence of irradiation creep is that of the creep compliance, which is shown below to be relatively weak. Finally, at too high temperatures (above some threshold T**) the in-reactor creep rate is dominated by the thermal contribution, which is not of interest here. Hence, the subsequent discussion is restricted to temperatures below T**.

The transition temperature T* can be defined from the condition $G \sim G_R$, which gives

$$k_B T^* \approx E_{mV} \ln^{-1}\left[\frac{Z_I^0 Z_V^0 D_V D_I \rho_d^2}{4 q_{IV} G}\right]. \qquad (1.19)$$

An estimate of T^* at typical parameter values D_{V0} = 1 cm^2/s (where D_{V0} is the prefactor in the vacancy diffusion coefficient), $\rho_d = 3\times10^{10}$ cm^{-2}, $q_{IV} = 5D_I/a^2$, a = 0.3 nm, $Z_\alpha^0 \approx 3$, and $G \approx 10^{-7}$ dpa/s gives

$$k_B T^* \sim E_{mv}/40.$$

The vacancy migration energy is known to correlate with the material melting temperature T_m, falling as a rule within the range of (6.5 ÷ 8) $k_B T_m$ [8] and hence the homologous critical temperature is $T^*/T_m \sim$ 0.16-0.2.

It can thus be seen that the only factor in equation (4.16) which is really sensitive to the mechanism providing the 'double anisotropy' of dislocation bias factors is the creep compliance B_{ij}.

Three possible reasons for the dislocation bias factor modification by external stress, answering the necessary requirements, have been suggested in the literature, as already mentioned in Section 3.4. They are known under the generic name 'Stress-Induced Preferred Absorption' or SIPA mechanisms, though initially this name referred to only that based on the stress-induced elastic modulus anisotropy of point defect interaction with dislocations [149,150,9-11]. The other two mechanisms consider the effect of anisotropic external stresses on the point defect mobility ("elastodiffusion") [151,152,12-16] and on the efficiency of point defect accumulation in dislocation cores [155,18-20]. Let us discuss them here in more detail.

a. Stress-modified modulus interaction of point defects with dislocations

Historically, this was the first mechanism suggested in the literature. It treats point defects as spherical inclusions (isotropic centers of a dilatation) with elastic constants distinct from those of surrounding matrix. Strictly speaking, interstitials in metals have a dumbbell (or even crowdion) configuration and can hardly be considered as spherical objects, but for isotropic (or cubic) materials the model can still be acceptable, if one takes an average over possible interstitial orientations. The idea of the mechanism is that the external loading 'polarizes' point defects, (see Figure 1). As a result, the dislocations of different orientations with respect to the applied stress become non-equivalent in terms of their elastic interaction with polarised point defects.

Figure 1. A schematic representation of the stress induced bias in the point defect-dislocation interaction [149]

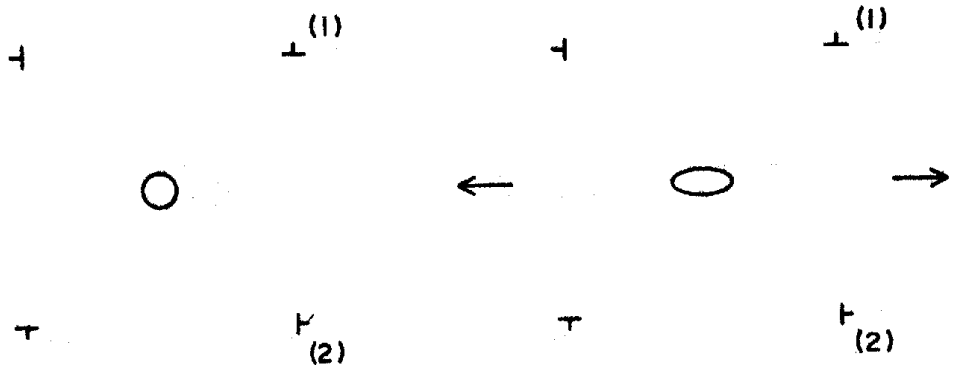

The energy of interaction of a polarised point defect with a k-type dislocation, U_α^k, looks like [11]:

$$U_\alpha^k = k_B T \frac{R_{d\alpha}^k}{r} \sin\theta, \qquad (1.20)$$

where r and θ are the polar coordinates related to the dislocation, and $R_{d\alpha}^k$ is the characteristic radius of dislocation interaction with point defects,

$$R_{d\alpha}^k = \frac{\mu\omega b}{\pi k_B T}\left(e_{\alpha 0} + p_\alpha^K \frac{\sigma}{E} + p_\alpha^\mu q^k \frac{\sigma}{\mu}\right), \qquad (1.21)$$

Here E is the Young modulus of the material, while p_α^K and p_α^μ are the factors, expressed either in terms of the bulk moduli (K, K_α) and shear moduli (μ, μ_α) of the matrix and the point defects of type α [11], or in terms of elastic polarisabilities of point defects P_α^K and P_α^μ [21]. The dependence of the interaction energy on the dislocation orientation is given by the factor q^k [22]:

$$q^k = 3\nu(\mathbf{t}^k\mathbf{s})^2 + 3(\hat{\mathbf{b}}^k\mathbf{s})^2 - (1+\nu), \qquad (1.22)$$

where $\boldsymbol{s}$ is the unit vector in the direction of applied load. As follows from relation (1.21), the anisotropy of dislocation interaction energy with point defects is due to the differences of shear moduli of point defects and the matrix.

Computer simulation of vacancy formation in α-Fe under the combined action of the external and dislocation stress fields [23] indicated no dependence of the vacancy formation energy on the stress direction. On the contrary, the dumbbell interstitial atoms that easily rotate on-site under the action of shear loads [24] are expected to be quite sensitive to the stress orientation. For the order of magnitude estimates one can usually assume $p^\mu_i \approx 0.5$ and $p^\mu_v = 0$ [10]. The estimate of p^μ_i and p^μ_v using the values for point defect polarisabilities in Al [25] also indicate that $p^\mu_i >> p^\mu_v$, though the values of p^μ_i are predicted to be one order of magnitude higher.

At the experimentally relevant temperatures the relation $r_0 << R_{d\alpha}^k << R_d$ holds, where r_0 is the radius of a dislocation core and $R_d \approx (\pi\rho_d)^{-1/2}$ is the average distance between dislocations. With this in mind, equation (3.101) for $Z_{\square}$can be expanded to the first order in small parameter σ/μ, providing the first derivative of the bias factor over stress in the form [152]:

$$\delta_\alpha^k = \frac{Z_\alpha^0 p_\alpha^\mu}{2\pi e_{\alpha 0}} q^k . \qquad (1.23)$$

As can be seen, $Z_{\square}^k$ does depend on both the type of point defects and the dislocation orientation. The irradiation creep compliance is then given by

$$B_{ij} = S_{ij}^{EMA}\left(\frac{Z_I^0 p_I^\mu}{2\pi e_{I0}} - \frac{Z_V^0 p_V^\mu}{2\pi e_{V0}}\right), \qquad (1.24)$$

where S_{ij}^{EMA} is the structure factor determined by the distribution of dislocation orientations with respect to the applied load,

$$S_{ij}^{EMA} = 3\nu\left\langle \hat{b}_i\hat{b}_j\left((\boldsymbol{ts})^2 - <(\boldsymbol{ts})^2>\right)\right\rangle + 3\left\langle \hat{b}_i\hat{b}_j\left((\hat{\boldsymbol{bs}})^2 - <(\hat{\boldsymbol{bs}})^2>\right)\right\rangle .$$

Using the estimates $p^\mu{}_i \approx 0.5$, $p^\mu{}_v = 0$, $Z_I^0 \approx 3$, and $e_{I0} \approx 1.2$, one obtains

$$B_{ij} \approx S_{ij}^{EMA} \sim 1 .$$

This value of the creep compliance is very similar to the estimates commonly reported for the in-reactor creep modulus in experimental publications, which was considered for some time as an experimental support for this mechanism. However, later on it became clear that the point defect generation rate by fast neutrons, when estimated using the common standards, turns out to be nearly an order of magnitude higher than it really is. Correspondingly, the analytical prediction of the creep compliance value should be at least an order of magnitude higher in order to really fit experimental data. Such a value cannot be reached by varying parameters entering (1.24) within reasonable limits. Together with the above mentioned inconsistency in the prediction of limiting stress σ^*, this rules out stress-induced elastic modulus anisotropy as a relevant mechanism of irradiation creep.

b. Stress-induced anisotropy of point defect diffusion

In this mechanism, the physical reason for the bias factor anisotropy is the modification of the energy barriers for point defect diffusion in the loading direction and perpendicular to it. In this case the diffusion is described not by a scalar diffusion coefficient but by a tensor of diffusion coefficients $D_{\alpha,ij}$, which can be written down in terms of individual diffusional jumps as [26]:

$$D_{\alpha,ij} = \nu_\alpha \sum_{\mathbf{h}} \lambda_{\mathbf{h}} h_i h_j \exp\left(-\frac{E_\alpha^h}{k_B T}\right), \qquad (1.25)$$

where ν_α is the vibration frequency of point defects in the lattice, h_i - the i-th component of a vector $\boldsymbol{h}$, connecting an equilibrium point defect position with one of the

neighbour equilibrium positions, $E_\alpha^{\boldsymbol{h}}$ - the energy barrier of diffusional jump in the direction $\boldsymbol{h}$, $\lambda_{\boldsymbol{h}}$ - the factor that takes into account a possibility of the point defect rotation (for interstitial atoms), and summation in (1.25) is performed over all nearest neighbour sites to which the point defect can jump. If the material is under the action of elastic deformations $e_{ij}(\boldsymbol{r})$, the energy $E_\alpha^{\boldsymbol{h}}$ can be written down as:

$$E_\alpha^h = E_\alpha^m - P_{\alpha,kl}^s(\boldsymbol{h})e_{kl} - \frac{1}{2}Q_{\alpha,klmn}^s(\boldsymbol{h})e_{kl}e_{mn}, \qquad (1.26)$$

where $P^s_{\alpha,kl}$ and $Q^s_{\alpha,klmn}$ are, respectively, the force tensor and the elastic polarizability tensor at a saddle point of a diffusional jump. Both these tensors can depend on the jump direction. According to relation (1.26), the diffusion coefficient dependence on the external load and the dislocation orientation can originate from two sources.

First of all, the strains e_{kl} in equation (1.26) are given by the sum of external strains ε^e_{ij} and the strains created by a nearby dislocation ε^d_{ij}. Though these two strains enter additively in the second term in (1.26), their effect on the diffusivity is not additive because in the vicinity of a dislocation core $P^s_{\alpha kl}\varepsilon^d_{kl} \geq k_B T$ and hence the exponential terms in (1.26) cannot be straightforwardly expanded in powers of the total deformation [26]. Because of this, the resulting corrections to the dislocation bias factors turn out to be dependent on both the point defect type and the dislocation orientation with respect to stress.

Second, the last term in the r.h.s. of Equation (1.26) depends on the strain products $\varepsilon^0_{kl}\varepsilon^d_{mn}$, which include interference terms that depend simultaneously on the external loading and the orientation of the dislocation. The account of such terms results, correspondingly, in corrections to the diffusion coefficients and to the dislocation bias factors, which satisfy the "double anisotropy" requirement and can contribute to irradiation creep [27]. Having in mind, however, that this effect is of the second order in strains, it is possible to neglect it as compared to the first-order one.

When the external stress is sufficiently low (i.e. $\sigma\omega / k_B T \ll 1$) and the crystalline lattice is cubic, the bias factors can be presented as [152]:

$$Z_\alpha^k = Z_\alpha^0\left(1 - \frac{(1+\nu)}{2(1-2\nu)}e_\alpha^s q^k \frac{\sigma\omega}{k_B T}\right), \qquad (1.27)$$

where ν is the Poisson ratio of the material, e_α^s - the point defect dilatation in the saddle point of diffusion jump, and the orientation factor q^k is defined by the relative orientation of the unit vector of dislocation orientation, $\boldsymbol{t}^k$, the unit vector $\boldsymbol{s}$ in the direction of applied stress and the basis vectors $\boldsymbol{e}_p$ (p = 1,2,3) of the crystalline lattice,

$$q^k = d_\alpha^{(2)}(\boldsymbol{s}\boldsymbol{t}^k)^2 + d_\alpha^{(3)}\sum_{p=1}^{3}(\boldsymbol{s}\boldsymbol{e}_p)^2(\boldsymbol{t}^k\boldsymbol{e}_p)^2, \qquad (1.28)$$

where $d_\alpha^{(2)}$) and $d_\alpha^{(3)}$ are the factors determined by point defect force tensors at the saddle points of a diffusion jump. Numerical values for $d^{(2)}$ and $d^{(3)}$, estimated using computer simulation values for copper and iron, are summarised in Table 1.

Table 1. Numerical estimates of $d^{(s)}$ for copper and α-iron [152]

	Cu*		α-Fe	
	V	*I*	*V*	*I*
$d^{(2)}$	-0.62(-0.35)	0.20(0.13)	0.88	0.60
$d^{(3)}$	-1.51(-0.85)	-0.24(-0.16)	-0.88	-0.60
*)The values in parentheses are estimated with the data from [28], all other values use the data from [29]				

According to Equation (1.28), the stress-induced modification of dislocation bias depends on the dislocation orientation with respect not only to stress, but to the crystal lattice axes as well. In a monocrystal, the creep compliance has the form [152].

$$B_{ij} = \frac{3K\omega}{4k_B T}\left[\left(e_I^s d_I^{(2)} - e_V^s d_V^{(2)}\right) S_{ij}^{(2)} + \left(e_I^s d_I^{(3)} - e_V^s d_V^{(3)}\right) S_{ij}^{(3)}\right], \qquad (1.29)$$

where $S_{ij}^{(2)}$ and $S_{ij}^{(3)}$ are structure factors, defined as:

$$S_{ij}^{(2)} = \left\langle \hat{b}_i \hat{b}_j \right\rangle \left\langle (\boldsymbol{ts})^2 \right\rangle - \left\langle \hat{b}_i \hat{b}_j (\boldsymbol{ts})^2 \right\rangle \qquad (1.30)$$

and

$$S_{ij}^{(3)} = \sum_{p=1}^{3} (\boldsymbol{e}_p \boldsymbol{s})^2 \left\{ \left\langle \hat{b}_i \hat{b}_j \right\rangle \left\langle (\boldsymbol{e}_p \boldsymbol{t})^2 \right\rangle - \left\langle \hat{b}_i \hat{b}_j (\boldsymbol{e}_p \boldsymbol{t})^2 \right\rangle \right\}. \qquad (1.31)$$

An estimate of the creep compliance at $T = 300^{o}$C using the point defect polarization data from [152] (see also Table 1) gives,

$$B_{ij} \approx 20 S_{ij}^{(2)} + 7 S_{ij}^{(3)}$$

and

$$B_{ij} \approx 70 (S_{ij}^{(2)} - S_{ij}^{(3)})$$

for copper and α-iron, respectively. The identical coefficients before structure factors constitute a general feature of bcc metals, where $d_\alpha^{(2)} = -d_\alpha^{(3)}$ due to the specific point defect symmetry at the saddle points of diffusion jumps [147].

In polycrystalline materials the expression for creep compliance should be additionally averaged over different grain orientations (that is – over $\boldsymbol{e}_p$ in (1.31)). Assuming the isotropy of grain orientations, one gets:

$$S_{ij}^{(3)} = \frac{2}{5} S_{ij}^{(2)},$$

so that the dependence on the creep compliance on lattice orientation is completely lost.

Since at temperatures up to 1000°C the relation $\mu\omega / k_B T \gg 1$ holds true, the value of creep compliance for the elastodiffusion mechanism correlates reasonably well with

experimental predictions, making it the most probable mechanisms for SIPA-type irradiation creep [152,16].

c. Stress-modified efficiency of point defect absorption by dislocations

Both preceding models implicitly assume that a dislocation absorbs any point defect jumping into its core. Actually, straight edge dislocations lying along low-index crystallographic directions have atomically smooth edges of extra-planes, divided by separate jogs and kinks, and the lengths of smooth segments considerably exceed the interatomic distance a [3]. A point defect entering the dislocation core on a smooth segment does not annihilate [30] and can diffuse along the extra-plane edge. Eventually, the defect either jumps out of the core back into the volume of material, or is absorbed at a dislocation jog, thus contributing to the climb of the dislocation (the direct electron microscopy observation of non-conservative movement of dislocation jogs was carried out e.g. in [31]).

Even when the concentration C_j of jogs on a dislocation line is rather low ($aC_j << 1$), the dislocation can act as a perfect sink for point defects, provided $\lambda_\alpha C_j \geq 1$, where λ_α is the average distance traveled by a point defect in the dislocation core. However, in the opposite limiting case ($\lambda_\alpha C_j << 1$) the dislocation captures point defects on a discrete set of jogs and only provided these defects enter the dislocation core at a distance smaller than λ_α from the nearest jog. The total absorbing length of such a dislocation is proportional to $\lambda_\alpha C_j$ [154,17], while the dislocation bias factors can be written down as [18]

$$Z_\alpha^k = z_\alpha^k \lambda_\alpha^k C_j^k , \qquad (1.32)$$

where $z_\square^k$ is the coefficient that depends on C_j^k and on the effective radius of elastic interaction of point defects with dislocation $R_{d\alpha}^k$, given by equation (1.21). An external load can influence the bias factors of a "discrete" dislocation by modifying both the defect diffusion in dislocation core and the linear density of jogs.

The dependence of jog concentration on the external load can result from variations of the energy barrier that must be overcome for the nucleation of new jog pairs on a straight segment of extra-plane edge [18]. Indeed, new jogs are nucleated in pairs when a cluster of Λ atoms is added to extra plane or a row of Λ vacancies "eats out" the extra-plane ($\Lambda \approx$ 2-3). The formation of such clusters on a dislocation with orientation k in the field of external loads σ_{ij} requires additional work $\delta A^k = -\Lambda\sigma_{nn}\omega$ or $\delta A^k = -\Lambda\sigma_{nn}\omega$, respectively, where $\sigma_{nn} = \hat{b}_i^k \hat{b}_j^k \sigma_{ij}$ is the stress acting normally to the dislocation extra-plane.

The mean free path of a point defect in the dislocation core, λ_α, is given by the relation [18]

$$\lambda_\alpha^k = a \exp\left(\frac{\Delta Q_\alpha^k}{k_B T}\right), \qquad (1.33)$$

where $\Delta Q_\alpha^k = (Q_\alpha^k - Q_\alpha^{dk})/2$, while Q_α^k and Q_α^{dk} are the sums of point defect formation and migration energies in the bulk and in the dislocation core, respectively. The external load can change the values of both formation and migration energies of point defects in dislocation cores, [32]. Expanding Q_α^{dk} to the first order in external strains ε_{ij}^e, and using Hooke's law for ε_{ij}^e, the orientational dependence of λ_α can be represented as

$$\lambda_\alpha^k \propto \exp\left\{\frac{1+\nu}{6(1-2\nu)}\frac{p_{\alpha,ij}^k \sigma_{ij}\Delta V_\alpha^d}{k_B T}\right\}, \qquad (1.34)$$

where $p_{\alpha,ij}^k = 3P_{\alpha,ij}^{dk}/\mathrm{Tr}P_{\alpha,ij}^{dk}$ and it is assumed that the relaxation volume of a point defect in the dislocation core, $\Delta V_\alpha^d = \mathrm{Tr}P_{\alpha ij}^{dk}/K$, is independent of dislocation orientation with respect to the applied load.

In the linear approximation in σ, each of three multipliers in the r.h.s. of eq. (1.32) depends on the dislocation orientation with respect to the loading direction. However, the contribution to the creep compliance from C_j vanishes because this parameter is independent of the point defect type. The stress enhanced jog nucleation affects the creep compliance only through the dependence of the factors z_α^k on the jog concentration [18]

$$B_{ij} = S_{ij}^{EJN}\frac{z_I^2 z_V^2}{2(4\pi)^4}\ln\left(\frac{e_{I0}}{|e_{V0}|}\right)\frac{\Lambda\mu\omega}{k_B T}, \qquad (1.35)$$

where $S_{ij}^{EJN} = <\hat{b}_i\hat{b}_j(\zeta(\mathbf{bs})^2 - <\zeta(\mathbf{bs})^2>)>$, ζ^k = 1 when a dislocation with orientation k climbs absorbing predominantly interstitials and ζ^k = -1 in the opposite case. Taking $z_I \sim z_V \sim 5$, $\Lambda = 2$, $e_{I0} \approx 1.3$, and $|e_{V0}| = 0.5$, one gets [18]

$$B_{ij} \approx 0.03 S_{ij}^{EJN}\frac{\mu\omega}{k_B T}.$$

The contribution to creep compliance from the orientational anisotropy of point defect pipe diffusion along dislocation cores, Equation (1.34), is:

$$B_{ij} = (e_I^d S_{I,ij}^{PDA} - e_V^d S_{V,ij}^{PDA})\frac{K\omega}{12k_B T}, \qquad (1.36)$$

where $e_\alpha^d = \Delta V_\alpha^d/\omega$ and the structure factors are defined as

$$S_{\alpha,ij}^{PDA} = \left\langle \hat{b}_i\hat{b}_j(p_{\alpha,11}^d - <p_{\alpha,11}^d>)\right\rangle. \qquad (1.37)$$

Here $p_{\alpha,11}^d$ is the component of polarisation tensor in the coordinate system with the axis 1 coinciding with the load direction. Information about polarization tensors of point defects in dislocation core is practically lacking in the literature. A very rough estimate of:

$$B_{ij} \approx 0.03\frac{\mu\omega}{k_B T}$$

can be obtained using the data for the effect of external load on vacancy diffusion along dislocations in α-Fe [33] and assuming isotropic distribution of dislocations over orientations. That is, the contribution to the irradiation creep compliance from the stress effect on point defect absorption by "discrete" dislocation sinks is expected to be comparable to that from elastodiffusion.

1.3. Steady-state irradiation creep: mechanisms based on climb-controlled dislocation glide

Dislocation glide in perfect crystals starts when the resolved shear stress in the dislocation glide plane exceeds a certain threshold value (Peierls barrier [34,35]) and the glide velocity V_{g0} is extremely fast (of the order of the sound velocity). However, in real metals the average glide velocity of dislocation, V_g, is usually much less than V_{g0}, due to the presence of various obstacles (impurity atoms, precipitates, voids, dislocation loops, other dislocations, etc.) in the dislocation glide plane. These obstacles serve as barriers hindering the glide. As a result, the limiting step in the dislocation glide motion is not the glide itself, but the barrier overcoming. A dislocation can come over a barrier either thermofluctuatively, or climbing into a parallel glide plane, where the current barrier is no more operative. For qualitative understanding of the physical picture it will be sufficient to restrict ourselves to the case, where the barriers of only one kind are present in the materials, because even in multi-barrier situation only the most strong barrier system limits the average dislocation slide velocity [34,35].

If the average time required for a dislocation to overcome a barrier is τ_b and the average distance glided by a dislocation between consecutive pinning barriers in the glide plane is L_g, then the average dislocation glide velocity is $V_g \approx L_g / \tau_b$. The time required for a dislocation to overcome a barrier can usually be defined as:

$$\tau_b = \frac{h}{|V_c|}, \qquad (1.38)$$

where V_c - the dislocation climb velocity and h - the barrier geometrical "height". As a result, the contribution to the irradiation creep rate from the climb-controlled glide of dislocations, as given by the second term in the r.h.s. of Equation (4.5), can be written down as:

$$\dot{\varepsilon}_{kl}^{I} = \frac{1}{2}\rho b \left\langle (\hat{b}_i n_j + n_i \hat{b}_j) |V_c| \frac{L_g}{h} \right\rangle . \qquad (1.39)$$

A similar relation (without the averaging over dislocation orientations) was first proposed for the description of thermal creep [36,37], but its derivation did not depend on the particular mechanism of dislocation climb and so it is equally applicable to irradiation creep [38-40].

As follows from relation (1.39), in order to find the irradiation creep rate in the framework of the climb-controlled glide model, one must know not only the dislocation climb rate, but also the "glide factor", L_g/h, determined by the type and the parameters of the barrier system that provides the strongest hindrance for the glide.

Various components of the defect microstructure of irradiated material can behave as obstacles for dislocation glide, including both those not directly related to irradiation (impurity atoms [35], network dislocations [41], secondary phase precipitates [42,43]) and those appearing as a result of irradiation (cascade depleted zones [39,44,45], dislocation loops [46-50], voids [44]). Each of the barrier types has its own efficiency of dislocation stopping, which can be characterised by the minimum shear stress, σ_y, necessary for the athermal break-through of a dislocation through the ensemble of barriers. In fact, σ_y characterises the maximum stress at which a given system of barriers can prevent the glide of dislocations. At stresses larger than σ_y this barrier system becomes inactive.

In order to estimate the *average glide distance* of an unpinned dislocation before its recapture by the obstacles, let us consider a model, where a straight edge dislocation glides under the action of external shear stress τ in its glide plane, overcoming a grid of obstacles (see Figure 2). The gliding dislocation is considered as a flexible string with a constant linear tension γ (it is usually accepted that $\gamma \approx \mu b^2/2$ [51]). To simplify the discussion, let us assume first that the obstacles make a square lattice in the glide plane and the distance between the neighbour barriers equals L_b. This is shown schematically in Figure 2.

Figure 2. A schematic representation of a dislocation (dark black line) gliding through the array of obstacles (gray spheres) under the action of shear stress τ

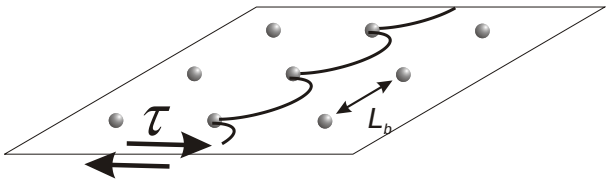

In an unloaded material the dislocations are generally not fixed by barriers, but the application of shear stress τ sufficient to overcome the Peierls barrier which makes the dislocation glide until it reaches the nearest obstacles and bends forward between them. When the barriers are strong enough to pin the dislocation at the applied stress level (i.e. $\tau < \sigma_\psi$), no further glide in the same plane is allowed and the strains due to dislocation segment bending are recoverable. If the barrier system makes a square lattice in the glide plane and the distance between the neighbour barriers equals L_b, the average deflection ΔL_e of a pinned dislocation segment grows linearly with the stress level [52,53]

$$\Delta L_e = \frac{L_b^2}{4b}\frac{\tau}{\mu}. \qquad (1.40)$$

Following [41], this average deflection ΔL_e is often treated as the dislocation glide distance (see e.g. [40]). However, such an assumption is incorrect. Indeed, overcoming (e.g. by climb) the first chain of barriers, the dislocation hangs up on a similar set of barriers in the new glide plane, keeping, on the average, the same deflection. Hence, the dislocation glide distance is simply the average distance between barriers in the glide plane ($L_g = L_b \sim C_b^{-1/3}$, where C_b is the atomic concentration of the barriers) and does not depend on the load level up to $\tau = \sigma_y$.

A more complicated situation arises, when the barriers are randomly (though uniformly) distributed in space. First of all, in this case the average distance between barriers at a dislocation, L_s, depends on the applied shear stress as [54-56]:

$$L_s = \chi_s \left(\frac{3\mu b L_b^2}{\tau} \right)^{1/3}, \quad (1.41)$$

where L_b is, as before, the average distance between barriers in the dislocation glide plane, and $\chi_s \sim 1$ is weakly dependent on the stress (varying from $\chi_s \approx 0.9$. at $\tau \to 0$ to $\chi_s \approx 1.2$ at $\tau \to \sigma_y$ [56]). Second, the force acting on a barrier is sensitive to the positions of neighbouring barriers. As a result, the stresses necessary to overcome some of the barriers can be less than the critical one and the athermal unpinning of a dislocation from these barriers occurs even before the stress level σ_y is achieved. In turn, the released dislocation segments act with the increased force on the neighbouring barriers (since these forces are proportional to the length of the free dislocation segment), resulting in a series of correlated unpinning acts ("unzipping" effect [57]). Due to the unzipping effect, the dislocation unpinned from the obstacles can glide, on the average, farther than the average inter-barrier distance before it is re-captured by barriers in the new glide plane. It is clear, however, that this effect should be noticeable only for stresses sufficiently close to σ_y. Indeed, numerical simulations of a dislocation break-through through a randomly distributed system of obstacles [35,58] indicate that at low stresses the progress of dislocation is limited by the deflection of its pinned segments according to relation (4.40), whereas at sufficiently large stresses ($\tau > 0.5\sigma_y$) the dislocation can cover distances exceeding L_b after a single unpinning act.

Thus, the dislocation glide distance in the case $\tau < \sigma_y$ can be described by the relation

$$L_g = L_b \Psi \left(\frac{\tau}{\sigma_y} \right), \quad (1.42)$$

where $\Psi(x) = 1$ at $x \le 1$ in the case of the ordered obstacle system. In the case of random obstacle distribution $\Psi(x) = 1$ only at $x < 0.5$, while for higher values of x the increase of Ψ with increasing x is predicted, as shown in Figure 3.

Figure 3. The average dislocation glide distance as a function of the relative shear stress (σ/σ_y) in the dislocation glide plane [35]

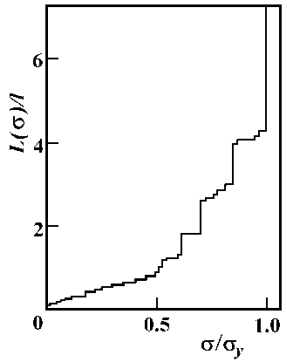

The *barrier height h* is determined by two factors, namely the actual geometrical size of the barrier and the strength and extension of its elastic field.

In the literature it is usually postulated that h for "forest" dislocations (extended barriers) is of the order of the average distance between dislocations, i.e. $h \approx (\pi\rho_d)^{-1/2}$ [41]. However, such choice is completely arbitrary. It seems more reasonable to assume that in this case h is infinite (or comparable to the grain size in real-life materials). However, as demonstrated in the final part of this section, forest dislocations are usually the weakest obstacles for the dislocation glide and can be overcome relatively easily even without the assistance of irradiation.

In the case of three-dimensional obstacles, the barrier height can be limited either by the own size of the barrier, or by the size of its elastic field. The latter is more typical for barriers with small cross-section, but strong elastic fields, such as dislocation loops and some kinds of precipitates. The same situation is met when a gliding dislocation interacts with a parallel dislocation in a nearby gliding plane.

In the case of stopping by elastic fields, the barrier height can be estimated according to the approach proposed in [41]. Let us assume that a dislocation glides in a plane located at distance h from the center of a barrier, such that h exceeds the characteristic barrier size R_b. The dislocation is under the simultaneous action of an external shear stress τ and the resistance force from the barrier, $F_b(h)$, which changes as the dislocation moves in the glide plane. The stresses from a three-dimensional stress source fall as h^{-3} and act on a dislocation segment of length ~ h, so that $F_b(h) \propto h^{-2}$. Accordingly, the maximum force of dislocation pinning by the barrier can be written down as:

$$F_b^{max} = A_b \frac{\mu |\Delta V_b| b}{h^2}, \quad (1.43)$$

where ΔV_b is the volume misfit of the obstacles causing elastic stresses in the matrix, and A_b is the numerical factor determined by a particular kind of the interaction law between the barrier and the gliding dislocation. Figure 4 shows the simplest law of interaction of an edge dislocation with a point-size center of dilatation in an isotropic material. Here, as can be easily checked, $A_b = 3\sqrt{3}/8\pi \approx 0.2$. However, the account of anisotropy of both the force tensor of a point defect and the elastic constants of material can result in much more complicated forms of the interaction law [230]. In such cases, the calculation of parameter A_b is a separate task requiring the application of numerical methods.

Figure 4. The force acting on an edge dislocation gliding past an isotropic dilatation centre

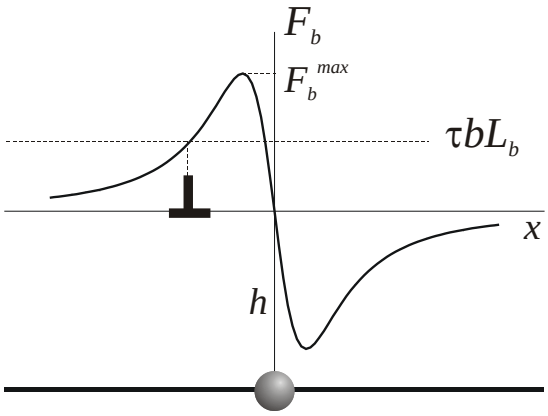

The curve shows schematically the force F_b acting on the dislocation as a function of dislocation position x. The glide barrier is at a distance h below the dislocation glide plane.

The minimum distance from the glide plane to the barrier that allows the dislocation to pass the barrier without being pinned (i.e. the height of the barrier h) is defined by the balance between the maximum pinning force $F_b^{max}(h)$ and the force from the external loading, i.e.

$$F_b^{\max}(h) = \tau b L_b . \qquad (1.44)$$

Combining relations (1.41) and (1.44) and taking into account that the average distance between the obstacles in a glide plane is given by

$$L_b \approx (N_b h)^{-1/2}, \qquad (1.45)$$

where N_b is the volume density of glide obstacles, one gets

$$h = \chi_0 \left[\frac{N_b \Delta V_b^3}{b} \right]^{1/5} \left(\frac{\mu}{\tau} \right)^{2/5}, \qquad (1.46)$$

where $\chi_0 = (A_b^3/3\chi_s^3)^{1/5}$.

The relation (1.46) for the barrier height remains valid as long as the stress remains below a certain critical value σ_{yh}, which can be easily determined by substitution of (1.46) into the relation $h = \xi R_b$, where the factor ξ accounts for the relative orientation of the dislocation and the barrier ($\xi = 1$ for spherically symmetric stress sources and $\xi < 1$ for dislocation loops). For the most interesting case of point-size barriers (impurity atoms) it is possible to set $\xi = \chi_s = 1$, $A_b = 0.2$, $R_b = b$, and $\Delta V_b = e_b \omega$, where e_b is the absolute value of the barrier dilatation, so that

$$\sigma_{yh} / \mu \approx 0.55 e_b^{3/2} C_b^{1/2} . \qquad (1.47)$$

For $\tau > \sigma_{yh}$ the elastic fields of the barriers do not block dislocation glide and the dislocation can be stopped only by the barriers themselves, i.e. at high stresses one has

$$h \approx \xi R_b. \qquad (1.48)$$

For stresses not too close to σ_y, it is possible to set $\Psi = 1$ in Equation (1.42). Then, taking into account (4.45), one gets

$$L_g / h \approx (N_b h^3)^{-1/2}. \qquad (1.49)$$

For the case of dislocation pinning by elastic fields of barriers (that is - at low stresses, $\tau < \sigma_{yb}$) one obtains for the glide factor the relation

$$\frac{L_g}{h} = \chi_0^{-3/2} \left(\frac{b}{\Delta V_b^3} \right)^{0.3} N_b^{-0.8} \left(\frac{\tau}{\mu} \right)^{0.6}. \qquad (1.50)$$

A similar relation was first proposed in [46]. On the contrary, when dislocations are stopped by the barriers themselves and the load is not too close to σ_y, one has

$$\frac{L_g}{h} = \xi^{-3/2} \left(N_b R_b^3 \right)^{-1/2}, \qquad (1.51)$$

so that the glide factor is independent of the applied load.

One can meet in the literature also other expressions for the glide factor, which are generally presented in the form of a power law,

$$\frac{L_g}{h} = \vartheta_g \left(\frac{\tau}{\mu} \right)^m, \qquad (1.52)$$

where both the prefactor ϑ_g and the power m depend on the particular considered system of glide barriers and on the possibility for gliding dislocation to form pile-ups. Most often $m = 1$ is suggested, though one can meet other values as well (e.g. $m = 0.5$ [47] or $m = 1.2$ [46]).

The obtained expressions for the "glide factor" make it possible to estimate the contribution to irradiation creep from the climb-controlled glide (CCG), which is often alternatively referred to as "climb-induced" glide (CIG). Substituting (4.13) and (1.52) into (1.39), and using the general representation of bias factors in the form of (1.15), one obtains for the CCG contribution to irradiation creep

$$\dot{\varepsilon}_{kl}^I = B_{kl}^G \left(\frac{\sigma}{\mu} \right)^{1+m} G\Phi\left(\frac{G}{G_R} \right), \qquad (1.53)$$

where the creep compliance B_{kl}^G is

$$B_{kl}^G = \frac{\vartheta_g}{2} \left\langle (\hat{b}_k n_l + n_k \hat{b}_l) \left| \delta_i - \delta_v - \langle \delta_i - \delta_v \rangle \right| \left((\mathbf{ts})(\hat{\mathbf{bs}}) \right)^m \right\rangle. \qquad (1.54)$$

The estimates of the creep compliance are not as trivial as in the case of climb-only creep mechanisms and the author is not aware of any attempts of their calculation reported in the literature.

The most important feature of the irradiation creep rate in the case of climb-controlled glide is its non-linear dependence on the applied stress. Due to the relation $\sigma/\mu \ll 1$, the CCG mechanism is weaker than SIPA type mechanisms at lower stresses. On the other hand, climb-controlled glide can dominate the irradiation creep at high stresses due to both the stress nonlinearity and the fact that the prefactor ϑ_g usually noticeably exceeds unity. This mechanism change is usually invoked to rationalise the stress exponents in the range $1<m<2$, as observed at the stresses above a certain threshold σ^* (see Section 2.3). An example is presented in Figure 5.

Figure 5. Comparison of creep rate between theoretical values and the experimental ones, as a function of stress. The hatched areas indicate the experimental values for the alloy 7807 and type 316 SS. The symbol σ* denotes the critical stress; the dashed lines are theoretical predictions for SIPA-type mechanism and solid lines – for climb-controlled glide mechanism [101]

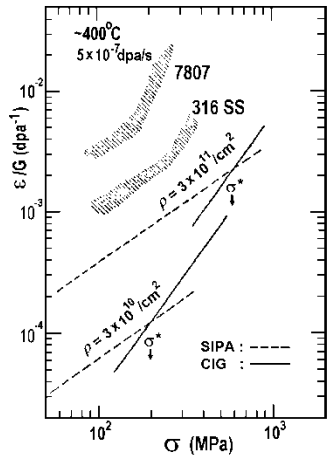

To conclude this section, let us discuss in more detail the relative efficiencies of different microstructural features as dislocation barriers. In a simple model of a regular square mesh of obstacles, as shown in Figure 2, the gliding dislocation is blocked at an obstacle, if the following condition is satisfied:

$$\tau b L_b \le F_b, \qquad (1.55)$$

where F_b is the resistance force of a single obstacle. The applied shear stress forces the free dislocation segments to bend forward. Treating the dislocation as a flexible string, it is easy to show that the curvature radius of the bent dislocation section is $R_c = \gamma/b\tau \approx \mu b/2\tau$ [60]. Thus the force acting on an obstacle from two adjacent free dislocation segments is equal to $F = 2\gamma\cos(\varphi/2)$, where φ is an angle between these adjacent dislocation segments. Then the critical stress for dislocation unpinning can be written down as

$$\sigma_y = \mu\frac{b}{L_b}\cos(\varphi_b/2). \qquad (1.56)$$

where the critical angle φ_b is defined by the relation $F_b = 2\gamma\cos(\varphi_b/2)$. When the glide barriers are distributed in the bulk randomly, L_b in this relation should be replaced with parameter L_s defined by Equation (1.41), so that

$$\sigma_y = \frac{1}{\sqrt{3}\chi_s^{3/2}}\frac{\mu b}{L_b}\cos^{3/2}(\varphi_b/2). \qquad (1.57)$$

This relation nicely correlates to the empirical law received in numerical simulations of dislocation break-through through a system of randomly located point-size obstacles [60]:

$$\sigma_y = \frac{4}{5}\frac{\mu b}{L_b}\left[1-\frac{\varphi_b}{4\pi}\right]\cos^{3/2}(\varphi_b/2). \qquad (1.58)$$

It is seen that the random arrangement of barriers results in the reduction of the critical stress in comparison with the ordered arrangement for all φ_b and this reduction is especially pronounced for weak barriers (when $\varphi_b \to \pi$).

The critical angle φ_b differs for different barriers and can be considered as a measure of the relative strength of individual barriers. It is a common practice to separate barriers into three classes [61]:

weak barriers (with $\cos(\varphi_b/2) < 1/4$): network dislocations, impurity atoms in FCC metals;

intermediate barriers ($1/4 < \cos(\varphi_b/2) < 1/2$): coherent precipitates, interstitial impurity atoms in bcc metals;

strong barriers ($\cos(\varphi_b/2) > 1/2$): incoherent precipitates, Frank loops, voids.

The values of critical angles for the dominant glide obstacles can be obtained experimentally because in this case σ_y is nothing but the yield stress. For example, for Frank dislocation loops an experimental estimate gives $\cos(\varphi_b/2) \approx 0.5\text{-}0.8$, while for voids $\cos(\varphi_b/2) \approx 1$ [62,63]. The estimate for voids correlates nicely with the numerical simulation prediction of $\cos(\varphi_b/2) \approx 0.95$ [64].

One should keep in mind, however, that when a material contains several different barrier types, the selection of the obstacle systems responsible for the dislocation glide blocking depends not only on the strength of individual obstacles, but also on the obstacle density in the dislocation glide plane. As follows from Equation (1.56), a large number of weak barriers can block the dislocation glide more efficiently, than a small number of strong obstacles.

Let's estimate the value σ_y for the principal components of defect structure present in the material at various stages of irradiation creep.

-For *network dislocations* $L_b \approx (\pi\rho)^{-1/2}$, which gives $\sigma_y/\mu \approx 10^{-3}$ -10^{-4} at typical values of $\varphi_b = 5\pi/6$ [35] and $\rho = 10^8$ - 10^{10} cm^{-2}. These estimates correspond to the lower limit of loads used in irradiation creep experiments, so that the stopping of gliding dislocations by a dislocation "forest" is rather of theoretical interest.

-For *three-dimensional barriers* (point defects, small clusters thereof, second phase particles, voids, faulted loops, etc.), which are randomly distributed in the bulk of the material and have the characteristic size h and the volume density N_b, the average distance between barriers in a glide plane is given by Equation (1.45). For voids and faulted dislocation loops, which are strong barriers for dislocation glide ($\cos(\varphi_b/2) \approx 1$) and have characteristic number densities of $N_b \sim 10^{15}$ cm^{-3} and sizes $h \sim$ 10-100 nm, one gets $\sigma_y/\mu \geq 10^{-3}$, i.e. at the relevant experimental stresses these microstructural features efficiently block dislocation glide only when they are sufficiently large. Indeed, the measurements of material hardness (the most direct indication of dislocation mobility) show that a certain increase of hardness in void-containing alloys occurs only at higher swelling levels [65].

-In the case of *impurity atoms*, $h \sim b$ and $\sigma_y/\mu \approx C_s^{1/2} \cos(\varphi_b/2)$, where C_s is the atomic concentration of impurity. If the barrier strength of the impurity is not extremely low and the impurity concentration is in the percent range, impurity atoms act as the principal barriers for dislocation glide.

1.4 Primary (transient) irradiation creep

At the initial stage of irradiation creep the strain rate is determined by the combined effect from the climbing network dislocations and the growing dislocation loops. The addition of dislocation loops to the defect microstructure can influence irradiation creep in two ways. First of all, the volume densities of nucleated loops can depend on loop orientation with respect to the loading direction. Usually this effect is described as [66]

$$N^k = N_0^k \exp\left(\frac{m\tilde{\sigma}_{nn}\omega}{k_B T}\right), \qquad (1.59)$$

where N_0^k is the volume density of k-type loops in a stress-free material, $\tilde{\sigma}_{nn}$ is the component of deviatoric stress tensor normal to the loop extra-plane, and m = 2-3. Such dependence is observed in some electron microscopy studies [39,67-75], but not always (see e.g. [76-78]) and its explanation is not at all obvious. Initially this kind of stress dependence was ascribed to the effect of stress on the free energy barrier for loop nucleation. However, in the case of interstitial dislocation loops the formation of a critical nucleus (di-interstitial) involves no energy barrier. A more probable explanation seems to be the reorientation of very small interstitial clusters (of only several interstitial atoms) into an energetically more favourable orientation with respect to the applied load [79]. Such thermally activated reorientation of di- and tri-interstitial clusters was indeed observed in MD simulation studies [80-83].

The stress-induced preferred nucleation (SIPN) of dislocation loops was one of the first microstructural mechanisms proposed for the explanation of irradiation creep [84]. However, being considered as an independent creep mechanism, SIPN is a poor alternative to mechanisms of SIPA type. Indeed, the nucleation of extra loops with a preferred orientation with respect to external load weakly contributes to the strain of material [46,66]. The subsequent growth of these loops can result in a certain amount of creep [85], but the material creep rate in this model should depend only on stresses acting during loop nucleation, and not on the instantaneous stress values. The same is true for

any model based on the initial anisotropy of loop orientations, such as that where the loop anisotropy is a consequence of preferred unfaulting reaction of small Frank loops [86]. Because loop nucleation takes very short time, such models would predict no creep if the material is loaded after the onset of irradiation [85]. Also, load variations during irradiation (even the complete unloading) should have no effect on the creep rate. Both these consequences of the SIPN model contradict observations. In any case, the anisotropic nucleation of loops can have influence on creep only as long as the loops are being nucleated; i.e. SIPN can not operate beyond the transient stage of irradiation creep. In fact, the contribution from SIPN to irradiation creep can be noticeable only at small irradiation doses in well-annealed metals with very low initial density of other point defect sinks [87]. Much more productive was the idea to combine SIPN with SIPA-type mechanisms, which ensure the sensitivity of point defect absorption to the loop orientation and thus affect the growth of differently oriented loops.

For the analytical description of dislocation loop kinetics at the early stages of irradiation creep it is necessary to modify the point defect balance equations (4.10) so as to include the growth of dislocation loops. Since the majority of loops nucleates at very short irradiation times, one can assume that the loop number density N_L instantly saturates at a constant value and the distribution of loops over sizes is sufficiently narrow in order to assign approximately the same size R^m to all loops of the same orientation m. Then the rate of growth for dislocation loops can be written down as

$$V_l^m \equiv \frac{dR^m}{dt} = b^{-1}\left(\eta_I^m D_I C_{I0} - \eta_V^m D_V (C_{V0} - C_{V0}^{th})\right), \qquad (1.60)$$

where $\eta^m{}_\alpha$ is the bias factor for point defects of type α at the loops with orientation m. The balance equations (4.10) can be rewritten as

$$G - k_\alpha^2 D_\alpha (C_{\alpha 0} - C_{\alpha 0}^{th}) - q_{IV} C_{I0} C_{V0} = 0, \qquad (1.61)$$

where $k_\alpha^2 = \langle Z_\alpha \rangle \rho_d + 2\pi N_L \langle \eta_\alpha R \rangle$ is the total sink strength for point defects that takes into account both network dislocations and dislocation loops. Because we are not interested here in the contribution of loops into thermal creep, the dependence of thermal vacancy concentration on the loop size and orientation is neglected.

Combining Equations (1.60)-(1.61), the dislocation loop growth rate can be expressed as [88]

$$V_l^m(R) = \frac{G\Phi(G/G_R)}{b k_I^2 k_V^2}\left(A^m \rho_d + B^m \rho_l\right), \qquad (1.62)$$

where $A^m = \eta_I^m \langle Z_V \rangle - \eta_V^m \langle Z_I \rangle$, $B^m = (\eta_I^m \langle \eta_V R \rangle - \eta_V^m \langle \eta_I R \rangle)/\langle R \rangle$, $G_R = k_I^2 k_V^2 D_I D_V / 4 q_{IV}$, $\rho_l = 2\pi N_L \langle R \rangle$ is the total dislocation density in loops and function Φ is the same as in Equation (1.13).

Eq. (1.62) implies that the loop kinetics reflects the competition of two processes:

(i) diffusional interaction of loops with network dislocations, specified by parameter A^m. Usually $A^m > 0$ because dislocation loops interact with interstitials more efficiently

than network dislocations [79,89]. The preferential interstitial absorption on loops as compared to network dislocations contributes to the growth of all loops, independent of their orientation.

(ii) diffusional interaction between loops of different orientations, specified by parameter B^m, which depends only on the loop bias factors. When the external load is absent, η_α are independent of loop orientation and $B^m = 0$. Under the effect of external stress the loop bias factors become sensitive to the loop orientations and B^m becomes non-zero. As a result, there occurs a redistribution of point defects between the loops oriented "favorably" (at $B^m > 0$) and "unfavorably" ($B^m < 0$) with respect to loading direction.

At the early stages of irradiation, when ρ_l is low, the first mechanism dominates and all loops grow due to their preferential absorption of interstitials with respect to network dislocations. For example, when the temperature is sufficiently high to neglect the recombination of point defects, the dependence of the average loop radius R^m on the irradiation dose φ is given by relation [88]:

$$R^m \approx R_c\left[(1+\varphi/\varphi_c)^{1/3}-1\right], \qquad (1.63)$$

where $R_c \approx 0.1\ \rho_d/N_L \approx$ 1-10 nm and $\varphi_c \approx 10^2$- $10^3\rho_d^2 a/N_L \approx 10^{-5}$- 10^{-1} dpa at $\rho_d \approx 10^8$-10^{10} cm^{-2}, $N_L \approx 10^{15}$ cm^{-3} and $a \approx 0.2$ nm. In other words, at small irradiation doses the loop size increases linearly with time, whereas at higher doses the growth rate slows down to $R^m \propto \varphi^{1/3}$. Such qualitative behaviour of the loop sizes is very typical for the experimental observations of loop kinetics in irradiated materials [173,174,90].

As loops become larger, the redistribution of point defects between loops grows in importance. Accordingly, the unfavorably oriented loops tend to grow slower than those oriented favorably. This effect was also demonstrated experimentally [70,71], as well as in numerical calculations in the framework of cluster dynamics [91] (see Figure 6).

Figure 6. Calculated dependencies of loop radius variation under the effect of uniaxial stresses of 0, 110 and 220 MPa

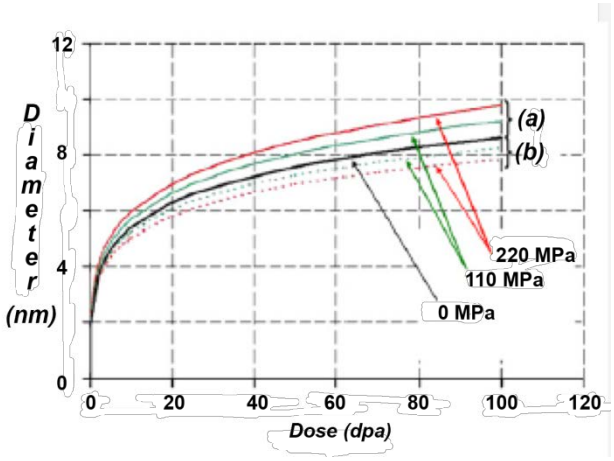

Solid curves are for well oriented loops, and dashed curves - for badly oriented loops. At zero stress the curves are superposed [91].

Moreover, as shown in [88], when the external tension exceeds some critical value σ^*, the defect redistribution between loops of different orientations can be so strong that at a certain dose the growth rate of unfavorably oriented loops becomes negative before these loops grow large enough to become a part of the dislocation network. As irradiation continues, these loops can dissolve completely, creating strongly anisotropic dislocation distribution over orientations. The characteristic doses of loop dissolution are of the order of $\varphi_R \approx 10^{-9}\rho_d\sigma^3/N_L\mu^3$, while the maximum size of unfavorably oriented loops is $R_{max} \sim 2\times10^{-3}\,\rho_d\mu/N_L\sigma$. The shrinkage of unfavorably oriented loops is possible, if $R_{max} < (\pi\rho_d)^{1/2}$, or, equivalently

$$\frac{N_L}{\rho_d^{3/2}}\frac{\sigma}{\mu} < 0.1. \qquad (1.64)$$

This relation gives the estimate of $\sigma^* \sim 5\times10^{-3}\mu$ for the minimum stress required for the observation of the loop dissolution [88]. At $\rho_d \approx 10^8$ cm^{-2}, $\sigma/\mu \approx 5\times10^{-3}$ and $G = 10^{-3}$ dpa/s the characteristic time of loop redistribution is of the order of 10^4-10^5 s. This time is sufficiently low to allow the observation of this effect in annealed metals subject to intensive irradiation (e.g. in High-Voltage electron microscopes or on fast particle accelerators).

The re-solution of dislocation loops was indeed observed in annealed nickel samples irradiated in the electron microscope [90]. The rate of damage creation in that experiment reached 2×10^{-3} dpa/s and the loads were as high as 50 MPa (corresponding to $\sigma/\mu \approx 6\times10^{-3}$). Though the volume density of loops was not reported, a rough estimate based on electron micrographs presented in [90] gives $N_L \approx 10^{15}$ cm^{-3}. In other words, the set of experimental parameters satisfied relation (4.64). The kinetics of growth of several separate loops is shown in Figure 7.

Figure 7. The dependence of individual loop sizes in electron irradiated Ni on irradiation time

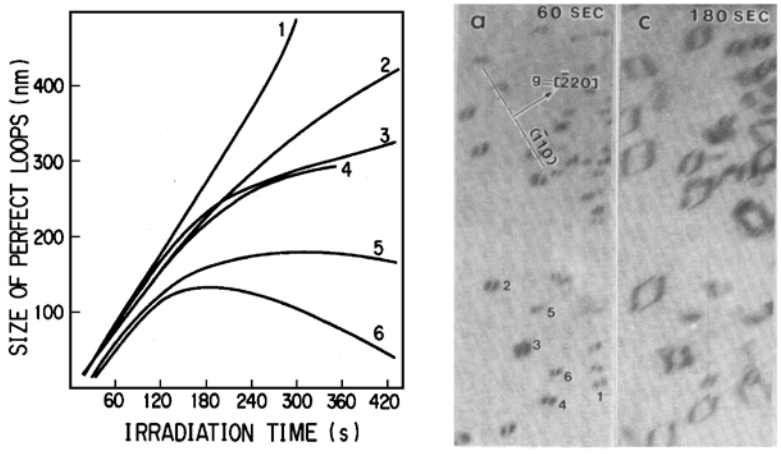

Numbers at the curves indicate the loops shown in TEM micrographs [90].

The first stage of loop kinetics, when loops grow mainly due to their diffusional interaction with dislocations, promotes the transient irradiation creep [88]. The character of the dose dependence of creep is highly sensitive to both the point defect absorption biases for loops and dislocations, and to the possible orientational anisotropy of loop nucleation. Figure 8 demonstrates some trends that are predicted by the theoretical investigation of irradiation creep at the transient stage.

Figure 8. (a) The qualitative behaviour of irradiation creep modulus B (normalised per steady-state value B_0) as a function of time t at the transient stage

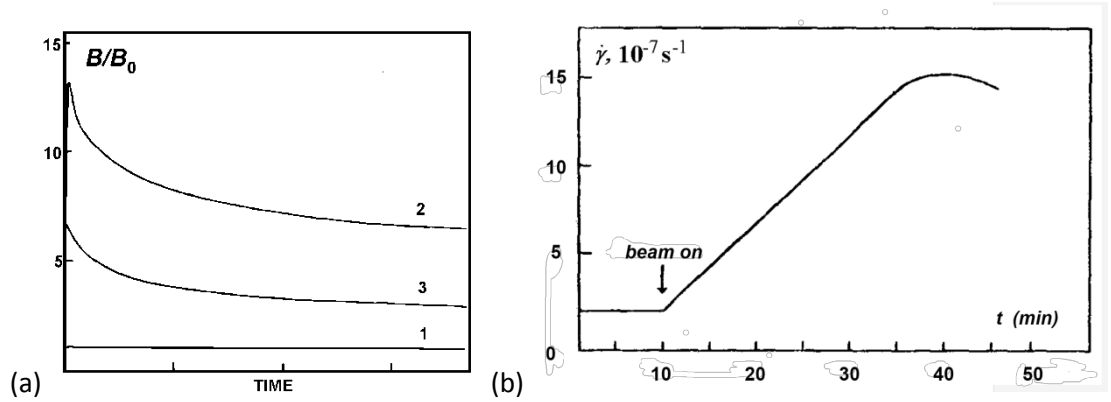

Numbers on the curves correspond to different limiting cases: 1 - without preferential nucleation of aligned dislocation loops; 2 - with preferential nucleation of aligned dislocation loops; 3 – with the account of point defect absorption limitations in dislocation cores. (b) The initial stage of creep in a twisted Al wire irradiated with 2 MeV electrons at a rate of 10^{13} $e^-/(cm^2\ s)$ [92].

When the mechanisms leading to point defect absorption bias are identical for loops and dislocations and the orientational dependence of loop nucleation is neglected, no creep rate sensitivity to irradiation dose is expected. This is quite evident because in this case loops and network dislocations capture point defects in the same way (i.e. $\eta_\alpha \approx Z_\alpha$), while the variations of relative densities f'' of dislocation loops and dislocations at the initial stage of loop growth is insignificant (even though the absolute values of dislocation densities, ρ_d and ρ_b, can strongly change).

A sharp increase of the creep rate practically immediately after the switch-on of irradiation is predicted, when the loop nucleation dependence on stress orientation is taken into account (see curve 2 in Figure 8(a)). The rate of irradiation creep during some irradiation time ($\sim 0.1\Phi_i$) grows practically linearly with dose, and then gradually decreases. It is interesting to compare this analytical prediction to results of [92], where the creep of annealed Al was investigated at 40-150°C during irradiation with 2 MeV electrons (defect production rate $G \sim 10^{-9}$ dpa/s). The authors of [92] overtly assign the observed irradiation creep to the interstitial loop growth (with loop density $N_L \sim 10^{15}$ cm^{-3}) and to the climb of dislocations. It is easy to check that the experimental conditions allow neglecting point defect recombination. The general behaviour of the dose dependence of irradiation creep rate shown in Figure 8(a) resembles very much the experimental dependence shown in Figure 8(b). The measured time of the creep rate increase also

correlates well with the theoretical estimate, which for the specified values of G and N_L and for dislocation density of 10^8 cm^{-2} (as typical for annealed metals) constitutes ~10^4 s.

The irradiation creep rate noticeably falls with increasing dose also where the point defect absorption biases strongly differ for loops and dislocations. In particular, curve 3 in Figure 8(a) demonstrates the behavior of irradiation creep rate for the case, where the bias of loops is due to the point defect elastic modulus anisotropy effects, while the point defect capture by network dislocations is limited by the availability of jogs in the dislocation cores. In the latter case the asymmetry of loop nucleation changes only the magnitude, but not the general behavior of irradiation creep rate.

1.5 Accelerated creep and the interrelation between irradiation creep and swelling

The evolution of the dislocation system is often accompanied at the later stages of irradiation with the development of voids and/or gas bubbles that promote the volume change of irradiated material. The competition for point defects between dislocations and voids directly affects the dislocation climb rate and thus the irradiation creep. This section deals with the third stage of irradiation creep, which occurs in parallel with the swelling.

The total strain rate of the material due to dislocation climb, $\dot{\varepsilon}_{ij}$ (i,j = 1,2,3), is determined by the first term on the r.h.s. of equation (1.5). The irradiation creep rate should be deduced from the total strain rate by the extraction of the rate of volume change (swelling). If one follows convention (1.1) and assumes swelling to be completely isotropic, one obtains

$$\dot{\varepsilon}_{ij}^{I} = \rho_d b(\left\langle \hat{b}_i \hat{b}_j V_c \right\rangle - \frac{1}{3}\delta_{ij} \left\langle V_c \right\rangle). \qquad (1.65)$$

It can be easily shown, however, that such a definition of irradiation creep can cause problems. Indeed, let us consider the case where no external stress is acting on the material. Then all dislocations climb at the same rate $V_{c0} = \left\langle V_c \right\rangle$ irrespective to their orientation, so that

$$\dot{\varepsilon}_{ij}^{I} = (\left\langle \hat{b}_i \hat{b}_j \right\rangle - \frac{1}{3}\delta_{ij})\rho_d b V_{c0}. \qquad (1.66)$$

When the dislocation structure is isotropic, the irradiation creep rate thus defined vanishes, as it should. However, if the dislocation structure is anisotropic, Equation (1.66) predicts a non-zero rate of shape distortion even though no strains are applied to the material. In order to avoid this problem, one can re-define the swelling rate $\dot{\varepsilon}_{ij}^{S}$ as:

$$\dot{\varepsilon}_{ij}^{S} = \rho_d b\left\langle \hat{b}_i \hat{b}_j \right\rangle V_c, \qquad (1.67)$$

which is automatically reduced to the usual relation $\dot{\varepsilon}_{ij}^{S} = \delta_{ij}\dot{S}/3$, when the dislocation structure is isotropic. When an external load is applied to the material, it is reasonable to retain eq. (1.67) as a definition of the swelling-induced strain rate and write down the irradiation creep rate as [93]:

$$\dot{\varepsilon}_{ij}^{I} = \rho_d b(\left\langle \hat{b}_i \hat{b}_j V_c \right\rangle - \left\langle \hat{b}_i \hat{b}_j \right\rangle \left\langle V_c \right\rangle). \qquad (1.68)$$

As shown below, two different definitions of the irradiation creep rate, eqs. (1.65) and (1.68) can give very different predictions about the irradiation creep behaviour at the late stages of irradiation.

Let us restrict ourselves to a simple model, where only dislocations and voids constitute the defect microstructure of the material. As before, there are K different dislocation orientations and the corresponding partial dislocation densities ρ_d^k ($1 \le k \le K$) are maintained at a constant level. All voids are assumed to have the same radius R_c, while the volume density of voids N_c is assumed to be constant because the void density saturation occurs relatively soon after the swelling onset.

The climb velocity of a dislocation of the k-th orientation is given by equation (1.8), while the rate of void growth is described by the commonly used relation

$$\frac{dR_c}{dt} = \frac{1}{R_c}\Big[D_V (C_{V0} - C_{V0}^{th}) - D_I C_{I0} \Big]. \qquad (1.69)$$

The mean-field point defect concentrations, $C_{\alpha 0}$, are given by the balance equations

$$G - k_\alpha^2 D_\alpha (C_{\alpha 0} - C_{\alpha 0}^{th}) = 0, \qquad (1.70)$$

where $k_\alpha^2 = \langle Z_\alpha \rangle \rho_d + 4\pi N_c R_c$ is the total sink strength for the α-type point defects. In writing down (4.70) we neglect point defect recombination, which is of no importance in the temperature range, where swelling occurs. Also, the dependence of thermal emission of vacancies from sinks on sink parameters is neglected, since it gives no contribution to SIPA irradiation creep.

Substituting the values of point defect concentrations, as defined by equation (1.70), into eqs. (1.69) and (1.5), one easily obtains from Equation (1.68) the relation between the irradiation creep and swelling rates that closely resembles Equation (2.1), that is

$$\dot{\varepsilon}_{ij}^I = B_{ij} \frac{\langle Z_I \rangle \langle Z_V \rangle \rho_d^2}{k_I^2 k_V^2} G + D_{ij} \dot{S}, \qquad (1.71)$$

where the swelling rate is defined as

$$\dot{S} = \langle Z_I - Z_V \rangle \frac{4\pi N_c R_c \rho_d}{k_I^2 k_V^2} G \qquad (1.72)$$

and the structure factors B_{ij} and D_{ij} are

$$B_{ij} = \frac{\langle \hat{b}_i \hat{b}_j Z_I \rangle}{\langle Z_I \rangle} - \frac{\langle \hat{b}_i \hat{b}_j Z_V \rangle}{\langle Z_V \rangle} \qquad (1.73)$$

and

$$D_{ij} = \frac{\langle (Z_I - Z_V) \hat{b}_i \hat{b}_j \rangle - \langle Z_I - Z_V \rangle \langle \hat{b}_i \hat{b}_j \rangle}{\langle Z_I - Z_V \rangle}. \qquad (1.74)$$

Let us suppose now that the material is under the action of uniaxial stress σ (the discussion of the general loading case can be found in [93]). When these stresses are lower than the threshold stress value σ^* (equal either to the material shear modulus μ [199], or to $k_B T/\omega$ [16,19]), the bias factors can be expanded to the first order in stresses, see eq. (1.15). Substituting this expansion into Equations (1.73) and (1.74) and taking into account that the stress-free dislocation bias for interstitial absorption $\Delta Z = (Z_i^0 - Z_v^0)/(Z_i^0 + Z_v^0) \ll 1$, one obtains for the creep rate along the loading axis :

$$\dot{\varepsilon}^I = BG\frac{\sigma}{\mu}, \tag{1.75}$$

with the creep compliance B being equal to

$$B = B_0\left(\frac{1}{(1+r_c)^2} + \frac{1}{2\Delta Z}\frac{dS_0}{d\phi}\right), \tag{1.76}$$

where $\phi = Gt$ is the irradiation dose, $\dot{S}_0$ is the stress-free swelling rate,

$$\dot{S}_0 = \frac{2\Delta Z G r_c}{(1+r_c)^2}, \tag{1.77}$$

$r_c = R_c/R^*$ is the normalised void radius, $R^* = 4\pi N_c / \overline{Z}\rho$, $\overline{Z} = (Z_I^0 + Z_V^0)/2$ and B_0 is the value of creep compliance in the absence of swelling, which depends on the selected mechanism of stress-induced dislocation bias anisotropy and, in some cases, on the lattice crystallography. For example, in a completely isotropic material the use of equation (1.23) results in

$$B_0 = \frac{2(2-\nu)}{30\pi}\left(\frac{Z_I^0 p_I^\mu}{e_{I0}} - \frac{Z_V^0 p_V^\mu}{e_{V0}}\right), \tag{1.78}$$

which gives $B_0 \approx 0.05$ for typical parameter values. Alternatively, when the effect of point defect polarisation at the saddle-points of diffusion jumps is considered, the crystalline lattice of the metal is cubic and the material is polycrystalline, one can use the bias factor expansion over stresses in the form of equation (1.27) and use the averaging over all possible grain orientations, thus getting

$$B_0 = \frac{(1+\nu)\mu\omega}{45(1-2\nu)k_B T}\left[e_I^s(d_I^{(2)} + \frac{2}{3}d_I^{(3)}) - e_V^s(d_V^{(2)} + \frac{2}{3}d_V^{(3)})\right]. \tag{1.79}$$

After simple transformations, equation (1.76) can be reduced to another form,

$$B = B_0 + D^c\frac{dS_0}{d\phi}, \tag{1.80}$$

where the creep-swelling coupling factor D^c is

$$D^c = -\frac{B_0}{2\Delta Z}(1+r_c). \tag{1.81}$$

Note that the absolute value of the coupling factor thus defined does not exceed ~100, while the factor itself is negative.

Equation (1.76) reveals the advantages of irradiation creep rate definition according to (1.68). First of all, the creep rate thus defined is related to the stress-free swelling rate, which can be measured much easier than the swelling rate of a stressed material. Moreover, if the dislocation anisotropy during swelling is maintained only by SIPA-induced point defect partitioning between differently oriented dislocations (or dislocation loops) as suggested in [94,95], the degree of dislocation anisotropy is proportional to external stress. Consequently, the anisotropy of dislocation structure can in this case be neglected.

The dependence of B on the normalised void radius r_c can be converted to the dose dependence wia straightforward integration of Equation (1.69) with point defect concentrations defined by Equation (1.70):

$$r_c^2 + \frac{4}{3} r_c^3 + \frac{1}{2} r_c^4 = 4\Delta Z(\phi - \phi_{in}) \qquad (1.82)$$

where $\phi = \varphi / \Phi_c$ is the normalized dose, ϕ_{in} is the incubation dose for void nucleation and

$$\Phi_c = \frac{(\bar{Z}\rho_d)^3}{64\pi^2 \Delta Z N_c^2}. \qquad (1.83)$$

At the typical values of $\rho_d \approx 3\times10^{10}$ cm^{-2} and $N_c \approx 10^{15}$ cm^{-3} one gets $\Phi_c \approx 5$ dpa. The predicted dependencies of the creep compliance and the total material strain on irradiation dose are shown in Figure 9. It is seen that the SIPA-based mechanisms predict the reduction of irradiation creep due to swelling, which correlates to experimental observations of creep cessation at high irradiation doses [15,40,41,96].

Figure 9. Dose dependence of the normalised creep compliance B/B_0 (a) and total strain (b) with (curve 1) and without (curve 2) account of the swelling rate enhancement by stress

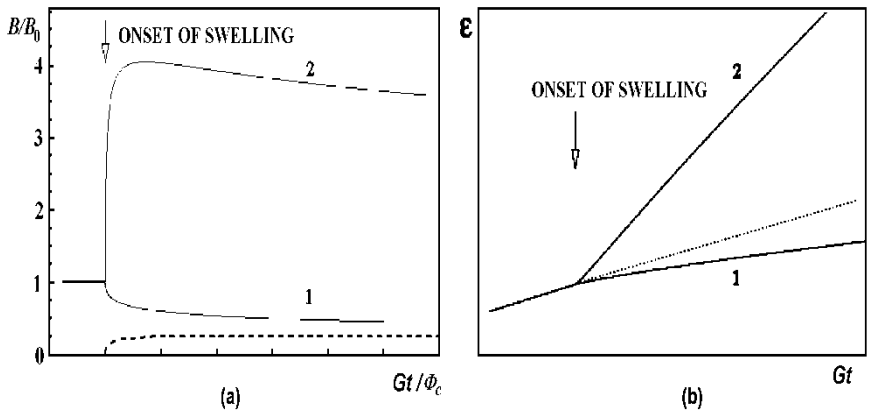

The dashed line in (a) is the stress-free swelling rate, the dotted line in (b) - the swelling-free trend [93].

In contrast, when the creep rate is defined using equation (1.65) instead of (1.70), the creep compliance looks like:

$$B = B_0 + D^c \frac{dS_0}{d\phi} + \frac{\mu}{\sigma}\left(\left\langle \hat{b}_1^2 \right\rangle \frac{dS}{d\phi} - \frac{1}{3}\frac{dS_0}{d\phi} \right), \qquad (1.84)$$

where $dS/d\phi$ is the actual (i.e. stress-affected) swelling rate. As compared to (1.80), equation (1.84) contains an additional contribution, which can be non-zero for at least two reasons.

First of all, the swelling rate in the loaded material can differ from the stress-free one. At relatively low stresses (<100 MPa) the swelling is known to depend on stress as (see Section 2.3):

$$S = S_0(1 + D^s \frac{\sigma}{\mu}), \qquad (1.85)$$

where D^S is a material constant. If D^S is time-independent and the dislocation structure is isotropic ($\left\langle \hat{b}_1^2 \right\rangle = 1/3$), equation (1.84) has the form

$$B = B_0 + \left(D^c + \frac{D^s}{3} \right) \frac{dS_0}{d\phi}. \qquad (1.86)$$

Equations (1.80) and (1.86) have the same functional form, but now the creep-swelling coupling factor includes a correction $D^S/3$, which can be of the same order of magnitude as the experimentally observed values of ~10^4. Figure 1.9 shows that equation (1.86) predicts both the increase of creep compliance and the growth of the total strain with the irradiation dose after the onset of swelling.

Another source of the creep rate modification, by the last term in the r.h.s. of eq. (1.84) can be the anisotropy of the dislocation structure. According to both experimental observations [39,71,97,98] and theoretical predictions [70,88,99,100], such anisotropy can result from SIPA-induced preferential growth of interstitial loops. A detailed investigation of the anisotropic dislocation structure kinetics and its contribution to creep-swelling coupling was undertaken in [94,95]. Strictly speaking, some of the assumptions used in these papers do not fit in the experimental picture. For example, the enhanced growth of favourably oriented dislocation loops in the presence of voids is hardly probable, even assuming the continuous interstitial loop nucleation in irradiation produced collision cascades [101,102]. Nonetheless, if for some reason the SIPA-induced anisotropy of dislocation orientations arises at the steady-state swelling stage, additional contribution to irradiation creep modulus can be expected.

To demonstrate this, let us assume that the relative density of dislocations with the Burgers vector along the loading direction is by Δf higher than the otherwise isotropic dislocation density. Then, even when the swelling rate is not influenced by stress, Equation (1.84) provides an additional contribution to the creep modulus,

$$\Delta B^g = \frac{2\Delta f}{3\sigma}\frac{dS}{d\varphi}. \qquad (1.87)$$

The dislocation anisotropy factor Δf can reach values up to 0.8-0.9 [97], so that at the stresses of the order of 100 MPa the expected contribution to the creep-swelling coupling factor is again of the same order of magnitude, as its experimental value. Since the dislocation anisotropy is the direct product of dislocation structure evolution under the action of external stresses, the contribution given by (1.87) cannot be eliminated by swelling measurements on unloaded samples. Moreover, if only one component of the strain tensor is measured, one cannot even check whether this systematic error is present or not.

Summing up, the way in which the total strain is separated into contributions from the irradiation creep and swelling can crucially influence the correlation between these phenomena. When the irradiation creep rate is defined as the difference between the total strain rate and the stress-modified swelling, the swelling decreases SIPA irradiation creep rate with the increase of irradiation dose. On the contrary, when the stress-free value of swelling is subtracted from the total strain rate, the predicted correlation between creep and swelling is described by equation (1.84) with the creep-swelling coupling factor of the same order of magnitude as that observed experimentally.

Finally, let us briefly discuss the effect of voids on the "climb-controlled glide" mechanisms of irradiation creep.

In the absence of voids, the dominant mode of dislocation motion at the steady-state creep stage is climb and only at stresses close to the irradiation-modified yield stress of material the climb-controlled glide can noticeably contribute to irradiation creep. The situation becomes more complicated, when voids appear in the material. The accumulation of vacancies into voids is accompanied by large currents of uncompensated interstitials to all dislocations, so that the relative role of stress-induced misbalance of interstitial redistribution between differently oriented dislocations becomes less pronounced and a decrease of the SIPA-type contribution to irradiation creep is expected [93,100,103]. On the other hand, the absolute values of dislocation climb velocities increase, simplifying climb-controlled glide. It is a long-lasting tradition to ascribe irradiation creep acceleration by swelling to the action of CCG creep mechanism [41,46,104-106].

Indeed, in the case when point defect concentrations are defined by Equation (1.70), the absolute value of dislocation climb rate is expressed in terms of the swelling rate dS/dt simply as:

$$V_c = \frac{1}{b\rho_d}\frac{dS}{dt}, \qquad (1.88)$$

where the dislocation bias dependence on the dislocation orientation is neglected. Correspondingly, the irradiation creep due to the CCG mechanism in the presence of swelling is given by:

$$\dot{\varepsilon}_{ij}^{I} = \frac{1}{2}\left\langle (\hat{b}_i n_j + n_i \hat{b}_j)\frac{L_g}{h}\right\rangle \frac{dS}{dt}. \qquad (1.89)$$

Note that in the case of the climb-controlled glide it is not necessary to subtract the swelling contribution from the total strains in order to get the true creep strains, since dislocation glide is, by definition, volume conserving.

The most striking feature of relation (1.89) is that the stress dependence of the creep rate is completely determined by the glide factor. Very often [41,46,104-106] a linear stress dependence of the glide factor is postulated and the resulting swelling contribution is reduced to the standard form. However, as discussed in Section 1.3, quite different stress dependencies of the glide factor can be observed. In particular, glide stopping by impurity atoms involves no stress dependence of the glide factor, so that no dependence of the CCG creep rate on stress should be expected in this case.

On the other hand, the increase of the dislocation climb is not the only reason for void effect on the irradiation creep. At the same time, the efficiency of dislocation pinning by voids increases with the increase of the average void size and at a certain swelling level the voids become the principal obstacle set for gliding dislocations. In this situation dislocation segments terminate on voids [40,107] and cannot be detached by glide because the voids are strong obstacles to dislocation motion. The climb of pinned dislocation segments is also largely reduced due to pipe diffusion of point defects to voids along dislocations, so that the unpinning of dislocations from voids is expected to be practically suppressed when the swelling reaches ~ 30% [108]. Therefore, the acceleration of irradiation creep in the framework of the climb-controlled dislocation glide mechanism, even if observed, is no more than transient and should be eventually suppressed as the swelling increases. It is no wonder, therefore, that the irradiation creep cessation at high swelling levels is observed.

2. Summary

The safe operation of nuclear reactors requires dimensional stability of their structural and functional materials operating in heavy radiation environment. The radiation resistance of these materials is limited by such physical phenomena as swelling, irradiation creep, radiation embrittlement, etc. All these phenomena are caused by the production of primary radiation damage by external irradiation with fast particles, which in turn promotes the transformation of material microstructure, including nucleation and growth of defect clusters in the form of voids, gas bubbles and dislocation loops.

This chapter summarises the main trends of irradiation swelling and creep reported in the literature and describes the available theoretical models developed for the explanation of swelling and creep behaviour of reactor materials. In particular, the influence of experimental conditions on parametric dependencies of irradiation swelling and creep are discussed and correlated to the underlying microstructural evolution, which causes both these effects.

The ability of the existing theoretical models of irradiation swelling and creep to reproduce the observed dose, temperature, and stress dependencies of these effects is critically assessed. It is demonstrated that theoretical models are able to give a reasonable description of both swelling and irradiation creep in a broad range of material operation parameters, both in qualitative and often even in quantitative terms.

The knowledge of the main features of irradiation swelling and creep and of the microscopic reasons responsible for that or other mode of material response to particular experimental conditions (such as irradiation dose, flux, temperature, etc.) is helpful not only for qualitative predictions of irradiated material performance in nuclear facilities, but provides as well a reliable basis for correlation of experiments and measurements undertaken in strongly different conditions (e.g. in simulation experiments on fast particle accelerators vs. actual in-reactor behaviour).

References

[1] T. Mura, Int. J. Eng. Sci. 1, 371 (1963).

[2] W.G. Wolfer, Philos. Mag. A 43, 61 (1981).

[3] J. Hirth, J. Lothe, Theory of Dislocations (McGraw-Hill, NY, 1967).

[4] T. Diaz de la Rubia, M.W. Guinan, A. Caro, P. Scherrer, Rad. Effects Def. Sol. 130-131, 39 (1994).

[5] W.J. Phytian, R.E. Stoller, A.J.E. Foreman, A.F. Calder, D.J. Bacon, J. Nucl. Mater. 223, 245 (1995).

[6] D.R. Harries, J. Nucl. Mater. 65, 157 (1977).

[7] G.W. Lewthwaite, D. Mosedale, in: Irradiation Behaviour of Metallic Materials for Fast Reactor Core Components, Proc.Int.Conf., Ajaccio, France, 1979, p.399.

[8] R.A. Johnson, J. Phys. F 3, 295 (1973).

[9] P.T. Heald, M.V. Speight, Philos. Mag. 29, 1075 (1974).

[10] R. Bullough, M.R. Hayns, J. Nucl. Mater. 57, 348 (1975).

[11] R. Bullough, J.R. Willis, Philos. Mag. 31, 855 (1975).

[12] E.J. Savino, Philos. Mag. 36, 323 (1977).

[13] Z.K. Saralidze, Fiz. Tv. Tela 20, 2716 (1978).

[14] N.A.Demin, Yu.V.Konobeev, in: Radiation Defects in Metals (Nauka, Alma-Ata, 1981), p.128. (in Russian)

[15] C.H. Woo, U. Gosele, J. Nucl. Mater. 119, 219 (1983).

[16] C.H. Woo, J. Nucl. Mater. 120, 55 (1984).

[17] A.I. Ryazanov, V.A. Borodin, Rad. Effects 55, 157 (1981).

[18] A.I. Ryazanov, V.A.Borodin, Rad. Effects 56, 179 (1981).

[19] V.A. Borodin, A.I. Ryazanov, J. Nucl. Mater. 135, 46 (1985).

[20] V.A. Borodin, A.I. Ryazanov, in: Effects of Radiation on Materials. 15th Int. Symp., ASTM STP 1125 (ASTM, Phil., 1992) p.530.

[21] E. Kroner, Physik der Kondensierten Materie, Band 2. 1964, s.262.

[22] C.H. Woo, AECL-6791 (1980).

[23] E. Kuramoto, J. Nucl. Mater. 122, 422 (1984).

[24] J. Holder, A.V. Granato, L.E. Rehn, Phys. Rev. B 10. 363 (1974).

[25] H. Wenzl, in: Vacancies and Interstitials in Metals, Eds. A.Seeger et al. (North-Holland, Amsterdam, 1970) p.363.

[26] P.H. Dederichs, K. Schroder, Phys. Rev. B 17, 2524 (1978).

[27] E.J. Savino, C.N. Tome, J. Nucl. Mater. 108-109, 405 (1982).

[28] M.P. Puls, C.H. Woo, J. Nucl. Mater. 139, 48 (1986).

[29] H.R. Schober, J. Nucl. Mater. 126, 220 (1984).

[30] E.Ya. Mikhlin, V.V. Nelaev, in: Computer Modeling of Defects in Crysatals (LFTI, Leningrad, 1979) p.166 (in Russian).

[31] H. Saka, T. Kondo, N. Kiba, Philos. Mag. A 44, 1213 (1981).

[32] A. Seeger, in: Defects in Crystalline Solids, Proc.Int.Conf., Univ. of Bristol, July 1954 (London, 1955), p. 392.

[33] V.A. Borodin, V.V. Kolomytkin, Yu.R. Kevorkyan, A.I. Ryazanov, J. Nucl. Mater. 187, 131 (1992).

[34] Yu.S. Pyatiletov, Fiz. Met. Metalloved. 50, 646 (1980).

[35] V.V. Kirsanov, Yu.S. Pyatiletov, O.G. Tyupkina, Phys. Stat. Sol. (a) 64, 735 (1981).

[36] J. Weertman, J. Appl. Phys. 26, 1213 (1955).

[37] G.S. Ansell, J. Weertman, Trans. AIME 215, 838 (1959).

[38] S.D. Harkness, J.A. Tesk, C.-Y. Li, Nucl. Appl. Techn. 9, 24 (1970).

[39] W.I. Duffin, F.A. Nichols, J. Nucl. Mater. 45, 302 (1972/73).

[40] L.K. Mansur, Philos. Mag. A 39, 497 (1979).

[41] J.H. Gittus, Phiosl. Mag. 25, 345 (1972).

[42] D.O. Northwood, L.E. Bahen, R.G. Fleck, J.Nucl.Mater. 66, 209 (1977).

[43] B. Burton, Philos. Mag. A 43, 1 (1981).

[44] C.C. Dollins, Rad. Effects 11, 123 (1971).

[45] C.C.Dollins, R.R.Tucker, J.Nucl.Mater., 52, 277 (1974).

[46] W.G. Wolfer, J.P. Foster, F.A. Garner, Nucl. Techn. 16, 55 (1972).

[47] W.G. Wolfer, A. Boltax, in: Irradiation Embrittlement and Creep in Fuel Cladding and Core Components (BNES, London, 1972) p.283.

[48] J.A. Hudson, R.J. McElroy, R.S. Nelson, in: Application of Ion Beams to Materials. Inst. of Phys. Conf. Ser. N 28, London, 1975, p. 251.

[49] C.H. Henager, Jr., E.P. Simonen, E.R. Bradley, R.S. Stang, J. Nucl. Mater. 104, 1269 (1981).

[50] C.H. Henager,Jr., E.P. Simonen, E.R. Bradley, R.G. Stang, J. Nucl. Mater. 122, 413 (1984).

[51] A.H. Cotterill, Dislocations and Plastic Flow in Crystals (Oxford Univ., Oxford, 1953).

[52] N.V. Mott, Philos. Mag. 43, 1151 (1952).

[53] J. Friedel, Philos. Mag. 44, 444 (1953).

[54] R. Labusch, Z. Phys. 167, 452 (1962).

[55] A.S. Argon, Philos. Mag. 25, 1053 (1972).

[56] A.I. Landau, V.N. Vydashenko, Metallofizika 4, 3 (1982).

[57] J.E. Dorn, P. Guyot, T. Stefansky, in: Physics of Strength and Plasticity, A.S.Argon, ed. (MIT, Cambridge, 1969) p.133.

[58] A.J.E. Foreman, M.J. Makin, Canad. J. Phys. 45, 511 (1967).

[59] V.M. Chernov, M.M. Savin, Phis. Stat. Sol. (a) 53,113 (1979)

[60] A.J.E. Foreman, M.J. Makin, Philos. Mag. 14, 911 (1966).

[61] A.L. Bement, Rev. Roum. Phys. 17, 361 (1972).

[62] J.J. Holmes, R.E. Robbins, J.L. Brimhall, B. Mastel, Acta Met. 26, 955 (1968).

[63] M.B.Toloczko, G.E. Lucas, G.R. Odette, R.E. Stoller, M.L. Hamilton, in: Effects of Radiation on Materials: 17th Int.Symp., ASTM STP 1270 (ASTM, Phil., 1996), p.902.

[64] R.O. Scattergood, D.J. Bacon, Acta Met. 30, 1665 (1982).

[65] F.A. Garner, M.L. Hamilton, N.F. Panayotou, G.D. Johnson, J. Nucl. Mater. 103-104, 803 (1981).

[66] G.W. Lewthwaite, J. Nucl. Mater. 46, 324 (1973).

[67] P.R. Okamoto, S.D. Harkness, J.Nucl.Mater. 48, 204 (1973).

[68] Yu.N. Socursky, L.N. Protsenko, J. Brit. Nucl. Energy Soc. 14, 137 (1975).

[69] T. Tabata, Y. Nakajima, T. Hida, H. Fujita, in: High Voltage Electron Microscopy 1977 (Tokyo 1977) p.519.

[70] F.A. Garner, W.G. Wolfer, Trans. ANS 28, 144 (1978).

[71] F.A. Garner, W.G. Wolfer, H.R. Brager, in: Effects of Radiation on Structural Materials, Proc. 9th Int.Symp., ASTM STP 683, Eds. J.A.Sprague and D.Kramer (ASTM, Phil., 1979) p.160.

[72] D. Caillard, J.L. Martin, B. Jouffray, Acta Met. 28, 1059 (1980).

[73] D. Caillard, J.L. Martin, J. Microsc. Spectrosc. Electron. 6, 361 (1981).

[74] L. Le Naour, P. Grosjean, V. Levy, CEA-CONF-7170 (1984).

[75] M. Suzuki, S. Sato, J. Nucl. Mater. 172, 97 (1990).

[76] J. Chen, W. Hoffelner, J. Nucl. Mater. 392, 360 (2009).

[77] J. Garnier, Y. Bréchet, M. Delnondedieu, A. Renault, C. Pokor, P. Dubuisson, J.-P. Massoud, J. Nucl. Mater. 413, 70 (2011).

[78] J. Chen, P. Jung, W. Hoffelner, J. Nucl. Mater. 441, 688 (2013).

[79] W.G. Wolfer, J. Nucl. Mater. 90, 175 (1980).

[80] B.J. Whiting, D.J. Bacon, Mat. Res. Soc. Symp. Proc. 439, 384 (1997).

[81] Yu.N. Osetsky, A. Serra, V. Priego, Mat. Res. Soc. Symp. Proc. 527, 59 (1998).

[82] A.V. Barashev, Yu.N. Osetsky, D.J. Bacon, Mat. Res. Soc. Symp. Proc. 540, 697 (1999).

[83] A.V. Barashev, Yu.N. Osetsky, D.J. Bacon, Philos. Mag. A 80, 2709 (2000).

[84] R.V. Hesketh, Philos. Mag. 7, 1417 (1962).

[85] A.D. Brailsford, R. Bullough, Philos. Mag. 27, 49 (1973).

[86] G.W. Lewthwaite, Scripta Met. 7, 75 (1973).

[87] R. Bullough, M.H. Wood, J. Nucl. Mater. 90, 1 (1980).

[88] A.I. Ryazanov, V.A. Borodin, Rad. Effects 59, 13 (1981).

[89] L.A. Maximov, A.I. Ryazanov, Rad. Effects 33, 7 (1977).

[90] S. Jitsukawa, Y. Katano, K. Shiraishi, F.A. Garner, in: Effects of Radiation on Materials. 15th Int. Symp., ASTM STP 1125 (ASTM, Phil., 1992) p.1034.

[91] J. Garnier, Y. Bréchet, M. Delnondedieu, C. Pokor, P. Dubuisson, A. Renault, X. Averty, J.-P. Massoud, J. Nucl. Mater. 413, 63 (2011).

[92] Yu.M. Platov, S.V. Simakov, A.B. Tsepelev, Fiz. Khim. Obrab. Metal., n.1, 11 (1989).

[93] V.A. Borodin, J. Nucl. Mater. 225, 15 (1995).

[94] C.H. Woo, F.A. Garner, J. Nucl. Mater. 191-194, 1309 (1992).

[95] C.H. Woo, F.A. Garner, R.A.Holt, in: Effects of Radiation on Materials: 16th Int. Symp., ASTM STP 1175 (ASTM, Phil., 1994), p. 27.

[96] M.B. Toloczko, F.A. Garner, J.Nucl.Mater. 212-215, 509 (1994).

[97] D.S. Gelles, in: Effects of Radiation on Materials. 12th Int. Symp., ASTM STP 870, vol.1 (ASTM, Phil., 1985) p.98.

[98] F.A. Garner, D.S. Gelles, J. Nucl. Mater. 159, 286 (1988).

[99] W.G. Wolfer, L.K. Mansur, J.A. Sprague, in: Radiation Effects in Breeder Reactor Structural Materials, Proc.Int.Conf., Scottsdale, AZ, 1977 (Met. Soc. of AIME, 1977), p.841.

[100] C.H. Woo, Philos. Mag. A 42, 551 (1980).

[101] C.A. English, W.J. Phytian, A.J.E.Foreman, J. Nucl. Mater. 174, 135 (1990).

[102] T. Diaz de la Rubia, M.W. Guinan, Mat. Sci. Forum 97-99, 23 (1992).

[103] R. Bullough, M.R. Hayns, J. Nucl. Mater. 65, 184 (1977).

[104] S.D. Harkness, R. Grappel, S.G. McDonald, Nucl. Techn. 16, 25 (1972).

[105] P.T. Heald, J.E. Harbottle, J. Nucl.Mater. 67, 229 (1977).

[106] L.K. Mansur, W.A. Coghlan, in: Dimensional Stability and Mechanical Behaviour of Irradiated Metals and Alloys. Proc. BNES Conf., vol.2 (BNES, London, 1984) p.65.

[107] D.L. Porter, F.A. Garner, in: Influence of Radiation on Material Properties : 13th Int. Symp., part II, ASTM STP 956 (ASTM, Phil., 1988) p. 11.

[108]V.A. Borodin, A.I. Ryazanov, J. Nucl. Mater. 165, 164 (1989)

Chapter 8.

Nano-scale mechanisms in irradiation-induced strengthening

Y.N.Osetsky[1], D.J.Bacon[2]
[1]Materials Science and Technology Division, Oak Ridge National Laboratory, US,
[2]Department of Engineering, University of Liverpool, Liverpool, UK

Abstract

The microstructure of metals exposed to radiation in reactor cores contains defects such as cavities, dislocation loops, stacking fault tetrahedra and precipitates. These resist dislocation motion and give rise to changes in mechanical properties. The size and spacing of these defects are typically on the nanoscale, and so atomic-level details of dislocation-obstacle interactions can be studied by molecular dynamics (MD). We present examples. To model at the coarser mesoscale, i.e. dislocations moving under stress in random arrangements of obstacles, the continuum approximation of elasticity theory has to be used. Older line-tension approaches are inadequate and this has led to dislocation dynamics (DD) computer simulation. For realism, parameters and mechanisms in DD codes can be validated by results from MD. Examples of this multi-scale modelling framework are presented.

1. Introduction

Structural core materials in nuclear power plant experience an intensive flux of energetic atomic particles and this results in primary damage in the form of displacement cascades, i.e. nanoscale regions (~few nm) containing high super-saturations of vacancies and self-interstitial atoms (SIAs) – see Chapter 2. Depending on the material and temperature, the evolution of primary damage leads to a microstructure containing defect clusters, such as voids, dislocation loops (DLs), stacking fault tetrahedra (SFTs), gas-filled bubbles and precipitates and an increase in the total dislocation network density – see Chapter 3. The presence of this microstructure affects motion of dislocations, the subject of this chapter, and so changes mechanical properties, such as yield stress, ductility, creep behaviour and the ductile-to-brittle transition temperature – see Chapters 4, 5, 6, 9 and 10. Examples of the first two effects are provided by the stress-strain plots for Cu (face-centred cubic, FCC) and α-Fe (body-centred cubic, BCC) in Figure 1. Furthermore, if the density of

obstacles to dislocation motion is sufficiently high, plastic deformation requires operation of dislocation sources that are not active in the unirradiated state. The stress to operate them is high and this gives rise to new mechanisms such as yield drop, plastic instability and concentration of plastic deformation in narrow bands ('dislocation channelling') that are cleared of visible defects.

Figure 1. Stress strain curves for (a) proton-irradiated single crystal copper and (b) neutron-irradiated polycrystalline iron [41]

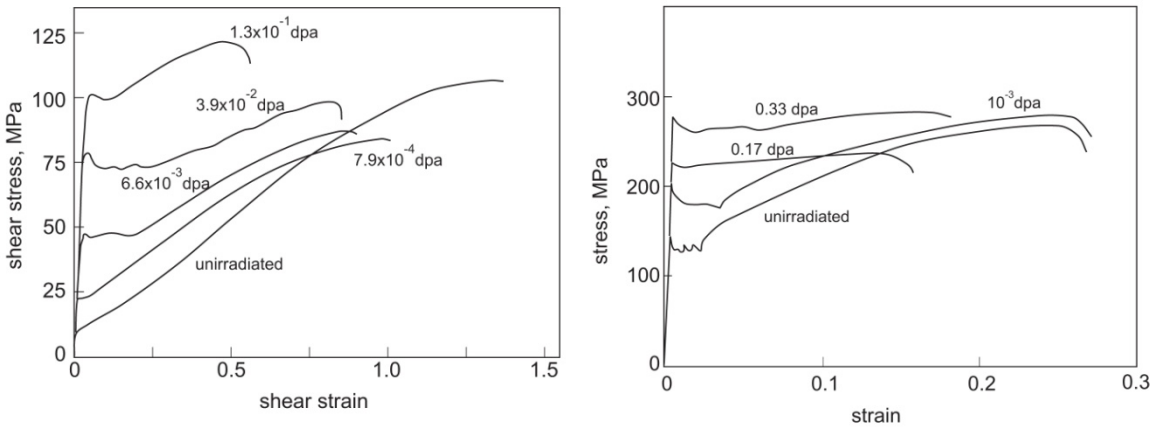

(a) (b)

A promising approach to understanding and predicting these effects is that based on multiscale materials modelling (MMM), in which phenomena are treated by computer simulation or theoretical methods appropriate for the length and times scales of the processes involved. The aim is to link the scales by either using parameters and/or mechanisms obtained for one scale in models for others, or validating assumptions used for one scale by calculations for another. The lowest level treats individual atoms by first principles, *ab initio* methods by solving Schrödinger's equation for moving electrons and ions. Calculations based on electron Density Functional Theory (DFT) take into account local chemical and magnetic effects and provide the most accurate computational techniques for studying single point defects, small clusters of point defects (up to ~10) and dislocation core structure. However, they are limited to systems containing up to ~1000 atoms, much too small for modelling properties of irradiated bulk materials, which involve phenomena acting over much longer length and time scales.

Atomic-scale modelling provides the first step to plugging this gap. Modelling at this level uses computer methods such as molecular statics (MS) and molecular dynamics (MD) to simulate up to millions of atoms over times of nanoseconds (ns) to microseconds (μs). In MS, a crystal at temperature $T = 0$ K is simulated, i.e. atoms have no kinetic energy, and the equilibrium of the system is found by minimising the potential energy. Atoms in MD have mean kinetic energy determined by T, i.e. $3kT/2$ where k is the Boltzmann constant and their trajectories evolve in a sequence of time-steps, in each of which their next position is predicted from the force on them using Newton's second law (acceleration = force/mass). The atomic energy and forces required for these methods are calculated from empirical interatomic potentials, which are designed to produce realistic

descriptions of the metals in question. This is achieved in part in the MMM approach by fitting the empirical parameters to chemical, defect and structural properties obtained *ab initio*. Fortunately, the scales involved in dislocation-damage interactions in irradiated metals are ideally suited to MD and MS because the defect clusters are typically a few nm in size and their density is ~10^{22}–10^{24}m^{-3}, i.e. spacing a few tens of nm. MD can be used to investigate the influence of temperature and applied stress on these interactions.

Mechanisms and parameters determined by MD modelling can be used in the MMM framework to inform dislocation dynamics (DD) models based on elasticity theory, for which the material is treated as a continuum. DD codes can be used to simulate many more dislocation-obstacle interactions than is possible with MD and can model multi-dislocation processes that occur over μm scales. They can also mesh at the next level with finite element methods for larger volumes of material.

In this chapter, we concentrate on MS and MD simulation of interactions between moving dislocations and obstacles to their motion. The aim is to provide an atomic-level detail of the mechanisms involved and show by way of examples what this has revealed. We also review some recent DD studies. First, we summarise the methods. Comprehensive introductions to dislocations and methods for modelling them are to be found in [12,13,5,3]: two examples of defects studied by the *ab initio* approach are [8,19].

2. Methods

2.1. Atomic-level modelling

The MS and MD models most widely used to simulate dislocation behaviour in metals are based on the periodic array of dislocations (PAD) scheme [3,22]. Periodic boundary conditions (PBCs) are used in the direction of the initially straight dislocation line so that it is effectively infinite in length. If the model also contains one obstacle, the length, L, of the model in the line direction represents the centre-to-centre obstacle spacing along an infinite row of obstacles. PBCs are also applied in the direction of dislocation glide, so that the dislocation is one of a periodic, two-dimensional array of identical dislocations. The success of PAD models is due to their simplicity and computational efficiency. With typically ~10^6–10^7 mobile atoms, it is possible to simulate dislocation interaction with obstacles of size up to ~10 nm and spacing up to ~100 nm, i.e. dimensions relevant for interactions in irradiated materials, using either parallelised or sequential codes on modern computers.

MD with the PAD scheme allows external shear stress (or strain) to be applied and the resultant elastic and plastic strain (or stress) and energy of the crystal to be calculated. With PBCs in the direction of dislocation glide, the dislocation can move over long distance without hindrance from the model boundary. Details of model construction can be found in [3,22]. Figure 2 illustrates models for edge or screw dislocations with Burgers vector $\boldsymbol{b}$ interacting with obstacles in BCC and FCC metals. The dimension L is shown parallel to the edge dislocation: it would be parallel to the screw dislocation for glide of the screw under shear stress τ. There are two types of dislocation loop in the BCC and FCC metals: they have Burgers vector $\boldsymbol{b}_L$ = ½<111> or <100>, and ½<110> or ⅓<111>, respectively. The first three are perfect dislocations, and therefore glissile, whereas the ⅓<111> Frank loop is faulted and sessile. These loops are commonly

formed by SIAs in irradiated metals and most studies in the literature have therefore simulated interstitial loops. Radiation damage in FCC metals can also contain Stacking Faults Tetrahedra (SFTs). They are formed by vacancies and consists of six stair-rod partial dislocations bounding four triangular stacking faults on {111} faces (see [13] for more detail on these defects).

Figure 2. Schematic of MD and MS models for screw and edge dislocations in (a) BCC and (b) FCC crystals

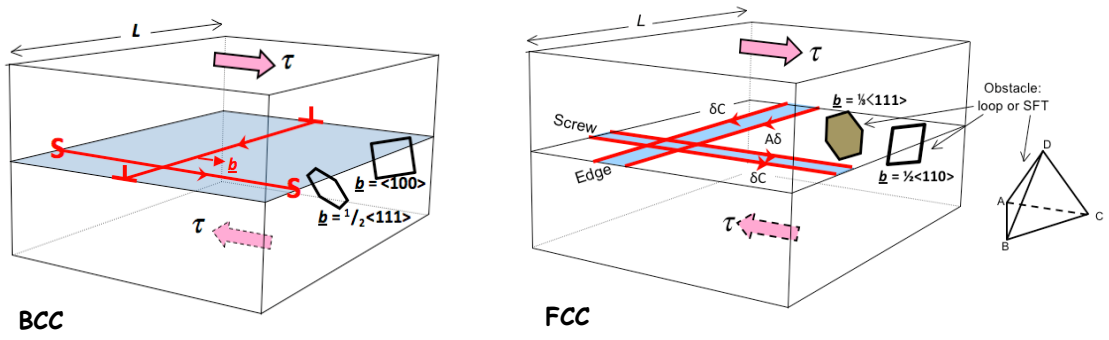

(a) (b)

The dislocations are dissociated into Shockley partials in (b). Examples of dislocation loops and an SFT, and sense of applied shear stress, τ, are indicated.

Visualisation techniques for studying atomic-scale mechanisms are necessary. The important atoms involved are usually identified by having high energy (potential or kinetic) and/or an environment of high stress, and/or near-neighbour atom co-ordination that is far from perfect. Thus, many computational techniques have been developed for visualization [3]. The images shown in Section 3 mainly use deviation from perfect co-ordination.

There are limitations to what can be achieved with atomic-scale modelling. One arises from computer CPU time available. In MS (T = 0 K), the computation efficiency that can be achieved with energy minimisation codes limits model size to a few million atoms. In MD (T > 0 K), in which the real trajectory of atoms is followed, computing resource limits both the model size and simulated time, t. For the model size range described above and time-steps ~1-5 fs, t is limited to typically ~10-100 ns. This, in turn, limits the minimum strain rate, $\dot{\varepsilon}$, that can be applied in order to attain a total strain ε in time t. Consider a typical simulation of dislocation-obstacle interaction in an Fe crystal, for which b = 0.248 nm. For L = 41 nm, a model containing $2\text{x}10^6$ atoms would have a cross-section area of $5.73\text{x}10^{-16}$ m^2, the reciprocal of which is the dislocation density ρ_D = $1.75\text{x}10^{15}$ m^{-2}. If the model size in the glide direction is $120b$ = 29.8 nm, the height perpendicular to the glide plane is 19nm. For the dislocation to travel across the slip plane once in 10 ns, say, its velocity v_D = 2.98 ms^{-1} and the corresponding strain rate given by the relation $\dot{\varepsilon} = v_D \rho_D b$ is $1.29\text{x}10^6$ s^{-1}. Thus, the lowest strain rate and dislocation

velocity studied by MD are ~6-10 orders of magnitude higher than those usually applied in laboratory tensile experiments and more than 10 orders higher than for the creep regime. This, at the moment, is an unresolvable problem for atomic-scale modelling. Note, however, that whereas the *average* velocity of dislocations in experiments is much lower than 1 ms^{-1}, their velocity in free flight under the levels of applied stress involved is compatible with that achieved in MD. What MD cannot replicate is the long time dislocations may wait for release from obstacles in real materials.

The other important limitation is associated with the interatomic potentials used, for they determine all the physical properties of the simulated system. Ideally, a potential should accurately describe the energy and forces associated with an atom for any configuration it may encounter. It should also have a form that lends itself to computational efficiency. A reasonable compromise is achieved with potentials based on the widely-used embedded-atom-method (EAM), in which the empirical parameters are fitted to experimental properties such as crystal structure, lattice parameter and elastic constants, and *ab initio* data such as vacancy and SIA formation energy, alloy energy and stacking fault energy, e,g, [15]. Effects due to magnetism have been much harder to incorporate for magnetic materials [6]. Thus, although ferritic steels (BCC) and austenitic steels (FCC) are major materials for structural components of current and planned nuclear reactors, potentials that accurately reflect all their defect and alloy properties have not been developed as yet. Simulation to date has been dominated by models of α-Fe (BCC) and Cu and Ni (FCC), in order that mechanisms associated with crystal structure and, in the FCC case, effects of stacking fault, could be investigated. Examples of these will be presented here.

2.2. Continuum-level simulation

In DD simulation, the discrete atomic structure of a crystal is neglected and the material is treated as an elastic continuum. The distortion created by a dislocation outside its core region is predicted with reasonable accuracy by linear elasticity theory and the force on it that makes it move in response to stress can be calculated in the same framework. Dislocations under stress bend when pinned at obstacles, but it is generally not possible to obtain analytic solutions for properties of curved dislocations in elasticity theory and a numerical treatment has to be used. The construction used in DD is illustrated schematically in Figure 3. Dislocations are represented by nodes (drawn as circles) connected to each other by straight dislocation segments. Each segment is characterised by its Burgers vector and direction in space between two nodes. Nodes move in response to forces on them from their own line, other dislocations and external stress. (The force per unit length is b times stress.) The stress due to adjacent and more distant segments is calculated in DD from linear elasticity theory. Force arising from core energy can also be included. The computation involved is non-trivial and several computationally-efficient methods have been developed [5].

Several factors determine how well real dislocations are simulated in DD. One is the way in which the dislocation changes shape if the force on a node is unbalanced. This can be allowed for this by giving the node a velocity proportional to the force and inversely proportional to a drag coefficient. Realism can be introduced by setting the drag coefficient for climb (in response to a force component out of the glide plane) to be much larger than that for glide, and allowing the coefficient for glide to vary with line

direction between edge and screw orientations. Temperature effects can also be incorporated with a *T*-dependent drag coefficient and by probability-determined waiting times for thermally-activated processes. The density of nodes that define the dislocation line is also important. The number of nodes should be as small as possible for computational efficiency, but the node density should be large for accurate shape representation. Node density needs to be high in regions where line curvature is strong (see Figure 3). Thus, the code has to be able to add or remove nodes in response to dislocation shape change. Furthermore, segments on the same or different dislocations can react to either annihilate or form new segments, and again nodes have to be added or removed.

Figure 3. DD construction of flexible dislocations represented by nodes (circles) connected by straight segments

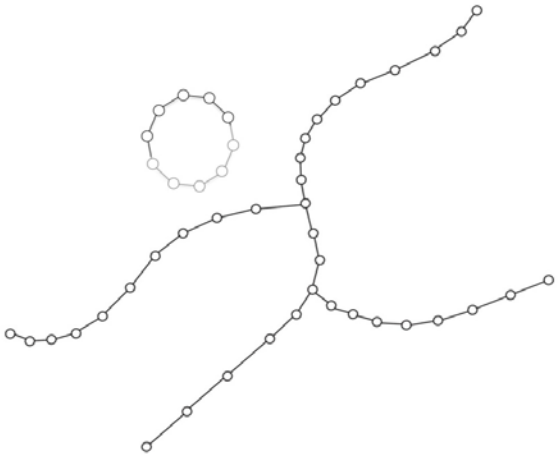

A dislocation loop is shown intersecting the glide plane.

Thus, although DD is similar to MD in that objects (atoms or nodes) move in a chosen time-step according to the force on them, DD is more complex. The number of atoms is constant in MD, whereas the changing number of nodes in DD requires that the inventory of nodes, nodal coordinates and segment $\boldsymbol{b}$ be updated after every time-step. The choice of boundary condition can also be problematic. On the other hand, longer length and time scales can be modelled with DD and, as will be seen later, nanoscale processes can be simulated in much less time than with MD.

3. Atomic-scale simulation of dislocation-obstacle interaction

Obstacles induced by irradiation affect moving dislocations in a variety of ways and can be categorised for convenience into two types.

- Inclusion-like defects, such as voids, bubbles and precipitates, have relatively short-range strain fields and provide the simplest dislocation-obstacle interactions. Obstacles that are not impenetrable to dislocations are usually sheared and steps defined by $\boldsymbol{b}$ of the dislocation are created on the obstacle-matrix interface. Unstable precipitates, such as those formed by Cu in Fe, may also suffer structural

transformation. These obstacles do not usually modify dislocations significantly, although they may cause climb of edge dislocations (see below). Inclusion resistance to dislocation motion is actually utilized in oxide dispersion strengthened (ODS) alloys by processing to produce a high concentration of rigid, impenetrable oxide particles: ODS materials may provide components in future-generation reactors.

- New dislocation segments can occur when a dislocation reacts with dislocation loops or SFTs. These obstacles have dislocation character and their strength depends on the Burgers vectors involved, edge/screw character of the dislocation, and interaction geometry, i.e. obstacle position and orientation relative to the dislocation glide plane. In addition to causing hardening, the reaction can modify both dislocation and obstacle structure. SFTs are three-dimensional defects and have short-range strain fields, whereas loops have relatively long-range strain fields and interact with dislocations over distances much greater than their size. A further complication is that dislocation loops with perfect Burgers vector $\boldsymbol{b}_L$ are glissile, in principle, and can move to, from or with dislocations, whereas SFTs and faulted loops are sessile.

3.1. Inclusion-like obstacles

Temperature T = 0 K

Many simulations of dislocation-void interaction have been reported in the literature [23]. Examples of stress-strain curves (τ vs ε) when an edge dislocation encounters and overcomes voids of diameter D in Fe and Cu at 0 K are presented in Figures 4(a) and (b), respectively. For these MS simulations, shear strain was applied to the model incrementally and τ to maintain each strain was calculated after each energy minimisation from the force exerted by the mobile atoms on rigid crystal blocks on the top and bottom surfaces of the model. The four distinct stages in τ vs ε and the difference in behaviour between the two metals, which is due to core dissociation into Shockley partials in Cu but not in Fe, are described in [23].

Voids are strong obstacles and at maximum ('critical') stress, τ_c, an edge dislocation in Fe at 0 K bows out strongly between the obstacles, creating parallel screw segments in the form of a dipole pinned at the void surface, as seen in the visualisation of core atoms for voids with D in the range 0.9-5 nm in Figure 5.

Figure 4. τ vs ε for edge dislocation-void interaction at 0 K in (a) Fe with L = 41.4 nm and (b) Cu with L = 35.5 nm

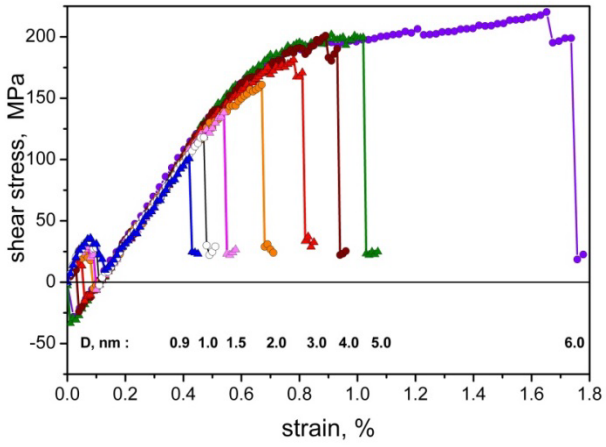

(a)

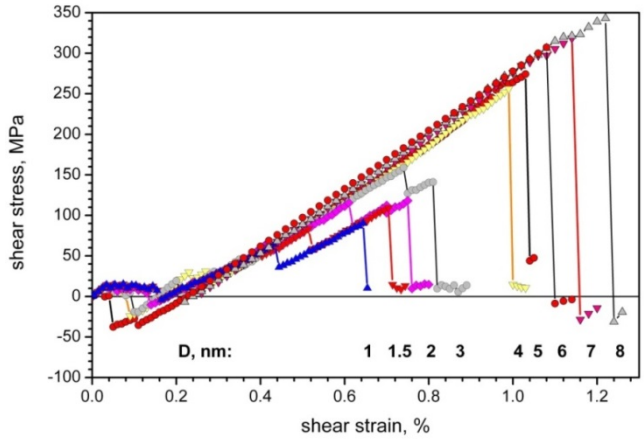

(b)

Values of void diameter *D* are indicated below the individual plots [23,24].

The screw arms cross-slip in the final stage when the dislocation is released from the void and this results in dislocation climb and a reduction in void size. In contrast with this, a Shockley partial cannot cross-slip. Partials of the dissociated dislocation in Cu interact individually with small voids ($D \leq$ partial spacing ~2nm), thereby reducing τ_c. Stress drops are seen in the plots in Figure 4(b). The first occurs at low τ when the leading partial breaks from the void and forms a 1/6<112> step on the exit surface. Breakaway of the trailing partial controls τ_c. For larger voids the two partials leave the void together at τ_c. However, extended screw segments do not form and the dislocation does not climb in this process. Consequently, large voids in Cu are stronger obstacles than those of the same size in Fe, as can be seen in Figure 6, and the number of vacancies in the sheared void in Cu is unchanged.

Figure 5. Critical line shape in the $(1\bar{1}0)$ glide plane for a dislocation passing a row of either spherical voids or Cu precipitates of different size in Fe at 0 K

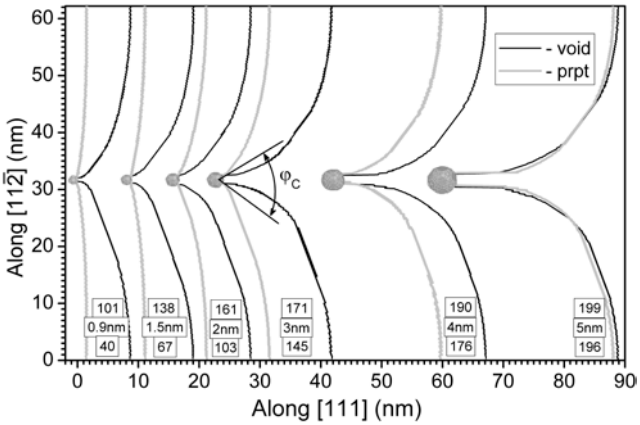

L is 62 nm and *D* varies from 0.9 to 5nm. Black line - shape for voids: grey line - shape for precipitates. The labels for each pair of shapes indicate τ_c for void, *D* and τ_c for precipitate, in descending order [2].

Figure 6. Critical stress τc (in units Gb/L) versus the harmonic mean of D and L (unit b) for voids and Cu precipitates in Fe and voids in Cu [2,23,24]

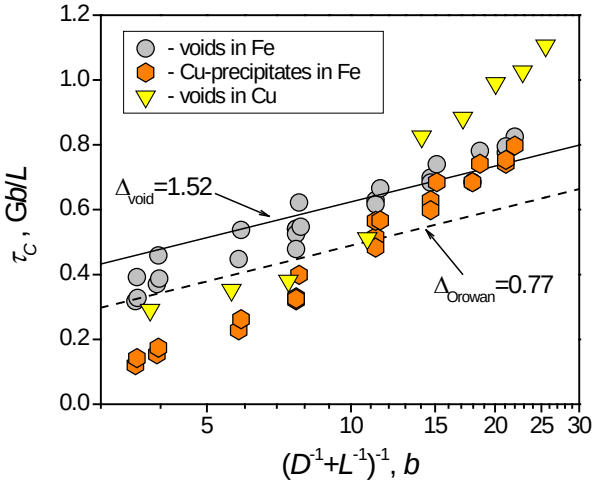

Cu precipitates in Fe have been studied extensively due to their importance in raising the yield stress of irradiated reactor pressure vessel (RPV) steels and the availability of suitable interatomic potentials for the Fe-Cu system [2]. The precipitates are BCC and coherent with the surrounding Fe matrix when small, and their interaction with an edge dislocation is similar to that for voids in Fe. The elastic shear modulus, *G*, of BCC Cu is lower than that of Fe and the dislocation is attracted into the precipitate. Stress is required to release it and form a step *b* on the Fe-Cu interface. τ_c is lower than for a void, however, for which *G* is zero and the void surface energy relatively high. Thus, τ_c for small

precipitates (≤3 nm) is insufficient to draw out screw segments (angle $\phi_c > 0$ in Figure 5) and the dislocation is released without climb. Larger BCC precipitates are unstable, however, and their structure is partially transformed towards the more stable FCC form when penetrated by a dislocation at $T = 0$ K. Transformation of Cu increases the obstacle strength and results in a critical line shape that is close to that for voids of the same size (Figure 5). Under these conditions, a screw dipole is created and effects associated with this, such as climb of the edge dislocation described above for voids in Fe, are observed.

MS simulation ($T = 0$ K) is comparable with continuum modelling of dislocations in which the equilibrium configuration is obtained by minimising elastic energy. An early example of the latter was the modelling of a dislocation under increasing τ overcoming impenetrable ('Orowan') particles and voids [1,30,31]. It was found that τ_c fits the relationship

$$\tau_c = \frac{Gb}{2\pi AL}\left[\ln(D^{-1} + L^{-1})^{-1} + \Delta\right], \quad (1)$$

where G is the elastic shear modulus and Δ is an empirical constant; A equals 1 and (1 - ν) for edge and screw dislocations, respectively; and ν is Poisson's ratio. D and L are the obstacle diameter and spacing along the dislocation line (see Figure 2) respectively. In fact [1,30,31] used dimensionless size and spacing D/r_0 and L/r_0 (r_0 is the dislocation core size) which is rather close to D and L values in unit b as it is presented in Figure 6. The interpretation is that voids and impenetrable particles are 'strong' obstacles in that the dislocation segments at the obstacle surface are pulled into parallel, dipole alignment ($\phi_c = 0$) at τ_c by self-interaction. For every obstacle, the forward force, $\tau_c bL$, on the dislocation has to match the elastic tension of dipoles of spacing D and L, so that $\tau_c bL$ correlates with $Gb^2\ln(D^{-1} + L^{-1})^{-1}$.

The same correlation is tested for the MS simulations in Figure 6. Good agreement is seen for D down to about 2 nm for voids in Fe and 3-4 nm for Cu precipitates. The explanation lies in the fact that these obstacles are strong at $T = 0$ K and dipole alignment occurs at τ_c. The smaller obstacles in Fe are too weak to be treated by Equation (1). The effect of dissociation in Cu results in a change of dependence on D and L for larger voids. Thus, the atomic-scale mechanisms that operate for small and large obstacles depend on their nature and metal and are not necessarily predicted Eq. (1).

The void and precipitate centre was placed on the dislocation glide plane in MS simulations above. Readers are referred to [9] for effects of changing the distance of the centre from the glide plane.

Temperature $T > 0$ K

Modelling by MD provides the ability to investigate effects of temperature (and strain rate within the limits described in Section 2.1). Results for the T-dependence of τ_c for an edge dislocation and 2 and 6 nm voids in Fe and Cu, and Cu precipitates in Fe are presented in Figure 7. Obstacle strength decreases with increasing temperature, although the mechanisms involved are not the same in all cases. Cu precipitates in Fe are particularly interesting [2]. Small precipitates (D < 3nm) are stabilised in the BCC state by the Fe matrix and are weak, shearable obstacles. The resulting T-dependence of τc is small

(Figure 7). At T = 0 K (see above), larger precipitates are unstable with respect to a dislocation-induced transformation towards the FCC structure driven by the difference in potential energy of BCC and FCC Cu. The free energy difference between the two phases decreases with increasing T until a temperature is reached at which the transformation does not occur. Thus, large precipitates are strong obstacles at low T and weak ones at high T, as shown in Figure 7. Some experimental observations can be interpreted by these results [2].

Figure 7. τ_c versus T for voids in Fe and Cu, and Cu precipitates in Fe. D is as indicated, L = 41.4 nm and $\dot{\varepsilon}$ = 5x10^{6}s^{-1}. [2,23,24]

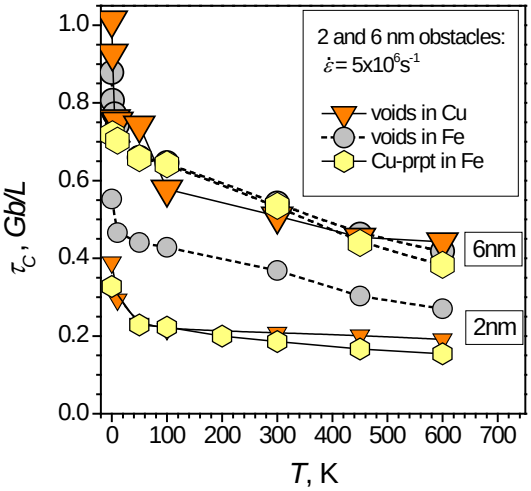

Other obstacles with inclusion-like properties have been studied less intensively. Cr-rich α′ precipitates in α-Fe have the BCC structure coherent with the matrix. Unlike Cu in Fe, G of Cr is higher than that of Fe, and so an edge dislocation is repelled by Cr precipitates. It stops at the precipitate-matrix interface until it shears the precipitate at τ_c [36,37]. Only 2.8 and 3.5 nm precipitates in the size range D = 0.6-3.5 nm had τ_c comparable with values given by Equation (1): the others were much weaker.

Helium-filled bubbles are common in irradiated metals but there is a lack of information on their equilibrium state, i.e. He/Vac ratio as a function of size and T, and their effect on mechanical properties. Interaction between an edge dislocation and 2 nm cavities with He/Vac ratios up to 5 in Fe at T between 10 and 700 K was considered in reference [32] simulated. It was found that τ_c has a non-monotonic dependence on the ratio He/Vac, dislocation climb increases with this ratio and interstitial defects are formed in the vicinity of the bubble. Recent works [33,34] with a new interatomic potential has shown that the equilibrium concentration of He is much lower than expected, e.g. He/Vac = 0.5 for a 2 nm bubble at 300 K which is quite close to experimentally estimated values of He/Vac ~ 0.6 for 1.3 nm He-bubble [42] and He/Vac~0.25-0.85 for bubbles of 2-5 nm in diameter [7]. Simulation of 2 nm bubbles with He/Vac in the range 0.2-2 and T between 100 and 600 K [27] has revealed that edge dislocation interaction with under-pressurized bubbles is similar to that with voids, in that the dislocation climbs up by absorbing some vacancies on breakaway, and τ_c increases with increasing He/Vac.

In the interaction with over-pressurized bubbles, the dislocation climbs down, i.e. it absorbs interstitials in order to reduce bubble pressure, and τ_c decreases with increasing He/Vac. Equilibrium bubbles (He/Vac ~ 0.5 for 2 nm bubble) are therefore the strongest.

As noted above, impenetrable particles such as those in ODS alloys, are another important example of inclusion-like obstacles. Simulation of 2 nm particles in Fe has been carried out by Osetsky (2009, unpublished). The obstacle was constructed from Fe atoms held stationary relative to each other and moved according to the total force on it from matrix atoms. The mechanism observed was close to the Orowan process, with formation of an Orowan loop that either shrinks quickly if the obstacle is small and spherical, or remains around the obstacle or is elongated in the direction perpendicular to the dislocation slip plane when D is large (≥4 nm). This is quite different from earlier findings for rigid obstacles in Cu [10], but the modelling conditions were different in that work, in that the obstacles were fixed with respect to the surrounding crystal and did not move in response to it.

Figure 8 compares τ_c for an edge dislocation to overcome 2 nm spherical obstacles of different nature in Fe at 300 K. A small coherent Cu precipitate is the weakest; a rigid particle is the strongest; and τ_c is higher for an equilibrium He-bubble than a void of the same size, as explained above.

Figure 8. Comparison of τ_c for an edge dislocation in Fe overcoming different 2 nm obstacles at T = 300K, L = 41.4 nm and $\dot{\varepsilon}$ = 5x10^6 s^{-1}

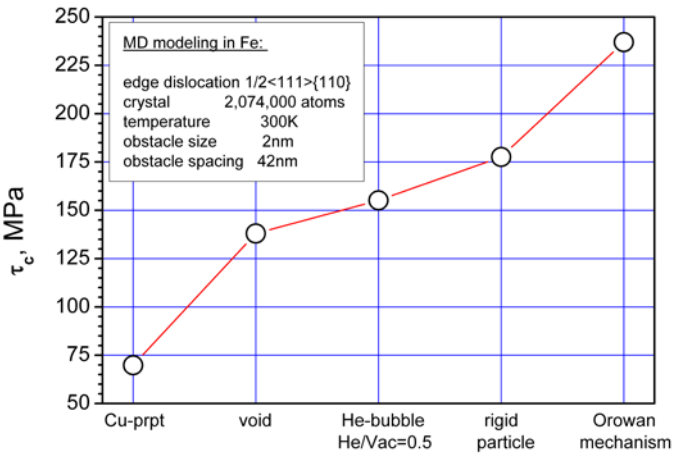

'Orowan mechanism' refers to a simulation when the rigid obstacle cannot be overcome via a screw dipole.

We are aware of only one study of a screw dislocation interacting with an inclusion-like obstacle, namely a void in Cu [11]. It was found that voids are quite strong obstacles, with mechanisms dependent on temperature. The screw dislocation keeps its original slip plane when breaking away from a void at low T, but cross-slip is activated when T is >300 K. Changing interaction mechanisms result in τ_c increasing with increasing T. However, in a model with PBCs, cross-slipped segments on screws can propagate through the

boundary and interact with the other side of the obstacle, and the effects of this require further study.

3.2. Dislocation-type obstacles

Simulations of interactions between moving dislocations and these obstacles have shown that favourable reactions between interacting segments follow Frank's rule for Burgers vectors [13]. This rule was derived using elasticity theory, but has now been shown to apply even for nanoscale segments. The outcome of these interactions varies widely, from no effect on the dislocation or obstacle to complete disappearance of the obstacle and significant modification of the dislocation. Analysis of numerous MD simulations (T > 0 K) for FCC and BCC models shows that reactions can be classified into five types [3,26]:

R1: edge or screw dislocation and obstacle unchanged

R2: edge or screw obstacle changed; dislocation unchanged

R3: edge partial or full absorption of obstacle by dislocation (superjog formation)

R4: screw temporary absorption of obstacle by dislocation (helical turn formation)

R5: edge drag of defect by dislocation

We give some examples for illustration, but emphasise that the details presented can change with temperature and strain rate, and with the geometry of dislocation-obstacle contact. This is particularly so for SFTs, for which the distance of the slip plane from the SFT base is important.

R1: dislocation and obstacle unchanged

The defect is sheared by $\boldsymbol{b}$ of the dislocation but is fully reconstructed after the dislocation unpins. This has been observed for both screw and edge dislocations with SFTs and Frank loops in FCC metals [3], and for edge dislocations interacting with large (331-SIA) ½<111> loops that have $\boldsymbol{b}_L$ inclined to the glide plane in Fe at 100 K [4]. Figure 9 shows the interaction sequence of a ½<110> screw dislocation with an SFT in Cu when the dislocation slip plane is close to the SFT apex. ½<110> ledges form on two SFT faces but are mobile and disappear at face edges. The obstacle and dislocation thus remain unchanged and τ_c is low.

Figure 9. Sequence in shear of an SFT in Cu at 100 K by a screw dislocation (*b* = AC), followed by full restoration

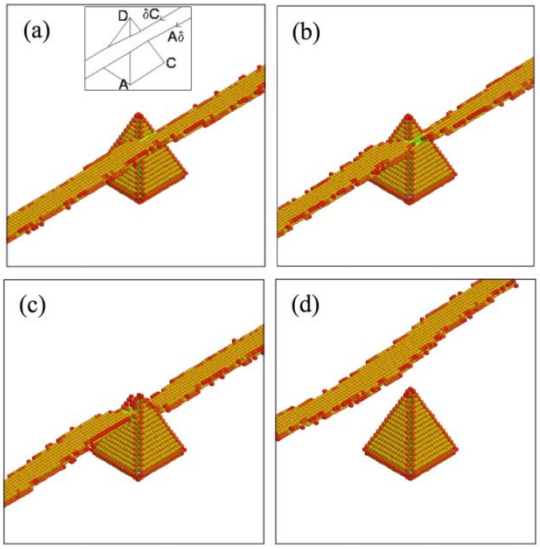

The inset in (a) shows the Thompson tetrahedron used to represent Burgers vectors.

R2: obstacle changed; dislocation unchanged

One example of this occurs when the screw dislocation slip plane above is a relatively long way from the SFT apex. Then, the ledges created on the SFT faces are stable and the obstacle is sheared into two by multiple reactions with dislocations on the slip plane. Another example is seen for some loops with $\boldsymbol{b}_L$ = <100> in Fe. They are transformed by an edge dislocation into conjoined <100>/<111> loops, as demonstrated by the reaction in Figure 10.

Figure 10. Sequence in the interaction between a ½[111] edge dislocation and a [100] loop in Fe at 300 K [37]

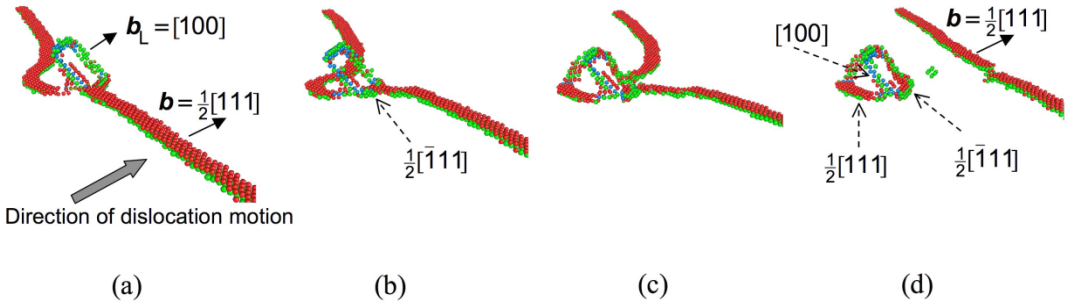

R3: partial or full absorption of obstacle by dislocation (superjog formation)

The formation of superjogs transfers some or all of the point defects from the obstacle to the dislocation. An example of this occurs when SFTs with their base above the slip plane of a positive ½<110> edge dislocation are absorbed as a pair of glissile superjogs, as illustrated in Figure 11.

Figure 11. Sequence in the partial absorption of an SFT by an edge dislocation with b = CA in Cu [26]

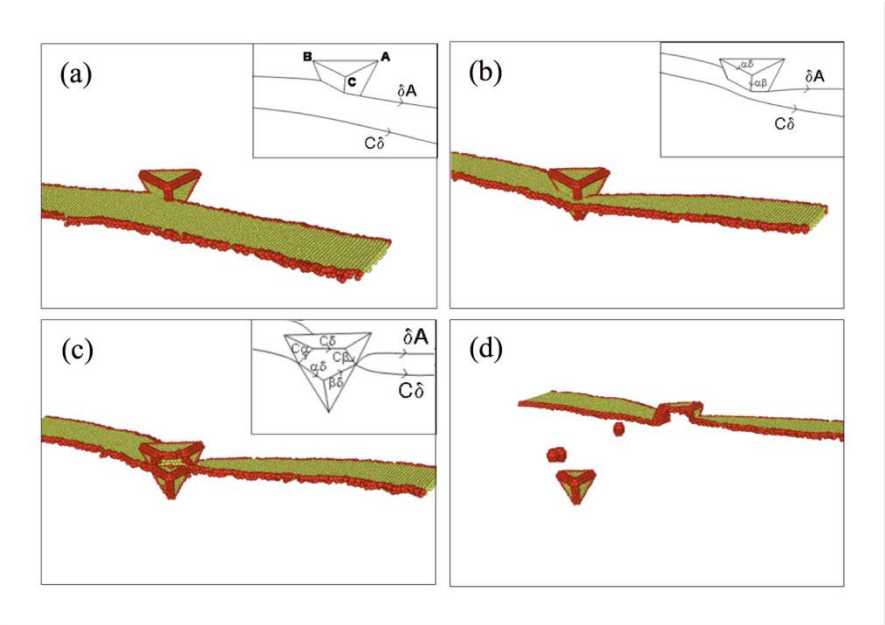

It can also occur when the obstacle is a glissile loop with $\boldsymbol{b}_L$ inclined to the dislocation glide plane, for it can be attracted to the dislocation by the dislocation stress field. For *small* loops (up to a few tens of SIAs), their $\boldsymbol{b}_L$ changes on contact with the dislocation to become that of the dislocation itself. They are weak obstacles. *Large* loops, however, are unable to change $\boldsymbol{b}_L$ because of the energy required. As illustrated in Figure 12 for a ½ $\mathbf{[1\,\bar{1}\,1]}$ loop in Fe, the favourable Burgers vector reaction ½[111] + ½$\mathbf{[1\,\bar{1}\,1]}$ = [010] occurs between the reacting segments. However, the new [010] segment cannot glide on the $\mathbf{(1\,\bar{1}\,0)}$ slip plane of the dislocation and so acts as a strong obstacle. As in the case of voids, a screw dipole is drawn out on the dislocation as τ increases. The dipole arms eventually cross-slip at τ_c, which is high, and the [010] segment moves on its (101) glide plane, transforming the loop into a glissile double superjog on the edge dislocation. Transformations in which a dislocation absorbs a loop after transforming $\boldsymbol{b}_L$ to its own can also occur for <100> loops in Fe [37].

Figure 12. Visualisations of spontaneous glide and transformation of a 331-SIA ½ [111] loop in Fe at T = 300 K. A [010] segment formed in (b) slips downwards as the dislocation side arms in screw orientation glide down in (c) and (d) [4]

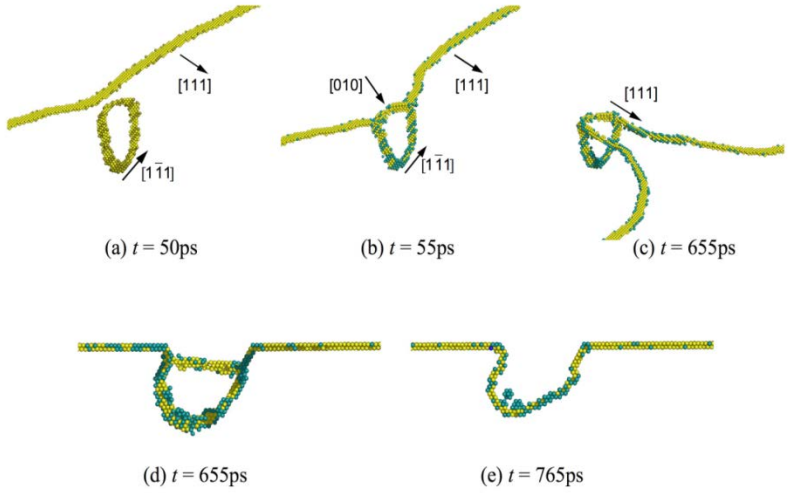

R4: temporary absorption of obstacle by screw dislocation (helical turn formation)

This is the most common outcome for screw dislocations and occurs when the obstacle has either the same Burgers vector as the dislocation or its vector can be transformed to that of the dislocation as the reaction proceeds. It has been observed for SFTs in Cu [26], Frank loops in Ni [28], and ½<111> loops and <100> loops in Fe [16,35]. In the latter case, shown in Figure 13, the screw dislocation reacts initially with a [010] loop ABCD to form a sessile segment AD by a reaction ½[111] + $\mathbf{[0\bar{1}0]}$ = ½$\mathbf{[1\bar{1}1]}$, which pins it. As τ is increased, the pinned side arms slip round the loop and it is absorbed as a helical turn (Figure 13(c)).

The ability of a screw dislocation to absorb defects in a helical turn is important because the turn can glide only in the direction of its $\boldsymbol{b}$, i.e. $\pm x$ in Figure 13, and so cannot be carried forward with the dislocation. The dislocation can only continue to glide if τ can force the turn to close, thereby releasing the line and leaving a loop behind (Figure 13(d)). Such reactions are characterised by high τ_c. Furthermore, if the line on one side of the turn moves ahead of the other side, the turn is pushed along the line, which provides a mechanism for fast mass transport (see Section 4). Additionally, if a screw dislocation absorbs both vacancy and interstitial clusters, the helical turns have opposite sense and so annihilate when they meet (either totally or partially, depending on the number of vacancies and SIAs in each). This provides an efficient recombination mechanism for the two components of radiation damage.

Expansion of a helical turn along a screw dislocation has a practical significance for MD modelling because of the PBCs employed to simulate bulk material. If a turn exits through one boundary (along the x-axis in Figure 13 say), it re-enters through the opposite boundary and can re-interact with remnants of the original obstacle. Care has to be exercised in interpreting the result of dislocation-obstacle interaction with these

conditions [3]. This difficulty does not exist when free boundaries are used instead, as in the successful simulation of dislocation-SFT interaction in thin films [25].

Figure 13. Interaction between a ½[111] secrew dislocation and a [010] SIA loop, which is absorbed (b-c) and then reformed with b = ½[111] (d)

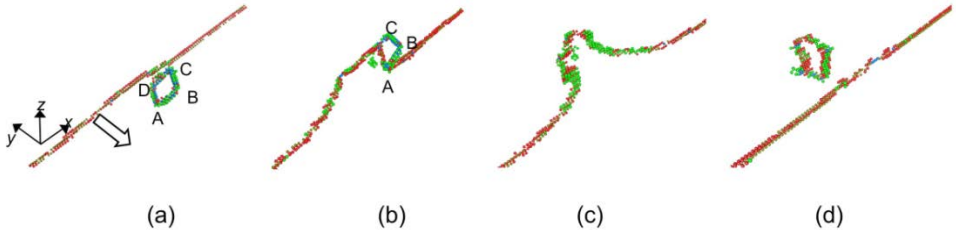

The screw dislocation glides in the -*y* direction shown by the double arrow [35].

R5: drag of defects by dislocation

An edge dislocation with dislocation loops in its vicinity interacts with them as a result of its strain field. As a result, loops with $\boldsymbol{b}_L$ parallel to the dislocation glide plane can be dragged or pushed as the dislocation moves. The process dynamics have been investigated and correlations found between cluster and dislocation mobility [29]. The maximum speed at which a dislocation can drag a loop is achieved by a compromise between dislocation-loop interaction force and loop friction, and varies at T = 300 K from ~180 ms^{-1} in Cu to >1000 ms^{-1} in Fe for loops containing a few tens of SIAs. An important consequence of drag is that a moving dislocation can transport glissile loops through the material. This does not contribute significantly to irradiation hardening but does assist recombination of SIA loops and vacancy SFTs in Cu by annihilation, for instance. MD simulation has shown that a loop dragged at speed by a gliding dislocation can annihilate the part of an SFT that intersects the loop glide cylinder. Such annihilation does not occur without the assistance of drag.

Obstacle strength of dislocation-type obstacles

As is clear from the extent of dislocation bow-out before release in the visualizations shown above, obstacle strength associated with loops and SFTs can depend strongly on parameters such as loop/SFT size, position relative to the dislocation slip plane, $\boldsymbol{b}_L$, [illegible] and T. Unlike the situation for inclusion-like obstacles, a simple correlation between size and strength does not exist for loops and SFTs. Comparative strength data for particular sets of conditions for ½<111> and <100> loops in Fe are available and a comparison has been made with the obstacle strength of voids [37,38]. There are cases when loop strengthening is comparable to or even exceeds that of voids containing the same number of point defects, confirming the conclusion that dislocation loops are an important component of radiation-induced hardening.

4. Continuum simulation of dislocation-obstacle interaction

DD simulations provide a suitable vehicle to link the nano- and meso-scales in the framework of MMM. Its validity rests on the fact that linear elasticity gives a good description of the strain field of dislocations outside their core. One of the earliest applications of the technique to study dislocation obstacle interaction has been mentioned already in relation to Equation (1). This showed the importance of interaction between segments of the same dislocation ('self-interaction') in determining τ_c, but did not include dynamic effects, i.e. it was equivalent to MS. Current DD codes incorporate dynamics ($T > 0$ K) with algorithms to model dislocation mobility and mechanisms such as constriction of partial dislocations, cross-slip and thermal-activation over barriers [5]. Applications to investigate dislocation-obstacle interactions relevant to irradiated metals have been less extensive than those at the atomic-level, but the following illustrate the scope for DD in this field.

Carbides in RPV steels

A dislocation mobility law is required for DD simulations and this poses a particular problem for BCC metals. Mobility follows a simple viscous drag law in FCC metals, but mobility for Fe depends strongly on T and dislocation character. Edge dislocations and screws at high T ($\geq$ 300 K) exhibit athermal viscous behaviour, but the motion of screw dislocations at low T occurs through nucleation and propagation of kink-pairs, which is thermally-activated, and so mobility decreases strongly with decreasing T. A multiscale approach was adopted to develop a mobility algorithm for Fe in [18]. *Ab initio* calculations were used to determine the Peierls potential of screw dislocations and thus validate the interatomic potential used in MD simulations to compute the velocity of dislocations as a function of τ and T. The mobility laws obtained in this way were applied in DD simulations to predict the effects of dislocation interactions with carbides particles on the flow stress of Fe at low and high T. Although not created by radiation damage, carbide particles are an intrinsic component of the microstructure of RPV steel. They are incoherent with the Fe matrix and therefore impede dislocations by the Orowan mechanism. The average particle size (100 nm) is of the same order of magnitude as the average particle spacing.

Impenetrable carbides were modelled as spheres with infinite shear resistance. In simulations of dislocations moving on their primary slip plane in the athermal regime ($T \geq$ 300 K), it was found that carbide strengthening raises the flow stress above that for material without carbides, for which the principal obstacles are 'forest' dislocations on other planes. As T is lowered, the obstacle resistance experienced by edge dislocations remains almost unchanged because a screw dipole is drawn out as the dislocation overcomes the particle, as explained in Section 3.1, and the stress required to extend the dipole depends only weakly on T. This is clear from the data in Figure 14(a) for the increase in strength as a function of particle spacing, L, at 50 and 250 K. The data follows a harmonic-mean dependence on L and D, as in Eq. (1) developed by [1] and shown by the curve BKS. The obstacle strength for screw dislocations depends strongly on both L and T, as shown in Figure 14(b). It falls below the BKS curve even at 250 K and has a stronger L-dependence because the probability of nucleation and propagation of kink-pairs increases with L. At low T, screw segments remain almost straight when L is large,

as is the case in the absence of carbides. Thus, DD simulations predict that carbide strengthening is well described by Eq. (1) in the athermal regime and is of the same order of magnitude as forest strengthening. Furthermore, it decreases with decreasing T such that the effect of carbides on the mechanical properties can be neglected in RPV steel at low T.

Figure 14. Orowan strengthening vs carbide spacing at 50 and 250 K for (a) edge and (b) screw dislocations

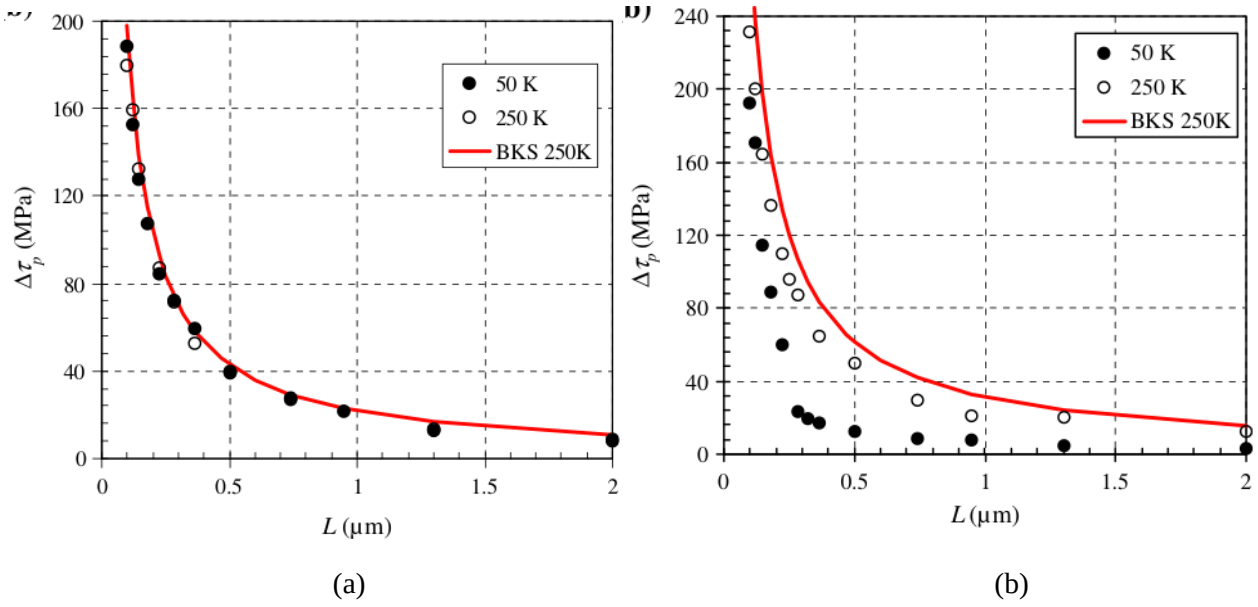

(a) (b)

The solid line is the prediction of the BKS model at 250 K [18].

Obstacle strength of SFTs

D and DD were exploited in the MMM framework in a different way [17]. As noted earlier, SFTs are common vacancy-type defects produced by irradiation of FCC metals and alloys, and their interaction with gliding dislocations affects strength and ductility. A few examples of outcomes of this interaction have been presented in Section 3.2, but, bearing in mind all the possibilities, MD studies have not provided a systematic account of obstacle strength. Marian et al. addressed this problem by utilising the power of DD to simulate the interaction of a dislocation with a single SFT in a much shorter time than is possible with MD, thereby allowing a large number of interaction geometries to be treated. In order to validate the methodology of the DD code, a small number of MD and DD simulations were undertaken for the same interactions.

One such is shown in Figure 15, which compares the sequences obtained by DD (left) and MD (right) of a screw dislocation encountering a face of a 4.6 nm SFT in Cu at 100 K and eventually passing it. τ was 300 MPa on the primary slip plane and $300/\sqrt{3}$ MPa on the cross-slip (SFT face) plane. Despite model differences, including PBCs in MD and bowing line of a Frank-Read source in DD, the agreement between the methods is striking. The interaction proceeds in both simulations by mechanisms that involve

constriction and dissociation, and reactions between Shockley and stair-rod partials that enable Shockley partials to form and sweep across SFT faces. The SFT is partly destroyed in the process.

The relatively small amount of computer processor time required by DD allowed Marian et al. to carry out simulations for screw, edge and 60°-mixed dislocations, three SFT sizes and three dislocation line lengths, L, and for a range of distances of the dislocation glide plane from the SFT base. It was found that the obstacle strength is approximately inversely proportional to the distance between the glide plane and SFT base; the strength is highest for screw dislocations and lowest for edge dislocations; and the strength is higher when the dislocation first meets an SFT on a face (as in Figure 15) than an edge. Furthermore, the geometrical parameter that determines obstacle strength for a given L was found to be the area, A, of the triangle intercepted by the glide plane, resulting in the empirical relation $\tau_c = PA^Q$, where P and Q depend on the character of the dislocation. Furthermore, τ_c varies with L as $\beta Gb/L$ (as in Equation (1)), where β depends on A and dislocation character. In this way, DD simulations, validated by MD runs, provided extensive data to enable empirical strength parameters to be extracted for better prediction of radiation hardening of Cu. Recent *in situ* nano-compression testing of proton-irradiated Cu has produced yield stress values consistent with this [14].

Figure 15. Visualisation sequences demonstrating good agreement between simulation by DD (left) and MD (right) of the interaction between a screw dislocation and a 4.6 nm SFT in Cu at 100 K [17]

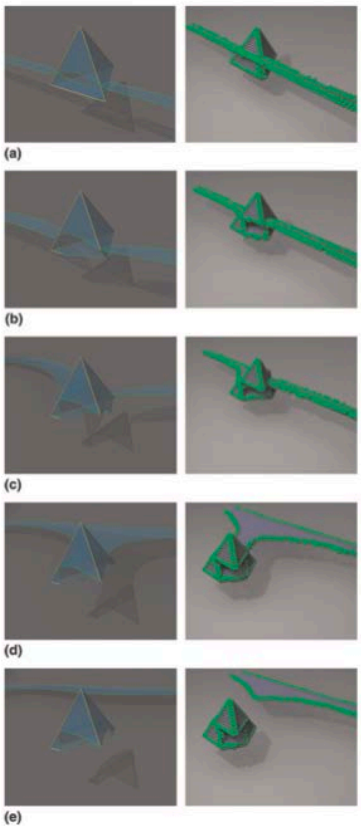

Clear band formation in FCC metals

As a final example, we turn to the localization of plastic deformation into clear bands. The mechanisms that form and widen such bands have long been a mystery, but MD and DD simulations have provided details that were not available previously. MD studies have shown that edge dislocations can absorb loops as superjogs and screw dislocations can absorb loops as helical turns (see Section 3.2), but these observations do not explain the absence of damage in clear bands and the observed uniform band thickness. These issues have been addressed for Cu by a combination of MD and DD [21].

The loops were 10 nm Frank loops ($\boldsymbol{b}_L$ = ⅓<111>) with 50 nm spacing, and the DD cell size was 0.6x0.6x0.24 μm^3, the last dimension being that perpendicular to the (111) primary glide plane. MD simulations [20] have shown that sessile Frank loops remain faulted but sheared after interaction with an edge dislocation, but are unfaulted and transform into a glissile helical turn by interaction with a screw dislocation (similar to a perfect loop in Fe (Figure 13)). This was mimicked in the DD simulations by initially treating the loop sides as immobile. When interacting with a dislocation, the sides were freed if the dislocation was near-screw (angle between $\boldsymbol{b}$ and line <20°) and loops were observed to become helical turns. For other dislocations, loops remained immobile and dislocation unpinning was allowed to occur when the angle between the side arms reached ϕ_c = 100°, as found in MD studies.

The interaction for a single screw dislocation ($\boldsymbol{b}$ = ½$[10\bar{1}]$) pinned at both ends and 200 nm long is illustrated in Figure 16. Under increasing τ the dislocation bows and contacts a loop, which becomes free and transforms spontaneously into a helical turn (Figure 16(a)). This consists of two segments in (111) primary planes and three superjogs on $(1\bar{1}1)$ cross-slip planes. As τ increases further, the bowing line absorbs more loops and is pinned by the helical turns because the superjogs can glide only in the $[10\bar{1}]$ direction of $\boldsymbol{b}$. Unpinning at τ_c requires activation of the segment in the (111) plane above the original screw glide plane (Figure 16(b)) and as it bows out the superjogs are pushed towards the cell borders. As shown in [20], this pushing is important for clear band formation.

Two sets of simulations were undertaken for a random array of loops. In one, the stress τ_{nucl} to nucleate a second dislocation from a source was chosen to be high (1000 MPa), well above the loop resistance of the previous paragraph. With that condition, the single dislocation glides through the loop array, shearing them or absorbing them as helical turns, depending on the character of its segments. It does not form a cleared band parallel to the primary glide plane because it is repeatedly re-emitted in upper (111) planes, as a result of which its effective glide plane is inclined to the primary (111) plane.

Figure 16. Interaction between a screw dislocation and Frank loops. (a) 60 MPa, 155 ps: the dislocation comes into contact with a loop that is absorbed as a helical turn; (b) 340 MPa, 680 ps: a segment in an upper (111) plane is activated and pushes the superjogs to the sides [21]

(a) (b)

In the other study, τ_{nucl} was chosen to be low (90 MPa). For a constant applied strain rate, the first dislocation in that situation acquires helical turns but becomes pinned until τ rises to τ_{nucl} and a second dislocation is nucleated. The plastic strain due to its movement causes τ to fall until it too becomes pinned, so that τ rises again until a third dislocation is nucleated, and so on. The stress concentration at the leading dislocation due to the pile-up formed in this way allows the dislocations to move through the DD cell. The first ones clear a band by forming helical turns and pushing the jogs towards the cell borders upon unpinning. Later dislocations glide in the region already cleared and contain few jogs, but as members of a pile-up play a key role in magnifying the stress on the leading dislocations. The leading dislocations unpin in (111) planes above the original (111) plane, as in Figure 16, and so a cleared band of finite thickness develops parallel to the primary glide plane, as found experimentally. Details of several collective effects of the pile-up are presented in [21].

5. Other issues

Computer simulation provides a powerful tool for investigating and predicting material properties that cannot be achieved by experimental techniques or other theoretical methods. The primary obstacles to dislocation motion in metals in a reactor core have size and spacing that are compatible with atomic-scale simulation. The examples of Section 3 illustrate how detailed information on dislocation-obstacle interaction and obstacle strength can be gained by this. The mechanisms found expose a difficulty of using simple elasticity-based formulae for yield stress at the mesoscale. Even Equation (1) for the Orowan limit of strong obstacles, which has been demonstrated to be valid for low temperature, would have to be scaled to allow for kinetic effects and its use for weak obstacles such as small loops is not appropriate.

Tensile test data for irradiated metals has often been used to validate a simple theoretical formula for yield stress: $\tau_c = \alpha Gb/L$, which is based on the line-tension approximation [13]. The interaction between dislocation segments is ignored in this and obstacle strength (α) is proportional to $\cos\phi_c$. When the observed ϕ_c (Figure 5) is used with this approximation, the predicted value of τ_c is too large. Thus, α does not have a

firm theoretical basis and must be treated as an empirical parameter obtained by fitting τ_c to experimental data. The results reviewed here show that for a microstructure consisting of nanoscale defects, the line-tension approach is inadequate for predictive modelling. This problem can be overcome by continuum-based DD simulation, in which dislocation stress field and self-force are incorporated properly. However, as seen in Section 4, correct modelling of dislocation mobility, obstacle resistance and thermal activation requires a framework based on parameters obtained by MD studies. This is a challenging task, but real progress is being made.

Despite the progress achieved to date, MD and DD face several challenges. One is associated with limits on length and time scales imposed by computing speed. This is particularly acute for MD and, although computer power is continually improving, it seems unlikely that this technique will supplant DD for mesoscale modelling in the near future. Another key issue for MD is concerned with the interatomic potentials used to calculate energy and forces. In order to maximise length and time scales of simulations, potentials have to be simple to compute, which is possible for metals because interatomic forces are short-ranged and the bonds are not usually strongly directional. However, metals used in many applications are complex alloys of numerous elements and there are many alloy systems for which suitable potentials do not exist. Other properties of metals that are difficult to capture with relatively simple potentials are phase changes and magnetism. This is an area where *ab initio* calculations are playing an increasing key role by providing information to validate potentials.

Finally, there is another consequence of dislocation activity related to microstructure changes that occur. While this may be not important in *post-mortem* experiments on irradiated materials, it can be important in real devices operating under irradiation. It is obvious that internal and external stresses can accumulate during irradiation of complicated devices due to high temperature, radiation growth, swelling and transition periods of operation e.g. shut down and restart. Creep is usually taken into account but microstructure changes due to dislocation activity during irradiation are not. This activity affects the whole process of microstructure evolution and should therefore be taken into account in predicting the effects of irradiation. The validity of this statement is demonstrated by recent in-reactor straining experiments on some BCC and FCC metals and alloys [39,40]. It is not possible at the moment to formulate unambiguous conclusions and more experimental work will be necessary for this. Nevertheless, it is clear that dislocation activity during irradiation directly affects the radiation damage process.

Acknowledgements

Most of work by YO described in this chapter (modelling and analysis) was carried out with support of the Office of Basic Energy Sciences (dislocation model development, voids and dislocation-type obstacles) and Office of Fusion Energy Sciences (He-filled bubbles precipitates and rigid inclusions) U.S. Department of Energy, under contract DE-AC05-00OR22725 with UT-Battelle, LLC.

References

[1] Bacon D.J., Kocks U.F. and Scattergood R.O., Philos. Mag. 28 (1973) 1241.

[2] Bacon D.J. and Osetsky Yu.N., Philos. Mag. 89 (2009) 3333.

[3] Bacon D.J., Osetsky Yu.N. and Rodney D., Dislocation-Obstacle Interactions at the Atomic Level, Chap. 88: *Dislocations in Solids,* Ed. by J.P. Hirth and L. Kubin, 2009, 1-90.

[4] Bacon D.J., Osetsky Yu.N. and Rong Z., Philos. Mag. 86 (2006) 3921.

[5] Bulatov V.V. and Cai W., Computer Simulations of Dislocations, Oxford University Press, Oxford, 2006.

[6] Dudarev S.L. and Derlet P.M., J. Phys.: Condens. Matter 17 (2005) 7097.

[7] Fréchard S., Walls M., Kociak M., Chevalier J.P., Henry J. and Gorse D., J. Nucl. Mater. 393 (2009) 102.

[8] Frederiksen S.L. and Jacobsen K.W., Philos. Mag. 83 (2003) 365.

[9] Grammatikopoulos P., Bacon D.J. and Osetsky Yu.N., Modelling Simul. Mat. Sci. Eng. 19 (2011) 015004.

[10] Hatano T., Phys. Rev. 74 (2006) 020102.

[11] Hatano T., Kaneko T., Abe Y. and Matsui H., Phys. Rev. B 77 (2008) 064108.

[12] Hirth J.P. and Lothe J., Theory of Dislocations, Krieger Publishing Company, 1982.

[13] Hull D. and Bacon D.J., Introduction to Dislocations, 5th edition, Butterworth-Heinemann, Oxford, 2011.

[14] Kiener D., Hosemann P., Maloy S.A. and Minor A.M., Nature materials 10 (2011) 608.

[15] Kim S-G., Horsmeyer M.F., Baskes M.I. et al,, J. Eng. Mater. and Techn. 131 (2009) 041210-1.

[16] Liu X.-Y. and Biner S.B., Scripta Mater. 59 (2008) 51–54.

[17] Marian J., Martinez E., Lee H-J. and Wirth B.D., J. Mater. Res. 24 (2009) 3628.

[18] Monnet G., Domain C., Queyreau S., Naamane S. and Devincre B., J. Nucl. Mater. 394 (2009) 174.

[19] Nguyen-Manh, D., Horsfield, A.P. and Dudarev, S.L., Phys. Rev. B 73 (2006) 020101.

[20] Nogaret T., Robertson C. and Rodney D., Philos. Mag. 87 (2007) 945.

[21] Nogaret T., Rodney D., Fivel M. and Robertson C., J. Nucl. Mater. 380 (2008) 22.

[22] Osetsky Yu.N. and Bacon D.J., Modelling Simul. Mat. Sci. Eng. 11 (2003) 427.

[23] Osetsky Yu.N. and Bacon D.J., Philos. Mag. 90 (2010) 945.

[24] Osetsky Yu.N. and Bacon D.J., Atomic-Level Dislocation Dynamics in Irradiated Metals, Chap. 29: *Encyclopedia of Comprehensive Nuclear Materials*, Ed. by R. Konings, Elsevier (2011).

[25] Osetsky Yu.N., Matsukawa Y., Stoller R.E. and Zinkle S.J., Philos. Mag. Lett. 86 (2006) 511.

[26] Osetsky Yu.N., Rodney D. and Bacon D.J., Philos. Mag. 86 (2006) 2295.

[27] Osetsky Yu.N. and Stoller R.E., J. Nucl. Mater, (2015) submitted.

[28] Rodney D., Nucl. Instr. Phys. Res. B 228 (2005) 100.

[29] Rong Z., Osetsky Yu.N. and Bacon D.J., Philos. Mag. 85 (2005) 1473.

[30] Scattergood R.O. and Bacon D.J., Philos. Mag. 31 (1975) 179.

[31] Scattergood R.O. and Bacon D.J., Acta Metall. 30 (1982)1665.

[32] Schaublin R. and Chiu Y.L., J. Nucl. Mater. 362 (2007) 152.

[33] Stewart D., Osetsky Yu.N. and Stoller R.E., J. Nucl. Mater. 417 (2011) 1110.

[34] Stoller R.E. and Osetsky Yu.N., J.Nuclear. Mater, 455 (2014) 258.

[35] Terentyev D.A., Bacon D.J. and Osetsky Yu.N., Philos.Mag. 90 (2010) 1019.

[36] Terentyev D.A., Bonny G. and Malerba L., Acta Mater. 56 (2008) 3229.

[37] Terentyev D.A., Grammatikopoulos P., Bacon D.J. and Osetsky Yu.N., Acta Mater. 56 (2008) 5034.

[38] Terentyev D.A., Osetsky Yu.N. and Bacon D.J., Scripta Mater. 62 (2010) 697.

[39] Singh B.N., Edwards D.J., Tahtinen S. et al., Risø Nat'l. Lab. Report: Risø-R-1481 (EN), 2004.

[40] Trinkaus H. and Singh B.N., Risø Nat'l. Lab. Report: Risø-R-1610 (EN), 2008.

[41] Victoria M., Baluca N., Bailata C. et al., J. Nucl. Mater. 276 (2000) 114.

[42] Wu Y., Odette G.R., Yamamoto T., Ciston J., Hosemann P., An Electron Energy Loss Spectroscopy Study of Helium Bubbles in Nanostructured Ferritic Alloys, Fusion Reactor Materials, Semiannual Progress Report DOE/ER-0313/54, Oak Ridge National Laboratory (2013) 173.

Chapter 9.

Irradiation-induced embrittlement: Fracture mechanics under irradiation

S.R. Ortner
National Nuclear Laboratory, UK

Abstract

It is often not feasible to obtain sufficient mechanical property measurements on irradiated material, e.g. reactor pressure vessel (RPV) steels, to carry out structural integrity assessments based on such data alone, so a number of assumptions concerning toughness behaviour and the viability of surrogate measurements must be made. These are discussed briefly. Fracture modelling and prediction is desirable to support the use of assumptions and indicate the limits of their validity. A number of fracture models in current use/development in the field of RPV embrittlement are described, together with their advantages and limitations. Likely future progress in fracture modelling is then considered.

Introduction

The safe operation of a nuclear power plant (NPP), as of any engineering structure, necessitates an assurance of its structural integrity. It must be designed to resist flaw growth, distortion, plastic collapse and corrosion. In the case of the NPP's reactor pressure vessel (RPV), proof of resistance to flaw growth is the major necessity. In a modern structural integrity assessment, such proof requires knowledge of the RPV steel's toughness and flow properties as a function of relevant temperatures.

It is particularly difficult to achieve such knowledge in the case of irradiated material because (i) RPV steels' toughness and ductility decrease with exposure to radiation, while their flow stresses increase and (ii), there are limited opportunities for monitoring the changes in mechanical properties due to irradiation. The changes in the flow curve are related to the introduction of the hardening centres discussed in Chapters 3, 4 and 5. The change in flow properties and the change in grain boundary segregation (discussed in Chapter 10) lead to a decrease in toughness at a given temperature (or increase in the ductile-to-brittle transition temperature, DBTT) as illustrated in Figure 1.

The monitoring of flow and toughness is carried out using samples irradiated in surveillance capsules held close to the inner wall of the RPV. These are withdrawn periodically for testing. Fewer than five capsule withdrawals are likely within the lifetime of most reactors, so the number of exposure conditions characterised will be small (see [3] for a full description of different countries' programme designs and standards). In addition, there will be limited space within each capsule, so the number of specimens of each monitored material which may be tested will also be small, and there is a strong driving force to test small samples.

Figure 1. Sketch illustrating the characteristics of fracture toughness versus temperature curve for a RPV steel, and the effect of irradiation

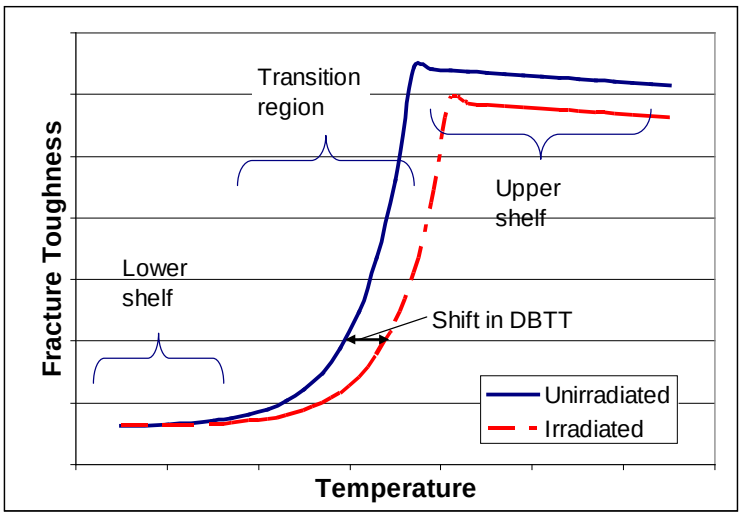

Valid measurements of uniaxial flow properties (tensile tests) may be made using small specimens and small numbers of tests. This is not always the case for toughness measurements. Standardising bodies identify limits to the sizes and shapes of specimens which may be used to produce valid measurements of elastic-plastic stress-field-characterising parameter J for the onset of crack advance [1]. Desirable materials which require higher values of toughness to initiate brittle fracture in the ductile to brittle transition (DBT) region require increasingly large specimens to produce valid measurements. High measurement variability in this temperature range means that using capsule space for a small number of large specimens rather than a larger number of small specimens is of little advantage. A particular source of concern to RPV operators and regulators has, therefore, been the extent to which data acquired using physically small specimens may be used to characterise toughness.

Even if it were theoretically possible to fit suitably large fracture toughness specimens within a surveillance capsule, many capsules do not contain such specimens. At the time of the design of many currently-operating reactor surveillance schemes, embrittlement was characterised using Charpy impact testing. A second concern to RPV operators and regulators is, therefore, the use of surrogate measurements (Charpy impact, yield, hardness) to characterise embrittlement.

In the face of these concerns, many test programmes have been set up to characterise the fracture toughness behaviour of RPV materials under irradiation, with the result that

certain assumptions have been found to be generally supported by experimental observations. These include:

- The shape of the median fracture toughness versus temperature curve (K vs. T) in the DBT region, and the distribution of measurements about the median value, are both unaffected by the absolute value of the DBTT.

With this assumption, it is necessary to test only sufficient samples to identify the location of the curve on the temperature axis (i.e. the DBTT), not the larger number of samples required to characterise the shape of the K *vs.* T curve for each condition. The most well-known of these curves is the Master curve [14,31], given in Equation (1), in which the characterising temperature is T_0. The Master curve relations define the value of K_J measured with probability, p, in a specimen containing a crack front of length, B, at temperature, T to be:

$$K = \sqrt{(JE')} = K_{min} + \{31 + 77\exp[0.019(T - T_0)] - K_{min}\}\left\{\frac{B}{25}\right\}^{0.25}\{-\ln(1-p)\}^{0.25} \qquad (1)$$

in which E'=E in plane strain; $E/(1-\nu^2)$ in plane stress; E=Young's modulus, ν=Poisson's ratio.

Equation (1) is considered appropriate for MnMoNi, CrMoV, CrMo and some 9Cr and 12Cr steels, at least for irradiation-induced shifts in T_0 up to at least 100°C [16,20], although there is some question concerning the scatter description for bounds lower than ~5% [34]. An illustration of radiation-invariant K *vs.* T curve with a flatter lower shelf and steeper transition, used for CMn steels, is given in (Wootton 2008). The reduced activation ferritic-martensitic Eurofer 97 steel may show a similarly sharper temperature dependence than Equation (1). All of the curve shapes mentioned are derived empirically from large numbers of measurements. The different curve shapes for different materials have been ascribed to: data misinterpretation; varying amounts of intergranular fracture; large variations in yield stress.

- Consistent size corrections may be made when small specimens are used to determine fracture toughness (or when test specimen data are applied to large structures).

The size effect in Equation (1) applies to the case in which fracture is dominated by a weakest link process (most likely in the lower transition region, and in components with moderate crack front lengths), where the material exhibits only small-scale yielding prior to fracture and the plastic zone is fully constrained within an elastic ligament. There is discussion concerning whether the size/yield stress limits for measurement validity in various standards do truly ensure small-scale yielding (see [20] for more discussion).

For measurements of upper shelf toughness, J-integral values at the onset of ductile crack extension can be measured. If the measurements are valid according to the ASTM procedure, then no size effect on initiation J is anticipated [1,2,17].

- Surrogate measurements may be used.

Linear relations between the irradiation-induced shift in T_0 (or the temperature at which the median K is 100MPa$\sqrt{m}$) and the DBTT shift measured using Charpy impact

tests (ΔT_{41J}) have been derived for a large number of materials [28]. Linear relations between the radiation induced increase in the lower yield stress, or the hardness [19,20], and the DBTT shift have also been measured, although the constants of proportionality may vary with material. Again, the limits to the applicability of the relations are unclear, and it is unclear whether the scatter in the correlations reflects measurement uncertainty or uncharacterised biases in different types of material.

- It is possible to predict DBTT shifts using dose-damage relations

Dose-damage relations (DDRs) or embrittlement trend curves (ETCs) take advantage of the assumption that only a DBTT shift is of importance, and correlate measures of the DBTT (or DBTT shift) against material and irradiation variables (e.g. material composition, irradiation temperature, neutron dose…). The form of the DDR may be based entirely on the statistical analysis of a large amount of surveillance data, or informed to varying extents by the mechanistic understanding of hardening and segregation processes as discussed in other chapters of this book. Different countries or Regulatory regimes utilise different DDRs [3].

With a DDR applicable to the RPV steel and radiation conditions of interest, a confidence that the fracture toughness is describable by a constant curve shape, and that the DBTT is correctly identified by the available measurements, it is possible to perform a structural integrity assessment. Unfortunately all of the evidence supporting assumptions 1-4 above is empirical. There is always some doubt concerning the margin which should be associated with the use of the assumptions, and the conditions under which the empirical observations will cease to apply. It would, therefore, improve confidence in the use of these assumptions if a valid model of RPV steel fracture could be used to underpin the assumptions, or clarify the limits of their applicability.

Modelling brittle fracture in RPV steels

Mechanism of brittle fracture

Fracture in low alloy steels at low temperatures requires little energy input, occurs extremely rapidly and results in a relatively smooth fracture surface. It is therefore described as brittle. It has, however, been known for many years, that the low temperature fracture of Fe and low alloy steels is consequent on yield. Steel fracture is thus not purely brittle in the manner shown by solids such as glasses or ceramics. The role of yield appears to be the redistribution of stresses that occurs when a polycrystalline aggregate containing a flaw deforms, and when a hard, elastic particle is surrounded by a deforming matrix. This latter aspect is important because brittle fracture in low alloy steels has been observed to initiate at cracked second-phase particles, e.g. carbides [15,23], nitrides, inclusions [8], pearlite colonies [7] and carbide aggregates), as illustrated in Figure 2. The very largest particles in the relevant particle population act as initiators.

Figure 2. Sketch illustrating a) particle cracking under loading from the matrix and b) subsequent extension of the microcrack into the matrix

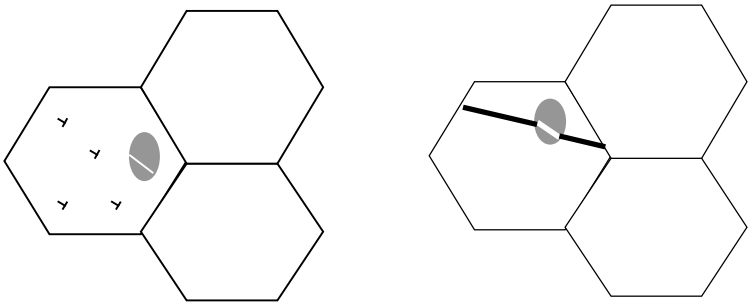

a) b)

While particle cracking is necessary to form a dynamic microcrack, it is not always sufficient to cause in overall fracture. Microcrack extension from the particle into the ferrite matrix requires a favourable balance between plasticity on the one hand and brittle crack growth on the other. If, as a result of a low yield stress, or a suitably-oriented slip band, plasticity can occur, then the microcrack blunts and slows down, the driving force is diverted, and cleavage is suppressed. The suppression can occur at the particle-matrix interface, within the first few microns of microcrack extension (i.e. within the first grain), or as the crack reaches a location at which either plasticity becomes easier or the loading on the microcrack reduces [15]. A high angle grain boundary is frequently cited as an example of the latter two conditions combining. It is also possible that the speed of the particle-sized microcrack affects the balance between plasticity and ferrite cleavage.

Modelling low temperature fracture in steels has been carried out at different scales. Historically the most frequently used approach has been at the level of the homogeneous continuum. It has also taken as its basis purely brittle behaviour, as illustrated in the following sections.

Continuum Modelling Of Brittle Fracture Using Stress Criteria

Griffith's analysis [12] leads to the criterion that, if a brittle material contains an atomically sharp flaw of half-length, r, then failure will occur under a fracture stress σ_F, given by Equation (2)

$$\sigma_F = \sqrt{\frac{2E'\gamma}{\pi r}} \quad \text{in which } \gamma\text{=material surface energy,} \qquad (2)$$

E'=E (plane stress) or $E/(1-\nu^2)$ (plane strain,

E=Young's modulus, ν=Poisson's ratio

Orowan suggested that this analysis could be extended to a material which was not truly brittle by replacing γ with an "effective surface energy", γ_{eff} [21]. γ_{eff} incorporates a plastic work term, i.e.

$\gamma_{eff}=\gamma+w_p$ where w_p is the plastic work expended when a crack advances (3)

These analyses lead to the formulation of a number of stress-based models of fracture in steel, of which the simplest is that due to Ritchie, Knott and Rice, RKR [26]. They found that requiring that a critical stress be exceeded at some location in a specimen did not lead to plausible predictions of macroscopic fracture behaviour. They therefore suggested that the critical stress (σ^*) had to be exceeded over a critical distance (X*) if failure were to occur. By fixing σ^* and X* as temperature-independent parameters, they found that they could predict a dependence of fracture toughness on temperature, induced by the temperature-dependence of the flow stress. Increasing the temperature decreased the flow stress, and so changed the relation between stress and distance within the plastic zone. Their predictions fitted their experimental data on 4-point bend specimens in the lower transition. As the test temperature approaches the DBTT, however, this analysis progressively underestimates the fracture toughness or cleavage stress. The same problem is encountered with more sophisticated treatments which utilise a critical area (A*) or critical volume (V*). The stress distribution in the applications of these models may be calculated using analytical methods for one- or two-dimensional calculations or, more commonly, finite element simulations for treatments of complex geometries.

The Beremin Local Approach [4] uses the same basic stress criterion within a probabilistic description of a material containing a distribution of weak links. In this analysis, the overall probability of failure (P_f) in a stressed sample is given by

$$P_f = 1 - \exp\left[-\left(\frac{\sigma_W}{\sigma_u}\right)^m\right] \quad (4a) \quad \text{or} \quad P_f = 1 - \exp\left[-\left(\frac{\sigma_W - \sigma_{\min}}{\sigma_u}\right)^m\right] \quad (4b)$$

in which m characterises the distribution of weak links, σ_u is a normalising constant incorporating contributions from the weak link distribution, γ_{eff} and other material parameters, and σ_W is the Weibull stress. This characterises the stress in the sample according to

$$\sigma_W = \sqrt[m]{\Sigma_j \left(\sigma_1^j\right)^m \frac{V_j}{V_0}} \quad (5)$$

In Equation (5) the summation is over volume elements, j, of size V_0 in the plastic zone; σ_1^j is the principal tensile stress in the j^{th} element. The two-parameter version of the model (Equation 4a) was the form originally developed. The three-parameter version (Equation 4b), incorporating a lower limiting stress, σ_{min}, is sometimes used as a means of improving correspondence with data.

As with the original RKR model, when the Local Approach in this form is used to predict fracture toughness, there is a tendency to under-predict in the transition region when the lower temperature data are well-described, i.e. the more sophisticated treatment of the stress distribution in the specimen has not solved the problem. The problem of under-prediction becomes particularly acute when this approach is used to describe radiation-induced hardening. If values of m and σ_u are derived by fitting to fracture toughness data distributions measured on an un-irradiated steel, and the role of irradiation is only to change the flow properties, then the fracture toughness of the irradiated steel

may be calculated readily. In this case, however, the under-prediction of toughness occurs ever closer to the lower shelf.

The Beremin group correlated the under-prediction with an influence of plastic strain, and modified the stress in Equation (5) with a strain-related scaling factor

$\sigma_W = \sqrt[m]{\sum_j \left(\sigma_1^j\right)^m \frac{V_j}{V_0} \exp\left[-\frac{m\varepsilon_1^j}{2}\right]}$ in which ε_1^j is the principal tensile strain in the jth element (6)

This correction is not generally used. It is more common to ascribe a temperature-dependence to σ_u, although a mechanistic justification for this is rarely given. In essence, it is equivalent to making the γ_{eff} temperature-dependent.

The WST model [29] was more mechanistically explicit than the RKR or Beremin models in that it correlated the weak links in the microstructure with the distribution of carbides in the steel under study, and applied a Griffith-Orowan type criterion to the probability of a particle-sized crack extending under the locally-prevailing principal tensile stress. As found previously, if the temperature-dependence of the flow properties changing the stress distributions in the specimen was the only effect of temperature, then fracture toughness at higher temperatures was under-predicted. WST dealt with this problem by explicitly introducing a temperature-dependence in γ_{eff}. Although it is plausible that w_p (see Equation 3) should increase with temperature, there is no successful derivation of this parameter from first principles. WST found it necessary to ascribe an exponential temperature-dependence to γ_{eff} to obtain the necessary temperature-dependence in fracture properties. While they could rationalise this form, they did note that data they considered relevant did not support it.

Later development of the WST model [30] added a term describing the initial cracking of particles. Since the particles themselves could be considered brittle, particle fracture was treated with Weibull statistics. At this stage, the stress acting on the particle was related to the shear flow stress in the matrix. The prediction thus contains two separate stress-dependences. Even with this addition and the closer link to the microstructure, it remained necessary to ascribe an otherwise unsupported temperature-dependence to the effective surface energy. These models provide the basis for the distribution of K measurements at a given temperature used in the Master curve.

For either σ_u in the Beremin models or γ_{eff} in RKR or WST, different temperature dependences are required to correlate predictions with fracture data from different steels, even within a given class.

More recently, Odette and co-workers (see [20] for a summary) have used an RKR-type critical stress over a critical area requirement, σ^*-A*, to model fracture. They do not consider that σ^* varies with temperature because of a requirement for a minimum plastic work contribution to crack extension. Instead they postulate that σ^* should be temperature-dependent because of a relation with crack arrest. However, neither the direct transfer of data from crack arrest measurements on single crystals nor a correlation with the dynamic yield stress (derived from an argument based on the postulate

concerning crack arrest) provided predictions of fracture toughness with the temperature dependence required by the postulated relation.

As a result of these difficulties, the required temperature-dependence of w_p, σ_u, σ^* etc. is usually determined by comparing the measured and predicted values of toughness. (There are also a number of scaling parameters in each of the models which must also be determined by comparison with fracture data.) This makes the use of the stress-based approaches descriptive of fracture rather than predictive. Thus they cannot be used to assess the conditions under which the empirical assumptions discussed in the Introduction will cease to hold. If the assumptions concerning fracture trends are applicable, however, these models can be used in the transfer of test data to conditions of different geometry or constraint such as a defect in the RPV [10,11,20].

In essence, all of the purely stress-based models are applications of a successful brittle fracture model to a system which is not purely brittle. The modifications required to incorporate the influence of plasticity involve adapting some significant stress value. In addition, experimental observation of fracture surfaces, however, shows that the separation between the pre-crack tip in a fracture sample and the brittle fracture initiation site increases as the DBTT approaches [22]. This suggests that the fracture process zone changes with temperature in a manner not fully described by stress criteria alone. The next stage in continuum fracture modelling has therefore been the treatment of plasticity effects as separate contributors to the fracture process.

Continuum modelling of brittle fracture using stress and strain criteria

Several models have been developed which incorporate strain explicitly, in addition to stress. In a series of publications beginning in 1990, Chen, Wang and co-workers investigated the characteristics of fracture in low alloy steels, chiefly CMn base and weld metals [7,8,9,33][18]. They noted that the stages in fracture (particle cleavage, microcrack extension into the matrix, microcrack extension past grain boundaries) which appeared critical varied not only with material, but also with specimen geometry and temperature. This led them to the conclusion that fracture occurred when three separate conditions were fulfilled. The first condition was that, as in the models already considered, it was necessary for the principal tensile stress to be above a critical value. This condition was taken to govern only microcrack propagation across the first grain boundary. The second criterion was that the stress triaxiality, T, should be low, with the critical level (T_{crit}) defined by $\sigma_m / \bar{\sigma} = T > T_{crit}$, where σ_m is the average principal stress and $\bar{\sigma}$ the effective shear stress, or equivalent stress. This condition was taken to govern the extension of the particle-sized microcrack into the matrix. Finally, the plastic strain was required to be above a given value for a particle to crack. The conditions $\varepsilon_{pl} \geq \varepsilon_{crit}$, $T>T_{crit}$ and $\sigma \geq \sigma_{crit}$ define the limits to a fracture process zone. At low loads, there may be no overlap between the regions in which $\varepsilon_{pl} \geq \varepsilon_{crit}$ and $\sigma \geq \sigma_{crit}$ are satisfied in a notched sample, even if the region in which $T>T_{crit}$ overlaps each. With increasing load, complete overlap is possible, whereupon the probability of failure increases as the width of the process zone increases. The model has been used to rationalise trends in fracture stress or fracture

[18] A representative selection, not an exhaustive list of these authors' publications on this subject.

toughness, and initiation site locations with changes in specimen geometry, temperature, loading rate and prestrain. There do not appear to have been any uses of the model by Chen, Wang or co-workers for quantitative predictions of fracture toughness or the fracture stresses in notched bend samples.

Although this model involves three parameters, it is not clear from the various illustrations of the process zone whether there are any situations in which the $\varepsilon_{pl} \geq \varepsilon_{crit}$, and $\sigma \geq \sigma_{crit}$ criteria are met, but the triaxiality criterion is not met. In the EOH model [23], there are separate stress and strain criteria, but no hydrostatic stress criterion. In EOH, particle cracking (as in WST) is taken to be stress-dependent, but the particle stress is now considered to be related to the local matrix strain. Microcrack extension is again governed by a Griffith-Orowan criterion, but γ_{eff} is taken to be temperature-independent. Introducing an independent strain term alone does not eliminate the under-estimate of fracture toughness as temperatures approach the DBTT. Within EOH, the problem was addressed by introducing an upper limit (r_{max}) to the particle size distribution (c.f. the 3-parameter Beremin approach, Equation 4b). The upper limit was suggested to result from the likelihood that the thermal stresses induced during quenching would crack very large particles prior to material use/testing. In support of this suggestion, the values of r_{max} required to match predicted with measured toughnesses decreased with increasing quench rate.

The EOH model has the advantage that γ_{eff} becomes constant not only with temperature, but also within similar classes of steel. Unfortunately, although trends in r_{max} appear predictable, absolute values have not been. Similarly, although ε_{crit}, and σ_{crit} are determined from fracture surface measurements, there are still some scaling parameters required, so the model cannot be considered fully predictive. The model has been used to describe the DBT behaviour of a number of MnMoNi steels. It has not, however, predicted irradiation-induced shifts in the DBTT.

Bordet and co-workers [5,6] also concluded from their analysis of the literature that particle cracking was a function of strain, and that there should be a maximum to the microcrack size. The treatment of nucleation rates and microcrack extension is more sophisticated than in EOH, while within their formulation it is not necessary to specify whether the extending microcrack refers to a cracked particle, lath, lath packet or grain. They considered the probability of particle cracking to be proportional to plastic strain (ε_p), with the yield stress (σ_Y) providing the constant of proportionality. Combining this with the Beremin description of microcrack extension produces:

Probability of failure in a volume element experiencing stress σ_1 and maximum plastic strain

$$\varepsilon_{p,u} = P_{failure}(\sigma_1, \varepsilon_{p,u}) \propto \int_0^{\varepsilon_{p,u}} \frac{\sigma_Y}{\sigma_{Y0}} \left\{ \left(\frac{\sigma_1}{\sigma_u} \right)^m - \left(\frac{\sigma_{\min}}{\sigma_u} \right)^m \right\} \exp\left[-\frac{\sigma_Y}{\sigma_{Y0}} \cdot \frac{\varepsilon_p}{\varepsilon_{p0}} \right] d\varepsilon_p \qquad (7)$$

Somewhat surprisingly, despite the introduction of the strain term and the maximum microcrack size, and the number of terms which may be varied (σ_{Y0}, σ_u, σ_{min}, m, ε_{p0}) to fit to low-temperature toughness data, this model still underestimates the temperature-dependence of toughness, although it reproduces the strain rate dependence well in a low

alloy steel. A temperature-dependence must be introduced in ε_{p0} and/or σ_u to reproduce the higher-temperature values of toughness or to allow for radiation-induced hardening.

In summary, there are several formulations of continuum models of fracture which incorporate strain effects, and do so in explicit reference to the different observed stages in the brittle fracture of steel. Transferability from one material/geometry to another may well be improved over the simple stress-only models, but each model still contains a number of scaling parameters (not all mentioned explicitly in the preceding text) which must be derived by comparison with data. In addition, the modelling of irradiation-induced shifts in the DBTT still requires the modification of parameters calibrated using unirradiated steel data.

It is possible that the inadequacies in prediction exhibited by all of these models to date indicate that there is insufficient information at the homogeneous continuum level to describe the fracture process sufficiently. It is, therefore, worth considering insights gained from modelling at other levels of detail.

Models of fracture at more detailed levels

The investigation of low alloy steel fracture at levels other than that of the homogeneous continuum has involved the investigation of individual stages in fracture rather than the overall process. The redistribution of stresses and strains at yield has been studied by aggregate modelling [25]. In aggregate modelling, the representative volume (e.g. V_0 in Equation 5) is taken to consist of a number of individual grains. The stress and strain distributions in the aggregate must, therefore, include strain concentrations caused by discontinuities of flow at grain boundaries or particles within the aggregate. The choice of grain shapes, misorientations across boundaries and particle distributions may all be informed by reference to the properties of actual steels. Early results of such modelling indicate that the ranges of stress and strain seen within a specimen may vary considerably from those predicted for a homogeneous continuum.

The cracking of individual particles was studied by Laukkanen and Wallin [13]. They used Finite Element simulations to relate the stress in an elastic particle to the stresses and strains in a surrounding plastic continuum. The precise relation between the particle stress and the stresses/strains in the matrix varied somewhat with particle aspect ratio and loading, but the results could be reasonably summarised by the generally-applicable expression [32]:

$$\sigma_p \approx \sqrt{1.3 \cdot \sigma_{matrix} \cdot \varepsilon_{matrix} \cdot E_{particle}} \tag{8}$$

in which σ_{matrix} and ε_{matrix} are the principal tensile stress and total principal tensile strain that would be present in the plastic matrix at the particle location in a particle-free sample (i.e. a homogeneous continuum) and $E_{particle}$ is the Young's modulus of the particle.

The use of Equation 8 permitted Wallin and Laukkanen to clarify the apparent temperature-dependence of particle cracking found in the literature. In addition, if a critical value of $\sigma_{matrix} \cdot \varepsilon_{matrix}$ is taken as the particle cracking criterion (rather than simply a critical value of ε_{matrix}) in EOH, better convergence is found between the behaviour of different steels, improving predictability of the model parameters [24]. It is possible that

such a particle cracking criterion would avoid the necessity of introducing a temperature-dependent value of ε_{p0} (or its equivalent) in the Bordet model.

The effect of lattice dislocations on the stress experienced by a crack or flaw has been studied by many workers. In particular, Roberts et al. [27] considered the emission of dislocations from sources close to a small finite crack when it is subject to a distant load. Dislocations generated from sources at each end of the microcrack were emitted onto planes above and below the microcrack. The stress experienced at each microcrack tip was, therefore, the sum of the stresses due to all the emitted dislocations (i.e. dislocations on all planes, and from both ends of the microcrack), and to the applied stress. In effect, the dislocation distribution shielded the crack tips from the external stress, reducing the stress intensity actually experienced at the microcrack tips. The degree of shielding was affected by the dislocation velocity i.e. by the activation energy for dislocation movement, the friction stress, the applied shear stress and the temperature. (These parameters may be measured independently of the fracture process). Overall, the degree of shielding (i.e. the difference in the K actually experienced at the crack tip and that which would be calculated from the crack length and external load alone) increased with increasing temperature. The crack extension condition was the achievement of the simple Griffith condition at the microcrack tip (i.e. Equation 1, using the independently-measurable, true surface energy, not an effective energy). The external load corresponding to the achievement of the Griffith condition increased with temperature, because the (quantitatively calculated) shielding increased with temperature, and a DBT resulted. The degree of shielding was also affected by the separation between the dislocation arrays at each end of the microcrack (i.e. the microcrack length, d). The end result was that the external stress required to extend the crack (σ_F) did not follow a Griffith-type $\sigma_F \propto \sqrt{1/d}$ (Equation 2) relationship, as used in many of the continuum models discussed above.

Noronha et al. [18] extended the Roberts et al work to the situation in which the load on the microcrack was applied by the stress field around a macroscopic crack. Dislocations were also generated at sources around the macroscopic crack tip, shielding it. The extension force on the microcrack ahead of a macroscopic crack was, therefore, affected by dislocations at both the macroscopic and microscopic crack tips, as well as on the external load. Finally, Noronha et al. considered the attraction of some of the generated dislocations to the macro-crack, which produced macro-crack extension and blunting and, hence, altered further the stress experienced by the microcrack. It proved necessary to include all of these factors to predict the observed upswing in the externally-measured fracture toughness with temperature.

None of the insights into the fracture process discussed in this section could have been acquired by homogeneous continuum modelling. It is, however, possible to inform improved continuum modelling with those insights: an assessment of the strain inhomogeneities caused by microstructural features such as grain boundaries; a more soundly-based particle cracking criterion; a microcrack extension criterion more applicable to partly-brittle material than the Griffith-Orowan criterion; the necessity to include effects of crack blunting/extension during loading.

Conclusions

Materials modelling is most informative when it is carried out at the correct scale (in length or time) for the process modelled. This is not necessarily the same scale as that at which the information must be used. Continuum-scale models are most readily usable for the transfer of fracture data from test specimens to structures. This chapter has surveyed the development of continuum models of fracture in low-alloy steels. The earliest, derived from descriptions of purely brittle fracture, incorporate only a single, characterising stress. Later models utilise information derived from microscopic observations of the fracture process in low alloy steels to introduce modifications to the characterising stress, or to define new strain parameters which may be incorporated into the models in mechanistically meaningful ways. As discussed, even the latest models remain descriptive rather than predictive. While this is useful, it does not provide the support necessary to underpin use of the assumptions currently made to produce RPV structural integrity assessments. Valid results on relevant materials in well-designed surveillance programs remain vital.

The limited success of the continuum models suggests that modelling at finer scales is necessary to provide a true description of a fracture process which is not purely brittle. Examples of models describing fracture at the grain, particle and dislocation level have been given. While most of these models are still under development, they have already provided insights which could be incorporated into the continuum models.

References

[1] ASTM Standard E1921-11a, "Standard Test Method for Determination of Reference Temperature, T_0, for Ferritic Steels in the Transition Range" (2011a).

[2] ASTM Standard E1820-11, "Standard Test Method for Measurement Of Fracture Toughness" (2011b).

[3] A. Ballesteros et al, *IAEA Nuclear Energy Series No NP-T-3.11 Integrity of Reactor Pressure Vessels In Nuclear Power Plants: Assessment Of Irradiation Embrittlement Effects In Reactor Pressure Vessel Steels,* pub IAEA, Vienna (2009).

[4] F. M. Beremin, Metall. Trans., 14A, 2277-2287 (1983).

[5] S. R. Bordet, A. D. Karstensen, D. M. Knowles and C. S. Wiesner, Engg. Fract. Mech., **72,** 435-452 (2005).

[6] S. R. Bordet, A. D. Karstensen, D. M. Knowles and C. S. Wiesner, Engg. Fract. Mech,. **72,** 453-474 (2005).

[7] J. H. Chen, G. Z. Wang and H. Ma, Metall. Trans., 21A, 321-330 (1990).

[8] J. H. Chen, L. Zhu, G. Z. Wang and Z. Wang, Metall. Trans., 24A, (1993) 659.

[9] J. H. Chen, G. Z. Wang and Q. Wang,, Metall. Mater. Trans., 33A, 3393-3402 (2002).

[10] R. E. Dolby, C. S. Wiesner, R. A. Ainsworth, F. M. Burdekin, J. Hancock, I. Milne and N. P. O'Dowd, Int. J. Press. Vess. & Piping, 82, 496-508 (2005).

[11] X. Gao and R. H. Dodds, Engg. Fract. Mech., 68, 263-283 (2001).

[12] A. A. Griffith, Phil. Trans. Roy Soc. Lond. A, 221, 163-198 (1920).

[13] A. Laukkanen and K. Wallin, VTT Report BTUO72-051372 (2005).

[14] D. E. McCabe, J. G. Merkle and K. Wallin, *An Introduction to the Development and Use of the Master Curve Method*, pub. ASTM International, ISBN No 0-8031-3368-5 (2005).

[15] C. J. McMahon, Jnr. And M. Cohen, Acta Metallurgica, 13 (1965) 591.

[16] R. K. Nanstad, M. Sokolov and D. E. McCabe, J. ASTM Intl., (2008)

[17] B. K. Neale, Engg. Fract. Mech., 69, 497-509 (2002).

[18] S. J. Noronha and N. M. Ghoniem, , Int. J. Mech. Material Design, 4, 1-12 (2008).

[19] G. R. Odette, M. Y. He and T. Yamamoto, J. Nuclear Mater., 367-370(A), 561-567 (2007).

[20] G. R. Odette, H. J. Rathbun, M. Hribernik, T. Yamamoto, M. He and P. Spatig, *Materials Issues for Generation IV Systems*. Ed V. Ghetta, pub. Springer 203-226 (2008).

[21] E. Orowan, *Fatigue & Fracture Of Metals* Ed. W. M. Murray, pub. John Wiley, 139-154 (1950).

[22] S. R. Ortner and C. A. Hippsley, Mater. Sci. Tech., 12, 1035-1042 (1996).

[23] S. R. Ortner, FFEMS, 29 (9/10), 752-769 (2006).

[24] S. R. Ortner, FFEMS, doi:10.1111/j.1460-2695.2011.01565.x

[25] N. Osipov, A.-F. Gourges-Lorenzon, B. Marini, V. Mounoury, F. Nguyen and G. Cailletaud Philos. Mag., 88, 3757-3777 (2008).

[26] R. O. Ritchie, J. F. Knott and J. R. Rice, J. Mech. Phys. Solids, 2, 395 (1973).

[27] S. G. Roberts, S. J. Noronha, A. J. Wilkinson and P. B. Hirsch, Acta Mater., 50, 1229-1244 (2002).

[28] M. A. Sokolov, R. K. Nanstad, *ASTM STP 1325*. Eds Nanstad et al, pub ASTM, 167-190 (1999).

[29] K. Wallin, T. Saario and K. Törrönen, Met. Sci. 18 (1), 13-16 (1984).

[30] K. Wallin, T. Saario and K. Törrönen, Int. J. Fract., 32, 201-209 (1987).

[31] K. Wallin, Int. J. Press. Vess. & Piping, 55, 61-79 (1993).

[32] K. Wallin and A. Laukkanen, FFEMS, 29 (9/10) 788-798 (2006).

[33] G. Z. Wang, X. C. Ren and J. H. Chen, Metall. Mater. Trans., 35A, 1765-1778 (2004).

[34] T. Williams, D. Swan and G. Dixon, IAEA Specialists Meeting, Moscow (2004).

[35] M. R. Wootton, R. Moskovic, C. J. Bolton and P. E. J. Flewitt, Energy Materials 3 (1), 45-56 (2008).

Chapter 10

Embrittlement without hardening: Grain boundary embrittlement

M. Yamaguchi
Center for Computational Science and e-Systems, Japan Atomic Energy Agency, Japan

Abstract

The aggregation (segregation) of a small amount of solute or impurity elemental atoms along grain boundaries in metals causes cracking along GBs, which is sometimes called non-hardening (GB) embrittlement. Although a number of atomistic studies have been done for many years, the mechanism of the GB embrittlement is still controversial. Recent progress of computers and first-principles codes has suggested that the change in the cohesive energy of GB caused by solute segregation may be a key factor controlling the GB cracking. Although the GB cohesive energy is only a small portion of the total fracture energy, the GB cohesive energy is considered to have a valve-like effect on the fracture energy that mainly consists of energy dissipation by plastic deformation due to dislocation activities.

Introduction

In the previous chapter, the embrittlement of metals caused by hardening is described. In this chapter, the embrittlement of metals that does not associated with the hardening is discussed. Among the non-hardening embrittlement, grain boundary (GB) embrittlement by solute segregation is considered to be the most important one, because it brings about the catastrophic failure of structural materials due to a substantial decrease of fracture toughness, which defines the resistance to brittle crack propagation.

It is well known that the mechanical properties of structural alloy steels can be drastically changed by a small amount of solute (or impurity) elements which are dissolved in those steels. By exposing the steels to elevated-temperature and/or neutron irradiation environments for a long period, some solute elements diffuse and then segregate (become trapped) at GBs. From the analyses of Auger electron spectroscopy (AES) on the fracture surfaces of the GB cracking in steels, the segregation of sulphur (S), phosphorous (P), tin (Sn), Antimony (Sb), and some other elements in steels are known to cause the GB

embrittlement, while the segregation of boron (B) and carbon (C) is known to suppress the GB embrittlement [16]. It is considered that those segregated elements change some atomistic properties along GBs. However, it is not known why and how such elements change the atomistic properties in the grain boundaries, and why its change brings about a large reduction of fracture toughness.

Many theoretical (computational) studies of GB embrittlement of metals by solute segregation have been done over 30 years. Losch proposed the idea that solute-induced changes in the electronic structure (or chemical bonding) could be responsible for the embrittlement in metals for the first time [10]. After his work, a large number of electronic structure calculations were performed and many kinds of atomistic mechanisms have been proposed as the origin of the GB embrittlement. However, whereas most works just pointed out the change in the atomistic and electronic properties caused by the solute segregation along GBs, those works do not explain the relationship from the macroscopic change in the mechanical properties of metals to the change in the atomistic and electronic properties of GBs. The considerations from atomistic (microscopic) to macroscopic fracture mechanics are necessary to understand the mechanism of GB embrittlement.

In the following section, some introductory topics about GB embrittlement are described. Then, some theoretical works will be introduced. Finally, the author's understandings will be shown, which is obtained from the author's recent first-principles calculations and considerations based on microscopic and macroscopic fracture mechanics [7,8].

Backgrounds

Grain boundary segregation of solute/impurity elements and its energetics

Most metallic materials are polycrystalline materials, which consist of many grains as shown in Figure 1(a). The grain is either a single crystal or has microstructure. The size of grain is usually more than several tens of micrometres. A GB is the interface between two grains, and in most cases the atomic structure of GB is severely distorted compared to the bulk lattice. For this reason, the GB has a positive excess energy (GB energy, γ_{gb}) with respect to the perfect crystal (Figure 1(b)).

Solute or impurity elemental atoms in grains are hard to dissolve when their atomic radius is much different from metal atoms. This is because the difference in atomic radius induces positive (unstable) elastic strain energy. The nature of chemical bonding for solute also affects its energetic stability in grains. When the solute/impurity elemental atoms in grains can diffuse owing to high temperature and/or neutron irradiation, those atoms tend to segregate (be trapped) along GBs, because they can be stabilised energetically by the release of the elastic strain energy at the GBs and/or by some chemical bonding effects (Figure 1(a)(b)). This stabilisation energy is called as GB segregation energy (ΔE^{seg}_{gb}), which is inherently negative in value.

When fracture occurs, two fracture surfaces are created. The energy of the two fracture surfaces ($2\gamma_s > 0$) is higher than that of GB. If the solute-segregated GB breaks, the segregated solute atoms appear on the fracture surfaces (Figure 1(b)). The fracture surface energy is also affected by the surface segregation energy (ΔE^{seg}_{s}) of solute atom. If

the surface segregation energy (< 0) is much larger (in negative direction) than the GB segregation energy for a solute elemental atom, this atom can decrease the pure GB cohesive energy ($2\gamma_{int}^{0}$) as,

$$2\gamma_{int} = 2\gamma_{int}^{0} + (\Delta E^{seg}_{s} - \Delta E^{seg}_{gb})\,\Gamma. \qquad (1)$$

Here, the GB cohesive energy ($2\gamma_{int}$) is defined as the energy difference between the two surface states after fracture and the grain boundary state before fracture as shown in Figure 1(b). Γ indicates the coverage of GB segregation. The $2\gamma_{int}$ is considered to define the strength of cohesion (chemical bonding) of atoms along the GB, as will be more described later.

Figure 1. Schematic illustrations for (a) solute segregation along GB, and (b) the relations between GB energy (γ_{gb}), fracture surface energy (γ_s), GB/fracture-surface segregation energy of a solute atom ($\Delta E^{seg}_{gb/s}$)

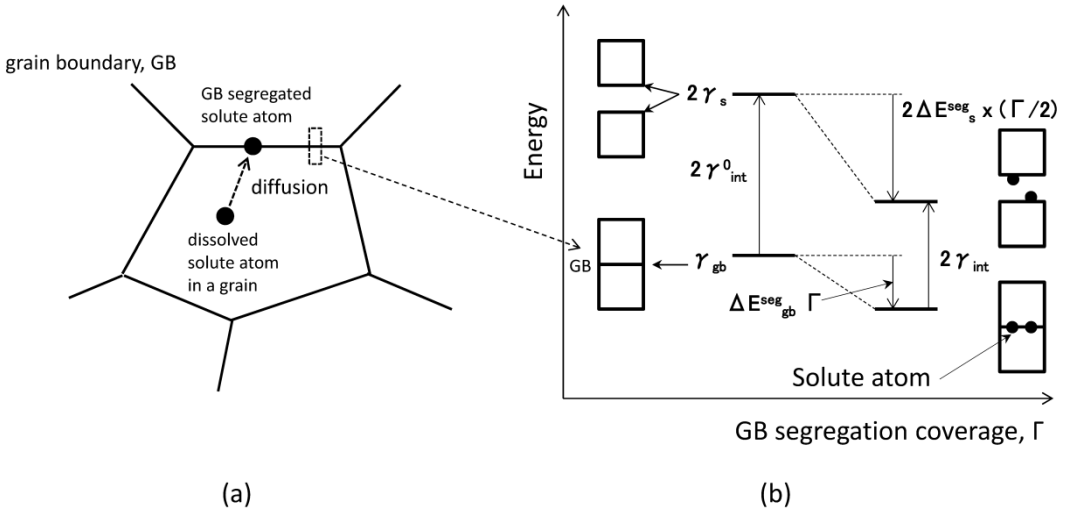

Intergranular embrittlement (grain boundary embrittlement)

Catastrophic failures in engineering materials can be caused by GB fracture. A well-known example of GB fracture is the rotor failure of the Hinkley Point Power Station turbine generator as shown in Figure 1 [6,16]. The broken rotor is reassembled as shown in Figure 1(a). The fracture occurs along prior austenite grain boundary path with little plastic deformation as shown in Figure 2(b). This fracture is caused by the thermally induced segregation of solute and/or impurity elements in the steel to the grain boundary.

Figure 2. (a) The reassembled 3Cr1/2Mo rotor that initiated the turbine failure at Hinkley Point [16] and [6] (b) Scanning electron micrograph of the fracture surface of the failed rotor (field view 200 microns [16]

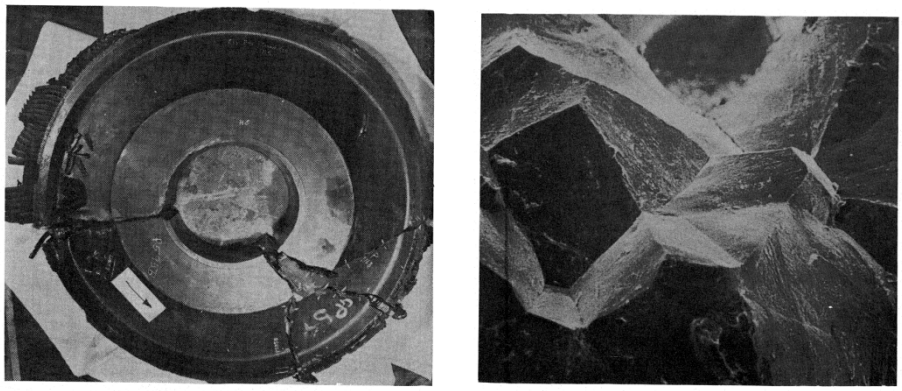

(a) (b)

Nowadays, this kind of GB embrittlement can be suppressed by reducing of the concentration of embrittling impurity elements in alloy steels. However, the fundamental mechanism of GB embrittlement still remains unclear. Furthermore, neutron irradiation in the nuclear reactor induces GB segregation in the temperature range at which thermally induced segregation does not occur. It is still not known whether the GB embrittling effect by solute segregation is the same or not as thermally induced segregation and irradiation induced segregation.

History of the study for the atomistic mechanism of GB embrittlement

As briefly described in the Introduction section, the idea that solute-induced changes in the electronic structure of GB could be responsible for the GB embrittlement in metals was firstly proposed by Losch [10]. Then, the first study using electronic structure calculations was done by Messmer and Briant (Messmer, 1982). In this work, they calculated the electronic structure and chemical bonding in the small and binary metal-solute clusters including several metal atoms (iron (Fe), nickel (Ni)) and a single solute atom (carbon (C), phosphorous (P), sulphur (S), etc.) surrounding vacuum environment. From these calculations, they obtained the conclusion that the strong embrittling element like S makes a strong bonding with metals, resulting in the reduction of electrons in metal-metal bonds that may cause GB embrittlement.

After that, different points of view were presented by some researchers by using similar cluster-model calculations. Eberhart et al. [82] pointed out from their Ni-S cluster-model calculations the effect of solute on the cohesive and shear strength in the crack tip region. Their calculations indicated that embrittling elements may suppress the dislocation emission at the crack tip, leading to GB embrittlement. On the other hand, Painter and Averill [14] showed that from Ni-S and Ni-B cluster calculations the restoring force of the clusters against lattice expansion were enhanced by B while weakened by S. This is consistent with experimental observations that B is a cohesion enhancer and S is an embrittling element. These calculations indicated that B/S strengthens/weakens the chemical bonding along the GB. Since the computer and codes for electronic structure calculations had been not well developed in the 1980s, their calculations were limited

within such a cluster model and thus did not give an electronic structure of GB in polycrystalline materials.

Other than the cluster-model calculations, the electronic structures of GB in bulk phase (under three dimensional periodic boundary condition) have been calculated by some researchers. Hashimoto et al. [4] calculated the electronic structure of a realistic bcc Fe Σ5(013) symmetrical tilt GB with/without P segregation, and supported the conclusion by Messmer and Briant; bond weakening (decohesion) occurs across the GB due to charge transfer by solute segregation. On the other hand, Crampin et al. [2] calculated the electronic structure of fcc Ni Σ5(012) GB with/without S segregation and suggested that the anisotropy of chemical bonds due to solute segregation inhibited the dislocation motion across the GB, leading to embrittlement.

The above studies focused on the change of chemical bonding along GB by solute segregation and tried to get some insights on the GB embrittlement. However, these calculations cannot give physical understandings in connection to the reduction of fracture stress, fracture toughness, and the upward shift in ductile-brittle transition temperature, which define the phenomenon of macroscopic GB embrittlement.

The theoretical model in order to understand the change in one of the macroscopic mechanical property, ductile-brittle transition temperature, by solute segregation along GB was proposed by Rice and Wang [15]. This Rice-Wang model assumes that the GB embrittlement is basically controlled by the cohesive energy of the GB (or the ideal work of GB fracture in other words); the energy difference between GB energy before fracture and two fracture surfaces' energies after fracture ($2\gamma_{int}$), which are influenced by solute segregation as shown in Figure 1(b). They estimated the change of $2\gamma_{int}$ by solute segregation from experimental segregation energies, and found that the change of $2\gamma_{int}$ is correlated to the shift of ductile-brittle transition temperature experimentally observed in iron and steels.

Several years later, Wu et al. [17] performed first-principles calculations for the change of ideal work of fracture for a bcc Fe GB by solute segregation of P and B. They found that B increases the ideal work while P decreases, which are consistent with experimental facts (B: cohesion enhancer, P: embrittling element). After this work, a number of similar calculations have been done for various embrittling and toughening elements along some kinds of metal GBs. Most of calculations support the Rice-Wang model; the cohesion enhancing elements (B, C in Fe GB) increase the ideal work of GB fracture, while embrittling elements (H, P, S in Fe and Ni GBs) decrease it.

Although the Rice-Wang model has been supported by many calculations, the multiscale understanding of GB fracture from atomistic to macroscopic aspects is still lacking. It is not well known that the Rice-Wang model is based on a more fundamental concept (hypothesis) suggested by Jokl et al. [5]; the plastic work associated with brittle crack propagation must be dependent on the GB cohesive energy. In the brittle crack propagation in metallic materials, this plastic work is inevitable. This hypothesis has been not yet established sufficiently by theoretical [5] and experimental [13] findings. For this reason, it is still controversial as to the atomistic mechanism of GB embrittlement, and thus different and new mechanisms still continue to be suggested one after another [1,3].

In the next section, the author's understanding will be shown based on fracture mechanical consideration with the hypothesis suggested by Jokl et al.

Understanding of GB embrittlement from fracture mechanical point of view

Macroscopic/Microscopic Fracture Mechanics of GB cracking

It needs a long story to explain why the reduction of the GB cohesive energy ($2\gamma_{int}$) controls a much larger reduction in the macroscopic fracture toughness or energy. One understanding is shown in Figure 3. The macroscopic fracture toughness is denoted by K_{Ic} that consists of macroscopic fracture stress (σ_{frac}) and macroscopic crack length (a_{macro}), and geometrical factor (*F,f*). This macroscopic crack can propagate if the K_{Ic} satisfies the crack propagation condition ($(1-\nu^2)K_{Ic}^2/E = G_{Ic}$ in Figure 3), in which G_{Ic} is macroscopic strain energy release rate, ν is Poisson's ratio, and E is Young's modulus. The local fracture stress σ_{local} is the concentrated stress ahead of the notch in the specimen, which produces plastic deformation. If there is an inclusion along GB under the maximum σ_{local}, the pile up of dislocations or cracking of inclusions can nucleate an atomistic sharp microcrack, which can propagate if the microscopic crack propagation condition is satisfied ($(1-\nu^2)k_{Ic}^2/E = g_{Ic}$ in Figure 3). In this condition, the microscopic strain energy release rate g_{Ic} consists of the GB cohesive energy $2\gamma_{int}$ and the plastic work term γ_p associated with the brittle crack propagation. This plastic deformation is produced by the stress concentration ahead of the microcrack.

Macroscopic K_{Ic} (strain energy release rate G_{Ic}) is much larger than the microscopic k_{Ic} (g_{Ic}), and furthermore the k_{Ic} (or γ_p) is much larger than the GB cohesive energy ($2\gamma_{int}$). It is well known that solute segregation of the embrittling element along the GBs can cause a large reduction of macroscopic fracture toughness. It is easy to understand that the solute segregation can change the GB cohesive energy ($2\gamma_{int}$), because the segregation is limited along GB within a few atomic layers. However, an important question is why the solute segregation can reduce k_{Ic} and K_{Ic}? The volumetric size of the plastic work region for $k_{Ic}(\gamma_p)$ near the fracture surfaces is a few microns in diameter, which is much wider than the segregation region (a few Angstroms). Furthermore, the plastic work region for K_{Ic} is much larger than that of k_{Ic}. For this reason, it is hard to imagine that segregated solute elements along a GB can affect the dislocation nucleation and motion far from the GB region.

This question can be resolved if the size of the plastic work term (γ_p) depends on the size of GB cohesive energy ($2\gamma_{int}$). Theoretical evidence of this assumption was given by Jokl, Vitek, and McMahon [5]. They suggested that the plastic work term (γ_p) was a monotonically increasing function of the GB cohesive energy from the analysis using the Dugdale-Billy-Cottrell-Swinden model as shown in Figure 4(b). Their model suggests that a large decrease in the plastic work term is induced by a small decrease of the GB cohesive energy from the competition in velocity between bond breaking and dislocation emission at the microcrack tip region. This is also supported by the measurement of X-ray line broadening near GB fracture surfaces in which the residual lattice strain is reflected by the plastic deformation near the fracture path [13]. Similar dependence can be seen between the macroscopic K_{Ic} and microscopic k_{Ic} as shown in Figure 4(a), which is an experimental analysis in the embrittlement of Ni-Cr steel by P, Sn, and Sb segregation

observed by Kameda [8]. This is roughly explained from the strain-hardening behaviour at the macroscipic crack tip region. From these theoretical and experimental results, it is suggested that the GB cohesive energy $2\gamma_{int}$ has a valve-like effect on the much larger plastic work term γ_p, and γ_p (or microscopic k_{Ic}) has also a similar effect on the much larger macroscopic K_{Ic}.

Figure 3. Schematic illustration for macroscopic and microscopic fracture mechanics of GB cracking

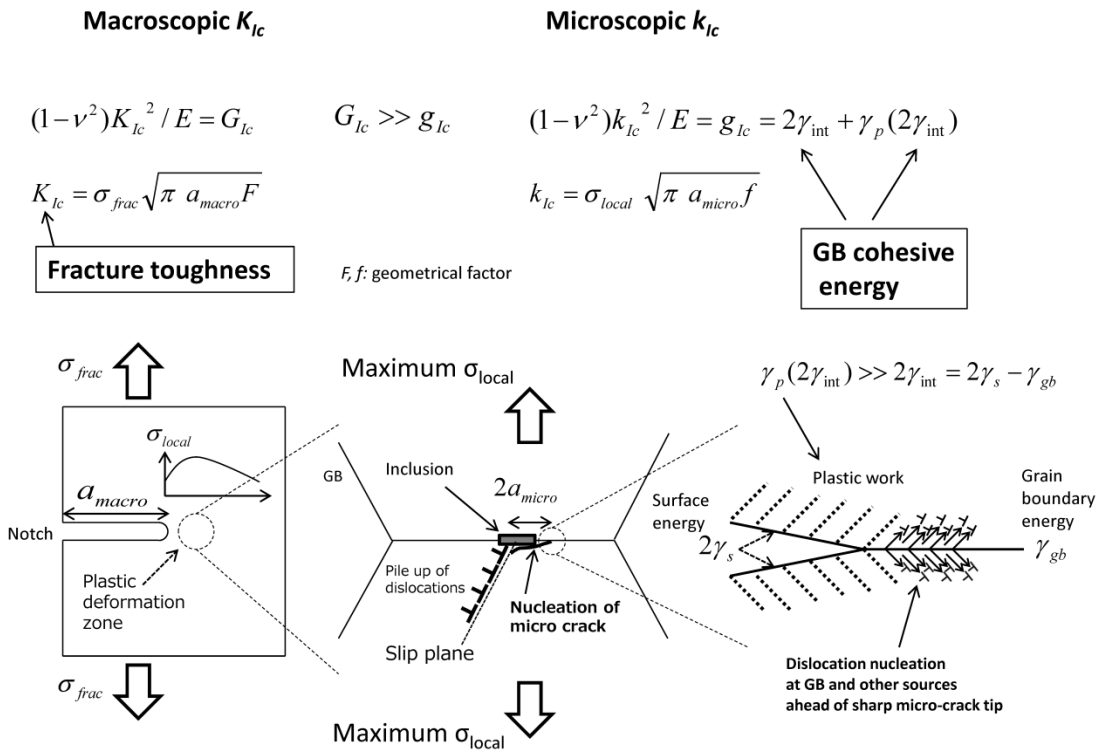

Figure 4. (a) A "valve-like" effect of the microscopic fracture toughness (k_{Ic}) on the macroscopic fracture toughness (K_{Ic}) [8], (b) A similar effect of the GB cohesive energy ($2\gamma_{int}$) on the plastic work term (γ_p) associated with a brittle microcrack propagation [5], because of $(1-\nu^2)k_{Ic}^2/E = 2\gamma_{int} + \gamma_p$, macroscopic K_{Ic} is considered to be controlled by $2\gamma_{int}$ from the above two relationships

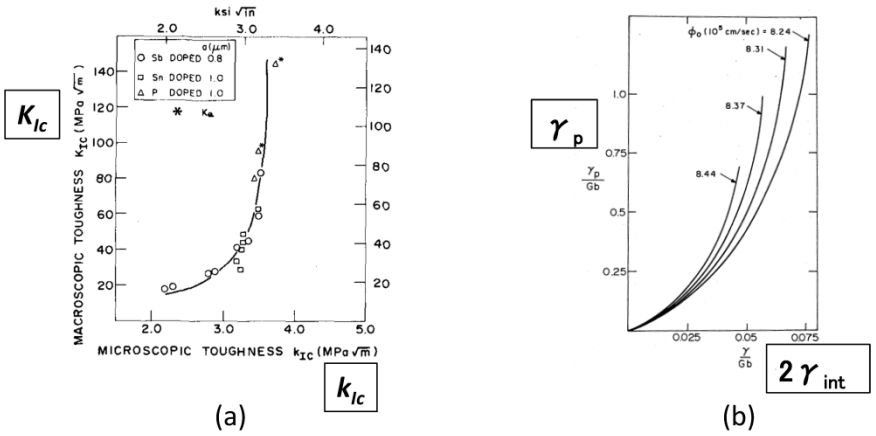

Ductile-to-brittle transition temperature (DBTT)

Although the atomistic modelling of the mechanisms of ductile-brittle transition is still missing, a phenomenological understanding of DBTT can be shown as in Figure 5. The ductile-to-brittle transition is considered to occur at the intersection of the two lines of brittle fracture stress (σ_{local}) and yield stress (σ_Y); the brittle fracture stress does not largely depend on temperature while the yield stress (σ_Y) depends very much. As shown above, the decrease of $2\gamma_{int}$ causes the large decrease of $2\gamma_p$. It results in the decrease of brittle fracture stress (σ_{local}) and then brings about the increasing shift of DBTT. In this way, the shift in DBTT is considered to be caused by the reduction of $2\gamma_{int}$.

Figure 5. Schematic illustration of the relation of DBTT and local fracture stress

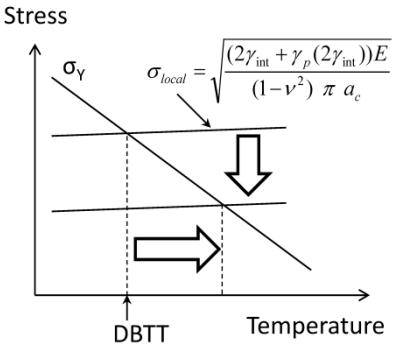

Recent Calculations of GB cohesive energy from first-principles

In the previous section, the importance of the GB cohesive energy was described. The GB cohesive energy has a "valve-like" effect on the plastic work term (γ_p) and the microscopic fracture toughness (k_{Ic}), and similarly the k_{Ic} has the same effect on the macroscopic fracture toughness (K_{Ic}). Consequently, the GB cohesive energy ($2\gamma_{int}$) is a key factor controlling the GB embrittlement. Jokl et al. [5] tried to estimate the GB cohesive energy change by solute segregation using their theoretical model in the analysis of the experimental results of the embrittlement in the Ni-Cr steel with P, Sn, and Sb segregation. Nowadays, however, the GB cohesive energy can be easily calculated from first-principles calculations as stated below.

Modelling of grain boundary structure

The unit cell including bcc Fe Σ3(111) symmetrical tilt grain boundary is shown in Figure 6 (a-b). The tilt angle is 70.5 deg, and the rotation axis is <1-10>. In the upper and lower regions of this cell, a vacuum region is introduced to allow the GB sliding along the GB plane. The calculated energy of this GB (γ_{gb}) is 1.52 J/m^2, and the energy of its fracture surface (γ_s) is 2.69 J/m^2. Thus, the calculated cohesive energy of the GB ($2\gamma_{int} = 2\gamma_s - \gamma_{gb}$) without segregation is 3.86 J/m^2. This GB is chosen because the structure is simple but the GB energy is relatively high.

Figure 6. Modelling of BCC FeΣ3 (111) symmetrical tilt grain boundary [18]

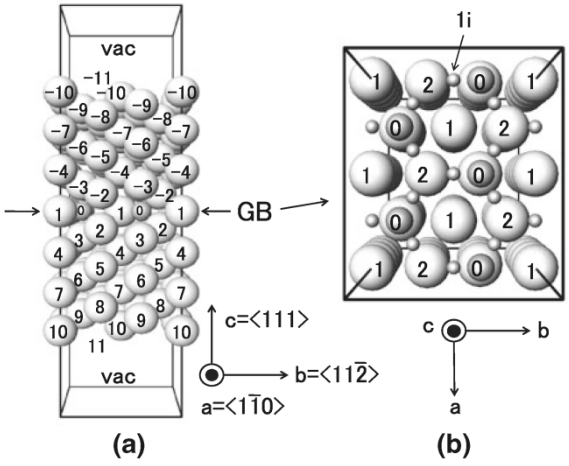

Calculations of segregation energy and tensile test calculations from first-principles

The details of first principles calculations are described in [18]. Here, a rough procedure of calculations will be explained below.

1. The segregation energy of solute atom at each atomic site in the cell (Figure 6) is calculated (The calculated segregation energies are not shown in this article.) The preferable segregation atomic sites along the GB and fracture surfaces are found.

2. The segregation energy of solute atoms with increasing segregation is calculated. Here, the most energetically stable segregation configuration is found at each segregation concentration.

3. From the tensile test calculations as shown in Figure 7(b), the GB cohesive energy is calculated as the energy difference between solute-segregated GB before fracture and two fracture surfaces after fracture. Here, several different fracture planes are used for tensile test calculations and finally the lowest GB cohesive energy is chosen.

It should be noted here that the important physical quantity for the GB embrittlement may be not the maximum tensile stress but the GB cohesive energy. Many first-principles calculations have been done focusing on the maximum tensile stress. As stated above, however, the maximum tensile stress seems not to have a direct connection to microscopic/macroscopic fracture toughness. This is due to the fact that the microcrack propagation is dominated by the energy balance condition, not by the condition of stress criterion. The stress criterion is considered to be easily satisfied by a very large stress concentration at the sharp microcrack tip in atomistic scale. For this reason, one should be careful to distinguish between the maximum tensile stress that breaks the atomic bond at the microcrack tip and the local fracture stress that appears in the microcrack propagation condition as shown in Figure 7(a). The region on which the latter stress (local fracture stress) is applied is about the whole size of a microcrack.

Figure 7. (a) Schematic illustration for the ideal stress to break atomic bonds at micro crack tip and local fracture stress. (b) Tensile test calculations from first-principles [18]

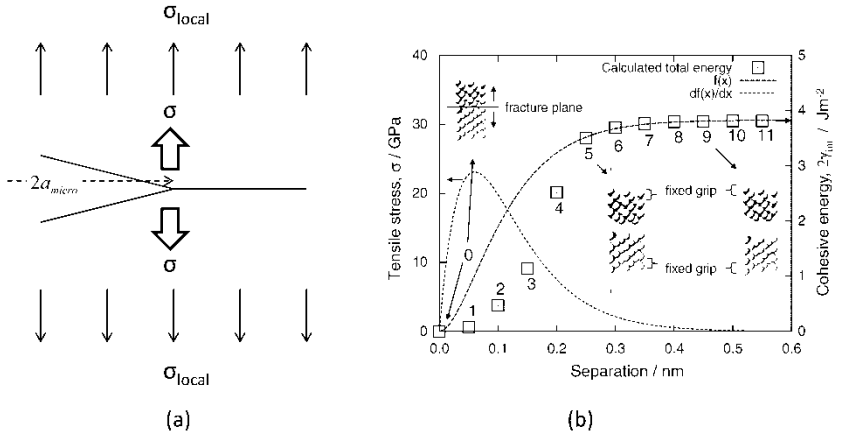

Calculated GB cohesive energy with increasing segregation

In Figure 8, the calculated GB cohesive energy and the maximum tensile stress are shown for each segregation concentration (N_x = 0 to 8) from tensile test calculation. N_x (X=B, C, P, S) is the number of segregated solute atoms within the unit-cell area (A= 0.565 nm^2). In the tensile test calculations, several fracture planes are tested and then the fracture plane that gives the lowest cohesive energy is chosen. In the case of no segregation, the fracture plane between the atomic site 0(1) and site 2 (Figure 6) gives the lowest cohesive energy, 3.8 J/m^2. The maximum tensile stress is about 22 GPa, which is an ideal strength of the iron GB. We can see that the maximum tensile stress is roughly proportional to the cohesive energy.

For the S segregation case, the most likely fracture plane is the plane between the site 0 and site 2 (Figure 6). For the P case, the most likely fracture plane is the plane between site 0 and site 2 for N_P = 1 to 6 and the plane between site 0 and site _2 for N_P = 7 to 8. This indicates that S and P are likely to appear on the fracture surfaces; these behaviours can be understood from the fact that the calculated surface segregation energies of S and P are very large in negative. In addition, the energetic stability of S and P on fracture surfaces are stronger than that at the GB, resulting to decrease the GB cohesive energy with increasing segregation as shown in Figure 8(a)(b).

B and C are also likely to appear on the fracture surfaces after fracture in the tensile test calculations. For the B case, the most likely fracture plane is the plane between the site 0 and site 2(2i). For the C case, the most likely fracture plane is the plane between site 1i and site 2. However, B and C can be more stable energetically at the GB rather than on the fracture surfaces. This leads to the increase of the GB cohesive energy with increasing segregation up to four atoms on the unit-cell area (N_x = 4). More segregation over four atoms is difficult to realize from the consideration of segregation energy (not shown here).

Figure 8. Calculated GB cohesive energy ($2\gamma_{int}$) with increasing segregation, indicated by bars. The solid circles with line indicate the approximate maximum tensile stress that breaks atomic bonds at the crack tip, which corresponds to the ideal strength of grain boundary. (a) S, (b) P, (c) C, (d) B [18]

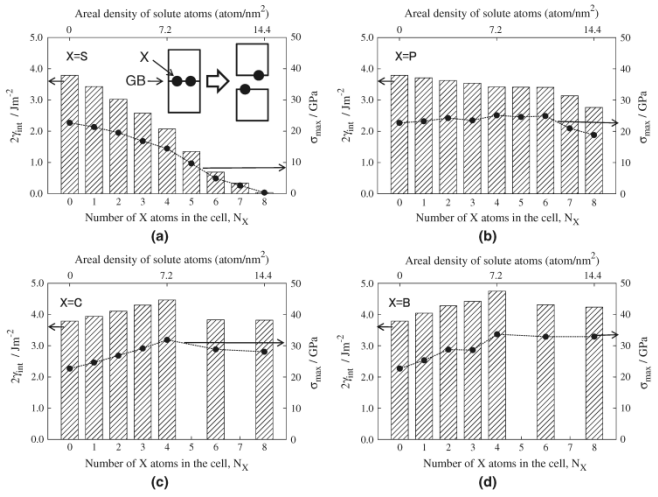

Correlation between GB cohesive energy and DBTT

From Figure 9, it is found that the cohesive energy of the GB decreases for P and S cases (N_x = 0 to 8, X=S, P) and conversely increases for B and C cases with increasing segregation concentration (N_x = 0 to 4, X=B, C). These trends are in agreement with the experimental facts that P and S are embrittling elements, while B and C are toughening elements for iron GBs. The change in the GB cohesive energy with increasing segregation is considered to be correlated with the shift in the DBTT, as described in Figure 5. In order to show such a correlation, the rate of increase/decrease of the calculated GB cohesive energy with increasing segregation is estimated from Figure 9(a). In Figure 9(b), we compare these estimated data with the experimental shift of DBTT with increasing segregation for a high-purity iron [9]. A good correlation between calculations and experiments can be seen. This indicates that the GB cohesive energy plays a key role in the GB embrittlement of metals with solute segregation, as suggested by Rice and Wang [15].

Figure 9. (a) Calculated GB cohesive energy with increasing segregation [19], (b) Comparison between the rates of increase/decrease in the calculated GB cohesive energy with increasing segregation and the experimentally observed DBTT shift with segregation in high-purity iron [18]

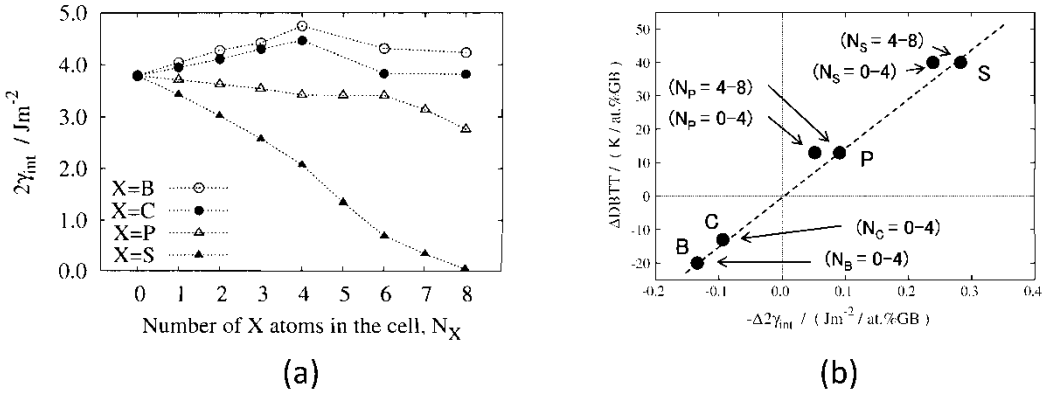

Origin of embrittling/toughening effect of segregated solute

From the above results, it is considered that the difference of energetic stability of solute element between the GB and the fracture surface controls GB embrittlement; the embrittling solute is more energetically stable on the fracture surface than on the GB, while the toughening solute prefers the GB to the fracture surface. The difference of energetic stability is considered to originate from the two factors; the elastic strain energy and the chemical bonding energy of solute element.

The elastic strain energy is induced from the mismatch in atomic radius between solute and metal atoms. This energy has a positive value, which means that solute atom is energetically unstable in the bulk lattice. If the radii of solute and metal are much different, the solute atom is hard to dissolve in metal because of its high strain energy. In this case, the strain energy of the solute can be released at the GB, because the structure of the GB is distorted compared to the bulk lattice. Furthermore, the strain energy is fully released if the solute atom appears on the fracture surface. From this consideration regarding only

the strain energy, all solute elements tend to be more stable on the fracture surface than at the GB, indicating that most elements are easy to become an embrittling solute.

On the other hand, the toughening effect of C can be understood from its chemical bonding effect. Due to the electronic structure of C atoms, they have a strong tendency to have three or four covalent bonds with the surrounding metal atoms. The numbers of surrounding metal atoms around C in BCC Fe are eight in the bulk lattic, and one or two on the fracture surface. This number, called the co-ordination number, can be three or four at the GB because of the distorted structure of GB, which can be the most preferable environment for chemical bonds of C atom. Therefore, C can be a cohesion enhancer of the GB. A similar effect can be expected for B, because the electronic structure of B is close to that of C.

Conclusions

Although the atomistic mechanisms of GB embrittlement of metals by solute segregation are not well understood over many years, recent calculations from first-principles have found that the cohesive energy of a GB may be a key factor controlling the mechanism of GB embrittlement. The author's calculations show that the toughening elements like boron (B) and carbon (C) in iron increase the GB cohesive energy while the embrittling elements like phosphorous (P) and sulphur (S) decrease it. The rate of increase/decrease in the calculated GB cohesive energy is well correlated with the experimentally observed downward/upward shift of ductile-to-brittle transition temperature in a high purity iron.

From the fracture mechanical considerations and first-principles calculations, the correlation between the microscopic GB cohesive energy and the macroscopic mechanical properties (ductile-brittle transition temperature, etc.) can be explained. It is considered that the GB cohesive energy has a valve-like effect on the much larger macroscopic fracture energy. However, the atomistic modelling on this correlation is still missing. In addition, the irradiation effect on the segregation and the resulting embrittlement is also not clear. Further studies are necessary to understand GB embrittlement from a multiscale point of view.

(Note added in proof) Based on the author's idea shown in this chapter, the combined analysis with fracture mechanics experiments and first-principles calculations for an alloy steel were performed in a recent literature [Yamaguchi, 2014].

References

[1] [Chen, 2010] H. -P. Chen, R. K. Kalia, E. Kaxiras, G. Lu, A. Nakano, K. -i. Nomura, A. C. T van Duin, P. Vashishta, Z. Yuan, Phys. Rev. Lett. 104(2010)155502.

[2] [Crampin, 1989] S. Crampin, D. D. Vvedensky, J. M. MacLaren, M. E. Eberhart, Phys. Rev. B40(1989)3413.

[3] [Duscher, 2004] G. Duscher, M. F. Chisholm, U. Alber, M. Ruehle, Nature Mater. 3(2004)621.

[4] [Hashimoto, 1984] M. Hashimoto, Y. Ishida, S. Wakayama, R. Yamamoto, M. Doyama, and T. Fujiwara, Acta Metall. 32(1984)13.

[5] [Jokl, 1980] M. L. Jokl, V. Vitek, and C.J. McMahon, Jr., Acta Metall., 28(1980)1479.

[6] [Kalderon, 1972] D. Kalderon, Proc. Instn Mech. Engrs., 186(1972)341.

[7] [Kameda, 1980] J. Kameda and C. J. McMahon, Jr., Metall. Trans. A, 11(1980)91.

[8] [Kameda, 1981] J. Kameda, Metall. Trans. A, 12(1981)2039.

[9] [Kimura, 1993] H. Kimura, J. ISIJ, 79(1993)N754. (in Japanese)

[10] [Losch, 1979] W. Losch, Acta Metall. 27(1979)1885-1892.

[11] [Messmer, 1982] R. P. Messmer, and C. L. Briant, Acta Metall. 30(1982)457.

[12] [McLean, 1957] D. McLean, Grain Boundary in Metals, Oxford Univ. Press, 1957.

[13] [Ogura, 1984] T. Ogura, and C. J. McMahon, Jr., Metal Sci. 18(1984)37.

[14] [Painter, 1987] G. S. Painter, and F. W. Averill, Phys. Rev. Lett. 58(1987)234.

[15] [Rice, 1989] J. R. Rice, and J.-S. Wang, Mater. Sci. Eng., A107(1989)23.

[16] [Seah, 2000] M.P. Seah, AES in Metallurgy, in Practical Surface Analysis (Second Edition), John Wiley & Sons Ltd., 1990, 311-356.

[17] [Wu, 1994] R. Wu, A. J. Freeman, and G. B. Olson, Science 265(1994)376.

[18] [Yamaguchi, 2011] M. Yamaguchi, Metall. Trans. A, 42(2011)319.

[19] [Yamaguchi, 2011,a] M. Yamaguchi, ISIJ 15(2010)755.

[20] [Yamaguchi, 2014] M. Yamaguchi, J. Kameda, Phil. Mag. 94(2014)21.

Chapter 11.

Irradiation assisted stress corrosion cracking

C. Pokor[1], **A. Herbelin**[1], **T. Couvant**[1], **Y. Kaji**[2]
[1]EDF-R&D, France
[2]JAEA, Japan

Abstract

Internal components of PWR vessels closest to the core (core barrel, baffle plates, formers, bolts, etc.) are exposed to a high neutron flux; the most highly irradiated zones of some of these components may be exposed to doses reaching about 80 dpa after 40 years of operation and 120 dpa after 60 years. This neutron irradiation changes their microstructure and their mechanical properties: hardening, loss of ductility, loss of toughness, irradiation creep, etc. Furthermore, these variations appear to cause sensitivity to stress corrosion (irradiation assisted stress corrosion cracking- IASCC) which led to cracking of some baffle-former bolts. The purpose of this document is to summarise acquired knowledge about Irradiation Assisted Stress Corrosion Cracking of austenitic stainless steels under neutron irradiation.

Introduction

Irradiation Assisted Stress Corrosion Cracking (IASCC) is the term used to describe the intergranular cracking, with little or no sign of ductility, which can occur in the irradiated structure components of nuclear power plants. In the case of PWR power plants, cases of baffle bolt cracking are proven for the French CP0 type units and this type of cracking remains potentially damaging for the other PWR type. Ultrasonic inspections of the baffle bolts are performed periodically on all of the CP0 type units and on a sample of units of the other type.

In a first part, the characteristics of cracking by IASCC encountered in power plants are discussed. Then the main experimental programmes concerning IASCC are described. A review of the IASCC mechanisms as well as the main influencing factors is done in order to propose an IASCC sensitivity criterion in the next part.

Definition of IASCC

IASCC is a particular case of Stress Corrosion that may affect the materials exposed to a neutron flux. IASCC is a mechanism that can explain the intergranular characteristics of cracking seen on site and that can be reproduced in the laboratory. This is a complex phenomenon needing different parameters to occur: operating parameters (temperatures, stresses, etc.), the environment (chemistry, etc.) and the properties of the materials, with each of these elements experiencing changes under irradiation. A schematic diagram is proposed in Figure 1. In this figure, the three central circles are the factors traditionally necessary for stress corrosion sensitivity: the encountering of a material, an environment and a stress under particular conditions. In the case of IASCC, the outer circle represents the additional modifications by irradiation necessary of these factors.

Figure 1. Diagram illustrating the different parameters necessary for IASCC

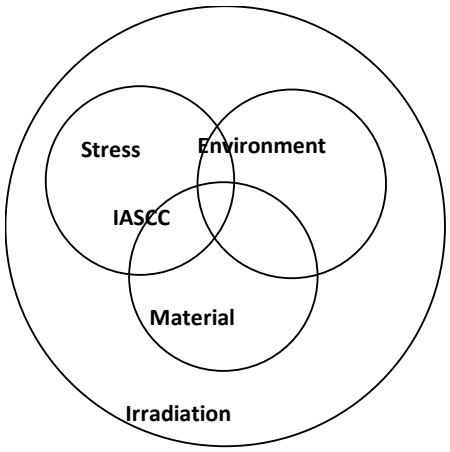

Figure 2. Representation of possible crack tip interactions during IASCC propagation [8]

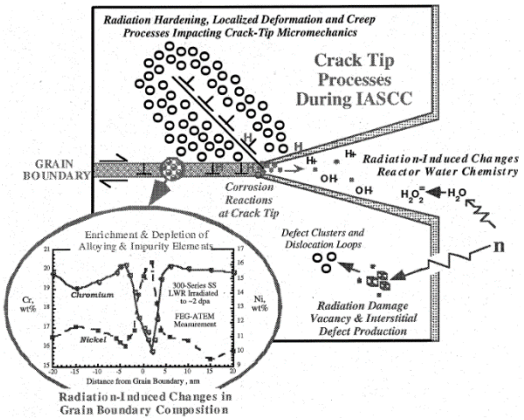

Reports on IASCC [69,78] describe the knowledge concerning cases of cracking by IASCC on site and for the laboratory tests. These summaries show the limited number of experiments with well-controlled test conditions conducted on well-characterised materials. No mechanism model is yet able to justify all cases of cracking, and the fine microstructural changes produced by irradiation that would control IASCC still remain partially unknown. In particular, the mechanisms for interaction between the environment and the material at the tip of the crack remain to be determined (Figure 2).

The reproduction of crack cases in the laboratory on materials irradiated in a reactor indicates that the persistent effects of irradiation on the materials (change in microstructure) are very important for IASCC sensitivity, although specific effects of irradiation simultaneous with oxidation and load can also have a role in cracking in operation.

IASCC phenomenology

IASCC causes the intergranular (IG) cracking of stainless steel (SS) core components exposed to high-energy neutron flux and primary water environment (Figure 3). The cracking is similar to IG in-service cracking observed in the SCC of non-irradiated strain-hardened material [18], adding irradiation effects to the susceptible material conditions.

Figure 3. Cracked baffle-former bolt 316 SS from Tihange-1, after 17 cycles irradiated to 8.5 dpa [75]

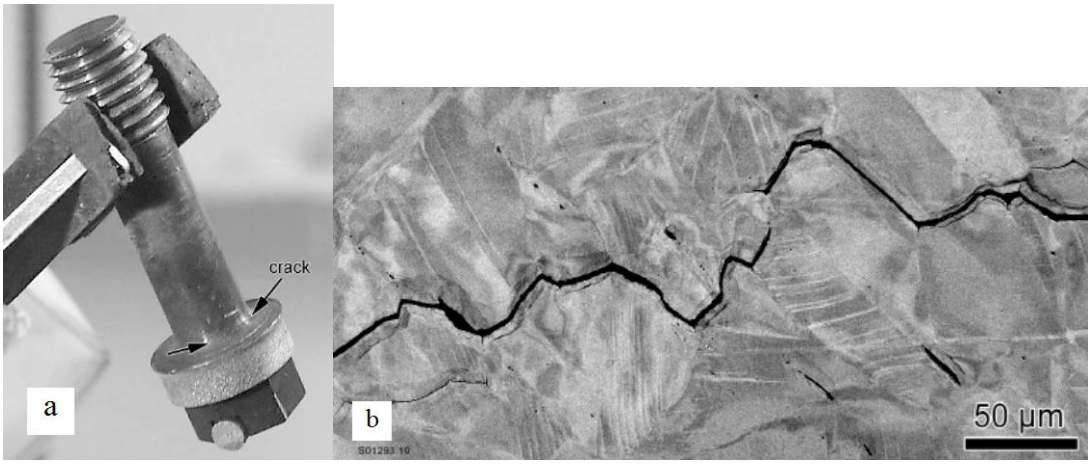

Crack initiating at the bolt-head/shank junction. SEM micrograph showing the IG crack and the deformation microstructure.

The main components affected by IASCC in EDF PWRs are baffle-former bolts; these bolts make the link between the baffles close to the outermost fuel rods, and the formers, maintaining the baffles and fixing them on the core barrel (Figure 4).

The baffle-former bolts are made of AISI 316 austenitic stainless steel (Table 1). The bolts are machined in forged bars, so they have already undergone extensive cold work and as such have attained a significant hardness (typically 240 HV). They are also submitted to high stresses during the various stages of the cycles. Finally their position in the core exposes them to significant radiations without shielding from other components: their heads are submitted to the majority of the radiation dose. The relative thickness being higher due to the assembling, γ radiations induce a substantial temperature increase, raising the local stresses and changing the material reaction to neutron irradiation.

Table 1. Composition ranges for AISI 316 and the available AISI316L SS (W%)

Grade		C	Mn	Si	P	S	Cr	Mo	Ni	N
316	Min	-	-	-	0	-	16.0	2.00	10.0	-
	Max	0.08	2.0	0.75	0.045	0.03	18.0	3.00	14.0	0.10
316L	Min	-	-	-	-	-	16.0	2.00	10.0	-
	Max	0.03	2.0	0.75	0.045	0.03	18.0	3.00	14.0	0.10

Figure 4. Baffle-former bolts location in the core

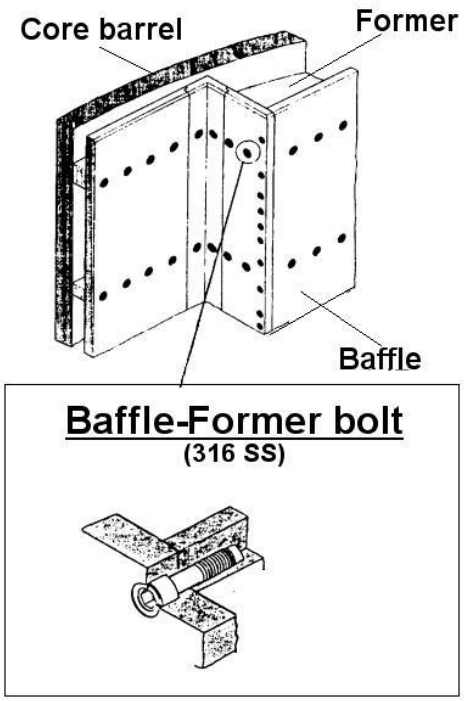

The first cracked bolts were revealed in 1988 in Bugey Unit 2 (PWR, France), during ultrasonic investigations (UT) in the baffle plates involved at that time in a water flow issue. After this discovery, several bolts were extracted for further evaluations [13,36,55,61,64] and a periodic inspection and replacements programme was set up in the affected reactor types. This regular assessment of the damage affecting the bolts revealed that significant differences in cracking behaviour exist between the various reactors. For instance, taking into account the number of cracked bolts, Bugey Unit 2 (100 bolts in 140 000 hrs) and Fessenheim Unit 2 (46 bolts in 140 000 hrs) are the most affected reactors (mostly under 30 for the rest of the reactors); additionally, their bolts are made from the same process, pointing towards the influence of initial composition and microstructure.

Based on these data, studies were conducted in order to correlate the location of the cracked bolts and the time to initiation to the corresponding operating parameters of the reactors. The main conclusions of this work are:

- Results of the periodic inspections:
  - Cracked bolts are very localised; 96% are located in the four inferior forming plates. This points out that particular conditions are needed to initiate IASCC mechanism.
  - Inspection data analysis seems to indicate that a threshold dose can be defined for IASCC cracking, slightly above 4 dpa.
  - Significant differences in cracking behaviour exist between the various reactors. For instance, Bugey 2 and Fessenheim 2, that have bolts made from the same heat, are the most affected ones.
  - Cracks propagate relatively fast; a bolt detected with a UT indication during an inspection is detected cracked at the next inspection, resulting in an average crack growth rate of $3\ 10^{-10}$ m/s.
- Evaluation of the influence of the operating conditions:
  - Neutron flux appears to have an influence on crack initiation: bolts exposed to higher flux, and thus reaching higher damage doses, crack earlier.
  - Using a simple calculation method on the case of the four inferior former plates, a correlation between the evaluated stress and the number of cracked bolts seems to stand out.
  - Time to initiation appears to be related to temperature by an Arrhenius type law (only in the case of the four inferior former plates).
- Characteristics of the bolts:
  - Cracks initiate on the bolt-head/shank junction and tend to propagate towards the head. The cracks are clearly intergranular.
  - Cracked bolts do not show any anomaly of chemical composition and mechanical properties compared to unaffected bolts.

- The microstructures of bolts irradiated in the same conditions, cracked or unaffected, do not differ. No specific phase precipitation was detected in the cracked bolts.
- No substantial deformation or mechanical damage due to the handling was observed on the bolts heads.

This study, based on an empirical approach, gives qualitative elements regarding the cracking of the bolts. The individual influence of each parameter (material, temperature, stress or irradiation flux) is difficult to quantify and experimental data with well-controlled testing conditions are needed to confirm the pointed-out tendencies.

Experimental programmes

There are three major categories of tests for studying IASCC: tests in pile, tests after irradiation, and tests on non-irradiated materials having undergone treatments to reproduce some effects of irradiation. The first tests require very complex equipment, are very expensive, and consequently do not allow parametric studies. Tests after irradiation rely on the assumption that the permanent effects of irradiation are mainly responsible for IASCC sensitivity. These tests are also difficult to implement because of the high activity of irradiated materials, but they constitute the biggest part of the available tests. The third category of tests is made up of experiments simulating irradiation by using other particles (protons or ions) or using cold working or heat treatments. The difficulty remains in demonstrating the representativity of this treatment in relation to neutron irradiation.

There is no unique indicator for IASCC sensitivity. The different indicators vary according to the laboratory and the type of test used (Table 2). Stress corrosion tests on irradiated materials for the study of IASCC mainly belong to three categories: initiation tests with load or displacement imposed on smooth specimens, propagation tests with load imposed on notched specimens and tests with imposed displacement rate (initiation and propagation). The choice of test types and their conditions are of great importance as part of the explanations of the slow progress in IASCC knowledge comes from the lack of well-defined data from tests on irradiated specimens well-characterised under well-determined conditions. The use of complementary tests based on load is a bearing resource in this lack of data (for example, complementary constant load tests [42] and imposed displacement [43]. The different characteristics of these tests are reviewed:

- Static initiation tests on smooth specimens.

Constant load tests use tensile specimens (flat or cylindrical) or annular specimens (O ring tests). These tests make it possible to obtain time to failure curves based on the stress. Time to failure is a measurement of IASCC sensitivity. Time to failure includes both the time necessary for the true initiation of the crack and the time necessary for its slow then fast propagation. It is also possible to determine a minimum stress in order to obtain the cracking for a given type of environment. Imposed displacement tests allowing for the relaxation of stresses during the propagation of a crack and accordingly its arrest can be used to characterise the behaviour of a material for stress cracking. This type of test is not used very much for the study of IASCC, undoubtedly because of the possible long test durations.

- Static tests of propagation on notched specimens.

For these tests, a constant load or a fixed crack opening is imposed on a pre-notched sample, most often a CT (Compact Tension) type, used for fracture toughness tests. Crack length is measured based on the time, thus allowing for the expression of a crack propagation rate based on the stress intensity factor. IASCC sensitivity is then expressed based on the propagation rate of the crack for a given environment. With this type of test, no information is collected on the crack's initiation. These tests make ipossible to have the behaviour of a material under different conditions (temperature, environment, intensity factory) during a single test. Note that electrical monitoring of the crack's development does not give an absolute value of the propagation and that some adjustments, sometimes significant, are necessary in order to cross-check with the true propagation of the crack, known once the test is over.

- Slow Strain Rate tests.

For slow strain rate tests in the environment, the load rates traditionally used are of the order of magnitude of 1.10^{-7} s^{-1}. The strain rate test results are interpreted in terms of a percentage of the fractographic aspect of the fracture surface presenting an intergranular character or in terms of change in the ductility in comparison with tests in an inert environment. Strain rate test are severe tests, since stress and cold working increase during the test. This test makes possible a quick comparison of the stress corrosion sensitivity among different pre-irradiated materials. The use of these results to measure the lifetime of a component is difficult.

It is also possible to use swelling mandrels [35]. Under flux, the B4C mandrels swell, thus imposing a deformation. The time to crack is then measured as an IASCC sensitivity criterion. In order to use the information of these tests, it is necessary to attain the development of stress in the tube being tested through complex modelling [31,32].

Table 2. IASCC sensitivity criteria and types of tests used

Criterion	Test type
% Intergranular on the fracture surface	Slow strain rate (SSRT slow strain rate test or CERT constant elongation rate test)
Distributed elongation	Slow strain rate (SSRT)
Time to fracture	Constant load, O ring
Time to cracking	Swelling mandrels
Propagation rate	Measurement of crack growth rate (CGR)

Main elements of the IASCC mechanism

In the absence of knowledge of a chaining of well-defined elementary events leading to cracking by IASCC, accepted by the international community, it is important to first describe and discuss the main elements of the IASCC mechanism. A diagram showing the interactions of the different mechanisms described in the rest of the chapter is provided (Figure 5). At a second stage, these elements will be connected with the different parameters of the triptych of the material/stress/environment IASCC.

Figure 5. Interaction of the different possible mechanisms leading to IASCC

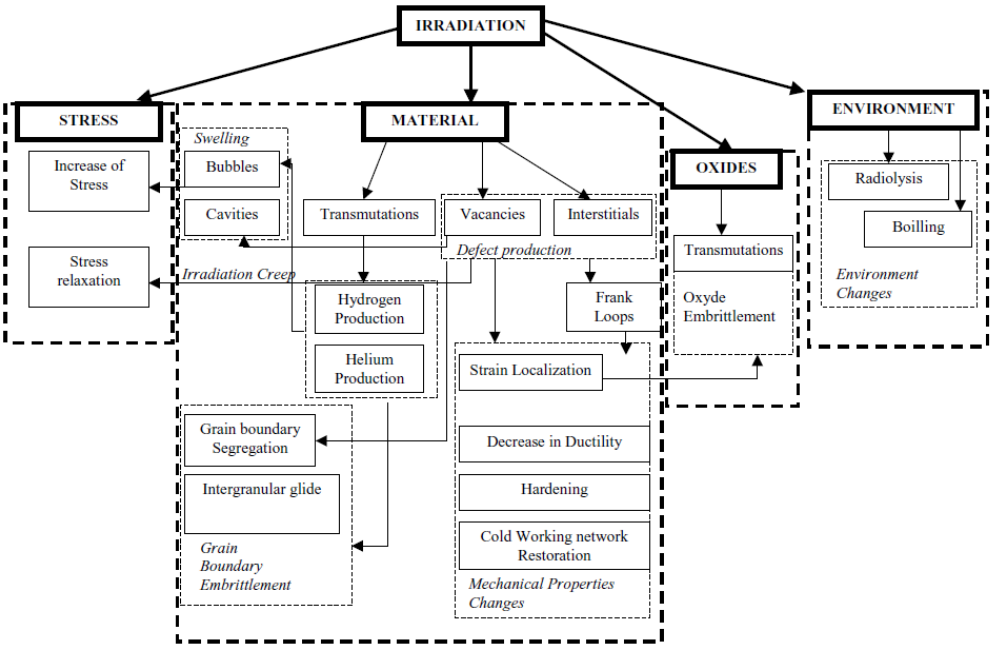

Water radiolysis

Primary water absorbs ionising radiations produced by nuclear reactions (neutrons, γ rays); these interactions induce dissociation reactions of the water: H_2O ◊ H_2, H_2O_2, e^-_{aq}, H, OH, H^+. These products interact in series of low activation energies reactions; thus, only H_2, H_2O_2 and O_2 formed by these interactions remain in the water. The stability of water regarding these interactions increases with increasing temperature, so yields of reaction product (H_2, H_2O_2 and O_2) are accordingly reduced.

Radiolysis has an effect in boiling water reactors (BWR), where it raises oxygen concentration (up to 200 ppm). Formation of oxidising species in higher concentrations under irradiation increases the electrochemical corrosion potential. The potential controls the kinetics of corrosion reactions; therefore the effect is an increase of SCC rate (Figure 6). However, in PWRs and specific BWRs operating under Hydrogenated Water Chemistry (HWC) the dissolved hydrogen suppresses the radiolytic dissociation [69]. As a result, shown in Figure 7, concentrations in oxidising species are greatly reduced and no increase of the corrosion potential is expected.

Figure 6. Shift in corrosion potential due to irradiation (BWR, 304 SS) [69]

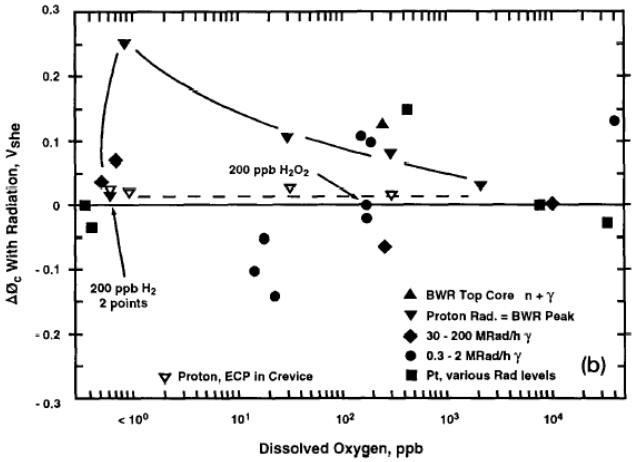

Figure 7. Steady state concentrations of several radiolysis products in PWRs versus the initial hydrogen concentration [69]

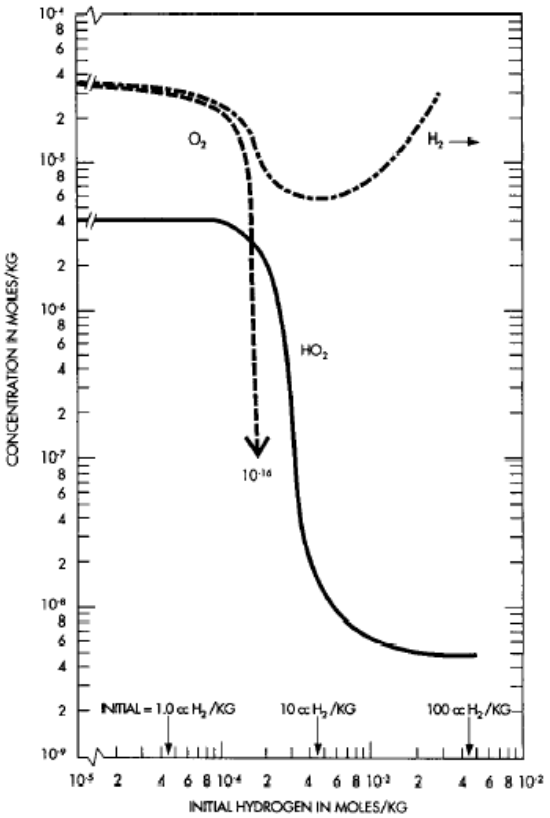

Local chemistry modifications

Radiolysis is suppressed in HWC when nominal conditions are considered. There are situations in which ionising radiation could lead to a local change in the water chemistry, and thus influence corrosion:

- Local boiling: γ radiations are a by-product of the fission reaction and can lead to an increase in temperature in exposed material; some components can undergo a temperature increase locally due to their design and induce water boiling on their surface. Boiling could modify local concentrations in boric acid and lithium hydroxide and cause an increase in pH. Temperature calculations have estimated the temperature at 360°C in baffle-former bolt heads: in this case, a local boiling cannot be dismissed. However, evidence of local boiling in cracked components is yet to be demonstrated, either at the surface or in the cracks.
- Occluded environment: there are areas in the reactor design where the water flow is not present or at a too low level to insure exchange with the nominal primary water. In these areas, the water chemistry could develop under the effects of corrosion reactions with the surrounding components and by radiolytic dissociation due to irradiation, possibly further enhancing corrosion or causing different phenomena to operate. The design of the components has been adapted - namely in the case of baffle-former bolts - to avoid such confined environments to appear. Moreover, IASCC occurrence does not seem to require occluded conditions, as cracking is still observed in baffle-former bolts after the modifications and in other components.

Figure 8. Local boiling in an enclosed space due to γ heating in the bulk of the material

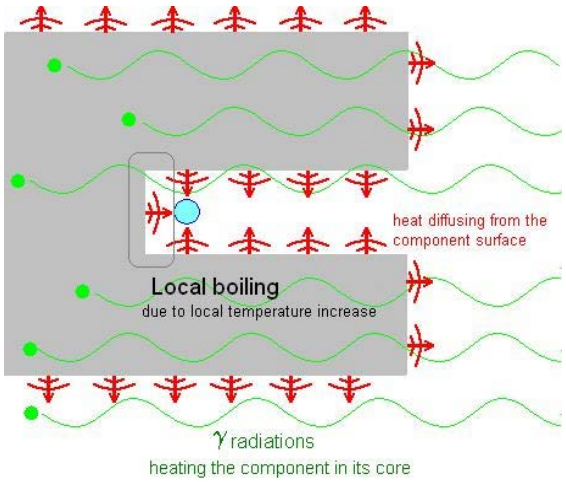

Figure 9. Example of a possible occluded area under the bolt head, inducing a change in the local chemistry

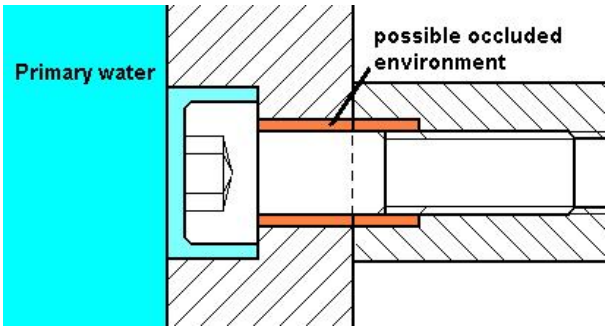

The issue of local chemical modifications only involves the CP0 type, for which there is a confined environment in the thread of the bolts. From the CPY type, this confined environment was removed for most of the baffle/former bolts. The fluid flow calculations show good flow in the CPY type bolts [68]. Beyond these theoretical considerations, not much is known about the local chemistry of the primary fluid in the bolts.

Radiation Induced Segregation (RIS)

An important consequence of neutron irradiation is the redistribution of alloy elements and impurities in the material.

By analogy with the stress corrosion phenomena of the thermally sensitised steels, the search for a link between the evolution of the compositions of the grain boundaries and the IASCC sensitivity was checked in numerous studies [7,80]. A study was conducted as part of the CIR programme [19]. This involves a statistical analysis of a large set of cracking data. This analysis tends to show that dechromisation of the boundaries makes it possible to explain the cases of cracking observed in the BWR-NWC (normal water chemistry conditions oxygenated) environment but is not enough to explain the cases of cracking in the BWR-HWC (hydrogenated) environment or PWR environment.

From an experimental standpoint, the role of dechromisation on IASCC sensitivity does not have a consensus: corrosion tests on 304 steel sensitised by thermal treatment confirm that there would be no corrosion in the hydrogenated environment [3], but materials with a chemical composition identical to the composition of the grain boundaries after segregation appear sensitive to stress corrosion in the primary environment even in the absence of irradiation [81].

In the case of BWRs, the development of the chemical composition of the grain boundaries could be linked to IASCC sensitivity in several cases [44,50]. In the case of PWRs, the situation is less clear. Post-irradiation annealing experiments made it possible to vary hardness through suppression of the irradiation defects while maintaining segregation with the grain boundaries [79]. In the studied cases, IASCC sensitivity decreases like hardness, while segregation does not develop (Figure 10).

These measurements, which remain qualitative, show that in the PWR environment, segregation with the grain boundaries is probably not the principal cause of sensitivity to intergranular cracking. Thus, Figure 11 illustrates the scattering that can exist between the chromium measurements in the grain boundaries and the IASCC sensitivity. However, these modifications of the grain boundary composition can only amplify the difference of behavior between the grain and the boundary and contribute to increase the grain boundary's load. In addition, the effect of segregation at the grain boundaries could become significant for high doses, which could explain the increase in IASCC sensitivity with the dose even if the mechanical properties no longer change with irradiation after a certain dose.

Figure 10. Variation of segregation induced by irradiation, density of dislocations, and hardness based function of the annealing measured by the diffusion distance of the iron $(D_{Fe}t)^{1/2}$, for different annealing conditions [79]

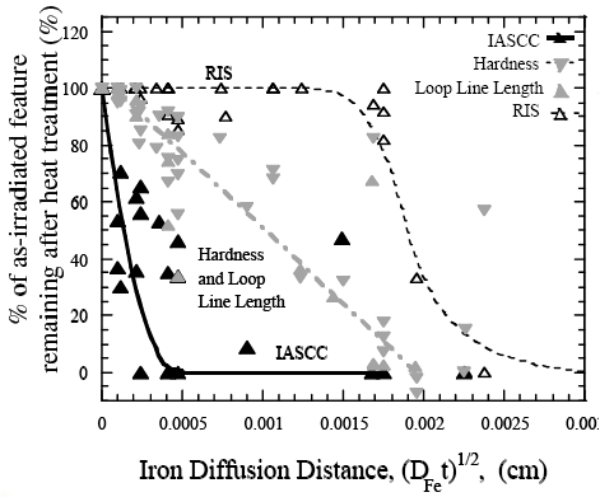

Figure 11. IASCC sensitivity measured by the percentage of intergranular rupture on a slow strain rate specimen feature in the environment based on the minimum rate of Cr in the grain boundaries measured by AES and FEG AAEM on power plant components [14]

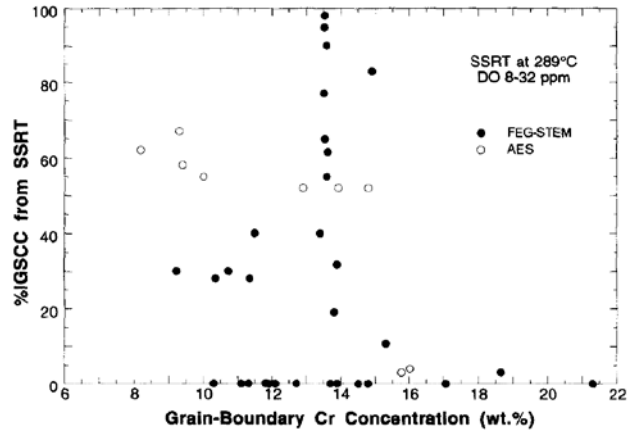

Microstructures and hardening induced by irradiation

During irradiation, high-energy neutrons create cascade displacements that lead to the formation of two types of point defects: vacancies and interstitials. In the range of power plant operating temperature, these point defects can develop: they are recombined, annihilated, and agglomerated on defect clusters already existing. These movements result in a modification of the microstructure and the creation of new microstructural objects of the dislocation loops (interstitial loops, Frank loops) faulted, sessile (not susceptible to sliding), created by recombination of interstitials. The development of the density is asymptotic with saturation between 10 and 15 dpa.

The created defects cause great hardening of the material. The yield stress and the ultimate tensile strength increase quickly and become very close, near 800 to 1000 MPa according to the steel and the irradiation temperature. Irradiation also results in a loss of ductility with very high degradation of the uniform and total elongations.

In the PWR reactors, hardening under irradiation by contributing to a significant load of the grain boundary is generally considered an important element of IASCC sensitivity. By analogy with other stress corrosion phenomena, work has been done to correlate the hardening of the material with IASCC sensitivity, mainly in the case of BWR power plants [27]. In the absence of irradiation, it is possible to correlate the stress corrosion sensitivity (measured by the crack propagation rate) with the yield stress.

As a part of the CIR programme (Cooperative IASCC Research), the statistical analysis of a large database of available test results was pursued in order to determine the influence of hardening on the cracking sensitivity [20]. In the conclusion of this study, it seems that the dose parameter constitutes a better indicator of stress corrosion sensitivity than the hardening parameter. A yield stress greater than 600 MPa is generally required so that the material becomes sensitive to intergranular cracking. Hardening is undoubtedly a necessary condition for the sensitisation of steel, but it is not sufficient to explain the behaviour in the PWR environment of these steels. In fact, all of the attempts at simulating hardening under irradiation by cold working, or thermal treatments resulting in hardness similar to that of irradiated materials, do not make it possible to reproduce their behaviour in the PWR environment satisfactorily. The mechanisms for hardening under irradiation and by cold working are very different.

In addition, IASCC sensitivity continues to increase with the dose of irradiation, while the hardening saturate towards 10 dpa, revealing the effect of other secondary mechanisms, possibly like segregation at the grain boundaries or on the dislocation loops, or even additional embrittlement by helium or hydrogen.

Strain localisation

In addition to the increase in yield stress, irradiation hardened SS undergoes a strong loss of ductility, as shown in Figure 12. The irradiation-induced microstructure greatly affects the mechanical behaviour: the hardening induces alternative deformation modes, in addition to the already complex behaviour of austenitic stainless steels related to their low stacking fault energy (SFE).

Figure 12. Stress-strain after tensile testing at 330°C curves for 304 SS irradiated to doses ranging from 0 to 3.4 dpa [62-64]

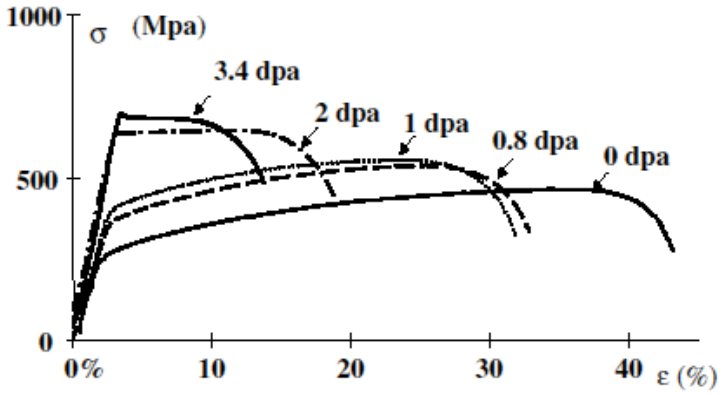

Therefore, in addition to the tangled dislocations, dislocation pileups, stacking faults and twins, the presence of the Frank loops can induce channelling as an additional deformation mode, as seen in Figure 13. This mechanism occurs as the Frank loops impeding the movement of dislocations are locally disposed to stop a sufficient number of gliding dislocations (i.e. are able to induce a sufficient stress, by their impeding process). Under the stress loading, the moving dislocations can glide through the Frank loop, forming a channel and clearing it from the Frank loop: the "clear band" formed is therefore the stage of preferential deformation, drastically decreasing the ductility by reducing the deformation accepted by the total matrix to a limited number of clear bands.

Each of the deformation mechanisms depends on the mechanical and dose conditions. A local situation strongly impeding movement has a stronger chance of inducing a localised deformation mode, should the higher stress requirement be met. Figure 14 shows a map synthesising the results of tests and observations [11]. However, in the dose domains relevant to IASCC (>3 dpa), only channelling and twinning seem dominant in 316 SS, and both result in the formation of a zone cleared from Frank loops.

Another observation indicating the influence of localised deformation on GBs: intergranular cracking has been reported in an inert environment on highly irradiated steel: 304 SS, 1.2×10^{20} n/cm², 290°C, 3.5×10^{-7} s^{-1} SSRT [57] and 304 SS, 30 dpa, 340°C, 700 MPa constant load [76]. Both indicated on the intergranular fracture zones the presence of linear features, identified by TEM as twins and channels (Figure 15). It is additionally reported [57] that lower- and unirradiated samples tested under the same conditions fractured in a ductile manner and showed no signs of localised deformation. Moreover, a potential effect of strain rate has been reported [76] in view of the various tests performed under various conditions. The results are reported on a schematic Strain-rate - Temperature map (Figure 16) indicating fracture morphology: IG fracture seems to occur under the lowest (constant load), indifferently at room and lower temperatures (100% IG in tensile and impact tests) and under the effect of PWR environment; complete dimple fracture occurred in the tensile tested sample at 300°C (moderate strain-rate, high temperature).

Figure 13. TEM observations in 316 SS after irradiation and deformation at room temperature [11] (a) Dislocation tangles in unirradiated material after 10% bend deformation. (b) Stacking faults in 0.15 dpa irradiated material after 10% bend deformation. (c) Channels (clear bands) and twins (in dark) in 0.15 dpa irradiated material after 10% tensile deformation. (d) Twins in 15 dpa irradiated material after 10% bend deformation

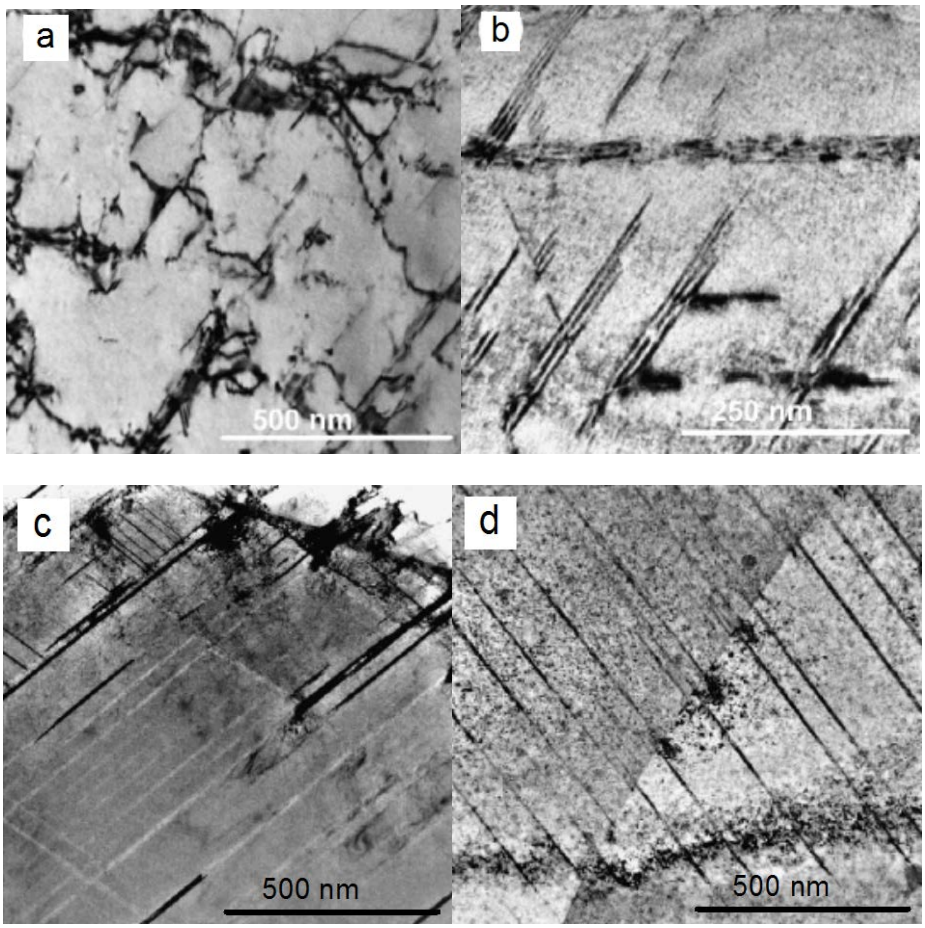

Figure 14. A deformation map of 316 SS in the true stress–dose space [11]

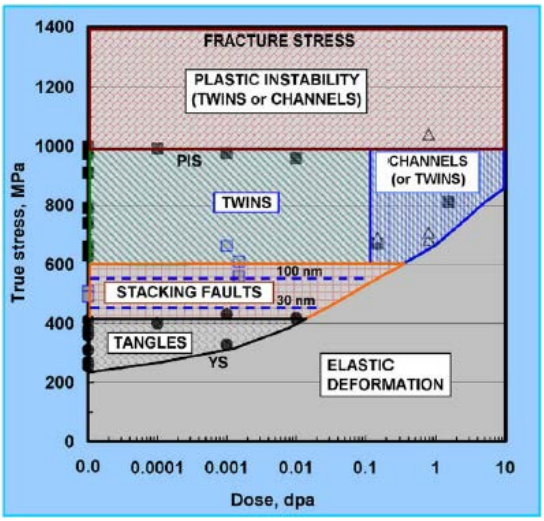

Figure 15. SEM observation of the intergranular fracture zone, on the constant-loaded specimen at 340°C in Argon atmosphere [76]

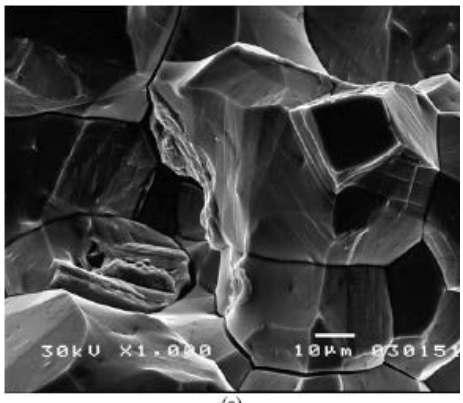

(a)

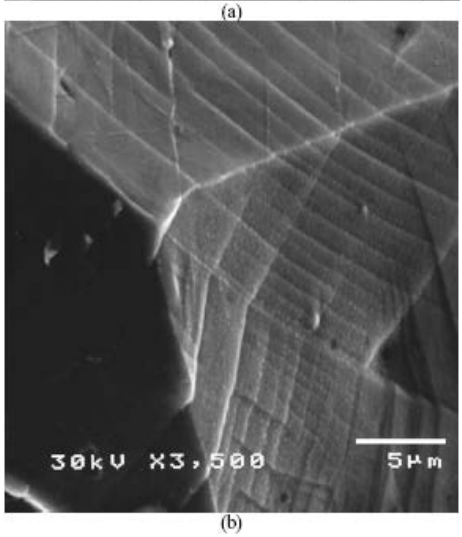

(b)

Figure 16. A schematic map of strain rate - temperature - fracture morphology dependencies [76]

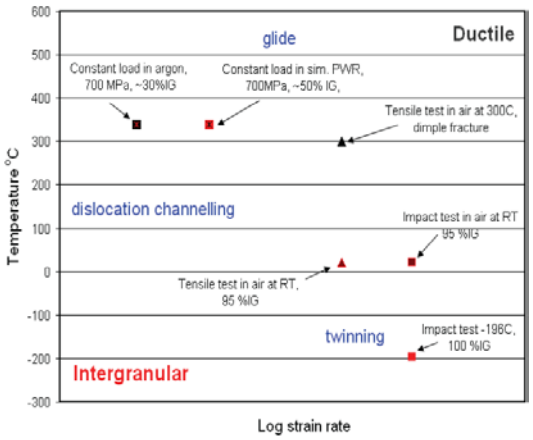

The influence of localised deformation mode on IASCC would be an increase in local stress concentration on grain boundaries. As seen in crack-tip observations, the various shear bands intersecting cracked boundaries (mainly twins) create steps on the interface and show a minor preferential corrosion attack (Figure 17). This means the corrosion occurred after the deformation and suggests that the presence of steps promoted the oxide penetration across the boundary.

Figure 17. Schematic diagram of the interaction between positioned deformation bands and rupture of the oxide film

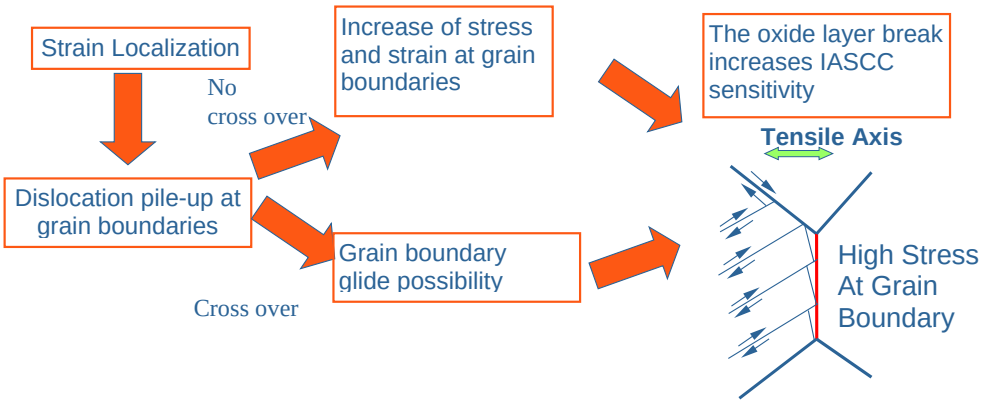

Helium and hydrogen

In operation, different mechanisms may result in the presence of hydrogen and helium in the austenitic steels of the pressure vessel internals. The major source of helium for high doses comes from the transmutation of nickel, and its rate of production is proportional to the nickel composition. The production of helium from the boron occurs quickly and also saturates quickly based on the thermal neutron flux. The hydrogen coming from transmutation of the nickel depends on the composition in this element and the ratio of thermal neutrons and fast neutrons [37]. The hydrogen also comes from environmental sources, particularly in the PWR environment because of the excess hydrogen pressure.

The hydrogen's mobility is elevated at the temperatures of the PWRs. Also the amount of hydrogen that actually remains in the steel is difficult to estimate, as it depends on the effectiveness of the trapping, particularly through the defects created under irradiation (bubbles, dislocations, possible martensitic phase created under deformation, etc.). The hydrogen and helium measurements in the irradiated austenitic steels are difficult and the existing data are scattered. Nevertheless, recent results [30] show that the hydrogen concentration in the steels can be much greater than predicted by the balances with the partial hydrogen pressures in the environment (Sievert's law). The hydrogen can be stored in the cavities and bubbles that form under irradiation.

Under some conditions, the hydrogen can have an embrittling effect which could contribute to a possible stress corrosion mechanism (embrittlement by hydrogen is encountered particularly in martensitic steels; in the case of austenitic steels, this embrittlement could occur if martensite created by deformation appears). This effect is significant primarily at low temperatures for austenitic steels (less than 100°C). Cracking associated with embrittlement by hydrogen would only be encountered during reactor shutdowns. However, it is less likely that the cracking of bolts will occur at this time because of the lack of stress. To date, considering the little experimental work on the topic, there are few objective elements making it possible to accuse embrittlement by hydrogen of being an operating mechanism of IASCC in PWRs.

With the difference of the phenomena of segregation under flux, hydrogen and helium production is linked to the irradiation spectrum (Figure 18). Also, a method for studying the effect of these elements constituted a comparison of the IASCC sensitivity of irradiated materials in the fast spectrum reactor (fast breeder reactor, low production of helium and hydrogen) and in the light water reactor (PWR, BWR, high production of helium and hydrogen).

The summary of available studies seems to suggest two stages of spectrum sensitivity:

- For low doses (< 10 dpa), the Slow Strain rate tests in the environment of material testing reactor specimens do not show any different behaviour between the specimens with high or low rates of hydrogen and helium, the other conditions (temperature, materials, flux) being equal (Figure 19).
- For higher doses (> 10 dpa), several elements seem to indicate a higher IASCC sensitivity of irradiated materials in the mixed spectrum compared to the fast spectrum. First, tests on materials irradiated in the reactor then loaded with hydrogen make it possible to show a possible influence of hydrogen, particularly for crack initiation. The IASCC sensitivity measured by the percentage of intergranular fracture surface after Slow Strain rate tests in the environment is highly decreased for materials irradiated with fast spectrum conditions (Figure 20). This difference in behavior is attributed to the presence of bubbles at the grain boundaries appearing for doses higher than 40 dpa [26].

The presence of bubbles can be due to the boron, an element present in the form of impurities, preferentially located in the grain boundaries. Under flux, transmutation of boron into helium is possible and can lead to an accumulation of helium in the grain boundary. This hypothesis remains to be validated, particularly because the significant recoil energy could disperse the helium atoms far from the grain boundaries.

This difference in behaviour between materials coming from different reactors is found in the results of tests on O-ring specimens conducted by Westinghouse on irradiated materials in PWR (Thimble tube) and in the BOR 60 fast neutron reactor. For the same test conditions, all of the specimens coming from the Thimble tube crack, and those coming from the BOR 60 reactor do not.

The role of hydrogen and helium on IASCC sensitivity could explain the increase in IASCC sensitivity after the apparent saturation of the mechanical properties [16] beyond 65 dpa [25,72].

Figure 18. Relationship between the dose and the hydrogen and helium contained in the materials for irradiation conditions in the PWR reactor and fast breeder reactor (the graphic's references are: "this study" [11,25,26]

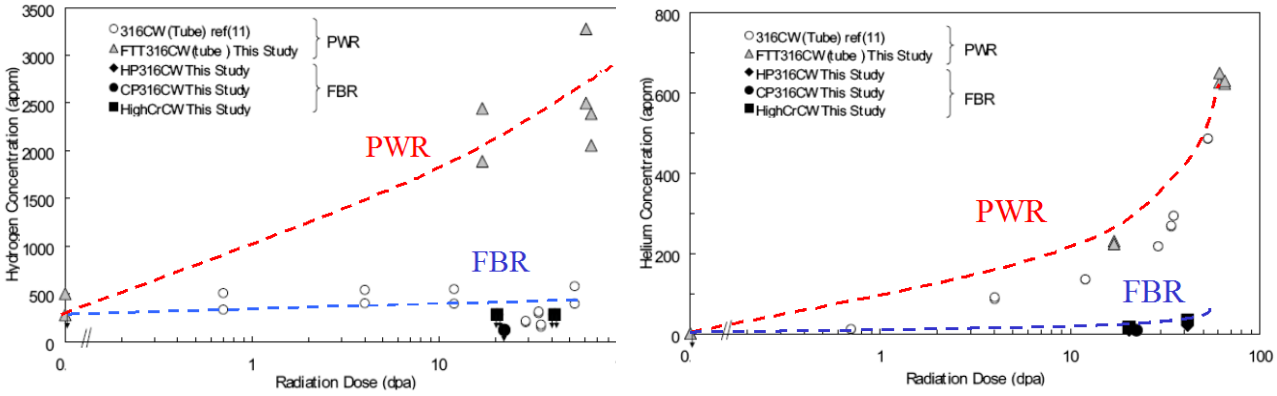

Figure 19. Air tensile curves and slow strain rate curves in the PWR environment for SAMARA experiment samples with various H and He levels a) CW 316 b) SA 304. No effect of helium and hydrogen on IASCC sensitivity has appeared for these specimens around 5 dpa [54]

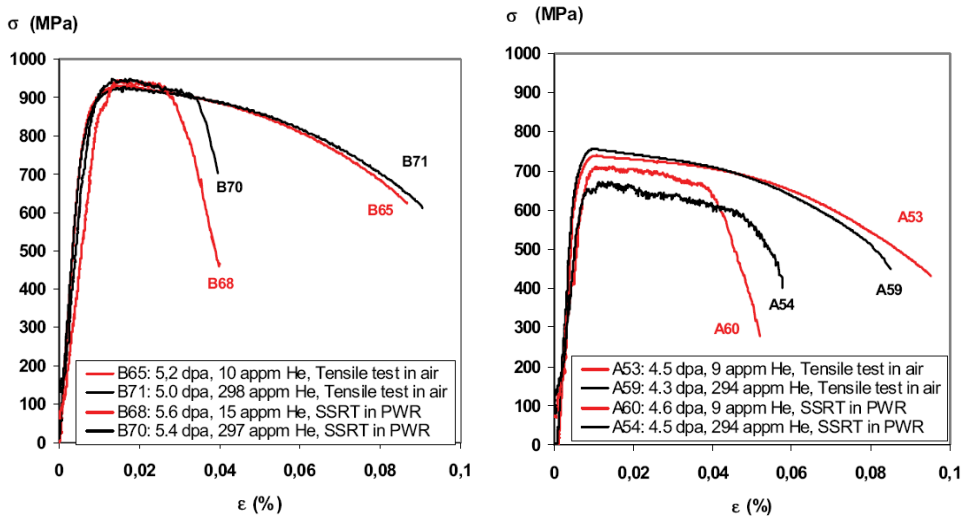

Figure 20. Comparison between the IASCC sensitivity of the materials irradiated in PWR and in the fast breeder reactor (FBR) [26]

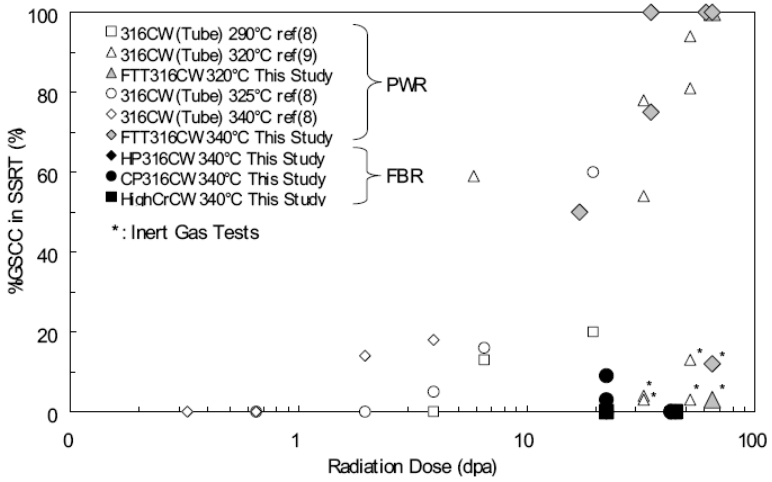

The experimental points of "This Study" correspond to reference [26], those of [8] in [72], and those of [9] in [28].

IASCC sensitivity parameters

In this chapter, the different variable parameters that can undergo a measurement or calculations (composition of materials, temperature, stress, primary chemistry, irradiation fluence) are reviewed with a view to quantifying their influence on IASCC sensitivity.

Materials

The evolution in the materials under flux constitute the main element of IASCC sensitivity [26]. The strain localisation, segregation under flux, and hardening could constitute elements of the IASCC mechanism and all depend on the components of the materials and their thermomechanical conditions. The differences in sensitivity to cracking between the different inspected units and the significant dispersions of the irradiated material stress corrosion test results are often attributed to possible "material effects". The influencing parameters (elements of chemical composition, thermal treatment, etc.) are rarely identified. The objective of the following paragraphs is to review the knowledge on these various parameters.

Thermomechanical treatments: solution annealed and cold working, and 316/304 differences

In the absence of experimental proof without ambiguity, there is no consensus on the effect of cold working during manufacture on IASCC sensitivity.

Proton irradiation tests for low irradiations show that cold working hinders IASCC sensitivity with regard to irradiation [10]. This result remains contradictory with the relationship between the yield stress and IASCC sensitivity, which is sometimes advanced for the initial stages of irradiation, while the cold worked steels systematically have a yield stress higher than that of solution annealed steels. The effect of cold working on IASCC for low doses (3-5 dpa) could be due to the restoration of the cold working dislocation network. An initial high density of dislocations first limits the formation of interstitial

loops but does not prevent it. These dislocations go up and self-destruct under flux, and above around 10 dpa, the cold working dislocation network seems to be completely restored for the operating temperatures of the PWR internals (330°C) [62,63].

On average, the 316 cold worked, 304 solution annealed, and 347 solution annealed materials behave in rather similar ways [48]. This is the conclusion that also comes from the crack propagation rate measurements under the CIR programme, although it is often difficult to compare the tests (variation of stress intensity factors, dose, etc.). In Figure 21, there is a summary of the crack rate measurements as a function of the stress intensity factor for different doses and irradiation conditions: the results for 304 and 316 steels are not distributed in a differentiated manner.

Although, as has been seen, not much is known about the effect of cold working and solution annealing on IASCC, it must be noted that proton studies on 304 and 316 steels as well as tests in the BWR environment of neutron irradiated specimens [45], show greater IASCC sensitivity in the SA 304 compared to the CW 316.

The cracked bolts of the baffles of the CP0 type units are made of cold worked 316 steel, but some of the stress corrosion tests on irradiated materials were done on specimens made of solution annealed 304. The elements presented in this paragraph do not significantly call into question the representativity of these tests with regard to cases of cracking on site.

Figure 21. Comparison of cracking rates based on the stress intensity factor for solution annealed 304 and 307 steels and cold worked 316 [46]

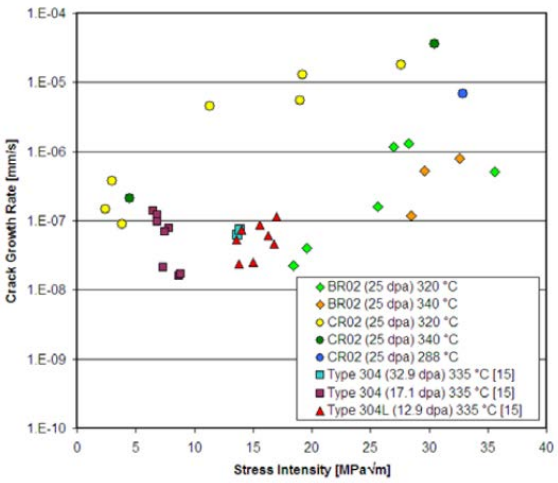

Effect of heat and alloy contents

Following the controls of the baffle/former bolts of the CP0 type units, analyses of the chemical compositions of these bolts were conducted. These analyses tend to show an effect linked to the heat of the bolts [53]. For the six CP0 units, it is possible to distinguish different trends (Table 3): the bolts of the units most affected by cracking (group A) come from heat prepared in the air (in a high-frequency furnace) showing lower levels of chromium and phosphorous than the others (group B). Nevertheless, the lack of statistical data does not allow for a complete conclusion on this point, all the more so

given that the recent Bugey 3 measurements (group B) show a less stable behaviour than Bugey 4 and 5, which are not part of the presented analysis.

Table 3. Chemical composition of the cracked bolt heats of the French CP0 units

Groups	Units	Mass levels in chemical elements of heats (%)								
		C	Cr	Ni	Si	Mn	S	P	Mo	Co
Group A	BUG2 and FES2	0.028	16.90	12.20	0.62	1.77	0.013	0.015	2.60	0.07
	FES1 and TIH1	0.026	16.80	12.10	0.64	1.81	0.016	0.017	2.56	0.05
Change from A to B		□	□	□		□		□	□	□
group B	BUG3	0.030	17.40	11.75	0.50	1.66	0.017	0.023	2.46	0.10
	BUG4	0.025	17.40	11.63	0.47	1.64	0.017	0.030	2.48	0.13
	BUG5	0.033	17.55	12.18	0.62	1.65	0.010	0.032	2.51	0.14

Attempts to identify this material effect have been undertaken as part of the CIR programme [9], for which high-purity model materials with controlled addition of solutes (Si, Ni, P, Mo, Ti, Nb, etc.) have been prepared and irradiated and will be tested for their resistance to intergranular cracking. The somewhat systematic studies for determining the influence of particular chemical elements on IASCC sensitivity, pertaining to, above all, the BWR conditions and therefore the influence of the elements, is considered mainly in terms of segregations at grain boundaries. The main conclusions are rather scattered.

- Ti: This is an element that is placed as a substitution in the crystalline lattice; it limits the amplitude of the segregation under flux and may decrease IASCC sensitivity [51].
- Nb: This is also a substitution element. In the conclusion of the work performed on swelling mandrels tested in reactor and in environment [35], it is recommended to have a ratio of niobium to carbon of around 20: 1 in order to limit stress corrosion in the BWR environment of pre-irradiated materials.
- Mo: A statistical link between IASCC sensitivity and the stability of austenitic to martensitic transformation is noted in the reference [1]. This link could result in better resistance to sensitivity of 316 steel compared to 304 steel.
- Cr: The influence of chromium outside of its depletion in the grain boundary is not known.
- Si: can have a beneficial effect [17] but work in the PERFECT project shows that Si can be considered an element with a negative effect. In this project, the alloys contain more than 2.5% Si and are therefore within a completely different composition range from that of the steels of the internals [49].
- C: In the range of steel concentrations for pressure vessel internals, the increase in interstitial carbon could have a beneficial effect in the BWR environment [14]. This point is illustrated in Figure 22: the rate of intergranular cracking in the BWR environment for slightly irradiated specimens decreases with the rate of interstitial carbon. There is not sufficient evidence to transpose this effect in a PWR environment.

In conclusion, there seems to be a material effect, but the direct link between the material characteristics of a heat and its IASCC sensitivity remains to be examined more in depth.

Effect of the grain size

Among the different processes by which the grain size could have an influence on IASCC sensitivity, two main mechanisms can be considered:

- The segregation of elements that decrease the IASCC resistance in the grain boundaries is all the more important since the grain is large.
- When the grain size decreases, the irradiation creep rate should increase, so the applied stress has more possibility of relaxing. In this case, the decrease of the grain size has a beneficial contribution for IASCC resistance. However, in the case of stress corrosion of cold worked stainless steels (not irradiated) in the PWR environment, it is known that a decrease of the grain size leads to the increase of intergranular cracking sensitivity. This was also observed in cases of austenitic stainless steels exposed to the BWR oxidising environment. This phenomenon probably results from the increase of plastic strain incompatibilities caused by the decrease of the grain size.

The polarization curves of sensitised 304 and 316 steels show that the passive current density is larger when the grain is small, which constitutes another assumption on the beneficial effect for stress corrosion of a large grain size.

To the knowledge of the report's author, the only available result in the literature on the effect of grain size on IASCC involves swelling mandrel experiments in the PWR environment. These complex tests, putting into play a large number of variable parameters, seem to show a beneficial link between low grain size and IASCC resistance.

Considering the various contradictory qualitative analyses, and in the absence of clear experimental results, it is therefore not possible to reach a consensus on the effect of grain size on IASCC.

Figure 22. Link between carbon and intergranular crack sensitivity (Slow strain rate tests) [14]

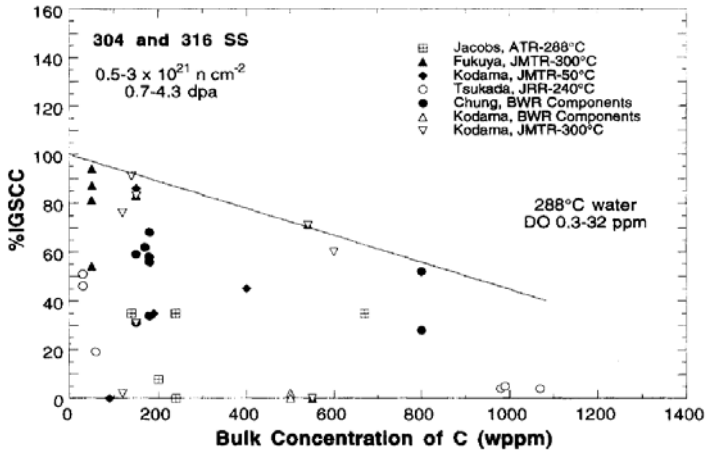

Environment

PWR and BWR primary environments

Cases of IASCC cracking are encountered both for BWRs and PWRs. It has previously been seen that the influence of chromium depletion was often the main cause of IASCC in the case of BWR reactors. Nevertheless, the evaluation of the fracture surface shows no difference due to either of the environments. Studies show that there is indeed a link between the dissolved oxygen (characteristic of the BWR environment in normal chemistry) and IASCC sensitivity [15], but decreasing the rate of dissolved oxygen is not enough to completely eliminate IASCC sensitivity [52]. One of the conclusions of the CIR programme [60] is that in the laboratory, propagation by SCC in the PWR environment and the BWR environment of pre-irradiated materials is phenomenologically continuous without fundamental change of the mechanisms between the two environments but with a change in the response kinetics to the changes of chemistry of the environment and the potential.

Primary environment

Beginning with the first cases of cracking on site, there has been a question as to whether a purely mechanical phenomenon was involved or stress corrosion.

For a long time, the possibility of purely mechanical intergranular cracking in the neutral environment for irradiated materials was debated, and some teams have been unable to have cracking other than ductile in the neutral environment for irradiated materials [15,48]. Several recent studies still make it possible to define the possibility of obtaining, under low slow strain rate (less than 10^{-7} s^{-1}), an intergranular cracking in the neutral environment and at the temperature of 330°C on highly irradiated materials [26,28,29,57]. A constant load specimen in the neutral environment on a Chooz A corner sample (30 dpa) developed an intergranular crack without completely break in 1000 hours, while the same test in a PWR environment cracks in five hours [76,77]. It appears that the environment accelerates the cracking.

Operating conditions

Irradiation conditions

Observation of the UT inspection results of the baffle/former bolts shows the existence of a cracking threshold dose that is slightly greater than 4 dpa. This dose is identical regardless of the former and it does not seem to be influenced by how long it stays in the reactor. This value is slightly higher than the value determined by laboratory tests around 2 - 3 dpa [72]. This threshold value can be approached with some developments of the microstructure, such as significant hardening and a change in the deformation modes. In the BWR environment, this threshold value is lower, on the order of 1 to 2 dpa [8,58,69].

After this threshold, IASCC sensitivity increases with the dose [72]. This increase continues beyond 10 dpa, which marks the saturation of the development of the mechanical properties with the dose. Tests on Thimble tubes show this increase in IASCC sensitivity at least until 65 dpa [26,28].

Temperature

By analogy with other stress corrosion mechanisms, attempts have been made to express the influence of temperature on IASCC sensitivity through an apparent activation energy of the phenomenon.

Data from the literature [72] indicate a reduction of the critical dose of intergranular cracking sensitivity when the temperature increases from 290 to 340°C. (this critical dose is supposed to mark a threshold under which there is no intergranular cracking characteristic of IASCC: an estimate of this measurement is obtained through slow strain rate tests and by measuring the rate of intergranular fracture on the fracture surface; the critical value is reached when the intergranular fracture rate becomes significant, i.e. measurable). These tests help determine an apparent activation energy for the phenomenon of around 70 kJ/mol (between 40 and 140 kJ/mol). The determination of the apparent activation energy on the fracture time was also performed on samples from the Chooz A corner [66]. The estimation is based on two tests which were both carried out with a stress of 700 MPa but at temperatures of 290°C and 340°C, respectively. The difference in time to failure indicates an activation energy of approximately 86 kJ/mol. There is only one test datum, so the uncertainty on the activation energy is significant. The order of magnitude for these estimates is comparable to the value of the activation energy for the crack growth rate measured for K constant on specimens of cold worked 316 (non-irradiated), 90 kJ/mol [6]. This result is consistent with the field experience: the cracked bolts are preferentially the hottest and the most irradiated [53] (Figure 23). However the range of values obtained is lower than the one coming from the field experience analysis: the activation energy was more likely to be between 100-180 kJ/mol taking into account inspected PWR.

This point remains to be confirmed by complementary tests and the resumption of the field experience analysis based on the temperatures calculated with better accuracy on the entire baffle assembly. In addition, in cases of cracking on site, it is difficult to separate the temperature effect from the irradiation effect (the temperature being linked in large part to the gamma energy deposit) and also the purely mechanical effects, since some of the stress on the bolts is linked to the differential thermal expansions between baffles and formers.

Figure 23. Empirical relationship between the temperature of a bolt in a former and the rate of cracking of this bolt for the CP0 type [53]

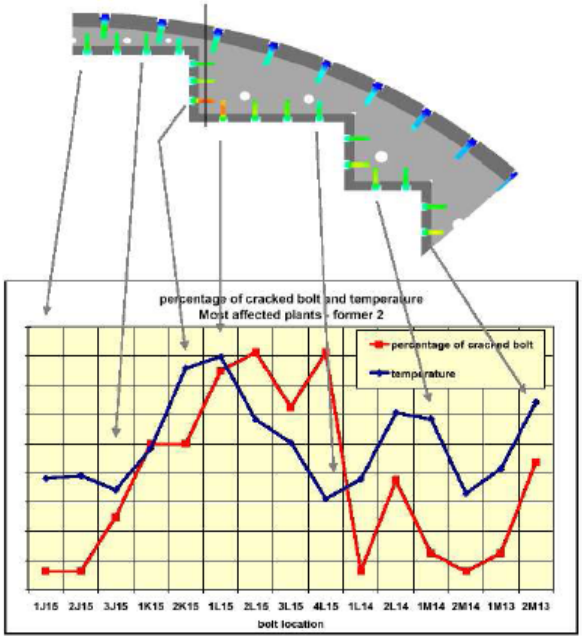

Stress

In the studies on the life-time of pressure vessel internals, particular effort has been put into determining the influence of stress on IASCC sensitivity. In fact, the quantification of this influence is necessary for any engineering analysis on the resistance of internals. The existence of a threshold stress below which cracking by IASCC is not encountered was still recently debated in the scientific community. The recent results of constant load tests make it possible to specify the existence of this limit.

The available PWR environment O-ring tests on Thimble tubes and constant load tests on sampled pieces of the Chooz A corner are represented in Figure 24. The constant load tests (Chooz A) and O ring tests (noted Beaver Valley, HB Robinson, and Ringhals in Figure 24) are mainly initiation tests. All of the tests were conducted between 290 and 340°C. The threshold stress is brought to the yield stress of the material at the test temperature and at the dose in question in order to be able to compare materials with different tensile properties.

There are three different sensitivity regions:

- Between 0 and 10 dpa, some available results seem to show low IASCC sensitivity below a lower applied stress at least at the yield stress.
- Between 10 and 25 dpa, the IASCC sensitivity region seems to extend for ratio of stress to yield stress decreasing with the dose.
- Beyond 25 dpa, the threshold stress seems to stabilise around a stress value of 40 to 50% of the yield stress of the material at the dose in question.

There is good consistency between the results of the Chooz A corner (solution annealed 304) and those on the Thimble tubes (cold worked 316).

The exploitation of the relationship between time to rupture and stress for a single irradiation dose shows that the greater the stress, the faster the cracking (Figure 25). The cracking times are very short, and cases of cracking beyond one thousand hours are rare. However, inspections of the bolts show cracking after several years of operation. Also, efforts are currently being put into better interpretation of the representativity of laboratory tests with regard to the position of bolts.

Figure 24. Summary of the O Ring test results (316 CW Thimble tubes H.B. Robinson, Beaver Valley, Ringhals [24]) or constant load tests (304SA Chooz A corner [77]) conducted in the PWR environment at 330°C)

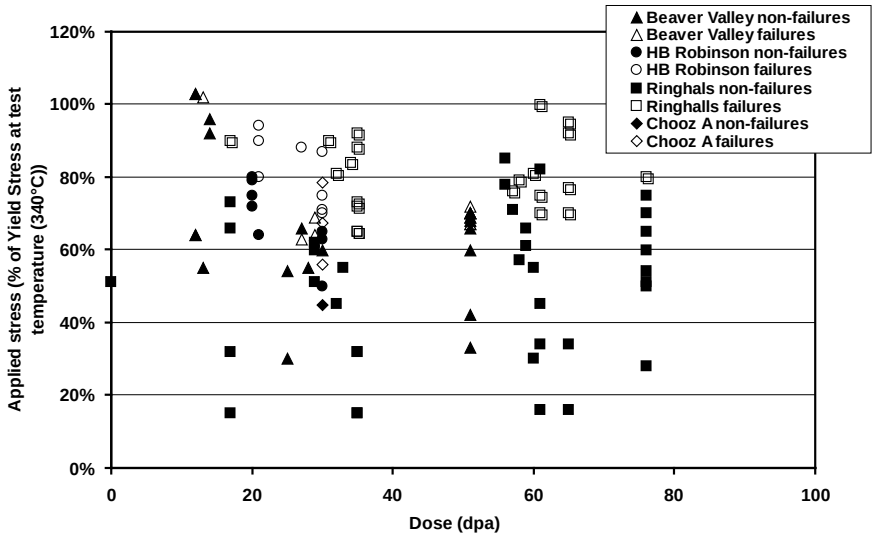

Figure 25. Constant load tests conducted at 340°C on Chooz A corner specimens (304L - 30 dpa) [66]

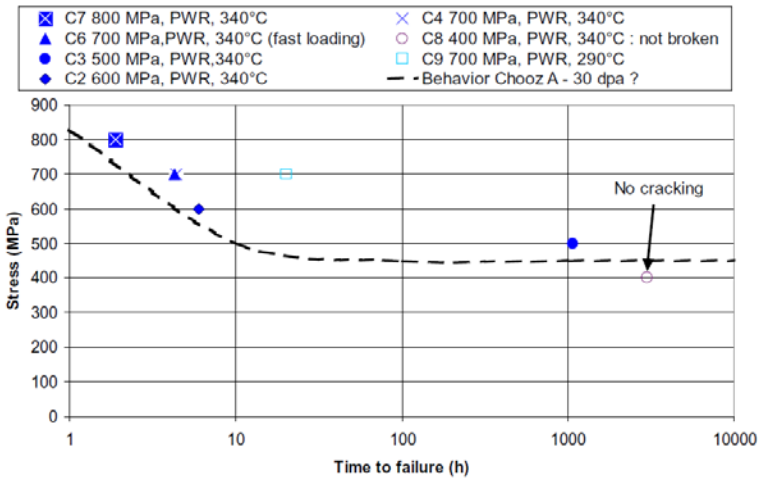

Criterion for IASCC sensitivity of austenitic steels in a PWR environment

Considering the various elements available on IASCC, no complete mechanism appears to explain and anticipate cracking by IASCC. Nevertheless, some IASCC sensitivity criteria have been proposed [60,65] that rely on the different thresholds shown experimentally and that is based on data combinations of neutron dose and stress leading to IASCC of austenitic stainless steels in PWR primary water.

Therefore, a single cracking criterion, which depends on the yield stress of the material, is proposed for solution annealed 304 and cold worked 316, independent of the possible variations of chemical composition of these steels within their specifications.

An IASCC sensitivity region is defined by EDF [65] based on the ratio of the stress applied to the yield stress at the temperature in question and the dose. The sensitivity region is defined in part in the stress/dose/temperature space as follows: a bolt with the operating conditions (σ_x, $dose_x$, T_x) with σ_x the applied stress - by simplification the Tresca stress (MPa) is be considered (that is used to characterise the O ring tests) - $dose_x$ the dose (dpa) and T_x the temperature (°C), this bolt belongs to the IASCC sensitivity region if:

- $dose_x$ < 4 dpa and $\frac{\sigma_x}{R_{P0.2}(T_x, dose_x)} > 1$ with $\mathbf{R}_{P0.2}$ the yield stress of the material at temperature T_x and at the dose "$dose_x$"
- or 4 ≤ $dose_x$ < 25 dpa and $\frac{\sigma_x}{R_{P0.2}(T_x, dose_x)} > -0.024 * dose_x + 1.095$
- or 25 ≤ $dose_x$ and $\frac{\sigma_x}{R_{P0.2}(T_x, dose_x)} > -0.0025 * dose_x + 0.545$.

A representation of the IASCC sensitivity area is given in Figure 26. Before 4 dpa, IASCC sensitivity is not expected. However, Stress Corrosion phenomena, independent of irradiation, remain possible above the elastic limit. This is why it was chosen to define a corrosion sensitivity region above the yield stress when the dose is less than 4 dpa. The decrease from 4 to 25 dpa corresponds to the increase in IASCC sensitivity. The parameters of the IASCC sensitivity region have been chosen in order to be consistent with experimental test results considered (Figure 28). The change in slope above 25 dpa, is due to the presence of a point corresponding to a test on a C ring specimen at 70 dpa presented in [73]. This is the only point that shows cracking at 40% of YS for a high dose. This point is somewhat atypical and must be confirmed by further tests.

Figure 26. Definition of the IASCC sensitivity area [65]

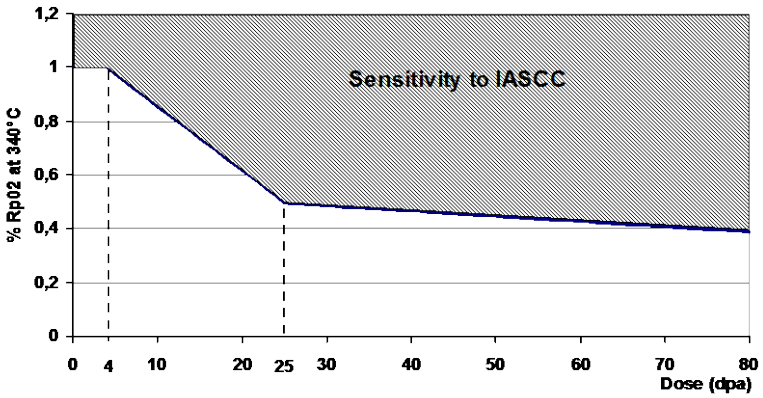

A similar criterion is used by the Electrical Power Research Institute (EPRI) [60] that is represented in Figure 27, based on mainly the same data points.

Figure 27. IASCC Flaw Initiation Stress vs. Dose – Constant Load Tests [60]

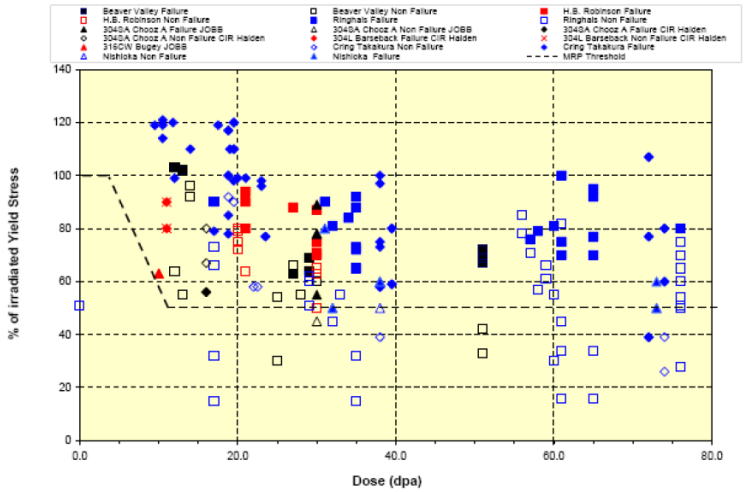

A comparison between both criterion is presented in Figure 28. The main differences are that for low irradiation doses, the EPRI criterion is more conservative than the EDF one. For high doses, the EDF criterion takes into account a change of the sensitivity to IASCC with the dose different to that of the EPRI criterion. This difference is due to two factors:

- the first is based on the hypothesis made by EDF that the increase of sensitivity to IASCC with the dose (measured through the percentage of intergranular fracture surface after slow strain rate test in environment) leads also to the diminution with the dose of the required stress for cracking due to IASCC. This origin is based on a hypothesis and has not been validated by experimental measurements.
- the second origin is the integration in the EDF criterion of an experimental point presented in [73], that was only available after establishing the EPRI criterion.

Figure 28. Comparison of the IASCC sensitivity area with the experimental points

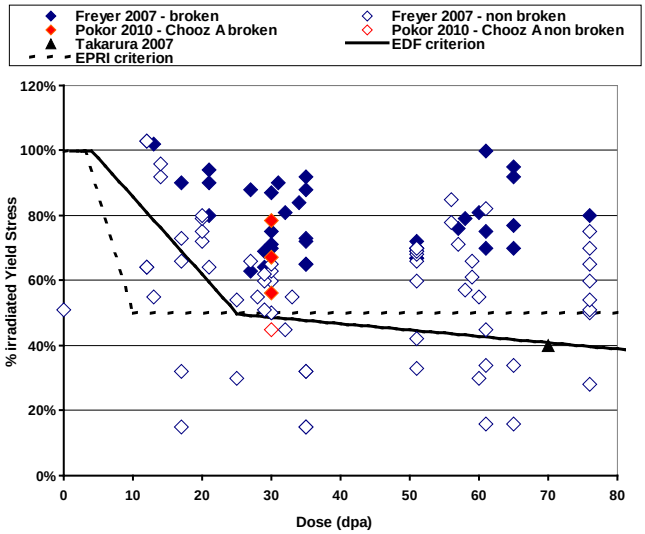

Additional testing and data are necessary to verify this apparent saturation of IASCC susceptibility for a PWR end-of-life dose up to approximately 125 dpa (including the license renewal period or up to 60 years). More data are needed to define IASCC susceptibility more precisely, especially at higher dose and longer times. Nevertheless, the results from this study can currently be used by the nuclear industry to assess the effects of irradiation on austenitic stainless steels in PWR systems as an indicator of the combination of stress and neutron dose at which IASCC could occur.

IASCC propagation behaviour in a BWR environment

As BWR plants age, certain locations in the mid-plane of the core shroud experience fluence levels at which the materials become susceptible to IASCC. The BWR Vessels and Internals Project (BWRVIP) has developed crack growth disposition methodologies for evaluating intergranular stress corrosion cracking (IGSCC) in the internal components of BWRs. The focus of these efforts has been the austenitic stainless steels used in the core region [12] and the Alloy 600/Alloy 182 materials used in the construction of the shroud support and the reactor pressure vessel attachment welds [59]. Figures 29 and 30 display the summary plots of the crack growth rates (CGRs) determined to be relevant for each of the two key environments – normal water chemistry (NWC) and hydrogen water chemistry (HWC). The fluence range of the specimens is $5x10^{24}n/m^2$ to $3x10^{25}n/m^2$. These figures also show the proposed CGR disposition curves for irradiated materials up to a fluence of $3x10^{25}n/m^2$. Figure 31 compares the field determined CGRs as a function of depth against the predicted CGRs based on an assumed stress state of 1.6ksi membrane stress and weld residual stresses relaxed 30% due to irradiation in conjunction with the K-dependent crack growth curve for NWC. The figure establishes that the crack growth predictions are bounded very well with the membrane stress and weld residual relaxation assumptions.

The Japan Nuclear Energy Safety organization (JNES) has been conducting a project related to IASCC as a part of safety research and development study for the aging management and maintenance of the nuclear power plants. The CGR tests has been

carrying out with neutron irradiated compact tension (CT) specimens under constant load and crack growth was measured using the reversing dc potential drop (DCPD). Irradiation was conducted in the core region of the Japan Materials Testing Reactor (JMTR) in simulated BWR water environments. The specimens were irradiated to fluences ranging from $5x10^{24}n/m^2$ (0.7dpa) to $1x10^{26}n/m^2$ (E>1MeV)(14dpa). CGR of Type 304L and Type 316L stainless steels (SSs) were formulated as a function of fluence and stress intensity factor. The CGR data showed that the CGR data tendency is influenced by the amount of the dose, stress intensity factor, water chemistry as shown in Figures 32 and 33. The CGRs in NWC increased with increasing fluence in the range of about 0.7-2dpa for Type 304L SS and 0.7-4dpa for Type 316L SS. Slight K dependence on the CGRs was observed in NWC. Clear reduction in the CGRs were measured with decreasing electrochemical corrosion potential (ECP) levels from ECP>+140mV_{SHE} to ECP<-200mV_{SHE} level.

Figure 29. Summary of screened crack growth data under NWC binned by fluence and proposed disposition curve for irradiated materials [60].

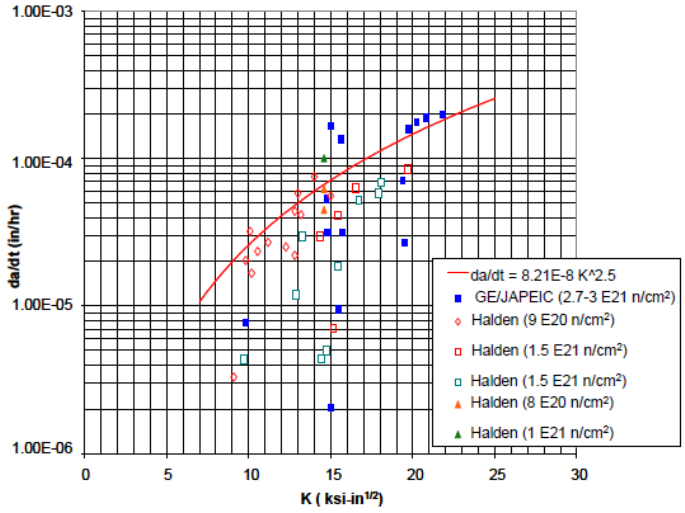

Figure 30. Summary of screened crack growth data under HWC binned by fluence and proposed disposition curve for irradiated materials [60]

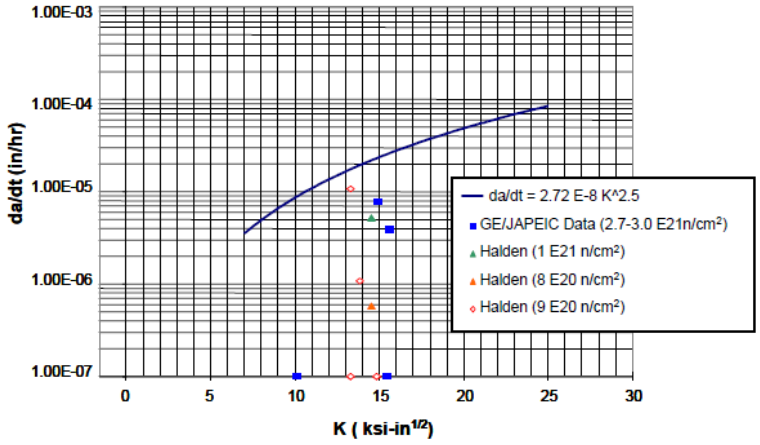

Figure 31. Comparison of calculated K-dependent rates as a function of average normalised depth with the field data plotted against average depth [60]

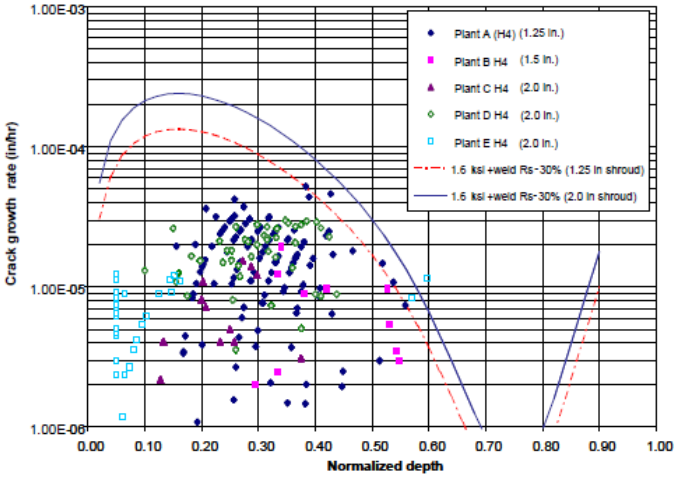

Figure 32. K dependence of CGR for Type 304L and Type 316L SSs [74]

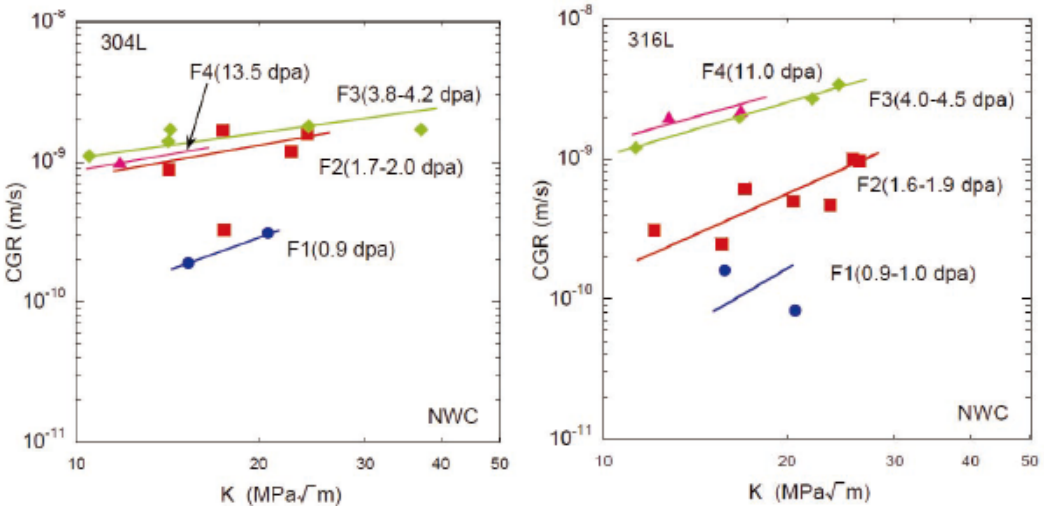

Figure 33. Fluence dependence and effect of ECP on CGR for Type 304L and Type 316L SSs [74]

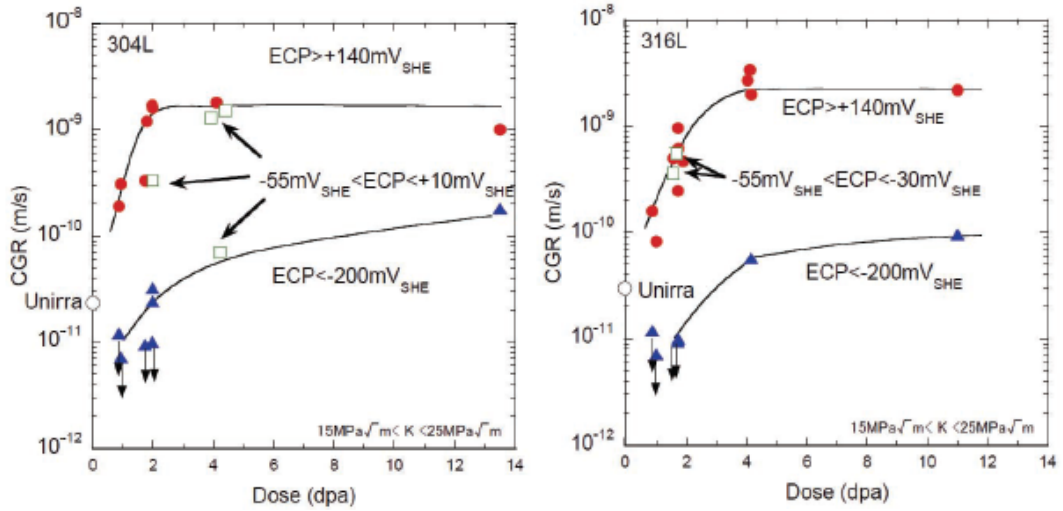

IASCC modelling and simulation

Andresen and Ford proposed a prediction model for SCC growth rates for austenitic alloys, including sensitised Type 304 SSs in simulated BWR environments by considering the slip/oxidation mechanism and crack tip strain rate [2,23]. For slip-dissolution/oxidation mechanism, the CGR equation has been proposed as shown in the next equation:

$$\frac{da}{dt} = \left[\frac{M \cdot i_0}{z \cdot \rho \cdot F \cdot (1-m)}\right]\left(\frac{t_0}{\varepsilon_f}\right)^m \{\dot{\varepsilon}\}^m$$

where a: crack length, M: atomic weight, i_0: reactive surface oxidation current density, z: change in charge due to oxidation, ρ: density of the material, F: Faraday's constant, m:

slope of the oxidation rate decay curve, t_0: time for the onset of current decay, ε_f: fracture strain of the protective film, ε: strain.

Shoji et al. reformulated a theoretical equation for stress corrosion crack growth rate of austenitic alloys in high temperature water based on crack tip asymptotic fields and crack tip transient oxidation kinetics [71]. The calculated results are compared with the experimental CGR data, which shows some consistency between the calculation and the reformulated theoretical CGR equations based on the asymptotic fields proposed by Gao and Hwang [33], Gao, Zhang and Hwang (GZH) [34] and that proposed by Hutchinson, Rice and Rosengren (HRR) [40,67]. For an example, if the transient oxidation follows a power law solid state oxidation mechanism, a theoretical CGR equation (Fracture Research Institute Theoretical Stress Corrosion Cracking, or FRI, model) based on HRR crack tip field can be derived as the follows:

$$\frac{da}{dt} = \left[(k_1)^{(1-m)} \cdot (\varepsilon_d)^{(-m)}\right] \times \left\{ \beta \left(\frac{\sigma_y}{E}\right) \left(\frac{n_{GH}}{n_{GH}-1}\right) \left\{ \ln\left[\left(\frac{\lambda}{r_0}\right)\left(\frac{K}{\sigma_y}\right)^2\right] \right\}^{\frac{1}{n_{GH}-1}} \left[\left(\frac{2}{K}\right)\dot{K} + \frac{\dot{a}}{r_0}\right] \right\}^m$$

where k_1: oxidation rate constant, ε_d: threshold strain for degradation of the protective film, β, λ: dimensionless constants in plastic strain calculation, σ_y: yield stress, E: elastic modulus, n_{GH}: strain-hardening exponent defined by Gao and Hwang, r_0: characteristic distance for formulating crack growth, K: stress intensity factor, $\dot{K}$: change in K with time, $\dot{a}$: CGR. The general schematic of the oxidation/mechanics interactions for SCC in high temperature water is shown in Figure 34. Depending on combinations of material/environment/loading conditions for SCC systems, the transient oxidation can take different kinetic laws, and the enhancement of crack tip oxidation can be realised via either a physical degradation mode, physical-chemical degradation mode or both. Experimental [2] and calculated CGRs with the FRI theoretical CGR equations based on the solid state oxidation mechanism and the HRR crack tip asymptotic field, for sensitised Type 304 SS in oxygenated pure water at 288°C are shown in Figure 35. The calculated CGRs are in generally agreement with the experimental data. More fundamental data for oxidation kinetic laws and crack tip mechanics are necessary to improve the accuracy of the input parameters in the CGR equations. Furthermore, Shoji et al. developed a 3D-finite element method (FEM) code for evaluation of environmentally assisted cracking (EAC) crack growth based on the crack tip deformation/oxidation mechanism in conjunction with a nodal force releasing technique that simulates the metal dissolution/oxidation mechanism [70]. Hashimoto, et al. modified mathematically the FRI model to eliminate the numerical divergence that occurs when the exponent of the oxidation current decay curve approaches 1 [38]. The procedure was applied to the IGSCC growth data obtained in a cold-worked Type 316L stainless steel and also the IASCC growth data obtained in a irradiated Type 316L stainless steel [39]. Crack growth calculations for a CT specimen under constant-load condition exhibited good agreement with the measured responses. Eason et al. presented a hybrid model of PWR primary water stress corrosion cracking (PWSCC) in unirradiated Ni alloys [21]. The overall form of the hybrid model is shown in the following equation, with the exponent m=1 and a model parameter A that is a function of material, test conditions (laboratory and test series) and environment (T, dissolved hydrogen):

$$\dot{a} = A\dot{\varepsilon_{ct}}^{m} = C_i(heat, lab, test\ series)exp\left[-\frac{Q}{R}\left(\frac{1}{T}-\frac{1}{T_{ref}}\right)\right]f(T,H_2)\dot{\varepsilon_{ct}}$$

Figure 34. A schematic of the SCC sub-processes of austenitic alloys in high temperature water [71]

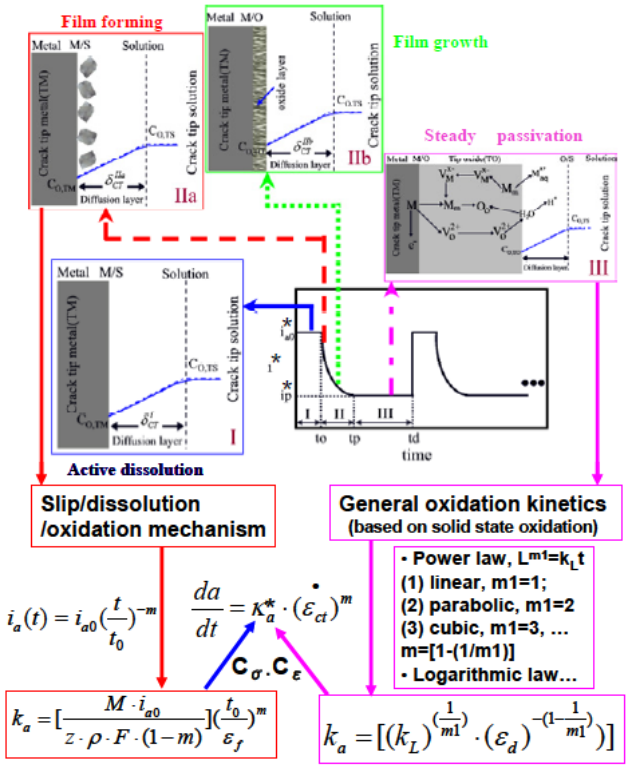

Figure 35. Experimental and calculated crack growth rates with FRI theoretical equations based on the solid state oxidation mechanism and the HRR crack tip asymptotic field for sensitised Type 304SS in oxygenated pure water at 288°C [71]

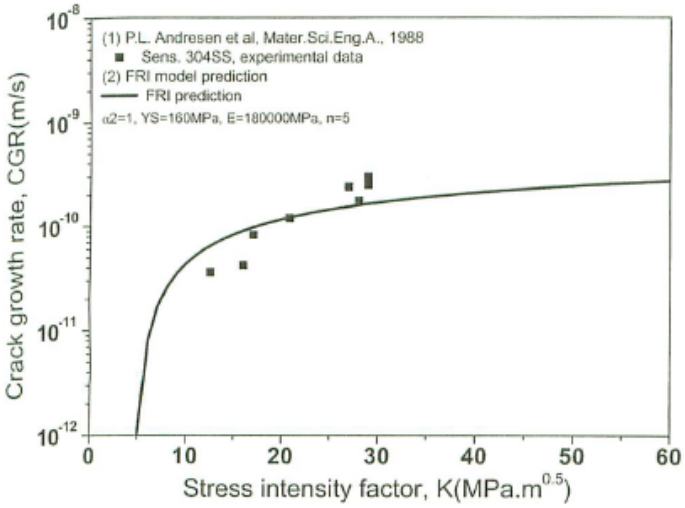

The coefficient on the hybrid model, Ci is different for each model calibration data set with a different heat, different laboratory, or substantially different test conditions. Variables that were considered for explicit modelling, such as T, K, and H2 concentration, were not assigned separate overall coefficients Ci.

The model shows significantly reduced scatter and reasonable agreement with Alloy 600 and Ni alloy weld metals data sets. The hybrid model has been extended to irradiated stainless steels in PWR primary environments [22]. The IASCC model is an empirical/theoretical hybrid strain rate model and the major differences from the PWSCC model include using the Rice-Drugan-Sham (RDS) theoretical expression for strain rate near a growing crack in elastic-perfectly plastic materials and including an empirical dose function.

Jivikov et al. developed a meso-scale mechanical model for intergranular stress corrosion cracking to investigate crack bridging and its effects on crack propagation in microstructures with different fractions of special boundaries [47]. The calculated results showed that both grain refinement and increase in the fraction of special boundaries are important for improving microstructure resistance. Itakura, et al. investigated the process of slow intergranular crack propagation by a three dimensional finite element method model and showed that branching is induced by partial arresting of a crack front owing to the geometrical randomness of grain boundaries as shown in Figure 36 [41].

Figure 36. Geometry of a simulation cell and fractured surface observed in the simulation projected onto the X-Z plane [41]

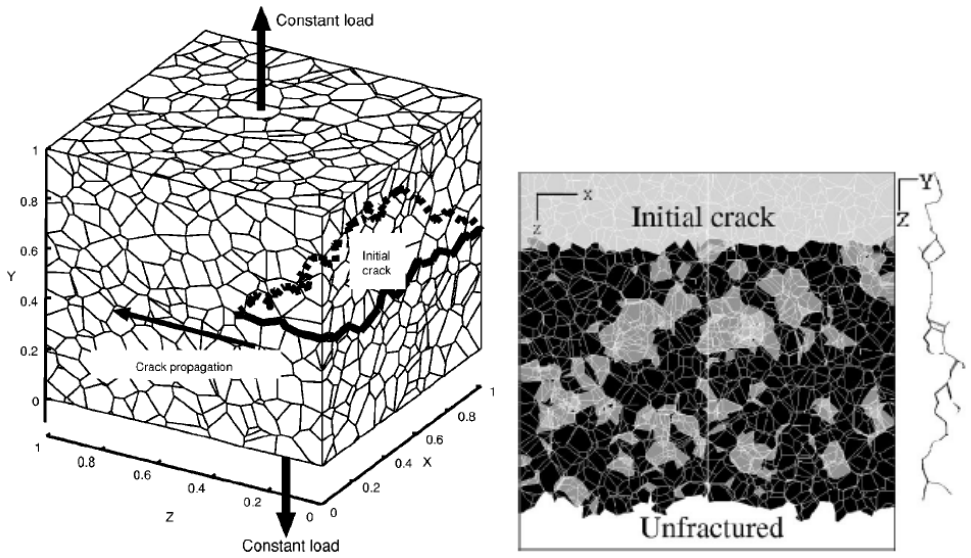

Aoyagi et al. proposed a crystal plasticity model expressing IGSCC by considering information about the oxidation along the grain boundaries and the failure of an oxide film caused by the localization of a deformation [5]. Introducing the oxygen reaction-diffusion model, the local criterion of crack propagation, and the oxide film failure model into a crystal plasticity model makes it possible to numerically reproduce the generation and propagation of cracks assuming the occurrence of IGSCC as shown in Figure 37. Although the crack propagation stops at one point, the crack propagates again as a result

of the oxidation corrosion of the grain boundary. They also conducted crystal plasticity simulations for a copper single crystal under simple tensile condition and investigated the effect of radiation defects and dislocation behaviour on the processes of strain localisation. In this study, considering information of radiation defects and disappearance of radiation defects due to dislocation movement, the macroscopic stress-strain responses of irradiated material such as increase of yield stress and decrease of work-hardening ratio can be numerically reproduced [4].

Figure 37. Distribution of (a) equivalent stress and (b) equivalent plastic strain (t = 49.84 Ms) [5]

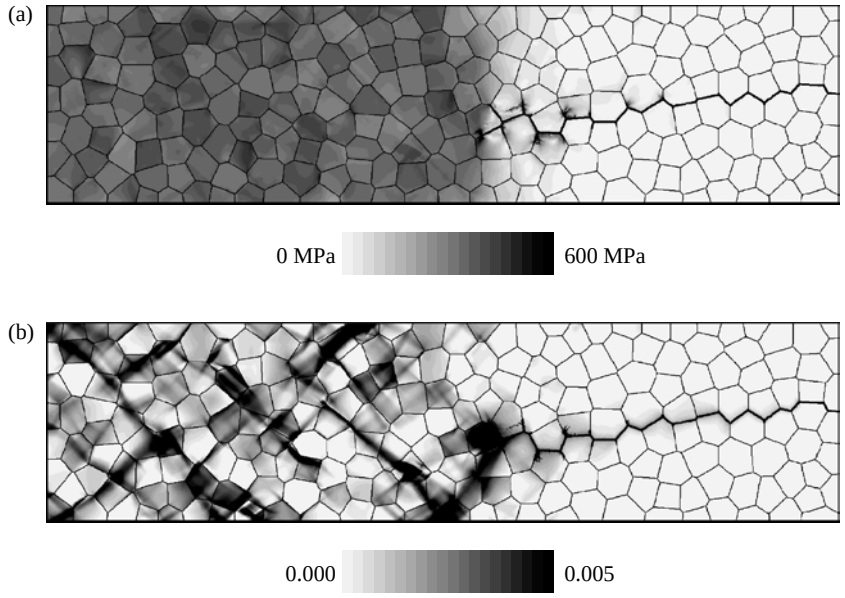

Conclusion

Internal components of PWR vessels closest to the core (core barrel, baffle plates, formers, bolts, etc.) are exposed to a high neutron flux; the most highly irradiated zones of some of these components may be exposed to doses reaching about 120 dpa after 60 years of operation. This neutron irradiation changes their microstructure and their mechanical properties: hardening, loss of ductility, loss of toughness, irradiation creep, etc. Furthermore, these variations appear to cause sensitivity to stress corrosion (irradiation assisted stress corrosion cracking- IASCC).

IASCC is now the main mechanism capable of causing cracking with intergranular surfaces that has been reproducibly established in laboratory tests.

Even if no complete mechanism has been found to explain and anticipate IASCC cracking, considering the various available elements, some criteria for sensitivity to IASCC have been proposed based on the different thresholds put forward experimentally and that have been partly confirmed by operating experience (appearance of materials, operating conditions, environment). These criteria must be interpreted as indicators capable of identifying trends on the risk of cracking of bolts and not as an absolute threshold to predict cracking.

In aged BWR plants, certain locations in the mid-plane of the core shroud experience fluence levels at which the materials become susceptible to IASCC. BWRVIP (Boiling Water Reactor Vessel Internals Program) has developed crack growth disposition methodologies for evaluating intergranular stress corrosion cracking (IGSCC) in the internal components of BWRs and JNES has been conducting a project related to IASCC CGR data as a part of safety research and development study for the aging management and maintenance of the nuclear power plants.

Although many investigators proposed prediction models for SCC and IASCC growth rates for austenitic stainless steels and Ni alloys, even more improvements of models are necessary as compared with the detailed experimental results, because these models are still preliminary models.

References

[1] J. Anders, L.G. Ljungberg, K. Pettersson, J. Walmsley, "Effects of austenite stability on sensitization to irradiation assisted stress corrosion cracking" 8th Int. Conf. Env. Degr. of materials in nuclear power systems-water reactors, American Nuclear Society, Amelia Island Plantation, 1997.

[2] P. L. Andresen, F. P. Ford, "Life Prediction by Mechanistic Modeling and System Monitoring of Environmental Cracking of Iron and Nickel Alloys in Aqueous Systems", Mater. Sci. Eng. A 103(1988) 167-184.

[3] P.L. Andresen, "Stress Corrosion Cracking – Material Performance an Evaluation", ed. R.H. Jones (ASM, 1992) p.181.

[4] Y. Aoyagi, T. Tsuru and Y. Kaji, "Crystal Plasticity Simulation Considering Crystal Defect Induced by Irradiation", Proc. 25th Symposium on Effects of Radiation on Nuclear Materials, ASTM, Anaheim, June 15-17, 2011.

[5] Y. Aoyagi and Y. Kaji, "Crystal Plasticity Simulation Considering Oxidation along Grain Boundary and Effect of Grain Size on Stress Corrosion Cracking", Materials Transactions, Vol.53, No. 1, 161-166, 2012.

[6] K. Arioka, Y. Kaneshima, T. Yamada, T. Terachi, "Influence of boric acid, hydrogen concentration and grain boundary carbide on IGSCC behaviours of SUS 316 under PWR primary water", 11th Int. Conf. Env. Degr. of materials in nuclear power systems-Water reactors, American Nuclear Society, La Grange, 2003.

[7] S.M. Bruemmer, "Grain-boundary segregation in austenitic stainless steels and effects on intergranular stress corrosion cracking in light-water reactor environments", Nace, Papier 138, Corrosion 1998.

[8] S.M. Bruemmer, E.P. Simonen, P.M. Scott, P.L. Andresen, G.S. Was, J.L. Nelson, "Radiation-induced material changes and susceptibility to intergranular failure of light water reactor core internals" Journal of Nuclear Materials 274 (1999) p.299-314.

[9] J.T. Busby, G. Was, "Irradiation-Assisted Stress Corrosion Cracking in Model Austenitic Alloys with Solute Additions", 11th Int. Conf. Env. Degr. of materials in nuclear power systems-Water reactors, American Nuclear Society, La Grange, 2003, pp. 995-1014.

[10] J.T. Busby, G. Was, "Effect of metallurgical condition on irradiated stress corrosion cracking of commercial stainless steels", 12th Int. Conf. Env. Degr. of materials in nuclear power systems-Water reactors, American Nuclear Society, Salt Lake City, 2005.

[11] T. S. Byun, N. Hashimoto, K. Farrell, "Deformation mode map of irradiated 316 stainless steel in true stress–dose space", Journal of Nuclear Materials, 351(1-3), 303-315, 2006.

[12] R. Carter, R. Pathnia, "Technical basis for BWRVIP crack growth correlations in BWRs", PVP2007-26618, Proc. PVP2007, 2007 ASME Pressure Vessels and Piping Division Conference, San Antonio, Texas, July 22-26, 2007.

[13] R. Cauvin, O. Goltrant, Y. Rouillon, E. Verzaux, A. Cazus, P. Dubuisson, P. Poitrenaud, S. Bellet, "Endommagement des structures internes inférieures soumises à fortes fluences: apports de l'expertise", Proc. International Symposium Fontevraud III, Société Française d'Energie Nucléaire, 1994, p.54.

[14] H.M. Chung., W.E. Ruther, J.E. Sanecki., A. Hins, N.J. Zaluzec, T.F. Kasner, "Irradiation-induced stress corrosion cracking of austenitic stainless steels : recent progress and new approaches" Journal of Nuclear Materials, Volume 239, 1 December 1996, Pages 61-79.

[15] H.M. Chung, R.V. Strain, W.J. Shack, "Tensile and stress corrosion cracking properties of type 304 stainless steel irradiated to a very high dose" Nuclear Engineering and design 208 (2001) p.221-234.

[16] J. Conermann, R. Shogan, K. Fujimoto, T. Yonezawa, Y. Yamaguchi, "Irradiation effects in highly irradiated cold worked stainless steel removed from a commercial PWR" 12th Int. Conf. Env. Degr. of materials in nuclear power systems-Water reactors, American Nuclear Society, Salt Lake City, 2005.

[17] J.M. Cookson, R.D. Carter, D.L. Damcott, M. Atzmon, G. Was, "Irradiation assisted stress corrosion cracking of controlled purity 304L stainless steels" Journal of Nuclear Materials, vol. 202, p.104-121, 1993.

[18] T. Couvant, P. Moulart, L. Legras, P. Bordes, J. Capelle, Y. Rouillon, T. Balon, "PWSCC of austenitic stainless steels of heaters of pressurizers", Proc. International Symposium Fontevraud VI, Société Française d'Energie Nucléaire, 2006.

[19] E.D. Eason, E.E. Nelson, "Radiation induced segregation, hardening and IASCC", 7th Int. Conf. Env. Degr. of materials in nuclear power systems-Water reactors, American Nuclear Society, Breckenridge, 1995.

[20] E.D Eason, "Development, evaluation and analysis of the initial CIR-IASCC database", EPRI Report TR-108749, Oct. 1998.

[21] E. D. Eason and R. Pathania, "A Preliminary Hybrid Model of Nickel Alloy SCC Propagation in PWR Primary Water Environments", 14th Int. Conf. Env. Degr. of materials in nuclear power systems-Water reactors, American Nuclear Society, Virginia Beach, 2009.

[22] E. D. Eason and R. Pathania, "A Preliminary Hybrid Model of Irradiation-Assisted Stress Corrosion Cracking of 300 Series Stainless Steels in PWR Primary

Environments", 15th Int. Conf. Env. Degr. of materials in nuclear power systems-Water reactors, TMS, Colorado Springs, 2011.

[23] F. P. Ford, "Quantitative Prediction of Environmentally Assisted Cracking", Corrosion 52 (1996) 375-395.

[24] P. D. Freyer, T. R. Mager, and M. A. Burke, in: T. R. Allen, P. J. King, L. Nelson, 13th Int. Conf. Env. Degr. of materials in nuclear power systems-Water reactors, Canadian Nuclear Society, Toronto, 2007, Paper No. P0034.

[25] Fujii, K., K. Fukuya, G. Furutani, T. Torimaru, A. Kohyama, and Y. Katoh, "Swelling in 316 Stainless Steel Irradiated to 53 dpa in a PWR", 10th Int. Conf. Env. Degr. of materials in nuclear power systems-Water reactors, American Nuclear Society, Lake Tahoe, 2001.

[26] K. Fujimoto, T. Yonezawa, E. Wachi, Y. Yamaguchi, M. Nakano, R. P. Shogan, J. P. Massoud, T. R. Mager, "Effect of the Accelerated Irradiation and Hydrogen/Helium Gas on IASCC Characteristics for Highly Irradiated Austenitic Stainless Steels", 12th Int. Conf. Env. Degr. of materials in nuclear power systems-Water reactors, American Nuclear Society, Salt Lake City, 2005.

[27] K. Fukuya, S. Shima, K. Nakata, A.J. Jacobs, G.P. Wozaldo, S. Suzuki, M. Kitamura, "Mechanical properties and IASCC susceptibility in irradiated stainless steels", 6th Int. Conf. Env. Degr. of materials in nuclear power systems-Water reactors, American Nuclear Society, San Diego, 1993.

[28] K. Fukuya, K. Fujii, M. Nakano, N. Nakajima, M. Kodama "Stress corrosion cracking on cold worked 316 stainless steels irradiated to hight fluence", 10th Int. Conf. Env. Degr. of materials in nuclear power systems-Water reactors, American Nuclear Society, Lake Tahoe, 2001.

[29] G. Furutani, N. Nakajima, T. Konishi, M. Kodama "Stress corrosion cracking on irradiated 316 stainless steel", Journal of Nuclear Materials, Volume 288, Issues 2-3, February 2001, Pages 179-186.

[30] F.A. Garner, E.P. Simonen, B.M. Oliver, L.R. Greenwood, M.L. Grossbeck, W.G. Wolfer, P.M. Scott "Retention of hydrogen in FCC metals irradiated at temperatures leading to high densities of bubbles or voids", Journal of Nuclear Materials, 356 (2006) 122-135.

[31] J. Garnier, Y. Bréchet, M. Delnondedieu, C. Pokor, P. Dubuisson, A. Renault, X. Averty, J.P. Massoud, "Irradiation creep of SA 304L and CW 316 stainless steels: Mechanical behaviour and microstructural aspects. Part I: Experimental results", Journal of Nuclear Materials 413 (2011) 63–69.

[32] J. Garnier, Y. Bréchet, M. Delnondedieu, A. Renault, C. Pokor, P. Dubuisson, J.-P. Massoud, "Irradiation creep of SA 304L and CW 316 stainless steels: Mechanical behaviour and microstructural aspects. Part II: Numerical simulation and test of SIPA model", Journal of Nuclear Materials 413 (2011) 70-75.

[33] Y. C. Gao, K. C. Hwang, "Elastic-plastic fields in steady crack growth in a strain hardening material", in:D. Francois (Ed.), Advances in Fracture Research, Vol.2, Fifth International Conference on Fracture, p.669-682, 1981.

[34] Y. C. Gao, X. T. Zhang, K. C. Hwang, "The asymptotic near-tip solution for mode-Ill crack in steady growth in power hardening media", Int. J. Frac. 21, p.301-317, 1983.

[35] F. Garzarolli, P. Dewes, R. Hahn, J.L. Nelson, "Deformability of high purity stainless steels and Ni-base alloys in the core of a PWR", 6th Int. Conf. Env. Degr. of materials in nuclear power systems-Water reactors, American Nuclear Society, San Diego, 1993.

[36] O. Goltrant, R. Cauvin, D. Deydier, A. Trenty, " Eléments internes inférieurs : apports de l'expertise d'une cornière de Chooz A", Proc. International Symposium Fontevraud III, Société Française d'Energie Nucléaire, 1994.

[37] L.R. Greenwood, F.A. Garner, "Hydrogen generation arising from the ^{59}Ni(n,p) reaction and the impact on fusion-fission correlations", Journal of Nuclear Materials 233-237 (1996) p. 1530-1534.

[38] T. Hashimoto and M. Koshiishi, "Modification of the FRI Crack Growth Model Formulation from a Mathematical Viewpoint", Journal of Nuclear Science and Technology, Vol.46, No.3, p.295-302, 2009.

[39] T. Hashimoto and M. Koshiishi, private communication, 2011.

[40] J. W. Hutchinson, "Singular behavior at the end of a tensile crack in a hardening material ", J. Mech.. Phys. Solid 16, p.13-31, 1968.

[41] M. Itakura, H. Kaburaki and C. Arakawa, "Branching mechanism of intergranular crack propagation in three dimensions", Physical Review E 71, 055102-1-055102-4, 2005.

[42] A.J. Jacobs, G.P. Wozaldo, Wilson S.M., "Stress corrosion testing of irradiated type 304 SS under constant load", Corrosion, vol. 49, n°2, 1993.

[43] A.J. Jacobs, G.P. Wozaldo, G.M. Gordon, "Use of constant deflection test to evaluate susceptibility to irradiation-assisted stress corrosion cracking", Corrosion, vol. 48, n° 8, 1993.

[44] A. Jensen, G. Ljungberg, "Irradiation assisted stress corrosion cracking of stainless steel alloys in BWR normal water chemistry and hydrogen water chemistry" 6th Int. Conf. Env. Degr. of materials in nuclear power systems-Water reactors, American Nuclear Society, San Diego, 1993.

[45] A. Jensen, L.G. Ljungberg, "Irradiation assisted stress corrosion cracking. Post irradiation CERT tests of stainless steels in a BWR test loop", 7th Int. Conf. Env. Degr. of materials in nuclear power systems-Water reactors, American Nuclear Society, Breckenridge, Colorado, 1995.

[46] A. Jenssen, J. Stjärnsäter, R. Pathania, "Crack growth rate testing of fast reactor irradiated type 304L and 316 SS in BWR and PWR environments", 14th Int. Conf. Env. Degr. of materials in nuclear power systems-Water reactors, American Nuclear Society, Lagrange Park, 2009.

[47] A. P. Jivkov, N. P. C. Stevens and T. J. Marrow, "Meso-scale mechanical model for intergranular stress corrosion cracking and implications for microstructure engineering", J. Pressure Vessel Technol., 130, 31402-31408, 2008.

[48] H. Kanasaki, I. Satoh, M. Koyama, T. Okubo, T.R. Mager, R.G. Lott, "Fatigue and stress corrosion cracking behaviors of irrradiated stainless steels in PWR primary water", 5th international Conference on Nuclear Engineering, ICONE5, May 26-30, 1997.

[49] R. Kilian, B. Devrient and Partners of WP 5, "Preliminary Experimental Data on Crack Initiation", PERFECT (F16O-CT-2003-508840), Deliverable (D-N°: C31 + C35a), June 2007.

[50] M. Kodama, S. Nishimura, J. Morisawa, S. Suzuki, S. Shima, M. Yamamoto, "Effects of fluence and dissolved oxygen on IASCC in austenitic stainless steels" 5th Int. Conf. Env. Degr. of materials in nuclear power systems-Water reactors, American Nuclear Society, San Diego, 1991.

[51] M. Kodama, K. Fukuya, H. Kayano, "Influence of impurities and alloying elements on IASCC in neutron irradiated austenitic stainless steels" 16th international conference "Effects of radiation on materials", 1993.

[52] M. Kodama, R. Katsura, J. Morizawa, S. Nishimura, S. Suzuki, K. Takamori, S. Shima, T. Kato, "IASCC susceptibility of irradiated austenitic stainless steel under very low dissolved oxygen" 7th Int. Conf. Env. Degr. of materials in nuclear power systems-Water reactors, American Nuclear Society, Breckenridge, 1995.

[53] E. Lemaire, J-P. Massoud, "Ageing management of Internal Structures in EDF PWRs", IAEA, Erlangen, 6 October 2004.

[54] J-P. Massoud, M. Žamboch, P. Brabec, V. K. Shamardin, V. I. Prokhorov, P. Dubuisson, "Influence of the neutron spectrum on the tensile properties of irradiated stainless steels, in air, and in PWR environment" 12th Int. Conf. Env. Degr. of materials in nuclear power systems-Water reactors, American Nuclear Society, Salt Lake City, 2005.

[55] I. Monnet, G.M. Decroix, P. Dubuisson, J. Reuchet, O. Morlent, "Investigation of the Chooz A nuclear power plant bolts" , Proc. International Symposium Fontevraud IV, Société Française d'Energie Nucléaire, 1998, p 371.

[56] H. Nishioka, K. Fukuya, K. Fujii, T. Torimaru, 13th Int. Conf. Env. Degr. of materials in nuclear power systems-Water reactors, Canadian Nuclear Society, Toronto, 2007, Paper No. P0040.

[57] T. Onchi, K. Dohi, N. Soneda, J. R. Cowan, R. J. Scowen, M. L. Castaño, "Fractographic and microstructural characterization of irradiated 304 stainless steel intergranularly fractured in inert gas", Journal of Nuclear Materials, 320(3), 194-208, 2003.

[58] R. Pathania, K. Gott, P. Scott, "An Overview of the Cooperative IASCC Research (CIR) Program", 13th Int. Conf. Env. Degr. of materials in nuclear power systems-Water reactors, American Nuclear Society, Canadian Nuclear Society, Toronto, 2007.

[59] R. Pathania, R. G. Carter, "Nickel alloy crack growth rate correlations in BWR environment and application to core support structure welds evaluation", PVP2008-61299, Proc. PVP2008, 2008 ASME Pressure Vessels and Piping Division Conference, Chicago, IL, July 27-31, 2008.

[60] R. Pathania, R. Carter, A. Demma, "Overview of EPRI research on effects of irradiation on LWR internals", O01-A102-T02, Proc. International Symposium Fontevraud VII, Société Française d'Energie Nucléaire, 2010.

[61] G. Pironet, A. Heuzé, O. Goltrant, R. Cauvin, "Expertise des vis de liaison cloison renfort de la centrale de Tihange 1", Proc. International Symposium Fontevraud IV, Société Française d'Energie Nucléaire, 1998, p.195.

[62] C. Pokor, Y. Bréchet, P. Dubuisson, J.-P. Massoud, A. Barbu, "Irradiation damage in 304 and 316 stainless steels: experimental investigation and modeling. Part I: evolution of the microstructure", Journal of Nuclear Materials. 2004, Vol 326/1, pp19-29.

[63] C. Pokor, Y. Bréchet, P. Dubuisson, J.-P. Massoud, X. Averty, "Irradiation damage in 304 and 316 stainless steels: experimental investigation and modeling. Part II: irradiation induced hardening" Journal of Nuclear Materials, Vol 326/1, pp30-37, 2004.

[64] C. Pokor, Y. Thébault, C. Pujol, E. Lemaire, N. Ligneau, "Metalurgical examination update of baffle bolts removed from operating French PWR", Proc. International Symposium Fontevraud VI, Société Française d'Energie Nucléaire, 2006.

[65] C. Pokor, G. Courtemanche, JL. Fléjou, M. Tommy-Martin, I. Rupp, B. Tanguy, J-P. Massoud, N. Monteil, "IASCC of Core Internals of PWRs: EDF R&D and Engineering program to assess internals lifetime management", Proc. International Symposium Fontevraud VII, Société Française d'Energie Nucléaire, 2010.

[66] C. Pokor, A. Toivonen, M. Wintergerst, U. Ehrnstén, W. Karlsen, J-P. Massoud, "Determination of the time to failure curve as a function of stress for a highly irradiated AISI 304 stainless steel after constant load tests in simulated PWR water environment", Proc. International Symposium Fontevraud VII, Société Française d'Energie Nucléaire, 2010.

[67] J. R. Rice, G. F. Rosengren, "Plane strain deformation near a crack tip in a power-law hardening material", J. Mech. Phys. Solids 16, p.1-12, 1968.

[68] I. Rupp, C. Peniguel, M. Tommy-Martin, "Large Scale Finite Element Thermal Analysis of Bolts of a French PWR Core Internal Baffle Structure", Nuclear Engineering and Technology – Vol 41 Number 9 – p 1171-1180 – Korean Nuclear Society Nov 2009.

[69] P. Scott, "A review of irradiation assisted stress corrosion cracking", Journal of Nuclear Materials, vol. 211, p. 101-122, 1994.

[70] T. Shoji, T. Yamamoto, K. Watanabe, Z. Lu, "3D-FEM simulation of EAC crack growth based on the deformation/oxidation mechanism", 11th Int. Conf. Env. Degr. of materials in nuclear power systems-Water reactors, Stevenson, WA, Aug. 10-14, 2003.

[71] T. Shoji, Z. Lu, H. Murakami, "Formulating stress corrosion cracking growth rates by combination of crack tip mechanics and crack tip oxidation kinetics", Corrosion Science 52, p. 769-779, 2010.

[72] I. Suzuki, M. Koyama, H. Kanasaki, H. Mimaki, M. Akiyama, T. Okubo, Y. Mishima, T.R. Mager, "Stress corrosion cracking of irradiated stainless steels in simulated PWR

primary water", Intern. Conf. on Nucl. Engineering, Vol. 5, pp. 206-213, ASME 1996.

[73] K. Takakura, K. Nakata, M. Ando, K. Fujimoto, E. Wachi, "Lifetime Evaluation for IASCC Initiation of Cold Worked 316 Stainless Steels BFB in PWR Primary Water", 13th Int. Conf. Env. Degr. of materials in nuclear power systems-Water reactors, American Nuclear Society International Conference on Environmental Degradation of Materials in Nuclear Power Systems, Canadian Nuclear Society, Toronto, 2007.

[74] K. Takakura, S. Tanaka, T. Nakamura, K. Chatani, Y. Kaji, "IASCC evaluation method for irradiated core internal structures in BWR power plants", PVP2010-25293, Proc. PVP2010, 2010 ASME Pressure Vessels and Piping Division Conference, Bellevue, Washington, July 18-22, 2008.

[75] L.E. Thomas, S. M. Bruemmer, "Analytical transmission electron microscopy characterization of stress corrosion cracks in an irradiated type 316 stainless steel core component", Proc. International Symposium Fontevraud V, Société Française d'Energie Nucléaire, 2002, p. 347-359.

[76] A. Toivonen, U. Ehrnsten, W. Karlsen, P. Aaltonen, J.-P. Massoud, J.-M. Boursier, "Fractographic observations on a highly irradiated AISI 304 steel after constant load tests in simulated PWR water and argon and after supplementary tensile and impact tests", 12th Int. Conf. Env. Degr. of materials in nuclear power systems-Water reactors, American Nuclear Society, Salt Lake City, 2005.

[77] A. Toivonen, P. Aaltonen, W. Karlsen, U. Ehrnstén, J-P. Massoud, J-M. Boursier, "Post irradiation SC investigations on highly irradiated core internals", Proc. International Symposium Fontevraud VI, Société Française d'Energie Nucléaire, 2006.

[78] G. Was, S.M. Bruemmer, "Effects of irradiation on intergranular stress corrosion cracking", Journal of Nuclear Material, vol. 216, 1994.

[79] G. Was, "Recent Developments in Understanding Irradiation Assisted Stress Corrosion Cracking" 11th Int. Conf. Env. Degr. of materials in nuclear power systems-Water reactors, American Nuclear Society, La Grange, 2003.

[80] S. Watanabe, N. Sakagushi, K. Kurome, M. Nakamura, H. Takahashi, "On the mechanism of radiation-induced segregation", Journal of Nuclear Materials Volume 240, Issue 3, p.251-253, Février 1997.

[81] T. Yonezawa, K. Fujimoto, H. Kanasaki, T. Iwamura, S. Nakada, K. Ajiki, K. Sakai, "SCC susceptibility of irradiated austenitic stainless steels for PWR" 8th Int. Conf. Env. Degr. of materials in nuclear power systems-Water reactors, American Nuclear Society, Amelia Island Plantation, 1997.

[82] M. E. Eberhart, K. H. Johnson, and R. M. Latanision, "A molecular orbital model of intergranular embrittlement", Acta Materialia Vol. 32. No.6, pp.955-959, (1984).